

Combustion and Sustainable Development
XXV Event of the Italian Section of The Combustion Institute



Sala del Tempio di Adriano
Rome, June 3-5, 2002

Combustion and Sustainable Development:
XXV Event of The Italian Section of The Combustion Institute

ISBN 88-88104-02-X

Front Cover:
“Lady Flame”
Artistic photo of propane flame
By Domenico Giordano, Rome 2002

Combustion and Sustainable Development

25th Event of the Italian Section of the Combustion Institute

Sala del Tempio di Adriano, Rome

June 3-5, 2002

organised by

Italian Section of the Combustion Institute

with:

ENEA

and with organizational support of :

IFRF - Italian Committee

CNR - Istituto di Ricerche sulla Combustione

with support of:

Università degli Studi di Napoli "Federico II"

ABB SpA

ENEL SpA

ENEA



A. D. MCCXXIV

ABB



THE COMBUSTION INSTITUTE

Prof. Chung K. Law, President
Prof. Brian S. Haynes, VP / President Elect
Prof. Sébastien Candel, VP Sectional Affairs
Prof. Catherine P. Koshland, Secretary
Prof. Toshisuke Hirano, Secretary Sectional Affairs
Dr. James Ekmann, Treasurer

EXECUTIVE OFFICE

5001 Baum Boulevard, Suite 435, Pittsburgh, Pennsylvania 15213
Telephone: (412) 687-1366
Mrs. Sue S. Terpack, *Executive Secretary*

Associazione Sezione Italiana del Combustion Institute

Prof. Piero Salatino, Presidente
Dr. Raffaele Ragucci, Segretario/Tesoriere
Prof. Umberto Arena, Consigliere
Prof. Tiziano Faravelli, Consigliere
Dr. Stefano Giammartini, Consigliere
Dr. Sauro Pasini, Consigliere
Prof. Leonardo Tognotti, Consigliere

Martine van Hapert, Segretaria Esecutiva

Associazione Sezione Italiana del Combustion Institute ONLUS c/o Dipartimento di Ingegneria Chimica - Università di Napoli "Federico II"

P.le V. Tecchio, 80 - 80125 Napoli - Italia

Tel. [39] [081] [768 2263/2258/2247] - Fax [39] [081] [5936936] - e-mail: martine@combustioninstitute.it

www.combustioninstitute.it

CONTENTS

Novel Fuels and Processes

Preliminary Kinetic Analysis of Biogas Combustion under Diluted Condition <i>G. Calchetti, V. Visentin, S. Giammartini</i> ENEA - C. R. Casaccia, Sec. ING-TECO, Roma - ITALY	I.1
Mathematical Modelling of Electric Field-Activated Combustion Reactions <i>M. Pisu*, A. Cincotti**, A. M. Locci**, R. Orru*, and G. Cao**</i> * CRS4, UTA, Cagliari, Italy ** Dipartimento di Ingegneria Chimica e Materiali, Università degli Studi di Cagliari, Italy	I.5
Mild Combustion in a Laboratory-Scale Apparatus <i>A. Effuggi, D. Gelosa, R. Rota</i> Dip. CMIC / CIIRCO, Politecnico di Milano, Italy	I.9
Extinction of N2 Diluted N-Heptane Non-Premixed Counterflow Flames <i>P. Berta*, I.K. Puri*, S. Granata**, T. Faravelli**, E. Ranzi**</i> * University of Illinois at Chicago, USA ** Dipartimento di Chimica, Materiali e Ingegneria Chimica, Politecnico di Milano, Italy	I.13
Flameless Combustion: from Furnaces to New Applications <i>A. Milani, J.G. Wunning</i> WS GmbH, Germany	I.17
Experimental Identification of Bifurcation Points in Methane Oxidation <i>M. de Joannon*, A. Tregrossi*, A. Cavaliere**</i> * Istituto di Ricerche sulla Combustione - CNR, Napoli, Italy ** Dipartimento di Ingegneria Chimica, Università di Napoli "Federico II", Napoli, Italy	I.21
Numerical Simulation of a H2/Air Turbulent Non-Premixed Flame <i>R. Malagnino*, E. Giacomazzi**, C. Bruno*, G. Calchetti**, M. Ruffoloni**</i> * Department of Mechanics and Aeronautics - Università "La Sapienza", Roma - Italy ** ENEA - C. R. Casaccia, Sec. ING-TECO, Roma - Italy	I.25
Study of the Stabilising Effect of Hydrogen in Lean Premixed Combustors <i>A. Di Benedetto</i> Istituto di Ricerche sulla Combustione - CNR, Napoli, Italy	I.29

Combustion in Practical Systems

Kinetic Modelling of Liquid Fuel Combustion <i>S. Granata, R. Del Rosso, T. Faravelli, E. Ranzi</i> Dipartimento di Chimica, Materiali e Ingegneria Chimica, Politecnico di Milano, Italy	II.1
Validation of a Discrete Ordinate Flux Method for Design and Performance Prediction of Cylindrical Combustors <i>M. Filla</i> Dipartimento di Processi Chimici dell'Ingegneria, Università di Padova - Italy	II.5
Cooling Control of Hot Exhaust Gases for Low NO2 Emissions <i>E. Baraldi, G. Fogliani</i> Worgas Bruciatori, Formigine (MO) - Italy	II.9

Characterization of Chemical Compounds Produced in a Steam Generator Tested in Reburning Conditions <i>E. Ricci*, G. Giammartini*, C. Benedetti*, F. Di Carlo*, A. L'Insalata**, A. Saponaro**, L. Fortunato**</i> * ENEA - C. R. Casaccia, Roma, Italy ** ANSALDO CALDAIE - Centro Combustione Ambiente, Gioia del Colle, Italy.....	II.13
LES of an Industrial Burner <i>E. Giacomazzi, G. Calchetti, M. Rufoloni</i> ENEA - C. R. Casaccia, Sec. ING-TECO, Roma, Italy	II.17
Numerical Simulation of Strong Swirling Confined Flame by CFD Calculation <i>A. Frassoldati*, S. Frigerio*, T. Faravelli*, E. Colombo**, F. Inzoli**</i> * Dipartimento di Chimica, Materiali e Ingegneria Chimica, Politecnico di Milano, Italy ** Dipartimento di Energetica, Politecnico di Milano, Italy	II.21
Comparison between PIV Measurements and CFD Simulation on a Model of GT Annular Burner <i>D. Giordano, S. Giammartini, M. Rufoloni, G. Calchetti, F. Manfredi, E. Giacomazzi</i> ENEA - Engineering Division CR Casaccia, Roma, Italy	II.25
Fluid Dynamic and Thermal Analysis of an Industrial Gas Burner <i>P. Gennaro*, G. Scribano**, L. Galfetti**, A. Coghe**, G. Solero**</i> * C.I.T.T. Impianti Srl , Bollate MI, Italy ** Dipartimento di Energetica, CIIRCO, Politecnico di Milano, Italy	II.29
A Swirl Natural Gas Flame as a Test-Case for Experimental Analysis and Numerical Simulation <i>A. Frassoldati, G. Solero, A. Coghe, T. Faravelli</i> CIIRCO - Centro Interdipartimentale di Ricerche sulla Combustione, Politecnico di Milano, Italy	II.33
Analysis and Prediction of Flash-Back in Premix Porous Burners for Domestic Appliances <i>M. Bizzi, G. Saracco, V. Specchia</i> Dipartimento di Scienza dei Materiali ed Ingegneria Chimica, Politecnico di Torino, Italy	II.37
DME Combustion in Domestic Cooking Appliances: Comparison with LPG <i>G. Migliavacca*, E. Parodi*, M. Marchionna**, L. Pellegrini***</i> * Stazione Sperimentale per i Combustibili, San Donato Milanese MI, Italy ** SNAM Progetti SpA, San Donato Milanese MI, Italy *** Agip Petroli SpA, San Donato Milanese MI., Italy.....	II.41
Prediction of Flammable Limits of Mixtures in Non Standard Conditions <i>M. Milli, M. De Lucca, R. Rota</i> Dip. CMIC / CIIRCO, Politecnico di Milano, Italy.....	II.45
Effects of Different Fuels in a Trapped Vortex Combustor <i>M. Losurdo*, C. Bruno*, G. Calchetti**, E. Giacomazzi**, M. Rufoloni**</i> * Department of Mechanics and Aeronautics - Universita "La Sapienza", Roma - Italy ** ENEA - C. R. Casaccia, Sec. ING-TECO, Roma - Italy.....	II.49
Turbulent Structures Characterization in a Bluff-Body Premixed Flame <i>E. Giacomazzi*, V. Battaglia**, C. Bruno***</i> * ENEA - C. R. Casaccia, Sec. ING-TECO, Roma - ITALY ** CRS4 - Cagliari - ITALY *** Department of Mechanics and Aeronautics - University "La Sapienza", Roma - Italy	II.53
Interaction of Combustion and Atomization Processes in Electrospays Burning <i>R. Ragucci*, A. Cavaliere**, O. Campagna**</i> * Istituto di Ricerche sulla Combustione - CNR, Napoli, Italy ** Dipartimento di Ingegneria Chimica, Università di Napoli "Federico II", Napoli, Italy	II.57
Mathematical Modelling of Flameless Combustion for Micro-CHP System Development <i>M. Malfa*, M. Venturino*, V. Tota**</i> * ABB Service Srl – Research Division - Sesto San Giovanni, Milano - Italy ** Dipartimento di Energetica – Politecnico di Milano, Milano - Italy.....	II.61

Internal Combustion Engines

Modeling of Spark Ignition Engines with Tumble Swirl

*U. Martin**, *R. Rota**, *S. Carra**, *A. Dominici***

* Dip. CMIC / CHIRCO, Politecnico di Milano, Italy

** Ferrari Spa..... III.1

CFD Modelling of a Lean-Lean-Premixed-Staged Combustion Chamber

*D. Valentini**, *A. Barresi**, *E. Carrea***

* Politecnico di Torino

** Alstom Power Technology Center, Baden-Daettwil, Switzerland..... III.5

NOx Formation in the Rich Quench Lean Combustion Mode: Chemical Kinetic Modelling

*L. Miccoli**, *A. Barresi**, *E. Carrea***

* Politecnico di Torino

** Alstom Power Technology Center, Baden-Daettwil, Switzerland..... III.9

Combustion Control by Multiple Injection in Common Rail D.I. Engines

*C. Beatrice**, *P. Belardini**, *C. Bertoli**, *M.na Migliaccio**, *C. Guido***

* Istituto Motori - CNR Napoli, Italy

** D.I.M.E. Università di Napoli "Federico II", Napoli, Italy..... III.13

Further Knowledge on the Effect of Fuel Formulation on Diesel Combustion

*C. Beatrice**, *C. Bertoli**, *N. Del Giacomo**, *M. Lazzaro**, *C. Guido***

* Istituto Motori - CNR Napoli, Italy

** D.I.M.E. Università di Napoli "Federico II", Napoli, Italy..... III.17

DEAL: A New Concept For Diesel Combustion

C. Beatrice, *C. Bertoli*, *N. del Giacomo*, *M.na Migliaccio*

Istituto Motori - CNR Napoli, Italy..... III.21

Coal, Biomass and Waste

Modeling of Molecular Weight Distribution of Tars from Coal Pyrolysis

*G. Migliavacca***, *E. Parodi***, *L. Bonfanti****, *T. Faravelli**, *E. Ranzi**

* Dipartimento di Chimica, Materiali e Ingegneria Chimica, Politecnico di Milano, Italy

** Stazione Sperimentale dei Combustibili. S. Donato Milanese, Italy

*** ENEL Produzione-Ricerca, Pisa, Italy..... IV.1

Kinetic Modelling of Emissions from Liquid Fuel FBC

*A. Frassoldati**, *T. Faravelli**, *E. Ranzi**, *M. Miccio***, *F. Miccio****

* Dipartimento di Chimica, Materiali e Ingegneria Chimica, Politecnico di Milano, Italy

** Dipartimento di Ingegneria Chimica ed Alimentare, Università di Salerno, Italy

*** Istituto di Ricerche sulla Combustione - CNR Napoli, Italy..... IV.5

Sound Assisted Fluidized Bed Combustion

A. Cammarota, *M. Urciuolo*, *R. Chirone*

Istituto di Ricerche sulla Combustione - CNR, Napoli, Italy..... IV.9

Loss of Gasification Reactivity Towards O₂ and CO₂ upon Heat Treatment of Carbons

*O. Senneca**, *P. Salatino***

* Istituto di Ricerche sulla Combustione - CNR, Napoli, Italy

** Dipartimento di Ingegneria Chimica, Università di Napoli "Federico II", Napoli, Italy..... IV.13

Puff Production During Incineration of Sewage Sludge Spiked with Chlorinated Hydrocarbons	
<i>G. Mininni*, G. Mascolo**</i>	
* Istituto di Ricerca sulle Acque, CNR, Roma, Italy	
** Istituto di Ricerca sulle Acque, CNR, Bari, Italy	IV.17
Metal Enrichment in Solid Residues Produced in Sludge Incineration by a Fluidized-Bed Furnace	
<i>D. Marani, C.M. Braguglia, G. Mininni</i>	
Istituto di Ricerca sulle Acque, CNR, Roma, Italy	IV.21
The Influence of the Hydration Time on Spent Sorbents Reactivation for Fluidized-Bed Desulphurization Processes	
<i>F. Montagnaro*, P. Salatino*, S. Russo**, F. Scala**, C. Zucchini**</i>	
* Dipartimento di Ingegneria Chimica, Università di Napoli "Federico II", Napoli, Italy	
** Istituto di Ricerche sulla Combustione - CNR, Napoli, Italy	IV.25
Selective Depolymerization of Polyethylene	
<i>D. Pedol, P. Canu</i>	
Dipartimento di Principi e Impianti di Ingegneria Chimica, Università di Padova, Italy.....	IV.29
Fuels and Combustible Wastes	
<i>G. Mininni*, R. Chirone**</i>	
* Istituto di Ricerca sulle Acque, CNR, Roma, Italy	
** Istituto di Ricerche sulla Combustione - CNR, Napoli, Italy	IV.33
Characterization of Biomass Residue after Devolatilization in Different Operative Conditions	
<i>E. Biagini, L. Tognotti</i>	
Dipartimento di Ingegneria Chimica, Università di Pisa, Italy	IV.37
Sub-Models for the Devolatilization of Biomass Fuels	
<i>E. Biagini, C. Grassi, L. Tognotti</i>	
Dipartimento di Ingegneria Chimica, Università di Pisa, Italy	IV.41
Deposit Prediction from Coal-Biomass Co-Combustion	
<i>A. Bianchi, M. Cioni, N. Pintus</i>	
ENEL Produzione S.p.A. - Ricerca, Pisa, Italy.....	IV.45
Combustion Behaviour of Fast Pyrolysed Coal, Biomasses and their Blends	
<i>P. Ciambelli, V. Palma, P. Russo, S. Vaccaro, V. Vaiano</i>	
Dipartimento di Ingegneria Chimica e Alimentare, Università di Salerno, Fisciano, Italy.....	IV.49
The Environmental Performance of Alternative Solid Waste Management Options: A Life-Cycle Assessment Approach to the Study	
<i>U. Arena, M.L. Mastellone, F. Perugini</i>	
Dipartimento di Scienze Ambientali, II Università di Napoli, Italy	IV.53
Chemical Characterization of Liquids Products from Wood Pyrolysis	
<i>C. Branca</i>	
Dipartimento di Ingegneria Chimica, Università degli Studi di Napoli "Federico II", Napoli, Italy.....	IV.57
Modelling the Combustion of Moist Wood	
<i>A. Galgano</i>	
Dipartimento di Ingegneria Chimica, Università degli Studi di Napoli "Federico II", Napoli, Italy.....	IV.61
Development of a Commercial FB Boiler for Combustion of Renewable Fuels at Small Scale	
<i>A. Cante*, A. De Riccardis**, C. Liccardi*, F. Miccio*, A. Silvestre*</i>	
* Istituto di Ricerche sulla Combustione - CNR, Napoli, Italy	
** Tekne srl, Galatina LE, Italy.....	IV.65
Char Combustion Kinetics of Biomasses: a Database for Industry	
<i>N. Rossi*, M. Falcitelli**, P. Ghetti*</i>	
* ENEL S.p.A. Produzione Ricerca, Pisa – Italy	
** Consorzio Pisa Ricerche, Pisa – Italy.....	IV.69

Catalytic Combustion and Combustion Synthesis of Materials

Detailed Surface Chemistry and CFD Simulation of CO Catalytic Combustion

*S. Segato**, *M. Perini**, *H. Kusar***, *P. Canu**

* Dipartimento di Principi e Impianti di Ingegneria Chimica, Università di Padova, Italy

** Royal Institute of Technology, Dept. of Chemical Engineering and Chemical Technology, Stockholm, Sweden.....V.1

Mechanisms and Kinetics of Catalytic Combustion of Diesel Soot

D. Fino, *P. Fino*, *G. Saracco*, *V. Specchia*

Dipartimento di Scienza dei Materiali ed Ingegneria Chimica, Politecnico di Torino, ItalyV.5

Catalytic Combustion of Light Alkanes in a Fluidized Bed Reactor under Fuel-Lean Conditions

*M. Iamarino**, *R. Chirone***, *R. Pirone***, *P. Salatino****, *G. Russo***

* Dipartimento di Ingegneria e Fisica dell'Ambiente, Università degli Studi della Basilicata, Potenza, Italy

** Istituto di Ricerche sulla Combustione - CNR, Napoli, Italy

*** Dipartimento di Ingegneria Chimica, Università degli Studi di Napoli "Federico II", Napoli, ItalyV.9

Combustion Synthesis of Perovskite Catalysts

S. Biamino, *A. Civera*, *M. Pavese*, *P. Fino*, *G. Saracco*, *C. Badini*

Dipartimento di Scienza dei Materiali ed Ingegneria Chimica, Politecnico di Torino, ItalyV.13

Combustion Diagnostics

Absolute Concentrations of Radical C₂ in Atmospheric Pressure Hydrocarbon Flames

*M. Marrocco**, *M. D'Apice**, *S. Giammartini**, *M. Magaldi***, *G. P. Romano***

* ENEA - Engineering Division CR Casaccia, Roma, Italy

** Department of Mechanics and Aeronautics - Università "La Sapienza", Roma - ITALY VI.1

Optical Emission Spectroscopy On a MILD Combustor

M. Marrocco, *V. Visentin*, *M. D'Apice*, *S. Giammartini*

ENEA - Engineering Division CR Casaccia, Roma, Italy VI.5

PIV Post Processing Methods Applied on High Turbulent GT Burners Flames

*D. Giordano**, *C. Willert***, *S. Giammartini**, *R. Gallodoro****

* ENEA - Engineering Division CR Casaccia, Roma, Italy

** DLR, Koln, Germany

*** Department of Mechanics and Aeronautics - Università "La Sapienza", Roma - ITALY VI.9

Multangular Light Scattering Measurements from Soot Fractal Aggregates in Laminar Diffusion Flames

S. De Iulius, *F. Cignoli*, and *G. Zizak*

Istituto per l'Energetica e le Interfasi - CNR Sez. Milano, Italy..... VI.15

Extra Situ-DLS Measurements on Nanoparticles Produced in Laminar Premixed Flames

*D. Cecere**, *P. Minutolo***, *A. D'Alessio**

* Dipartimento di Ingegneria Chimica, Università degli Studi di Napoli "Federico II", Napoli, Italy

** Istituto di Ricerche sulla Combustione - CNR, Napoli, Italy VI.19

Characterization of Combustion Produced Nanoparticles by Atomic Force Microscopy

C. Barone, *A. D'Alessio*, *A. D'Anna*

Dipartimento di Ingegneria Chimica, Università di Napoli "Federico II", Napoli, Italy..... VI.23

Matrix-Assisted Laser Desorption/Ionization Time-of-Flight (MALDI-TOF) Mass Spectrometry in the Analysis of

Fuel-Rich Combustion Products: a Preliminary Study

*B. Apicella**, *M. Millan***, *A.A. Herod***, *R. Kandiyoti***

* Istituto di Ricerche sulla Combustione - CNR, Napoli, Italy

** Department of Chemical Engineering, Imperial College, London, United Kingdom..... VI.27

Diagnostics of Gas Mixing in Bubbling Fluidized Bed <i>R. Solimene*</i> , <i>A. Telesca*</i> , <i>A. Marzocchella*</i> , <i>R. Ragucci**</i> , <i>P. Salatino*</i> * Dipartimento di Ingegneria Chimica – Università di Napoli "Federico II", Napoli, Italy ** Istituto di Ricerche sulla Combustione - CNR, Napoli, Italy	VI.31
Identification of Average "Hidden" Features of Multiphase Flows Through High Order Statistical Momenta of Quantitative Images <i>R. Ragucci*</i> , <i>A. Cavaliere**</i> , <i>A. Sgambati**</i> * Istituto di Ricerche sulla Combustione - CNR, Napoli, Italy ** Dipartimento di Ingegneria Chimica, Università di Napoli "Federico II", Napoli, Italy	VI.35
Ultraviolet Light Absorption in Flames, Engine Exhausts and Urban Atmosphere <i>A. Borghese*</i> , <i>G. Basile**</i> , <i>A. D'Alessio**</i> * Istituto Motori - CNR, Napoli, Italy ** Dipartimento di Ingegneria Chimica, Università di Napoli "Federico II", Napoli, Italy	VI.39

Pollutant Formation and Control

Dry Flue Gas Desulfurization: Adsorption Mechanism and Sorbent Reactivation <i>M. Derudi*</i> , <i>M. Suardi*</i> , <i>D. Gelosa*</i> , <i>R. Rota*</i> , <i>S. Malloggi**</i> , <i>E. Sani**</i> * Dip. CMIC / CHIRCO, Politecnico di Milano, Italy ** ENEL DP / Ricerca, Pisa, Italy.....	VII.1
Kinetic Scheme of Thermal Decomposition of Polyvinylchloride <i>A. Marongiu, F. Robecchi, T. Faravelli, G. Bozzano, M. Dente, E. Ranzi</i> Dipartimento di Chimica, Materiali e Ingegneria Chimica, Politecnico di Milano, Italy.....	VII.5
Wall-Flow Catalytic Traps for Diesel Particulate Abatement from Mobile Sources <i>E. Cauda, D. Fino, N. Russo, G. Saracco, V. Specchia</i> Dipartimento di Scienza dei Materiali ed Ingegneria Chimica, Politecnico di Torino, Italy	VII.9
Emissions from Light Oil Fluidized Combustion: Preliminary Application of an Optical Technique <i>C. Allouis*</i> , <i>F. Beretta*</i> , <i>F. Miccio*</i> , <i>M. Miccio**</i> , <i>G. Olivieri**</i> * Istituto di Ricerche sulla Combustione - CNR, Napoli, Italy ** Dipartimento di Ingegneria Chimica ed Alimentare, Università di Salerno, Italy	VII.13
Carbonisation Rates of Carbonaceous Particles in Premixed Laminar Flames of Ethylene-Air <i>A. Rolando*</i> , <i>G. Basile*</i> , <i>P. Minutolo**</i> , <i>A. D'Anna*</i> , <i>A. D'Alessio *</i> * Dipartimento di Ingegneria Chimica, Università degli Studi di Napoli "Federico II", Napoli, Italy ** Istituto di Ricerche sulla Combustione - CNR, Napoli, Italy	VII.17
Aspetti Ambientali della Combustione Stazionaria <i>F. Beretta*</i> , <i>A. Borghese**</i> , <i>G. Cascio***</i> , <i>A. D'Alessio****</i> , <i>A. Pini***</i> * Istituto di Ricerche sulla Combustione - CNR, Napoli, Italy ** Istituto Motori - CNR, Napoli, Italy *** Agenzia Nazionale per la Protezione dell'Ambiente **** Dipartimento di Ingegneria Chimica, Università degli Studi di Napoli "Federico II", Napoli, Italy	VII.21
Self-Propagating Reactions for Environmental Protection: State of the Art <i>D. Carta, R. Orru, G. Cao</i> Dipartimento di Ingegneria Chimica e Materiali, Università di Cagliari, Italy.....	VII.25
Modelling In-Duct Mercury Removal by Activated Carbon Injection in Coal-Fired Power Plants Flue Gas <i>F. Scala</i> Istituto di Ricerche sulla Combustione - CNR, Napoli, Italy.....	VII.29
Pilot-Scale Tests of Mercury Removal in Coal Flue Gas through Sorbent Injection <i>N. Pintus*</i> , <i>A. Bianchi*</i> , <i>V. Borghini**</i> * ENEL Produzione S.p.A. - Ricerca, Pisa, Italy ** Università degli Studi di Pisa, Italy.....	VII.33

Size-Dependent Coagulation of Small Carbonaceous Particles at High Temperature.	
<i>M. Mancini Tortora, A. D'Anna, A. D'Alessio</i>	
Dipartimento di Ingegneria Chimica, Università di Napoli "Federico II", Napoli, Italy.....	VII.39
Optical and Spectroscopic Characterization of a Coflow Ethylene/Air Flame	
<i>C. Allouis*, F. Beretta*, A. D'Alessio**, A. D'Anna**, P. Minutolo*</i>	
* Istituto di Ricerche sulla Combustione - CNR, Napoli, Italy	
** Dipartimento di Ingegneria Chimica, Università di Napoli "Federico II", Napoli, Italy	VII.43
Molecular Weight Evaluation of Combustion Related Materials	
<i>B. Apicella, R. Barbella, R. Ciajolo, A. Tregrossi</i>	
Istituto di Ricerche sulla Combustione - CNR, Napoli, Italy	VII.47
Co and Ag Exchanged Zeolites in Lean CH₄-SCR of NO_x	
<i>P. Ciambelli, D. Sannino, M.C. Gaudino, I. Buonomo</i>	
Dipartimento di Ingegneria Chimica e Alimentare, Università di Salerno, Fisciano, Italy.....	VII.51

AUTHOR'S INDEX

Allouis, C.	VII.13, VII.43	Del, Giacomo, , N.	III.17, III.21
Apicella, B.	VI.27, VII.47	Del, Rosso, R.	II.1
Arena, U.	IV.53	Dente, M.	VII.5
Badini, C.	V.13	Derudi, M.	VII.1
Baraldi, E.	II.9	Di, Benedetto, A.	I.29
Barbella, R.	VII.47	Di, Carlo, F.	II.13
Barone, C.	VI.23	Dominici, A.	III.1
Barresi, A.	III.5, III.9	Effuggi, A.	I.9
Basile, G.	VI.39, VII.17	Falcitelli, M.	IV.69
Battaglia, V.	II.53	Faravelli, T.	I.13, II.1, II.21, II.33, IV.1, IV.5, VII.5
Beatrice, C.	III.13, III.17, III.21	Filla, M.	II.5
Belardini, P.	III.13	Fino, D.	V.5, VII.9
Benedetti, C.	II.13	Fino, P.	V.5, V.13
Beretta, F.	VII.13, VII.21, VII.43	Fogliani, G.	II.9
Berta, P.	I.13	Fortunato, L.	II.13
Bertoli, C.	III.13, III.17, III.21	Frassoldati, A.	II.21, II.33, IV.5
Biagini, E.	IV.37, IV.41	Frigerio, S.	II.21
Biamino, S.	V.13	Galfetti, L.	II.29
Bianchi, A.	IV.45, VII.33	Galgano, A.	IV.61
Bizzi, M.	II.37	Gaudino, M.C.	VII.51
Bonfanti, L.	IV.1	Gelosa, D.	I.9, VII.1
Borghese, A.	VI.39, VII.21	Gennaro, P.	II.29
Borghini, V.	VII.33	Ghetti, P.	IV.69
Bozzano, G.	VII.5	Giacomazzi, E.	I.25, II.17, II.25, II.49, II.53
Braguglia, C.M.	IV.21	Giammartini, S.	I.1, II.13, II.25, VI.1, VI.5, VI.9
Branca, C.	IV.57, I.25, II.49, II.53	Giordano, D.	II.25, VI.9
Buonomo, I.	VII.51	Granata, S.	I.13, II.1
Calchetti, G.	I.1, I.25, II.17, II.25, II.49	Grassi, C.	IV.41
Cammarota, A.	IV.9	Guido, C.	III.13, III.17
Campagna, O.	II.57	Herod, A.A.	VI.27
Cante, A.	IV.65	Iamarino, M.	V.9
Canu, P.	IV.29, V.1	Inzoli, F.	II.21
Cao, G.	I.5, VII.25	Kandiyoti, R.	VI.27
Carra, S.	III.1	Kusar, H.	V.1
Carrea, E.	III.5, III.9	Lazzaro, M.	III.17
Carta, D.	VII.25	Liccardi, C.	IV.65
Cascio, G.	VII.21	L'Insalata, A.	II.13
Cauda, E.	VII.9	Locci, A.M.	I.5
Cavaliere, A.	I.21, II.57, VI.35	Losurdo, M.	II.49
Cecere, D.	VI.19	Magaldi, M.	VI.1
Chirone, R.	IV.9, IV.33, V.9	Malagnino, R.	I.25
Ciajolo, R.	VII.47	Malfa, M.	II.61
Ciambelli, P.	IV.49, VII.51	Malloggi, S.	VII.1
Cignoli, F.	VI.15	Mancini Tortora, M.	VII.39
Cincotti, A.	I.5	Manfredi, F.	II.25
Cioni, M.	IV.45	Marani, D.	IV.21
Civera, A.	V.13	Marchionna, M.	II.41
Coghe, A.	II.29, II.33	Marongiu, A.	VII.5
Colombo, E.	II.21	Marrocco, M.	VI.1, VI.5
D'Alessio, A.	VI.19, VI.23, VI.39, VII.17, VII.21, VII.39, VII.43	Martin, U.	III.1
D'Anna, A.	VI.23, VII.17, VII.39, VII.43	Marzocchella, A.	VI.31
D'Apice, M.	VI.1, VI.5	Mascolo, G.	IV.17
De, Iulius, S.	VI.15	Mastellone, M.L.	IV.53
de, Joannon, M.	I.21	Miccio, M.	IV., 5, VII.13
De, Lucca, M.	II.45	Miccio, F.	VII.13, IV.5, IV.65
De, Riccardis, A.	IV.65	Miccoli, L.	III.9
		Migliaccio, M.	III.13, III.21

Migliavacca, G.	II.41, IV.1	Russo, P.	IV.49
Milani, A.	I.17	Russo, G.	V.9
Millan, M.	VI.27	Russo, N.	VII.9
Milli, M.	II.45	Salatino, P.	IV.13, IV.25, V.9, VI.31
Mininni, G.	IV.17, IV.21, IV.33	Sani, E.	VII.1
Minutolo, P.	VI.19, VII.17, VII.43	Sannino, D.	VII.51
Montagnaro, F.	IV.25	Saponaro, A.	II.13
Olivjeri, G.	VII.13	Saracco, G.	II.37, V.5, V.13, VII.9
Orru, R.	I.5, VII.25	Scala, F.	IV.25, VII.29
Palma, V.	IV.49	Scribano, G.	II.29
Parodi, E.	II.41, IV.1	Segato, S.	V.1
Pavese, M.	V.13	Senneca, O.	IV.13
Pedol, D.	IV.29	Sgambati, A.	VI.35
Pellegrini, L.	II.41	Silvestre, A.	IV.65
Perini, M.	V.1	Solero, G.	II.29, II.33
Perugini, F.	IV.53	Solimene, R.	VI.31
Pini, A.	VII.21	Specchia, V.	II.37, V.5, VII.9
Pintus, N.	IV.45	Suardi, M.	VII.1
Pintus, N.	VII.33	Telesca, A.	VI.31
Pirone, R.	V.9	Tognotti, L.	IV.37, IV.41
Pisu, M.	I.5	Tota, V.	II.61
Puri, I.K.	I.13	Tregrossi, A.	I.21, VII.47
Ragucci, R.	II.57, VI.31, VI.35	Urciuolo, M.	IV.9
Ranzi, E.	I.13, II.1, IV.1, IV.5, VII.5	Vaccaro, S.	IV.49
Ricci, E.	II.13	Vaiano, V.	IV.49
Robecchi, F.	VII.5	Valentini, D.	III.5
Rolando, A.	VII.17	Venturino, M.	II.61
Romano, G.P.	VI.1	Visentini, V.	I.1, VI.5
Rossi, N.	IV.69	Wunning, J.G.	I.17
Rota, R.	I.9, II.45, III.1, VII.1	Zizak, G.	VI.15
Rufoloni, M.	I.25, II.17, II.25, II.49	Zucchini, C.	IV.25
Russo, S.	IV.25		

Preliminary kinetic Analysis of biogas Combustion under diluted Condition

G. Calchetti, V. Visentin, S. Giammartini

ENEA, Casaccia - Engineering Division, Rome - ITALY

ABSTRACT

The paper deals with the application of the mild combustion technique to CO/H₂ mixtures. The objective of the work is the estimation of the main process characteristics in view of the experimental activity on a 100 kW burner for biomass gasification gases which will work in the flameless modality.

Different kinetic mechanisms, namely GRI and Miller & Bowman (1989) have been considered. The CHEMIN package was used to perform the calculation of ignition delay times and pollutants (CO and NO_x) formation rates along with a sensitivity analysis. Some preliminary results are presented in view of a more extensive activity which will cover also the acquisition of experimental data.

INTRODUCTION

A great deal of discussion is currently going on about the technical and economical feasibility of the biomass derived gases (with LCV 5-7 MJ/Nm³) in CHP plants. A promising application is their utilisation in the supplementary firing stage of the gas-turbine cogenerative systems. The main advantages of such a technology are those of high efficiency and low pollutants emissions [8].

When trying to exploit these gases for power generation purposes some problems arise because of their characteristics, namely the reduced combustion temperature, low burning rates and narrow stability limits. In industrial application the typical approach is to raise the heating value by addition of high grade fuels or by burning them in two stage systems where a high calorific value gas is used for flame stabilisation in the LCVG-air mixture. Another solution is the recirculation of energy between products and reactants so that the diluted combustion seems to be the most suitable technique.

The effectiveness of mild combustion has been widely demonstrated for the industrial furnaces fed with natural gas, but the application to LCVG needs to be investigated both experimentally and numerically.

In fact flameless oxidation will be employed in a lower temperature field than that typical of the process industry so that special attention on NO_x has to be paid since the aforesaid low temperature regime could bring about the conversion of NO to NO₂. Another matter of concern is the production of N₂O, one of the most harmful among the greenhouse gases [4].

The following paragraphs describe a simple kinetic study that we've undertaken in order to investigate into the combustion chemistry of the biogas under diluted conditions. Indeed various detailed and validated mechanisms exist for methane and natural gas, the most used of which is the GRI one. But LCVG has a large content of inert and only 2-5% of CH₄. It seems reasonable that such a mixture could be described by means of slightly different sets of intermediate species and reactions also in light of the mild modality of fuel processing. However these literature available schemes are the compulsory starting point.

KINETIC CALCULATION

The fuel is a typical wood chips gasification gas whose lower calorific value and density are 3974 KJ/Nm³ and 1.145 Kg/Nm³ respectively. A classical gas-turbine discharge gas (15% vol O₂) is used as oxidant. In table 1 the composition of both the biogas and the vitiated air are reported. The oxidant stream is available at 770 K.

The traditional combustion of such a fuel-oxidant mixture has relevant ignition delay times, which range from 0.83 s to 0.1 ms for an initial temperature of 850 K and 1300 K respectively (these values are calculated with the Senkin routine). The material and energy balances have been performed with reference to the scheme in Fig. 1, which represents the conceptual model of a trapped-vortex burner. Part of the main oxidant stream coming from the turbine discharge is entrained into the vortex established inside the combustion cavity where the mixing with the recirculation products and with the fuel takes place. The entrained air is 16% of the whole oxidant so that a stoichiometric air-fuel mixture is realised, while the remaining oxidant stream does not participate to the combustion. The recirculation ratio of the combustion products (K_v) is 60% of the global flow which undergoes the reaction into the vortex. The simulation of the flameless process requires an iterative calculation for the solution of mass and energy balances to find out the stationary working conditions starting from a conventional flame. The combustion reaction has been simulated in adiabatic atmospheric conditions by means of the Senkin module [6] of the CHEMKIN software. Two kinetic mechanisms have been implemented: the GRI-3.0 model [3] and the Miller and Bowman [2]. The residence time for the Senkin routine was chosen equal to 50 ms.

The iterative procedure converges in both cases to the same temperatures upstream and downstream of the reaction block: the hot products recirculation rises the fresh reactants mixture temperature up to 1295 K; the O₂ molar fraction of the mixture is 4.5%. The temperature increase, due to combustion reactions, is about 400 K and an outlet value of 1728 K results, with 1.3 % for the O₂ molar fraction; the final temperature is 1030K downstream of the burner.

Mol Frac. (%)	H ₂	CO	CH ₄	CO ₂	N ₂	O ₂	H ₂ O	NO
<i>Biogas</i>	14	18	2	8	58	-	-	-
<i>Oxidant</i>	-	6E-04	-	3	76.5	15	5.5	47E-04

Tab. 1. Volumetric composition of the fuel and of the oxidant.

		CO	NO	N ₂ O	NO ₂
In	Miller	2.96E-02	3.19E-05	3.97E-08	1.31E-08
	GRI	1.51E-02	3.58E-05	2.79E-08	1.77E-08
Out	Miller	0.0002183	3.44E-05	6.79E-08	2.24E-08
	GRI	0.0001273	4.12E-05	4.77E-08	3.04E-08
Final	Miller	5.67E-05	4.40E-05	1.63E-08	5.36E-09
	GRI	3.69E-05	4.82E-05	1.15E-08	9.07E-09

Tab.2. Molar fractions of some species at stationary working condition. With reference to fig.1, In is the stream before "reaction", Out is the stream after "reaction" and Final is the flue gas stream.

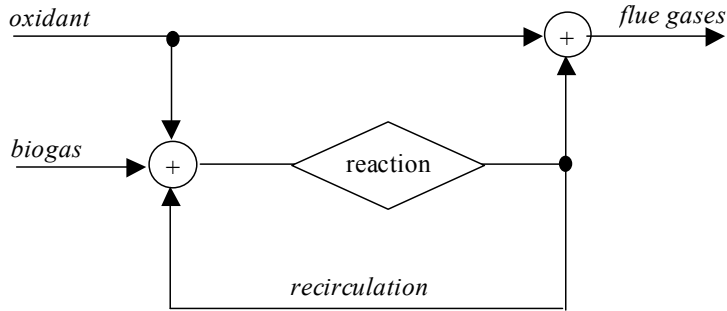


Fig.1 Schematic representation of a mild combustion burner.

RESULTS

The first observation is that pollutants emission is not a problem in the diluted combustion modality. Considering the NO species the final concentration is about 50ppm (see tab. 2) for both the mechanisms so that the biogas combustion does not increase the initial NO content of the oxidant stream (47 ppm). This behaviour is not valid for the CO, which has a final concentration of 30 ppm while the inlet oxidant stream has only 6 ppm. This means that a 50 ms reaction time is not sufficient for the CO consumption at these relatively low temperatures. As far as the reaction block is considered the GRI mechanism gives a slightly higher estimate (about 10 ppm, see fig.2) than that of Miller and Bowman for the NO while NO₂ and N₂O present minor discrepancies (fig. 3 left).

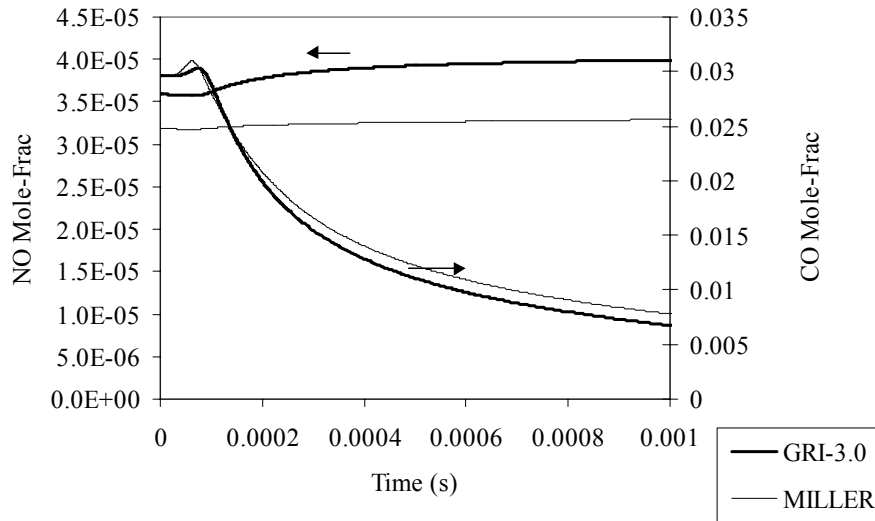


Fig.2: NO and CO molar concentration vs time. Initial condition of the mixture are reported in the first two row in tab.2

The sensitivity plots in fig.4 can give reason of this evidence. In fact in the Miller mechanism NO mole fraction is mostly sensitive to reaction $N+O_2 \rightarrow NO + O$ (G233 in fig.4 left) which is a key step in the thermal path, but in the application under study the temperature is relatively low. Considering the GRI sensitivity it turns out that the thermal steps are not involved, rather a sequence of reaction that comprises the decomposition of N₂O is the relevant phenomenon (reaction G38, G185 and G208 in fig. 4 right: $H+O_2 \rightarrow O+OH$, $N_2O (+M) \rightarrow N_2 + O$, $NNH + O \rightarrow NH + NO$). A further effort is needed for the interpretation of these results in light of the peculiarity of this application.

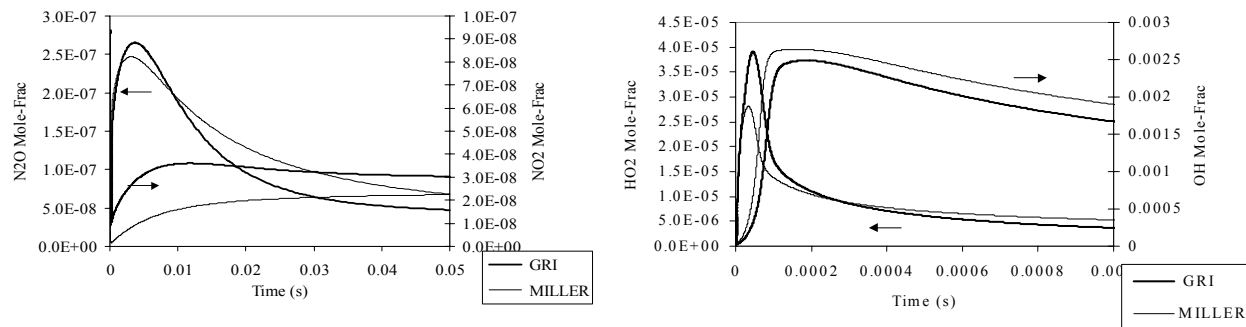


Fig.3 : N2O and NO (left side), HO2 and OH (right side) time profiles. Initial conditions are in tab.2.

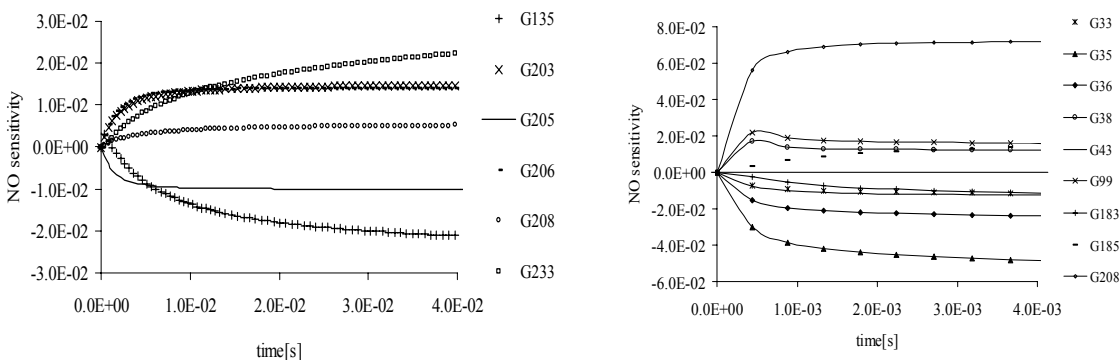


Fig. 4: NO sensitivity plots for the Miller mechanism (left side) and for GRI mechanism (right side).

CONCLUSIONS

We have discussed a work in progress about the combustion chemistry of biogas mixtures under diluted condition. The initial calculation with the Chemkin package show that the NO_x are not a concern from the environmental point of view, while the complete combustion of the CO may become a drawback because of the slow rate of the reaction $\text{CO} + \text{OH} \rightarrow \text{CO}_2 + \text{H}$. This issue requires further analysis aimed at the refinement of the process residence time. From the point of view of the reaction mechanism other schemes will be taken into account, first of all that of Glarborg (1998) [5].

Finally the comparison of our numerical simulation with experimental data should be made so that the more appropriate NO_x formation scheme can be found. On this subject the Enea Laboratory is actually engaged for the realisation of a test-rig for a trapped-vortex biogas burner.

REFERENCES

1. J. Chomiak, J. P. Longwell, A. F. Sarofim: *Prog. Energy Combust. Sci.*, **15**:190(1989).
2. J. A. Miller, C. T. Bowman: *Prog. Energy Combust. Sci.*, **15**:287 (1989).
3. G. P. Smith, D. M. Golden, M. Frenklach et al.: http://www.me.berkeley.edu/gri_mech/
4. G. Löffler, V. J. Wargadalam, F. Winter, H. Hofbauer: *Comb. Flame*, **120**:427(2000).
5. P. Glarborg, M. U. Alzueta, K. Dam-Johansen, J. A. Miller: *Comb. Flame*, **115**:1(1998).
6. A. E. Lutz, R. J. Kee, J. A. Miller: *Senkin, Sandia Rep. SANDD87-8248*(1988).
7. A. Cavaliere M. de Joannon: *3rd CREST Int. Symposium*, **E3**:1, Yokohama (2000).
8. A. V. Bridgwater: *Fuel*, **74**:631(1995)

Mathematical Modelling of Electric Field-Activated Combustion Reactions

¹M. Pisu, ²A. Cincotti, ²A. M. Locci, ²R. Orrù and ^{1,2}G. Cao

1 CRS4, Center for Advanced Studies, Research and Development in Sardinia, Uta, Cagliari - ITALY

2 Dipartimento di Ingegneria Chimica e Materiali, Centro Studi sulle Reazioni Autopropaganti (CESRA) and Unità di Ricerca del Consorzio Interuniversitario Nazionale di Scienza e Tecnologia dei Materiali - Università di Cagliari - ITALY.

INTRODUCTION

Self-propagating High-temperature Synthesis (SHS) is a well known technique for the synthesis of advanced materials characterized by highly exothermic reactions [1-3]. The modeling of SHS processes is really complex since it involves the description of different physico-chemical phenomena such as melting and diffusion of reactants, chemical reactions with formation of intermediate phases, nucleation and grain growth, etc. Considerable effort has been made both in experimental and modeling directions in order to understand the basic mechanisms occurring during self-propagating reaction [3].

Recently, a new method, based on the use of an electric field to activate self-propagating reactions in less-exothermic systems, was developed [4]. This method, known in literature with the acronym FACS (Field Assisted Combustion Synthesis), allows one to synthesize materials heretofore not possible by normal SHS (e.g. SiC, SiC-AlN, MoSi₂-SiC, Ti₃Al, B₄C-TiB₂ and TaC). In FACS systems the electric field is applied on the sample simultaneously with the ignition source. The reaction front propagates through the sample only in the presence of the electric field and in a direction perpendicular to it. Since we are dealing with systems that are not self-sustaining, when the field is turned off during wave propagation, the combustion front stops immediately. Although SHS and FACS techniques appear really advantageous for industrial applications, process scale-up, as well as the optimization of the operating conditions and process control may not be straightforward because of the lack of knowledge in terms of reaction and structure formation mechanisms. At the experimental level a relevant effort has been addressed to highlight all physico-chemical steps and mechanisms involved during self-propagating reactions. To this aim the combustion front quenching technique, which is based on the rapid extinction of the combustion front during its progress, is often used. This technique may provide a relatively accurate picture of the physico-chemical phenomena involved during reaction evolution. By investigating product microstructure and composition at different areas relative to the location of the frozen reaction wave, it is possible to identify intermediate species and phase transformations taking place. For systems characterized by low reaction heat, which can be synthesized through the FACS technique, quenching of the reaction can be obtained by turning off the electric field during front evolution [5,6].

With the aim of contributing towards the development of a reliable model of the FACS process, which may become a simple but powerful tool to support the investigation of electrically activated self-propagating high-temperature reactions, we present in this paper a two-dimensional model of the FACS technique which is able to simulate the rapid quenching of the reaction during its progress as the applied field is turned off.

MODELING OF FACS PROCESSES

A schematic representation of the FACS system and its use for the quenching of the combustion front is shown in Figure 1. Powders of elemental reactants are typically mixed in stoichiometric amounts and pressed into round-ended rhombohedral pellets. The sample, which is placed between two graphite electrodes, is ignited by means of a tungsten coil placed few millimeters away from one end. The electric field is applied, simultaneously, with the ignition source which is turned off immediately after the reaction is initiated. The reaction front propagates through the sample only in the presence of electric field and in a direction perpendicular to it. Since we are dealing with systems that are not self-sustaining, when the field is turned off during wave propagation, the combustion wave stops immediately. The process evolution is measured from video recordings using a time-code generator. Real-time current (I) and voltage (V) data are also acquired during wave propagation.

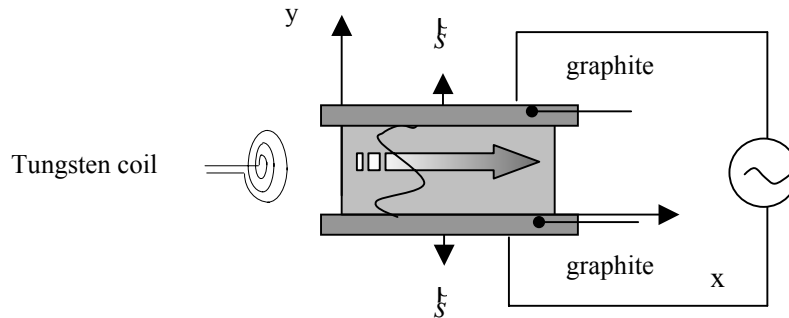


Figure 1

With the assumption of an isotropic powder mixture of the elemental reactants and by neglecting the mass diffusion of the solid reactants and products, the energy balance may be written as follows:

$$\rho C_p \frac{\partial T}{\partial t} = \left(\frac{\partial}{\partial x} k \frac{\partial T}{\partial x} \right) + \left(\frac{\partial}{\partial y} k \frac{\partial T}{\partial y} \right) + (-\Delta H) C_{B0} \frac{\partial \eta}{\partial t} + \sigma |\nabla \phi|^2 - 2 \frac{[h(T - T_0) + \nu(T^4 - T_0^4)]}{w} \quad (1)$$

This energy balance takes into account the heat conduction, the heat generation by chemical reaction, the Joule heat induced by the electric field, as well as the heat dissipation due to natural convection and radiative cooling from the sample surface [6]. Equation (1) is coupled with the following mass balance based on a kinetic model which describes the reaction between a low melting component (A) and a high melting component (B) [7]:

$$\frac{\partial \eta}{\partial t} = \begin{cases} a \geq 1, & \frac{6}{\rho_B} \frac{1+2\beta}{\beta} \frac{D_0}{d_{p0}^2} \exp\left(-\frac{E}{RT}\right) \frac{(a-\eta)(1-\eta)^{1/3}}{(a-\eta)\frac{1}{\rho_A} + (b+\eta)\frac{1}{\rho_P}} \\ a < 1, & \frac{6}{a\rho_B} \frac{1+2\beta}{\beta} \frac{D_0}{d_{p0}^2} \exp\left(-\frac{E}{RT}\right) \frac{(1-\eta)(1-a\eta)^{1/3}}{(1-\eta)\frac{1}{\rho_A} + \left(\frac{b}{a} + \eta\right)\frac{1}{\rho_P}} \end{cases} \quad (2)$$

where $\eta = 1 - (d_p/d_{p0})^3$ for $a > 1$, $\eta = [1 - (d_p/d_{p0})^3]/a$ for $a < 1$, with $C_A = C_{B0}(a-\eta)$, $C_B = C_{B0}(1-\eta)$, $C_P = C_{B0}(b+\eta)$. Equations (1) and (2) can be solved considering the following IC and BCs:

$$t = 0 \quad \forall x, \forall y \quad T = T_0 \quad \eta = 0 \quad (3)$$

$$x = 0 \quad \forall y, \forall t > 0 \quad T = g(t) \quad (4)$$

$$x = L_x \quad \forall y, \forall t > 0 \quad -k \frac{\partial T}{\partial x} = h(T - T_0) + \nu(T^4 - T_0^4) \quad (5)$$

$$y = 0 \quad \forall x, \forall t > 0 \quad k \frac{\partial T}{\partial y} = U(T - T_0) \quad (6)$$

$$y = L_y \quad \forall x, \forall t > 0 \quad -k \frac{\partial T}{\partial y} = U(T - T_0) \quad (7)$$

The Joule heating term which appears in the energy balance (1) can be calculated by considering the electric potential ϕ , obtained from the solution of the following equation:

$$\left(\frac{\partial}{\partial x} \sigma \frac{\partial \phi}{\partial x} \right) + \left(\frac{\partial}{\partial y} \sigma \frac{\partial \phi}{\partial y} \right) = 0 \tag{8}$$

Equation (8) is coupled with the boundary conditions:

$$y = 0 \quad \forall x, \quad \forall t < t_1 \quad I = - \iint_{y=0} \sigma \bar{\nabla} \phi \, dS^p = \frac{V_{in} - V}{R_{in}^p}; \quad V = \int \bar{\nabla} \phi \, dl^p \tag{9}$$

$$y = L_y \quad \forall x, \quad \forall t < t_1 \quad I = \iint_{y=L_y} \sigma \bar{\nabla} \phi \, dS^p = \frac{V}{R_o} \tag{10}$$

$$y = 0 \quad \forall x, \quad \forall t \geq t_1 \quad \iint_{y=0} \sigma \bar{\nabla} \phi \, dS^p = 0 \quad y = L_y \quad \forall x, \quad \forall t \geq t_1 \quad \iint_{y=L_y} \sigma \bar{\nabla} \phi \, dS^p = 0 \tag{11}$$

$$x = 0 \quad \forall y, \quad \forall t > 0 \quad \frac{\partial \phi}{\partial x} = 0 \quad x = L_x \quad \forall y, \quad \forall t > 0 \quad \frac{\partial \phi}{\partial x} = 0 \tag{12}$$

The dependence of the thermophysical properties, such as thermal conductivity, electrical conductivity, and heat capacity on temperature and composition, as well as the mixing expressions are taken from the literature [6]. The equations (1) and (2) are solved simultaneously by adopting a finite difference scheme at the internal node points and integrating the resulting system of ordinary differential equations by means of standard routines. For each time step the system of algebraic equations arising from the discretization of equation (8) is solved using a band matrix solver. An appropriate finite-difference scheme also applies to the boundary condition appearing in equation (5), where non-linearities are handled with the Newton method. The computation was generally performed by considering 3600 (120x30) spatial discretization points. Higher values of the internal node points did not cause any change in the results [8].

RESULTS AND DISCUSSION

The reaction $Si + C \rightarrow SiC$, which does not involve the formation of intermediate phases, in accordance with the adopted kinetic equation, is considered as model system, while physico-chemical data, model parameters and operating conditions used for simulation runs are reported in the literature [7]. The function $g(t)$ appearing in equation (4) is obtained by interpolating the entire temperature profile at the base where the sample is ignited. In agreement with experimental results [5], the proposed model predicts that in the absence of an imposed field no self-sustaining combustion waves take place. These waves can be activated when an electric field is applied above a minimum (threshold) value, i.e. 7.8 V/cm. Typical modeling results concerning the output of current and voltage during FACS are shown in Figure 2 (dotted lines) for the case when the electric field is maintained throughout the process.

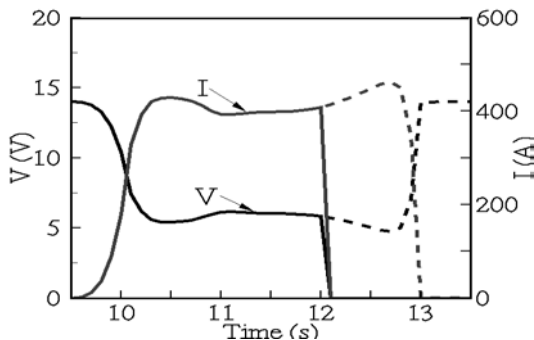


Figure 2

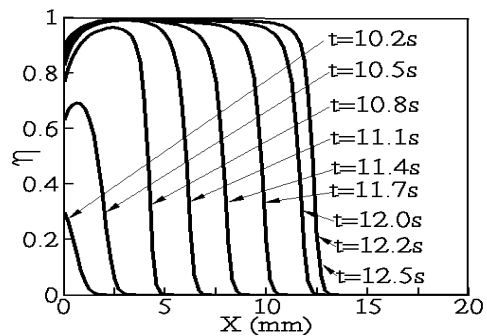


Figure 3

It is seen that when the wave is initiated, the current increases rapidly and then reaches a relatively flat level during wave propagation before the wave reaches the opposite side of the sample. When the field is turned off during the propagation of the combustion wave, the extinction of the reaction front occurs rapidly as it may be seen in Figure 2 (solid lines). This effect is clearly illustrated in Figure 3 where the time-space conversion profiles are depicted. The wave velocity rapidly decreases after the time when the electric field is turned off (i.e. $t = 12$ s), until the front is stopped. For the case when the electric field is maintained throughout the process, the temperature levels of the sample during combustion wave propagation at a given time (i.e. $t = 12.8$ sec) is reported in Figure 4. It is clearly shown that the temperature varies significantly along y-direction and therefore, in the description of a FACS process, the proposed two-dimensional model appears more suitable with respect to the one-dimensional approach [9].

The variation of the calculated ratio dp/dp_0 and the corresponding extent of conversion as a function of the spatial distance along the pellet axis at $t = 12$ s is shown in Figure 5. Moving from the region on the right corresponding to the reactants, the particle diameter of the solid component first sharply decreases in a relatively narrow region (about 1 mm thick) and then continues to decrease at a much slower rate, until the product region is approached.

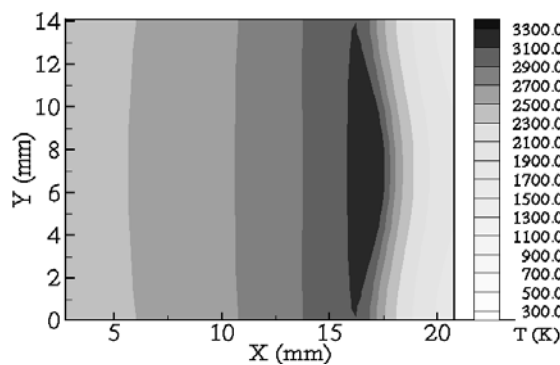


Figure 4

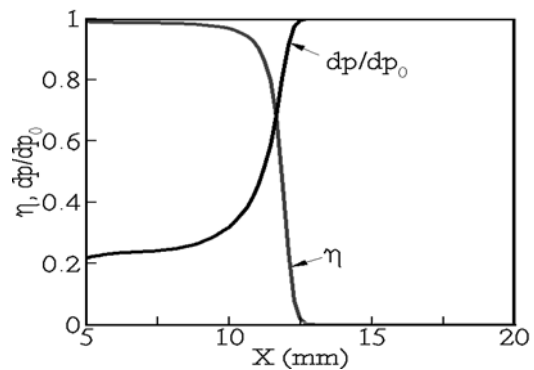


Figure 5

The development of a comprehensive model of the type proposed here and in previous studies available in the literature [9] may consequently provide an excellent tool to capture the essential features related to the microstructure evolution observed experimentally during FACS. Thus, together with appropriate experimental investigations, this approach may represent a good starting point towards the development of a more accurate description of the phenomena taking place during electric field-activated self-propagating reactions.

REFERENCES

1. Merzhanov, A.G., and Borovinskaya, I.P, *Dokl. Akad. Nauk SSSR*, 366 (1972).
2. Munir, Z.A., and U. Anselmi-Tamburini, *Material Sci. Report* **3**:277 (1989).
3. Varma, A., Rogachev, A.S, Mukasyan, A.S., and Hwang, S., *Adv. Chem. Eng.* **24**:79 (1998).
4. Munir, Z.A., Lai, W., and Ewald, K.H, *U.S. Patent N.5* 380 (1995).
5. Feng A., and Munir, Z.A., *B-Proc. Metallurgy and Mat. Proc. Science* **26B**:587 (1995)
6. Feng, A, Graeve, O.A., and Munir, Z.A., *Comp. Mat. Science* **12**:137 (1998).
7. Kanury, A.M., *Metallurgical Transactions A* **23A**:2349 (1992).
8. Pisu, M., Cincotti, A., Orrù, R., Cao, G., and Munir, Z.A, *Proc. of Int. Conf. on "Mass and Charge Tran. in Inorg. Materials"*, Ed. P. Vicenzini, TECNA, Faenza, Italy, 905 (2000).
9. Orrù, R., Cincotti, A., Cao, G., and Munir, Z.A, *Chem. Eng. Sci.*, **56**:683 (2001).

Mild Combustion in a Laboratory - Scale Apparatus

Alessandro Effuggi, Davino Gelosa, Renato Rota*

Politecnico di Milano

*Dip. di Chimica, Materiali e Ingegneria Chimica "G. Natta" / CIIRCO
via Mancinelli, 7 - 20131 Milano, Italy*

INTRODUCTION

In the recent years the focus of the energy research is set on the minimization of pollutant emissions of engines and power plants. Several innovative combustion systems have been investigated leading to a noteworthy improvement in both pollutant emissions and combustion efficiency. Among the others, it is worth mentioning the introduction of regenerative burners using hot flue gases to preheat the combustion air. However, regenerative burners leads to a very high production of nitrogen oxides through the classical Zeldovich pathway. This high production of thermal NO_x can be avoided by coupling regenerative burners with the so-called "flameless" or "mild" combustion. This new technology uses a recycle of burnt gases to dilute the high-temperature combustion air, thus leading to a good thermal efficiency combined with low NO_x emissions [1–13]. Real-size burners realize "flameless" conditions feeding the combustion air and the fuel through separated high-velocity jets into the combustion chamber. The air-jets entrain a large amount of burnt gases from the combustion chamber before reacting with the fuel. Consequently, the reactants concentration is lower than in traditional flames, while turbulence is higher. Therefore, chemical reactions occur with lower rates (comparable with mixing rates) in a larger space region and the heat generated is diluted in a larger mass. This avoids the formation of hot spots in the furnace and reduces thermal NO_x production without compromising thermal efficiency. The high temperatures of the gases recycled in the combustion chamber give ignition and stability of this kind of burners.

The fundamentals of this technology can be investigated using the well-controlled conditions achieved in laboratory-scale burners. In this work, an apparatus characterized by high internal recycle ratio, high back-mixing as well as the possibility of simulating external recycles of burnt gases is described, as well as the main results achieved.

LABORATORY SCALE-BURNER

Such as in real-scale burners also in a laboratory burner it is necessary to obtain a fast mixing of air and burned gases with the fuel to obtain similar mixing and reaction rates. This condition can be obtained with high turbulence, which allows a fast mixing of gaseous streams.

The adopted solution involves a single high velocity nozzle. This generates a high velocity flow of air (that can be vitiated with inert gases to simulate both internal and external burned gas recycle) inside a small pipe, into which the fuel stream is injected perpendicularly.

The laboratory-scale burner is sketched in figure 1; it is basically constituted by a close quartz cylinder divided in two section: the combustion chamber (A) and the air pre-heating section (B). Centrally, on the bottom of the combustion chamber the nozzle (C) is located from which the high velocity jet exits. In the nozzle the combustion air (D) and the fuel (F) partially pre-

* Telephone: +39 0223993154, Fax: +39 0223993180, E-Mail: renato.rota@polimi.it

mix before entering the combustion chamber. The combustion reaction cannot proceed inside the nozzle due to the small diameter of the pipe and the short residence time. The jet entrains a large amount of burned gases and this provides the fast dilution required by “mild” combustion. Due to the high velocity, no conventional flame can be stabilized on the nozzle tip and the combustion proceeds in the whole combustion chamber volume. In figure 1 a secondary inlet of air (E) is also evidenced that is used during the start-up of the system. Before switching to “flameless” conditions, the combustion chamber must be preheated using a conventional flame stabilized on the nozzle tip.

The two section of the burner are enclosed in refractory insulation equipped with electrical resistances. The lower oven provides the air preheating, while the upper one (whose temperature is always set below that of the combustion chamber) has been used to reduce heat losses from the combustion chamber.

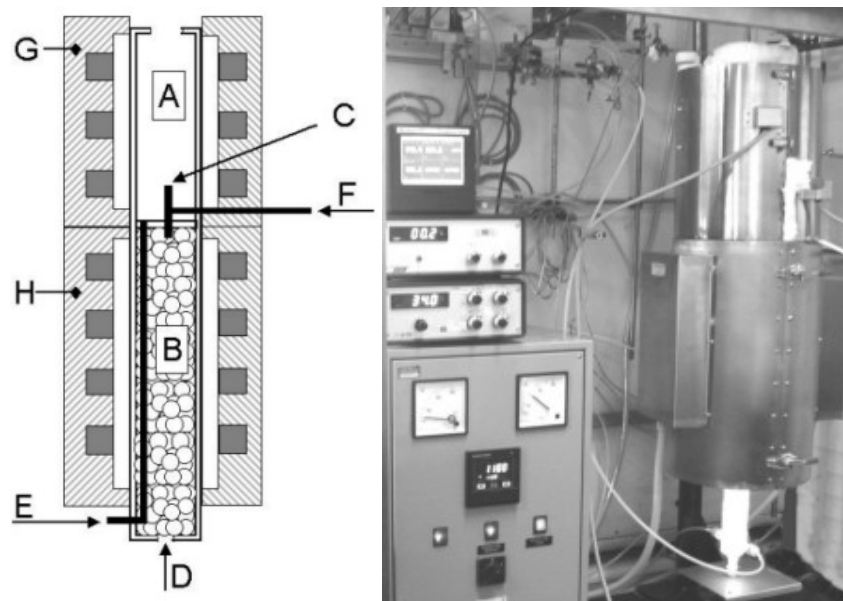


Fig 1 Sketch and picture of the laboratory scale apparatus.

RECYCLE RATIO ESTIMATION

An important parameter that can determine the performance of the laboratory-scale burner is the value of the recycle ratio inside the combustion chamber. To estimate the recycle flow rate into the combustion chamber, some calculations have been performed with a general-purpose code for computational fluid dynamics [14].

When the burner works in “flameless” conditions, the fluid dynamic regime of the system can be approximated as an isothermal confined turbulent jet where a recycle of the burnt gases takes place, increasing the flow rate of the jet. In Figure 2 a typical model result is reported as isovelocity contours for half the combustion chamber (since it is symmetric), where the location of the jet nozzle is $y = 0$ and $x = 0$. We can see that the high jet velocity close to the center of the combustion chamber rapidly decreases along the radial direction (that is, the y one) till zero. Behind this point a reverse flow is evidenced, leading to a recycle of the burnt gases into the jet. From these computations the recycle flow rate has been estimated as:

$$Q(x) = 2\pi \int_{R1}^R u_x(x, y) y dy$$

where the co-ordinate R and R_1 are defined in Figure 2. $Q(x)$ is the backflow rate, whose value depends on the axial co-ordinate, x , and it is equal to zero when the jet boundary hits the wall of the combustion chamber. Behind this point there is no backflow.

The recycle ratio, k , has been estimated as the ratio of the maximum value of $Q(x)$, Q_{\max} to the inlet jet flow rate, Q_{in} . For typical conditions used in all the experiments, this value has been found equal to about 5.

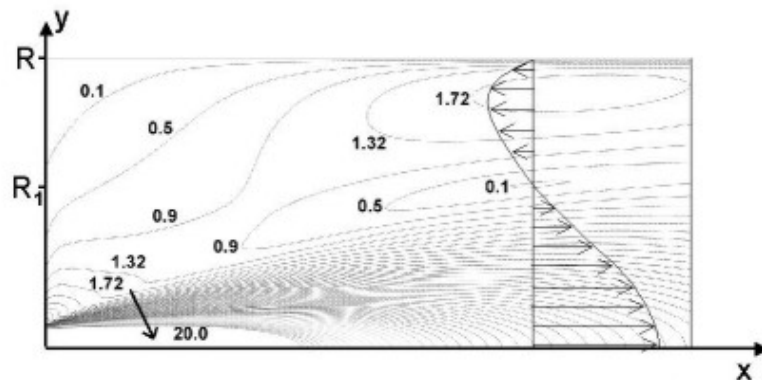


Fig 2 Velocity field of the confined turbulent jet in the combustion chamber.

TRANSITION FROM TRADITIONAL FLAMES TO “MILD” CONDITIONS

It is known that “flameless” industrial burners show different combustion regimes as a function of the average temperature in the combustion chamber and the amount of burnt gases recycled back into the air jets. Stable flames are possible over the whole range of combustion chamber temperature but only for a very low recycle ratio. For higher recycle ratio values, the flame becomes unstable, lifts off and finally blows out. However, if the furnace temperature is sufficiently high, the fuel can react in the very steady and stable form of “flameless” or “mild” combustion.

To determinate the recycle ratio value that enables the switch from conventional combustion to the “mild” one at a given air pre-heating temperature, we gradually switched from a low-speed jet able to stabilize a conventional flame on the burner tip without any entrainment of burned gases to an high velocity jet leading to a high recycle of burned gases and a volume combustion. This has been done by feeding at first through the nozzle only the fuel surrounded by secondary air fed through the inlet (E) (see figure 1). Then, the flow rate of the secondary air has been gradually reduced while augmenting that of the primary air through the nozzle, thus increasing the jet velocity and consequently the entrainment of burned gases. This mimics the variation of the recycle ratio in real-size burners.

A typical behavior evidenced experimentally is shown, for the sake of example, in figure 3 for methane and ethane combustion. In both the cases we can see that increasing the recycle ratio value leads to an homogeneous thermal profile in combustion chamber where the NO_x emissions show a drastic reduction. In particular, for methane combustion we can see that “mild” transition occurs for a recycle rate equal to about 3 – 4, while for the ethane combustion this value is slightly reduced to about 2,5 - 3,5. This behavior has been found in all the experiments carried out and clearly shows the possibility of achieving “mild” conditions for different fuels once provided a sufficient recycle of burnt gases.

The stability limits for “mild” conditions have been also determined for the two fuels. Once obtained the transition to “mild” combustion the air preheating has been gradually decreased looking for the combustion extinction. Using methane as a fuel “mild” combustion has been found to be stable down to a combustion chamber average temperature equal to about $800^\circ - 850^\circ\text{C}$, while using ethane as a fuel this temperature strongly decreases to $600^\circ - 650^\circ\text{C}$.

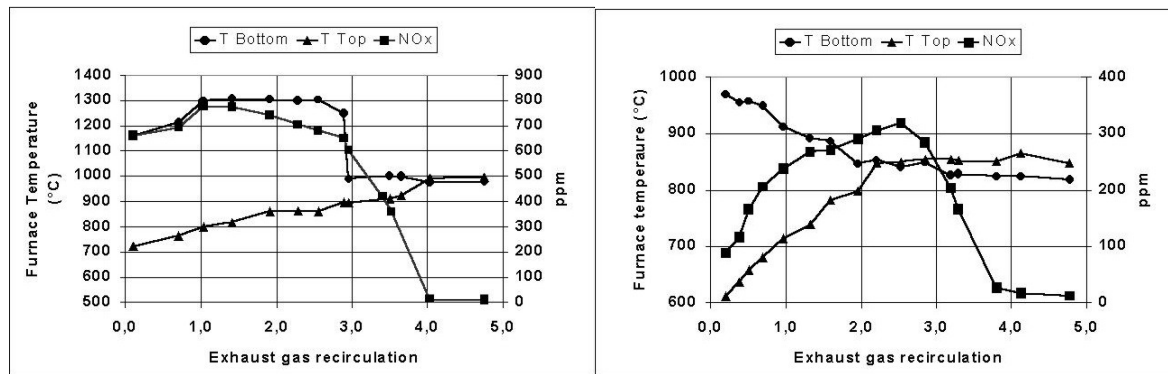


Fig 3 Typical transition to “mild” combustion for methane (left) and ethane (right).

CONCLUSION

A laboratory burner for mild combustion has been realized. Several experiments demonstrated that it is possible to reproduce also at a laboratory – scale the main phenomena observed in real - size flameless burners. Operating conditions for obtaining stable “mild” combustion with methane and ethane as a fuel have been investigated and operating parameters maps have been obtained. Work is in progress to investigate the feasibility of using “mild” combustion to reduce the emission of pollutants other than thermal produced NOx.

REFERENCES

- 1 Beer J. M., *Prog. Energy Combust. Sci.*, 26: 301 (2000).
- 2 Wüning J. A. and Wüning J. G., *Prog. Energy Combust. Sci.*, 23: 81 (1997).
- 3 Hasegawa T., Tanaka R. and Niioka T., AS.PA.C.C. (1997).
- 4 Milani A. and Wüning J. G., *Combust. Emiss. Control III*, 305 (1997).
- 5 Soroka B., Karp I., Roberts M., Cygan D. and Lisin F., AS.PA.C.C. (1997).
- 6 Coelho P. J. and Peters N., *Combustion and Flame*, 124: 503 (2001).
- 7 Katsuki, M. and Hasegawa, T., *Twenty-seven Symposium (Int.) on Combustion*, 3135 (1998).
- 8 Ishiguro T., Tsuge S., Furuhashi T., Kitigawa K., Arai N., Hasegawa T. and Gupta, A. K., *Twenty-seven Symposium (Int.) on Combustion*, 3205 (1998).
- 9 Plessing T., Peters N. and Wüning J. G., *Twenty-seven Symposium (Int.) on Combustion*, 3197 (1998).
- 10 Yasuda T., *Proceeding of 2nd Int. High Temperature Air Combustion Symp.*, B3 (1999).
- 11 Weber R., *Proceeding of 2nd Int. High Temperature Air Combustion Symp.*, C2 (1999).
- 12 De Joannon M., Langella G., Beretta F. and Cavaliere A., *Proc. of Mediterranean Combustion Symposium*, 347 (1999).
- 13 Cavaliere A. and De Joannon M., *3-rd CREST International Symposium* (2000).
- 14 *CFX Solver Manual*, AEA Technology, Harwell (UK), 1997.

Extinction of N₂ diluted n-heptane non-premixed counterflow flames

¹P. Berta, ¹I. K. Puri, ²S. Granata, ²T. Faravelli, ²E. Ranzi

1 University of Illinois at Chicago, Chicago - USA

2 Dipartimento di Chimica Industriale e Ingegneria Chimica - Politecnico di Milano - ITALY

INTRODUCTION

Liquid fuels are one of the most important energetic resources and are used in many applications. The characteristics of this combustion are very complex because the fuel is introduced into the combustion chamber in the form of a spray of fuel droplets of different sizes and the smaller droplets evaporate at a faster rate. This non-uniform evaporation process is very difficult to model and an investigation should start from simpler configurations. Such models always need to be proved and experimental results of flames of liquid fuels are not easy to find in literature [1,2]. Liquid fuels are blends of several components. For simplicity, n-heptane has been chosen as fuel surrogate in this study.

EXPERIMENTAL APPARATUS

The experimental results have been obtained on a counterflow burner. The separation distance between the nozzles is 15 mm and the nozzle diameter is 27.38 mm. The fuel nozzle is located at the bottom and nitrogen is flowed from an annular duct around the fuel nozzle in order to form a curtain to protect and isolate the flame. Nitrogen and burnt gases are ventilated from another annular duct around the oxidizer nozzle and cooled down.

The velocities of the two streams are selected in order to obey to the global strain rate definition [3],

$$a_g = \frac{2|V_o|}{L} \left(1 + \frac{|V_F|}{|V_o|} \sqrt{\frac{r_F}{r_o}} \right)$$

and to satisfy the momentum balance:

$$r_o V_o^2 = r_F V_F^2$$

The oxidizer is air at room temperature while the fuel stream is composed of a mixture of nitrogen and prevaporized n-heptane having different composition case by case, held at 400 K. The bottom part of the burner is heated and the temperature is accurately controlled to provide a constant fuel stream temperature.

Nitrogen and n-heptane are mixed in the prevaporizer, which consists of a stainless steel chamber electrically heated. The desired mass flow rate of n-heptane is introduced by a pump while the nitrogen stream is introduced from the bottom. Half of the chamber is full of glass beads in order to improve the residence time in the chamber and hence the heat transfer. The temperature of the exiting gas is constantly tracked by a thermocouple.

The temperature profiles of the flames have been obtained by a thin wire Pt-Rh thermocouple having bead diameter of 0.508 mm and wire diameter of 0.127 mm.

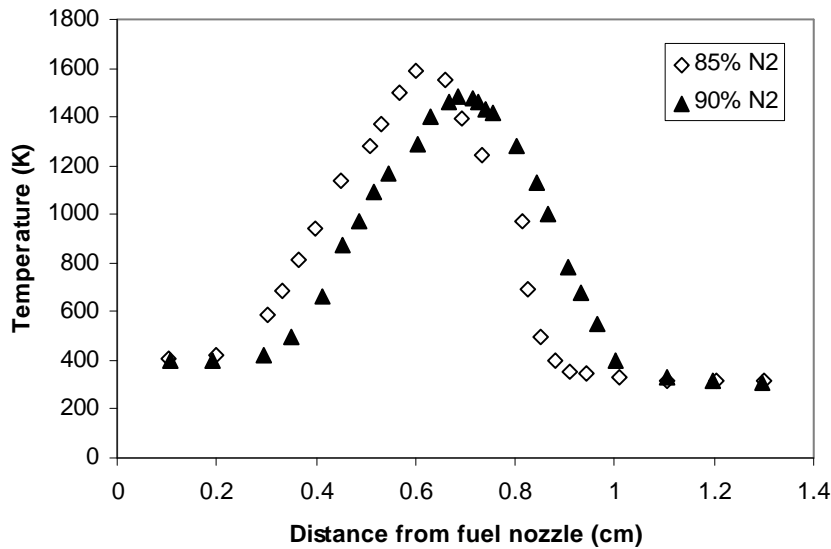


Fig. 1a Experimental temperature profiles at the strain rate 30 s^{-1} .

RESULTS AND DISCUSSION

In order to characterize the extinction point several experiments have been carried out varying the global strain rate and the nitrogen dilution.

Strongly diluted n-heptane flames show a faint blue color. The amount of nitrogen in fact is so high that even though the flame is non-premixed, pyrolysis reactions and soot growth cannot take place.

Figure 1a shows the experimental values of temperature for two flames having global strain rate 30 s^{-1} and nitrogen concentration in the fuel stream 85% and 90% respectively. Temperature measurements are not corrected for the thermocouple radiation heat loss.

With 90% dilution the temperature peak substantially decreases, this effect is to be expected as in this case the concentration of n-heptane is much less than with 85% dilution.

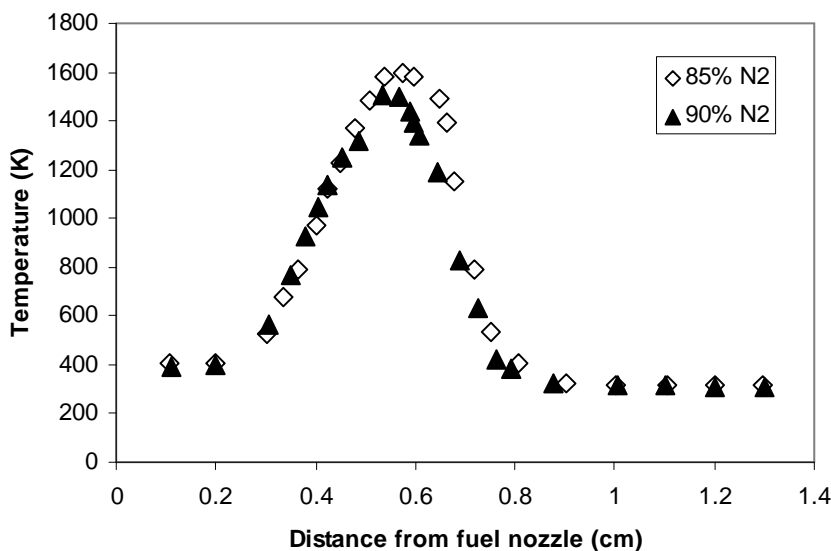


Fig. 1b Experimental temperature profiles at the strain rate 50 s^{-1} .

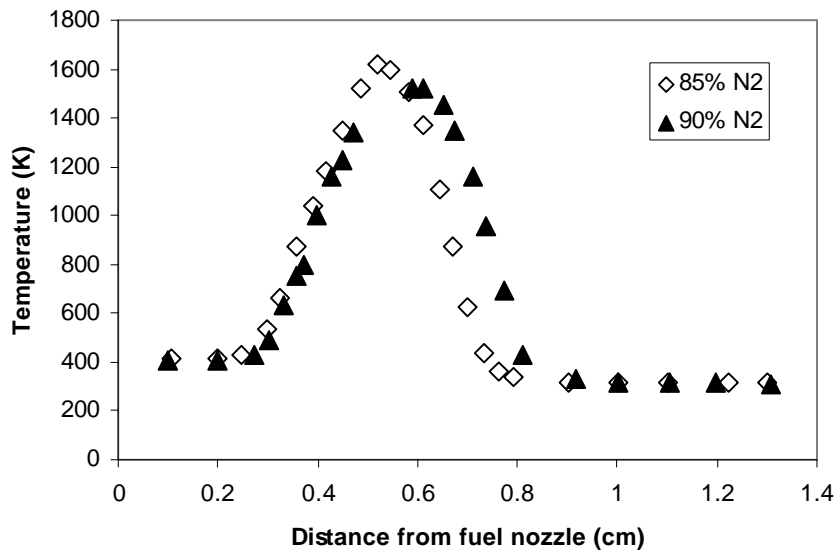


Fig. 1c Experimental temperature profiles at the strain rate 70 s^{-1} .

The same trend can be observed in figures 1b and 1c in which the same set of experimental results is presented for the strain rate cases of 50 s^{-1} and 70 s^{-1} respectively.

A study of the dependence of the extinction point has been carried out and the results are shown in figure 2. The nitrogen concentration reported is the value over which the flame cannot sustain any more.

From the diagram it seems that this value is constant and does not depend on the strain rate. Some authors however [4-6], found that for different fuels this value of critical concentration of dilutant should decrease at very low strain rates due to radiation heat loss.

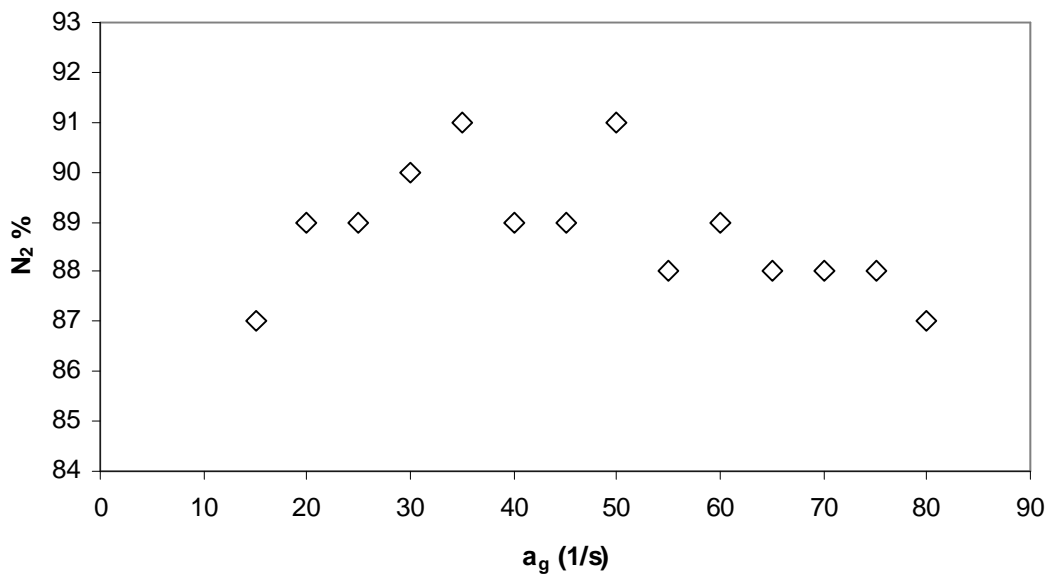


Fig. 2 Critical nitrogen dilution as a function of the strain rate .

A study of n-heptane flames at very low strain rates, however has not been possible since in these conditions the flame extinguished because of flow instabilities and buoyancy effects rather than nitrogen dilution.

Very preliminary model predictions are reported in Figure 3, for the 85% and 90% of nitrogen dilution at strain rate 30 s^{-1} . The comparison of temperature profiles shows large deviations between experimental results and model predictions, therefore further investigation is required. Nevertheless it seems relevant to observe the large differences in the predictions of benzene and naphthalene formation at the two different nitrogen dilutions.

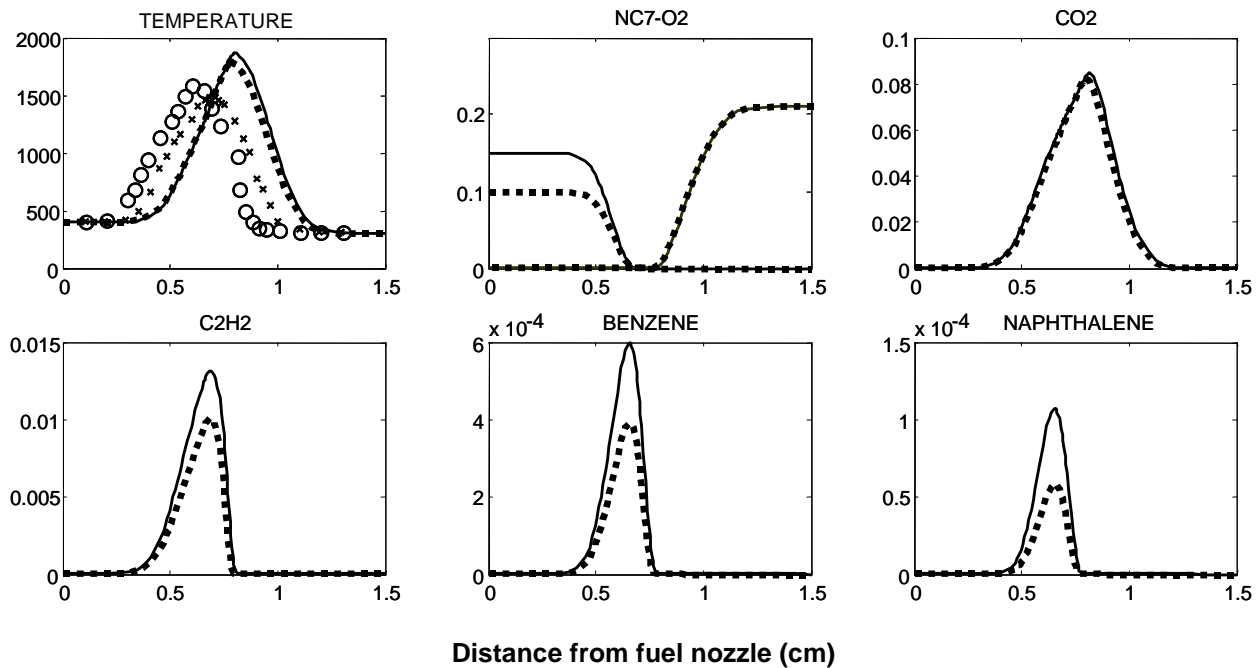


Fig. 3 Model predictions (temperature and mole fractions) and experimental temperature profiles at the strain rate 30 s^{-1} .

Experiments: \circ (85% N₂) and \times (90% N₂)

Predictions: Solid lines (85% N₂) and dotted lines (90% N₂)

REFERENCES

1. Seiser, R., Truett, L., Trees, D., and Seshadri, K.: *Proc. Comb. Inst.* 27:649 (1998).
2. Berta, P., Mukhopadhyay, A., Puri, I.K., Granata, S., Faravelli, T., and Ranzi, E.: *Proceedings of the 24th event of the Italian Section of the Combustion Institute*, V-3 (2001).
3. Chelliah, H.K., Law, C.K., Ueda, T., Smooke, M.D., and Williams F.A.: *Proc. Comb. Inst.* 23:503 (1990).
4. Chao, B.H., Law, C.K., and Tien, J.S.: *Proc. Comb. Inst.* 23:525 (1990).
5. Maruta, K., Yoshida, M., Guo, H., Ju, Y., and Niioka, T.: *Combust. Flame*, 109:639 (1998).
6. Pogliani, B.: *MS Thesis*, (2002).

Flameless Combustion: from furnaces to new applications

A. Milani, J.G. Wünnig

WS Wärmeprozessstechnik

Flameless combustion has been extensively employed now in high temperature process technology, basically heating and heat treatment furnaces in the steel and non-ferrous metals industry, for low NO_x purposes, where it was originally discovered and developed [1], and for exploiting the considerable energy saving potential (order of 25 to 50%) associated with the high combustion air preheat made feasible by the flameless technique. This main characteristic is accompanied by additional, advantageous features of the flameless combustion pattern that is unlike the conventional, burner-stabilised flame combustion (heat transfer uniformity, noise abatement, insensitivity to fuel and to equivalence ratio). Flammability limits are restricted as far as O₂ concentration *and* inert-gas concentration before reaction are concerned: this is certainly true for the stabilisation of a *flame front*. Assuming that the process is above self-ignition temperature (order of > ~ 800 °C for safety) and therefore *safe against explosion risk*, a combustion pattern different from the burner stabilised flame-front pattern can be devised. This is carried out by entraining a consistent rate K_v of recirculation products into the reactants *before* combustion.

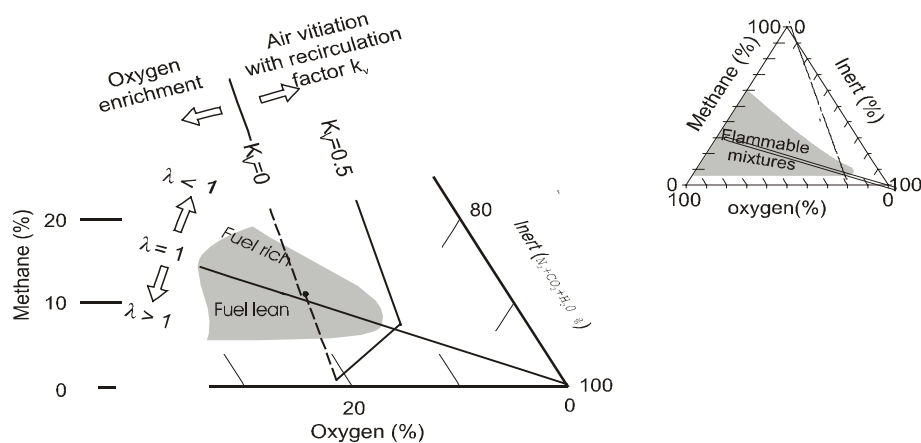


Figure 1 – Flammability triangle O₂-CH₄-Inert gas

By so doing, a flame front attached at the burner becomes unstable (Figure 1: moving into an *air vitiated* zone, very sensitive to *equivalence ratio* for $K_v > \sim 0.5$); then *lifted* flames (flame fronts “stabilised” by local turbulent structures) are still possible, but for K_v above the qualitative threshold $K_v > \sim 2.5-5$ a stable *flameless* combustion mode is set up, as shown in Figure 2. By entraining a large amount of recirculation gases, composed by CO₂+H₂O+excess O₂+ N₂, a large thermal ballast is added to the reacting partners and the temperature jump ΔT during reaction is inherently limited: it may be easily computed that ΔT is limited to ~ 200-400 °C in flameless conditions, with respect to ~ 800-1200 °C in flame conditions. No wonder that in the *flameless* case, thermal NO formation is abated by one order of magnitude; also chemistry and detailed kinetics and other pollutant formation are quite different from the

flame front case, where the bulk of radical related reactions are confined into a highly convoluted and stretched turbulent, “two-dimensional” layer with strong thermal gradients.

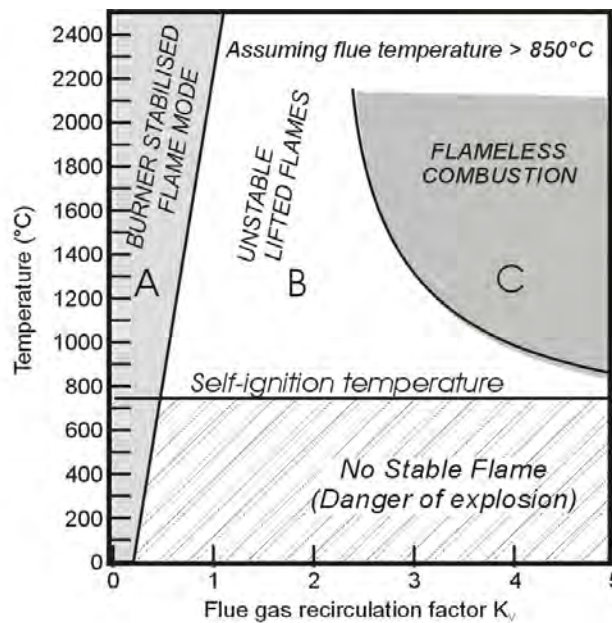


Figure 2 – Limits of flameless combustion vs recirculation rate

Flameless firing has been identified as *volume* combustion to stress that the reaction rate is smoothly distributed over a wide volume, unlike the *flame-front* firing pattern. WS prefers to avoid *mixed firing patterns* and tends to emphasize the difference between the two combustion modes, as it may be appreciated from the following picture; the burner may fire either in flame-mode (as it must indeed, for temperatures *below self-ignition*) or in flameless mode. A pure flameless mode does not use or require any pilot flame and it is not possible to monitor flameless combustion with any known flame detector. Only when temperature is safely above self-ignition threshold (~~ 850 °C), is it possible to switch from flame to *FLOX®* or flameless mode.

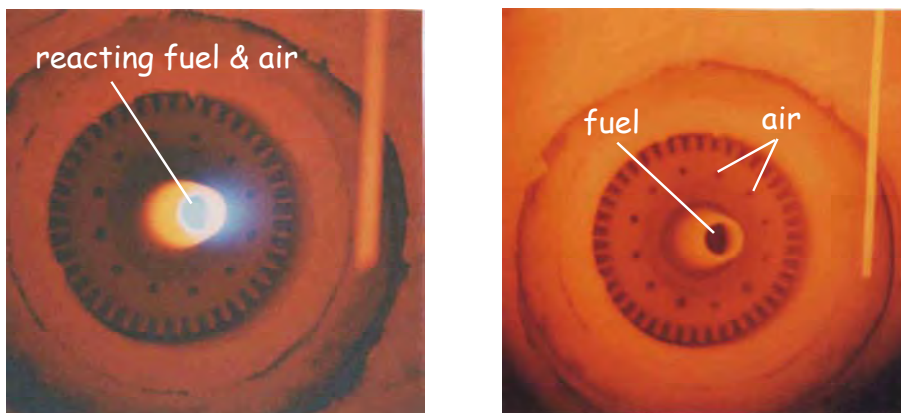


Figure 3 – Flame and *FLOX®* (flameless) firing modes

Figure 4 shows how this is carried out in a typical WS high velocity burner. Fuel gas can be injected radially to stabilise a flame into the primary chamber (flame mode) or axially in such a way that this central jet has no chance of creating a stable flame front (in absence of any flame holder or central recirculation vortex).

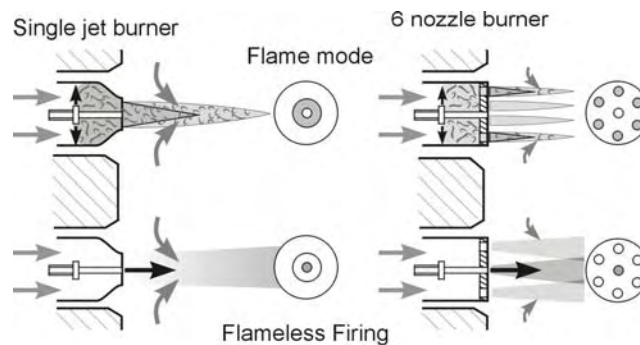


Figure 4 – High velocity burners: details of gas injection

Standard CFD computations (taking into account temperature controlled kinetics) confirm realistic and validated temperature predictions, as shown in Figure 5.

These design principles have been implemented in *several thousands burners* typically firing reheating furnaces (mainly large pieces of equipment) and heat treatment furnaces (usually dedicated, small scale, natural gas fired burners), as reported in the recent *HTACG4 Symposium* organised by ENEA (Rome, 26-30 November 2001).

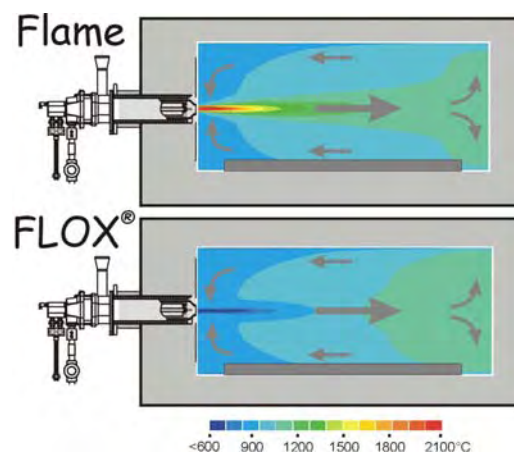
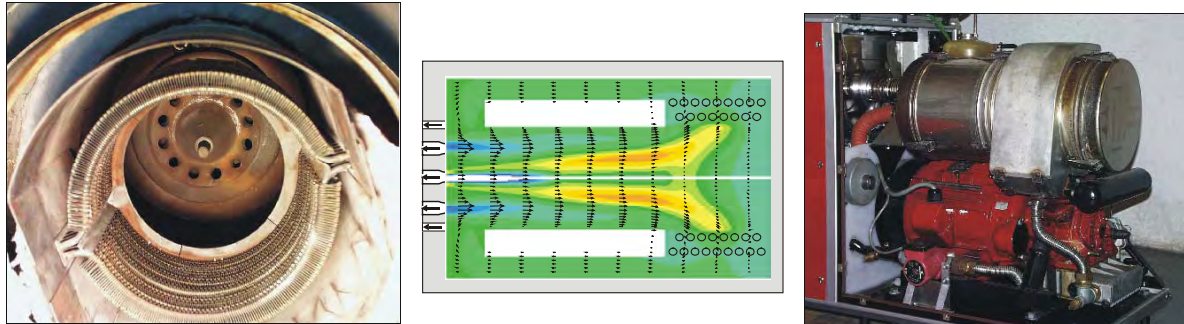


Figure 5 – Flame and flameless firing predictions

The design principle and the associated know-how (on materials for high temperature, manufacturing etc) lends itself to use in a multiplicity of other applications as well. A convenient field for WS concerns delivering “high quality heat” (i.e. at high temperature with high thermal efficiency (above $\sim 75\%$), good uniformity, compact design, flexibility and availability etc) to small or very small pieces of decentralised equipment. During a R&D project, a *FLOX®* burner for Stirling engines was developed (Figure 6); besides low NO_x -emissions and high efficiency, a compact design and the potential for low production cost, when produced in large series, were important. The Stirling engines are intended to be used as CHP-units (combined heat and power) for decentralized electric power generation. To use the advantages of a more uniform heat distribution from flameless oxidation for new, more

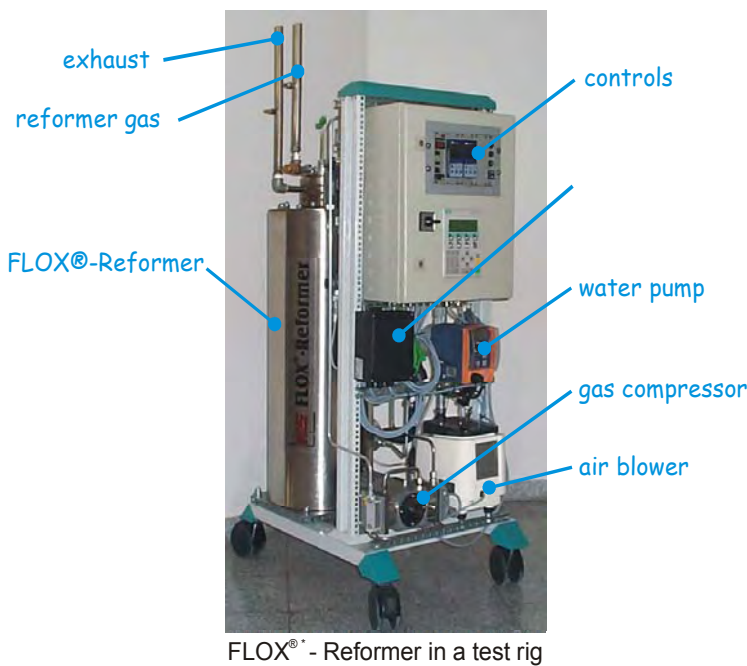
compact furnace designs was the topic of another R&D project called CFHU (compact fired heating units). The use of liquid fuels, produced from waste wood, was the topic an R&D project. Flameless Oxidation proved to be very applicable for difficult fuels since flame stability is usually one of the major problems when using special fuels.



Development will continue to improve recuperative and regenerative burners for furnaces:

Figure 6: Burner development for Stirling engines

rising energy costs should favour *regenerative concepts* (for air preheat) due to their higher potential for efficiency. For instance, regenerative radiant tubes which allow for internal recirculation, called *A-type-tubes*, are currently under development in WS' test hall and perform satisfactorily.



FLOX® - Reformer in a test rig

New concepts have been developed for:

- petrochemical furnaces (reformer)
- micro FLOX®-reformers for fuel cells (Figure 6)
- gas turbine combustion chambers
- waste gas disposal

Application of flameless to gas turbine combustors, for both small and large machines, is being seriously taken into consideration (see e.g. [2]). First tests of a newly developed FLOX® prototype is being successfully carried out at WS's experimental hall.

Figure 7 - FLOX® small reformer for micro H₂ generation

- FLOX® is a registered trademark of WS

References

[1] Wüning J. A., Wüning J. G - "Ten Years of Flameless Oxidation: Technical Applications and Potentials" - HTACG4 Symposium - Rome, 26-30 Nov 2001
 [2] Tabacco D., Cuoco F. and Bruno C - "Theoretical and numerical investigation on flameless combustion and its potential for applications to gas turbines" - HTACG4 Symposium - Rome, 26-30 Nov 2001

Experimental Identification of Bifurcation Points in Methane Oxidation

¹M. de Joannon, ¹A. Tregrossi, ²A. Cavaliere

1 Istituto di Ricerche sulla Combustione - C.N.R., Naples - ITALY

2 Dipartimento di Ingegneria Chimica - Università Federico II, Naples - ITALY

INTRODUCTION

The dynamic behavior of continuous stirred reactors occurring during the oxidation of most part of hydrocarbons have been extensively studied over the years. Although the thermokinetic effects related to periodic temperature oscillations are not yet completely understood, they have been clearly related either to the cool flames or multistage ignitions according to the operating temperature ranges.

In this analysis, smaller hydrocarbons, such as methane, have been disregarded because the oscillation phenomenology associated to these hydrocarbons were considered to occur in a temperature and pressure range not relevant for practical applications. As a matter of fact, only few papers on methane cool flames are present in literature. The only experimental data, reported by Vanpè [1] and confirmed by Egret et al. [2], were obtained in a batch reactor in rich, not diluted conditions. In these works methane ignition diagrams were obtained and one cool flame, two cool flames, slow combustion and ignition regions have been identified at a fixed C/O ratio. In more recent years, Vanpè extended the range of experimental parameters considered [3] by analysing the concentration effect and the influence of reactor dimension on the occurrence of oscillations. These results were modeled by Basevich et al. [4] and Lignola et al. [5] with success. More recently, Di Maio et al. [6] and Barbieri et al. [7] extended the detailed kinetic model of methane oxidation of Lignola et al. [5] in order to make it able to predict dynamic behavior (periodic ignition and complex oscillation) of the CH₄/O₂ system in a continuous stirred reactor in isothermal conditions. However, no experimental result in these conditions has been so far published to verify the effectiveness of the kinetic models.

The renewed interest toward such phenomenology in methane oxidation arises from the development of new combustion modes, stimulated by pollutant reduction and energy saving requirements. This is the case of Mild combustion concerning fuel oxidation evolving in very diluted, highly preheated conditions. These processes show several features that make them quite attractive from the scientific and practical point of view. For instance, they are characterized by extension of reaction zone where nearly homogeneous temperature and concentration profiles are present, by absence of the typical noise and flame luminosity and by high infrared emission. Therefore, the exploitation of this new combustion mode does claim for extension of the study of both physical and chemical processes occurring in these extreme working conditions. During the experimental evaluation of the influence of high temperature, very diluted conditions on methane oxidation kinetics, a significant temperature oscillation phenomenology was detected. Therefore, a characterization of oscillating regimes in methane combustion was experimentally done at different initial temperature and carbon/oxygen ratio in a continuous stirred reactor.

EXPERIMENTAL SET UP

CH₄/O₂/N₂ mixtures were injected in a spherical quartz Jet Stirred Flow Reactor with volume of about 0.1m³. The reactor was located inside a cylindrical (0.3m i.d.) electrically heated,

ceramic fiber wall oven, equipped with a temperature controller. A recirculation air system provides for an homogeneous temperature distribution in the oven which can reach a maximum temperature of 1300 K. The reactants pass through a pre-heating coil in the furnace so that the reactant temperature at the inlet of the reactor is nearly equal to oven temperature. Time resolved profiles of the reactor temperature were measured using a silica coated fine wire (40 μ m bead size) Pt-Pt13%Rh thermocouple. The temperature values were acquired by means of an A/D converter at a sampling rate of 50 Hz, then stored and analyzed by a personal computer.

The experimental tests were carried out at atmospheric pressure, different inlet temperatures and mixture compositions. In particular, C/O ratio was changed from 0.1 up to 1 while keeping constant the dilution and the residence time (τ). Hence, the nitrogen volumetric fraction was fixed at 90% of the inlet flow, whereas CH₄ and O₂ fractions were changed simultaneously in order to obtain a τ of 0.5 s. For each C/O ratio the inlet reactant temperature (T_0) was changed from 1020 K up to 1220 K.

RESULTS

The study of methane combustion in a continuous flow reactor in mild conditions revealed several characteristic behaviors that were classified by means of temperature temporal profile analysis. The regions corresponding to the different phenomenologies were pointed out in the bifurcation map reported in Fig.1 where inlet temperature and C/O ratio were considered as continuation parameters. The symbols correspond to conditions where experimental tests were performed.

On this map three different regions were identified. The first one, on the left side of the dotted line corresponds to the conditions where stable oxidation occurs (○). As expected at such high inlet temperatures, in this case a single step ignition leads the system to a steady working temperature that depends on the T_0 and C/O ratio. This is the only phenomenology occurring in the region of richer C/O ratios down to 0.8 in the whole temperature range analyzed.

At lower C/O ratios a second characteristic behavior was recorded corresponding to the region on the right side of the dotted curve (Δ , \blacktriangle , \bullet). As a matter of fact, starting from C/O=0.7 temperature oscillations can be found at T_0 higher than 1120K. The oscillating temperature region enlarges toward lower T_0 by decreasing the C/O ratio, thus covering almost the whole temperature range at leanest condition.

Several dynamic behavior were recognized in this region. For C/O between 0.7 and 0.4 a stable oscillation phenomenology with simple waveform was identified (\bullet). An example of temperature temporal profile corresponding to the point indicated as (a) on the bifurcation map is reported in Fig.2(a).

In the region around stoichiometric C/O ratio ($(C/O)_{\text{stoic}}=0.25$) stable temperature oscillations with complex waveform (Δ) were detected in the temperature range from 1100 K up to 1200 K. They generally show a double peak wave-shape such as shown by the temperature temporal profile reported in Fig.2(b), corresponding to the point (b) of Fig.1. In the same region irregular temperature oscillations were also detected (\blacktriangle). Also in this case a sort of periodicity can be recognized, such as shown by the temperature profile reported in Fig.2(c), corresponding to the point (c) of Fig.1.

Although point (d) in Fig.1 is representative of a stable oscillation with simple waveform, such as the point (a), the related temperature temporal profile (Fig.2(d)) is quite different from temporal profile collected in (a). As a matter of fact, the latter is symmetric with respect to the average value whereas the former presents a bell-shaped profile. These differences correspond to a different oscillation frequency that changes from 0.2Hz in (a) to 2.8Hz measured in (d).

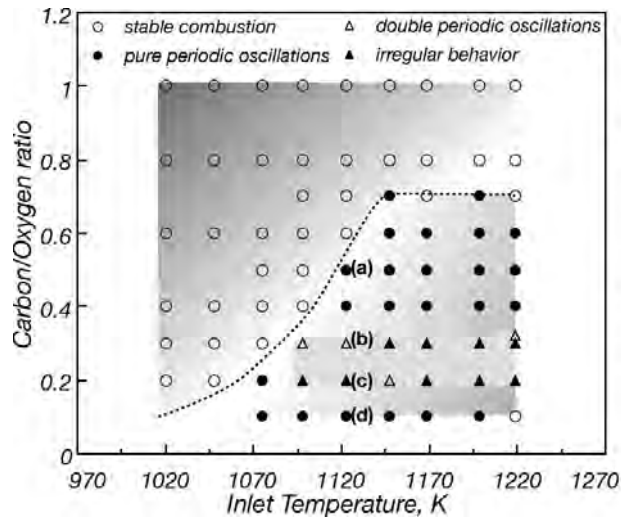


Fig. 1 Experimental bifurcation map for diluted methane combustion for inlet temperature and the C/O ratio as continuation parameters.

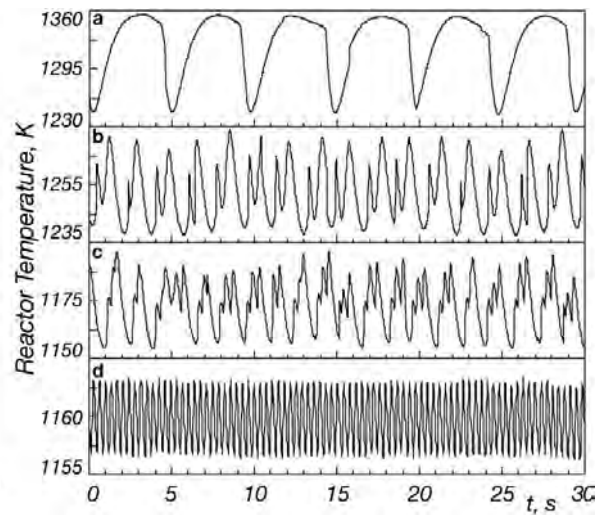


Fig. 2 Temperature temporal profiles corresponding to the points (a), (b), (c) and (d) of bifurcation map reported in Fig. 1.

Better information on system behavior can be pointed out by analysing the bifurcation diagram obtained by fixing one of the continuation parameters considered before. Therefore, in Fig. 3 reactor temperatures measured for C/O=0.1 (a) and 0.6 (b) were reported as function of T_0 . In respect of the symbolism generally used, the solid lines correspond to the stable working temperature or to stable static branch, whereas the dotted lines with full symbols represent the maximum and minimum temperatures measured during oscillation and, therefore, the stable periodic branch.

Low temperature increase, ranging from 25K at $T_0=1070$ K to few degrees at $T_0=1220$ K, were detected for C/O=0.1. The decrease of amplitude oscillation corresponds to an increase of oscillation frequency (f), such as shown by the frequency profile at C/O=0.1 reported in the bottom of Fig. 3 (▲). In this case, f rises from 1Hz at 1070K up to 4.7 Hz at 1150K, then it slightly decreases reaching a nearly constant value of about 3Hz. Similar behavior was shown by temperature profile related to C/O=0.6. Also in this case, the oscillation amplitude decreases with the increase of inlet temperature whereas f shows a monotonic trend passing from 0.53Hz at 1150K up to 2.7Hz at 1220K. The stable static and stable periodic branches obtained in present work were compared with the bifurcation diagram obtained by Lignola et al. [8] by means of a numerical analysis and represented in Fig. 3 with the curve (c). The LP and HP1 are representative of limit and bifurcation points respectively. Although this temperature profile was computed for inlet conditions different from the one considered in the present work, it is noteworthy that the temperature range where stable periodic branches have been experimentally detected is a subset of temperature range where this phenomenology has been already predicted without the support of any experimental data.

On the basis of these evidences a numerical simulation of these behavior were tentatively performed by using the methane oxidation model by Warnatz [9]. The system was schematized by means of Aurora configuration of the CHEMKIN package [10], that allows for the simulation of perfect stirred flow reactor in transient conditions. The temperature profile computed at $T_0=1070$ K and C/O=0.2 was compared in Fig. 4 with the profile measured in the same conditions. The model fairly well reproduces the oscillation frequency although it fails in the computation of temperature oscillation amplitude.

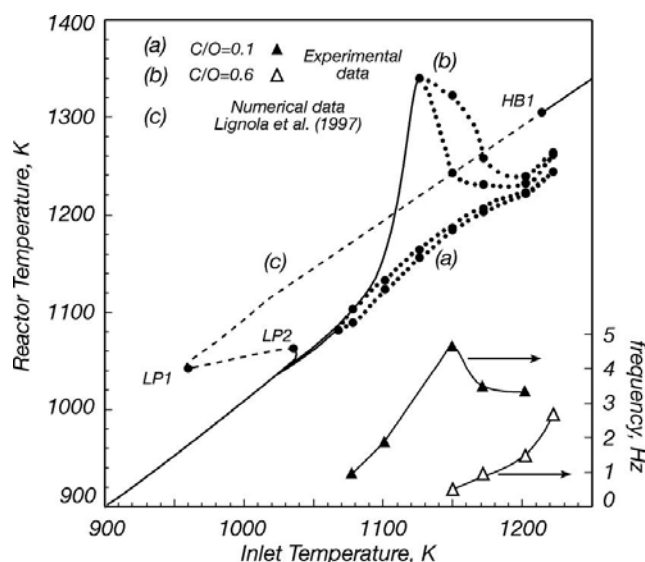


Fig.3 Experimental bifurcation diagram for methane combustion in a JSFR considering the inlet temperature as bifurcation parameter.

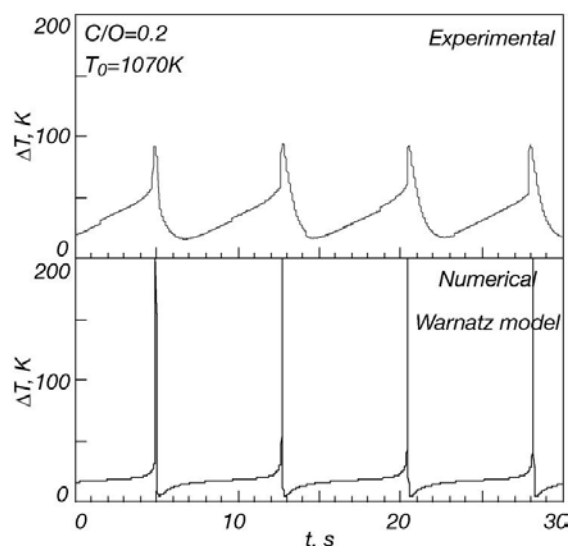


Fig.4 Experimental and numerical temperature temporal profile comparison.

CONCLUSIONS

Although an impressive number of papers on methane oxidation are present in literature, this is the first time that oscillation phenomenology has been experimentally recognized in methane combustion in a continuous flow reactor. The oscillations occur in high temperature range ($T > 1000\text{K}$) very different from the temperature range characteristic of oscillations related to most part of hydrocarbons. This experimental evidence can contribute to better understand the oxidation kinetic of small paraffins and represent a rigorous test for validation of kinetic models that must be able to predict the dynamic behavior of the reacting system, thus considering more stringent constraints. Moreover these results point out that mild combustion conditions do not exclude the occurrence of periodic behavior.

REFERENCES

1. Vanpè M.: *Compt. Rend.*, **243**:804 (1956).
2. Egret J., Sochet L.R., Lucquin M.: *Bull. Soc. Chim.*, 2205 (1965).
3. Vanpè M.: *Comb. Sci. Tech.*, **93**:363 (1993).
4. Basevich V.Ya., Kogarko S.M.: *Oxidation Communications*, **3-4**:199 (1983).
5. Barbieri G. Di Maio F.P., Lignola P.G., *Joint Meeting of the Italian and Portuguese Section of the Combustion Institute*, Salsomaggiore Terme, Italy, September, 220 (1994).
6. Di Maio F.P., Lignola P.G.: *Joint Meeting of the Italian Section of the Combustion Institute*, Stresa, 28th June-1st July (1993).
7. Barbieri G., Di Maio F.P., Lignola P.G., Loiacono M.L.: *Comb. Sci. Tech.*, 106:83 (1995).
8. Lignola P.G., Minale M., Rotondi R., *Analisi dinamica e sviluppo di reattori chimici e sistemi di controllo ad alta affidabilità*, Report P.R.I.N. project, MURST, F-11 (1997).
9. Warnatz J., Maas U., Dibble R.W., *Combustion: Physical and Chemical Fundamentals, Modelling and Simulation, Experiments, Pollutant Formation*, Springer, Berlin (1999).
10. CHEMKIN Collection, Release 3.6, Reaction Design, Inc., San Diego, CA (2000).

Numerical Simulation of a H_2/Air Turbulent Non-Premixed Flame

Raniero Malagnino, Eugenio Giacomazzi[†], Claudio Bruno
Giorgio Calchetti[†], Marco Ruffoloni[†]

* Department of Mechanics and Aeronautics - University "La Sapienza", Roma - ITALY

[†] ENEA - C. R. Casaccia, Sec. ENE-IMP, Roma - ITALY

Abstract

In the present work we want to investigate the use of hydrogen as fuel in turbulent combustion, focusing on flame stabilization and flame stretching. We numerically investigate a turbulent non-premixed flame of H_2/Air for which reliable point measurements are available. The fuel jet Reynolds number is 2208; its velocity is 25 m/s and that of air (coaxial) is 4 m/s . We solve the reactive 3 – D axisymmetric Navier-Stokes equations in RANS and LES approximations, assuming a Fast Chemistry approach for hydrogen oxidation (the error associated to neglecting non-equilibrium effects is usually small).

Results show good agreement with the experimental data available, revealing important aspects of combustion such as effect of heat-release rate, role of buoyancy, and Lewis-number effects during the flame-vortex interactions. In particular, we observed that a positive stretching on the outer side of the flame decreases temperature and a negative stretching (compression) increases temperature; the effects of stretching are opposite when the stretching is applied on the inner side of the flame.

1 INTRODUCTION

In this work we numerically simulate the double-concentric hydrogen-air jet diffusion flame experimentally studied by Takahashi [1]. This test case includes detailed velocity and temperature data for the validation of advanced turbulent combustion models capable of predicting high-order moments: the near-field turbulent structure has been investigated by using conditionally sampled, three-component laser Doppler velocimetry and coherent anti-Stokes Raman spectroscopy. The combustor consists of a central fuel tube (9.45 mm inner diameter, 0.2 mm lip thickness, 806 mm length) and a concentric annulus air tube (26.92 mm inner diameter), centered in a vertical test section ($150 \times 150\text{ mm}^2$ square cross section with rounded corners [quasi-octagonal], 486 mm length), through which external air is supplied. Hydrogen is injected axially.

At first we analyzed from a kinetical point of view by means of SENKIN [4] (a CHEMKIN package, that predicts the time-dependent chemical kinetics behavior of a homogeneous gas mixture in a closed system) three different mechanisms comparing them with a detailed 28 reactions mechanism: a single-step [2], a two-steps [2] and another two steps [3]. To simplify the CFD calculation we assumed the first two global mechanisms, i.e., a single-step and a two-steps [2]. Hydrogen kinetics is relatively simple when compared to that of hydrocarbons.

2 RESULTS

We used a standard industrial flow solver (FLUENT 5) for the simulations. We simulated the burner in 3 – D axisymmetric domain by means of the classical RANS $k - \epsilon$ and LES Smagorinsky [5] models. In the following we show our results obtained with the two different mechanisms chosen, with and without buoyancy effect, and compare them with experimental data.

We adopted the unstructured finite-volume solver, with second-order central differencing for convective momentum fluxes and second-order upwinding for scalar fluxes. The SIMPLE pressure-correction scheme is used for time-advancement; discretization of pressure in the correction step is second-order accurate.

For the RANS simulations we adopted the EDC combustion model [6] and the simple reactions without any modeling for turbulence - chemistry interactions: we did not observe any difference between the two approaches. The temperature field is shown in Fig. 1. The flame is anchored near the fuel tube exit on the air side of the dividing streamline; the predicted maximum temperature is in agreement with the adiabatic flame temperature.

The LES calculation is unsteady but formally 2 – D (to reduce CPU time) and therefore there is no vortex stretching; anyway these results are in agreement with the experimental data. In particular, the models have revealed important aspects of combustion such as effect of heat-release rate, role of buoyancy, and Lewis-number effects during the vortex-flame interactions. Fig 2 shows an instantaneous iso-temperature field evidencing the effect of buoyancy-driven structures. Once a vortex is developed it rolls along the flame surface while it is convected downstream. To compare our unsteady results with the experimental data, we computed ensemble averages of measured quantities. In each situation (different chemistry, with and without buoyancy) the flame base is anchored near the fuel tube exit on the air side (low-velocity region) of the dividing streamline (whose

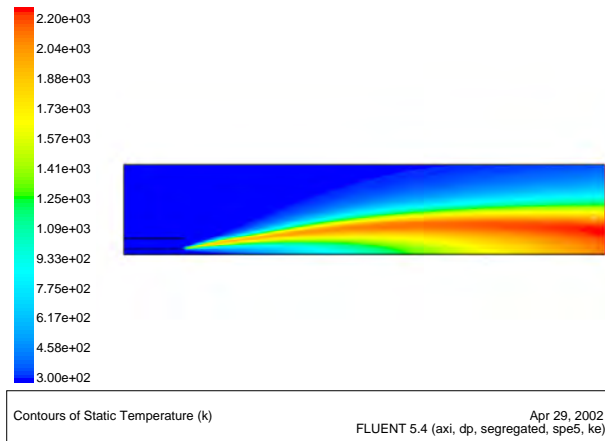


Figure 1: Temperature field for the RANS calculation.

radial distance from the axis: $y \approx 4.7\text{mm}$) as the sharp temperature peaks ($\sim 2000\text{ K}$ at $x = 1.5\text{mm}$, $y = 5$ to 5.5mm) indicate. The maximum temperature region shifts outward and broadens downstream. The rms temperature fluctuation is maximum (up to 900 K for the experimental case) in the outer thermal layer where the mean temperature gradient was large; this maximum is shifted more downstream in the simulations than in the experiments. The results obtained show an excellent agreement with the experimental data available in particular for the LES 1-step with gravity case. In Fig. 4 we compare average temperature, its rms values and axial velocity, of all our simulations with the measured data at one axial location (from the experiment there are seven axial locations, $x = 1.5, 10, 25, 50, 75, 150$ and 225 mm).

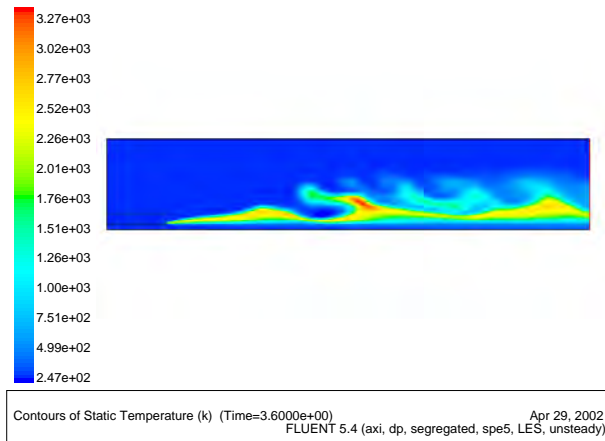


Figure 2: Temperature field for the LES calculation.

The transitional $H_2 - Air$ diffusion flame (see Fig. 2) is subjected to stretch by two types of vortices, one located on the fuel side of the flame and the other on the air side [7, 8]. Both types of vortices create positive (stretch) and negative (compression) stretch regions when interacting with the flame. The flame-stretch factor and temperature at different radial locations are plotted for the outer and inner vortex-flame interactions in Fig. 3. When the outer vortex interacts with the flame, the maximum stretch occurs at a location 25 mm upstream of the vortex center ($z \simeq 175\text{mm}$). The buoyancy-induced vortex in this case develops locally stretched flamelets having a stretch factor up to 210 s^{-1} and compressed flamelets having k as low as 90 s^{-1} ; the flame temperature decreases when the flamelet is stretched and increases when it is compressed. The outer vortex in this flame is associated with the fluid that rotates in the anti-clockwise direction, and induces an axial velocity in the flame zone that decreases with decreasing radial distance. The positive velocity gradient has more effect on the heat transport than on the mass transport in the $H_2 - Air$ diffusion flame that has a Lewis number less than unity on the fuel side. In this case, in fact, we have a Prandtl number of 0.85 and a Schmidt number of 0.7 , so the Lewis number is less than unity. The faster removal of heat from the flame zone, due to this velocity gradient in the stretched flamelet, decreases the flame temperature (Fig. 3) by about 150 K . Since the vortex is on the air-side, the flame has a convex curvature with respect to the incoming fuel. This results in an increased flame temperature in the compressed flamelet due to the fuel coming into the region faster than heat can escape. During the inner vortex-flame interaction, the flame is stretched in the regions where it is pushed radially outward.

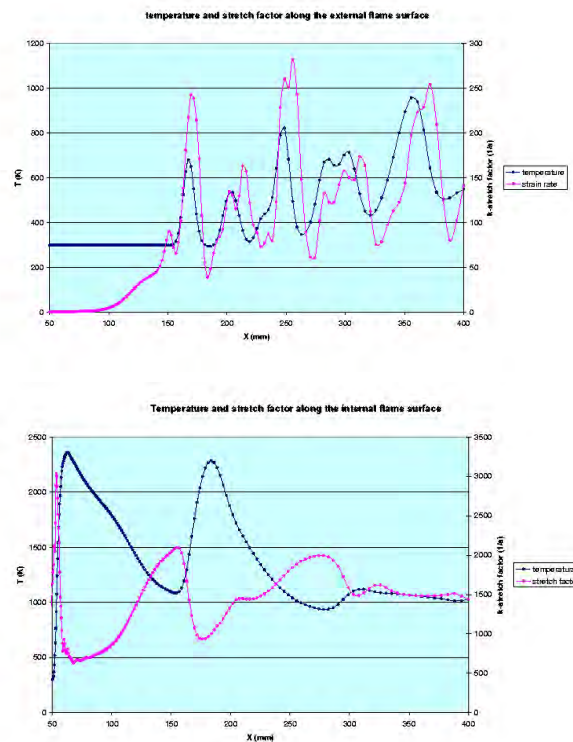


Figure 3: Profiles of the stretching factor and temperature along the flame surface.

When the flame is pulled back in the trailing edge of the vortex, the local flamelet is compressed. Note that the flame stretch is maximum at a location slightly downstream of the vortex center. Flame temperature, which is nearly constant in the steady-state flame, changes with the axial distance during this interaction. In contrast to the results obtained with the outer vortex-flame interaction, when the flame is stretched by the inner vortex, the temperature increases. Similarly, when it is compressed, the flame temperature decreases.

References

- [1] F.Takahashi,M.D.Vangsness,M.D.Durbin,W.J.Schmoll, *Structure of Turbulent Hydrogen Jet Diffusion Flames With or Without Swirl*, University of Dayton, Dayton, 1996
- [2] *FLUENT* (version 5.4), <http://www.fluent.com>
- [3] R.C.Rogers,W.Chinitz, *Using a Global Hydrogen-Air Combustion Model in Turbulent Reacting Flow Calculations*, AIAA 20th Aerospace Sciences Meeting, Orlando, pp. 586-592,1982
- [4] SENKIN, CHEMKIN Collection Release 3.6, SEN-036-1, Reaction Design, 2000
- [5] J. Smagorinsky, *General Circulation Experiments With the Primitive Equations. I. The Basic Experiment*, Monthly Weather Review, vol. 91, pp. 99-164, 1963
- [6] B. F. Magnussen, *The Eddy Dissipation Concept for Turbulent Combustion Modeling. Its Physical and Practical Implications*, Division of Thermodynamics, Norwegian Institute of Technology, N-7034, Trondheim, Norway, October 17, 1989
- [7] P.H.Renard,D.Thevenin,J.C.Rolon,S.Candel, *Dynamics of flame/vortex interactions*, Progress in Energy and Combustion Science, vol. 26, pp. 225-282, 2000
- [8] W.M.Roquemore,V.R.Katta, *Role of Flow Visualization in the Development of UNICORN*, International Conference on Optical Technology and Image Processing in Fluid, Thermal, and Combustion Flow, paper No.KL310, Yokohama,Japan, 1998

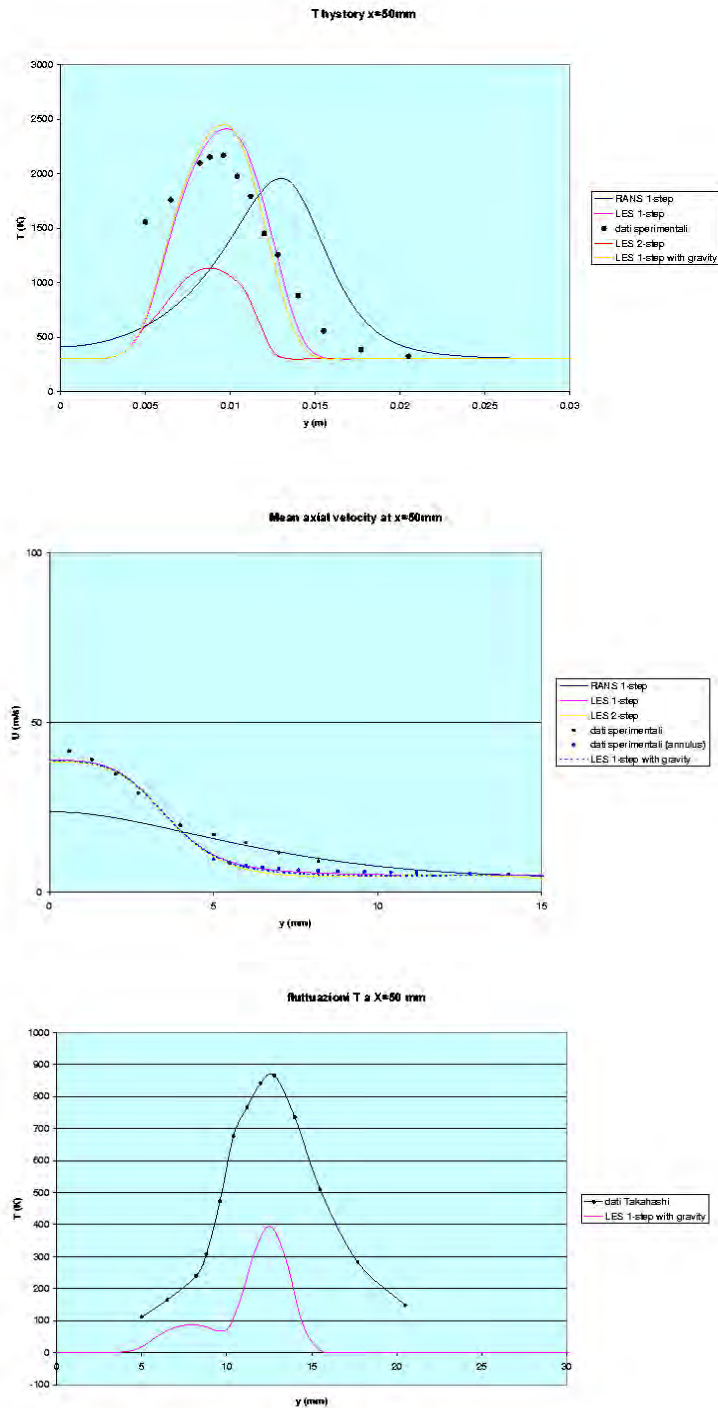


Figure 4: Comparison of radial profiles of temperature, axial velocity and its rms at one axial location.

Study of the stabilising effect of hydrogen in lean premixed combustors

Almerinda Di Benedetto

Istituto Ricerche sulla Combustione – CNR, via Diocleziano, 328, 80124 Napoli – Italy

Phone: [39] 081 7682947, Fax: [39] 081 7622915, e-mail: dibenede@irc.na.cnr.it;

INTRODUCTION

In the last years lean premixed combustion has received great attention as it results in lowering the flame temperature thus reducing NO_x emission. However, at low equivalence ratio values, a loss of stability can occur leading to spontaneous oscillations of temperature and pressure in the combustor. Pressure oscillations can be dangerous because they can lead to mechanical failures and high levels of acoustic noise. Many experimental and theoretical works have been developed in order to identify the physiochemical mechanism responsible for the dynamic behaviour of gas turbine combustors at lean conditions [1-3]. The main issue is to understand if the occurrence of large pressure oscillations experimentally observed in lean premixed combustors are driven unstable by unsteady release of heat and thus related to flame instability (intrinsic instabilities) or whether there is a feedback mechanism between acoustics and heat release from the flame (system instabilities). In a previous paper [4], we have addressed the oscillating heat release from the flame to the presence of heat losses in the combustors and to the reaction rate of the combustion and more specifically, to the positive feedback of temperature on reaction rate coupled with the negative feedback of fuel concentration on reaction rate. We have shown that a very simple model, based only on propane mass and energy balances, is able to simulate the oscillating behaviour. It seems reliable that in the next future biomass or by-products of combined-cycle coal gasification will be a significant source of fuels for gas turbines. Recently experimental runs have been performed in order to test the behaviour of combustors when mixture of hydrogen and hydrocarbons are fed [5]. It has been shown that the presence of hydrogen strongly stabilises the flame during lean combustion. In particular, it has been observed that by increasing hydrogen content in the mixture not only the region of existence of stable steady operating point is increased but also that oscillations are less likely to occur. The present work aims at theoretically studying the influence of hydrogen on both steady and dynamic combustor stability. The stability analysis of the combustor is performed by means of the bifurcation theory carried out by varying the residence time for mixture with different hydrogen contents.

MATHEMATICAL MODEL DEVELOPMENT

The combustor has been modelled as non-adiabatic WSR. The gas behaviour is assumed as ideal. Moreover, one-step reaction rates for both propane and hydrogen have been used. The model equations are the unsteady fuel mass balance and energy balances. They read:

Propane mass balance:

$$dY_p/dt = (Y_{p,in} - Y_p)/\tau - r_p/\rho \quad (1)$$

Hydrogen mass balance:

$$dY_h/dt = (Y_{h,in} - Y_h)/\tau - r_h/\rho \quad (2)$$

Energy balance:

$$dT/dt = C_p (T_{in} - T)/(\tau C_v) + \sum_{i=p,h}(\Delta H_{r,i} - R T) r_i/(\rho C_v) - h a_v (T - T_c)/(\rho C_v) \tag{3}$$

initial conditions:

$$@ t=0 \quad Y_i=Y_i^\circ, T=T^\circ \tag{4}$$

The reaction rate for propane used in the model is a one step kinetic equation evaluated according to Westbrook and Dryer [6]:

$$r_p = (k^\circ/\alpha) \exp(-E_a/R T) Y_p^{0.1} Y_{ox}^{1.65} \rho^{1.75} \tag{5}$$

where $k^\circ=2.8e8 \text{ kg/ m}^3 \text{ s}$; $E_a/R = 15098 \text{ 1/K}$. The reaction rate for hydrogen propane used in the model is a one step kinetic equation evaluated according to Marinov et al. [7]:

$$r_h = (k^\circ/\alpha) \exp(-E_a/R T) Y_h Y_{ox}^{0.5} \rho \tag{6}$$

where $k^\circ=1.8e13 \text{ kg/ m}^3 \text{ s}$; $E_a/R = 17614 \text{ 1/K}$. The parameter α takes into account the effect of microscale mixing limitations. The heat transfer coefficient (h) has been evaluated according to the Dittus-Boleter equation reported in Incropera and DeWitt, [8]. The bifurcation analysis of the proposed model, has been performed by means of the software AUTO97 based on the continuation method [9].

RESULTS

The residence time is assumed as bifurcation parameter. The combustor stability has been studied for the three mixtures reported in table1. The choice of mixture composition has been conducted by ensuring a constant combustor thermal load. In figure 1 the bifurcation diagram for mixture 1 in terms of the combustor dimensionless temperature is shown as function of residence time. The

Table1. Mixtures composition

Mixture	H ₂ (%)	C ₃ H ₈ (%)	Y _{C₃H₈}	y _{H₂}
1	0	100	0.036	0
2	100	0	0	0.014
3	50	50	0.018	0.007

occurrence of an isola with a stable steady state region can be observed besides the non ignited solution that has been omitted for the sake of clarity.

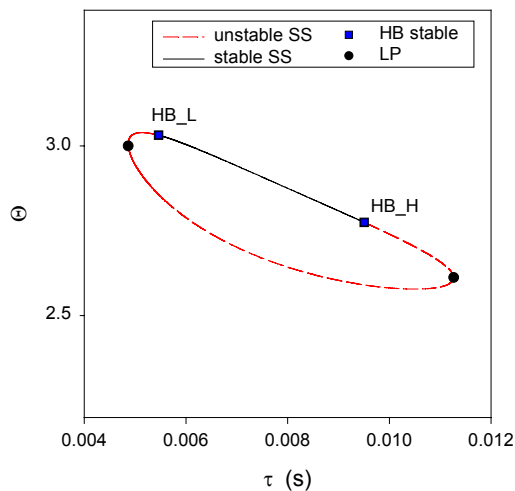


Figure1 –Bifurcation diagram of mixture 1:dimensionless temperature as function of residence time

On the isola extremes, two fold bifurcation points (or limit points, ●) are present. The lower temperature solution of the isola is a saddle point. The range of existence of a stable steady state hot solution extends from the HB_L point ($\tau = 4.86 \text{ ms}$) to the HB_H point ($\tau = 11.26 \text{ ms}$). These points are two stable supercritical Hopf bifurcations from which stable oscillations of temperature and pressure arise.

Blow out occurs when the region of existence of the stable limit cycles vanishes. Same calculations with respect to the dependence from the residence time have been performed for mixtures 2 and 3. In figure 2 the bifurcation diagram is shown for mixture 2, in terms of the combustor dimensionless temperature. The region of existence of a stable steady state point

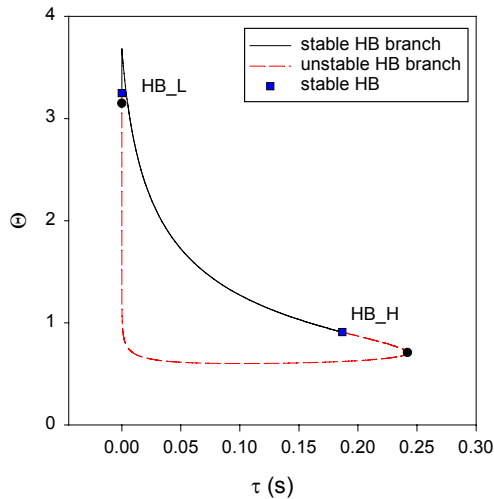


Figure 2 – Bifurcation diagram of mixture 2: dimensionless temperature as function of residence time

not possible in actual conditions. In figure 3 the bifurcation diagram for the mixture of propane and hydrogen (mixture 3) is shown. In this case the region of existence of an ignited solution is larger than the pure propane region (Fig.1) but narrower than the pure hydrogen mixture (Fig.2). Three Hopf bifurcation points (HB_L, HB_M and HB_H) can be detected. The point at low values of the residence time (HB_L, $\tau=8.8e-5s$), is unstable. This point corresponds to the HB_L

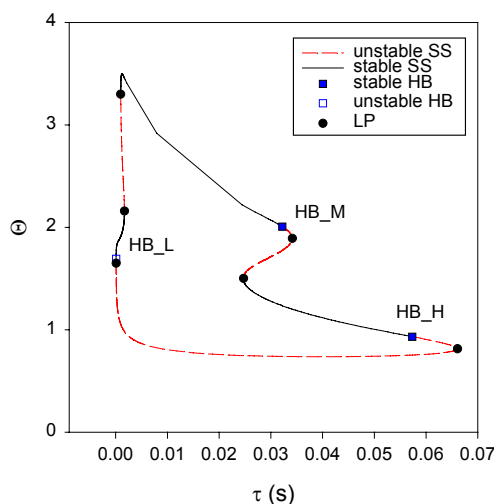


Figure 3 – Bifurcation diagram of mixture 3: dimensionless temperature as function of residence time

point of the pure propane bifurcation diagram (Fig.1). The presence of hydrogen, not only shifts this point to lower values of the residence time but also is able to destabilise it. As a consequence, from this point no stable oscillations are possible. At higher values of the residence time the two Hopf bifurcation points (HB_M and HB_H) are stable and then oscillations may arise. The HB_H point occurs at values of temperature ($T=870K$) and conversion degree ($x=0.015$) far away from the typical values of existing combustors. Point HB_M corresponds to the HB_H point in the pure propane bifurcation diagram (Fig.1). The presence of hydrogen, is able to shift this point at lower temperature (1300K) and higher values of residence time, enlarging the region of stable steady state operating conditions. Near point HB_M an hysteresis behaviour is possible, according to which by increasing the residence time from point HB_M oscillations occur followed by a jump on the lower stable branch of the isola instead of blow out. Comparison of the bifurcation results (Fig.1, 2 and 3) as function of the residence time shows that mixtures 1, 2 and 3 differ in terms of characteristics of the solutions and their stability. At the typical operating conditions, a pure propane mixture can give rise to oscillating behaviour, while pure hydrogen mixture, exhibits only steady state solutions. Mixture 3 has an intermediate behaviour because, differently from the pure hydrogen mixture, it can exhibit stable dynamic regimes but it has a much wider range of stable steady state operation points than pure propane. These results suggest that the presence of hydrogen in the feed mixture could stabilise the combustor in a steady state operating point reducing the possibility of oscillations. Tomczak et al. [5] have performed experimental tests in a gas turbine combustor by using pure methane, pure hydrogen and a mixture of methane and hydrogen (50%) at different

for pure hydrogen is wider than that obtained for pure propane, ranging from $\tau=3.4e-7s$ (HB_L) to $\tau=0.19s$ (HB_H). These points are stable supercritical HB bifurcation (HB_L and HB_H). The HB_H point is not interesting being an operating point characterised by low values of temperature ($T=855K$), far away from typical operating conditions in combustors. The low residence time Hopf bifurcation point (HB_L) occurs at a very low value of the residence time ($\tau=3.4e-7s$), never reached in a real combustor. As a consequence, it is possible to conclude that not only the blow out region is strongly reduced if compared to that one of pure propane but also that when H_2 is used oscillations are not possible in actual conditions.

In figure 3 the bifurcation diagram for the mixture of propane and hydrogen (mixture 3) is shown. In this case the region of existence of an ignited solution is larger than the pure propane region (Fig.1) but narrower than the pure hydrogen mixture (Fig.2). Three Hopf bifurcation points (HB_L, HB_M and HB_H) can be detected. The point at low values of the residence time (HB_L, $\tau=8.8e-5s$), is unstable. This point corresponds to the HB_L point of the pure propane bifurcation diagram (Fig.1). The presence of hydrogen, not only shifts this point to lower values of the residence time but also is able to destabilise it. As a consequence, from this point no stable oscillations are possible. At higher values of the residence time the two Hopf bifurcation points (HB_M and HB_H) are stable and then oscillations may arise. The HB_H point occurs at values of temperature ($T=870K$) and conversion degree ($x=0.015$) far away from the typical values of existing combustors. Point HB_M corresponds to the HB_H point in the pure propane bifurcation diagram (Fig.1). The presence of hydrogen, is able to shift this point at lower temperature (1300K) and higher values of residence time, enlarging the region of stable steady state operating conditions. Near point HB_M an hysteresis behaviour is possible, according to which by increasing the residence time from point HB_M oscillations occur followed by a jump on the lower stable branch of the isola instead of blow out.

values of load. Their results show that the presence of hydrogen in methane strongly reduces amplitudes of the oscillations.

CONCLUSIONS

The stability analysis of a lean premixed combustor for different fuel compositions has been performed by means of the bifurcation theory. The combustor has been modelled as an unsteady well stirred reactor. Three different fuel compositions have been compared and in particular, pure propane, pure hydrogen and a mixture of propane and hydrogen at the same value of thermal load. The results show that propane and hydrogen exhibit significantly different behaviour in terms of both blow-out and dynamic conditions. This behaviour has been addressed to the higher hydrogen reaction rate and wider flammability limits. It is to point out that to simulate the behaviour of a real combustor the effect of non homogeneous spatial distributions of compositions and temperature have certainly to be included. Furthermore, as a consequence of this kinetic instability, acoustic oscillations can also be excited. Therefore, the complete coupling with fluid flow and acoustic is needed in order to perform also a quantitative comparison with the experimental results.

AKNOWLEDGEMENTS

Author wish to express thanks to Dr. F.S. Marra for useful scientific discussions and Prof. G. Russo for his contribution in sustaining my ideas and coaching my work.

REFERENCE

- [1] Richards, G. A., Morris, G. J., Shaw, D.W., Keeley, S.A., and Welter, M. J., *Combust. Sci. Tech.*, 94: 57 (1993)
- [2] Lieuwen, T., Neumeier, Y., and Zinn, B.T., *Combust. Sci. Tech.*, 135:193 (1998)
- [3] Park, S, Annaswamy, A, and Ghoniem, A., *39th AIAA Aerospace Sciences Meeting & Exhibit*, Reno, NV, January, 2001
- [4] Di Benedetto A., Marra F.S. and Russo G., *Mediterranean Symposium on Combustion*, Sharm el Sheikh, January, 2002
- [5] Tomczak H.-J., Benelli, G., Carrai, L., and Cecchini, D., 13th IFRF Member's Conference (2000)
- [6] Westbrook, C. K. and Dryer, F. L., *Combust. Sci. Tech.* 27:31 (1981)
- [7] Marinov, N.M., Westbrook, C.K., and Pitz, W.J., *Transport Phenomena in Combustion*, Volume 1 S. H. Chan edited, Talyor and Francis, Washington, DC, (1996)
- [8] Incropera, F. P. and DeWitt D.; *Fundamentals of Heat and Mass Transfer*. John Wiley & Sons, 1996, p.445.
- [9] Doedel, E.J., Champneys A.R., Fairgrieve T.F., Kuznestov Y.A., Sanstede B., and Wang X., *AUTO97; Continuation and Bifurcation Software for Ordinary Differential Equations* (1997)

Kinetic Modeling of Liquid Fuel Combustion

S. Granata, R. Del Rosso, T. Faravelli, E. Ranzi

Dipartimento di Chimica, Materiali e Ingegneria Chimica-Politecnico di Milano – ITALY

INTRODUCTION

Liquid fuels (gasoline, jet fuels and diesel fuels) are complex chemical mixtures, often containing thousands of compounds. These fuels only meet broadly defined specifications, therefore their composition varies with crude oil source and also with season and year of production. The definition and use of surrogate blends allow the fuel composition to be accurately controlled and monitored, thus providing a model fuel useful for experimental and computational tractability and reproducibility. Surrogates need to meet physical and chemical properties of the real fuel in a given application. As an example, a surrogate blend of 6 pure hydrocarbons is found to adequately simulate the distillation and compositional characteristics of a realistic JP-8 [1].

Liquid fuels are mainly composed of paraffins, naphthenes and aromatics. Dodecane and tetradecane are typical reference components for linear alkanes, while iso-octane is often used as a model component for branched paraffins [2]. Cyclohexane and methyl cyclohexane are assumed as the reference molecules in the cycloalkane fraction while light alkyl-benzenes, such as xylenes, can represent the remaining aromatic fraction.

The detailed kinetic modelling of normal and branched paraffines has already been widely discussed and clarified in recent years, while the behaviour of aromatics and naphthenes, less defined and accurate, should require more attention.

The recent interest in the homogeneous charge compression ignition (HCCI) as a clean and valid alternative to spark ignition (SI) and diesel engine, imposes a deeper understanding of combustion characteristics of liquid fuels, naphthenes in particular because they are critical components for ignition delay times.

PROPERTIES OF LIQUID FUELS

Kerosenes are complex mixtures containing C₉ to C₁₆ hydrocarbons, their composition depends on the crude source and refinery process conditions. The typical distillation range is 145 to 300°C, therefore the boiling points of the carcinogenic 3 to 7 fused-ring polycyclic aromatic hydrocarbons (PAH) are well above this range [3].

The major components of kerosenes are branched and straight chain paraffins and naphthenes (cycloparaffins), these normally account for at least 70 to 80% by volume. Aromatic hydrocarbons, mainly alkylbenzenes and alkyl naphthalenes, do not normally exceed 20-25% by volume. Olefins are not present at more than 5% by volume. In fact, they are undesirable constituents of kerosenes since they are relatively unstable and can cause polymer and gum formation when burnt.

Kerosenes are essentially of two types: straight-run, obtained from crude oil by atmospheric distillation, and cracked, obtained from thermal or catalytic treatment of refinery streams.

The most important use of kerosenes is in blending aviation fuels. Such fuels have demanding specifications, both for civil and military aircraft. Common jet fuels, with a maximum aromatic content of 25% (vol), are:

- Jet A-1 : used in civil aircraft, maximum freezing point -47°C.
- Jet A : similar to Jet A-1, but with maximum freezing point of -40°C (available in North America).

- Jet B : wide cut type, used in civil aircraft, very limited availability.
- AVTAG/JP-4 : wide cut type, used in military aircraft.
- AVCAT/JP-5 : high flash point, used in naval aircraft.
- AVTUR/JP-8 : kerosene type used in military aircraft.

Jet fuels are blends of kerosene streams, sometimes supplemented with naphthas together with low concentrations of additives to improve stability and performance. All jet fuels must be free of contaminants, particularly water and must be pumpable at very low temperatures and stable at higher temperatures. Physical properties and specifications limits of jet fuels are summarized in table 1.

Property	Unit	Method (ASTM)	Jet A Jet A1	Jet B	JP-4	JP-5	JP-8
Distillation range 10% over	°C	D86	205	-	-	205	205
Distillation end point	°C	D86	300	-	270	300	300
Density at 15°C	kg/m ³	D4052	775-840	751-802	751-802	788-845	775-840
Reid vapor pressure at 37.8°C	kPa	D323	-	-	14-21	-	-
Closed cup flash point, min.	°C	D3828	38	-	-	60	38
Kinematic viscosity at -20°C, max.	mm ² /s	D445	8.0	-	-	8.5	8.0
Freezing point, max.	°C	D2386	-40(JetA) -47(JetA1)	-50	-58	-46	-47
Aromatics, max.	% v/v	D1319	25	25	25	25	25

Table 1 Specification limits and properties of typical jet fuels [3].

Gas oils are used primarily in the production of fuels for diesel engines and for both industrial and domestic heating [4]. Also gas oils are complex and variable mixtures of hydrocarbons, predominantly C₁₁ to C₂₅ with boiling temperatures in the range 150-450°C. Chemical composition depends on the nature of the crude and on the refinery processes that they have undergone. Gas oils must meet specifications based on technical performance requirements, their principal uses are: automotive fuels for diesel engines, heating oils, marine fuels. Physical properties of these fuels are given in table 2

Property	Unit	Method (ASTM)	Automotive gas oil	Heating oil	Distillate marine fuel
Boiling range	°C	D86	160-390	160-400	170-420
Kinematic viscosity at 40°C	mm ² /s	D445	2-4.5	2-7.4	1.5-7.4
Flash point, min.	°C	D93	56	56	60
Pour point, max.	°C	D97	-5	0	-6
Density at 15°C	kg/m ³	D1298	820-860	810-900	820-920
Vapor pressure at 40°C	KPa	D2889	ca 0.4	ca 0.4	-
Sulphur max [*]	% m/m	D1552	0.05	0.2	1.5-2.0

* Stricter maximum sulphur limits may apply in some countries.

Table 2 Typical properties of gas oils [4]

Gas oils contain straight and branched chain paraffins, naphthenes and aromatic hydrocarbons and also mixed aromatic cycloalkanes (e.g. indanes and tetraline). Olefins are usually present only in cracked gas oils. Performance requirements for gas oil fuels are defined primarily in terms of physical properties, the sulphur content typically being the only significant compositional parameter. Most commercial gas oils contain also PAH, mainly 2 and 3-ring compounds. The use of heavier atmospheric, vacuum or cracked gas oil components is likely to result in an increase in the content of 4 to 6-ring PAHs, some of which are known to be carcinogenic. Commercially available gas oils may contain low concentrations of performance additives such as flow improvers, corrosion inhibitors, defoamers, dyes/markers, anti-oxidants, stability improvers, cetane improvers, detergents and anti-static additives.

KINETIC MODEL

A large and general semi detailed kinetic scheme of hydrocarbon oxidation was already developed and discussed in earlier works [5]. The scheme uses a simplified description of the primary propagation reactions and primary intermediates for the reference fuels (n-heptane and iso-octane) and then treats the reactions of smaller species with a detailed elementary kinetic scheme. This semi-detailed approach, together with an extensive use of structural analogies and similarities within the different reaction classes, readily accommodates extensions of the kinetic model to different fuels and/or additives. Liquid fuel surrogates are usually defined in terms of a limited number of heavy reference components. On this basis, the extension of the scheme to include heavier paraffines (n-dodecane and n-tetradecane), naphthene reference components (such as cyclohexane and methylcyclohexane) and tetraline ($C_{10}H_{12}$) only required the analysis of their primary propagation reactions [1,6]. In order to show the possibility of the kinetic model, two different mixtures are analysed.

Methyl-cyclohexane/Toluene

The study of these simple blends containing substantial amounts of naphthenes and aromatics constitutes a key step towards the analysis of real fuels. Experimental data of methylcyclohexane (MCH)-toluene blends were obtained by Zeppieri et al.[7], in the Princeton Turbulent Flow Reactor. The model properly predicts the lower reactivity of toluene, both in the case of pure toluene and in the mixtures. As shown in figure 1, MCH conversion correctly decreases due to the addition of toluene; conversely, the mixture's effect increases the toluene reactivity.

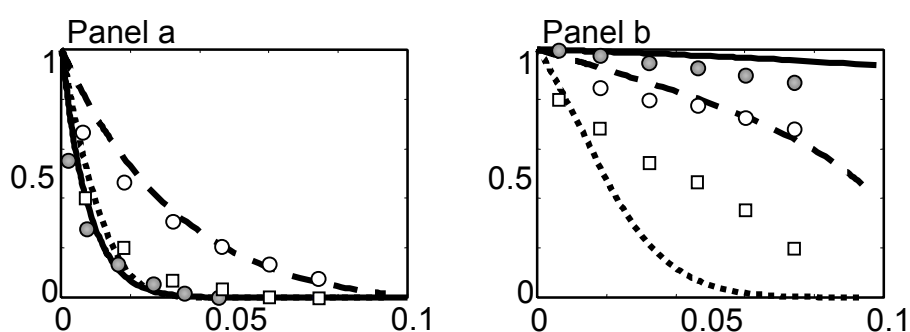


Figure 1 Mixture effect on MCH and Toluene oxidation in PFR at 1160 K; $\Phi=1.3$ [7]
 Normalized mole fractions of MCH (panel a) and Toluene (panel b) as a function of time [s].
 Pure MCH: 1815 ppm and pure Toluene 2559 ppm (solid lines and filled circles)
 Blend: MCH 1229 ppm - Toluene 1475 ppm (dotted lines and squares)
 Blend: MCH 240 ppm - Toluene 2592 ppm (dashed lines and empty circles)

Kerosene

The rich kerosene/O₂/N₂ laminar premixed flame ($\Phi = 1.7$) has been analyzed by Doute' et al.[8]. They report a broad chemical analysis of kerosene. On mole basis, the assumed fuel composition is 73.5 n-dodecane, 5.5 i-octane, 10 MCH, 1 benzene and 10 toluene. As shown in figure 2, the overall agreement between model predictions and experimental data is good. Olefins from C₂ to C₅ are correctly reproduced by the model, while acetylene, ethane and benzene are underestimated.

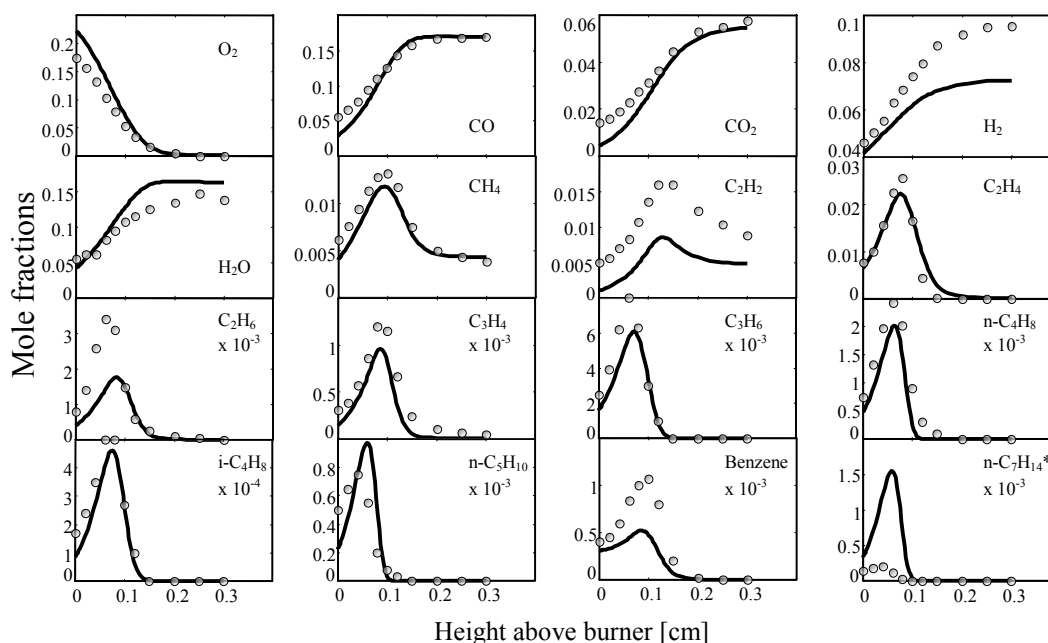


Fig. 2. Experimental (symbols) and predicted (lines) mole fractions of relevant species in a kerosene flame[8]

CONCLUSIONS

Real liquid fuels are complex mixtures of several components. Since they must meet broadly defined specifications, their composition varies not only with refinery source, but also with year of production. Therefore surrogate blends, which reproduce the chemical and physical characteristics of these fuels, are needed for experimental and computational studies. A semi-detailed kinetic model was tested against experimental data of methyl-cyclohexane/toluene mixtures and conventional kerosene giving satisfactory agreement between experimental data and model predictions.

REFERENCES

1. Violi, A., Yan, S., Eddings, E. G., Sarofim, A. F., Granata, S., Faravelli, T., and Ranzi, E., *Second Mediterranean Combustion Symposium*, Sharm El-Sheikh, January 2002
2. Edwards, T., and Maurice, L. Q., *J. of Propulsion & Power* 17:461 (2001).
3. Concaue, *Kerosines/jet fuels*, Report 94-106, (1994).
4. Concaue, *Gas oils (diesel fuels/heating oils)*, Report 95-107, (1995).
5. Ranzi, E., Dente, M., Goldaniga, A., Bozzano, G., and Faravelli, T., *Prog. Energy Combust. Sci.* 27:99 (2001).
6. Granata, S., Faravelli, T., and Ranzi, E 'A Wide Range Kinetic Modeling Study of Pyrolysis and Combustion of Naphthenes' 2002 (Submitted for publication).
7. Zeppieri, S., Brezinsky, K., and Glassman, I., *Combust. Flame* 108:266 (1997).
8. Doute', C., Delfau, J.-L., Akrich, R., and Vovelle, C., *Combust. Sci. Tech.* 106:327 (1995).

Validation of a Discrete Ordinate Flux Method for Design and Performance Prediction of Cylindrical Combustors

M. Filla

Dipartimento di Processi Chimici dell'Ingegneria, Universita' di Padova - ITALY

INTRODUCTION

Flux methods are approximate methods for the solution of the radiative transport equation, the simplifying approximation consisting in the assumption of the angular distribution of the intensity of incident radiation at a point in the medium. A second order partial differential *flux transport* equation is obtained by angular integration over the 2π solid angle centred about the positive and negative direction of each axis for the relevant component of the radiative flux vector, whose spatial distribution remains thus defined by the boundary conditions. A variety of flux methods is encountered in the literature as a consequence of different assumptions of the profile of incident radiation, as well as of different procedures of integration.

The discrete ordinate four-flux method for cylindrical axisymmetric coordinates in object is the present state of refinement of that originally developed in Ref. 1. The validation has been focused on the wall heat flux profiles obtained by assigned temperature distributions in the medium in view of the application to furnace design and performance prediction, where the main objectives are the heat flux profile at tube walls and the temperature of refractory walls. The ranges of absorption thickness and albedo of the radiating medium considered in this validation include any combination of combustion gases with the soot and fly ash content typical of atomized liquid and pulverized fuel flames, and with the dust loads found in the freeboard of fluidized bed combustors and in cement clinker rotary kilns.

GOVERNING EQUATIONS

The flux transport equations of the two components G_z and G_r of the average radiative flux \underline{G} , obtained by angular integration of the radiative transport equation in an absorbing/emitting and isotropically scattering medium of absorbing and scattering coefficients k_a and k_s after assigning our discrete ordinate intensity profile, are:

$$\frac{\partial}{\partial z} \left(\frac{B_z}{k_a} \frac{\partial G_z}{\partial z} \right) = \frac{k_a}{(1-\omega)^2} \Omega_{zz} \left(A_{zz} G_z + A_{zr} G_r - (1-\omega) \frac{2\sigma T^4}{\pi} \right)$$

$$\frac{\partial}{\partial r} \left(\frac{B_r r^2}{rk_a/(1-\omega) + B_r} \frac{\partial G_r}{\partial r} \right) = r \frac{k_a}{1-\omega} \Omega_{rr} \left(A_{rr} G_r + A_{rz} G_z - (1-\omega) \frac{2\sigma T^4}{\pi} \right)$$

where

$$\omega = k_s / (k_a + k_s),$$

$$\begin{aligned}
 A_{zz} &= W_{zz} - \omega(\Omega_{zz}W_{zz} + \Omega_{rz}W_{rz})/\pi, & A_{zr} &= W_{zr} - \omega(\Omega_{zz}W_{zr} + \Omega_{rz}W_{rz})/\pi, \\
 A_{rz} &= W_{rz} - \omega(\Omega_{zz}W_{zz} + \Omega_{rz}W_{rz})/\pi, & A_{rr} &= W_{rr} - \omega(\Omega_{zz}W_{zr} + \Omega_{rz}W_{rz})/\pi, \\
 B_z &= M_{zz}/\Omega_{zz}, & B_r &= M_{rr}/\Omega_{rr},
 \end{aligned}$$

the 2x2 matrices Ω , \mathbf{M} , and $\mathbf{W}(= \mathbf{M}^{-1})$ being functions of the geometry of the elementary volume only [1].

The boundary conditions for the flux transport equations above are:

$$\begin{aligned}
 \partial G_z / \partial z &= \pm \{ [2\varepsilon_{w,i} / (2 - \varepsilon_{w,i})] (G_z - E_{w,i}) \} / \{ 2B_z / [k_a / (1 - \omega)] \} \\
 \partial G_r / \partial r &= - \{ [2\varepsilon_{w,i} / (2 - \varepsilon_{w,i})] (G_r - E_{w,i}) \} / \{ 2B_r r^2 / [rk_a / (1 - \omega)] + B_r \}
 \end{aligned}$$

at walls of blackbody emissive power $E_{w,i}$ and emissivity $\varepsilon_{w,i}$ normal to the axis z and r , and

$$\partial G_r / \partial r = 0$$

on the symmetry axis.

The flux method above has been further extended to take into account the anisotropic scattering of radiation by large particles of a cloud compared to thermal wavelengths by delta-Eddington approximation of the relevant phase function. The rate of radiative heat transfer by such a medium is intermediate between that of the purely absorbing/emitting and of the absorbing/emitting and isotropically scattering medium of the same absorption thickness, as reported in Refs. 2 and 3 for the case of the freeboard of a fluidized bed combustor.

VALIDATION

The dimensionless heat flux at the isothermal black walls of the cylindrical chamber of diameter D and length L filled by a purely absorbing/emitting isothermal medium of absorption coefficient k_a gives the emissivity

$$\varepsilon_G = \varepsilon_G(k_a D, L/D)$$

whose dependence on the absorption thickness of the medium $k_a D$ and aspect ratio of the chamber L/D obtained by the flux method can be visualized in fig. 1. The sensitivity to the aspect ratio is a maximum for media of absorption thickness of the order of unity and tends to vanish in both the thin and thick medium limits. A number of exact values of the emissivity calculated by the zone method [4] are also reported in the Figure for the purpose of comparison. The agreement is particularly good when the absorption thickness is lower than 1., and still good even for large aspect ratios in fairly thick media, where the largest discrepancies occur (-5.2% for $L/D = 5$ and -6.6% for $L/D = 10$).

The results of a more demanding test on the case of a non-isothermal medium exhibiting the initial temperature rise followed by a fall after reaching a maximum, typical of a combustion chamber where the heat release by the flame exceeds the heat absorption by the cold walls up to a distance from the burner end between a half and two thirds of the length, are shown in fig. 2. The temperature profile is reported together with the heat flux profiles at the circumferential cold wall (at temperature $T_w = 500K$) of a furnace of diameter $D = 1m$ and length $L = 6m$ where the exact heat flux profiles have been calculated by Chui

et al. [5] for the three levels of the absorption coefficient $k_a = 0.1, 1., 10. \text{ m}^{-1}$. The comparison with those obtained by the flux method is very good for all values of the absorption coefficient, and hence over the whole range of absorption thickness that may be expected in the combustion chamber when fired by a lean gas flame ($k_a \approx 0.1 \text{ m}^{-1}$) or by a sooty oil or pulverized fuel flame ($k_a = 1. \text{ to } 10. \text{ m}^{-1}$).

The validation has been extended next to scattering media, two-phase media in this instance, such as solid particle laden combustion gases, where the functional dependence of the emissivity in the case of isotropic scattering becomes

$$\varepsilon_G = \varepsilon_G(k_a D, L/D, \omega)$$

the albedo ω being the ratio of the scattering to the extinction coefficient ($\omega = k_s/(k_a+k_s)$). Exact solutions are available in the literature for absorbing/emitting and isotropically scattering media, even if only in the limiting cases where the aspect ratio tends to zero or to infinity. The predictions of the flux method are compared with the exact solutions of Hottel and Sarofim [4] in the $L/D \rightarrow 0$ limit for a plane slab of a purely absorbing/emitting medium in fig. 3 and of an absorbing/emitting and scattering medium in fig. 4. In the first case (fig. 3) the flux method is shown to underestimate the emissivity toward the transparent medium limit, and to overestimate that of intermediate and high absorption thickness media. Quantitatively, the agreement is satisfactory, as the maximum discrepancies do not exceed -7% for $k_a L < 0.3$ and +5% for $k_a L > 0.3$. In the second case (fig. 4) it may be worth noting that the upper limit of the emissivity/absorptivity of an isotropically scattering plane slab is no longer that of the blackbody, but a lower value the higher the albedo, the complement being the reflectivity. The overall trend of the predictions of the flux method is reversed with respect to that observed in purely absorbing/emitting media, in that the emissivity is overestimated for low and intermediate values of the absorption thickness (below 5% for $\omega < 0.7$ and up to 9% for $\omega = 0.9$) and underestimated for thick media (with a maximum discrepancy of -2.7% for $\omega = 0.9$). In the case of the infinite cylinder the exact values of the emissivity of an absorbing/emitting and scattering medium reported in fig. 5 are those calculated by Azad and Modest [6]. The predictions of the flux method are in very good agreement in thin media, as well as over the whole range of absorption thickness for low values of the albedo. The underestimation observed in the range of intermediate and thick media does not exceed 8% even for such considerable scattering levels as $\omega > 0.5$.

CONCLUSIONS

A reliable discrete ordinate four-flux method has been developed for the purpose of design and performance prediction of cylindrical furnaces, in the light of the good agreement found with exact solutions of the radiative transport equation in the validation tests. The adoption of the method can thus be recommended for purely absorbing/emitting combustion products, such as gas species and soot, as well as for cases where the solid particles present in the flue gas reach concentration levels that confer appreciable scattering properties to the two-phase medium.

REFERENCES

1. Scalabrin, A., "Modellistica dello scambio termico per irraggiamento nel freeboard di combustori a letto fluidizzato", *Ph.D. Thesis*, Universita' di Padova, Padova (1995).
2. Filla, M., Scalabrin A. and Tonfoni C., *26th Symposium (Int.) on Combustion*, The Combustion Institute, Pittsburg, 3295 (1996).
3. Filla, M., Scalabrin A. and Bonora, S., *Frantic '97* (20th Annual Meeting of the Italian Section of the Combustion Institute), Chia Laguna (Italy), p. VI-6 (1997).

4. Hottel, H.C. and Sarofim, A.F., *Radiative Transfer*, McGraw-Hill, New York (1967).
5. Chui, E.H., Hughes, P.M. and Raithby, G.D., *Combust. Sci. Technol.*, **92**:225 (1993).
6. Azad, F.H. and Modest, M.F., *J. Heat Transfer*, **103**:350 (1981).

FIGURES

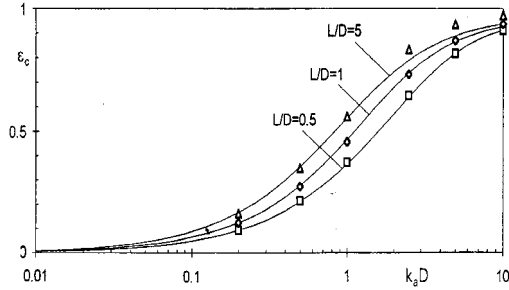


Fig. 1 - Emissivity of an absorbing/emitting cylindrical volume of absorption thickness $k_a D$ and aspect ratio L/D predicted by the flux method (full lines) and exact values [4] (symbols).

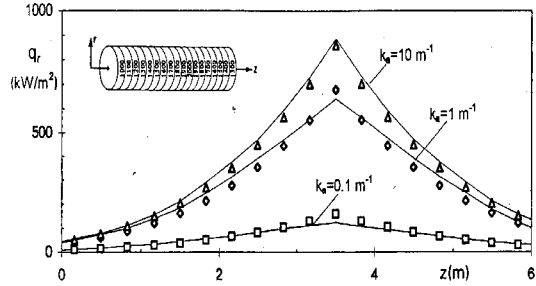


Fig. 2 - Heat flux profiles predicted by the flux method (full lines) and exact values [5] (symbols) at the circumferential wall of a $D=1$ m, $L=6$ m cylindrical chamber filled by a medium of absorption coefficient k_a with the temperature profile shown.

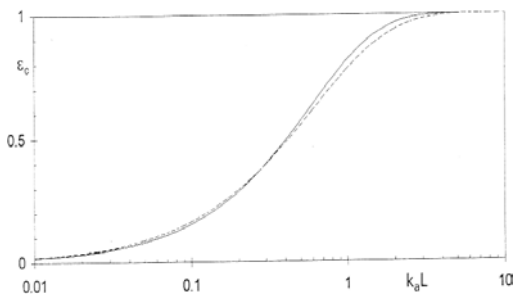


Fig. 3 - Emissivity of a plane slab of an absorbing/emitting medium of absorption thickness $k_a L$ predicted by the flux method (full line) and exact [4] (dotted line).

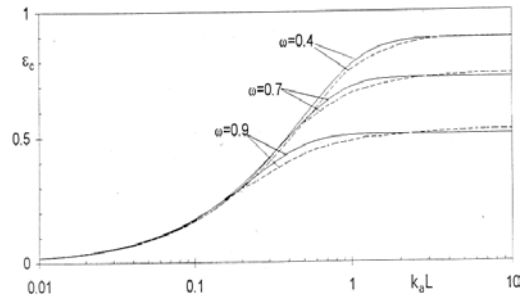


Fig. 4 - Emissivity of a plane slab of an absorbing/emitting and scattering medium of absorption thickness $k_a L$ and albedo ω predicted by the flux method (full lines) and exact [4] (dotted lines).

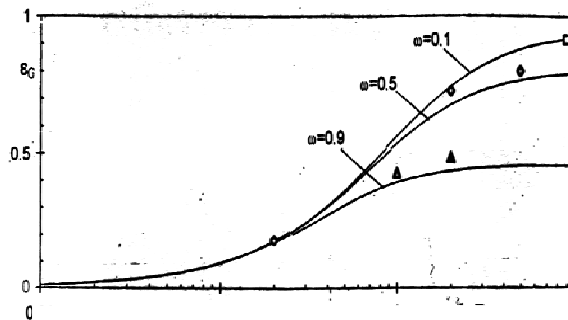


Fig. 5 - Emissivity of an infinite cylinder of an absorbing/emitting and scattering medium of absorption thickness $k_a D$ and albedo ω predicted by the flux method (full lines) and exact values [6] (symbols).

Cooling Control of Hot Exhaust Gases for Low NO₂ Emissions

E. Baraldi, G. Fogliani

Worgas Bruciatori, Formigine (MO) - ITALY

INTRODUCTION

Significant concentrations of NO₂ have been found in the products of range-top burners,¹ because a large proportion of NO is converted to NO₂; besides the final NO₂ concentration is likely to rise through rapid cooling of hot exhaust gases. Since NO₂ is believed to be a greater pollution hazard than NO, the question has some environmental significance especially on unvented gas space heaters because these appliances discharge exhaust gases in domestic environment causing a serious source of indoor pollution especially in the amounts of NO₂. Current research about NO₂ formation on domestic appliances, based on detailed kinetic modelling, indicates that the concentration of both NO₂ and NO fall sharply with increasing air equivalence ratio, λ , under fuel-lean conditions.²

The present paper reports the results of a possible way to reduce NO₂ emissions in the exhaust gases of an unvented room heater. In particular, the effects of the cooling conditions of the hot exhaust gases on NO-NO₂ conversion in unvented gas space heaters are fully investigated with both chemical kinetic calculations and experiments, in order to find a practical way to prevent NO to NO₂ conversion.

MODELLING CALCULATIONS

Natural cooling rate of exhaust gases coming out from the flame with surrounding air at ambient temperature has been modelled with a CFD code (Fluent), as shown in *Fig. 1a*). There are mainly two cooling rate profiles: the central and the lateral one of 20 K/ms and 90 K/ms respectively. To investigate NO to NO₂ conversion during the quenching process of hot combustion gases, the cooling rate profiles, expressed in terms of temperature gradient over time (dT/dt), were given, and the changes of species concentrations with time were calculated by the Chemkin code. The final gas temperature was fixed at 373 K. Twenty-five species and 96 reactions for only C1-chemistry and NO_x mechanisms important for NO₂ formation were considered, and in this study only those extracted from mechanism proposed by Miller & Bowman were used.³ The pressure was fixed at one atmosphere. The initial concentrations of chemical species, except for species containing nitrogen, have been verified to be almost the same as in condition of chemical equilibrium in the adiabatic flame for a methane/air mixture. Indeed we found that, except for the initial NO_x concentration, they exert little influence on important results. Initial NO and NO₂ concentrations were fixed arbitrarily. The total calculation time was fixed at one second, because this is long enough not to affect the results significantly. The degree of NO₂ formation is expressed by a NO₂ conversion ratio:

$$NO_2 [\%] = \frac{NO_2}{NO + N_2O + NO_2} * 100 \quad (1)$$

When exhaust gases are cooled gradually the NO₂ conversion ratio can be kept below 10%, as show in *Fig. 1b*). Thus the cooling rate of free flame in surrounding air should determine NO₂

conversion ratio under 20%, but the NO_2 experimental emissions do not match with this result. Indeed, this slow cooling simulation requires gradual and well controlled cooling, together with equilibrium conditions of heat transfer, but unfortunately the reaction chemistry in the case of combustion and cooling process in an unvented heater is not under equilibrium conditions. Therefore the time evolution of the combustion gases and heat radiative transfer become important in explaining the NO_2 formed by oxidation of NO . Besides commercial unvented heaters have a black internal surface that causes heat losses by exhaust gases.

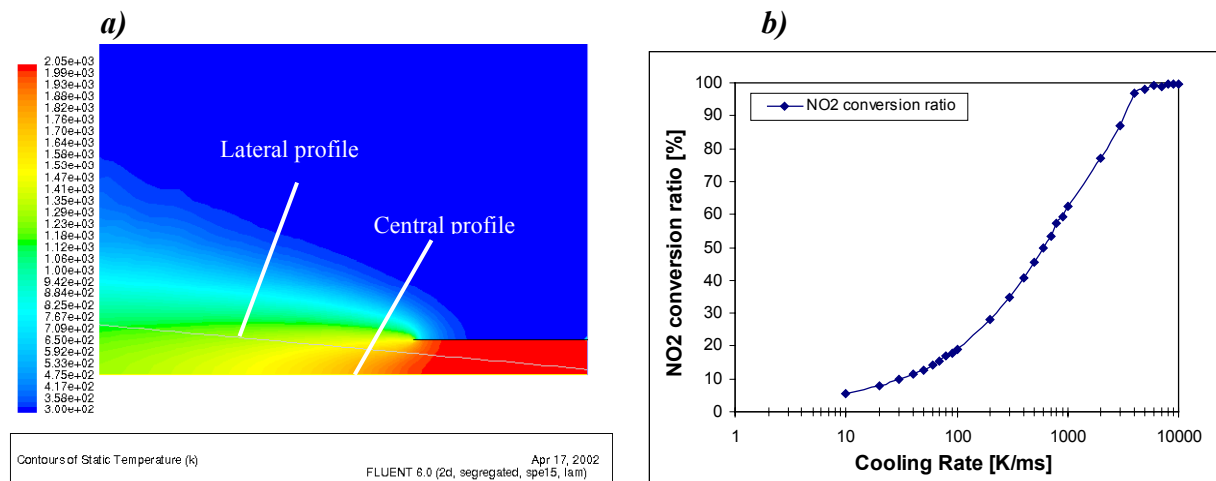


Fig. 1 – a) CFD simulation of exhaust gases coming out from the flame with surrounding air; y -axis = exhaust gases temperature and x -axis = exhaust gases axial position
b) NO_2 conversion ratio as a function of cooling rate of exhaust gases

In order to investigate a more realistic cooling system the effect of surrounding air temperature and consequently the radiative heat transfer are considered. The CFD simulations have proved that for a methane-air mixture the oxygen concentration in secondary air diffusing into the flame is 10%. This result has been used as input datum in Chemkin simulations where the conservation equations have been numerically solved to investigate the influence of unburned hydrocarbon presence and surrounding air temperature on NO to NO_2 conversion in the region where hot burned gases mix with surrounding air. The presence of unburned methane coming out from rich flame has been found to promote the conversion of NO to NO_2 and its conversion ratio NO_2/NO_x increases with increasing unburned methane. The NO_2 formation is instead suppressed by increasing the temperature of surrounding air with or without unburned methane. In Fig. 2a) the NO_2 concentration is expressed as a function of inlet air temperature. The NO_2 conversion passes through a minimum that is a function of air equivalence ratio. Through kinetic analysis we have verified which are the most important reactions in production and destruction mechanism of NO_2 . The NO_2 formation was found to be mostly controlled by the mixing process of hot burned gases with surrounding air and it is also related to the temperature gradient and the concentration of active species such as H , OH , HO_2 and O as well as NO in the burned gas. The NO_2 conversion ratio as a function of NO inlet concentration is shown in Fig. 2b).

Thermal radiation in gaseous media can be an important mode of heat transfer in high temperature chambers.⁴ Thermal radiation affects significantly the structure and extinction characteristics of a methane-air flame due to the radiative cooling mechanism; ignoring radiative transfer may introduce significant errors in the overall predictions. Post-flame radiative cooling has a strong effect in post-flame reactions.

Starting from these results we are developing a combustion system that permits to reduce heat

losses by exhaust gases, to increase a surrounding air temperature and to increase the residence time of exhaust gases at high temperature.

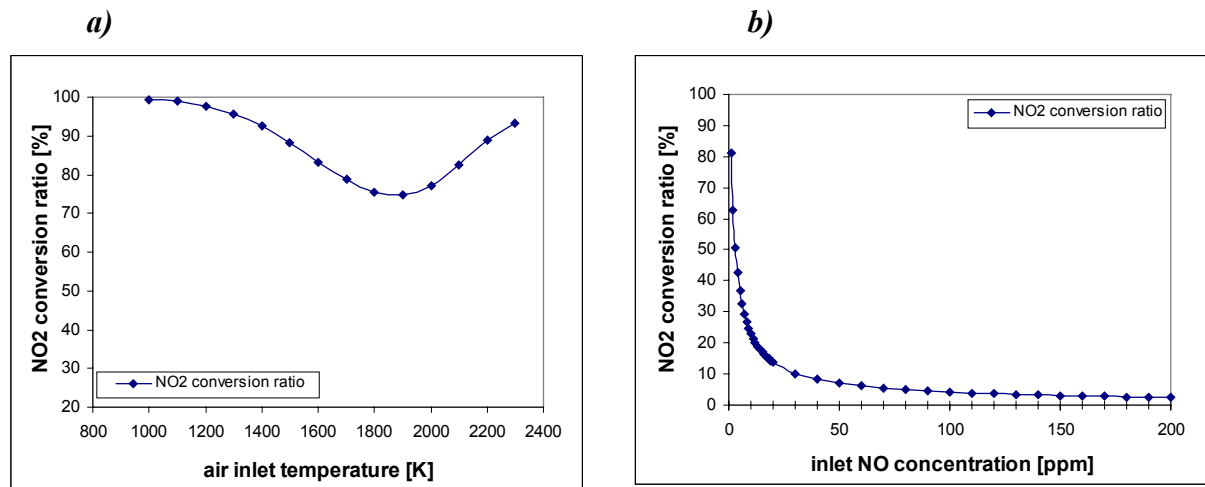


Fig. 2 – a) NO₂ conversion ratio as a function of surrounding air temperature
b) NO₂ conversion ratio as a function of NO inlet concentration

EXPERIMENTAL DETAILS

The experimental tests have been carried out with a modified commercial unvented room heater. Following the guidelines suggested by the simulations as described above, according to which a slow and controlled quenching of exhaust gases reduces the NO₂ formation, we have put inside the unvented heater a Worgas heat exchanger and a Worgas burner. Fig. 3 shows a photo of experimental facilities.



Fig. 3 – Photo of unvented room heater, with Worgas burner and Worgas heat exchanger, under regular hood for measurements according to ANSI standard

The tests have been carried out following the guidelines of the American standard ANSI Z21.11.2. This standard describes also a proposal draft to perform NO₂ emissions'

measurements for unvented room heaters. NO_x and NO concentration were determined in the sample gas by means of a chemiluminescent analyser and NO₂ concentration emissions by an unvented heater burning methane gas is obtained by the difference between the two data. The experimental results with original unvented room heater can provide fundamental data on NO₂ formation levels in combustion systems where the dilution/cooling processes occur. Such a high and rapid dilution of the flue gases with cold ambient air is a typical characteristic for unvented heaters and is mainly useful to cool down hot flue gases to prevent burn hazards for people. The results of the experimental tests are shown in *Table 1*.

Table 1

<i>Input Load 100%</i>	Commercial configuration (without heater exchanger)	Worgas configuration (with heater exchanger)
NO₂ air free [ppm]	33 ± 2	13 ± 2

This heat exchanger realises a NO₂ reduction of about 40% in respect to commercial room heater, confirming our expectation. Thus this is a solution to reduce NO₂ emission in this type of domestic appliances. The NO₂ production is reduced controlling the quenching of hot gases coming out from the flame, or controlling the surrounding air temperature. Thus the Worgas heat exchanger controls the cooling rate of the combustion products, reducing heat losses, and maintains both an appropriate residence time and residence temperature, which result in a reduced conversion of NO to NO₂.

CONCLUSIONS

We see the possibility of developing a Worgas heat exchanger and burner for room heaters to realise low NO₂ conversion controlling the interactions between appliance geometry and hot exhaust gas flux. This paper has emphasised how these results can help designing low NO₂ appliances in reference to ANSI Z21.11.2. To achieve this goal some parameters have been defined to design a heat exchanger that allows low NO₂ emissions in every unvented room heaters. As shown above one effective way of reducing the NO₂ emissions is reached through the use of the Worgas heat exchanger. This exchanger decreases heat losses by exhaust gases and increases the surrounding air temperature which determine low NO₂ conversion ratio. We are developing new Chemkin simulations in order to better understand the relations between the temperature and the diffusion made of secondary air towards the flame and the level of NO₂ concentrations in exhaust gases; we are also checking the effect of radiation. We will verify our results testing new prototypes of heat exchangers with new designs on the same gas room heater.

REFERENCES

1. Johnson, G.M., Smith, M.Y.: *Comb. Science Tech.*, **19**:67 (1978)
2. Baraldi, E., Fogliani, G., Costarella, B., Berthold., G.: *Proceeding of the Event of the Italian Section of the Combustion Institute*, **24**:VI-19 (2001)
3. Miller, J.A., Bowman, C.T.: *Prog. Energy Combust. Sci.*, **15**:287 (1989)
4. Keramida, E.P., Liakos, H.H., Founti, M.A., Boudouvis, A.G., Markatos, N.C., *Int. J. Heat and Mass Transfer*, **43**:1801 (2000)

Characterization of chemical compounds produced in a steam generator tested in reburning conditions

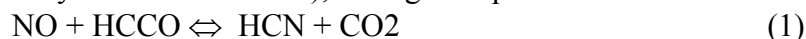
¹E. Ricci, ¹S. Giammartini, ¹C. Benedetti, ¹F. Di Carlo
²A. L'Insalata, ²A. Saponaro, ²L. Fortunato

¹ENEA - C.R. Casaccia - Via Anguillarese 301, 00060 S. Maria di Galeria (RM), Italy
²ANSALDO CALDAIE – Centro Combustione Ambiente – Via Milano km 1.600, 70023 Gioia del Colle (BA), Italy

INTRODUCTION

Reburning technology in combustion consists of a combined air and fuel staging, in which a part of the second one (about 10-20% called primary fuel) is injected over the combustion zone. In this section, called *reburning zone*, reconversion paths of NO to other nitrogenous compounds, such as N₂, NH₃, HCN, are favourite. Secondary fuel can be the same of the primary one, but generally methane is preferred because of his lack in N content. Combustion is completed in *burn-out zone* with an excess of "over-fire air" that determines the oxidation of unreacted species. In this section, HCN, N₂, NH₃ can reconvert to NO, but the total NO_x amount, measured at the stack in reburning conditions, results remarkably less than the one obtained in conventional combustion.

Global mechanism can be subdivided in two steps [1]. In the first one, NO is fastly covered to HCN (thanks to the presence of hydrocarbon radicals), through the paths:



In the second stage, the slower and therefore the limiting one for the process, HCN is transformed in NH_i and then in molecular nitrogen:



Since HCN is the principal product of NO reconversion, a measure of this compound in the reducing zone can be a good index of reburning efficiency.

THE EXPERIMENTAL CAMPAIGN

The experimental tests have been carried out in a steam production plant, which dimensions are: 13 m height, 13 m length and 7 m width. In the furnace body, natural circulation tubes for water vaporization are placed. The most part of the steam produced, at 224°C and 23 kg/cm², with a mass flow of 2.73 kg/s, is conveyed to an air condenser. A minor fraction is employed for atomization of the liquid fuel (with a low sulfur content), preheated at about 100°C.

A number of eight burners, all placed in the frontal part of the furnace, have been used: four MAIN burners (Low-NO_x kind, three swirled coaxial air flows), two reburning burners (RB, with two coaxial swirled ducts), and two overfired air ones (OFA, of the same RB kind with no fuel duct). Combustion products exit from the furnace at a temperature of about 550°C and are carried to a tubular exchanger in which air is preheated up to 290°C. In our tests, flue gases have been recirculated only to the RB burners (with an inlet temperature of about 350°C), while air has been conveyed to MAIN and OFA ones. Experimental campaign has been performed in two phases. In the first one, emissions have been monitored at the stack, while in the second one they have been directly sampled in the furnace body. In the first tests grid, plant operating conditions have been varied in order to find the best configuration, in

terms of the lowest NO_x emissions. Second phase was particularly finalized to an *in-flame* characterization of HCN distribution, after the introduction of air and fuel staging.

Measures collection has been carried out with a FTIR and a Chemical Ionization Mass Spectrometer, available on ENEA Mobile Lab, typically used for *in situ* online analyses.

<i>Mass Spectrometer</i>	<p>HCN</p> <p>VOC: Formaldehyde, Acetaldehyde, Propionaldehyde, Acetone, Crotonaldehyde, Butyraldehyde, Benzene, Toluene, Styrene, O,p-Xylene, Ethylbenzene, Propylbenzene, Ethyltoluene, Mesitylene, Trimethylbenzene, Butylbenzene.</p> <p>PAH: Naphthalene, Fluorene, Anthracene, Phenanthrene, Chrysene, Benzanthracene, Benzopyrene, Benzofluoranthene, Dibenzanthracene, Coronene</p>
<i>FTIR coupled to O₂ and CO₂ detectors</i>	NO, NO ₂ , N ₂ O, SO ₂ , CO, CH ₄ , HCl, HF, NH ₃ , H ₂ O, O ₂ , CO ₂

Tab.1: Chemical equipment employed in the experimental campaign

During the sampling, adduction lines connected with instrumentation were heated and kept at about 180°C, to prevent water and heavy polycyclic hydrocarbons condensation risk.

Emissions online monitoring at the stack

Seven plant configurations, summarized in the following table, have been tested:

<i>Baseline</i>	100% air and fuel to MAIN. No staging
<i>Ofa20%</i>	20% air to OFA, 100% fuel to MAIN
<i>Ofa25%</i>	25% air to OFA, 100% fuel to MAIN
<i>Ofa30%</i>	30% air to OFA, 100% fuel to MAIN
<i>Ofa30%Rb25%</i>	30% air to OFA, 25% fuel to RB
<i>Ofa30%Rb20%</i>	30% air to OFA, 20% fuel to RB
<i>Ofa30%Rb15%</i>	30% air to OFA, 15% fuel to RB

Tab.2: plant configurations tested

Total fuel and air mass flows were respectively 525 kg/h and about 7.5 tons/h. For each plant configuration, the stoichiometric ratio at the reburning zone has been changed by slightly modulating air mass flow to the MAIN and OFA burners. In such a way, the oxygen content at the outlet of flue gas duct has been monitored, until the minimum manageable value has been reached. This value is established as a compromise between the minimum NO_x content at the stack together with an acceptable CO level. PAH, VOC and macro-polluting species such as CO, CO₂, NO_x (calculated as a sum of NO, NO₂ and N₂O and expressed in terms of total N₂O), SO₂, HX (HCl, HF), NH₃ have been monitored for all the plant configurations. All the data have been normalized with respect a 3% oxygen content in the flue gas. Best performances were obtained with Of30%Rb20% configuration, as it can be observed in Fig. 1. For this specific configuration, the most convenient oxygen residual content in the flue gas was about 1.5%, in correspondence of which a NO_x abatement above than 60 % with respect to the Baseline operating conditions was reached (250 mg/Nm³@3%O₂ in comparison with 800 mg/Nm³@3%O₂).

With regard to the other pollutants, the following remarks can be made:

- benzopyrene, benzanthracene, benzofluoranthene and dibenzoanthracene, some of the most dangerous and carcinogenic substances belonging to the PAH group, kept always below the Italian regulation limit [2] of 0.1 mg/Nm³, established for steam generator of 50-500 MWt. No dependence with different plant configurations could be observed, probably because of their high molecular weight which caused them to condense in the flue gas adduction line to mass spectrometer;

- SO₂, HCl and HF kept below the limits respectively of 1700, 100 and 5 mg/Nm³ for all plant configurations;
- NH₃ was never found in the stack emissions;
- The total amount of the principal Volatile Organic Compounds (formaldehyde, acetaldehyde, crotonaldehyde) never went below the fixed limit of 20 mg/Nm³, as the formaldehyde content in the flue gas was always well beyond that value, except for the Baseline configuration, in correspondence of which it wasn't detected.

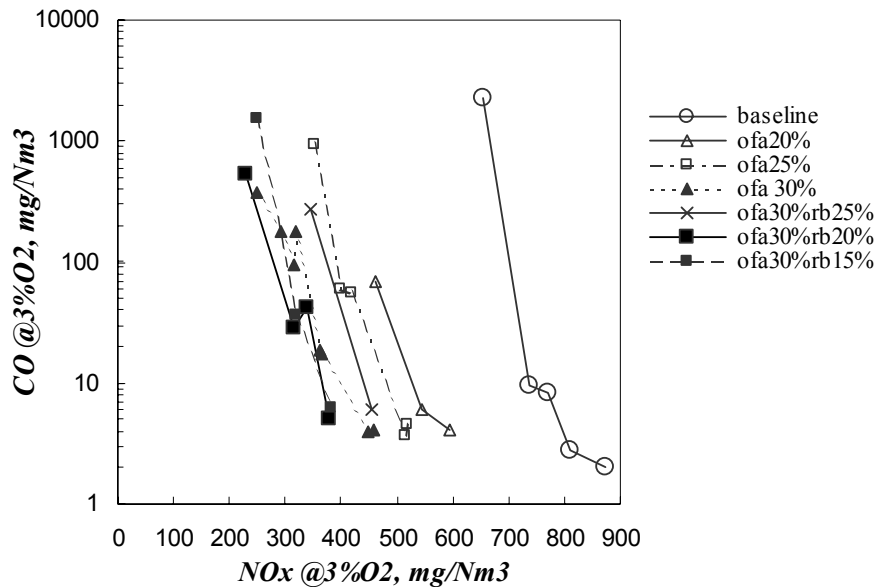


Fig 1: CO vs NOx emissions, for different plant configurations

In particular, it was observed that formaldehyde grew up, according to an exponential trend, with the oxygen residual content and the NO_x amount at the stack.

Such a trend can be explained by supposing that, in the reburning zone, the following reaction rules formaldehyde formation path:



In the burnout zone, the mean residence time is probably not long enough to let the CH₂O reconvert in CO and then CO₂.

In furnace characterization of HCN distribution

For three plant configurations (Baseline, Ofa30%, Ofa30%Rb20%) and 1.3 % residual oxygen content in the flue gas, a test grid has been performed, by sampling the gas inside the furnace body with a water cooled probe, supplied with a Pt/Rh thermocouple and connected to the mass spectrometer for chemical analyzation. HCN concentration was determined in correspondence of 45 points for each configuration, distributed on three rows of three inlet holes for each one (right, central and left sides), and five sinking in every hole.

The rows were placed as follows:

- 4th row: 0.12 m above the MAIN burners axis, at the gas exit from the main zone;
- 6th row: 0.21 m above the RB burners axis, at the gas exit from the reburning zone;
- 10th row: 1m above the OFA burners, at the gas exit from the burnout zone.

For Ofa30%Rb20% plant configuration, the following 'in furnace' distribution of HCN concentration was obtained, in correspondence of the 4th holes row section.

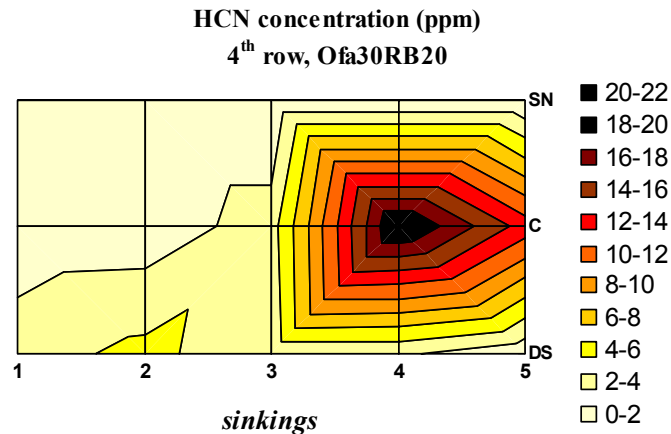


Fig. 2: In furnace HCN distribution: 4th holes section, reburning conditions.

For Baseline and Ofa30% plant configurations, no HCN could be detected.

Moreover, the HCN highest value, obtained in reburning conditions, is about 20 ppm. This result depends on fuel nitrogen content. The maximum is localized in the 4th holes row section that is the nearest one to the reburning zone.

CONCLUSIONS

An experimental campaign on reburning technology application has been carried out at the Ansaldo Caldaie facilities, on a 6MWt steam generator. The plant has been tested in seven different configurations, in order to find the best operating conditions in terms of NO_x reduction at the stack. The optimal ones have proved to be 30% of total air to OFA burners, 20% of total fuel to RB burners, 1.3 % of residual O₂ content in the flue gas.

For this configuration, a NO_x content in the flue gas composition of about 250-300 mg/Nm³@3%O₂ has been obtained, corresponding to an abatement above 60% with respect the Baseline conditions, in which the measured value was 800 mg/Nm³@3%O₂.

PAH, SO₂, NH₃, HCl, HF kept always below the fixed limits of italian regulation, but some troubles were found for VOC pollutants, as formaldehyde [3] exceeded the limit every time that air and fuel staging was introduced.

The second phase of the experimental campaign has been focused on 'in furnace' characterization of HCN distribution, as it represents an important intermediate compound in the reburning mechanism. At this purpose, a grid of sampling has been established, in order to achieve a sufficient amount of points inside the furnace body.

Three experimental configurations have been tested (Baseline, Ofa30% and Ofa30%RB20%), and HCN has been detected only in reburning conditions. A maximum value of 20 ppm has been found in correspondence of the 4th holes row, the nearest one to the reburning zone.

REFERENCES

1. Kilpinen P., Glarborg P., Hupa M. *Ind.Eng.Chem.Res.* **31**: 1477 (1992)
2. DM 12 Luglio 1990: *Linee guida per il contenimento delle emissioni degli impianti industriali e la fissazione dei valori minimi di emissione*. Italian reference regulation.
3. L'Insalata A., Saponaro A. *Atti del XI Congresso Internazionale Biologi*: 167-169 (1998).

LES OF AN INDUSTRIAL BURNER

EUGENIO GIACOMAZZI, GIORGIO CALCHETTI, MARCO RUFOLONI

ENEA - C. R. CASACCIA
SEC. ENE-IMP, S. P. 081
VIA ANGUILLARESE, 301
00060 - S. MARIA DI GALERIA, ROME (ITALY)

Abstract

The aim of the present work is to analyze turbulence - kinetics interaction on a Nuovo Pignone industrial burner, called K120, particularly focusing on the flame stabilization. The burner is fed by a primary jet consisting in a mixture of CH_4/Air , and by a secondary jet of CH_4 . We perform 3 - D Large Eddy Simulations considering both simple mixing and reacting cases. We model turbulence and combustion by means of the Fractal Model (FM) as SGS closure. We assume that chemical reactions take place only at the dissipative scales of turbulence, i.e., near the so called "fine structures" (Eddy Dissipation Concept). FM predicts the growth of the dissipative scales due to the heat release, enabling local DNS in the hot regions of the flow where spatial resolution increases.

THE BURNER

In this work we numerically simulate the DLN-K120 burner, designed by Nuovo Pignone (DLN stands for Dry Low NOx) for a gas turbine [1]. It is a scaled premixed burner. The air enters the burner by means of an annular duct, with a gas flow rate of 76.33 g/s and a velocity of 12.01 m/s. The CH_4 enters from 12 cylinders, located at uniform distance (30 degrees) along a circumference. Each cylinder has six holes with a diameter of 1 mm, three for each side. So the gas is injected perpendicularly to the air flow. There are also 12 blades to swirl the flow, if needed. The mixture enters the combustion chamber at ~ 60 m/s. The combustion chamber is cylindrical, 1 m long, with a diameter of 120 mm. In the wall near the burner head there are also 12 holes, with a diameter of 0.9 mm. By means of these holes some more CH_4 is injected into the combustion chamber with a direction parallel to the chamber axis, resulting in 12 diffusive pilot flames; without these pilot flames the combustion in the burner is unstable, due to the high excess of air (λ can have values from 1.2 to 2.1). The CH_4 flow rate from the pilot holes is normally not above 15% of the total CH_4 flow rate to limit the NOx production; in our case this flow rate is 2.6 g/s (7% of the total CH_4 flow rate); the resulting velocity inlet is 40.17 m/s. The inlet temperature of all reactants is 300 K.

Some measurements have been done in ENEA on this burner: temperature and velocity at four different axial positions, respectively 5, 80, 160 and 450 mm from the burner head. Therefore we compare the experimental data with results of our numerical simulations. We simulated a segment of the combustion chamber, 60 degrees wide, assuming periodic boundary conditions at the side axial planes. A segment of 60 degrees is sufficient to have a computational grid with a good skewness.

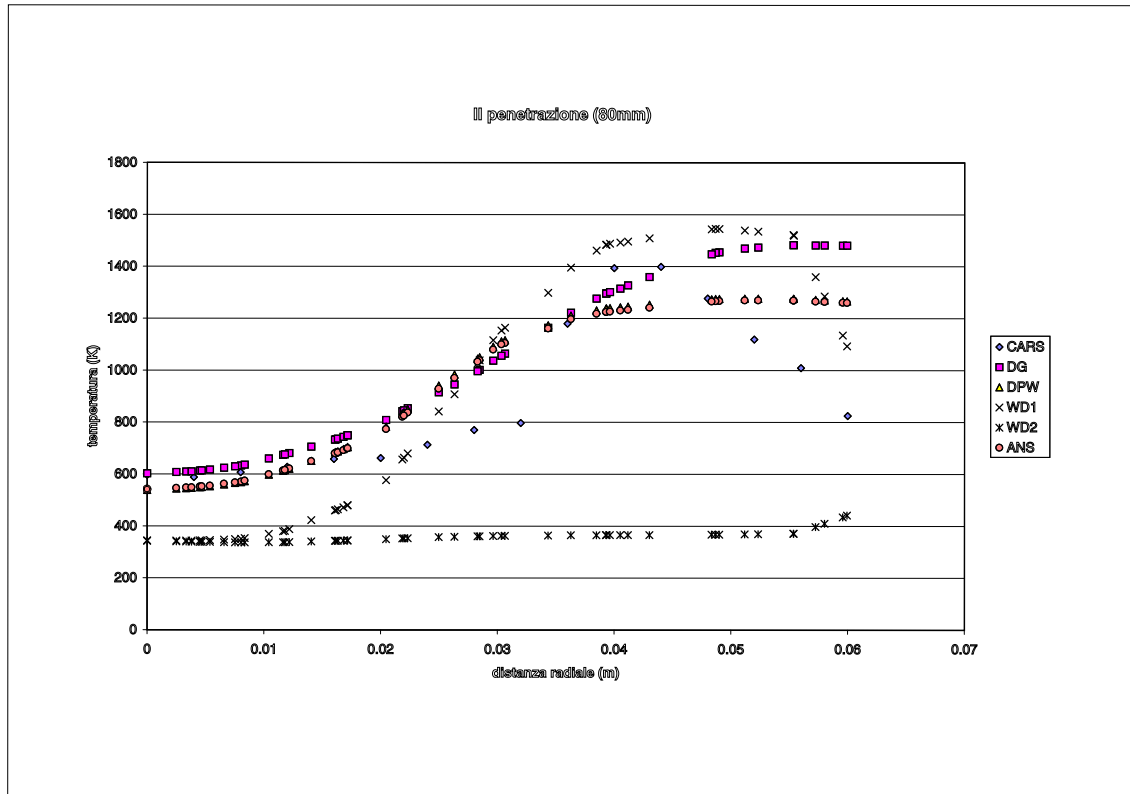


Figure 1: RANS temperature radial profiles at 80 mm from the burner head.

RANS RESULTS

In previous work we simulated [1] the burner by assuming the classical RANS $k - \varepsilon$ model and the Eddy Dissipation Concept [2, 3] to treat turbulence - chemistry interactions. In [1] we adopted five different reaction mechanisms to simulate CH_4 oxidation (in particular WD1 in the figures indicates the one-step global reaction [4]).

In Fig. 1 we compare predicted temperature radial profiles at 80 mm from the burner head with the experimental data. The axial velocity distribution at the same middle plane, is qualitatively in agreement with that of the other RANS simulations; but momentum loss is larger, resulting in a lower maximum axial velocity in the region near the burner head (60 m/s and not 90 m/s as predicted in the other results).

After having compared our predictions with the experimental data at different locations, we conclude that the chemical mechanism that gives results closer to the experimental data is the one-step of Westbrook & Dryer. The velocity field is well predicted, while the other chemical models give unsatisfactory results. The predicted maximum temperature is higher due to the single-step assumed (the other models give more realistic maximum temperatures), but the radial profiles are in good agreement with the experimental ones, showing temperature decreases near the external walls.

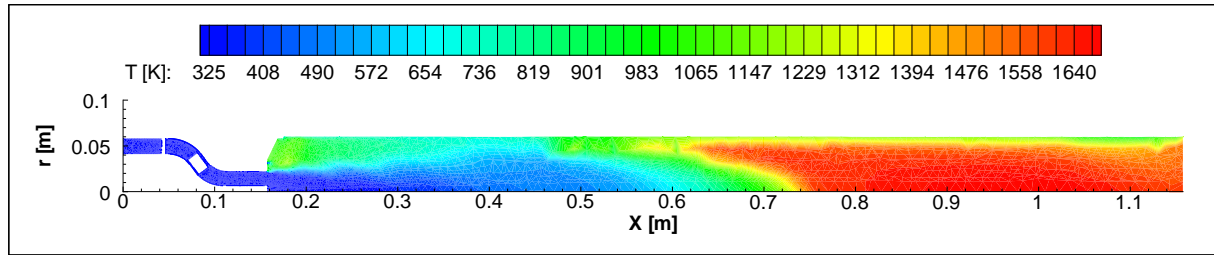


Figure 2: LES instantaneous temperature field for the adiabatic inlet duct case.

LES RESULTS

We have also simulated the burner by using *LES* and the Fractal Model (*FM*) [5, 6] for turbulence and chemical kinetics closures, assuming the same single-step mechanism [4] used in *RANS*. We want to investigate (1.) the unsteady nature of the physico - chemical mechanisms anchoring the premixed turbulent flame, and (2.) the turbulence - heat release coupling. Moreover, we investigate the effect of the main flow temperature at the inlet of the combustion chamber assuming adiabatic walls for the inlet ducts and walls at a fixed temperature (500 K, value derived from the experimental measurements). The different temperature changes combustion characteristics; when the walls are adiabatic the flow enters the chamber at 300 K and therefore the ignition delay time is not short and the flame stabilizes downstream of the step recirculation zone (see Fig. 2); assuming the inlet walls at 500 K, instead, produces a flow with temperature higher than the previous case, reducing the ignition time.

We performed the simulations presented here using a code [7] linked to a subroutine for our *SGS FM*. We adopted a finite-volume scheme, implicit, second order in time, and second order centered in space; the formulation is incompressible. Inlet *BCs* were velocity profiles, temperature and species mass fractions; pressure was extrapolated. Zero gradient was imposed to all variables at the exit. No-slip and zero normal velocity conditions were imposed at the walls; zero gradient to all the other variables; for the walls of the combustion chamber we considered radiative and conductive heat losses to calculate the wall temperature. The computational grid is the same of the *RANS* calculations and has ~ 300000 nodes.

In [5] we proposed a novel turbulence model based on fractal theory (*FM*), later extended to turbulent flames [6, 8]. *FM* is a *SGS* model: it generates a vortex cascade in each cell of a *CFD* domain, starting from the local cell dimension Δ and Reynolds number Re_{Δ} . The cascade ends at the dissipative scale η . We assume reactions take place in the “fine structures” η ; therefore, their state is different from the “filtered” state of the cell. *FM* can predict the growth of the dissipative scale [5] with increasing temperature, sensing the local regime and adapting to it, for instance turning itself off in laminar flow regions.

FM models subgrid stresses by means of an “eddy viscosity” μ_t , that goes automatically to zero in laminar regions and in particular at walls. μ_t is defined by [6]:

$$\mu_t = \sigma \cdot N_{\eta} \cdot \mu = \sigma \cdot \pi^{-2/3} \cdot \frac{u_{\Delta} \Delta}{\nu_{\eta}} \cdot \mu_{\Delta}. \quad (1)$$

where σ is the sole engineering “calibration constant” of the model. In our simulations $\sigma = 0.1$ and $\mu_t = 0$ for $Re_\Delta \leq 7$, because for $Re_\Delta = 7$ the model predicts a fractal dimension $D_3 = 2$, associated to laminar regime.

Combustion chemistry occurs close to dissipation scales. *FM* treats the reactive “fine structures” as a Perfectly Stirred Reactor; this idea is derived from the Eddy Dissipation Concept (*EDC*) of Magnussen and Hjertager [2, 3]. *FM* estimates the volume fraction γ^* occupied by the dissipative structures in each *CFD* cell, by means of

$$\gamma^* = \gamma_{N_\eta} \cdot \left(\frac{\Delta}{\eta} \right)^{D_3-3}. \quad (2)$$

Here γ_{N_η} is the ratio of the number N_η of η scales to the total number of scales generated locally, and D_3 is the local fractal dimension [6]. γ^* must tend to 1 at low Reynolds, because the cell scale Δ becomes then the dissipative scale. The Favre-filtered chemical source terms in the N species equations and in the energy equation are obtained by multiplying the molecular reaction rates inside the reactor times γ^* [6].

References

- [1] G. Calchetti, M. Rufoloni, REPORT ENEA su K120
- [2] B. F. Magnussen, B. H. Hjertager, *XVI Symposium (International) on Combustion*, Proc. The Combustion Institute, 719-729 (1976)
- [3] B. F. Magnussen, “The Eddy Dissipation Concept for Turbulent Combustion Modeling. Its Physical and Practical Implications”, Norwegian Institute of Technology, Division of Thermodynamics, Report N-7034, Trondheim, Norway, 17 October (1989)
- [4] C. K. Westbrook, F. L. Dryer, *Combustion Science and Technology*, 27:31-43 (1981)
- [5] E. Giacomazzi, C. Bruno, B. Favini, *Combustion Theory and Modeling*, 3,4:637-655 (1999)
- [6] E. Giacomazzi, C. Bruno, B. Favini, *Combustion Theory and Modeling*, 4:391-412 (2000)
- [7] *FLUENT* (version 5.4), <http://www.fluent.com>
- [8] E. Giacomazzi, C. Bruno, *XV ISABE Symposium, Joint Propulsion Conference*, Proc. AIAA, paper No. 1144 (2001)

Numerical simulation of strong swirling confined flame by CFD calculation

¹A. Frassoldati, ¹S. Frigerio, ¹T. Faravelli, ²E. Colombo, ²F. Inzoli

1 Dipartimento di Chimica, Materiali e Ingegneria Chimica – Politecnico di Milano – ITALY

2 Dipartimento di Energetica – Politecnico di Milano - ITALY

ABSTRACT

This paper is focused on the characterization of the flow, thermal and concentration species fields for swirled and confined natural gas diffusion flames, comparing different turbulence and combustion models. The experimental work developed within the German TECFLAM cooperation, concerning a swirl burner characterized by 150kW thermal load, 0.8 equivalence ratio, and 0.9 swirl number [1], has been used as reference for the numerical analysis.

The CFD analysis is performed using the commercial code FLUENT6, a multi purpose code based on the finite-volume approach widely used for different technical applications.

INTRODUCTION

The growing attention to the environmental protection is driving the research activity towards new strategies with the goal of minimizing combustion system impact. A promising strategy is represented by the application of a swirled velocity component to the flow. The resulting flame, shorter and with wider radial developments, leads to rapid homogenization of the mixture and stronger stability [2], improving control of the combustion process and minimizing the pollutant production, mainly related to NO_x.

The CFD analysis represents a useful tool to provide preliminary information, even if, due to the rapid changes in both the pressure and the velocity field, an accurate mathematical simulation of such complex flames is difficult, as also recent works have shown [3-5], and is one of the great challenge for modern CFD.

EXPERIMENT

The TECFLAM investigation is focused on a device similar to many combustion systems of practical importance. It consists of a cylindrical water-cooled chamber with an internal diameter $D = 0.5\text{m}$ and a height $L = 1.2\text{m}$, equipped with a swirl burner, which provides the flow with the effective swirl number $S_{\text{eff}} = 0.88$ [4]. The most evident feature of the flow is a recirculating zone close to the fuel inlet, that sustains the entrainment process of the outer stream into the inner one, enhancing the mixing process. The swirled flow field can be divided into three separate zones: the mixing zone between the oxidizer and the fuel streams; the inner recirculating zone; the outer recirculating zone [3].

RESULTS AND DISCUSSION

The simulation developed with FLUENT6 uses a non-uniform unstructured mesh. In particular the analysis is computed over a two-dimensional axial symmetric grid composed by 28000 cells. The grid has been adapted near the inlets and stretched close to the axis (Fig.1), to give high resolution where required and to save the computational effort elsewhere.

The boundary conditions of the inlet velocity assume the profiles experimentally measured at 1 mm below the burner inlet. That allows to further increase the computation accuracy.

In the present study reaction rates are computed from the Arrhenius rate expression and from the eddy dissipation concept of Magnussen and Hjertager either using the 1step or the 2steps combustion models. The Second-Order Upwind Scheme is adopted for the spatial resolution and the SIMPLE algorithm is assumed for the coupling between pressure and velocity [6]. PRESTO algorithm is used for the pressure interpolation at faces, as usually suggested for swirled flows [7]. A steady state simulation is performed. Since the experimental data show that roughly 60% of the thermal power of the flame is lost, thermal radiation is included in the simulation using P1 model, even if the simulations show that radiation does not significantly affect the flow field and the velocity profiles. A two standard equations k-ε model is used to model turbulence, and standard wall functions are used for the wall treatment.

To get the final solution, we adopt a convenient strategy, which can be summarized as in the following. Initial guess of combustion fields is assumed the solution of the isothermal cold conditions. Successively, the reactants are fed at high temperatures (1500K). A continuous method is then used to decrease the temperature down to the real inlet conditions (300K).

The comparison between the numerical and experimental data shows a general good agreement both in the temperature and in the velocity fields as shown by the two temperature maps of Fig.2. Both are characterized by a hot central core from the inlet up to 160-180mm, where the hot intermediate products are transported from the flame, and where the combustion process is completed.

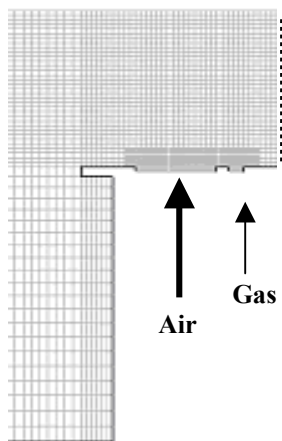


Fig.1 Adapted grid close to the inlets zone.

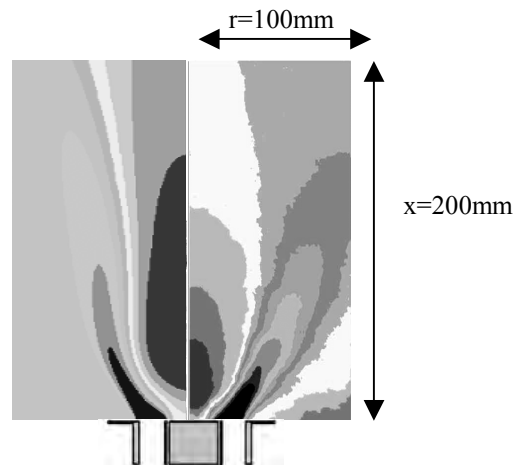


Fig.2 Favre averaged simulation (left side) and experiment (right side).

Mean Flow Fields

The analysis mainly refers to the zone closed to the inlets, characterized by the strong turbulent mixing process and the high degree of combustion intensity. Axial, radial and swirl velocity component are depicted at 10, 30 and 70mm.

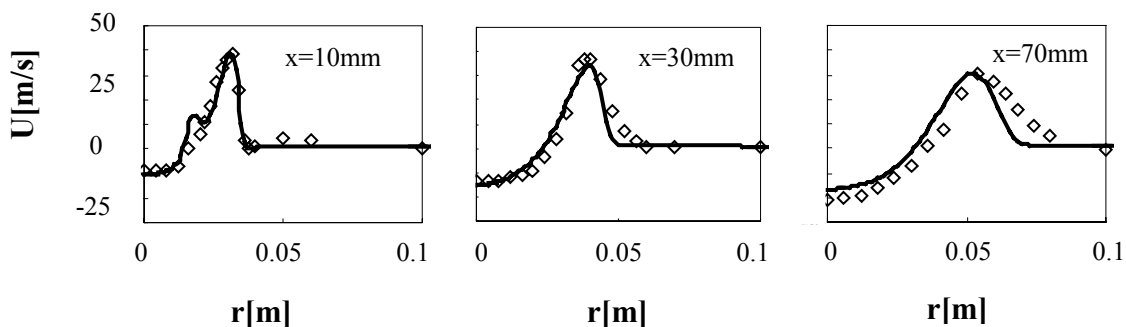


Fig.3 Radial distribution of mean axial velocity U at distance from the inlets (x) = 10, 30, 70mm. (— FLUENT6, ◊ Exp.)

Figure 3 shows the radial development of mean axial velocity U . The presence of the whirling zone near the axis, denoted by the negative values of U , is evident. As expected, diagrams reveal that the recirculation zone is more pronounced in the center of the eddy. The recirculation velocity peaks (-20m/s) in between 60-90mm. The computed U profile fits the experimental one, except in the central recirculating zone where the velocity is slightly underestimated (8%). The radial development of the simulated flame comes out wider, being the peak of the calculated U smaller than the measured, both at 30mm and 70mm. The analysis of the radial velocity V (Fig.4) also confirms the goodness of the prediction.

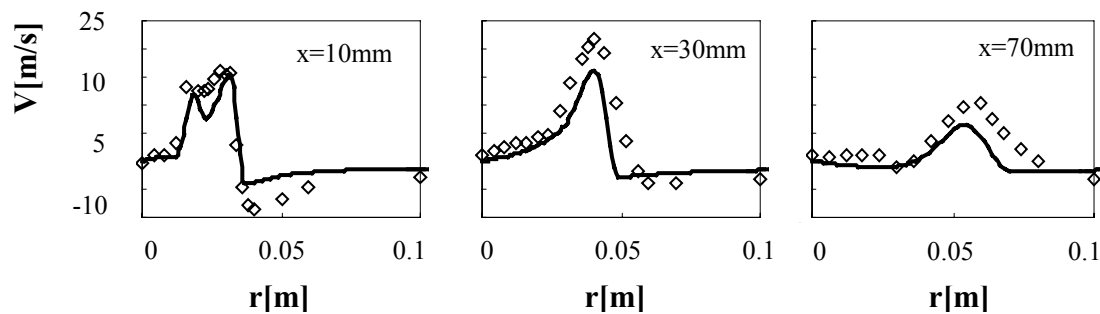


Fig.4 Radial distribution of mean radial velocity V at $x=10, 30, 70\text{mm}$. (—FLUENT6, \diamond Exp.)

The largest deviations from the experimental results are detected in the outer region of the flame ($r > 40\text{mm}$). The negative value of the real velocity is due to the air entrainment coming from the dead space on the back of the burner. The temperature boundary conditions at the wall partially affect these results.

The above considerations are also valid for the W profile. When $r > 40\text{mm}$, the simulated flow shows a more intensive tangential component.

Temperature field and species concentration

From Fig.5 it is evident that the predicted temperature distribution agrees quite well with the experiments (see also Fig.2). The analysis is performed comparing experimental data with the results achieved considering 2steps combustion model even if the 1step combustion model does not change significantly the obtained profiles.

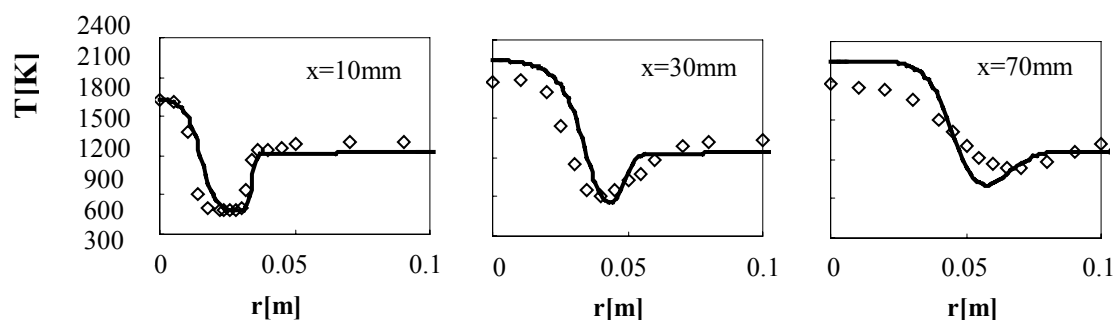


Fig.5 Radial distribution of mean temperature T at $x=10, 40, 90\text{mm}$. (—FLUENT6, \diamond Exp.)

FLUENT6 is able to simulate the inner recirculating zone and the region affected by the reaction. The radial development clearly shows the drop in temperature that underlines the differences of heat level between the first hot region constituted by the reactive mixture and the burnt recirculating gas and the second zone characterized by the air. Remarkable differences from experimental data are relative to the zone closed to the axis for $x > 30\text{mm}$. The simulation overestimates the experimental temperatures, both with 1step and 2steps

model. The simplified reaction model adopted partially explains the observed differences. The experimental data suggest that pyrolysis of CH_4 (to dehydrogenated heavier species) plays an important role at these high temperatures ($T > 1800\text{K}$). The pyrolysis endothermic reactions decrease the temperatures and cannot be simulated either by 1step or 2steps models. This consideration is partially confirmed by CO concentration levels (Fig.7). Experimental

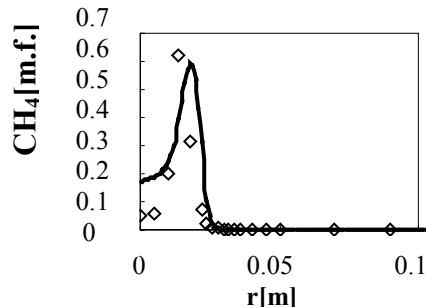


Fig.6 Radial distribution of mean CH_4 mass fraction at $x=10\text{mm}$.
(— FLUENT6, \diamond Exp.)

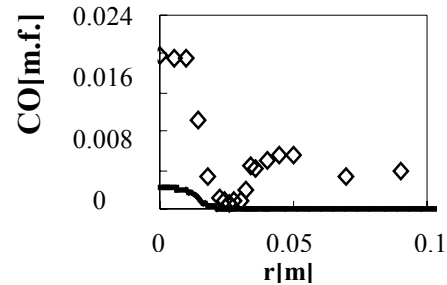


Fig.7 Radial distribution of mean CO mass fraction at $x=10\text{mm}$.
(— FLUENT6, \diamond Exp.)

CO data are strongly higher than simulated, mainly close to the axis. The formation of more reactive hydrocarbons in comparison with CH_4 allows faster oxidations and consequently an enhanced CO formation.

The use of a combustion model limited to 2 reactions comes out as inadequate and further kinetic details are needed to better represent the real temperature and concentration profiles.

Conclusion

The present investigation, developed by using a CFD approach, has shown the capability of FLUENT6 to predict flow and temperature fields of the high swirled TECFLAM flame. In particular the analysis focused on the turbulent mixing zone reveals a good agreement with experimental data. Mass fraction distributions of computed major species do not match the experimental data. The deviations from measured values are due to the simplified combustion model used (either 1step or 2steps). The introduction of more detailed reaction schemes will improve the results and grant reasonable predictions of pollutant formation.

Acknowledgments

This work has been carried out under MURST-COFIN (1999-2001) financial support. The authors acknowledge FLUENT ITALIA for the cooperation and the technical support.

REFERENCES

1. TECFLAM webpage, www.tu-darmstadt.de/fb/mb/ekt/tecflam
2. Antifora A., Coghe A., Faravelli T., Solero G., Ranzi E., Frassoldati A.: *6th Int. Conference on Technologies and Combustion for a Clean Environment*, Oporto (Portugal), July 9-12, 2001.
3. Meier W., Keck O., Noll B., Kunz O., Stricker W.: *Applied Physics B*, 71:725-731 (2000).
4. Landefeld T., Kremer A., Hassel E. P., Janika J., Schäfer T., Kazenwadel J., Shulz C., Wolfrum J., *Proc. Comb. Inst.*, 27:1023 (1998).
5. Repp S., Sadiki A., Schneider C., Hinz A., Landefeld T., Janika J.: *Int. Journal of Heat and Mass transfer*, 45:1271-1285, (2002).
6. Patankar S. V., *Numerical Heat Transfer and Fluid Flow*, (1980).
7. FLUENT6.0 User's Guide.

Comparison between PIV Measurements and CFD Simulation on a Model of GT Annular Burner

D. Giordano, S. Giammartini, M. Rufoloni, G. Calchetti, F. Manfredi,
E. Giacomazzi

*ENEA - Casaccia - Dipartimento di Energia
Via Anguillarese n.301, 00060 Casaccia (Roma), Italy*

ABSTRACT

A model of industrial burner for air breathing engines has been investigated experimentally and numerically. The combustor is formed by an external circular duct (obtained with the overimposition of a diffuser on a circular pipe) and a stabiliser (consisting of an inverted frustum of cone) fixed axially.

Burner shape has been designed to generate an abrupt increase of vorticity along the inner wall of the outletting annular jet. A ring like vortex steady evolves downstream the bluff body as a consequence of the strong velocity gradient of the outletting mixture (methane-air or LPG-air).

Exhaust gasses, coming from annular front flame, evolve in a central counter rotating zone (generated by the annular vortex) and form an "hot bubble" useful for flame stabilization.

A comparison between experimental PIV measurements and numerical calculations (RANS 2D, 3D and LES) allowed us to point out either flame base properties either numerical performances, with a description of GT burner behaviour (from a fluid mechanic, thermal and chemical points of view).

Key words: CFD simulation, PIV measurements, GT burner

INTRODUCTION

Recirculation zone properties, downstream a conical bluff body burner (applied on gas turbines combustion chambers), have been investigated with the joint venture of experimental measurements (PIV and LDA velocities measurements, thermocouples measurements) and numerical evaluations like: Reynolds Average Navier Stoke Simulation (RANS) and 3D Large Eddy Simulation (LES). Ring like vortex (steady evolving downstream an axial bluff body stabiliser) fixes the premixed flame at the burner exit by a maximum Reynolds number of $Re=12000$ and equivalence ratio (ϕ =fuel flow/air flow) changeable in the field $\phi=0.57-1.2$. Experiences showed in the following have been made on methane-air premixed flame with constant regime. This working condition corresponds to low pollutant emissions¹ (low NO_x and limited CO).

To put in evidence different numerical performances we compared the same mean experimental field with RANS and LES results to point out advantages and disadvantages.

EXPERIMENTAL SET-UP

PIV measurements have been acquired by means of the following set-up: CCD camera 484 x 768 pixels; double pulsed Nd:Yag lasers (energy = 300 mJ, wave length = 532 nm); air feeding systems (with Al₂O₃ air seeder); Dantec PIV 2000 cross correlation and synchronisation unit. Flame evolves inside a cylindrical test chamber (diameter = 0,4 m, height = 1,5 m), with a conical upper hood and a perforated base (porosity = 40%) and

outcomes from a conical bluff body burner placed axially 100 mm over the grid above mentioned. Burner quartz is formed by an external 23.4 mm steel pipe and an inner stabiliser formed by a 15 mm frustum of cone¹.

Air and fuel flow in downward the burner, in a premixing cylindrical volume, with a cross flow configuration. Fuel comes from the bottom while four air jets comes from the vertical walls, crossing the fuel axially.

EXPERIMENTAL AND NUMERICAL RESULTS

Experimental measurements have been done with the same $Re = 8000$ and equivalence ratio $\phi = 0,6$ (corresponding to low NO_x emission¹, limited CO production¹ and a steady flame evolution). Velocity field downstream the conical stabiliser shows the evolution of a counter rotating ring vortex (fig.2), where exhaust gasses evolve heating the axial "hot bubble".

This burning regime was chosen for low NO_x and CO emissions^{1,2,3} and steady flame evolution^{4,5}. To obtain a good numerical representation of flow evolution we measured the following boundary conditions: a. turbulence level of the outletting mixture at the burner exit is $u'/U_m = 13\%$ (measured by means of 2D LDA technique); b. mean velocity of the air incoming from the base of the combustion chamber is equal to 0,05 m/s.

To verify flame stability and properties we performed PIV acquisition and two dimensional (chosen for the symmetry of the burner shape) RANS simulations (useful for the rapidity of the result) on the same working regime. Numerical simulation was made without air entrainment from the base of the combustion chamber. The result of was an unsteady flame that burned out fastly (due to oxygen deficiency). As a matter of fact we considered the air entrainment and obtained a steady numerical configuration for flame behaviour. To validate numerical results we closed the base of the combustion chamber and verified the unsteady behaviour of the flame. This confirmed the usefulness of air entrainment for flame feeding and stabilisation (in figure1 there is a scheme of the base of the combustion chamber).

The first comparison between PIV and numerical data showed a great difference. This result was due to the angularity of the outletting mixture, ought to an error of angularity for burner pipe installation. As a consequence, several LDA measurements have been performed on the burner exit to control and optimize the symmetry of air-methane mixture outlet .

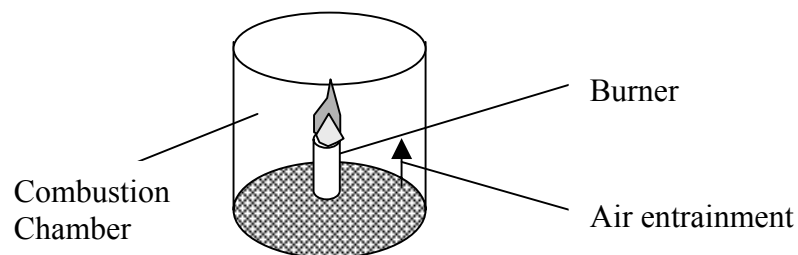


Fig. 1 Scheme of the base of the combustion chamber and entrainment

The final comparison between two and three dimensional RANS evaluation and the experimental mean trend (reported in fig.2 only for the 2D case for the sake of brevity) allowed us to point out the following results for the simulation :

1. Underestimation of the recirculation zone extension;
2. Fast reduction of momentum downstream the ring like vortex, while the real trend shows a annular jet maximum velocity quite constant.

Contrary of the real case this seems to be due to high turbulent viscosity that doesn't decrease with temperature.

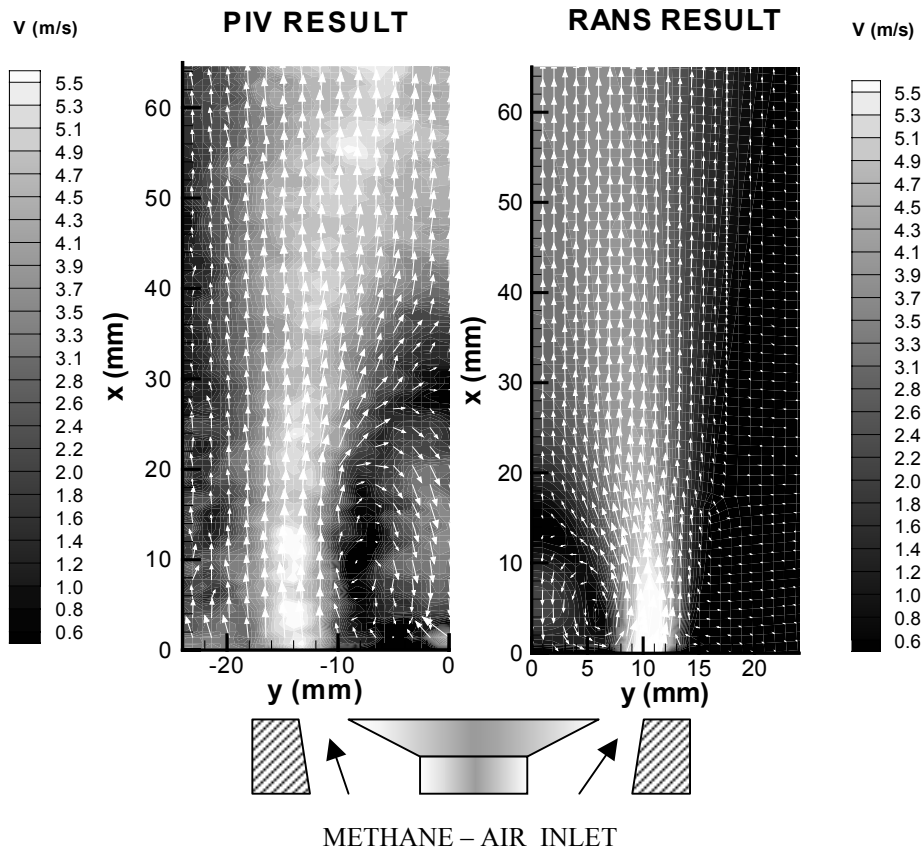


Fig. 2 Comparison between mean velocity field (calculated on the base of 60 PIV samples) and 2D RANS simulation ($Re=8000$, $\phi=0,6$)

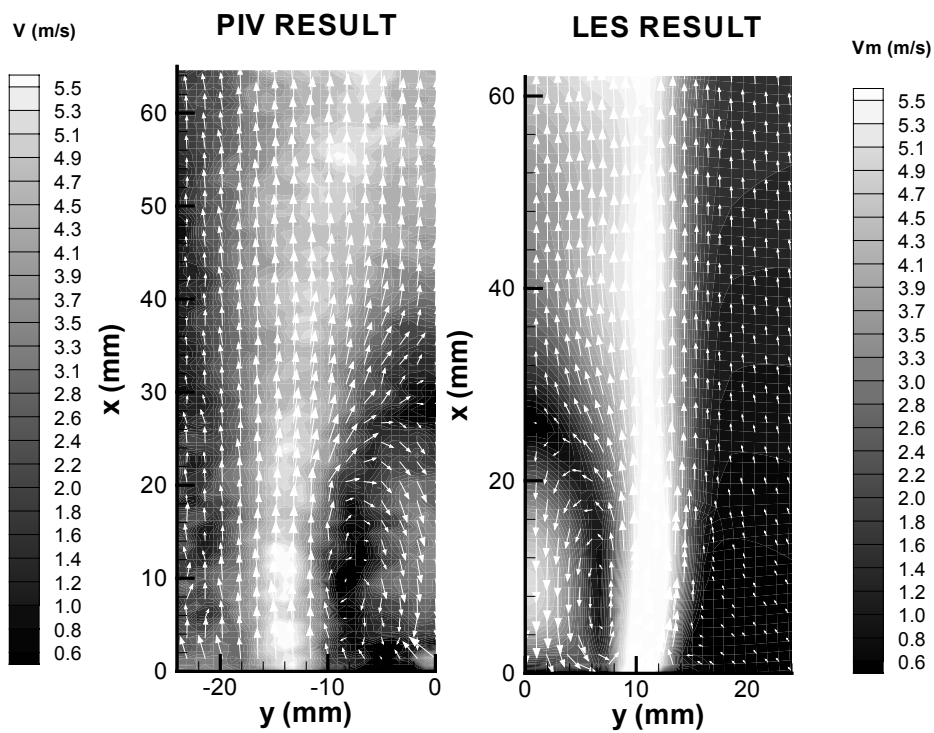


Fig. 3 Comparison between mean velocity field (calculated on the base of 60 PIV samples) and 2D LES simulation ($Re=8000$, $\phi=0,6$)

LES simulation was made in two and three dimension. We succeed to acquire the flame with a 2 D PIV for the symmetry of the phenomenon and the absence of swirl movements of outletting mixture. The comparison between 2D simulation and experimental samples shows a good agreement, even if we do not consider 3D vortex stretching typically considered with LES calculations (fig.3).

This simplification allowed us to obtain the same result of the 3D case but with a lower computational time.

Temperature field obtained with numerical simulation gave a good qualitative representation of temperature variation useful to predict pollutant emissions.

CONCLUDING REMARKS

Annular bluff body burner has been investigated by means of two dimensional PIV technique. Ring vortex rotates downstream the conical stabiliser, forced by burner shape. This recirculation zone creates an hot central volume crossed by exhaust gas. The provisional RANS simulation pointed out the relevancy of air entrainment (from the base of the combustion chamber) for flame oxygen feeding and stabilisation. An improved ventilation system was designed for hook duct to increase air intake downward the combustion chamber.

The comparison between RANS and LES simulation with PIV mean data allowed us to point out high turbulent viscosity of the first code in hot region with an apparent velocity reduction, causing an under estimation of the recirculation zone extension. Greater efficiency of LES simulation allowed us to have a quite good reproduction of the whole field.

Two dimensional application of LES code showed good performances due to the swirl absence. Squishing movements generate a rotation in plane that can be measured with 2D PIV too.

Numerical result for temperature field gave an over estimation of local values especially for hotter regions. The comparison between thermocouples measurements confirmed us the good qualitative representation of numerical result, useful to predict hottest regions (useful for NOx emission control and preview) and to detect ignition zone (useful for flame stabilisation and control).

ACKNOWLEDGMENT

We gratefully acknowledge Prof. F. Gori, Prof. P. Coppa and Prof. G. Bella who allowed us to perform numerical simulations at the University of Rome "Tor Vergata" and for insightful discussion about numerical results. We acknowledge Mrs R. Gallodoro for technical and scientific support.

REFERENCES

1. Giordano D., Giammartini S., Manfredi F.: *Sixth International Conference on Technologies and Combustion for a Clean Environment*, Oporto, Portugal, July, p.1487 (2001)
2. Giordano D., Giammartini S., Giacomazzi E., Manfredi F.: *Combustion and the Environment XXIV Event of The Italian Section of the Combustion Institute*, S. Margherita, Italy, September, p. V.7, (2001)
3. Lefebvre A. H., Ibrahim A. R. A. F. and Benson N. C.: *Combustion and Flames*, **10**, (1966).
4. Lefebvre A. H.: *Gas turbine combustion*, Mc Graw-Hill, New York (1983)
5. Chen R. H., Driscoll J.: *Proceedings of the Combustion Institute*, **22**:531 (1988):

Fluid dynamic and thermal analysis of an industrial gas burner

¹Paolo Gennaro, ²Gianfranco Scribano, ²Luciano Galfetti, ²Aldo Coghe, ²Giulio Solero

1 C.I.T.T. Impianti Srl – Bollate (Mi) – Italy

2 Dipartimento di Energetica, CIIRCO – Politecnico di Milano, Italy

ABSTRACT

This paper deals with the characterization of a natural gas burner used for steel thermal treatment. The burner is equipped with a screw-type swirl generator, providing the rotating motion to the air stream, and with a central fuel injector. The nominal thermal power of the device is 12 kW, with a feeding equivalence ratio equal to 0.85.

The flame generated, due to relative low swirl effect imparted to the air flux, is quite long ($L_{\text{flame}}/D_{\text{efflux}} \approx 10$) and is confined inside a radiant tube. The analysis of the device concerned:

- Velocity measurements by LDV, in order to study the fluid dynamic development of the combustion process;
- Thermal measurements in critical regions both for the flame and the surface of the radiant tube;
- Pollutant emissions (NO_x , CO) at the exhaust, varying the operating conditions of the burner (thermal power and equivalence ratio);
- Comparison between the experimental results and those derived from the numerical simulation of the device.

INTRODUCTION

In this work it has been investigated the flame produced by a burner used in the steel surface treatment industry. The interest of the work lies mainly in the fluid dynamic analysis of the device, characterised by a swirl motion imparted to the air stream. The burner is fed with natural gas and air; hence the major production of NO_x is due to Thermal NO_x and Prompt NO_x [1-2]. The aim of swirl motion is usually to enhance mixing process between the reactants increasing flame stabilization [3], contributing also to a reduction of pollutant emissions such as NO_x and CO. The flame was investigated through Laser Doppler Velocimetry (LDV), thermocouple temperature measurements and pollutant emissions measurements at the exhaust; the data obtained by this study have been compared with the results of numerical simulation performed through a commercial code (Fluent). The aim of the numerical approach is to validate the code, in order to have a useful tool to investigate ways for the burner optimisation.

EXPERIMENTAL SET-UP

Details about the burner analysed in this work are presented in figure 1. In this burner the swirl motion is produced by a screw type swirl generator, with the air flowing through six helicoidal channels, and the natural gas is injected through three apertures on an annular section coaxial with the inner tube. The flame produced is a typical diffusion flame. Centrally to the burner, it has been positioned a premixed pilot flame used to ignite the mixture and to prevent burnout. The combustion process is strictly confined by a flame tube ($D_{\text{tube}}/D_{\text{efflux}} = 1.2$) and the combustion products go backward through an annular enclosure and are used to pre-heat the incoming air stream.

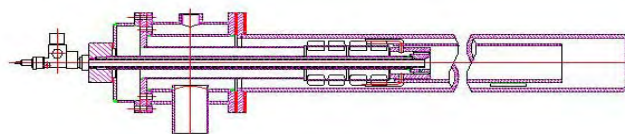


Figure 1: the burner geometry.

The nominal operating conditions of the device are listed in table 1.

	Air	Methane
Efflux Area [mm ²]	350	220
Flow Rate [Nl/min]	240	21.3
Reynolds Number	≈5200	≈500
Swirl Number S	0.85	0
Pilot Burner Flow Rate [Nl/min]	23.8	2.5
Equivalence ratio of the main burner Φ	0.85	

Table 1: burner working parameters.

Temperature and pollutant emissions measurements have been conducted for different input thermal powers (from 10 kW to 16 kW) and equivalence ratio (from 0.7 to 1).

Swirl number of the air flow, defined in [3], has been estimated by integration of axial and tangential velocity radial profiles, measured by LDV in isothermal conditions along the minimum available axial distance from the burner exit (3.5 mm), and resulted equal to 0.85. Further experimental investigations put into evidence that the swirl number is quite constant for different air flow rates in accordance with [4].

LDV measurements were carried out by means of a Argon-ion laser (Spectra Physics) coupled with a transmitting-receiving unit in back-scatter configuration. The Doppler signals were monitored by a BSA unit interfaced with a PC. Tracing particles have been produced by means of sub-micrometric Al₂O₃ powders dispersed in the air flow through a fluidised bed, and the tube used to confine the flame has been replaced by a glass transparent tube. Temperature measurements were performed by a B type thermocouple with a 350 μ m hot junction diameter (results presented have not been corrected for radiative and conductive losses).

Pollutant emissions measurements have been possible by means of a conventional apparatus: measurement techniques are based on chemiluminescence for NO_x analysis, infrared techniques for CO and CO₂, and paramagnetic properties for O₂.

EXPERIMENTAL RESULTS

Due to the complicated geometry of the burner efflux, the axial velocity profile depends on the angular position. This influence disappears at progressive increasing distance h from the burner efflux ($h=6$ mm) and for this reason in this paper are reported the profiles for a fixed angular position. Axial velocity profiles are reported in figure 2 and the tangential velocity profiles in figure 3, at increasing distances h from the efflux. For these measurements the pilot burner has been switched off and the equivalence ratio fed to the device is the nominal value 0.85.

It can be noticed the formation and progressive development of a CTRZ (Central Toroidal Recirculation Zone) characterised by negative values of axial velocity, due to air swirl effect. In the central zone the internal recirculation bubble is disturbed by the presence of a positive velocity region caused both by the high confinement and acceleration effect induced by the combustion process. Figure 3 shows a complex vortical field generated inside the flame tube.

Figure 4 shows a comparison between temperature profiles measured for different equivalence ratio, along the burner axis. For each condition it is possible to notice the presence of a temperature peak and a flat zone subsequent the maximum; the high temperature can be seen as the ignition zone (higher for $\Phi = 0.8$ and $\Phi = 0.85$). It is clearly visible the progressive development of the combustion reaction inside the flame tube at different operating conditions.

In figure 5 are reported the temperature profiles measured on the burner axis for different thermal powers: the temperature peak rises with the thermal power.

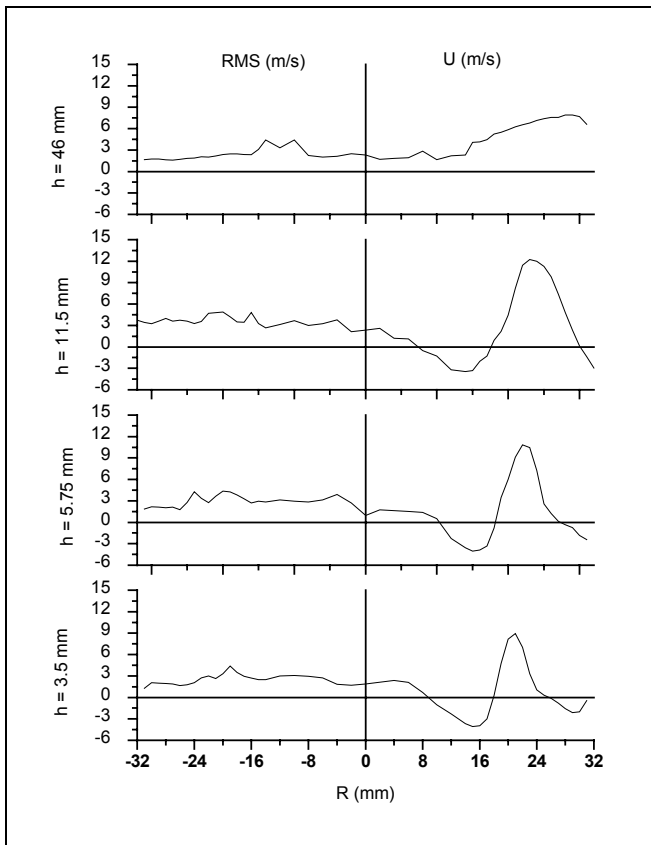


Fig. 2: mean axial velocity and turbulence intensity profile.

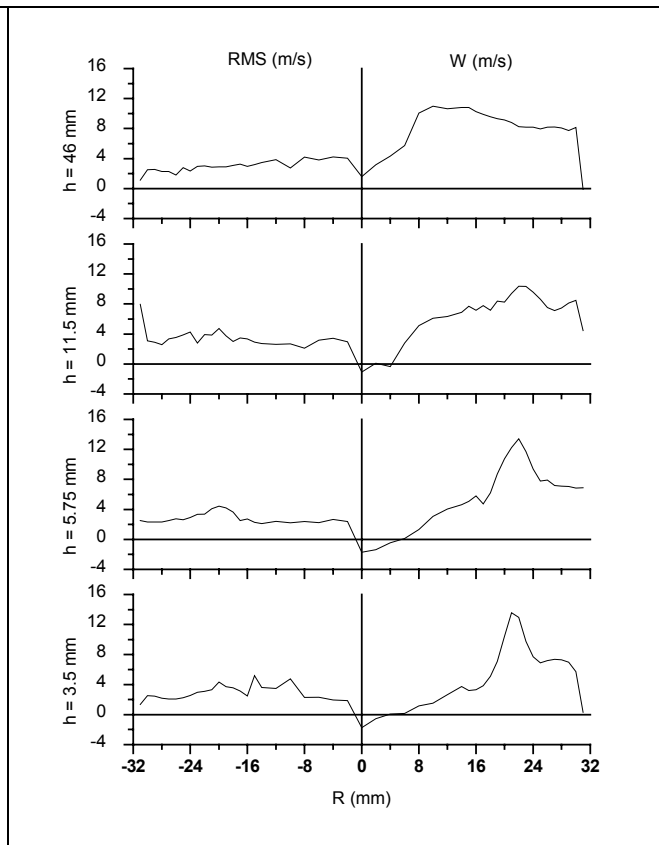


Fig. 3: mean tangential velocity and turbulence intensity profile.

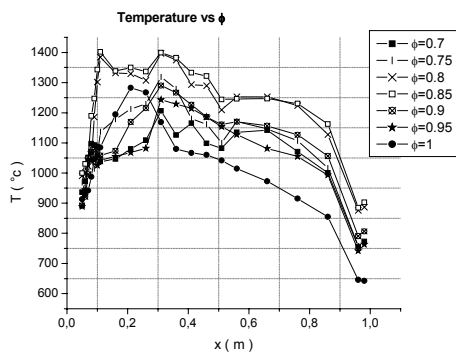


Figure 4: axial temperature profile for different equivalence ratio (Thermal Power=12.8 kW).

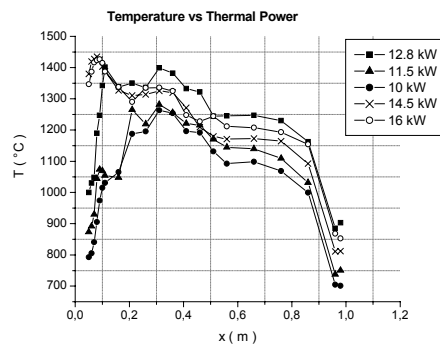


Figure 5: axial temperature profile for different Thermal Power ($\Phi = 0.85$).

Figures 6, 7 report the pollutant emissions measured at the exhaust of the burner. The represented values are CO percentage and NO_x expressed as NO₂ mg/Nm³ 3% O₂ dry basis. The measurements have been carried out for the same thermal power and equivalence ratio of the previous temperature profiles.

The trend shown in figure 6 is in quite good agreement with the temperature profile reported in figure 4: in fact, for equivalence ratio greater that 0.85, CO raises and the temperature decreases, probably owing to an incomplete combustion due to lack of optimal mixing conditions. Figure 7 shows a flat zone for equivalence ratio lower that 0.9 then an abrupt reduction due to the lower temperature caused by incomplete combustion.

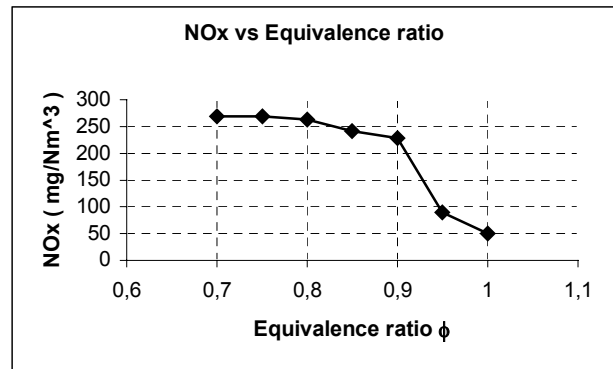
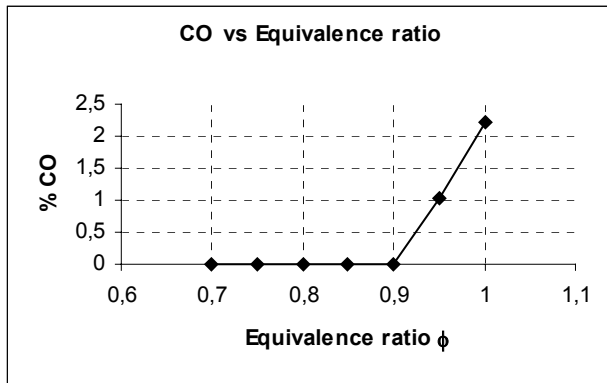


Figure 6: CO emissions for different equivalence ratio Figure 7: NO_x emissions for different E.R. (Thermal Power 12.8 kW).

Finally, Fig. 8 reports the results of preliminary computations relative to cold flow conditions, compared with the experimental data, which allowed the code tuning in term of initial and boundary conditions, mesh size (the best compromise was a mesh of approximately 400000 cells), turbulent model (“ $k-\epsilon$ ”). The conclusion of this first stage in the numerical approach is that the fluid-dynamic field is satisfactorily described.

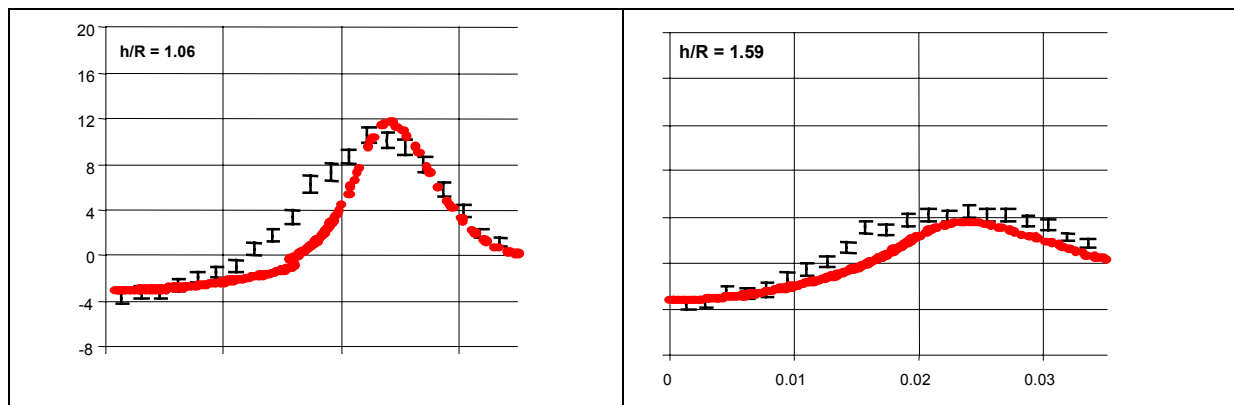


Fig. 8: comparison referred to axial velocity profile at different distances from the efflux between experimental and numerical data.

CONCLUSIONS

It has been performed the analysis (experimental and preliminary numerical) of a natural gas burner used for industrial applications, under different operating conditions (equivalence ratio and input thermal power). Future work will go on with the experimental characterization (probably upon an implemented release of the burner) and numerical simulation in the presence of combustion reactions.

REFERENCES

1. Zel'dovich Ya. B, Sadovnikov P Ya, Frank-Kamenetskii D A. Oxidation of nitrogen in combustion, translated by Shelef M, Academy of Sciences of USSR, 1947.
2. Miller JA, Bowman CT. Prog Energy Combust Sci 1989;15:287–338.
3. Gupta A.K., Lilley D.G., Syred N. (1984): “Swirl flows”, Abacus Press, Tunbridge Wells, 1984.
4. H.J. Sheen, W.J. Chen, s.Y. Jeng, T.L. Huang, “Correlation of Swirl Number for a Radial-Type Swirl Generator”, Experimental Thermal and Fluid Science, 1996.

A swirl natural gas flame as a test-case for experimental analysis and numerical simulation

A. Frassoldati, G. Solero, A. Coghe, T. Faravelli

CIIRCO – Centro Interdipartimentale di Ricerche sulla Combustione - Politecnico di Milano, Italy

ABSTRACT

A swirling natural gas flame has been selected as a test-case for experimental analysis performed by LDV, thin thermocouples and pollutant emissions (NO_x) measurement at the exhaust, comparing the obtained results with those derived from a CFD simulation of the combustion process. The burner under investigation is equipped with an axial + tangential air swirl generator and with a single fuel injector coaxial to the rotating air stream. The flame behavior has been analyzed under different operating conditions, that is varying air swirl number ($S = 0.7 - 0.85$), fuel-air momentum ratio and, consequently, equivalence ratio ($\phi = 0.5 - 0.84$).

INTRODUCTION

Among the methodologies under development to minimize the environmental impact of combustion systems, the most promising are those based on the improvement and optimization of the mixing process between the reactants and cold fresh combustible mixture with hot gas products. It is well known that, independently from the combustion technology used, any improvement of combustion performance relative to pollutant formation, stability and overall efficiency requires a careful study of the mechanism of mixing and entrainment in high turbulent reacting flows, especially in the presence of swirl motion. In fact, swirl is imparted to the air flow in order to increase fuel-air mixing and improve flame stabilization [1].

This paper reports on the main results of the characterization of both isothermal and reactive thermo-fluid dynamic field developed by a natural gas swirl burner, equipped with an axial + tangential entry swirl generator and with fuel injection coaxial to air stream (Fig. 1). This burner has been selected for both experimental analysis and numerical simulation: in fact, it can be observed that the device presents a geometry similar to that ones used in typical industrial appliances, but enough simple to allow a continuous match between experimental data and results from CFD simulations.

The experimental analysis of the device has been performed first in isothermal conditions through non intrusive optical techniques (LDV, PIV) in order to select a set of operative conditions, in terms of air swirl number S , fuel-air momentum ratio MR and, consequently, in order to detect the influence of the over mentioned operative parameters S and MR on the development of the turbulent flow and mixing field, on the generation of CTRZ (Central Toroidal Recirculation Zone) and on the entrainment phenomenon induced by the outflowing jet. Particularly, two values of swirl number S ($0.7 - 0.85$) and three values of fuel-air momentum ratio MR ($0.42 - 0.82 - 1.23$), corresponding respectively to equivalence ratio $0.5 - 0.7 - 0.85$ and input thermal power $12 \text{ kW} - 17 \text{ kW} - 21 \text{ kW}$, have been selected for detailed investigation. The characterization in the presence of combustion reactions has been carried out equipping the burner with a quartz cylindrical combustion chamber and natural

draught hood for continuous burned gases sampling. The analysis covered these points, inside the set of operative conditions identified by the isothermal study:

- Thermal local characterization of the flames through thermocouples. In this case, both shielded and nude junctions for high temperature (Pt-Rh) have been used;
- Measurement by LDV of the reactive flow field in order to analyze the influence of flame development upon the main flow parameters, such as the recirculation region;
- Burned gases sampling and analysis of the pollutant emissions (NO_x, HC and CO). It has to be noticed that the investigated burner is able to work with a stable flame under a high degree of dilution, due to air swirl effect, and with relatively low pollutant emissions (NO_x≈40 mg/Nm³ 3%O₂, CO≈5 mg/Nm³ 3%O₂);

Both in isothermal and hot conditions, a continuous match between experimental results and numerical ones has been performed for validation of the models used for the simulations. The CFD calculations were carried out by the Fluent 6.0 code, using an unstructured grid (about 14000 cells, see Fig. 2), under the hypothesis of axial symmetry. k-ε turbulence model and, in reactive conditions, 1 step kinetics and P1 radiative model have been used for the simulations.

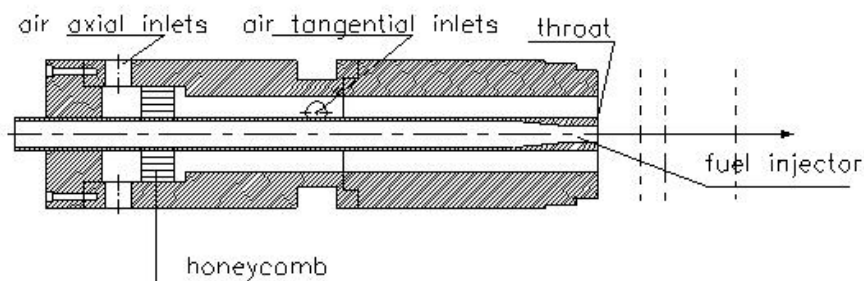


Fig. 1: schematic view of the burner.

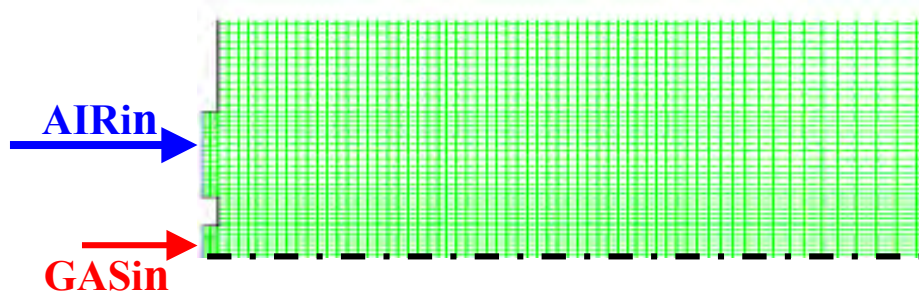


Fig. 2: the computational grid (zoom of the inlet zone).

RESULTS

Isothermal analysis

Figures 3 and 4 show the comparison between experimental results and numerical ones, referred, respectively, to mean axial and swirl velocity radial profiles at a distance from the efflux $x/R=0.16$, in the absence of the central fuel jet (that is $MR=0$). The results confirm a good agreement between experimental and numerical analysis, allowing the code validation.

In fig. 5 are shown the streamlines at different swirl number obtained from the numerical simulation. The formation and development of the central recirculation region (connected to the rotating motion of the air stream) is clearly visible: increase of swirl number induces a radial enlargement of this zone, with a slight influence upon its longitudinal extension. Flow confinement gives rise to a vortical region close to the chamber walls.

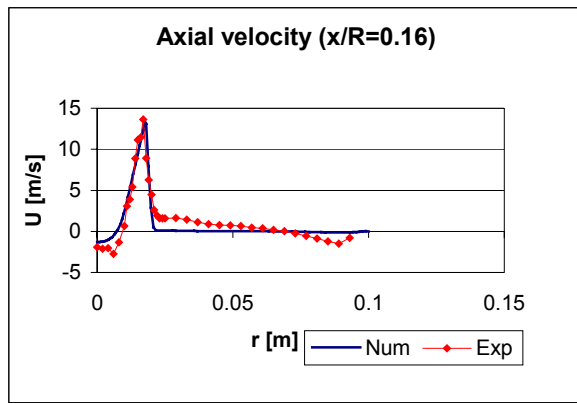


Fig. 3: mean axial velocity profile ($S=0.85$; $MR=0$)

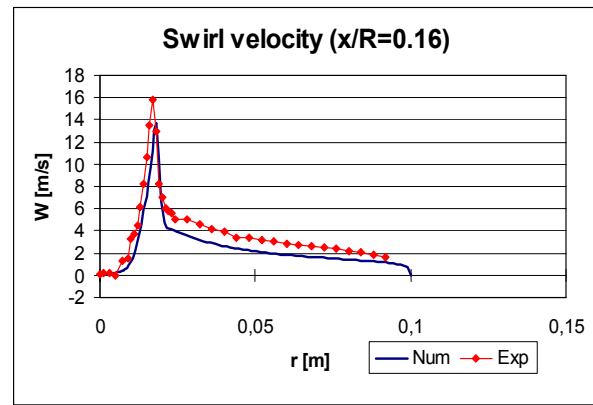


Fig.4: mean swirl velocity profile ($S=0.85$; $MR=0$)

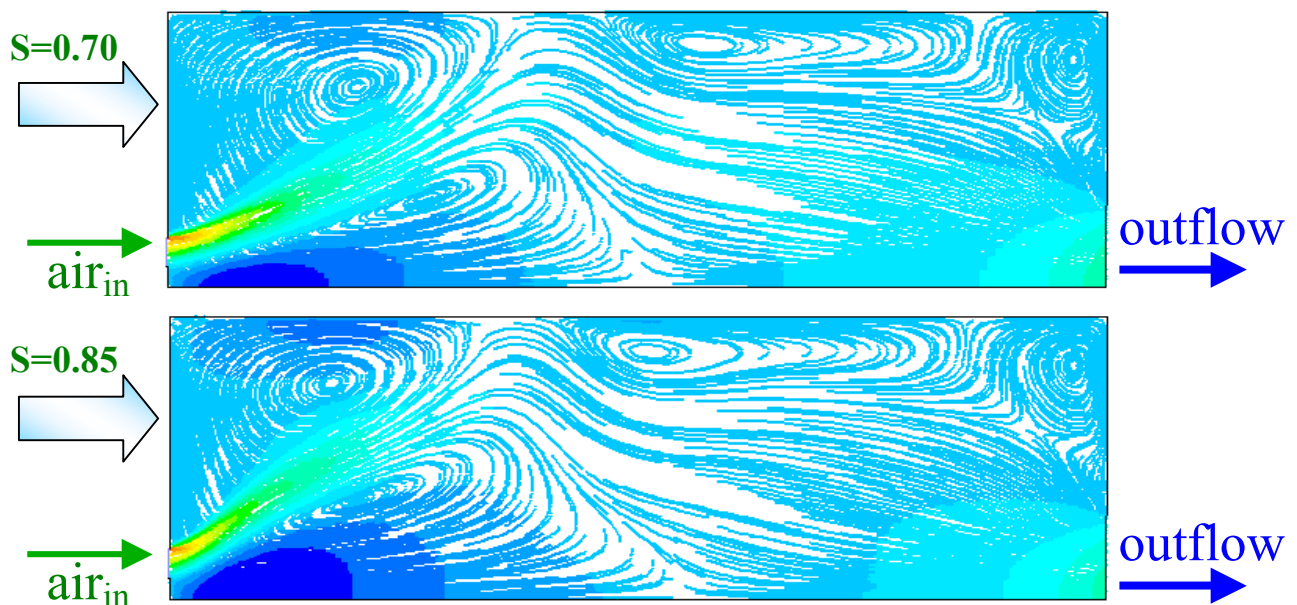


Fig. 5: streamlines at different swirl numbers.

Reactive conditions

Fig. 6 shows a qualitative comparison of the image flame and of the simulated thermal field. Central jet penetration, interaction with parallel swirling air stream and progressive development of the reaction front are clearly visible from the computations and comparable to flame visualization.

Fig. 7 is referred to a quantitative comparison between computed and measured temperature profile, at a distance $x/R=7$ from the efflux. In this case too, the agreement between the two techniques is good, almost in a traverse quite downstream the flame development.

Finally, fig. 8 reports the values of nitric oxide emissions (expressed as $\text{mgNO}_2/\text{Nm}^3$, 3% O_2) measured at different swirl numbers and equivalence ratio. It can be noticed that NO_x formation is more sensitive to swirl intensity rather than equivalence ratio. In fact, swirl effect presents a great influence upon the main features (stability, flow field, mixing process and, consequently, pollutant emissions) of a typical diffusion flame like that one under analysis. In any case, NO_x emissions are quite low (under $100 \text{ mgNO}_2/\text{Nm}^3$).

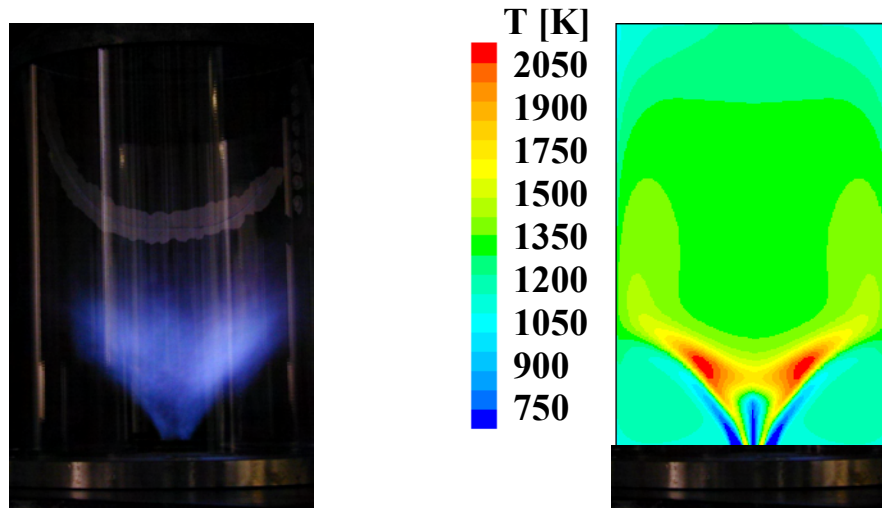


Fig. 6: comparison of flame image and simulated thermal field ($S=0.7$; $MR=0.42$, $\Phi=0.5$).

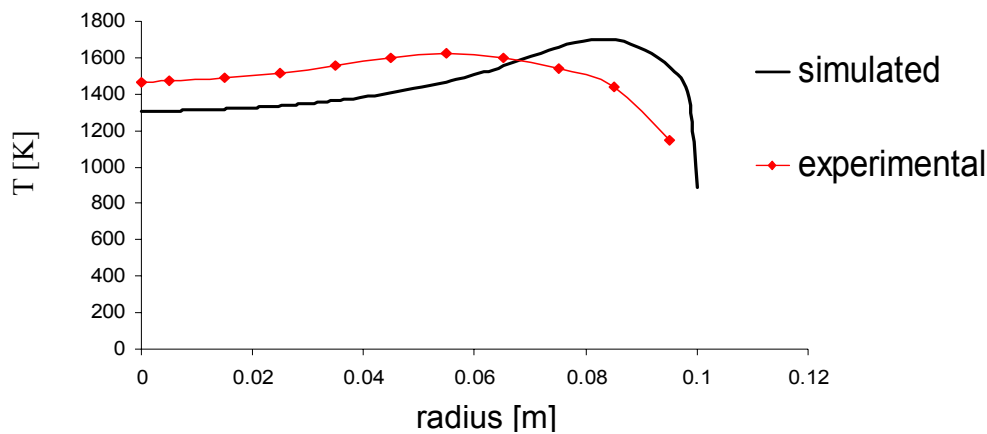


Fig. 7: mean temperature profile along a traverse at $x/R=7$ from the efflux.

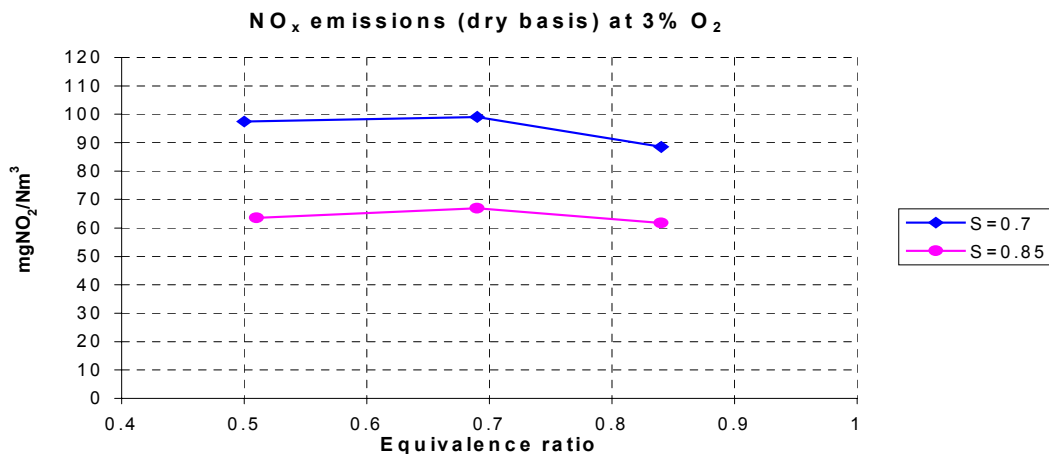


Fig. 8: NO_x emissions as a function of air swirl number and equivalence ratio ϕ .

CONCLUSIONS

Thermo-fluid dynamic experimental analysis upon the device allowed the achievement of a wide data-base for validation of numerical simulations, turbulence and reactive models.

REFERENCES

[1] Gupta A. K., Lilley D. G., Syred N., *Swirl flows*, Abacus Press, Tunbridge Wells, 1984.

Analysis and prediction of flash-back in premix porous burners for domestic appliances

Massimo Bizzi, Guido Saracco*, Vito Specchia

*Dipartimento di Scienza dei Materiali ed Ingegneria Chimica,
Politecnico di Torino, Corso Duca degli Abruzzi 24, 10129 Torino, Italy.*

** corresponding author: tel./fax: +39-011-5644654/99; e-mail: saracco@polito.it*

INTRODUCTION

Premixed radiant burners fed with natural gas or LPG offer superior performance compared to traditional diffusive-type ones in terms of thermal efficiency, environmental impact, and design flexibility [1]. Due to the considerable heat exchange between the gas and the porous medium, lower flame temperatures can be achieved, thus allowing a remarkable reduction of the NO_x emissions. The design of these devices may be approached by making more compact geometries of the combustion chamber and of the heat exchanger, and burners can be operated firing upwards, downwards or sideways, as opposite to diffusive-type ones. Moreover, the system can be operated at lower excesses of air, thus promoting high flue gas temperatures. This improves in turn the performance of the heat exchanger, due to the increment in the driving force of the heat transfer process, resulting in enhanced thermal efficiency.

However, these devices might suffer from serious flame stability problems typically associated with the occurrence of flashback phenomena, which take place as the result of the gas feedstock pre-heating. Once the flame front is stabilized at least in part within the porous medium, the upstream surface of the porous matrix reaches relatively high temperatures due to back-transfer of heat. Radiation of energy in the upstream direction determines a broad increase of the plenum chamber temperature which entails, in turn, a pre-heating of the gas stream entering the combustion system. Therefore, the flame front moves upstream within the porous medium, as a result of the increased inlet gas temperature that enhances chemical reactivity. This determines a further increase in the upstream surface temperature and in the upstream energy flux by radiation, eventually promoting the reactants ignition ahead of the porous medium (flashback).

In order to enhance the system performance and safety, an improved understanding of the principles governing radiant premixed burners has become imperative and extensive modelling activities were carried out for this purpose [2]. This paper presents a model of metal fibre burners for methane combustion, either in a non-catalytic form or catalytically activated with palladium. Experiments and simulations are presented and compared for model validation purposes. The validated model is used for a stability analysis of the burner, so as to single out the range of operating conditions that are necessary to avoid flashback. Since flashback is primarily related to thermal profiles in the system, the dependence of the burner temperatures on porosity, effective thermal conductivity, fibre dimension, and surfaces emissivity was assessed. The focus of the analysis was to point out an optimum strategy for materials and geometry selection for the sake of maximizing the flame stability.

MODELLING AND MODEL VALIDATION

The system description is achieved by means of equations for mass continuity, gas phase species conservation, separate gas phase and porous medium energy conservation, and the

ideal gas law. The model accounts for inter-phase heat transfer, internal radiation in the porous medium, longitudinal mass transfer phenomena in the gas phase and a detailed reaction mechanism [3] for methane combustion in the gas phase. The catalyst, when present, is assumed to promote the oxygen dissociation and therefore the formation of O[•] radicals. The heterogeneous reaction $O_2 \rightarrow 2O^{\bullet}$ is introduced on purpose, with a reaction rate that is assumed to be mass transfer limited, due to the very fast reaction rates of intrinsic kinetics typical of these systems.

Model calculations and experiments are compared at different values of excess of air E_a and of specific power input Q . The pilot plant and the procedures employed in the experiments are described in detail in [4]. The porous medium (the FeCrAlloy fibre mat NIT100S by ACOTECH, B) is placed horizontally, at the end of the plenum chamber, and is firing upwards. Since temperature measurement with thermocouples in a combustion system is known to be a challenging task, a correction to the measured values has been applied, on the basis of a thermal balance on the thermocouple tip according to the criteria suggested in [5]. Figure 1 shows typical calculated and measured temperatures of the downstream surface of the catalytic fibre mat at two excess of air values (E_a). Analogous model performance was obtained for the non-catalytic mat.

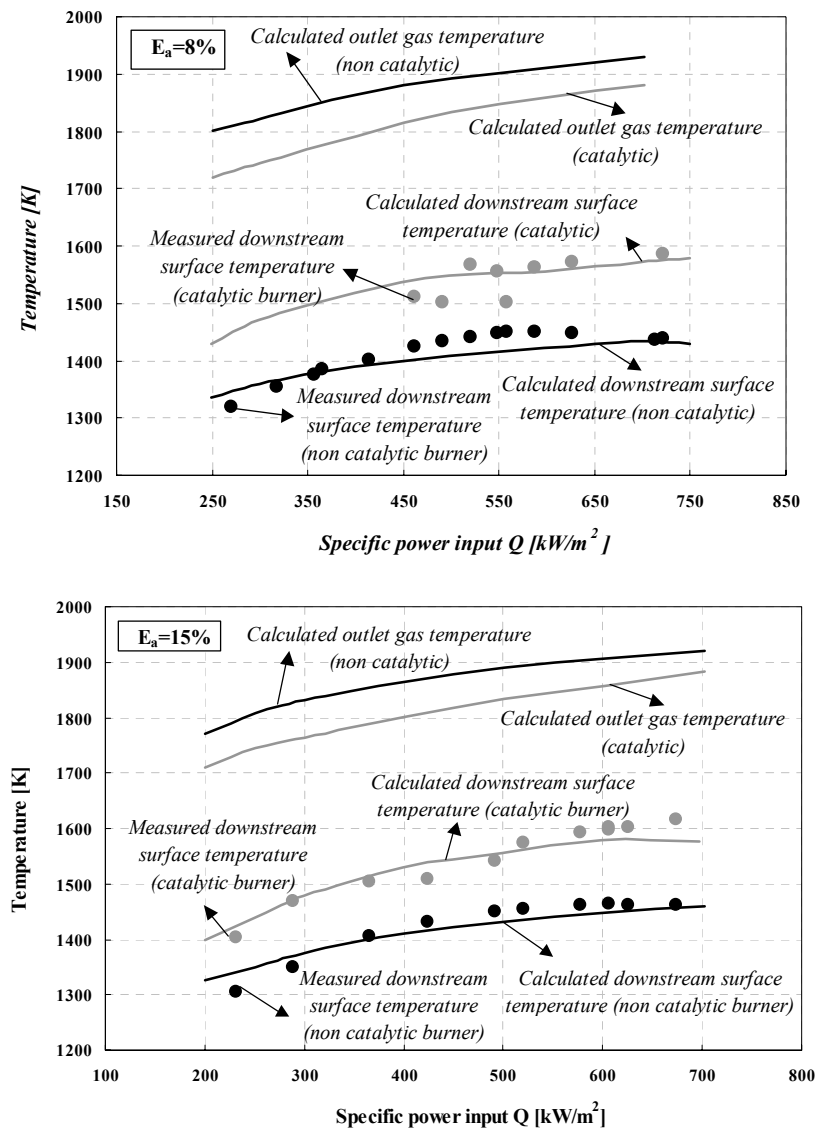


Fig. 1. Model validation for the catalytic burner operated at different E_a values (8 and 15 %).

MODEL CALCULATIONS

As far as the comparison between the catalytic and the non catalytic fibre burners is concerned it has to be stressed that the catalyst stabilizes the combustion more inside the porous medium by promoting the production of those radicals that are responsible of the ignition of the fuel mixture. As a consequence, the fibre mat receives more effectively the energy released by the reactive gas phase. Hence, higher surface temperatures are thus observed in the entire range of E_a and Q investigated, together with an improvement in radiant performance. To further emphasise this issue, Fig. 3 compares the absolute values and the fractions of energy transferred by the catalytic and the non-catalytic burners at various specific power inputs. This feature of the catalytic burner is positive, on the one hand, since it enables lower NO_x emissions, but negative, on the other hand, as it favours flashback.

The analysis of the burner flame stability has been carried out by model simulations according to the following procedure. The effect of the inlet gas temperature on the upstream surface temperature has been calculated and the results are shown in Fig. 4.

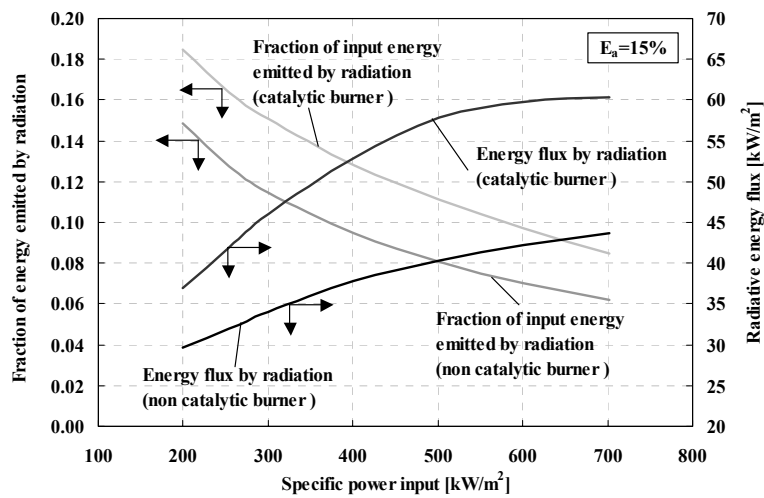


Fig. 2. Radiative output of the catalytic and non-catalytic fibre burners operating at different specific power inputs.

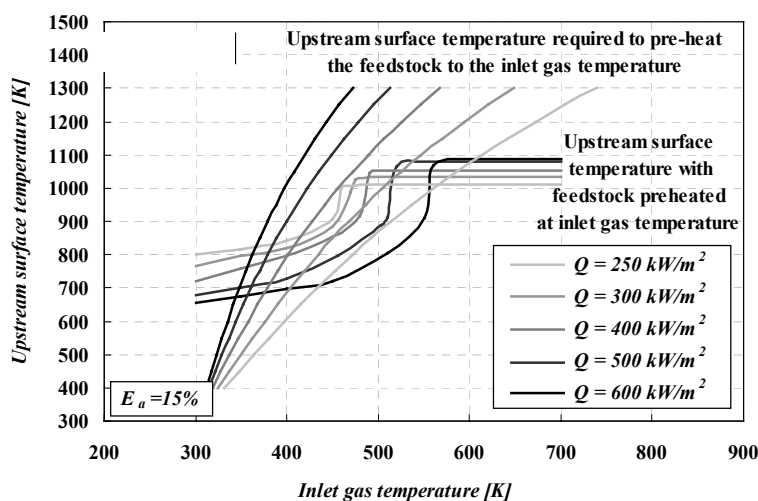


Fig. 3. Upstream surface temperature versus inlet gas temperature for the catalytic burner; the intersections between the curves represent steady state solutions.

When flashback occurs the upstream surface temperature becomes extremely high, and a steep increase in these plots can be noticed. The inlet gas temperature is strongly dependent

on the upstream surface temperature, which determines the backwards radiative flux responsible of the feedstock preheating and therefore of flashback. An energy balance equation can be formulated to relate these variables, thus obtaining the curves plotted in Fig. 3. Obviously, at each value of specific power input the system works at the intersection of these different curves. By this method, the region of operating conditions to avoid flashback has been determined for both the catalytic and the non catalytic fibre burners and represented in Fig. 4. By a comparison between Figures 4a and 4b, it can be observed that the curves limiting the regions of safe combustion and of flashback shift to the right direction in the case of the catalytic burner, which has thus a more limited range of operating conditions for safe operation.

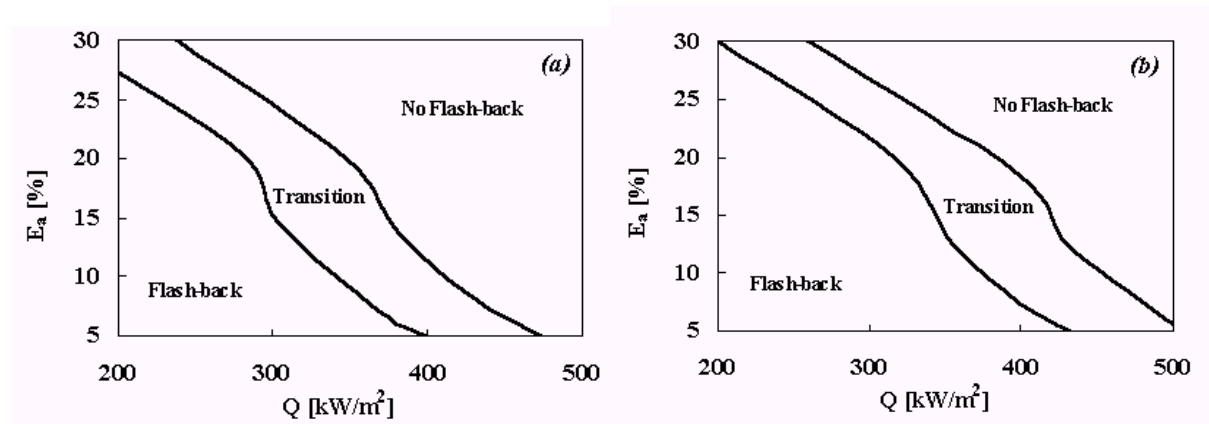


Fig. 4. Flashback charts in the Q - E_a plane for the non-catalytic (a) and the catalytic (b) burners.

The effects of the burner physical parameters (e.g. fibre diameter, burner density, thermal conductivity, emissivity, ...) on the system performance were finally assessed. The results of such investigations, not reported here for the sake of brevity, will be described in the congress presentation.

CONCLUSIONS

A model of catalytic and non-catalytic premixed fibre burner was presented and some general differences with non-catalytic systems were discussed. A criterion for the analysis of stability and flashback of a metal fibre burner was thus formulated. In particular, ranges of conditions of safe operation and a flashback region, in terms of E_a and Q , could be singled out for both catalytic and non-catalytic burners. Such operational maps are currently being used in selecting the most appropriate control systems for the burners in high-power-modulation boilers.

REFERENCES

1. Saracco, G., Cerri, I., Specchia V., Accornero, R.: *Chem. Eng. Sci.*, **54**: 3599 (1999).
2. Rumminger, M.D.: *Numerical and Experimental Investigation of Heat Transfer and Pollutant Formation in Porous Direct-Fired Radiant Burners*, Ph.D. dissertation, University of California at Berkeley (1996).
3. Kazakov, A., Frenklach, M. : *Reduced reaction sets based on GRI-Mech*, University of California at Berkeley. <http://www.me.berkeley.edu/drm>
4. Cerri, I., Saracco, G., Specchia, V., Trimis, D. : *Chem. Eng. J.*, **82**: 73 (2001)
5. Xiao, X., Choi, C.W., Puri, I.K. : *Comb. & Flame*, **120**: 318 (2000).

DME combustion in domestic cooking appliances: comparison with LPG

¹G. Migliavacca, ¹E. Parodi, ²M. Marchionna, ³L. Pellegrini

1 Stazione Sperimentale per i Combustibili, S. Donato Milanese - ITALY

2 SNAM Progetti SpA, S. Donato Milanese - ITALY

3 Agip Petroli SpA, S. Donato Milanese - ITALY

ABSTRACT

This work contains a brief description of a series of experimental and model studies performed to investigate the potential application of DME as a substitutive fuel in domestic appliances, commonly fed with LPG. Some results are presented about combustion tests performed with pure DME (Dimethyl Ether) and mixtures with propane and butane in variable concentrations, along with endurance and stability experiments, carried out to evaluate the safety and compatibility of this fuel. A particular attention is devoted to the results of numerical models, applied to forecast the combustion performances of the fuel mixtures and to predict the formation of not-measured pollutant species.

INTRODUCTION

DME, thanks to its good combustion properties, is considered a possible alternative fuel in many industrial fields: this work examines the various aspects connected to the possible use of this compound in substitution or in mix with commercial LPG, in the domestic cooking appliances. DME is the simplest compound of the aliphatic ether family, and it has the lowest C/H ratio after methane; it is chemically stable and it is a colourless liquid below 25.1°C: owing to this features, DME can be considered very similar to propane and butane, so that the same simple technologies can be used for its handling and storage. In the atmosphere it decomposes in few hours, so it cannot be considered a potential greenhouse gas; its toxicity is rather low and comparable with commercial LPG. DME is used nowadays as spray propellant in the dye, agriculture and cosmetic industries, as an ideal substitute of freon, but it is also utilised as refrigerant, reactant in the synthesis of high purity dimethyl-sulfate and as extracting solvent in many industrial processes. About 150000 tons per year are currently produced in the world. Industrial processes for DME production include direct synthesis from methanol or reforming reaction from methane or synthesis gas. Ethers, in general, are becoming more and more important the combustion applications, mainly in the field of internal combustion engines, where they can be used both as fuels and additives. DME was particularly studied as a possible substitutive fuel in the diesel engines, since it has a high cetane number and shows a low tendency to soot formation. This behaviour is favoured by the absence of C-C bonds and by the high internal oxygen amount, which enhances the oxidation and depresses the formation of carbonaceous compounds.

The problem of fuel inter-changeability is addressed to verify the good compatibility of all those chemical and physical properties of a fuel, which can influence its performances in terms of combustion properties, storage and handling or compatibility with commonly used materials, respect to another fuel already tested and commonly used.

SAFETY ON HANDLING, STORAGE AND UTILISATION OF DME

To safely produce, distribute and commercialise mixture of DME with LPG, it is necessary to verify that undesired reactions cannot take place inside the storage vessels or the mixing plants, under common environmental conditions. For this activity eight different gas mixture, binary and ternary, at different concentration of DME, propane and butane have been prepared. Small bottles, completely filled with very small iron alloy spheres to enhance surface contact with gas mixture, have been used for the storage of the gas mixtures. The bottles have been submitted to daily thermal cycles (10 and 40 °C) for four months, and periodically analysed for gas composition. The analytical results, carried out by gas chromatography among this time frame, have shown no change in the chemical composition of macro-elements and no new chemical compounds have been detected. From this result can be concluded that DME is stable, at standard storage conditions, in presence of LPG pure constituents (propane and butane).

DME & MATERIAL COMPATIBILITY

In this experimental section the endurance test to DME (the most severe condition) of gas governors and commercial flexible tubes has been evaluated. For the endurance test additional, not standard, equipment has been designed and build (see picture below), this apparatus allow to set seven governors and flexible tube as in typical the gas-cooking configuration (bottle, governor, flexible tube, burner) and to submit the equipment to periodical on-off cycle with pure DME.

Governors

After four months of testing the several type gas governors have not been damaged and they did not change the pressure adjustable capacity; very small, reversible (after air washing), modification of K-value have been noticed. Some dynamic test of pressure adjustment in pure DME have shown small pressure fluctuation (fraction of mbar). Gas governors with Hypalon[®] membrane did not show any pressure fluctuation.

Flexible tubes

Less encouraging results have been achieved with the flexible tube performance; the tube submitted to the same endurance test as for the gas governors showed small but meaningful losses in hydrogen permeability capacity, even that stay within the allowable range as required in the technical standard. For this type of equipment, in the presence of DME or also DME-LPG mixture, it will be necessary to set a more frequent item replacement.

COMBUSTION OF PURE AND MIXED DME

The combustion process of DME, pure and mixed with propane and butane, was studied both experimentally and theoretically, by means of direct in-flame measures and tests on cooking stoves and by modelling calculations using available and well-established numerical codes. These studies have been performed in order to better understand the chemical behaviour of this compound respect to the more commonly applied liquefied fuels and to directly measure the DME performances in the real appliances.

Numerical modelling

The DISMOKE Code [1], developed by the Department of Chemical Engineering of the Politecnico di Milano, was used for combustion modelling, starting from a kinetic scheme including hundreds of species and reactions and able to describe the combustion process of many different fuels, including DME whose reaction scheme was especially tuned and tested for this work. Other calculations were performed with the Chemkin III code using a restricted

kinetic scheme, including only DME reactions [2], in order to compare the different schemes. The flexibility of the model and its performances were validated by means of comparisons between model predictions and experimental results coming from the recent scientific literature and referring to experimental studies performed with many different devices operating in different experimental conditions (plug flow reactors [3], jet stirred reactors[2], shock tubes [4] and premixed burners).

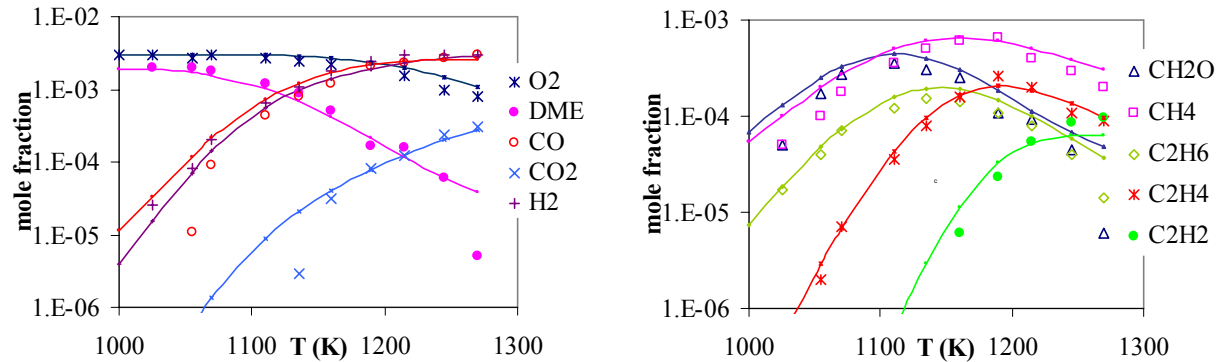


Figure 1 DISMOKE Model comparison for JSR [2] experiments ($DME = 0.2\%$ $\phi = 2$ $p = 1 \text{ atm}$ $\tau = 0.1 \text{ s}$)

Then, the effect of DME, on the premixed combustion mechanism of fuel mixtures containing propane and butane, is evaluated and a clear increase of reactivity is observed, as shown, in the first of the following figures, by the anticipated CO_2 production.

A particular attention was devoted to pollutant formation (like aldehydes and aromatic compounds). The former show a strong increase in the peak concentrations, certainly due to the presence of an oxygenated group which enhances its production and accumulation, although this effect is limited to the first flame region. An experimental measurement campaign would be useful to confirm this behaviour also under the real condition of combustion. On the contrary, a positive reduction effect, in the presence of DME, is observed respect to the aromatic hydrocarbon, as shown in the following figures relative to benzene and pyrene.

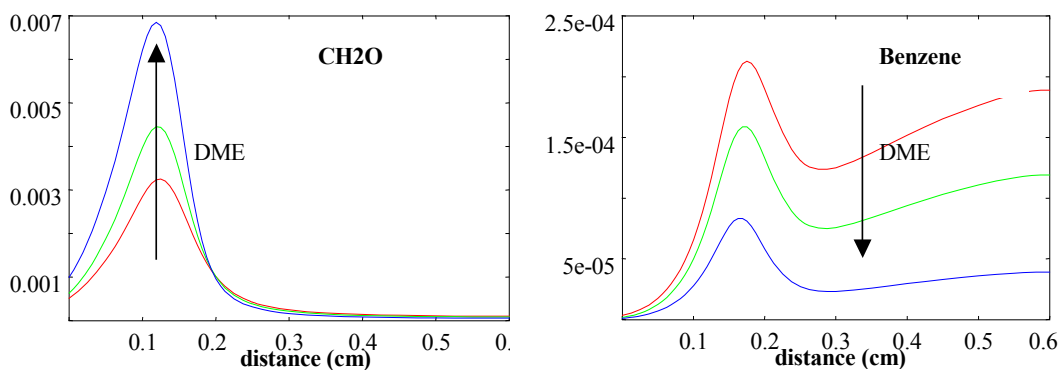


Figure 2 Calculated mole fractions of CH_2O and C_6H_6 at increasing DME concentrations

Flame diagnostic

Along with this merely model evaluation, an experimental study was carried out using the laser induced fluorescence (LIF) technique, in order to measure the OH radical concentration

varying the operating conditions and the fuel composition. Tests were performed on a flat flame premixed burner, using a porous sintering bronze matrix as flame stabiliser. Different stoichiometries and fuel compositions studied point out the similar behaviour of DME flames and common LPG flames: the radical concentration profiles for pure DME are very similar to the ones measured with butane flames (in both of the cases, more radicals are formed with respect to pure propane), clearly indicating the basic similarity among the processes taking place. In the figures below we can see the concentration trends of OH radical in some different flames, having different fuel feed or stoichiometric ratio. It is evident the drastic decrease of radical concentration switching from an oxygen rich mixture to a fuel rich one.

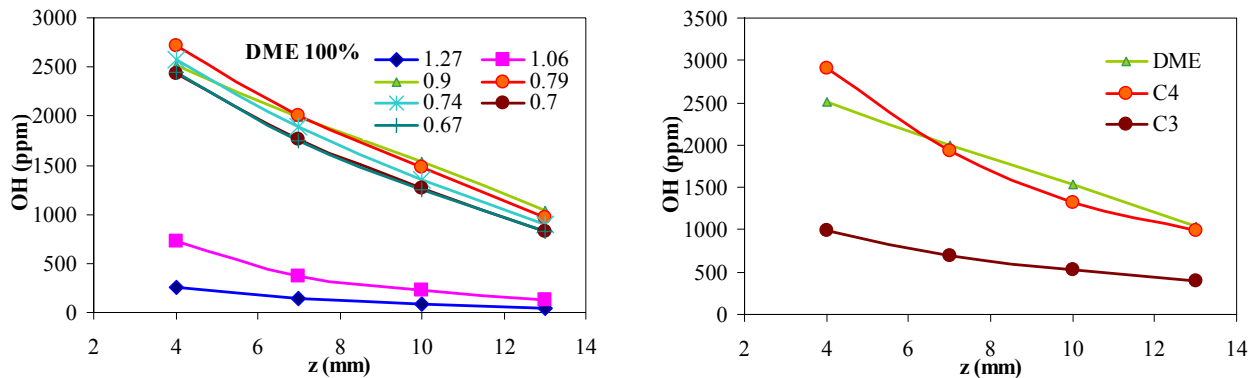


Figure 3 OH concentration profiles at various Φ ratios (left) and for different fuels (right)

Cooking hobs tests

Five cooking hobs, using different types of burners were tested: cup burner with fixed premixed air, cup burner with adjustable premixed air, classic burner with venturi adjustable premixed air. The combustion tests, using LPG, pointed out different critical points: thermal input out of nominal range, high pollutants levels and different performances for the different burners type and size. Butane showed the worst behaviour respect to CO production, while propane and commercial LPG mixtures showed lower and very similar pollution levels. The use of pure DME does not get the combustion worse, but requires to make some change to the cooking hobs set up. The study of LPG-DME mixtures points out the positive effects of DME addition respect to the combustion parameters and the CO emissions. This effect is mainly evident for those stoves having higher carbon monoxide emissions and in the presence of butane-rich mixtures; the cup burner with adjustable premixed air is the most flexible one for combustion setting as function of gas type.

ACKNOLEGMENTS

We are indebted with E. Ranzi, T. Faravelli and S. Granata (from Politecnico di Milano), for the useful contributions and discussions about the kinetic modelling and for the availability of the DSMOKE code and schemes used in this work.

REFERENCES

1. Ranzi E., Dente M., Goldaniga A., Bozzano G., Faravelli T., *Progr. En. Comb. Sci.*, p. 99 (2001)
2. Fischer S. L., Dryer F. L., Curran H. J., *International Journal of Chemical Kinetics*, (1999)
3. Dagaut P., Boettner J., Cathonnet M., *26th Symposium (Int.) on Combustion*, p. 627 (1996)
4. Pfahl U., Fieweger K., Adomeit G., *26th Symposium on Combustion*, p 781 (1996)

Prediction of Flammable Limits of Mixtures in Non Standard Conditions

M. Milli, M. De Lucca, R. Rota*

Politecnico di Milano

*Dip. di Chimica, Materiali e Ingegneria Chimica "G. Natta" / CIIRCO
via Mancinelli, 7 - 20131 Milano, Italy*

INTRODUCTION

Knowledge of flammability characteristics of raw materials, intermediate and products is important for the safety of all the process industries since flammable mixtures can be generated almost in any industrial unit operations, such as storage, transfer and handling of flammable compounds. Therefore, to prevent fires and explosions it is necessary to know the combustion characteristics of fuel-oxidant mixtures under general working conditions (that is, composition, temperature and pressure). Unfortunately, many factors influence the flammability limits of vapors mixture, such as mixture's chemical-physic proprieties, temperature, pressure, geometric characteristic and materials of the vessel, flame propagation direction, turbulence, and so on. For this reason one can find in literature different values of the LFL (lower flammability limit) and UFL (upper flammability limit) for the same compound. Moreover, most of the data available in literature were measured at standard temperature and pressure, and for "pure combustible" like methane in oxygen or air.

As previously mentioned, for what concerns the safety of industrial processes a predictive method for estimation of the LFL and UFL of generic flammable vapors mixture at different temperatures and pressures in different oxidative systems is required. In the past years several theoretical methods have been suggested to estimate the flammability limits of mixtures when no experimental data are available. However, these methods have some limits in their application; for example, the Le Chatelier's mixing rule for flammable limits yields good results only for LFL of mixtures of similar vapors in oxidative environment without any inert gas, and the results are not extendible to different pressures and temperatures. These methods can be grouped in three classes, for the prediction of flammability limits of:

- pure compounds in air at standard conditions;
- mixtures of fuels with or without inert gases;
- vapors mixed with air in different conditions from their values at standard T and P;
- any mixture using the Calculated Adiabatic Flame Temperature (CAFT).

In this work we have choose to investigate the possibility of estimating the LFL and UFL using the Calculated Adiabatic Flame Temperature due to its wide applicability to generic combustible-oxidative systems in different conditions. The main aim has been to identify a reliable procedure for applying this methods to a wide range of operating conditions, thus significantly enlarging its predictive capabilities. With this aim, the flammability limits of 126 pure chemical compounds and several their mixture in a range of temperature of 150-720 K and pressure of 0.16-125 bar have been investigated.

PREDICTION OF FLAMMABILITY LIMITS USING THE CAFT

This method comes from the old observation that lower paraffins have a nearly constant flame temperature. The basic idea on which the method is based is that if a vapors mixture reaches,

* Telephone: +39 0223993154, Fax: +39 0223993180, E-Mail: renato.rota@polimi.it

during combustion reactions, a flame temperature higher than an assumed threshold temperature, the mixture is able to propagate the flame and then it is inflammable [2]. One of the most relevant aspect of this model is that the method is intrinsically able to determine how the adiabatic flame temperature of a generic mixture of combustibles, comburents and inert, varies with the concentration, temperature and pressure.

Mathematical Model

The basic hypothesis of this method is that the chemical reaction rate and then the chemical heat generation rate are much greater than the energy and material transport rates. Therefore, it is possible to assume that in the reacting region thermodynamics equilibrium is reached without any heat losses. This method involves two steps: the first one requires the estimation of the adiabatic flame temperature at thermodynamic equilibrium (CAFT). To determine the CAFT, in this work the CHEMKIN-II software package [1] and more specifically the subroutines based on the STANJAN III code have been used.

The second step requires the definition of a threshold temperature. As previously mentioned, it is assumed that all the mixtures that can reach a CAFT greater than this threshold temperature are flammable. Therefore, once a representative value of the threshold temperature of the system is available, it is possible to determine the LFL and UFL. According to Melhem [2], the majority of experimental flammability limits correspond to threshold temperatures in the range of 1000 – 1500 K. One possible reason for this is linked to reaction mechanisms of carbon monoxide, the primary product formed in substantial amounts during any hydrocarbon oxidation process. Since the CO conversion to CO₂ controls a sizeable amount of flame energy release its limiting temperatures will control the overall flammable characteristics. The reaction $\text{CO} + \text{HO} = \text{CO}_2 + \text{H}$ does not occur appreciably up to about 1100 K and it is self sustaining above about 1400 K [3]. However, significant differences in the predicted values for both LFL and UFL can be obtained using temperature values in this range, thus evidencing the necessity of a reliable procedure for defining the threshold temperature as a function of the operating conditions.

The analysis carried out in this work has been articulated in two steps:

- evaluation of the exact threshold temperature for all available pure species, at different temperatures and pressures, and definition (from these results) of general rules for predicting threshold temperatures in a wide range of operating conditions; .
- prediction of the flammability limits for mixtures using these rules suitably mixed.

This job has been carried out with two aims: the first one was to estimate an “optimum” value of the estimated threshold temperature (ETT), that is, one able to give the best fit of the experimental data. The second one to estimate a “conservative” ETT value, that is the threshold temperature that allows an estimation of the flammable limits always conservative, that is, such as to assure safe working conditions. In the following, only results referring to the “optimum” ETT will be discussed. Similar results have been obtained for the “conservative” ETT investigation.

Results and Discussion

Almost all the “optimum” threshold temperatures (OTT) estimated in this work are in the range of 1000~1500 K. However, it has also been found that it is necessary the use of two different threshold temperatures for the lower and upper flammability limits predictions. Moreover, due to the particular form of the CAFT versus composition curve, the use of the threshold temperature of 1200 K, as recommended in the literature as a “rule of thumb” [2], yields reasonable results only for what concern the LFL, whereas gives definitely bad results in the estimation of the UFL. It has been also found that is suitable to subdivide the considered compounds into few classes (such as, alkanes, alcohols, aromatics etc.).

An example of the rules derived from the aforementioned analysis are shown in the following table.

Class	Working conditions	OTT	Validation range	Notes
<i>mean error in the estimation of the LFL = 8%</i>				
alkanes	298K; 1atm	1550 K		
	T; 1atm	$\begin{cases} 1865.1 - 1.158 \cdot T & T \leq 358 \text{ K} \\ 1450 \text{ K} & T > 358 \text{ K} \end{cases}$	150 K < T < 623 K	
	298K; P	$\begin{cases} 1466.86 - 564 \cdot \log P & P \leq 0.7 \text{ atm} \\ 1550 \text{ K} & P > 0.7 \text{ atm} \end{cases}$	0.16 atm < P < 125 atm	
<i>mean error in the estimation of the UFL = 11%</i>				
alkanes	298K; 1atm	1150 K		for CH ₄ :1650K for C ₃ H ₆ :1500K
	T; 1atm	1150 K		no CH ₄ & C ₃ H ₆
	T; 1atm	1650 K		only CH ₄
	298K; P	1769.39 – 376.38·logP	0.176 atm < P < 125 atm	only CH ₄
	298K; P	1301.77 – 220.63·logP	1 atm < P < 34 atm	only C ₂ H ₆
	T; P	1532.7 – 143.73·lnP	1 atm < P < 55 atm	only CH ₄

We can see that no “universal” ETT can be used without losing reliability, in particular for what UFL estimation concerns. Similar results have been obtained for all the other compounds investigated.

Figures 1 and 2 show a comparison between calculated (with the rules developed for defining the ETT) and the experimental values of both LFL and UFL for all the pure compounds data at different pressures and temperatures. Quite a good agreement has been found for all the data available, resulting in a mean error of about 10%.

The rules derived for pure compounds can be also used to predict the ETT of mixtures, provided that a suitable mixing rule to compute the mixture ETT from the ETTs of the single classes is established. We have found that a simple mixing rule, that is:

$$ETT_{MIX} = \left(\sum Y_i / ETT_i \right)^{-1}$$

is suitable to reasonably predict the experimental data with an average error equal to about 20%, as summarized in figure 3 where calculated and experimental flammability limits for several mixtures are compared.

It should be finally mentioned that an advantage of this method is that the presence of some inert gas is directly accounted for in a lower CAFT. In other words, the ETT_{MIX} of combustible-inert-comburent systems is the same of the combustible-comburent systems as computed from the inert free combustible molar fractions.

REFERENCES

1. Kee, R.J.; Miller, J.A.; Jefferson, T.H. *CHEMKIN: A General Purpose, Problem-Independent, Transportable, FORTRAN Chemical Kinetics Code Package*. The Sandia National Laboratories Technical Report SAND89-8009; Sandia National Laboratories: Albuquerque, NM, and Livermore, CA. (1989).

2. Melhem, G.A.: *A Detailed Method For The Estimation of Mixture Flammability Limits Using Chemical Equilibrium*. Arthur D. Little, Inc, Cambridge, Massachusetts 02140 (2000)
3. Mashuga, C.W., Crowl, D.A.: *Process Safety Progress* 19, 112, (2000).

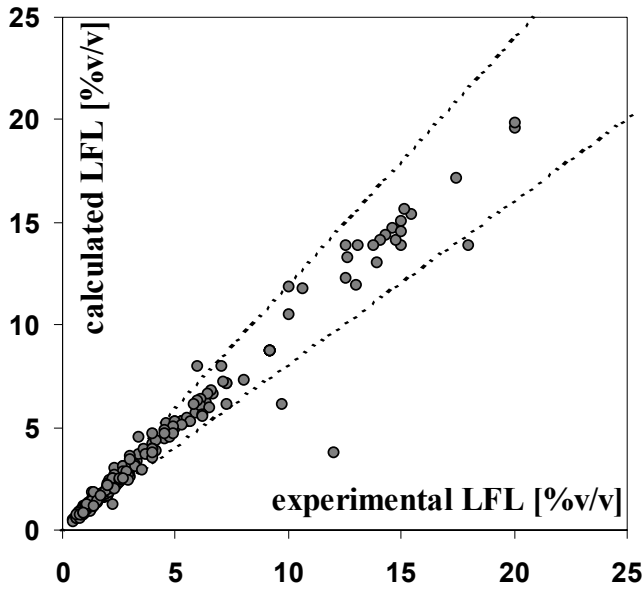


Fig.1: calculated experimental LFL for all pure compounds in different working conditions

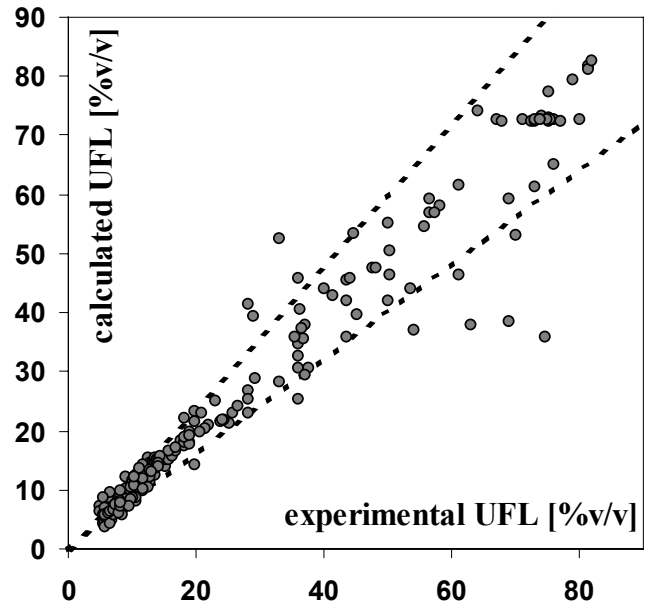


Fig.2: calculated experimental UFL for all pure compounds in different working conditions

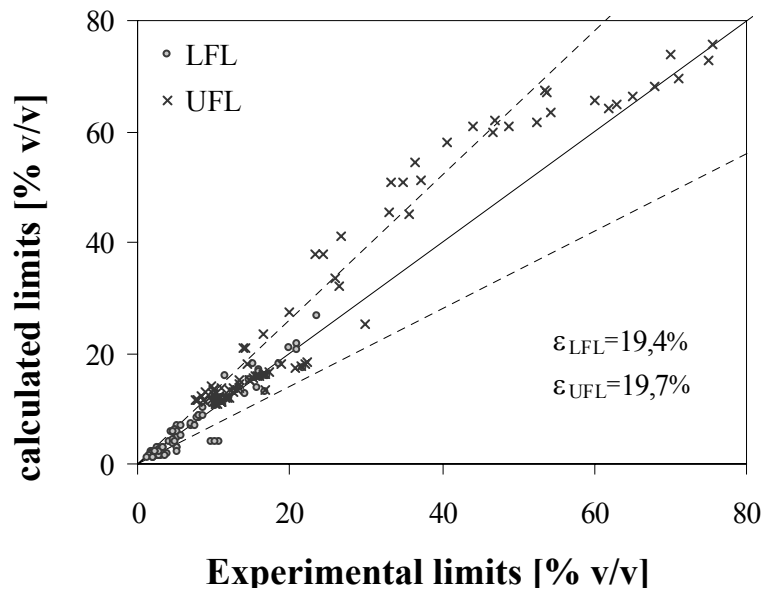


Fig. 3: calculated and experimental flammability limits for various mixtures in different working conditions

Effects of Different Fuels in a Trapped Vortex Combustor

*Marco Losurdo, Claudio Bruno

†Giorgio Calchetti, Eugenio Giacomazzi, Marco Rufoloni

* Department of Mechanics and Aeronautics - University "La Sapienza", Roma - ITALY

† ENEA - C. R. Casaccia, Sec. ING-TECO, Roma - ITALY

Abstract

The Trapped Vortex (TVC) strategy has the main effect to reduce the pressure drop in a combustor by generating a stable vortex within a cavity, where fuel and oxidant are injected, mix and react. The trapped vortex prevents vortex shedding from the cavity, the main mechanism responsible for the pressure drop. The aim of the present work is to analyze the fluid dynamics in a Trapped Vortex Combustor operated with different fuels (C_3H_8 , CH_4 , H_2) by numerically solving the reactive Navier-Stokes equations in a RANS approximation. Moreover, we investigate the possibility to achieve MILD-type combustion by using this TVC strategy. The actual geometry of the TVC comes from the studies of V. R. Katta and W. M. Roquemore. Results show that it is possible to burn different fuels without altering the effects of the combustion strategy.

INTRODUCTION

A Trapped Vortex Combustor (TVC) is a combustor consisting of a cavity where fuel and oxidant are injected and mixed inside a vortex system created by a main air flow blowing parallel to the top of the cavity. For certain cavity shapes a main stable vortex avoids vortex shedding along the combustor. When this occurs, reactants injected into the cavity burn with remarkably low pressure drop in the combustion chamber. The anchorage of the flame is due to the recirculation of hot combustion products whose temperature is above the autoignition temperature of the mixture [1, 2]. The aim of the present work is to numerically investigate this strategy in terms of low emission indexes, total pressure losses and residence times, using different fuels (propane, methane and hydrogen) without changing the combustor geometry.

In particular, in order to reduce NO_x emission [1], a MILD ("flameless") combustion [1, 3] approach was also simulated: this strategy introduces together with reactants hot combustion products (volume concentration of oxidant < 15%). The numerical results presented refer to two TVC geometries and were obtained solving reactive Navier-Stokes equations using RANS. The geometries (shown in Fig. 1) are composed by two or three axisymmetric disks mounted on the same axis, taken from Katta and Roquemore [4].

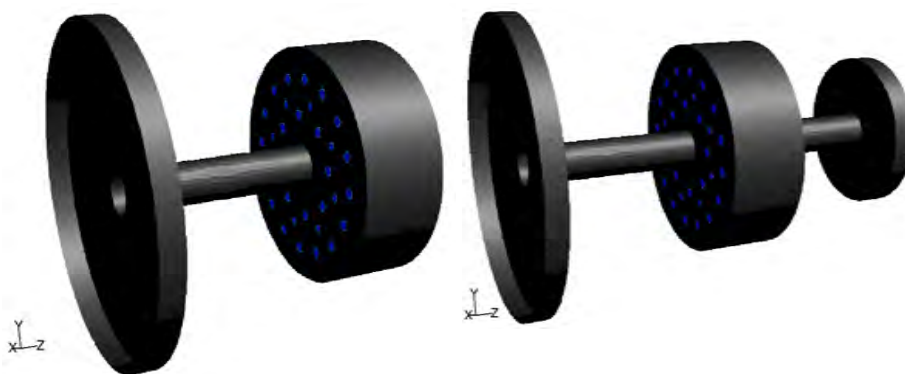


Figure 1: Geometries of the TVC burners simulated.

The geometry consists in annular cylinder (diameter=8 cm) and two disks (the larger, called "forebody", has a diameter of 7 cm, the smaller, called "afterbody", which has a diameter of 5.08 cm). The shorter geometry is 6.43 cm long, while the other one is 10 cm long by adding a third disk whose diameter is 3.81 cm. The second cavity, bordered by the two afterbodies, improves both combustion efficiency η_b and the main vortex stability in the first cavity. The blockage ratio $\frac{A_{forebody}}{A_{annular\ duct}}$ is 0.76, $\frac{d_{afterbody}}$

0.73, $\frac{h}{d_{forebody}} \Big|_{1^{st} \text{ cavity}} = 0.59$, $\frac{d_{afterbody2}}{d_{afterbody1}} \Big|_{2^{nd} \text{ cavity}} = 0.75$, $\frac{h}{d_{afterbody1}} \Big|_{2^{nd} \text{ cavity}} = 0.6$. The TVC model was validated using literature results for propane ($v_{C_3H_8} = 22 \frac{m}{s}$, $P = 35KW$, $p = 1atm$) [5]. The simulations with CH_4 and H_2 can be divided into **three groups of investigation**: (1) $v_{H_2} = v_{CH_4} = v_{C_3H_8} = 22 \frac{m}{s}$ at $p = 1atm$, (2) $P_{H_2} = P_{CH_4} = P_{C_3H_8} = 35KW$ at $p = 1atm$, (3) $P_{H_2} = P_{CH_4} = 350KW$ at $p_{H_2} = p_{CH_4} = 10atm$. In group (1) we simulated **only** conventional combustion (*annular air flow*, $T = 300 K$), in (2) we investigated **also MILD combustion** conditions and in (3) we simulated **only MILD conditions** (*combustion products as annular flow*, $T = 550 K$).

RESULTS

1st group : results indicate mixing depends only on momentum of annular air, fuel and primary air jets: if the momentum of the main vortex (whose mass comes from the annular air flow) is about *ten times* that of fuel or primary air, combustion takes place in the bottom of the cavity (as it happens in H_2 case, showed in the picture) instead in the main vortex. This stratifies combustion process (see Fig. 2) because stoichiometric conditions occur only the bottom of the cavity; vortex momentum doesn't allow fine mixing, crushing fuel and primary air on the cavity walls. Expansion of hot gases then ejects the main vortex (colder than the remain part of the cavity) and causes vortex shedding which is the main mechanism responsible for pressure drop in combustors.

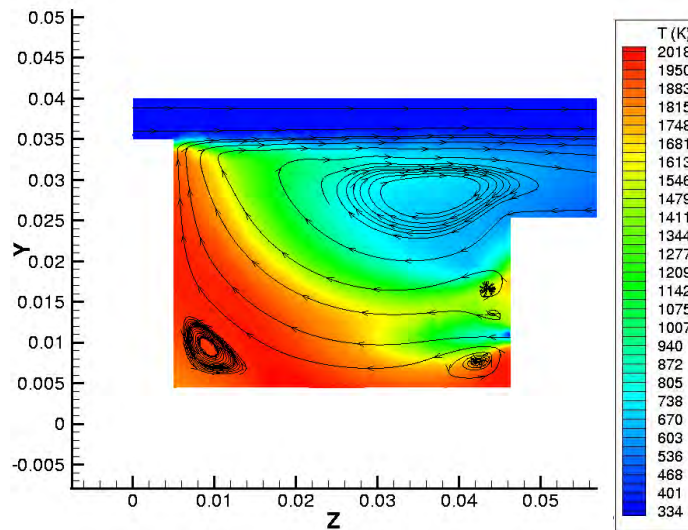


Figure 2: Contour plot of temperature for the case of H_2 at $22 m/s$.

In the case of C_3H_8 , combustion starts at the cavity bottom but it takes place inside the main vortex, where hot gases recirculate. Efficiency $\eta_b = 1 - \frac{\frac{dm_{fuel}}{dt} \Big|_{outlet}}{\frac{dm_{fuel}}{dt} \Big|_{inlet}}$, is very high: $\eta_b|_{C_3H_8} \simeq 86\%$, $\eta_b|_{CH_4} \simeq 90\%$, and $\eta_b|_{H_2} \simeq 94\%$. The fact that $\eta_b|_{C_3H_8}$ is $< 96\%$ reported in [4] is due to the two step kinetic of the combustion model used, while $\eta_b|_{C_3H_8}$ is the lowest in this case because of no ideal mixing condition was found in the cavity (this was true also for H_2 and CH_4 cases) but $\frac{dm_{fuel}}{dt} \Big|_{C_3H_8}$ and momentum are much higher than in the other cases ($\frac{\rho_{C_3H_8}}{\rho_{CH_4}} \simeq 2.71$, $\frac{\rho_{C_3H_8}}{\rho_{H_2}} \simeq 21.25$), so that resident time is too short for the kinetics used to make propane burn completely in the 1st cavity.

The behavior of methane is between those of hydrogen and propane: its momentum is a good compromise between ideal mixing (perfectly mixed), chemical kinetics and convective resident time. Most part of methane burns in the 1st cavity, even though expansion of the hot gas moves the main vortex to the top of the cavity, next to the exit lip: obtaining good mixing and stable combustion is the aim of diffusion combustion, while the Trapped Vortex combustion needs a stable main vortex mixing and burning the reactants;

it takes that fuel and primary air jets reinforce the main vortex with their momentum.

η_b predictions depend strictly both on fuel used and on the *reduced chemical mechanism chosen* (1-step or 2-step, etc...) on *momentum ratios* (mixing conditions) and on *residence time* inside the cavity.

Ideal burning condition is different from **ideal mixing condition** (for cold flow) because the latter depends only on momentum. **Ideal burning condition** depends on mixing (*momentum*), on kinetic energy of the flows and on chemistry (*chemical energy released*).

2nd group : results show that it is not possible to maintain constant power without making η_b (and mixing) worse. In this case the momentum of fuel and/or primary air jets is larger than that of main vortex thus the shape of the main vortex appears to be stretched along the cavity; the residence time decreases and the highest temperature occurs in the 2nd cavity where combustion can be completed. Reaching the highest temperature in the 2nd cavity results in a thermal NOx “pool”.

The *working-diagram* in Fig. 3 shows, along the combustor length, some of the unburned species mixing with the annular flow and exhausting without being captured by the 2nd cavity: this explains the η_b decreasing in atmospherical simulations. At 10 atm reaction rates increase and $\eta_b|_{10 atm} > \eta_b|_{1 atm}$.

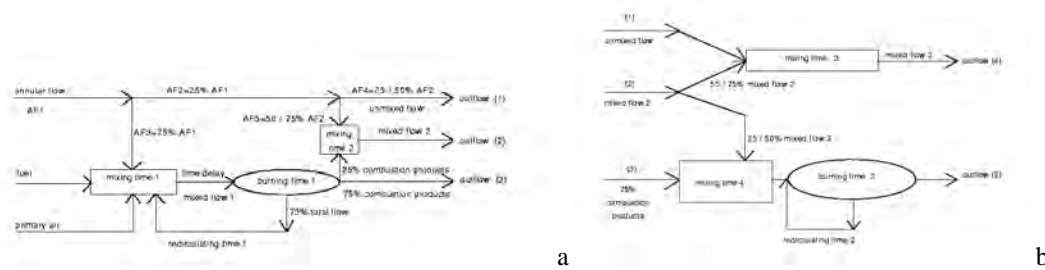


Figure 3: Working diagrams of the TVC burner.

MILD COMBUSTION RESULTS

MILD (“*flameless*”) combustion occurs at low oxidant concentration and moderate products temperature, since combustion should be delocalized within the combustor volume.

In order for MILD to occur in a TVC the kinetic energy of the annular flow (and therefore the parameter $K_{factor} = \frac{Kinetic\ Energy_{annular\ flow}}{Kinetic\ Energy_{fuel} + Kinetic\ Energy_{primary\ air}}$) should be kept constant with respect to conventional combustion. The temperature of annular flow in MILD cases is 550 K and its composition is $O_2 = 0.15$, $H_2O = 0.055$, $CO_2 = 0.0275$, $N_2 = 0.7675$ (molar fractions).

In MILD cases (annular flow of combustion products, $T = 550\ K$, $v = 52 \frac{m}{s}$) η_b decreases even more, because mixture is low in oxygen and residence time is a little lower than in conventional combustion (annular air flow, $T = 300\ K$, $v = 42 \frac{m}{s}$), the fact that in the 1st cavity no ideal mixing condition is achieved grows in importance.

MILD conditions lead to a lower NOx emission index, since this combustion strategy flattens temperature peak (in the present work we calculated only $NOx_{thermal}$ and NOx_{prompt} contributes).

The 3rd group refers to MILD combustion cases at 10 atm. The higher pressure doesn’t change vortex shape: this means that the kinetic parameter K_{factor} is quite independent of pressure. η_b is a little better than MILD at $p = 1\ atm$: equations are not linear, so even though pressure is increased ten times, the reaction rate grows but not as much as it should to burn completely a ten fold larger mass in the first cavity: most part of unburned fuel is in the flow path called *mixed flow 3* (see Fig. 3).

The results of 2nd and 3rd groups of simulation are summarized in Table 1.

The $EICO|_{MILD}^*$ is higher than conventional because combustion products were introduced as annular inlet; this fact leads to added CO_2 dissociating into CO ($2CO_2 \rightarrow 2CO + O_2$), so $EICO|_{MILD}^*$ grows about 27.2% compared to $EICO|_{conventional}^*$. A comparison between $EICO|_{MILD}^*$ and $EICO|_{MILD}^{**}$ shows that, even when pressure is increased ten times, $EICO|_{MILD}^{**}$ is only 11% greater than $EICO|_{MILD}^*$: the reason is that increasing pressure suppresses the dissociation of CO_2 , but increasing temperature promotes dissociation.

Pressure drops are lower in MILD cases (both for methane and hydrogen) because the heat released is more evenly distributed in the combustor volume than in conventional cases. This fact means that **pressure drop** doesn't depend on absolute pressure, but **only on how combustion is obtained**.

CONCLUSIONS

Mixing plays an important role in TVC to burning different fuels with very low pressure drops, since burner efficiency η_b depends on good turbulent mixing. The TVC strategy is intrinsic MILD from a recirculating point of view (as seen in Fig. 3): in fact, using a driven cavity as a combustion zone, it recirculates 96% ($K_v = 0.96$) of the whole mass injected (only) in the cavity, while typical MILD combustion requires a $K_v = 0.75$ [2]. **It is possible to burn different fuel** with high η_b using an injection plate with many holes, that can optimize fuel and primary air injection for every case, i. e., **without changing combustor geometry**. Since mixing is controlled by momentum while vortex shape and its persistence are controlled also by kinetic energy, a first constraint is that a stable TVC needs a $K_{factor} \simeq \circ(100)$: this could pose a problem, especially in MILD combustion. It is important to underline that **for no reactive flow** vortex shape, stability and mixing are controlled only by momentum: **for reactive flow** instead shape and stability (*persistence of vortex without shedding*) are controlled by kinetic energy since gas expansion in the cavity could expel the main vortex, so to prevent this it takes an annular fluidinamic "cowl" to hold the vortex inside the cavity: the "annular" kinetic energy must be enough to control both gas expansion and residence time.

References

- [1] "Diluted Combustion Technologies", by A. Milani, and A. Saponaro, IFRF Combustion Journal, article n.200101, Feb 2001, ISSN 1562-479X
- [2] "Flameless Combustion and Its Application to Aeroengines", C. Bruno, L. Vallini
- [3] "MILD Combustion of High Temperature Reactants", M. De Joannon, R. Ragucci, A. Cavaliere, submitted to: Comb. Sci. Tech., 1998
- [4] "Numerical Studies on Trapped Vortex Concepts for Stable Combustion", V. R. Katta, W. M. Roquemore, presented at: The ASME Turbo Asia 1996, Congress and Exposition, Jakarta, Nov. 5-7, 1996
- [5] "Performance of a Trapped Vortex Combustor", K. Y. Hsu, L. P. Goss, W. M. Roquemore, presented as Paper 95-0810 at the AIAA 33rd Aerospace Sciences Meeting, Reno, NV, Jan. 9-12, 1995.

*P = 35 KW **P = 350 KW	CH ₄ v _{CH₄} = 56 $\frac{m}{s}$ 10 cm	H ₂ v _{H₂} = 36 $\frac{m}{s}$ 10 cm	H ₂ v _{H₂} = 186 $\frac{m}{s}$ 6.43 cm
$\eta_{b conventional}^*$	0.7578	0.9	0.7374
$\eta_{b MILD}^*$	0.765	0.84	0.72843
$\eta_{b MILD}^{**}$	0.854	0.9439	
$\frac{\Delta P_{tot}}{P_{tot}}^*$	0.75%	0.78%	0.59%
$\frac{\Delta P_{tot}}{P_{tot}}^*_{MILD}$	0.593%	0.61%	0.458%
$\frac{\Delta P_{tot}}{P_{tot}}^{**}_{MILD}$	0.5886%	0.61%	
$\frac{E_{ICO MILD}}{E_{ICO conventional}}^*_{1 atm}$	1.272		
$\frac{E_{ICO MILD}_{10 atm}}{E_{ICO conventional}}^{**}_{1 atm}$	1.411		
$\frac{E_{ICO MILD}_{10 atm}}{E_{ICO}_{1 atm}}^{**}$	1.10927		
*P = 35 KW **P = 350 KW	CH ₄ v _{CH₄} = 56 $\frac{m}{s}$ 10 cm	H ₂ v _{H₂} = 36 $\frac{m}{s}$ 10 cm	H ₂ v _{H₂} = 186 $\frac{m}{s}$ 6.43 cm
$\frac{E_{INOx MILD}}{E_{INOx conventional}}^*_{1 atm}$	$5.5284 \cdot 10^{-3}$	$6.037 \cdot 10^{-1}$	$2.2831 \cdot 10^{-1}$
$\frac{E_{INOx MILD}_{10 atm}}{E_{INOx conventional}}^{**}_{1 atm}$	$1.783 \cdot 10^{-3}$	4.0747	
$\frac{E_{INOx MILD}_{10 atm}}{E_{INOx MILD}_{1 atm}}^{**}$	0.3225	6.75	
$\frac{E_{INOx MILD}}{E_{INOx conventional}}^*_{1 atm} thermal$	$5.564 \cdot 10^{-4}$	$6.27 \cdot 10^{-2}$	$5 \cdot 10^{-1}$
$\frac{E_{INOx MILD}}{E_{INOx conventional}}^*_{1 atm} prompt$	$4.51618 \cdot 10^{-3}$	$4.03 \cdot 10^{-2}$	$1.3725 \cdot 10^{-1}$
$\frac{E_{INOx MILD}_{10 atm}}{E_{INOx conventional}}^{**}_{1 atm} thermal$	$1.7821 \cdot 10^{-3}$	4.57	
$\frac{E_{INOx MILD}_{10 atm}}{E_{INOx conventional}}^{**}_{1 atm} prompt$	$2.085 \cdot 10^{-3}$	0.141	
$\frac{E_{INOx MILD}_{10 atm}}{E_{INOx MILD}_{1 atm}}^{**} thermal$	3.2	72.9	
$\frac{E_{INOx MILD}_{10 atm}}{E_{INOx MILD}_{1 atm}}^{**} prompt$	0.4617	3.498	

Table 1: Summary of results.

Turbulent Structures Characterization in a Bluff-Body Premixed Flame

¹Eugenio Giacomazzi, ²Valerio Battaglia, ³Claudio Bruno

¹ ENEA - C. R. Casaccia, Sec. ING-TECO, Rome - ITALY

² CRS4 - Cagliari - ITALY

³ Department of Mechanics and Aeronautics - University "La Sapienza", Rome - ITALY

Abstract

The aim of the present work is to analyze turbulence - kinetics interaction, and also effect of commonly made approximations, on bluff-body flame anchoring in a straight channel premixed burner having a rectangular cross section. We perform RANS and LES simulations in 3 - D and 2 - D , considering both simple mixing and reacting cases. The time-dependent *LES* results show three-dimensional vortex structures periodically shortening the recirculation zone downstream of the bluff-body and entraining fresh mixture into the hot recirculating region, stabilizing this flame. We also investigate the effects of assuming periodic boundary conditions along the spanwise direction, instead of the side walls, concluding that assuming periodic boundary conditions cannot capture secondary turbulence phenomena important to correctly predict wall heat transfer. Finally, comparing the "cold" and the reacting cases, we show that even simple kinetics creates a range of chemistry times interacting with those of turbulent structures. Compared with the simple mixing ("cold") case, heat release couples with turbulence via viscous and dilatational effects, flattening the macroscales and widening the inertial range by a factor ~ 2 in frequency. This effect works therefore in the same direction as a reverse energy cascade.

THE TEST CASE

The burner simulated in this paper [1] was purposely built to create an experimental database to validate numerical codes. The burner is a straight channel (length 1 m, rectangular cross section 0.12 m \times 0.24 m), where a prismatic bluff-body, having an equilateral triangular section (side 0.04 m), and located 0.55 m upstream of the outlet section (Fig. 1) anchors the flame. Premixed air and propane (equivalence ratio $\Phi = 0.65$) flow with air mass flow rate 0.6 kg/s. Inlet temperature is 288 K, velocity is 16.8 m/s, and turbulence intensity is 3 - 4 %. The nominal pressure is 1 atm. Temperature was measured by *CARS* and velocity by *LDA* [1]. The Reynolds number based on bluff-body dimension and on maximum velocity reached by the flow at the bluff-body location (30 m/s) is $\sim 10^5$; the resulting dissipative scales (from Kolmogorov's expressions at $T = 288$ K) are $\sim 7 \cdot 10^{-6}$ m and $\sim 3.6 \cdot 10^{-6}$ s.

We performed the simulations presented here using a code linked to a subroutine for our *SGS FM* [?, 3, 4]. We modeled fuel oxidation in the simplest, and crudest, way by means of a single step reaction [5]. We checked the importance of 3 - D effects by performing 2 - D simulations (41000 nodes), 3 - D over only 1/3 of the burner span (~ 273000 nodes, periodic boundary conditions in the spanwise direction) and fully 3 - D (~ 793000 nodes). The *LES* integration time step is 10^{-4} s for the nonreactive and $8 \cdot 10^{-5}$ s for the reactive case.

RESULTS

The flow is characterized by a recirculation zone downstream of the bluff-body periodically altered by vortex shedding. Shedding is asymmetric for the nonreactive case (predicted ~ 107 Hz, measured 105 Hz) and symmetric for the reactive case (predicted 140 Hz). We time-averaged our numerical results to compare them with time-averaged experimental data [1]. Because of the type of variables measured, the comparison is limited to the time-averaged component U_x and its *rms* values (not reported here for reason of length) for the non-reactive case, and also to time-averaged temperatures in the reactive case, at different locations downstream of the flame holder.

First, we investigated the effects of the small aspect ratio (= 2) of the channel in the "cold" case. We considered two subcases: a *LES* of only the central 1/3 of the burner span, assuming spanwise periodic *BCs*, and next, the complete (solid walls) geometry (Fig. 1). Results, not reported here for reasons of length, indicate 3 - D effects, associated to the "secondary" turbulence in the channel, cannot be neglected.

To check 3 - D effects of turbulence on combustion we simulated the reactive case also in 2 - D with the classical *RANS* $k - \epsilon$ model (yielding only the steady state time-averaged solution), the *LES* Smagorinsky model (both coupled to the *EDC* to treat turbulence - chemistry interactions), and our *FM*. After averaging, we concluded that all 2 - D simulations predict similar results downstream of the recirculation zone; within this zone instead the $k - \epsilon$ model

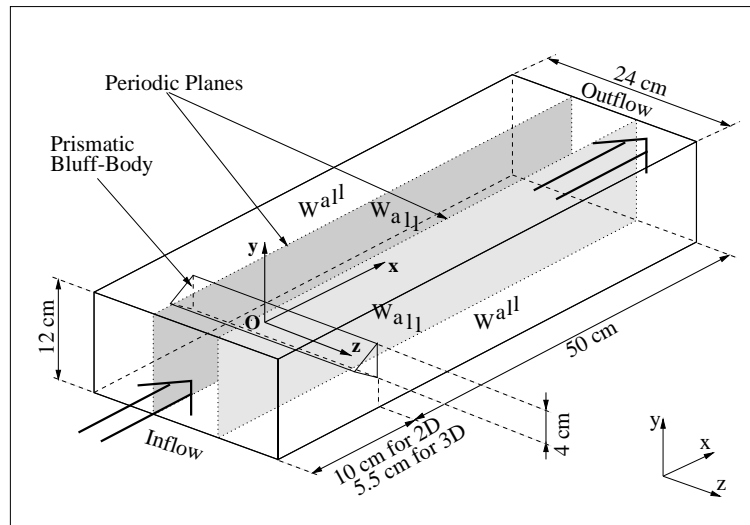


Figure 1: Three dimensional sketch of the burner geometry showing the boundary conditions implemented in our simulations.

is better at predicting the velocity field, partially compensating missing turbulence physics by its larger eddy viscosity. In fact, the $k - \varepsilon$ turbulent viscosity, proportional to k^2/ε , is overpredicted inside recirculation zones because k is large and ε is small. The FM predicts maximum temperature better, but it underestimates heat transfer along y ; heat transfer obtained by using the Smagorinsky model agrees better with the experimental data, but this is simply due to overestimating temperature in the reacting zones, and therefore its gradients near walls. $k - \varepsilon$ results are unsatisfactory as far as maximum temperature and heat transfer.

The recirculation zone length is overpredicted by the 2-D FM simulation because of missing 3-D turbulence effects immediately downstream of the bluff-body. Missing 3-D effects are not the secondary turbulence in the channel: both periodic and fully 3-D BCs LES predict well the recirculation zone length. The recirculation zone is overpredicted because stretching, the effective engine of turbulence controlling vorticity, is missing in 2-D simulations. Predictions near walls improve when boundary layer and corner vortices become large enough for the grid to resolve them; the boundary layers are thickened by near wall 3-D turbulence. We compared average rms values of U_x ; the fully 3-D case agrees better with data than the periodic BCs case, even though the averaged U_x profiles are not as good. Figure 2 shows temperature profiles. The fully 3-D simulation predicts the experimental data best. Thus accurately simulating secondary turbulence is critical to wall heat transfer predictions, as corners vortices, interacting with the reacting shear layer downstream of the flameholder, transport heat to the walls. The single-step chemistry used can apparently predict the average temperatures of this flow.

The flame in this paper is stabilized by (symmetric) vortex shedding. Vortices downstream of the bluff-body (tracked by their helicity in our investigation) tend to flatten near the upper and lower edges of the flameholder prism, and to become cylindrical near the center. Reaction occurs in the shear layers between wake and coflowing fresh mixture. Hot products are stored inside the wake, convected downstream and periodically mixed by the shed vortices with the coflowing fresh mixture. Pockets of reactants have additional time to burn further downstream within "isles" of fast kinetics indicated by the Damkoehler number field (not shown). Profoundly unlike the picture drawn based on time-averages, this mechanism is intrinsically unsteady.

Turbulent Kinetic Energy Spectra And Their Coupling With Chemistry

We estimated the range of frequencies injected into the flow from the reaction rate [5] adopted for the simulation: even though the chemistry is simple, it injects into the reacting flow a broad range of chemical frequencies. At

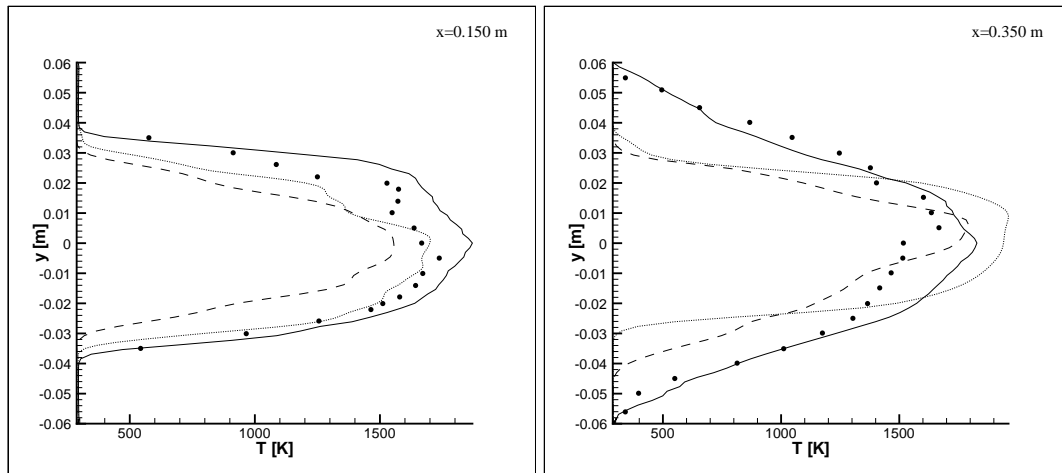


Figure 2: Comparison of temperature profiles at different locations with experimental data. Numerical results obtained by using the FM model. Solid line: complete 3 – D . Dashed line: periodic BCs 3 – D . Dotted line: 2 – D . Bullets: experimental data.

$p = 101325 Pa$, this range is $O(1)$ to $O(1000) Hz$.

These chemical scales interact with turbulence. We show this by means of the turbulent kinetic energy spectra of Fig. 3. We sampled turbulent kinetic energy in the fully 3 – D nonreactive and reactive cases at $x = 0.12 m$ and $y = 0.018 m$ in the $z = 0$ plane; this point is (in the average) inside the reacting shear layer downstream of the flameholder. Sampled signal FFT spectra were nondimensionalized by their rms and then normalized by the peak value in the nonreactive case. Due to the different sampling frequencies f_s of the two signals ($f_s = 10000 Hz$ for the “cold” and $f_s = 12500 Hz$ for the “hot” flow), cutoff frequencies, $f_s/2$, are different.

In the “cold” flow a large eddy at $\sim 250 Hz$ stores most of the energy; we expected this frequency because the velocity fluctuation close to the sampling location is $\sim 10 m/s$ and the length scale is $0.04 m$ (bluff-body and flow passage sizes): their ratio predicts the frequency of the large scale. Bluff-body size being the main scale, there is a rapid transfer of energy down to ~ 2000 , prior to reaching the wider inertial range from ~ 2000 to $\sim 4000 Hz$.

Analyzing the “hot” spectrum, this picture changes due to three effects:

1. The **local** density changes due to combustion expands products, locally accelerating the flow ($\nabla \cdot \underline{u}$ in the continuity equation). Therefore, **high heat release frequencies** at the sampling location pump kinetic energy in the frequency region from ~ 2000 to $\sim 6000 Hz$. At large scales no reactions occur, or, if they do, gradients are small; therefore pumping is small or negligible. This pumping implies **non-equilibrium** of **reactive fine structures**; in the “cold” flow these structures are instead in equilibrium. Spectra from literature [6] do not show this behaviour, due to the slow chemistry employed, or low sampling frequency, or large integration time step (these considerations apply also to experimental measurements). Non-equilibrium physics of reactive fine structures suggests every SGS model should be made time dependent within an integration time step if the local spatial resolution is insufficient to resolve reacting scales (i.e., at high Damkohler). Capturing these intermittent dilatational phenomena may reveal itself crucial to study certain type of *combustion instability*.

2. **Large scale fluctuations** are instead **damped** by viscosity increasing with temperature, and that is why their turbulent kinetic energy is lowered with respect to the “cold” case. This effect is well known.

3. The **inertial range** is **widened** (from ~ 300 to $\sim 2000 Hz$). This occurs because macroscales are damped by viscosity (effect # 2) and, mainly, due to a **reverse energy cascade**: heat released inside fine structures produces **local intermittent dilatation** (see #1) pumping energy into lower frequencies. This dilatation together with convective transport may contribute to counter-gradient diffusion. FM predicts this effect because it can perform local DNS

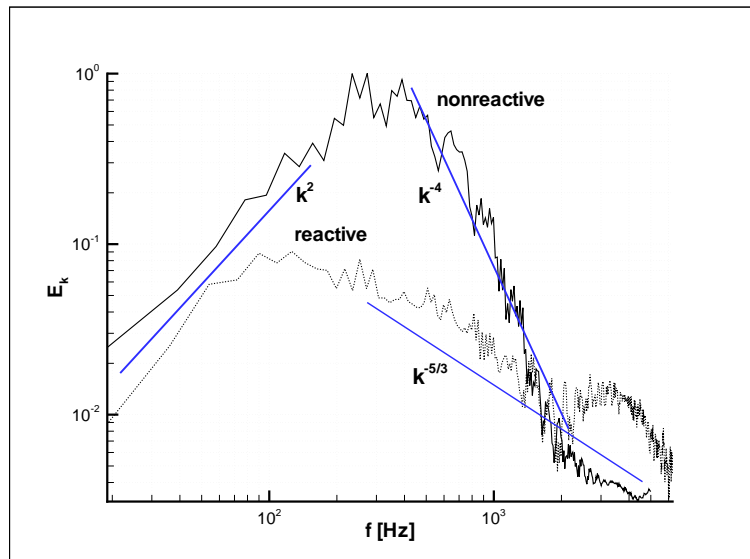


Figure 3: Turbulent kinetic energy spectra in the reactive and nonreactive case, nondimensionalized by their variance and normalized by the maximum value of the cold spectrum.

in the reactive hot zones with sufficient spatial resolution, i.e., including molecular and dilatational effects. This capability is shown by the high frequencies resolved in Fig. 3.

CONCLUSIONS

Our results show that the burner analyzed must be simulated without *BCs* approximations typical of *CFD* practice. 3 – *D* structures downstream of the bluff-body stabilize the flame by periodically mixing fresh mixture and hot products. This picture is substantially different from conclusions drawn based on time-averaged results/data. Secondary turbulence is important far downstream of the flame holder, altering wall heat transfer.

Frequency analysis inside the (average) reacting shear layer shows important differences between the “cold” and the “hot” flows, never reported before. These consist of three effects: first, realistic (fast) chemical reactions pump energy at high frequency; second, the temperature increase due to combustion dampens large scale fluctuations, decreasing the energy of the eddies; third, the energy pumping at high frequencies produces a significant reverse energy cascade, widening the inertial range in the case of reacting flow.

References

- [1] R. Ryden, L. E. Eriksson, S. Olovsson, *XI ISABE*, Proc. AIAA, 470-478 (1993)
- [2] E. Giacomazzi, C. Bruno, B. Favini, *Combustion Theory and Modeling*, 3,4:637-655 (1999)
- [3] E. Giacomazzi, C. Bruno, B. Favini, *Combustion Theory and Modeling*, 4:391-412 (2000)
- [4] E. Giacomazzi, C. Bruno, *XV ISABE Symp., Joint Propulsion Conference*, Proc. AIAA, paper No. 1144 (2001)
- [5] C. K. Westbrook, F. L. Dryer, *Combustion Science and Technology*, 27:31-43 (1981)
- [6] R. J. M. Bastiaans, L. M. T. Somers, H. C. de Lange, *ERCOFTAC Bulletin*, 48 (2001)

Interaction of Combustion and Atomization Processes in Electrospays Burning

¹R. Ragucci, ²A. Cavaliere, ²O. Campagna

1 Istituto di Ricerche sulla Combustione - C.N.R., Naples - ITALY

2 Dipartimento di Ingegneria Chimica - Università Federico II, Naples - ITALY

INTRODUCTION

During last few years theoretical and experimental exploration of potentials of electro-hydro-dynamic control of atomization attracted a high level of interest^{1,2,3}. Among the other reasons of this interest is the envisaged possibility of using this technology in order to control, by acting on the atomization, the evolution of a whole process. Examples of processes that could find advantages by the use of such control systems are the combustion of liquid fuels as well as material deposition technologies. To this aim the availability of a dispersion of droplets of a well defined size and electrically charged is potentially an excellent solution. As matter of fact the size control allows for a thorough control of evaporation and mixing processes along with a targeting based on deflecting systems acting on the droplet residual charge.

Nevertheless, the determination of a stable, effective and robust configuration of an electro spraying system that could be used successfully in practical combustion system is still lacking. Many configuration have been evaluated and several results can be found in literature but many problem are still open and will require further experimental and modelling activity.

One of the open questions is the effect of the mutual interaction of combustion and atomization processes. This interaction represents a key point in the assessment of realistic potentialities of electro spray systems exploitation in combustion systems.

The nature of this interaction is intrinsically complex and a thorough description of even its phenomenology is difficult. As a matter of fact, the pool of radicals formed during the chemical reactions taking place in the flame regions interacts with the charged droplet in a complicated way and can affect the droplet cloud shape and behavior. On the other hand the electric field itself interacts with the flame and, as a consequence, it can be expected that the flame be influenced by the electric field presence.

It can be envisaged that atomization and combustion processes cannot be decoupled and their characterization has to be attempted using a systematic approach. In this paper a systematic characterization of a well-defined nozzle configuration, operated either in isothermal and burning conditions while keeping the same feeding and applied voltage conditions, is presented. This paper aims both to identify the ranges of fuel flow rate and of applied voltage in which a stable combustion condition can be established and to determine the changes in the spray droplets size and velocities induced by the combustion process.

SET-UP OF THE ATOMIZING SYSTEM

The atomizer used in the experimental work is a simple coaxial system, sketched in Fig. 1, in which a stainless steel needle is used to feed the liquid fuel and the electric field is generated by applying a potential difference between the needle and a co-annular electrode. In the external part of the atomizer an air flow is used to prevent the accumulation of liquid and to shield the spray from external perturbations. The air flows through a glass balls bed and then through a metallic mesh that is posed to the same potential of the annular electrode. The fuel used was n-heptane, with an added percentage of 0.05 of an antistatic additive.

The air velocity has been kept constant and very low (with respect to the droplet velocities) in all the investigated conditions in order to avoid a significant interaction with the atomization and combustion processes.

A purposely realized voltage generator capable of supplying voltages up to 10 KV was used to generate the electric field, In a great part of the tests a positive voltage was applied to the needle while the remaining part of the nozzle was kept at ground level. Some of the tests were conducted inverting the polarization of the electrodes in order to evidence possible effects on the atomization and combustion processes.

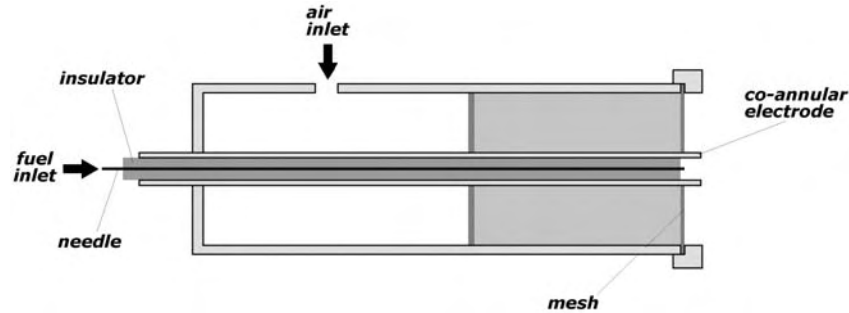


FIG. 1 Schematics of the nozzle.

FLAME STABILITY

A relevant part of the work aimed to the determination of the burner geometric configuration that could assure a satisfying functioning of system in terms of flame stability. A preliminary work made in isothermal conditions indicated that a reasonable performance of the system, in terms of atomization quality, could be achieved by using a needle with an outside diameter of 0.46 mm and an inside diameter of 0.25 mm. It was then decided to use this needle in the characterization of flame stability. To this aim the distances between the needle and the top of the co-annular electrode were changed in a systematic way and the interval of stable combustion were observed. It was thus individuated a suitable geometric configuration to be used for the subsequent characterization of the spray atomization and combustion.

In Fig. 2 is reported the domain of stable combustion, in terms of liquid flow rate and applied voltage, as it was observed for the above mentioned configuration.

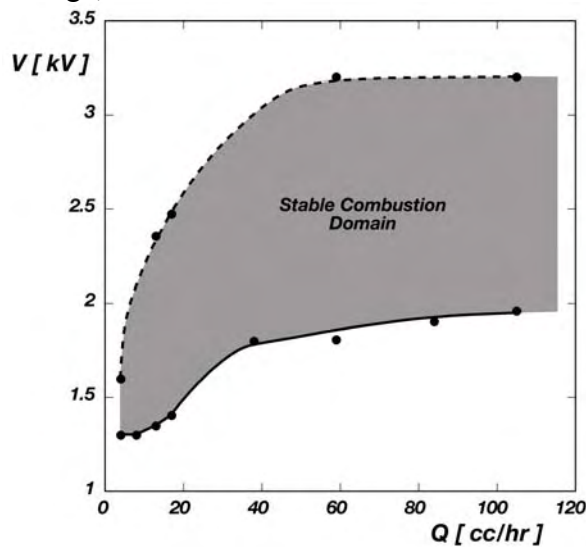


Fig. 2. Domain of stability for the spray in Combustion.

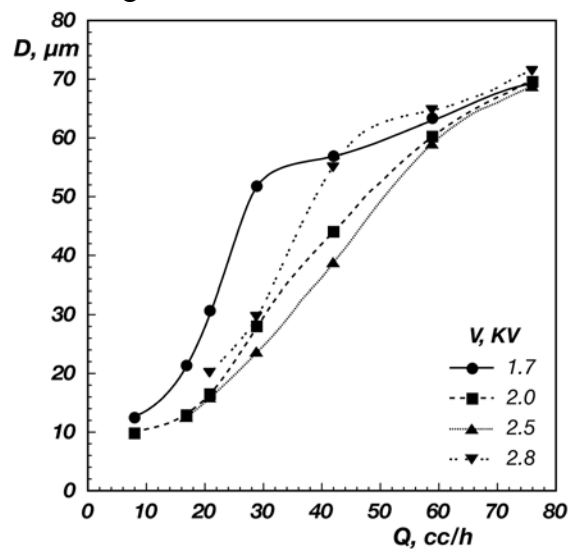


Fig. 3. Values of the mean diameter of droplets spray vs fuel flow rate.

The dotted line marking the upper limit of stable combustion region (in grey) indicates the

maximum voltage applicable at each liquid rate before the occurrence of an electrical discharge between the needle and the annular electrode. The continuous line marks the lower limit of applied voltage under which the flame became unstable and extinguishes due to the very poor atomization quality. It is noteworthy that it was not possible to find a real upper limit for the liquid flow rate in which the flame could be stabilized. Nevertheless at very high fuel flow rates the liquid jet was clearly visible very far from the needle and the flame was stabilized around the liquid jet.

An explanation of the observed stability domain can be found in the droplet size profiles obtained at different applied voltage as a function of the liquid flow rate reported in Fig. 3.

As shown in figure, the droplet diameter decreases with increasing voltage from 1.7 up to 2.5 KV due to the reduction of Taylor's cone apex angle at increasing voltage. Vice versa with increasing the flow rate an increase of final droplets diameter is observed due to the increase of this angle.

In view of these results it can be inferred that the increase in minimum voltage required to stabilize the flame observed at increasing the liquid flow rate (see solid line in Fig. 2) is due to the degradation of atomization quality with production of larger droplets.

From Fig.3 it can also be observed that a further increase in the applied voltage above 2.5 KV causes a significant increase of droplet size. This can be another explanation of the impossibility of stabilizing a flame at very high voltage. Finally, from Fig. 3 it can be observed that the size of the droplets does not depend on the applied voltage at high fuel rates. This is a fairly good explanation of the essential independence of the stability domain on applied voltage at high fuel flow rates (see Fig. 2).

ATOMIZATION-COMBUSTION INTERACTION

As reported in the introduction section the coupling of atomization and combustion processes is complex due to the multiple mutual effects acting simultaneously. An attempt to give at least a phenomenological description of such interaction two conditions were chosen and characterized in detail both in isothermal and burning conditions. The first condition (named A) correspond to a fuel flow rate of 17 cc/hr and an applied voltage of 1.7 KV. The second one (B) corresponds to 34 cc/hr and 2.5 KV. The two conditions have a very different atomization quality (see Fig. 3).

The mean diameter profiles in the two conditions are reported in Fig. 4 for both isothermal and burning cases. In isothermal conditions the difference in the droplet sizes of the two considered cases is not very significant and also the difference in their axial evolution is not relevant.

In presence of the flame for the condition A it can be observed a general decrease of droplet size with respect to the isothermal case. The axial profile of the droplet size in burning condition shows an increase of droplets dimensions. The analysis of the size histograms (not reported here for lack of room) reveals that this behaviour is due to a phenomenon of selective evaporation of smaller droplets with survival of droplets which have greatest dimensions.

In condition B it is possible to observe a strong increase of the droplet sizes passing from isothermal to combustion condition. An explanation of this peculiar behaviour is not simple. The effect of a selective evaporation is to exclude based on the analysis of the size histograms. Another possible explanation could be the selective drifting of smaller droplets toward the spray periphery, due to the combined effect of charge repulsion and electric field action, that was observed in cold conditions and can explain the convexity of the profile in isothermal condition in case A. In the case under discussion it has been verified the substantial absence of radial components of the velocity in combustion conditions and a selective spatial displacement of the droplets can not be invoked to explain the observed huge increase in the mean size.

The most probable explanation of this increase appears to be a change of the atomization regime induced by the presence of the flame. In fact, the applied voltage (2.5 KV) is close to the upper limit of stability for the flame at the 34 cc/hr fuel flow rate. In these conditions it is likely that the Taylor cone formed at the top of the needle is less stable than in the previous case^{4,5}. The double effect of the radiative heating from the flame and the modification in the electric field induced by the free charges present in the flame can lead to the destabilization of the cone and to a sensible decrease in the atomization quality. This effect is not dissimilar from the one observed at very high applied voltages (curve at 2.8 KV in Fig. 3) where the increased voltage disrupt the cone stability and produce an unstable atomization regime (either a multi-jet or a whipped regime) characterized by larger droplet sizes⁵.

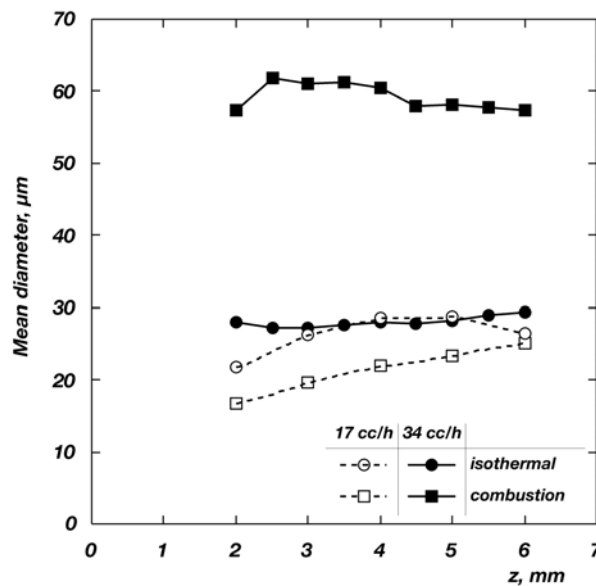


FIG. 4 Values of mean dimensions of droplets for conditions “A” and “B” in isothermal and combustion regimes.

REFERENCES

- Balachandran W., Hu D., Yule A.J., Shrimpton J.S., Watkins A.P. (1994): “Electrostatically produced fuel sprays for combustion applications”, ICLASS 94 Rouen, France, pp. 1010-1018.
- Gomez A. (1993): “The electro spray: Fundamental and applications”, Proceedings of 3rd Conference on experimental heat transfer, Fluid Mechanics and Thermodynamics, Honolulu.
- Gomez A., Chen G. (1994): “Monodisperse electro sprays: Combustion, scale-up and implications for pollutant formation”, Submitted for publication in a volume in honor of professor Irvin Glassman in the Combustion Science and Technology Book Series.
- Ragucci R., Fabiani F., Cavaliere A., Muscetta P., Noviello C. (2000): “Characterization of stability regimes of electrohydrodynamically enhanced atomization”, Experimental Thermal and fluid Science.
- Noymer P.D., Garel M. (1999): “Stability and atomization characteristics of electrohydrodynamically jets in the cone-jet and multi-jet modes”, J. Aerosol Sci., Vol 31, pp 1165-1172.

Mathematical Modelling of Flameless Combustion for Micro-CHP System Development

¹E. Malfa, ¹M. Venturino, and ²V. Tota

1 ABB Service S.r.l – Research Division, Sesto S. Giovanni – ITALY

2 Laureando c/o Dipartimento di Energetica – Politecnico di Milano, Milano - ITALY

INTRODUCTION

Thermophotovoltaic (TPV) conversion is a process by which heat radiation is directly transformed into electricity by means of photovoltaic generation. Recent interest in TPV has been stimulated by the availability of infrared PV cells and by the possibility of surrounding the source of heat by an “emitter” that re-radiates the energy in a narrow spectrum (selective emitter). ABB is leading the development of a Micro-CHP TPV unit, size of 1.5 kW, in which a recuperative burner [1] heats a cylindrical infrared emitter up to 1300°C. Multiple circuits of shingled GaSb infrared-sensitive cells [2] surround a refractory metal foil wrapped around the SiC support tube, creating an infrared emitter with a spectral output matched to the PV cells. [3, 4].

To maximize the micro-CHP conversion efficiency it is necessary to obtain uniform temperature along the emitter and to enhance the heat recovering in the flue gases. To reach these goals the commercially available WS FLOX[®] recuperative burner C100 has been selected for micro-CHP prototype development. The burner works using combustion air at temperature exceeding 800°C and reduced oxygen content by dilution with combustion gases. This results in a transparent flame (were the name “**FL**ameless **OX**idation”), characterised by uniform temperature along its axis and low NO_x and noise emissions.

The present paper relates to the validation of the CFD tool for flameless combustion and its application to the modelling of the combustion system for the TPV based micro-CHP unit in order to evaluate the proper match between the selected recuperative burner and the TPV Power Conversion Array (PCA)

FLAMELESS COMBUSTION MODELLING

The validation has been performed using experimental data available in literature [5] for a cylindrical furnace of 1m length and 0.5m diameter equipped with a “WS C100” recuperative burner (figure 1 and 2). This burner (min./max. output 15kW/25kW) is designed to operate either in conventional flame or in FLOX[®] mode.

CFD simulations, by means of FLUENT[™] code, have been performed using 2D axisymmetric approach. A mesh of about 16,000 quadrilateral cells, has been adopted to discretised the combustion chamber and the burner head.

Herein the results for three operational conditions in FLOX[®] mode, corresponding to process temperature of 900°C, 1000°C and 1100°C have been described. Table I reports the physical models used in the simulations, the numerical approach and the boundary conditions [6].

Temperature profiles along the furnace axis are compared with experimental data in figure 3, for the three process temperatures. The mixing of methane, air and

recirculating gas and the ignition delay (low-temperature zone) are well predicted for $T_{\text{proc}} \leq 1000^\circ\text{C}$. Figure 4 shows radial temperature profiles for $T_{\text{proc}} = 1000^\circ\text{C}$ on four different radial locations placed at 50mm, 200mm, 400mm and 950mm from the burner head.

<i>Physical models and reaction scheme</i>			
Flow	Incompressible		
Turbulence	k - ϵ Standard		
Reaction Scheme	$\text{CH}_4 + \text{O}_2 \rightarrow \text{CO}_2 + \text{H}_2\text{O}$ (1 Step)		
Chemistry	Eddy-dissipation / Arrhenius (Westbrook&Dryers)		
Discretization model	DOM (Discrete Ordinates Model)		
	WSGGM		
Wall boundaries	Wall functions		
<i>Numerical approaches</i>			
Grid type	Unstructured - quadrangular		
Order	Segregated		
Linearization	Implicit		
Discretization of non linear terms	second order up-wind scheme		
<i>Boundary conditions</i>			
	$T_{\text{process}} = 900 \text{ C}$	$T_{\text{process}} = 1000 \text{ C}$	$T_{\text{process}} = 1100 \text{ C}$
Flow (methane)	$T = 300 \text{ K}$; $m = 0.0005 \text{ kg/s}$ (25 kW)		
oxidizer (air)	$m = 0.009846 \text{ kg/s}$		
	$T = 858 \text{ K}$	$T = 923 \text{ K}$	$T = 988 \text{ K}$
Stoichiometric ratio	$\Phi = 1.15$		
Thermal conditions on burner walls	adiabatic		
Thermal conditions on combustion chamber walls	$q = - 12110 \text{ W/m}^2$	$q = - 12750 \text{ W/m}^2$	$q = - 13150 \text{ W/m}^2$

Table I. Physical model and reaction scheme, numerical approach and b.c. adopted in FLOX[®] mode simulations

The good agreement between numerical and experimental data for $T_{\text{proc}} \leq 1000^\circ\text{C}$ confirms that, despite of 1-step simplified reaction scheme, the Finite-Rate/Eddy-Dissipation model, in which the smallest of the Arrhenius rate and the mixing rate is used, is suitable for representing the kinetic controlled reactive flows. In fact the flameless combustion process in these cases is mainly dominated by slow kinetics due to autoignition delay (low temperature regime) and dilution of reacting mixture (high recirculation of flue gases) while the effects of turbulence has little influence on the prediction of temperature field. At higher process temperature ($T_{\text{proc}}=1100^\circ\text{C}$) the Finite-Rate/Eddy-Dissipation model gives a good prediction of position and value of temperature peak, however in the near burner zone the axial temperature is below the experimental data. This can be explained considering that the higher temperature of recirculating gases increase the kinetic rates while the higher combustion air jet velocity increases the turbulence mixing close to the burner head. As results of this, the two phenomena become simultaneous and the Finite-Rate/Eddy-Dissipation model appears to be less accurate.

Figure 5 shows the results of the simulation for WS C100 burner firing in a radiant tube either in flame and FLOX[®] mode. The working condition has been selected to match the TPV Power Conversion Array (PCA) needs in terms of power density and emitter temperature [4]. The longitudinal distribution of the emitter temperature in FLOX[®] mode appears to be flatter than in flame mode (max. ΔT in the active region $< 30^\circ\text{C}$). This confirms the potential for the application of recuperative burner

operating in FLOX[®] mode for micro-CHP TPV. By the end of this year, a test campaign will be performed in collaboration with ENEL in order to assess the combustion system performance. The laboratory test will also provide experimental data for further validation of CFD approach herein described.

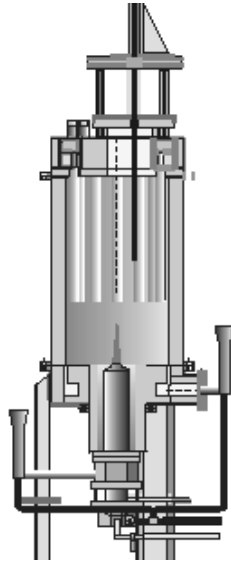


Fig. 1: WS experimental furnaces



Fig. 2: WS C100 burner

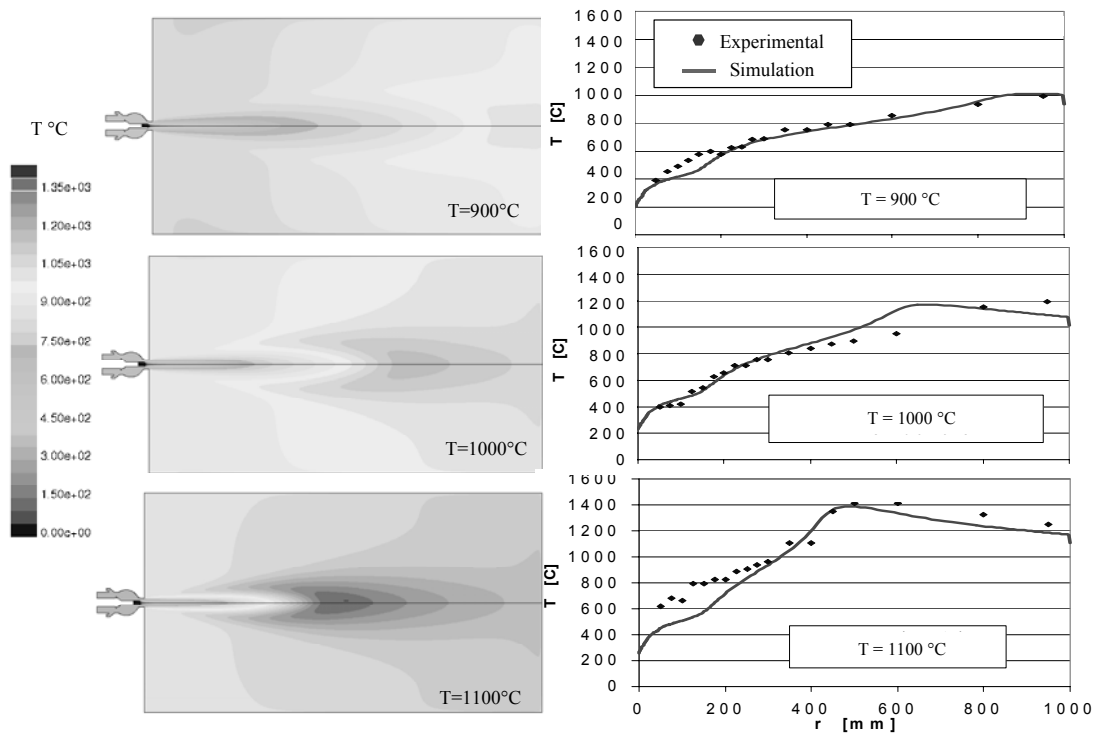


Fig. 3: WS C100 burner in FLOX[®] mode:
Temperature field and axial profiles for different T_{proc} .

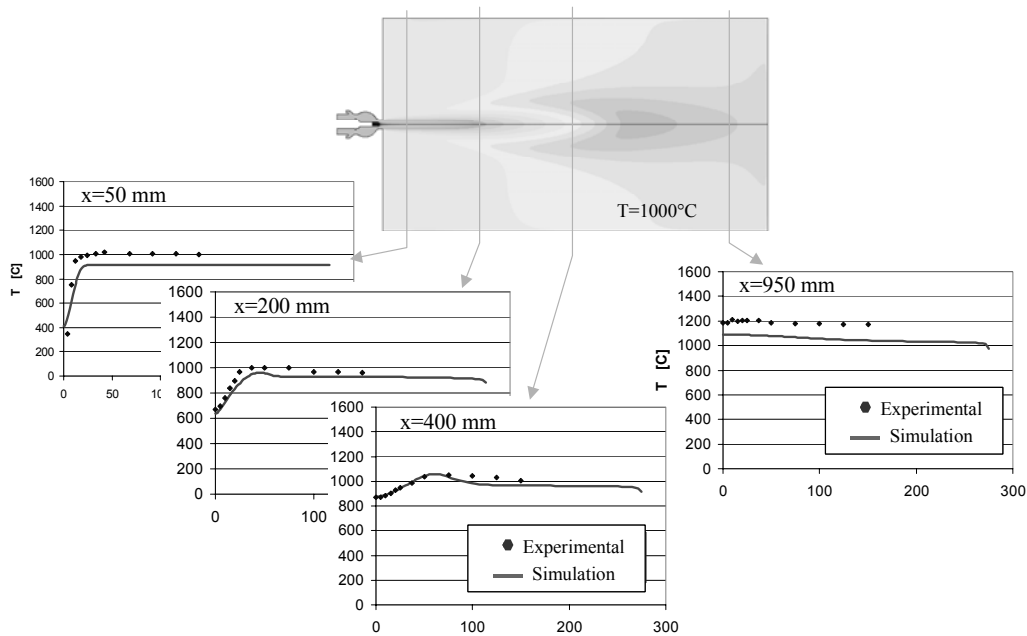


Fig. 4: WS C100 burner in FLOX[®] mode:
 Temperature field and axial profiles for $T_{proc}=1000^{\circ}\text{C}$

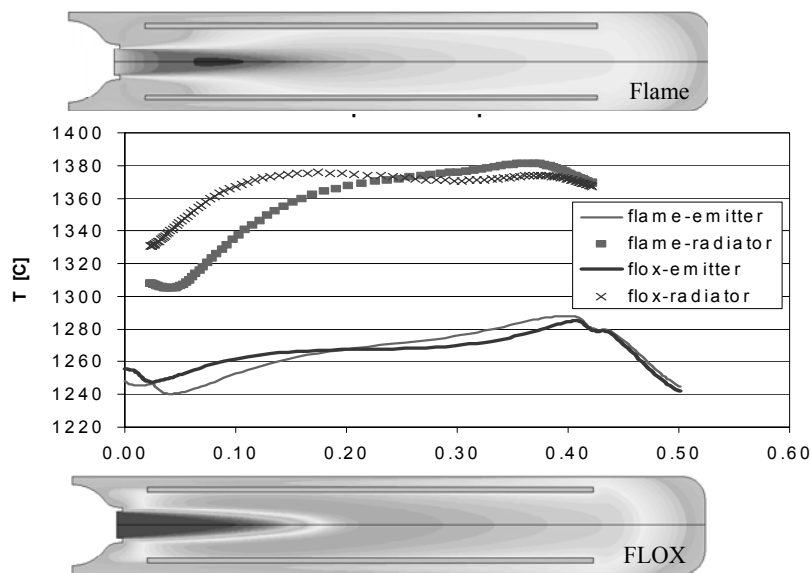


Fig. 5: WS C100 firing in radiant tube:
 Temperature field and axial temperature on emitter and flame tube

REFERENCES

1. Wunning J.A., Wunning J.G.: *Proc. 4th HTAG 2001*, Roma, November (2001)
2. Ferguson L., Fraas L.: *Proc. 3rd NREL Conference on TPV Generation of Electricity*, CP401, p. 169 (1997)
3. Fraas L., Malfa E., et al.: *17th European PhotoVoltaic Solar Energy Conference and Exhibition*, Monaco, October (1997)
4. Fraas L. et al.: *5th Conference on TPV*, Roma, To be published (2002)
5. Wunning J.G.: *Flammlose Oxidation von Brennstoff*, ISBN 3-89653-053-4, D82 (Diss. RWTH Aachen), (1996)
6. Tota V.: *Tesi di Laurea anno accademico 2002-2003*, Politecnico di Milano, Dip. Energetica, Relatore Prof. E. Macchi

Modeling of Spark Ignition Engines with Tumble Swirl

Ugo Martin, Renato Rota*, Sergio Carrà

Politecnico di Milano

*Dip. di Chimica, Materiali e Ingegneria Chimica "G. Natta" / CIIRCO
via Mancinelli, 7 - 20131 Milano, Italy*

and

Agostino Dominici

Ferrari S.p.A.

Via Abetone Inf. – 41053 Maranello (MO), Italy

INTRODUCTION

The homogeneous charge spark ignition apparatus is one of the most common and old kind of internal combustion engine. However, its functionality is not yet fully understood since it involves non-stationary turbulent reacting flows [1].

The main problem is that, as well known, the turbulence field has a fundamental influence on the flame speed and consequently on the engine efficiency. A detailed numerical simulation of multi-dimensional reacting flows could in principle solve all spatial and temporal scales of turbulence and chemistry, but this is yet far from the current computer technology.

A different approach accounting for these phenomena is to use a lumped parameters multiple-zones model representing the flame sheet propagation [2], which expands in an almost perfect spherical way with a velocity depending on the turbulence intensity. In this work the laminar flame speed has been modified in order to account for turbulence influence [3]. This model, which is based on physically founded relations, is inherently less dependant from a particular engine configuration and its results can be more easily generalized.

MODEL DESCRIPTION

We are interested in developing a multiple-zone lumped-parameters model resulting in a set of ordinary differential equations (ODE). Figure 1 shows the volume displaced by the system considered for the model development. Moreover since we are interested into the effect of the tumble intensity on the engine performances only the compression and expansion strokes have been considered in this work.

As usual for multiple-zones models this volume is divided into two perfectly stirred zones, relative to burned and unburned gases respectively, separated by an ideal flame sheet [2]. The composition of the burned mixture is assumed to be equal to the equilibrium one while that of the unburned one keeps the same global composition all over the process. In particular, 50 chemical species, involving also many radicals that can play a role at the high temperature values achieved in

* Telephone: +39 0223993154, Fax: +39 0223993180, E-Mail: renato.rota@polimi.it

combustion engines, have been considered.

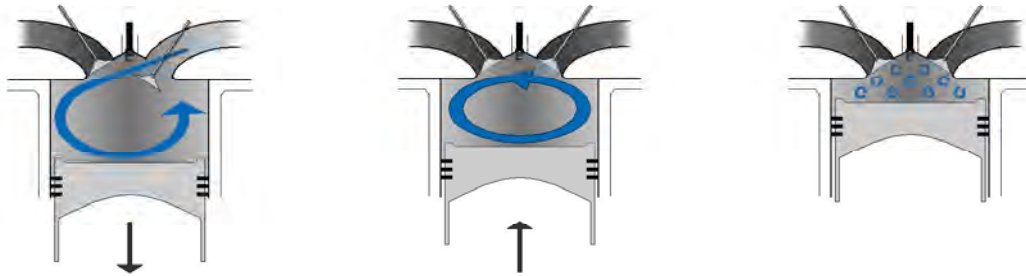


Fig. 1 Schematic representation of the control volume considered in the model development and schematic Tumble swirl's view during its generation and evolution

The basic equations of the model (that is the mass, energy and entropy equations) are similar to those discussed in a previous work for a different situation [4], and are discussed in detail elsewhere [6]. Based on the multi-connected flame front assumption, the mass burning rate equations can be expressed as [2]:

$$\frac{dm_b}{dt} = s_L \rho_u S_f + \frac{m_\mu}{\tau_b} \quad (1)$$

where all the symbols retains their intuitive meaning apart from m_μ , which is the amount of unburned gases entrained as small pockets into the flame front, and τ_b , which is the characteristic time for burning these small pockets and can be approximate as the ratio of the characteristic dimension of these pockets (that is, the characteristic length of the turbulent vortex) to the laminar burning rate. The rate of unburned gas entrainment determinates the increase of the flame speed with respect to the laminar value, and can be represented as [2]:

$$\frac{dm_\mu}{dt} = \rho_u S_f u_T \left(1 - e^{-\frac{t}{\tau_b}} \right) - \frac{m_\mu}{\tau_b} \quad (2)$$

where a second parameters, u_T , which is the entrainment velocity, has been introduced. These two parameters, τ_b and u_T , can be related to the turbulence parameters, which in turn are related to the velocity field in the cylinder. In this work we investigated the effect of the tumble vortex which is considered as a solid body rotating around its own central symmetrical axis (that is orthogonal to the cylinder axis) with a simplified velocity field [5]. This assumption allows for computing the three velocity components (which are required to compute the average value of the turbulence kinetic energy, as discussed in the following) at a given point in the cylinder as a function of a single variable, U .

The $k - \varepsilon$ turbulence model is constituted by the conservation equations for the turbulent kinetic energy, k , and for the rate of dissipation of turbulent kinetic energy, ε [4, 5]. To be congruent with the general lumped-parameters approach, the conservation equations have been integrated

over the chamber volume to find an average volume value of both k and ε :

$$\int_{VOL} \rho \frac{dk}{dt} dV = \int_{VOL} \left(\frac{2}{3} k \frac{\partial \rho}{\partial t} + \tau_{ij} \frac{\partial u_i}{\partial x_j} - \rho \varepsilon \right) dV - \int_{SUR} \rho v_{teq} \left(\frac{k - k_{eq}}{y_{eq}} \right) dS \quad (3)$$

Using the simplified velocity field it is possible to solve analytically the integrals above leading to the final formulation of the model. These equations allow for computing k and ε once U is known, which represents a new unknown thus requiring one more equation: the momentum balance of the tumble vortex.

EXPERIMENTS

To validate the model discussed in the previous section several experiments have been carried out. They involve two different 12 cylinder real engines that differ mainly in the intake and exhaust system shape thus leading to a markedly different intensity of the tumble vortex. Both the engines have been operated in a wide range of operating conditions, that is, from 1000 to 7000 rpm engine speeds and from +4 to -8 crank angle degree of spark timing. +4, 0, -4 and -8 refer to a standard set that was different for each engine speed.

RESULTS AND DISCUSSION

The starting turbulence intensity has been considered as the only adjustable parameter of the model to be tuned on some experimental data, namely three maximum pressure values. A typical comparison between experimental pressure profiles data and model results is shown in Figure 2.

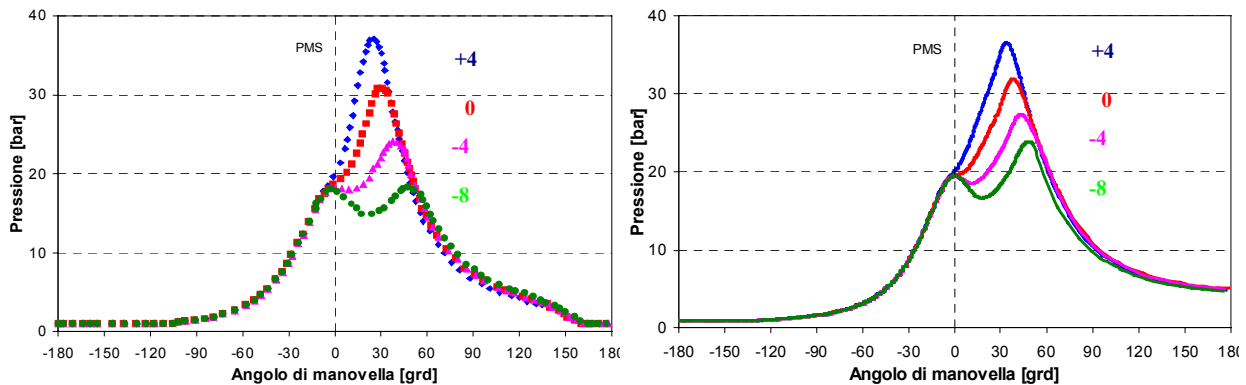


Fig. 2 Experimental (left) and model prediction (right) pressure profiles as function of crank angle for 1000 rpm and different spark times classes (+4, 0, -4, -8)

We can see that the agreement between experimental data and model calculation is definitely good. To confirm the capability of the model to predict the effect of changing the tumble intensity, a more meaningful validation has been carried out considering an independent set of measurements on a different engine. Since no data from this engine have been used in the tuning procedure, this comparison represents a more severe test for the model reliability.

An overall comparison among the model predictions and the experimental results is summarized in Figure 3. We can see that also in this case the average difference between model predictions and

experimental data is equal to about 4%, that is, of the same order of magnitude of that found for the first engine. All the findings concerning the model performances have been confirmed also by this second set of experiments.

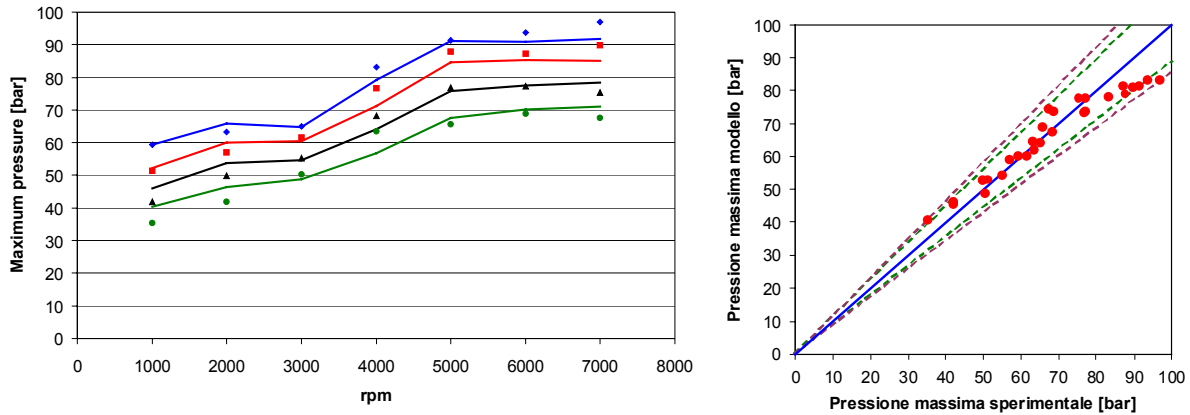


Fig.3 Comparison between maximum experimental pressure values (symbols) and model predictions (lines) for the second engine. Sparking time: +4(♦);0(■);-4(▲);-8(●)

CONCLUSIONS

On the basis of very few experimental information, the model developed has been able to foresee the influence of changing several engine operating conditions, such as the engine speed, the spark timing as well as the tumble ratio. Apart from a good quantitative agreement with the experimental findings, the model has been able to predict also the main trends evidenced experimentally, thus becoming a valuable tool for the daily design work.

BIBLIOGRAPHY

1. Heywood, J.B.: *Internal Combustion Engine*, McGraw-Hill (1988).
2. Keck, J.C.: *Proceedings of Nineteenth Symposium on Combustion*, p.1451, The Combustion Institute, (1982).
3. Launder, B.E., Spalding, D.B.: *Lectures in Mathematical Models of Turbulence*, Academic Press (1972).
4. Canu, P., Rota, R., Carrà, S. and Morbidelli, M.: *Comb. and Flames* 80: 40 (1990).
5. Benjamin, S.F.: C0465/013 *IMechE* (1993).
6. Martin U., Rota R., Carrà S., Dominici A., *Comb. and Flames* submitted (2002).

CFD Modeling of a Lean-Lean Premixed Staged Combustion Chamber

^{1,2}D. Valentini, ¹A.A. Barresi, ²E. Carrea

1 Dip. di Scienza dei Materiali e Ingegneria Chimica - Politecnico di Torino, Turin - ITALY

2 ALSTOM Switzerland, Technology Center Daettwil, Segelhof 1, CH-5405, Switzerland

INTRODUCTION

Lean premixed combustion is applied to gas turbines combustion systems as a proven DLN (dry low NOx) method [1].

In the present work, the influence of the combustion chamber geometry on pollutants (CO and NOx) emission is investigated. The system under analysis is based on a new mixer and swirl generator characterized by the presence of two sequential stages as shown in Fig. 1.

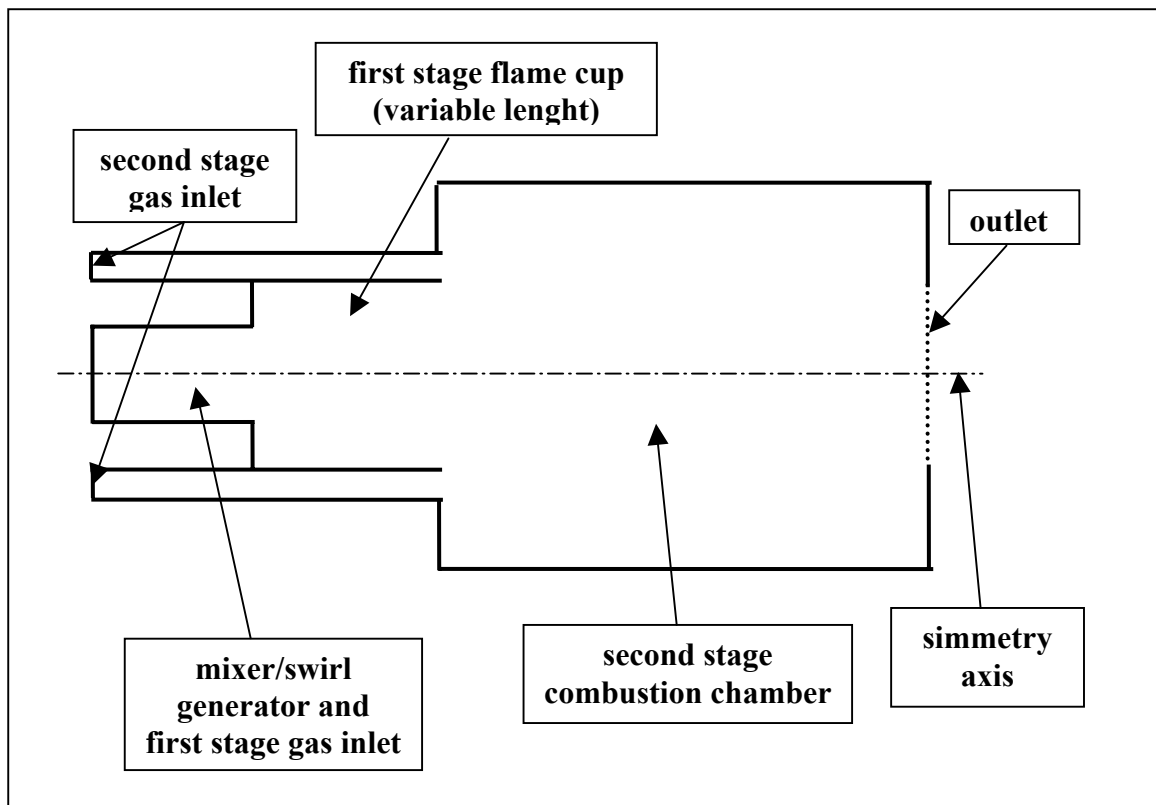


Figure 1. Scheme of the lean-lean premixed staged combustion chamber

The first stage operates at constant temperature, while the second stage operates at variable temperature depending on the load conditions, to keep a stable flame with low NOx emissions over a wide operation range. In the first stage the expansion ratio between the swirl generator and the flame cup allows a recirculation zone to be established to assure stable ignition and combustion in the first stage before cross-ignition with the second stage occurs.

The combustion simulations reproduce experimental tests carried out at atmospheric pressure. The correct reproduction of experimental data will allow the model to be used for further simulations as a reliable prediction tool.

CFD SIMULATIONS APPROACH

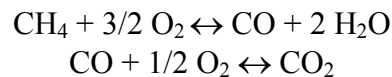
The system described above has been experimentally investigated at atmospheric pressure under a wide set of operating conditions [2]. This work reports the results of a CFD simulation approach for the same system; some of the experimental runs have been selected for the comparison. Simulations have been carried out using Fluent 6. A bi-dimensional, axial-symmetric grid has been considered. Measured velocity and mixture concentration profiles have been used as inlet conditions 90 mm upstream the swirler exit into the first flame cup.

Cold flow simulations: mesh and turbulence model validation

Mesh and turbulence model have been validated via comparison with experimental data of axial velocity measured with LDA method in a water channel [2]. The geometry considered in the simulations has a different scale, compared to the one used in the cold flow measurements, and the fluid considered was air instead of water. The comparison here attempted is based on the Reynolds similitude. Different turbulence models have been tested: standard $k-\varepsilon$, RNG $k-\varepsilon$ and Reynolds Stress Model. The choice of the standard $k-\varepsilon$ model is justified by the correct reproduction of shape and position of the vortex breakdown bubble.

Combustion simulations: choice of the combustion model

Combustion of the methane-air mixture has been modelled considering a lumped two-steps mechanism :



The "finite rate/eddy dissipation" model has been used [3].

Modified kinetic coefficients, derived by genetic algorithms, have been used [4]. NO_x post-processing considers exclusively the thermal NO_x formation mechanism.

RESULTS AND DISCUSSION

Figures 2 and 3 show the predicted CO emission trends compared with the experimental data. CO experimental trends are satisfactorily reproduced; but the model underestimates the absolute values (within an order of magnitude).

In the experimental system the cold air coming from the secondary stream has a stronger quenching effect on the CO burnout than in the simulations. This can be related to an uncorrected treatment of the interface between the two different streams by the software and to other reasons discussed in section 4.0.

Fig. 2 compares predictions and experimental CO emissions (dry @ 15% O₂ versus different lengths of the first stage flame cup, L). In this test only air without swirl component is introduced through the second stage. It is possible to observe that the longer residence time (longer first stage flame cup lengths) allows an almost complete CO burnout. At the same time a longer residence time of the gases in a high temperature zone increases the NO_x values.

Fig. 3 shows the comparison between predicted and experimental CO emissions at different adiabatic temperatures (dry @ 15% O₂). In this test a methane-air mixture of different compositions (to reach the different adiabatic temperatures desired), is introduced through the second stage. Differently from the previous case, the secondary air flow has a swirl component. At low adiabatic temperatures (corresponding to low fuel quantity introduced through the second stage) there is an under-estimation of the CO values (similarly to what observed in the previous case). On the other hand, for higher adiabatic temperatures CO emissions are overestimated, even if the model predicts correctly the overall trend. It can be observed that for these conditions the contribution of the second stage to the CO

production becomes relevant.

Fig. 4 shows the comparison between predicted and experimental NOx emissions at different adiabatic temperatures (dry @ 15% O₂). Also in this case the trend is correctly reproduced but there is a general under-estimation of the values. At low adiabatic temperature there might be a non-negligible contribution of other NOx formation mechanisms, other than the thermal one, which are not considered by the model. Modeling the second stage as perfectly premixed contributes to the overall NOx underestimation as this does not allow to take in account the presence of hot spots due to the non-perfect mixing (as observed in the experimental tests) that causes relevant NOx emissions.

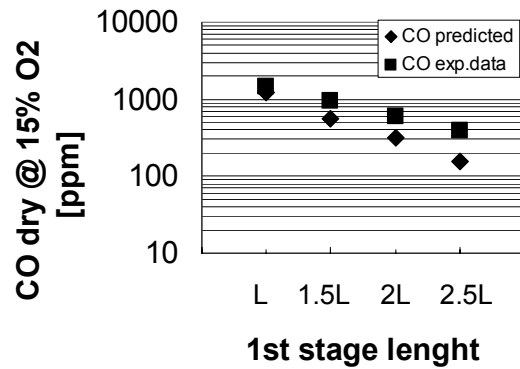


Figure 2. CO emissions versus the flame cup length of the first stage.

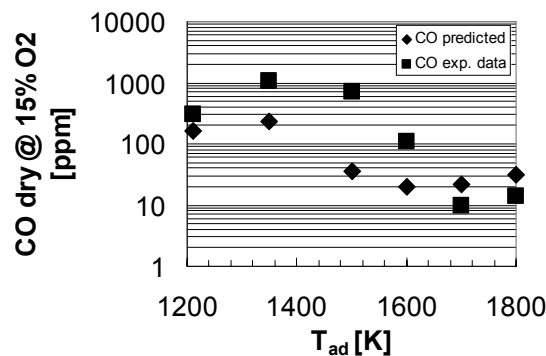


Figure 3. CO emissions versus adiabatic temperature.

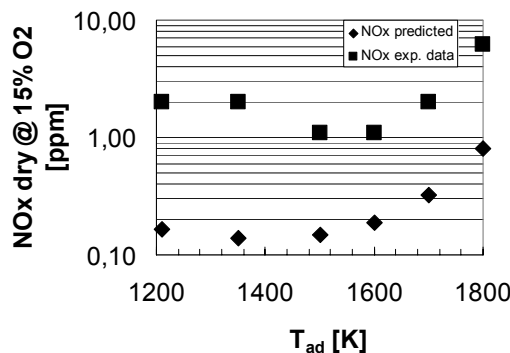


Figure 4. NOx emissions versus adiabatic temperature.

In general it is possible to observe a better agreement between simulations and

experimental data when the swirl component of the secondary flow is present. The high temperature zone shows a shorter length and is extended in the radial direction, indicating a faster mixing, enhanced by the secondary swirling flow.

CONCLUSIONS AND RECCOMENDATIONS FOR FURTHER WORK

A simplified model for the simulation of the combustion process in a lean-lean premixed staged combustor has been considered. The model results have been compared (at atmospheric pressure conditions) with experimental data. CO and NO_x emissions have been investigated for different temperatures, lengths of the first stage of the combustion chamber and presence (or absence) of swirl in the second stage. The results confirm that larger residence times have a positive effect on CO burnout, but increase NO_x production.

The simplified approach allows good predictions of CO and NO_x trends, but a perfect agreement between data and predictions still lacks. In particular quench effect of cold air, and CO production at low adiabatic temperature are underestimated. In the second stage, constant velocity and stoichiometry profiles have been considered, which do not account for the non-ideal profiles established in reality.

Especially regarding NO_x emissions values, there is an overall under-estimation of one order of magnitude, that can be caused by the fact that some NO_x formation mechanisms are neglected and the formation of hot spots in the second stage is not taken into account.

As concern the kinetics of the combustion process, a simplified 2-step reaction model has been used in this work. In order to improve the performance of the model, envisaged alternatives are:

- to include in Fluent a more detailed kinetic model via a user-defined subroutine implementation;
- to use a statistical approach with the partially premixed model available in Fluent 6 or other user-defined PDF methods;
- to use a fuel mixture (and relative kinetic model) with a composition similar to that of the natural gas used in the experimental tests (nowadays all simulations consider only the combustion of the methane-air mixture).

Further experimental data are also required in order to set up a complete picture of the system's behaviour. Including these improvements in the model would allow a better agreement with the experimental data to be gained.

Acknowledgements - Financial support from Alstom to one of the authors (D.V.) carrying out his master thesis at the Alstom Technology Center is gratefully acknowledged. The author wish to thank F. Biagioli, P. Flohr, D. Tabacco and M. Garay for valuable discussion and suggestions.

REFERENCES

1. Correa S. M.: Power generation and aeropropulsion gas turbines: from combustion science to combustion technology; *Twenty-Seventh Symposium (International) on Combustion / The Combustion Institute*,:1793-1807 (1998).
2. Staedtler A.: Diplomarbeit: Aerodynamische Untersuchungen an einem mager/mager gestuften Vormischbrenner für Industriegasturbinen; Lehrstuhl für Technische Thermodynamik Universität Erlangen-Nürnberg / Alstom Power Technology Corporate Research Baden-Daettwil, CH (2000).
3. Fluent User's Guide, Fluent. Inc (2001).
4. Polifke W., Geng W., Dobbeling K.: Optimization of rate coefficients for simplified reaction mechanisms with genetic algorithms. *Premix Flames Basic Project* , ABB Corporate Research, Baden-Daettwil CH, (1997).

NO_x formation in the Rich Quench Lean combustion mode: chemical kinetic modelling

^{1,2}L. Miccoli, ¹A.A. Barresi, ²E. Carrea

1 Dip. di Scienza dei Materiali e Ingegneria Chimica – Politecnico di Torino – ITALY
2 ALSTOM Switzerland, Technology Center Daettwil – Segelhof 1, CH-5405 – CH

INTRODUCTION

The Rich Quench Lean (RQL) technique is defined as a combustion mode whereby combustion is staged in two sequential phases:

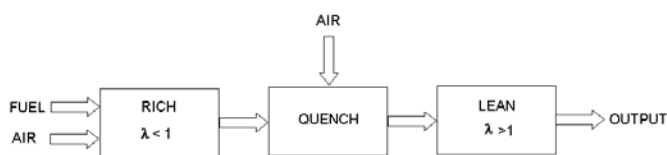


Fig. 1. RQL concept ($\lambda=1/\Phi$)

- ignition and combustion in rich conditions ($\Phi > 1$) which assures low NO_x production due to oxygen shortage

- combustion in lean conditions ($\Phi < 1$) where burnout is achieved with low NO_x formation due to the lean stoichiometry. Φ is the

equivalence ratio, defined as the fuel/air ratio normalised with respect to the stoichiometric one; in the following its reciprocal λ is used.

The switch-over from the rich phase into the lean burnout mode is accomplished via quick quench by air (fast quench is necessary to avoid the formation and persistence of stoichiometric gas zones).

The RQL combustion concept has been proposed since the 1970s; experiments by Fenimore [1] and other researchers [2-4] showed that is possible to control NO_x emissions from Fuel-Bound-Nitrogen (FBN) combustion under rich conditions.

In experimental studies by Novick *et al.* [5], NO_x emissions appeared to be controlled only by rich zone equivalence ratio, whereas CO and UHC (smoke) were influenced markedly by both rich-zone and lean-zone equivalence ratios. A minimum lean-zone equivalence ratio of 0.6 was needed to achieve acceptable smoke levels.

Jackson *et al.* [6] used the RQL at 10 atmospheres; the gas used had a nominal heating value of 4370 kJ/kg and included 4600 ppm (by vol) of ammonia (the FBN). They fixed an equivalence ratio of 1.25 in the rich phase and regulated the quenching on the outlet temperatures of exhaust gases finding a minimum value of NO_x emissions.

The RQL concept is currently studied for aircraft application by Pratt and Whitney Company and others laboratories in the USA. Most of the work carried out so far on RQL concept has confirmed its potential for low conversion of FBN into NO_x. RQL combustion systems are also being considered for suppression of thermal NO_x in high-speed civil transport [6].

In this work a chemical reactor simulation package (Chemkin) has been used with the GRI 3.0 kinetic mechanism. Two possible applications of the RQL have been considered:

- Rich Quench Lean run in a single combustion chamber (at constant pressure)
- Sequential RQL combustion: rich and lean combustion are carried out in two different combustors at different pressures (rich phase run at high pressure and lean phase at lower pressure). Between the two combustion chambers an expansion stage provides for energy extraction.

The two configurations are studied under several operating conditions in a systematic approach. The analysis of the RQL behaviour under real GT operating conditions will be the subject of future work.

Clean fuel and Fuel-Bound-Nitrogen (FBN) have been used; in particular FBN has been simulated adding different quantities of ammonia in the fuel.

Main objectives of the present investigation are:

- to identify the presence of an optimum operation point in the rich phase
- to investigate the influence of the residence time in the rich phase on NO_x emissions
- to study the response of the RQL combustion with different amount of NH₃ in the fuel.

Finally the NO_x emissions in the RQL technique have been compared with those obtained in a Lean-Premixed (LP) combustion under the same operating conditions.

MODEL SET-UP

Figures 2 and 3 show the Chemkin models used to simulate the single and sequentially staged RQL combustion, respectively.

As concerns the single combustion chamber model, the primary zone of the combustion (rich phase) has been simulated connecting a perfect stirred reactor (PSR, for ignition) and a plug flow reactor (PFR, for the secondary combustion zone).

Three different values of the residence time in the PFR_{RICH} have been used (5-10-15 ms). Simulations have been performed considering a rich stoichiometry range (equivalence ratio) of 0.5÷0.75. A mixer module connects the rich and the lean burnout phases simulating quenching by air intermediate feeding.

The lean phase has been carried out at $\Phi=0.5$ and with the residence time necessary to reach the condition: $CO=1.5*CO_{eq}$.

Rich and lean phase run at constant pressure. Two different pressures have been considered in the simulations: 1 and 20 bar. Clean (CH₄) and nitrogen fuel (CH₄+NH₃) combustion has been investigated. For Fuel-Bound-Nitrogen the ammonia concentration in the fuel has been varied within the range 0.3%÷0.5%.

Figure 3 shows the sequential RQL combustion model. The rich (PSR+PFR) and lean (PFR) stages are separated by an expansion stage (GT). The rich stage runs at 20 bar while the lean stage is operated at 10 bar. An isentropic expansion has been considered for the gas turbine stage. Also in this case the quench is regulated to obtain $\Phi=0.5$ in the lean phase.

In a last effort the single-chamber RQL model has been directly compared with a classic Lean Premix model set-up. The Lean Premix model consists of a connection of a PSR and a PFR reactor. The PSR simulates the well-mixed flame stabilisation zone, created by a vortex breakdown phenomenon, while the PFR reactor is used to model the eventual burnout. Overall residence time refers to the minimum value which allows a CO concentration 50%

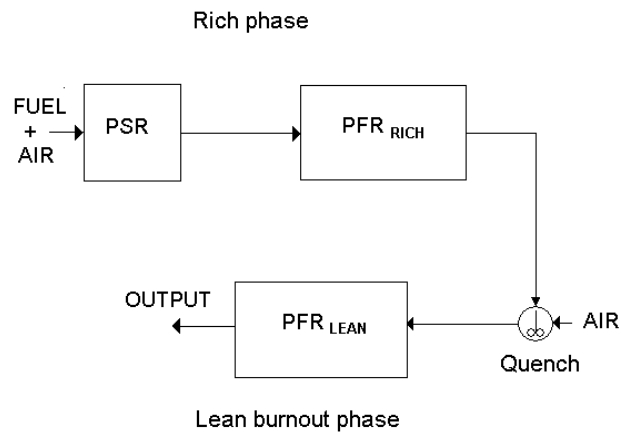


Fig. 2. Single combustion chamber

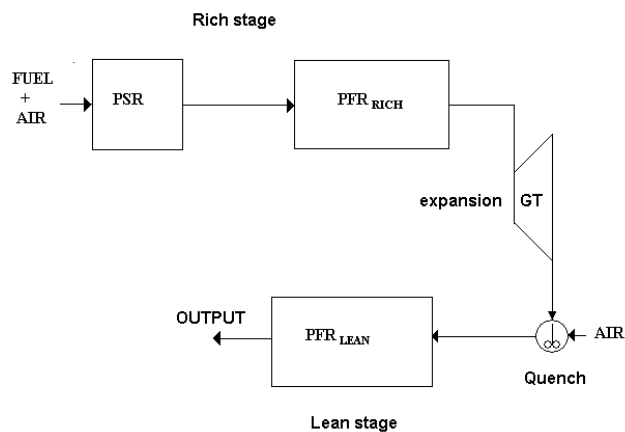


Fig. 3. Sequential RQL combustion

higher than the equilibrium value. Same inlet and operating conditions have been used to have a common basis of comparison.

RESULTS

Figure 4 and 5 show the NO_x emissions predicted for the single combustion chamber for $\tau_{\text{RICH}}=10$ ms and $\text{NH}_3=0.4\%$, as a function of the stoichiometry in the rich phase.

In the clean fuel case, the NO_x emissions increase approaching the stoichiometric conditions ($\Phi=1$) in the rich phase and decrease for high pressure (Fig.4a).

In the FBN case the presence of an optimum λ_{rich} value has been detected (this optimum being more evident at high pressure) (Fig.4b).

The influence of the residence time in the rich stage on NO_x emissions can be summarised as follows:

- for the clean fuel, at 1 bar, NO_x emissions increase with residence time, while at 20 bar, the influence of the residence time in the rich phase is negligible;
- for the FBN case, long residence times in the rich phase depress NO_x emissions (due to the onset of reburning mechanism); the effect is stronger in proximity of the optimum rich stoichiometry.

The influence of ammonia concentration is shown in Figures 5 and 6: high ammonia concentration in the fuel produces higher NO_x emissions; the effect is weaker for high pressure at the optimum λ_{rich} .

NO_x trends in the sequential RQL combustion are similar to those of the single combustion chamber: in the clean fuel case higher emissions for higher λ_{rich} are obtained, whereas with FBN the presence of an optimum point is confirmed.

Figures 5 and 6 report also the comparison between the RQL mode in a single combustion chamber and the Lean Premixed combustion. The results show that the Lean Premix mode is preferable in the clean fuel case (especially at atmospheric pressure), while in the FBN case the use of a RQL mode would help considerably reducing the NO_x emissions.

CONCLUSIONS

The RQL combustion allows to reduce NO_x emissions, especially at high pressure and when nitrogen-containing fuel is employed; in these cases it is advantageous with respect to Lean Premix combustion. The stoichiometry in the rich phase is very important, and an optimal value is observed for FBN, that is dependent on pressure. In conditions close to the optimal one, the system is only slightly affected by the nitrogen content of the fuel, and this

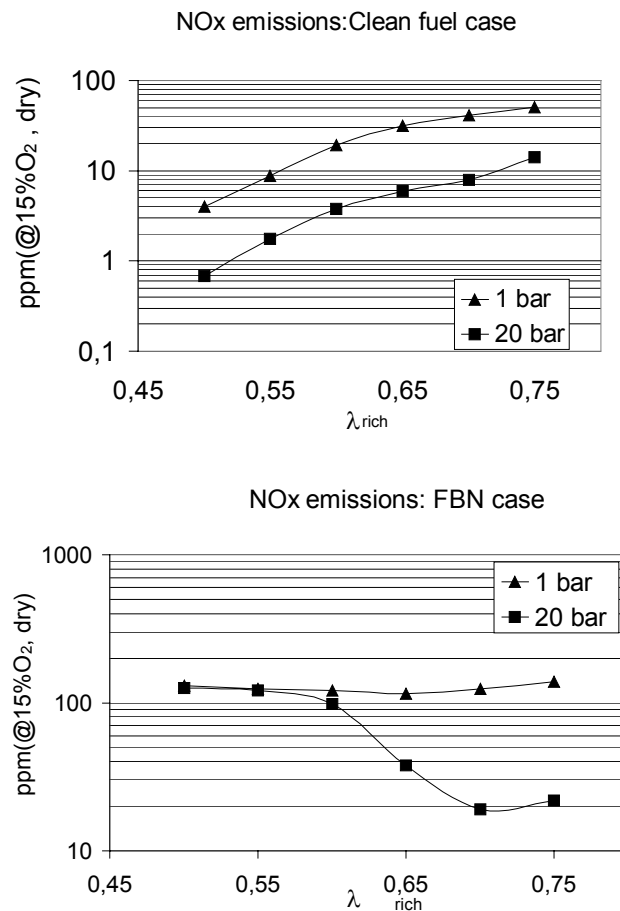


Fig. 4. NO_x predictions for the single combustion chamber, with methane (a) and FBN (b).

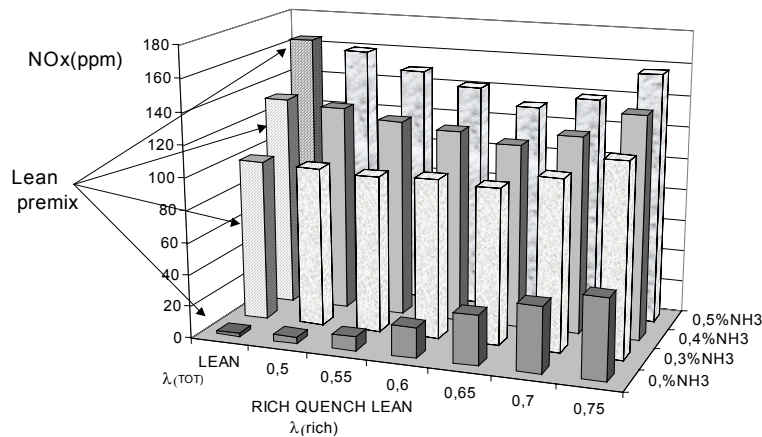


Fig. 5. Comparison RQL-Lean Premix: ppressure 1 bar

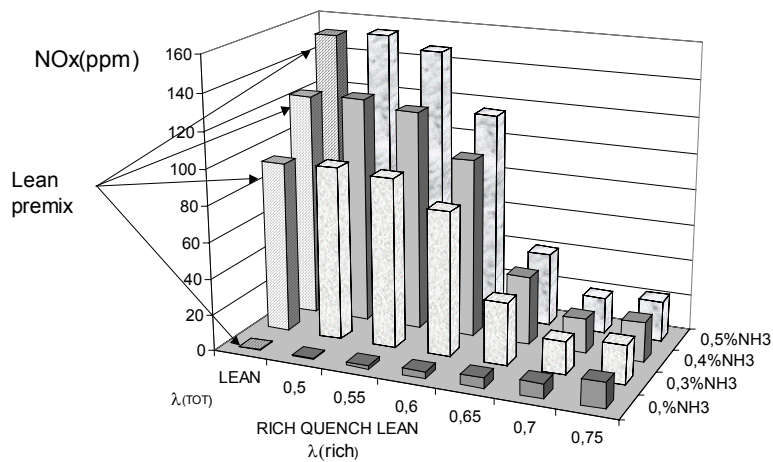


Fig. 6. Comparison RQL-Lean Premix: pressure 20 bar

could allow the design of flexible systems. The influence of the residence time is dependent on pressure and fuel composition.

The preliminary results suggest that RQL combustion can be very advantageous for NO_x control; future work will investigate the performance in real operating conditions.

Acknowledgements

Financial support from Alstom to one of the authors (L.M.) carrying out his master thesis at the Alstom Technology Center is gratefully acknowledged.

REFERENCES

1. Fenimore C. P., "Reaction of Fuel-Nitrogen in Rich Flame Gases": *Combustion and Flame*, **25**: 249 (1976).
2. Pierce, R. M. Smith, C. E. and Hinton, B. S., "Low NO_x Combustion Development for Stationary Gas Turbine Engines": *Proceedings of the Third Stationary Source Combustion Symposium EPA-600/7-79-050 C*, Vol. III (Feb. 1979).
3. Martin, F. J., and Dederick, P. K., "NO_x from Fuel Nitrogen in Two-Stage Combustion": *Proceedings of the Sixteenth Symposium (International) on Combustion*. The Combustion Institute, p. 191 (1976).
4. Takagi, T., Tatsumi, T., and Ogasawara, M., "Nitric Oxide Formation from Fuel Nitrogen in Staged Combustion: Roles of HCN and NH_i": *Combustion and Flame*, **35**: 17 (1979).
5. A.S. Novick, D. L. Troth, and H. G. Yacobucci, "Design and Preliminary Results of a Fuel Flexible Industrial Gas Turbine Combustor": *Journal of Engineering for Power* **104**: 368 (1982).
6. Jackson, M. R., Ritter, A. M., Abuaf, N., Lacey, N., Lacey, M. A., Feitelberg, A. S., and Lang, P., ASME paper 96-GT-219 (1996). Quoted from Correa, S. M., *Proceedings of the Twenty-Seventh Symposium (International) on Combustion*. The combustion Institute, p. 1793 (1998).

Combustion Control by Multiple Injection in Common Rail D.I. Engines

C.Beatrice¹, P.Belardini¹, C.Bertoli¹, M. Migliaccio¹ and C.Guido²

1 Istituto Motori - C.N.R., Naples - ITALY

2 D.I.M.E. - Università Federico II, Naples - ITALY

INTRODUCTION

In order to attain the future Emissions Standards (Euro 4 limits: CO/NO_x/PM = 0.5/0.25/0.025 g/km) for light-duty Diesel engine, a second generation of Common Rail F.I.E. that can manage multiple sequential injection appears efficient [2], [3], [4]. The flexibility of the system allows to split the main injection in a sequence of very closely coupled stages and manage, if needed, the injection stages at larger dwell time with respect to the main injection. The most diffused multiple injection strategy is characterised by a first injection (called "pre-injection") very near to the main injection and by an injection following the main one (called "after-injection") [2]. The multiple injection effects on soot formation and oxidation processes have been largely studied in the case of heavy-duty engines, [5], [6]. However in the literature, data about "swirl supported" light duty C.R. engines are practically absent. In this case the main processes leading to soot and NO_x evolution in the combustion chamber have not been fully explained. Very critical parameters to control the soot oxidation process are the best separation time (dwell time) between main and after injection, and the percent fuel mass distribution between all the described injections. In the present paper the influence of multiple injection control parameters on emissions of a 1.9 litres four-cylinder C.R. engine has been studied.

RESULTS AND DISCUSSION

This paper refers to the experimental results obtained using two DI diesel engines equipped with an advanced Common Rail system. The first engine is a four-cylinder engine with 1.9l of total displacement (Fiat 1.9 JTD-F3, 2 valves per cylinder), while the second is an optically accessible single-cylinder prototype engine, with a combustion system quite close to the four-cylinder engine one. The transparent engine was used to investigate on the injection and combustion processes, having as reference the detailed emission measurements carried out by the four-cylinder engine. Using different settings of the multiple injection strategy the influence of some injection parameters on the combustion patterns and emission levels has been evaluated.

In fig. 1 the Soot-NO_x trade-off is reported adopting different strategies, in particular splitting the main injection and varying the dwell time between the different injections. Tests are referred to the four-cylinder engine operating at 1500 rpm and 5 bar of B.M.E.P. The reference condition of a classical strategy of pilot-main injection is also shown in the same figure. Noise and BSFC for all conditions are also reported. As expected, global engine performance (emissions, noise and BSFC) are strongly dependent on the adopted injection strategy. Moreover, for each strategy the setting of injection parameters also influences the performance. The choice of the optimal injection strategy requires an enormous experimental effort in order to evaluate the effect of each single parameter. Therefore, in order to foresee the use of model based injection strategies, the in-cylinder mechanisms controlling the engine performance must be investigated. Starting from the best global performance of pre-main-

after injection strategy (from now on called ‘multiple’), our first study was focused on its effect on combustion and exhaust emissions. Fig. 2 shows a comparison between pilot-main and multiple strategies in terms of indicating signals and heat release rate. The injection parameter setting is also shown in the same figure. The EGR rate, taken on CO₂ concentration between inlet and exhaust ducts, was 17% and 19% for pilot-main and multiple injections, respectively. The higher EGR value in the second case was chosen in order to approach the NO_x EURO4 limits taking into account its pronounced effect on soot reduction. It can be noticed that the premixed combustion rate peaks are similar adopting the two different strategies. In fact, activating the pre-injection has the same or a better effect on combustion noise reduction than pilot injection, while at the same time reduces the BSFC.

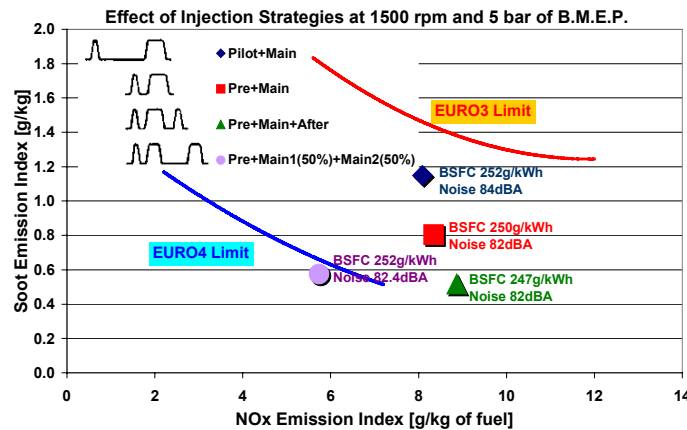


Fig. 1 Effect of different injection strategies on the four-cylinder engine performance at 1500rpm and 5bar of BMEP.

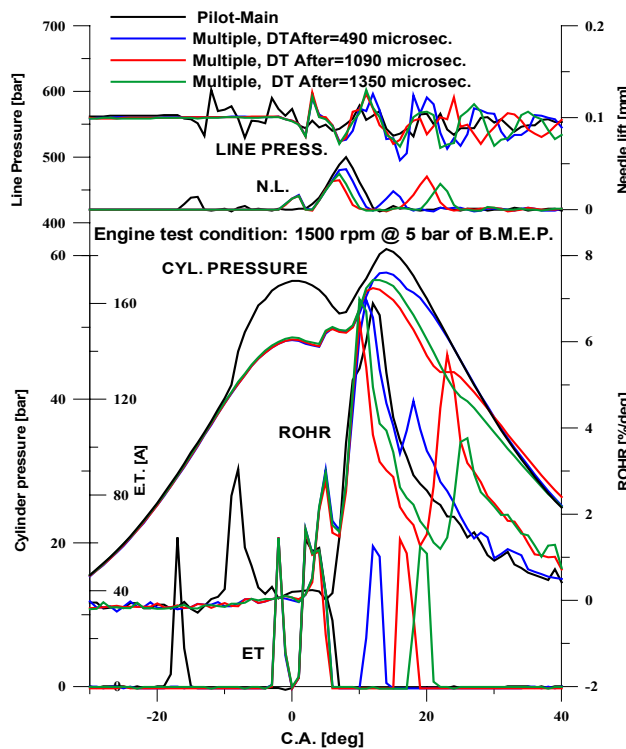


Fig. 2 Injection parameters, cylinder pressure and heat release rate for pilot-main and multiple injection strategies

Simultaneously multiple injection reduces both NOx and soot emissions. The main mechanisms that control this effect are not yet clearly explained at least for swirl-supported light-duty engines. However, it is common opinion that the two main mechanisms are the improvement of air utilisation due to the split of the main injection and the higher combustion temperature in the last combustion phase that promotes soot oxidation. Following the first mechanism, the split of the main injection in two injections (main and after) can produce an air entrainment in the spray path which reduces the extent of the over-rich fuel/air zones [7].

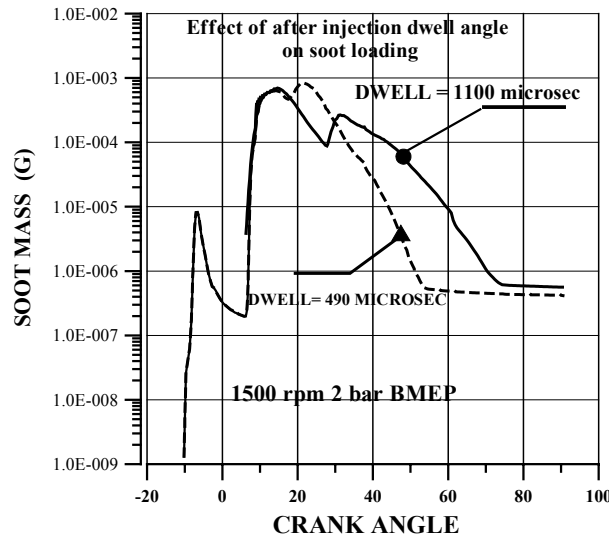


Fig. 3 Soot loading during combustion cycle for the two DTAfter (490 and 1090 μ s). Four cylinder engine simulation at 1500 rpm and 2bar BMEP.

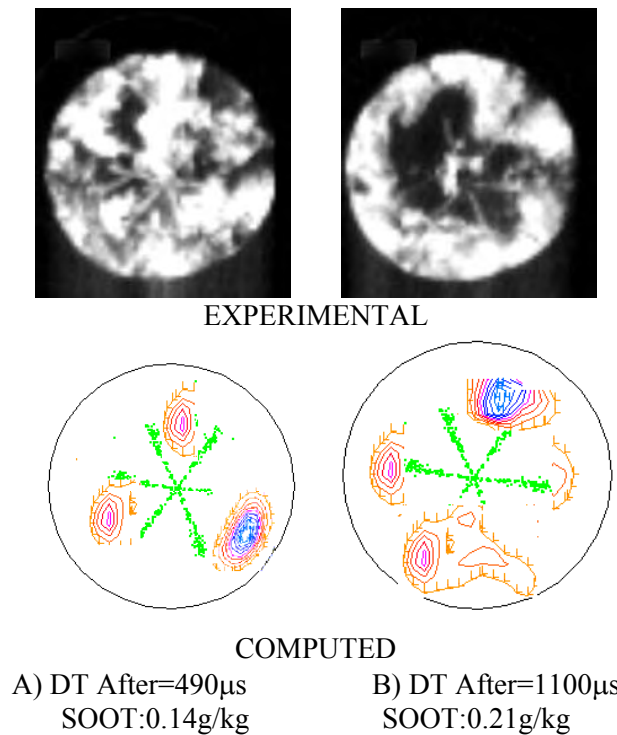


Fig. 4 Experimental and numerical visualisation of the relative position of soot clouds and incoming jets of the after injection at DT After of 490 (left) and 1090 μ s (right) at 1500rpm and 2bar of BMEP.

To investigate on these topics a joint numerical and experimental activity was set-up. The diesel engine combustion simulations were performed by an improved version of the Kiva3V code [1]. The effect of the dwell time interval between main and after injection (DT After) was deepened. Neglecting the test point with DT After of 1350 μ s because of its high exhaust emissions and poor BSFC, the effect of the two remaining DT After values (490 and 1090 μ s) on in-cylinder soot loading is shown in fig. 3. Retarding dwell time between main and after injection, even if the peak of soot formation is lowered, leads to an increase of net soot emitted due to the decrease of the oxidation process. Fig. 4 shows the visualisation of the relative position of the combustion products in the combustion chamber and the incoming jets of the after-injection for the two previously chosen DT After cases. On the bottom of the same figure the computed spatial soot distribution in the same conditions is shown. The agreement between computations and measurements is surprisingly good. In the case of DTAfter of 1090 μ s, the air utilisation for the combustion of the fuel jets deriving from the after-injection is worse. This effect together with the lower flame temperature justifies the decrease of the efficiency of the soot oxidation process for this dwell time.

The previous analysis suggests a simple conceptual model for a pre-setting of the DTAfter value. Starting from the knowledge of the in-bowl swirl ratio evolution during the expansion stroke, one can assume that the angular velocity of the combustion products of the main injection is of the same order of magnitude as the swirl velocity. So the optimum of the DTAfter value can be easily computed imposing (as suggested from figure 4) that, at the moment that after injection starts, the combustion products of the main injection are located in the middle of the angular sectors defined by the spray jet axes.

REFERENCES

Journals

1. Beatrice, C., Belardini, P., Bertoli, C., Lisbona, M.G., Rossi Sebastiano, G.M.: "Diesel Combustion Control in common rail engines by new injection strategies", *International Journal Engine Research*. (3), n. 1, (2002)

Combustion Symposium Proceedings:

2. Imarisio, R, Ricco, M, Rossi Sebastiano, G.M.: "Multiple Injection, a cost effective Solution for Emission Reduction of Common Rail DI Diesel Engines" *Proceedings of Aachener Kolloquium*. Aachen, Germany, October, (2000).
3. Hummel, K., Krieger, K., Hansen, N.: "Evolution of the Bosch Common Rail System for Passenger Cars". Paper 20A2012. Proceedings of International Symposium: *The Future of Diesel Engine Technology for Passenger Cars*. Porto Cervo, Italy, October, (2000).
4. Meissonnier, G., Bazinet, V.: "Injection Control in an Advanced Common Rail Injection Systems". Paper 20A2014. Proceedings of International Symposium: *The Future of Diesel Engine Technology for Passenger Cars*. Porto Cervo, Italy, October, (2000).

Conferences

5. Farrell, P.V., Chang, C.T., Su, T.F.: "High Pressure Multiple Injection Spray Characteristics". *SAE Paper 960860*, (1996).
6. Bakenhus, M., Reitz, R. D.: "Two-Color Combustion Visualization of Single and Split Injection in a Single-Cylinder Heavy-Duty D.I. Diesel Engine Using an Endoscope-Based Imaging System". *SAE Paper 1999-01-1112*, (1999).
7. Han Z, Uludogan A, Hampson GJ, Reitz RD: "Mechanism of Soot and NOx Emission Reduction Using Multiple-Injection in a Diesel Engine". *SAE Paper 960633*, (1996).

Further knowledge on the effects of fuel formulation on diesel combustion

C.Beatrice¹, C.Bertoli¹, N.Del Giacomo¹, M.Lazzaro¹ and C.Guido²

1 Istituto Motori C.N.R. Via Marconi 8, 80125 Napoli, Italy.

2 DIME, Università degli Studi "Federico II", Napoli, Italy.

INTRODUCTION

Aim of this study is to investigate the interaction between the modern diesel engine technology and the reformulated fuels, because the consolidate results in this area of research [1] may not be valid for the new Common Rail diesel engines. This paper describes the results of the research program named PNRA, sponsored by Italian Ministry of Environmental. Partners of the project with the Istituto Motori were Agip Petroli S.p.A. and Fiat Research Center (CRF). In Istituto Motori tests were done to evaluate the potentiality of five reformulated fuels burning in a EURO3 light-duty CR diesel engine and in two steady-state test points: 1500 rpm at 5 bar of B.M.E.P. and 2500 rpm at 8 bar of B.M.E.P.

ENGINE, EXPERIMENTAL APPARATUS AND TESTS POINTS

The Common Rail engine employed in the tests was a Fiat four-cylinder CR diesel engine (EURO3 version of 1910 cc). A new generation CRF electronic control unit (UNIJET2000) controls the injection system. Gaseous emissions were sampled upstream and downstream the catalyst. As above mentioned, the two chosen test points were: 1500 rpm at 5 bar of B.M.E.P. and 2500 rpm and 8 bar of B.M.E.P.. In these points, during the ECE15+EUDC cycle, the engine generates the highest emissions. So the improvement on emissions achievable in these points is more significant than in others. They were chosen as representative of the two main parts of the ECE15+EUDC cycle and for this reason the tests on the five fuels were run in these points.

THE FUELS

The fuels, provided by Agip Petroli S.p.A., were designed in order to evaluate the reduction of pollutant emission of some synthetic paraffin and oxygenated compounds. Table 1 shows the main fuel features. The tested fuels were prepared using a reference high quality fuel with low aromatic and sulphur content and a CN 51 (its label is BASE). To the base fuel two synthetic compounds, di-normal pentylether (fuel OETL60) and di-butyl carbonate (DBC) (fuels ODBC51/4 and ODBC51/2) and a pure paraffinic fuel (fuel HCSINT60) were blended.

	BASE	HCSINT60	OETL60	ODBC51/2	ODBC51/4
density @ 15°C	838.0	822	827	843	849
visc.@ 40°C (cSt)	3.3	2.9	2.4	2.8	2.6
Cetane number	50.4	60.8	60.5	51	51
Distillation 90% (°C)	328	315	316	325	320
BASE Fuel (% vol)	100	78	80	93	86
Linear Paraffins (% vol)	-	22	-	-	-
Di-N-Pentylether (% vol)	-	-	20	-	-
D-B-Carbonate (% vol)	-	-	-	7	14
Total-aromatics (% w)	27.2	18.6	23.3	23.2	22.1
Heat of combustion (Kcal/Kg)	10291	10328	10080	9982	9968
Oxygen (% w)	0	0	2	1.9	3.9

Table 1 Main fuel features.

Looking at the parameters affecting the emissions, for the base fuel and all blends it is possible to recognise two levels of cetane number (51 and 60), three classes of aromatic content and three classes of oxygen content. The addition of synthetic paraffins tends to reduce the aromatic content (responsible for smoke production) and to increase the cetane number. The same results are obtained adding DNPE that tends also to increase the oxygen content. As DBC reduces aromatics and increases oxygen content, the two blends at 7 and 14% were chosen in order to evaluate smoke reduction due to an increase of oxygen content.

RESULTS AND DISCUSSION

Figure 1 shows heat release rate, needle lift and injection line pressure in the two tested points, for all five fuels. It's clear that no remarkable differences can be found using all the five tested fuels. In particular, at low load (1500x5 case), the heat release (both premixed and diffusive phases) shows a well-marked peak for all fuels, while at high load (2500x8 case), the main combustion is completely controlled by the diffusive phase.

Looking at the main injection combustion, no significant ignition delay changes were observed varying the fuel cetane number (CN) from 51 to 60. However, the pilot injection activation reduces drastically the ignition delay time, hiding the cetane number influence.

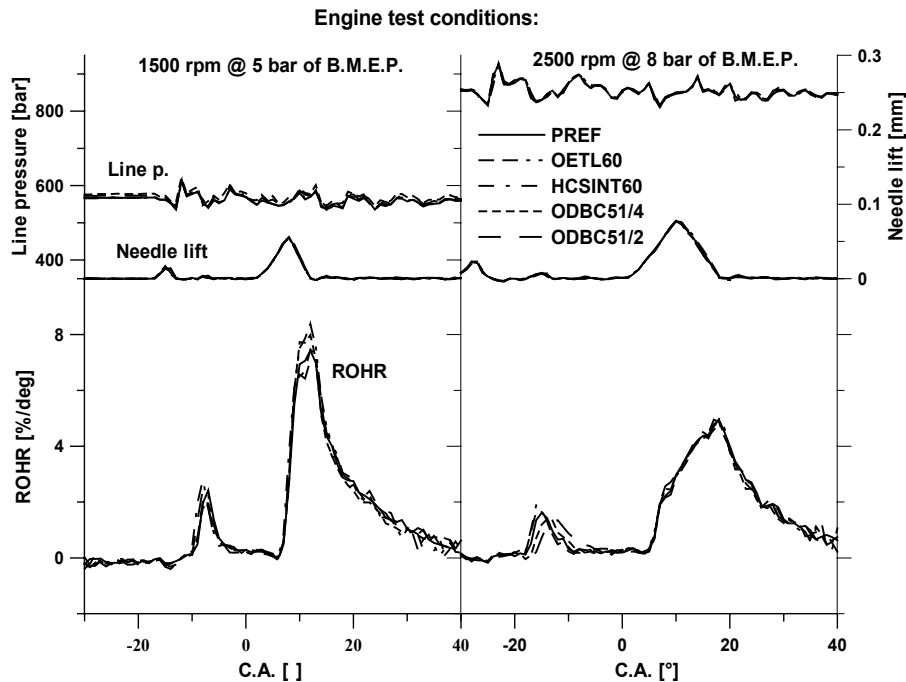


Figure 1 Heat release rate, needle lift and line pressure for all fuels and test conditions.

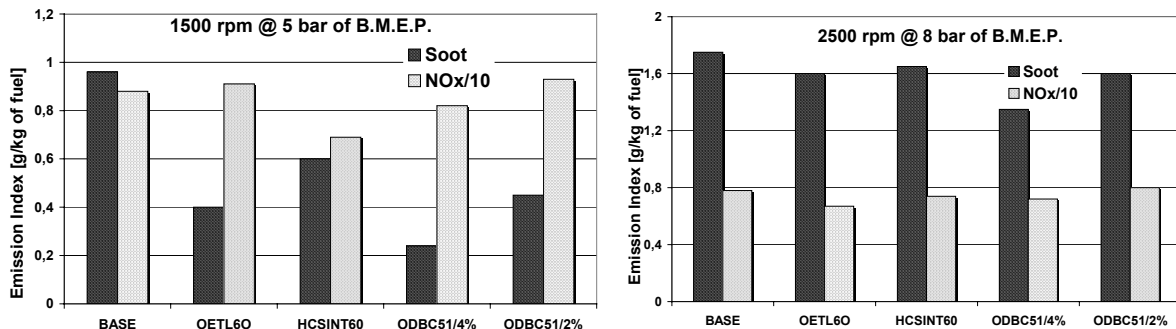


Figure 2 Soot and NOx emissions in the two tested points.

The improvement on Soot emission due to the fuel formulation can be seen in figure 2. The Soot emission sensitivity to the fuel quality is clear at low engine speed. The oxygen addition is effective in reducing Soot. In fact, in agreement with other previous studies [2, 3], Soot emission, burning oxygenated fuel, is lower than base fuel and decreases with oxygen content. At the same time, HCSINT60 behaviour shows that the reduction of aromatics content, by means of linear paraffin addition, contributes to soot decrease. At high load the engine is less sensitive to fuel quality change and this result depends on the increase of rail pressure and the decrease of EGR rate. It seems that NO_x emissions are not influenced significantly by fuel quality. It can be noticed that generally the presence of oxygen in the fuel tends to increase the flame temperature and than the NO_x emissions, but at the same time the use of EGR counteracts this effect. Moreover the lower heat content of oxygenated fuels increases the fuel consumption that in turns lowers the emission index. In figure 3 unburned gaseous emissions downstream catalyst are shown, at 1500x5 and 2500x8 respectively.

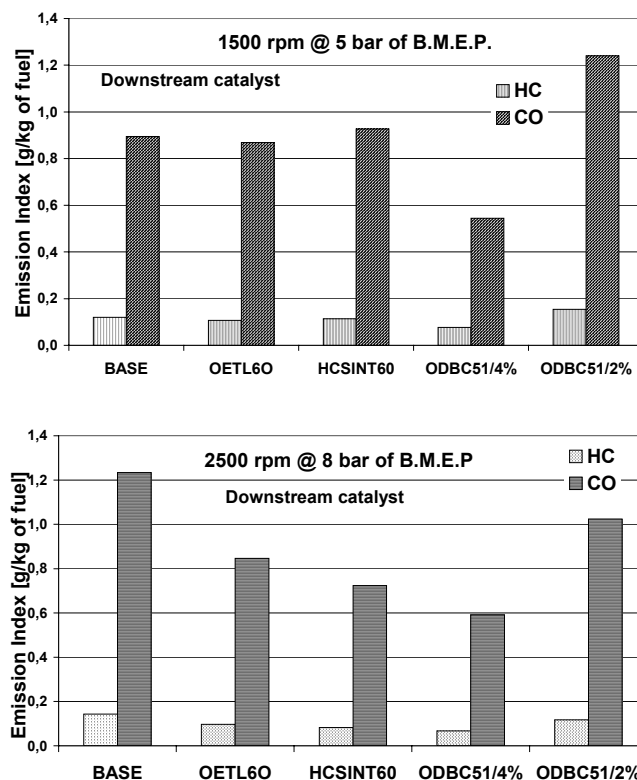


Figure 3 HC and CO emission index downstream catalyst at the two tested points.

The sensitivity of gaseous emissions to the fuel quality is always rather low and of the same order of magnitude. The effect of CN variation and of fuel oxygenation seems to be quit low. Only ODBC51/4% shows a marked emission reduction and this may be due to the DBC effect on the catalytic efficiency. NO_x-Soot trade-off for both engine test points, using all fuels is reported in figure 4, where the two area corresponding to EURO 3 and EURO 4 limits are also presented. At 1500 rpm and 5 bar of B.M.E.P. the best performance are found for ODBC51/4% and HCSINT60 which are very close to EURO4 zone. It must be noted that the higher fuel oxygen content (4%) characterises the first, while the second shows the lower aromatic content. At 2500 rpm and 8 bar of B.M.E.P. the improvements on trade-off are reduced, but not negligible. In particular, it's clear that by using OETL60 (characterised by high cetane number oxygenated compounds as DNPE), significant gains can be also achieved.

Therefore, with the new generation of DI diesel engines, the fuel oxygenation and aromatic purification tend to improve the NOx-Soot trade-off.

CONCLUSION

The analysis of all results confirms that fuel oxygenation and aromatic purification are an efficient way to improve the Soot-NOx trade-off. In particular, the influence of oxygen, and of synthetic paraffin, in reducing Soot, is more evident at low load and low speed test points. Fuel oxygenation doesn't appear so influential on NOx emissions. In fact, in modern engine management, the use of a relative high EGR ratio controls NOx formation. Future limits could be reached through an adequate fuel reformulation including the use of relative high percentage of synthetic oxygenated fuels.

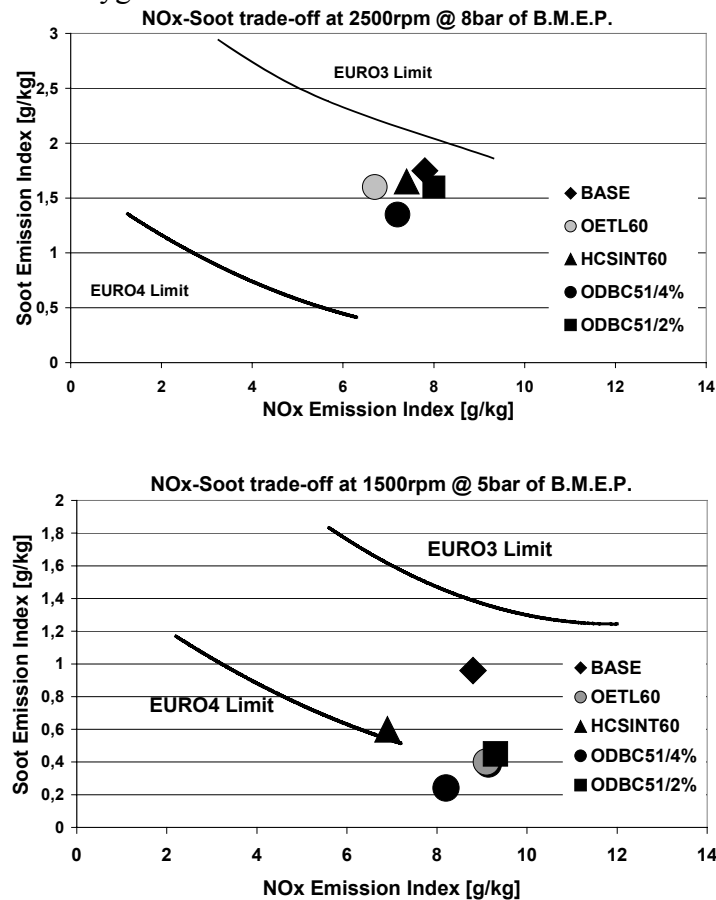


Figure 4 NOx-Soot trade-off for all fuels at 1500x5 and 2500x8 test points.

REFERENCES

1. Beatrice, C., Bertoli, C., Del Giacomo, N: "The influence of fuel formulations on pollutant of light duty D.I. Diesel engine". (1996). *SAE Paper 961972*.
2. Spreen, K.B., Ullman, T.L., Mason, R.L.: "Effects of cetane number, aromatics, and oxygenateds on emissions from a 1994 heavy-duty diesel engine with exhaust catalyst". *SAE Paper 950250*.
3. Miyamoto, N., Ogawa, H., Arima, T., Miyakawa, K.: "Improvement of diesel combustion and emissions with addition of various oxygenated agents to diesel fuels". *SAE Paper 962115*.

DEAL: A New Concept for Diesel Combustion

C. Beatrice, C. Bertoli, N. Del Giacomo, Mna. Migliaccio

Istituto Motori C.N.R., Naples - Italy

INTRODUCTION

High efficiency together with very low emissions are conflicting requirements considering only the technology options available today. Probably in U.E., in 2008, the NO_x emission limit for diesel will be at the level of 0.08 g/km and the particulate limit will drop near zero. On this way, two conceptually different approaches can be followed to match the goal of obtaining high efficiency ultra-low emission engines. The first one attains to the development of complex after-treatment systems that inducing a possible increase in fuel consumption. The second option is linked to the development of new combustion systems in order to cut directly the raw emissions. This second option is very attractive because probably it will presents, in terms of production costs, some advantages with respect to the former. Recently at Istituto Motori it was patented another new combustion concept, named *DEAL* (Diesel Emission At low Limit) [1]. This concept refers to a process where the goal of low flame temperatures is obtained acting on both the air-charge dilution with high EGR rate and the air-fuel mixing improvement. In the present paper the main characteristics of the combustion system are illustrated and the main constraints in developing new diesel combustion systems are discussed.

THE EXPERIMENTAL ENGINES

The tests were carried out on three different engines. The first engine (Engine A) is a medium duty single cylinder DI Diesel engine (Ruggerini RP170) equipped with a mechanical Bosch P type in-line pump. The engine was equipped with an EGR laboratory system whose layout was set-up in order to minimize the EGR drag losses. This engine was employed for a preliminary application of the DEAL concept. The second engine (Engine B) is modern four cylinder common rail prototypes equipped with a second generation F.I.E. apparatus. This engine has allowed a first application of the DEAL concept on a production engine.

RESULTS AND DISCUSSION

Engine A)

Tests with engine A were carried out at low load (4 bar of I.M.E.P.) and 1500 rpm varying the cooled E.G.R. rate from 0 to about 65%. In the figure 1 the apparent rate of heat release is shown at different E.G.R. rates. In the same diagram the needle lift curves versus crank angle are also reported. Looking at the figure it is possible to note that, adjusting the injection timing, a good thermodynamic efficiency can be maintained also at high EGR rate. Increasing the EGR rate over 50%, the ROHR (rate of heat release) curve was decreased and two peaks can be identified, indicating that the combustion was moving toward a smoothed premixed combustion. Probably the first peak in the rate of heat release pattern was due to the presence of cool flames that are typical of the HCCI combustion. Increasing the EGR up to the maximum sustainable limit, the combustion evolution pattern shows a reduced sensitivity to the injection timing variation and EGR rate variation (see curves over 60% of EGR). This is another indication that at high EGR rate the combustion process moves toward a premixed lean combustion. In Figure 2 Soot and NO_x emissions are displayed.

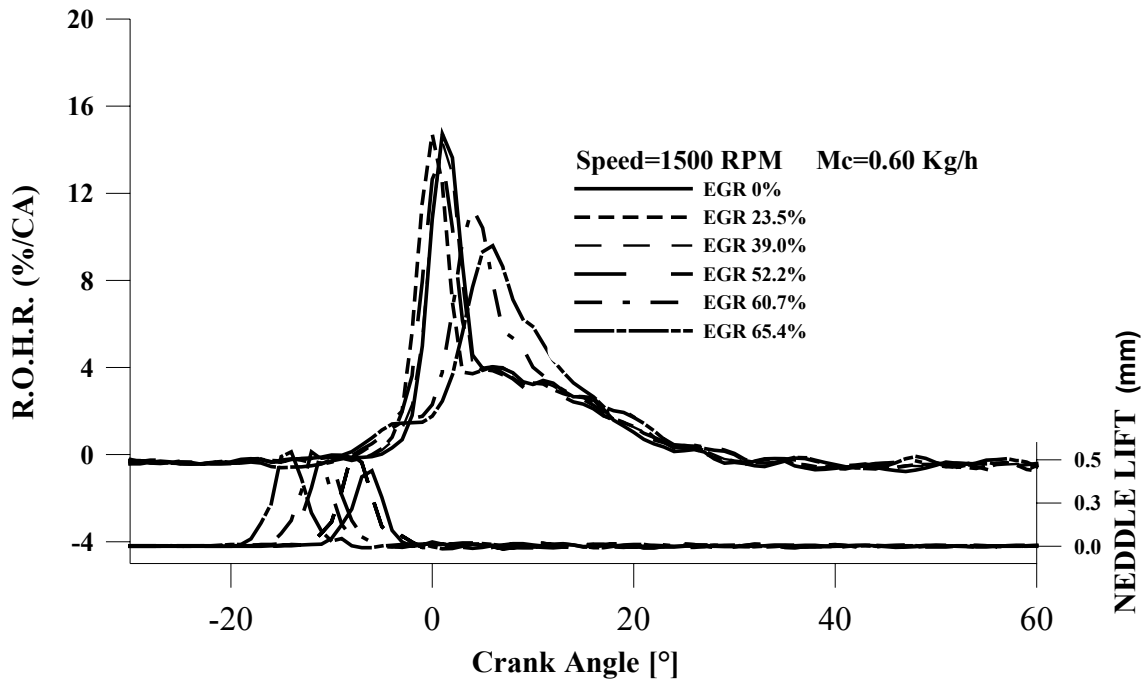


Figure 3: Rate of heat release at different E.G.R. rate for Engine A

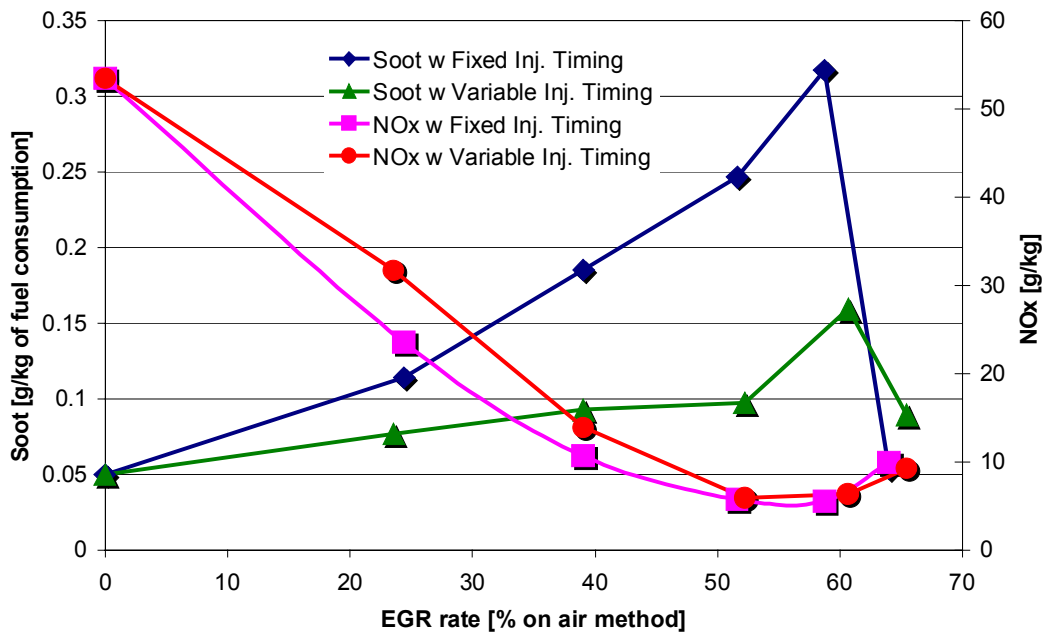


Figure 2: Soot and NOx emissions versus EGR rate for Engine A.

Exhaust emissions versus EGR rate are reported, with and without adjusting injection timing. Obviously increasing the EGR rate NOx emissions are reduced while soot emissions show a marked rise. This is true until 50% of the EGR rate. Over this value a drop of soot emissions can be observed with both fixed and variable injection timing. The soot emission reduction can be ascribed to two different mechanisms. As first, the reduction of mean flame temperature shifts to the left branch of the bell shape curve of the fuel sooting tendency versus temperature [2]. As second, the long ignition delay time at high EGR rates increases the air-fuel mixing falling down the over-rich mixture zones of the combustion volume. As a consequence a simultaneous reduction of NOx and soot are expected.

As well known, the HC and CO emissions (not reported here) in the exhaust increase by increasing EGR. But due to the reduced exhaust flow rate with EGR, the emissions indices,

expressed as grams per kg of burned fuel, show little variations until to about 50% of EGR rate. Up this value, the joint effect of low combustion temperature and high dilution air-fuel mixture causes a drastic rise of HC and CO. Clearly a better control of HC emissions is obtained by adjusting the injection timing value.

Engine B)

Tests were carried out on Engine B at the test point of 2bar of b.m.e.p. and 2000 r.p.m.. Tests were performed in DEAL conditions by varying rail pressure and main injection timing. The E.G.R. rate was adjusted at the maximum value allowing the engine stability. In the bar chart of figure 3 and 4 the Soot and NOx emission measurements are shown. In these figures a reference line represent the emission level obtained managing the engine control in a standard way, i.e. using the well known injection strategy pilot injection plus main injection.

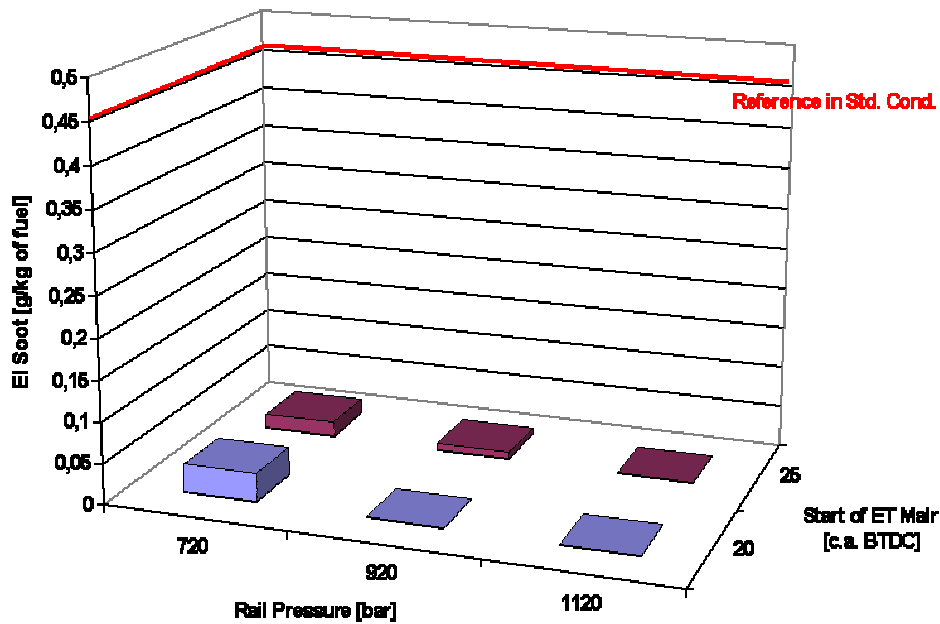


Figure 3 Engine B: Soot emission index at 2000 RPM 2bar B.M.E.P.

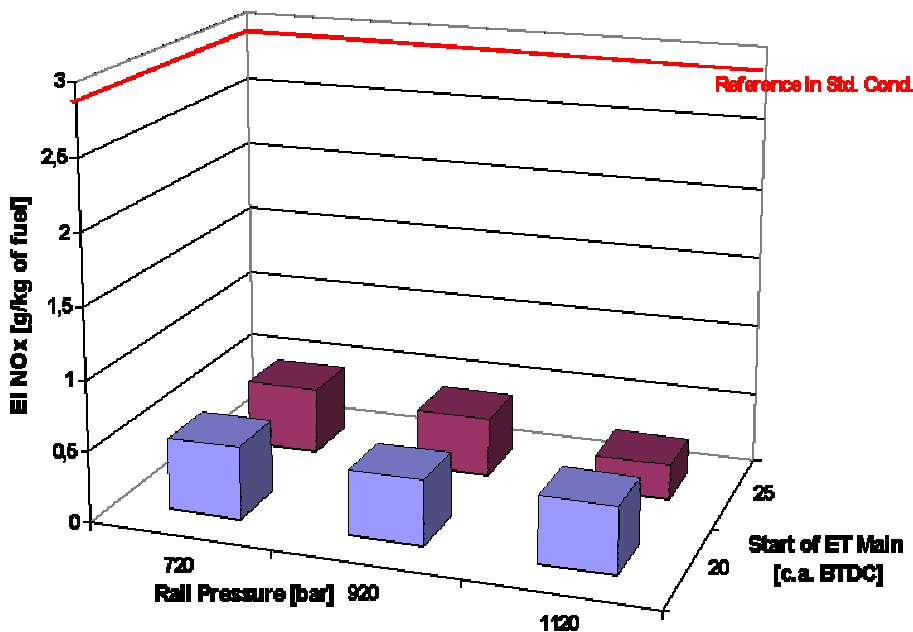


Figure 4 Engine B: NOx emission index at 2000 RPM 2bar B.M.E.P.

Results demonstrate the very high potential of the DEAL concept in controlling both soot and NOx emissions. NOx and soot emission levels are moderately affected by the choice of the setting value of injection timing and rail pressure. This can be probably ascribed to the quite good homogenization of air-fuel mixture realized in DEAL conditions. Anyway both NOx and Soot emissions present a dramatic reduction with respect to the standard engine settings. Specific fuel consumption was unmodified at low speed while at higher speed a little increase of this parameter was measured.

CONCLUSIONS

Recently, in the Diesel Engines and Fuel division of Istituto Motori, it was patented a new concept of Diesel combustion where the goal of low combustion temperatures is obtained acting on both the air-charge dilution with high EGR rate and the air-fuel mixing improvement. Tests were carried out on two different engines: a medium duty single cylinder engine equipped with mechanical injection apparatus and a common rail engines.

The main results obtained are the following:

- Increasing the EGR rate over 50%, the ROHR curve was decreased and two peaks were identified indicating that the combustion tends to move toward a smoothed premixed combustion, with the presence of cool flames before that the main hot combustion start;
- Soot emission shows a marked rise versus the EGR. This is true until to 50% of the EGR rate. After this value, a dramatic drop in soot emission can be detected. Simultaneously a strong reduction of NOx emissions can be achieved while HC and CO strongly rise;
- With common rail engines, at low load and speed, soot and NOx emissions in DEAL conditions are lowered by an order of magnitude with respect to the standard engine management.
- When DEAL conditions are reached a quite good air-fuel mixture homogenization is obtained that inducing a quite independence of soot and NOx emission to the injection parameters.
- Specific fuel consumption is unmodified at low speed while at higher speed was slightly increases;

REFERENCES

1. Bertoli C., Beatrice C., Belardini P., Del Giacomo N., Massoli P. DEAL - *Diesel Emission At low Limits (Diesel combustion system with high EGR rate)*. Patented CNR n. RM 2001 A 000420. July 13 2001.
2. Bauerle, St., Karasevich, Y., Slavov, St., Tanke, D., Tappe, M., Thienel, Th., and Wagner, H.Gg. (1994). *Soot formation at elevated pressure and carbon concentrations in hydrocarbon pyrolysis*. Proceedings of 25th Symposium (International) on Combustion. P. 627.

Modelling of molecular weight distribution of tars from coal pyrolysis

G. Migliavacca^{1,2}, E. Parodi², L. Bonfanti³, T. Faravelli¹, E. Ranzi¹

1 Dipartimento di Chimica, Materiali e Ingegneria Chimica-Politecnico di Milano – ITALY

2 Stazione Sperimentale per i Combustibili. S. Donato Milanese – ITALY

3 ENEL Produzione-Ricerca, Pisa– ITALY

ABSTRACT

The aim of this work is to present and discuss some specific aspects of a detailed kinetic mathematical model able to describe the devolatilization process of solid fuels, under pyrolysis conditions. The common chemical and structural aspects of these solid fuels are used as starting points to define the model fundamentals. The formation of light gases and liquid tars is the first step of the pyrolysis process. The model capability of describing relevant aspects of the gas and mainly of the tar phase are showed in comparison with the available experimental data. Molecular weight distributions and elemental composition of tars are analysed in respect of coal rank, pyrolysis temperature and holding times. The gas phase composition is also predicted with attention to NO_x, SO_x and pollutant formation.

INTRODUCTION

Models of coal devolatilization have moved on from simple empirical expressions of total mass release, involving one or two rate expressions (Anthony et al. [1], Kobayashi et al. [2]), to more complex descriptions of the chemical and physical processes. Pitt [3] first treated the coal as a mixture of a large number of species decomposing by parallel first order reactions with different activation energies. Similarly, Anthony et al. [4] proposed the Distributed Activation Energy Model (DAEM) and the succeeding DISCHAIN model (distributed-energy chain statistics). Niksa and Kerstein [5] introduced the flash distillation mechanism and developed FLASCHAIN model. Furthermore, Solomon et al. [6] combined the previous Functional Group model (used to describe the gas evolution) with the Depolymerisation-Vaporisation-Cross-linking (DVC) algorithm in the FG-DVC model. Coal dependent chemical structural parameters, deduced from solid state ¹³C-NMR experiments, are the starting point for chemical percolation and devolatilization (CPD) model developed by Fletcher et al. [7]. The tar formation and its chemical evolution represents a fundamental aspect in the overall devolatilisation process. Many studies were devoted to identify its nature and to quantify its amount as a function of coal rank and pyrolysis conditions. Despite this attention, several ambiguous and inconsistent results are often found in literature and different conclusions may be deduced from the available data and experimental evidences. For these reasons, a modeling analysis could be useful in order to clarify this confuse situation.

MODEL FORMULATION

The general features of the model were already presented elsewhere [8-9], but they are shortly proposed here for sake of completeness, along with recent modifications, implementations and upgradings.

Starting from the experimental evidence of the macromolecular nature of coal and from the analogies between coal pyrolysis and other processes involving the thermal degradation of hydrocarbon materials, like oils and polymers, we focused our attention on the possibility to develop a general and fundamental devolatilisation model, based on intrinsic-kinetic parameters. Specific information available on the coal structure is used to build up an array, which describes the main features of the starting material. The same array is also suitable to describe the successive transformations of the lattice during pyrolysis, gasification and even combustion processes. The different cells of this array represent a particular lump of aromatic sites, characterised by an average number of aromatic carbons, as well as by the number of intact bridges. Four structural classes of lumped species are considered here, depending on the number of intact bridges. The aromatic sites contain three attachments, which are intact bridges or side chains. All the species on the same matrix row have an aromatic cluster with the same number of carbon atoms. The internal distribution of the different pseudo-species describes the coal structure at any instant of the conversion process. The initial and starting distribution of different coals is defined on the basis of all the available experimental information. Experimental NMR data supply detailed and essential parameters, which can be also estimated from literature correlations [10]. Coals of different rank are represented by different starting distributions inside the structural array and by different chain compositions. The different array elements or pseudo-species are involved in several radical chain propagation reactions that progressively modify the coal matrix. In this way, the devolatilization process goes along with the coal evolution towards its final char structure. The overall pyrolysis process is described on the basis of only four main classes of propagation reactions:

- a Decomposition or fragmentation reactions.
- b Condensation reactions.
- c Cross linking reactions
- d Aromatisation reactions

The decomposition reactions account for the bond-breaking process which is progressively responsible of the tar formation. This reaction class is in competition with condensation and cross-linking reactions, responsible for the formation of heavier species with progressively larger aromatic sites. Condensation reactions act on species still connected, while the cross-linking ones reconnect free units with the coal matrix. Another reaction class, involved in the process, considers a progressive aromatisation of the structure by means of progressive inclusion of portions of the aliphatic side chain in the aromatic clusters. This reaction process progressively leads coal towards a graphite like structure.

During both condensation and cross-linking reactions, the pseudo-species lose a portion of their side aliphatic chains in the form of light gases and aliphatic compounds. A proper rule is applied to split among the gas species, according to the instantaneous composition of the aliphatic chains. Moreover, other specific pyrolysis reactions justify the formation of some permanent gases (CO, CO₂, H₂O), starting from specific functional groups or structural elements introduced in the model by means of rank dependent pseudo-species. These species are considered additional sources of light gases, according to independent reactions rates. Also some light tar species are introduced in the same way to account for guest molecules with weak bonds or physically adsorbed on the coal structure.

As described elsewhere [9], the extension of the model to treat also biomasses only required the coupling of cellulose and lignin devolatilisation kinetics with the coal pyrolysis process.

RESULTS AND DISCUSSION

The model performances are here challenged in respect to the experimental data coming from the work by Unger and Suuberg [11]. First of all the total volatiles and the tar fraction measured in some grid-reactor experiments, carried out at different temperatures, are compared with the model predictions, for the Bruceton bituminous coal. The simulation of the experimental conditions was achieved by means of a linear heating ramp (1000 K/s) from the room temperatures up to the experimental peak temperature, followed by a cooling phase at a constant rate of 200 K/s. Figure 1 shows the very good agreement in respect to the volatile yield, while some greater discrepancies are observed for tar, but limited to the temperature range between 700 and 850 K.

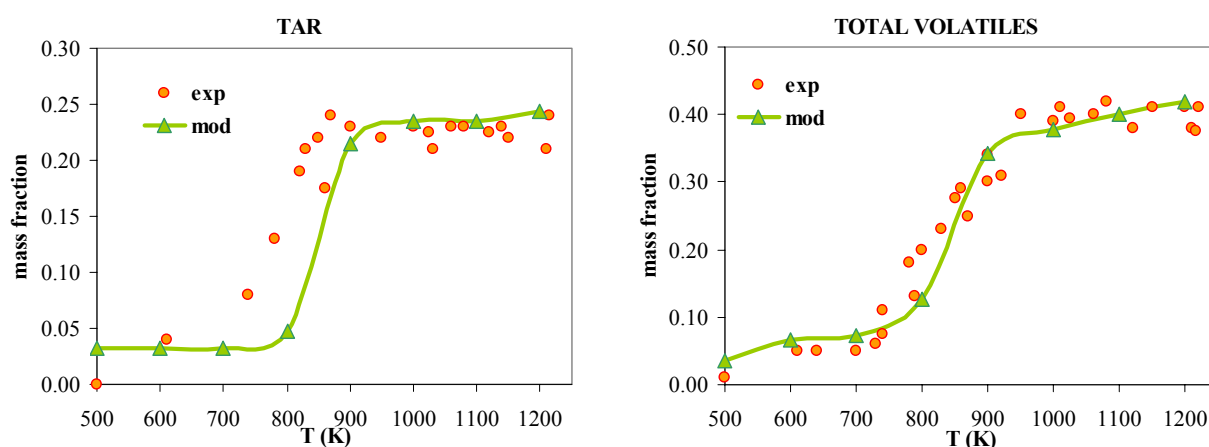


Figure 1 Comparisons of experimental data with model predictions for Tar and Total Volatiles of Bruceton coal [11]

The presence of a mixture of guest molecules with different structures, compositions, molecular weights and hence different boiling points may give a possible explanation for the observed discrepancy. The model actually includes only one guest pseudo-species, responsible for the predicted tar baseline, while a broader distribution of guest species could be used to justify the presence of large tar amounts at low temperatures where a relevant C-C bond cleavage can hardly occur.

The molecular weight distribution of tars is another important feature to account for in the coal pyrolysis modelling. The same paper by Unger and Suuber [11] supplies a very detailed analysis of the tar molecular weight released from different coals, under different experimental conditions. The experimental results for the Bruceton coal show distributions peaked around 500-700 a.u. with a slight shift towards higher weights with the temperature increase. A long tail, covering a range of thousands of a.u. is observed too. The corresponding model predictions are shown in Figure 2 where both massive and relative distributions are presented. The predicted distributions are in rather good agreement with the experimental evidences and confirm the relative invariance of the distribution shape, in the investigated temperature range. Model predicts a maximum position of the distribution curve at only 400 a.u. and also slightly underestimates the high molecular weight components. The experimentally observed heavy species (>2000 a.u.) and/or soot formation can be justified by secondary pyrolysis reactions of primary tars. This phenomenon is observed and reported by many authors [12] and represents a very reasonable explanation, since such heavy compounds

cannot be vaporised at these experimental temperatures, therefore cannot be directly released as primary tars.

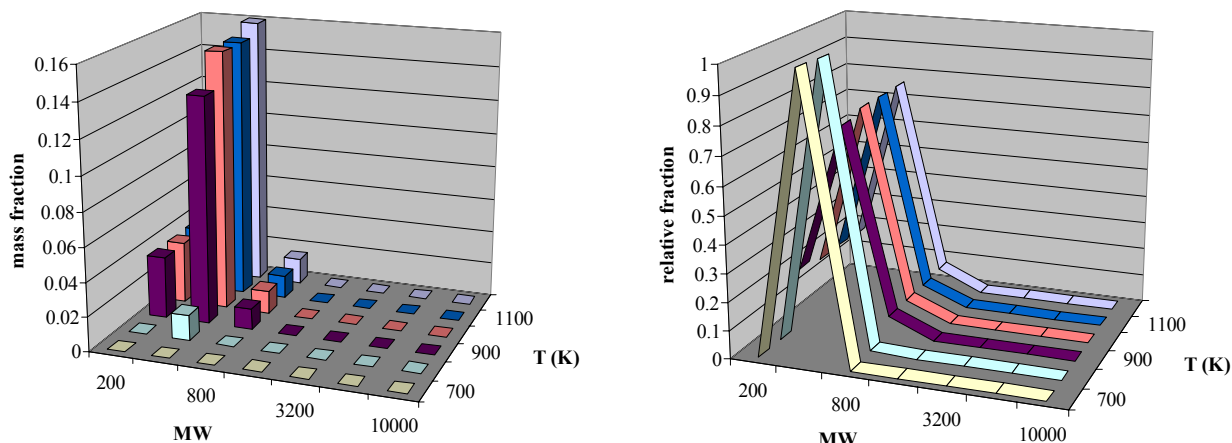


Figure 2 Absolute(left)and relative (right) tar molecular weight distributions for Bruceton coal [11] (guest molecules are not included)

Secondary pyrolysis reactions are not included in the model, but we plan to study also these gas phase reactions and to take them into account in future developments. Further indications could also arise from the analysis of the extract yields, since they can represent a finger print of the metaplastic phase where liquid phase pyrolysis reactions take place and form the primary tars.

ACKNOLEGMENTS

This work was financed by the fund established by the Italian Government to support research activities of general interest of the electric sector (Ministerial Decree 26 January 2000)

REFERENCES

1. Anthony, D.B., Howard, J.B., *AIChE Journal*, **22**, 4, p. 625 (1976)
2. Kobayashi, H., Howard, J.B., Sarofim, A.F., *16th Symp. Comb., Combustion Inst., Pittsburgh*, p. 411 (1977).
3. Pitt, J.G., *Fuel*; **41**, 267 (1962)
4. Anthony, D.B., Howard, J.B., Hottel, H.C., Meissner H.P., *15th Symp. (Int.) Comb., The Combustion Inst., Pittsburgh*, p.1303 (1975).
5. Niksa S., Kerstein A.R.). *Energy & Fuels*, **5**, 647 (1991).
6. Solomon, P.R., Hamblen D.G., Carangelo R., Serio M., Deshpande, G.V., *Energy & Fuels*, **2**, 405 (1988).
7. Fletcher T.H., Kerstein, A.R., Pugmire, R.J., Grant, D.M.. *Energy & Fuels* , **4**, 54 (1990).
8. Migliavacca, G., Faravelli, T., Pierucci, S., Ranzi, E., Bonfanti, L., Parodi, E.: *Technologies and Combustion for a Clean Environment* Paper 19.3, p 625-634, Oporto, July 2001.
9. Migliavacca, G., Sartori, V., Zanderigo, E., Faravelli, T., Ranzi, E., Parodi, E., *Combustion and the environment*, S. Margherita Ligure, 16-19 September, 2001
10. Genetti, D.B., Fletcher, T.H., Pugmire, R.J. *Energy & Fuels* 1999, **13**, 60-68, 1999.
11. Unger, P.E., Suuberg, E.M., *Fuel*, **63**, p. 606 (1984).
12. Mitra, A., Sarofim, A.F., *Aer. Sci. and Tech.* **6**, p.261-271 (1987)

Kinetic Modeling of Emissions from Liquid-Fuel FBC

¹A. Frassoldati, ¹T. Faravelli, ¹E. Ranzi, ²M. Miccio, ³F. Miccio

1 Dipartimento di Chimica, Materiali e Ingegneria Chimica-Politecnico di Milano, Italy

2 Ingegneria Chimica ed Alimentare - Università di Salerno, Italy

3 Istituto di Ricerche sulla Combustione - CNR Napoli, Italy

ABSTRACT

This paper discusses the results of a preliminary simplified model for the description of homogeneous combustion of different fuels in fluidized bed combustors (FBC). The assumption of the model is that fuel rich bubbles (endogenous) generated at the fuel injector travel inside a bubbling fluidized bed, at constant pressure, and undergo chemical conversion in presence of coalescence with air bubbles (exogenous). The model couples a conventional fluid-dynamic model based on the two-phase theory of fluidization for the prediction of typical mixing and residence times in the bed with a detailed kinetic model of gas phase combustion. Preliminary results concerning gasoil combustion confirm the experimental trend that the heat released in the freeboard decreases at increasing emulsion phase temperature. The model with detailed kinetic mechanism has the potentiality to investigate the pollutant formation (like NO_x and PAH) and to identify the optimal operative conditions for increasing the energy efficiency and reducing the emissions.

INTRODUCTION

The main interest in studying the fluidized bed combustion (FBC) of gaseous and liquid fuels lies in their potential benefit for pollutant reduction and for their efficiency and flexibility.

Premixed FBC of gaseous fuels has been extensively studied and accurately modeled [1-2]. Obviously, fluidized combustion of liquid fuels occurs under non-premixed conditions. Literature on non-premixed FBC of gaseous and, mainly, liquid fuels is still limited and many aspects remain unclear and worth of investigation.

Miccio et al. [3] carried out steady-state tests of FBC of gasoil at temperatures between 650°C and 850°C. They extensively analyzed all fuel-air phenomena, which take place from the fuel injection to the splash zone.

The aim of present paper is the development of a preliminary model of the FBC reactor, which is mainly centered on the fate of the rising fuel rich bubble and takes full advantage of a detailed kinetic scheme [4], which includes both the low and high temperature mechanisms of hydrocarbon oxidation.

KINETIC SCHEME AND BED MODEL

The detailed kinetic scheme, able to analyze partial oxidation and combustion of hydrocarbon mixtures up to JP8 and diesel fuels, is well described elsewhere [4]. This accounts for about 200 molecular and radical species involved in more than 5000 reactions.

Even though a high degree of simplifications is required, it is possible to analyze the behavior of the fuel bubble inside the FBC taking into account mass and energy exchange with the emulsion phase and coalescence with the other fuel and air bubbles. Mass and energy balance equations refer to a single spherical and homogeneous fuel bubble rising in the bubbling fluidized bed. The emulsion phase is assumed perfectly mixed, at a constant and assigned temperature T_e . Air bubble temperature is equal to T_e . Heat transfer by radiation is neglected.

-Mass balance equation of i -th species

$$\frac{dm_i}{dt} = k_{oi} \cdot (\omega_{i,e} - \omega_i) \cdot S_b + R_i \cdot V_b \cdot W_i + f_{f,f} \cdot m_i + f_{f,a} \cdot m_{i,a} \quad (1)$$

-Energy balance on the fuel bubble

$$\sum_i m_i \cdot c_{vi} \cdot \frac{dT}{dt} = \sum_i k_{oi} \cdot (\omega_{i,e} - \omega_i) \cdot S_b \cdot (h_{i,e} - u_i) - \sum_i u_i \cdot R_i \cdot V_b \cdot W_i + (h_{b,e} + h_s) \cdot (T_e - T) \cdot S_b + \sum_i (f_{f,a} \cdot m_{i,a} \cdot (h_{i,a} - u_i) + f_{f,f} \cdot m_i \cdot (h_i - u_i)) - \dot{W} \quad (2)$$

The coalescence frequency between the fuel bubbles with fuel or air bubbles ($f_{f,f}$, $f_{f,a}$) makes continuous the discrete and stochastic coalescence with both endogenous and exogenous bubbles. This model has been already discussed in Frassoldati et al. [5]:

The rate constants in the emulsion phase include a reducing factor, which takes into account the wall termination effect on free radicals. The mass transfer between the air bubbles and emulsion is considered extremely fast. As a consequence, emulsion phase benefits of O₂ content of exogenous bubbles, too. A better description of these transport phenomena would imply solving a larger (double) set of differential equations, i.e. the mass and energy balances for the air bubbles, whose definition is identical to equations (1) and (2).

The algebraic material balances on the emulsion phase allow to close the overall balances and provide a consistent set of mass fractions of the emulsion phase with a few iterations by using a simple under-relaxation method. Further, assuming a fixed T_e , it is possible to evaluate from the overall energy balance the contributions to the heat generated inside the bed and in the freeboard zone.

MODEL RESULTS AND PRELIMINARY VALIDATION

The kinetic model indicates that the reaction times are lower than the residence times of the bubbles inside the FBC, consequently the exchange with the emulsion and the coalescence influence the chemical evolution. As an example, figure 1 shows the temperature and species evolution inside a gasoil bubble traveling into the emulsion phase at 1000 K.

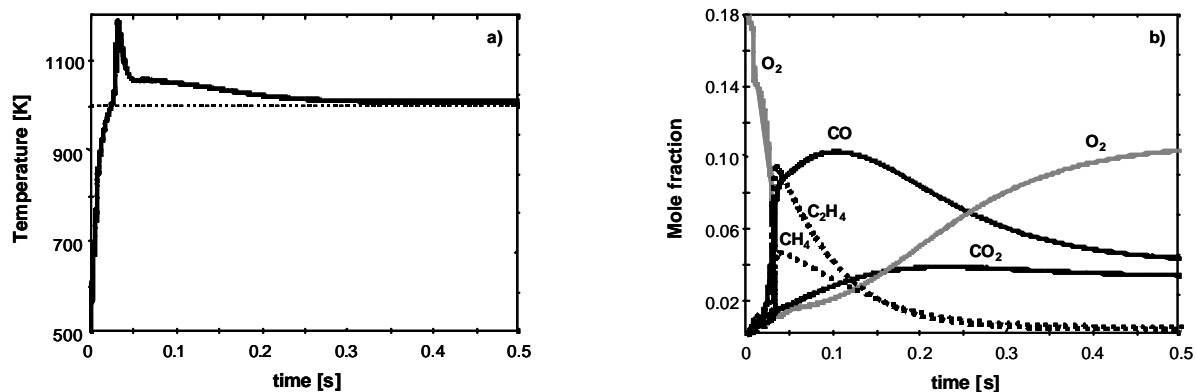


Figure 1. Theoretical temperature (a) and main composition profiles (b) of the fuel bubble rising in the reactor. Bubble initial conditions: $T=500$ K, $d_b=3 \cdot 10^{-2}$ m, 14% nC₁₂H₂₆ in air.

Coalescence frequency with air bubbles was fixed in order to reach $\Phi=2$ at the bed outlet. Gasoil composition is roughly assumed as pure n-dodecane. The initial conditions of gasoil bubble are: 14% mol nC₁₂H₂₆ in air, $T=500$ K, diameter $3 \cdot 10^{-2}$ m. The bed is in the bubbling regime at $U - U_{mf} = 0.5$ m/s. The endogenous bubble rise time is in the order of 0.5–1.0 s.

The composition of the emulsion phase and the endogenous bubble at the bed outlet (for species whose amount is larger than 100 ppm) are reported in table 1 and Fig. 1b,

respectively. In this simulation, the numerical convergence required 6 iterations with an under relaxation factor of 0.25.

N ₂	.7364	CO	.0369	C ₆ ⁺ olefins	.12x10 ⁻³	C ₂ H ₄	.48x10 ⁻²	CH ₃ CHO	.14x10 ⁻³
O ₂	.1210	CO ₂	.0247	pentenes	.15x10 ⁻³	C ₂ H ₂	.15x10 ⁻³	CH ₂ CO	.20x10 ⁻³
H ₂	.66x10 ⁻²	nC ₁₂ H ₂₆	.75x10 ⁻³	butenes	.17x10 ⁻³	C ₄ H ₆	.31x10 ⁻³	CH ₃ OH	.23x10 ⁻³
H ₂ O	.0587	CH ₄	.55x10 ⁻²	C ₃ H ₆	.85x10 ⁻³	C ₆ H ₆	.25x10 ⁻³	CH ₂ O	.99x10 ⁻³

Table 1 Mole fractions in the emulsion phase at the bed outlet. Conditions of figure 1

The following features can be singled-out:

- The sudden temperature rise from 750 K to 900 K is the effect of the low temperature oxidation mechanism. At about 900 K the reactivity of the system declines. The O₂ profile shows a very sharp jump from about .17 to .14. The temperature peaks at about 1200 K and 30 ms where CO formation sharply increases. This hot ignition is controlled by the total amount of oxygen inside the bubble and its diffusion limitation.
- Up to 500 ms the high temperature mechanism is mainly controlled by the coalescence mechanism, due to the low oxygen diffusion from the emulsion phase. Hydrocarbons formed from fuel pyrolysis, gradually decrease and form CO. The presence of pyrolysis and incomplete combustion products was experimentally confirmed by Van der Vaart [6].

Figure 2 shows the three contributions of heat released in the FBC in terms of cumulative fractions as a function of the emulsion temperature. The duty, i.e. the fraction of heat released inside the bed (bubble and emulsion phase), reaches the 60-65% only at T_e>1100 K. The sensible heat represents the fraction of the totally available combustion enthalpy needed for heating-up the flows entering the reactor to T_e.

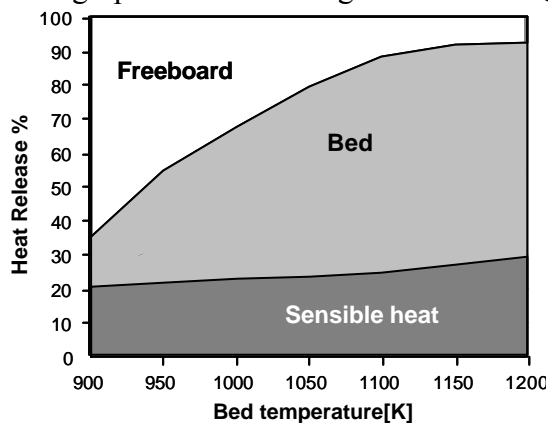


Figure 2. Cumulative fractions of heat released in the FBC

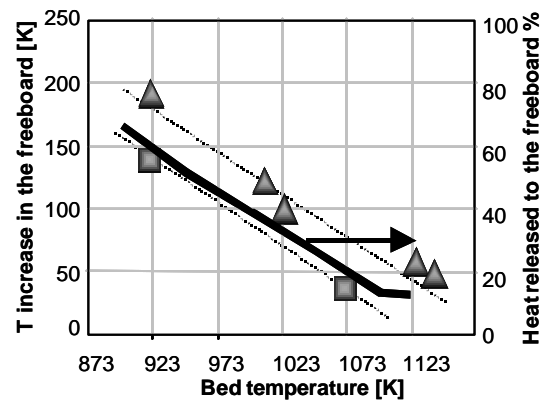


Figure 3. Heat released from the rising fuel bubbles and T increase vs. emulsion temperature.

Triangles: nozzle=2 mm; Squares: nozzle=4 mm

The heat released in the freeboard region closes to 100% the overall energy balance. According to the experimental observation of Dennis et al [7], less than 2-3% of the combustion takes place in the emulsion phase up to 1200 K. As already mentioned, this limited combustion in the emulsion phase is the result of the reducing factor applied to the gas phase reactions, due to free radical terminations on particle surface.

Steady-state combustion experiments of standard gasoil for automotive applications were carried out in a 370 mm ID bubbling FB combustor. A full description of the experimental facility can be found elsewhere [3], [8]. The fuel is under-bed fed by means of an air-assisted injector. A base case of experiments was considered at T=750 °C, U=0.73 m/s and Φ=0.79. Experimental results include measurements of T, P and gas concentrations (O₂, CO₂, CO, SO₂, NO_x, hydrocarbons) along the combustor.

The gas leaving the fluidized bed and entering the freeboard still contains unburned species. For instance, volumetric concentrations equal to 0.75%, 0.06% and 0.088% were measured at 750 °C for CO, CH₄ and C₂H₄, respectively. Concentration of unburned species is higher above the injection point and declines along the diameter. An increase of the temperature in the freeboard was always noted during combustion tests at different operating conditions [3].

This ΔT was attributed to diffusion flames above the bed surface that are observable through an optical access port. Figure 3 shows experimental values of ΔT versus the bed temperature for two different fuel nozzle sizes. ΔT decreases when increasing the bed temperature as a consequence of the faster oxidation. A larger injection nozzle depresses freeboard post-combustion due to longer jet penetration and better fuel dispersion. The degree of post-combustion in the freeboard, evaluated following Fiorentino and Miccio's approach [9], ranged between 10 and 20%. The model underestimates fuel conversion in the bed, CO and light hydrocarbons being higher than the experimental ones. This leads to overestimate the heat release in the freeboard (Fig. 4) with respect to post combustion degree. Anyway, the trends with temperature as well as the establishment of zones at different gas concentration (over jet region and emulsion phase) are correctly predicted by the model.

CONCLUSIONS

A quite simple model of bubbles rising a FBC allows to introduce a detailed chemistry including both the low and high temperature mechanisms. The preliminary results are in a qualitatively good agreement with the experimental observations.

The detailed kinetics is a useful tool to investigate and characterize new operative conditions and their impact on the heat released and on the emissions from this potentially clean combustion system. Different and more practical fuels, like surrogate blends, or complex mixtures with potentially dangerous compounds, like aromatics, can be easily analyzed on the basis of an already available kinetic mechanism. The formation of PAH or NO_x can be predicted and new strategies for their reductions can be addressed.

Finally the model has the potential capability to direct new experimental activity, to investigate and focus the critical parameters and phenomena inside FBC, especially as far as low operation temperature is concerned.

ACKNOWLEDGEMENTS

This work has been carried out under the MURST-COFIN (2001-2003) financial support.

REFERENCES

1. Zukowski W., *Fuel*, 79:1757 (2000).
2. Pre, P., Hemati, M., and Marchand, B., *Chem. Eng. Sc.*, 53:2871 (1998).
3. Miccio, F., Miccio, M., and Olivieri, G., paper FBC01-0178, *Proc. of the 16th International Conference on Fluidized Bed Combustion (FBC01)*, Reno, (Nevada USA), May 13-16, 2001.
4. Ranzi, E., Dente, M., Goldaniga, A., Bozzano, G., and Faravelli, T., *Prog. Energy Combust. Sci.* 27:99 (2001).
5. Frassoldati, A., Pagani, D., Faravelli, T., Ranzi, E., Miccio, F., Miccio, M., *Proc. of 24th event of the Italian section of the Combustion institute*, S.M. Ligure (Italy) September 16-19, 2001.
6. Van der Vaart, D. R., *Combust. Flame* 71:35 (1988).
7. Dennis J.S., Hayurst A.N., and Mackley I.G., *Proc. Comb. Inst.* 19:1205 (1982).
8. Miccio, F., Miccio, M., Repetto, L., and Traniello Gradassi, A., *Proc. of 15th Int. Conf. on Fluidized Bed Combustion*, ASME, Savannah (Georgia USA), May 16-19, 1999, p. 1354.
9. Fiorentino M. and Miccio F., *Combust. Sci. and Tech.*, 159:57 (2000).

SOUND ASSISTED FLUIDIZED BED COMBUSTION

A. Cammarota, M. Urciuolo, R. Chirone

Istituto di Ricerche sulla Combustione – C.N.R., Naples - ITALY

Dipartimento di Ingegneria Chimica – Università Federico II, Naples - ITALY

INTRODUCTION

The combustion and/or gasification of solid fossil fuels in fluidized beds may be considered a technology already mature (Abdulally I. F. and Reed K., 1995). However its extension to the case of not conventional fuels: Refuse Derived Fuel (RDF), Tyre Derived Fuel (TDF), biomass and industrial or civic residues, is the challenge to the operators of the sector and to researchers (Antony E. J., 1995). The main feature of such fuels and, more in general of high-volatile fuels, is the generation of large amount of fine particles during their conversion. A limit situation is the case of TDF: the total amount of carbon present in the bed under steady state operation is made of fine particles, whatever the feed size (Salatino P., et al., 1997). On the other hand the efficiency and the environmental impact of the combustion is mainly related to elutriation of solid carbon.

Aim of the present work is to investigate the practical usefulness of using sound assisted fluidized beds to increase carbon conversion degree and to reduce the amount of fine particles escaping the reactor as unreacted carbon, when fuels of different characteristics are used.

Table I - Characteristics of the materials used.

PROXIMATE ANALYSIS, % WEIGHT (as received)			
	T.D.F.	SULCIS	PET. COKE
Moisture	0.9	4.3	0.5
Volatile matter	65	35.3	6.7
Fixed carbon	30.7	36.4	92.2
Ash	3.4	24.0	0.6
ULTIMATE ANALYSIS, % WEIGHT (dry basis)			
Carbon	86.8	49.2	93.9
Hydrogen	6.8	4.6	2.4
Nitrogen	0.3	1.4	1.2
Oxygen	0.8	14.6	0.4
Sulfur	1.9	6.2	1.5
Ash	3.4	24.0	0.6
Density, kg/m ³	940	1370	1050
U.H.V., kJ/kg	38600	17600	35000
L.H.V., kJ/kg	38200	17350	34850
d _p (Sauter), μm	9.9	45.2	151
Bed inert material		Silica sand	
Particle size range, μm		300 ÷ 400	
Particle density, kg/m ³		2600	

MATERIALS

Table I reports the characteristics of the three fuels tested: a Tyre Derived fuel (TDF), a Sulcis Lignite and a Petroleum Coke. Main features of the fuels are :

- i. TDF particles turn into a multitude of fines (average size less than 100 μm) during devolatilization stage.
- ii. Reactivity increases passing from Petroleum Coke to TDF fines and to Sulcis Lignite.
- iii. Abrasion of Petroleum Coke is rather limited.

EXPERIMENTAL APPARATUS AND PROCEDURE

The experimental apparatus consists of a 40 mm I.D. stainless steel sound assisted fluidized bed reactor (fig.1). Experiments were conducted under steady state condition. A data acquisition system is used to process signals from on line analysers (CO, CO₂, NO_x, O₂, CH₄, SO₂). Tests were carried out by feeding particles in the size range 0 – 1 mm into a bed made of 180 g of silica sand in the size range of 300 ÷ 400 μm. Superficial gas velocity and temperature were fixed to 0.4 m/s and 850°C, respectively. Combustion tests were carried out with or without

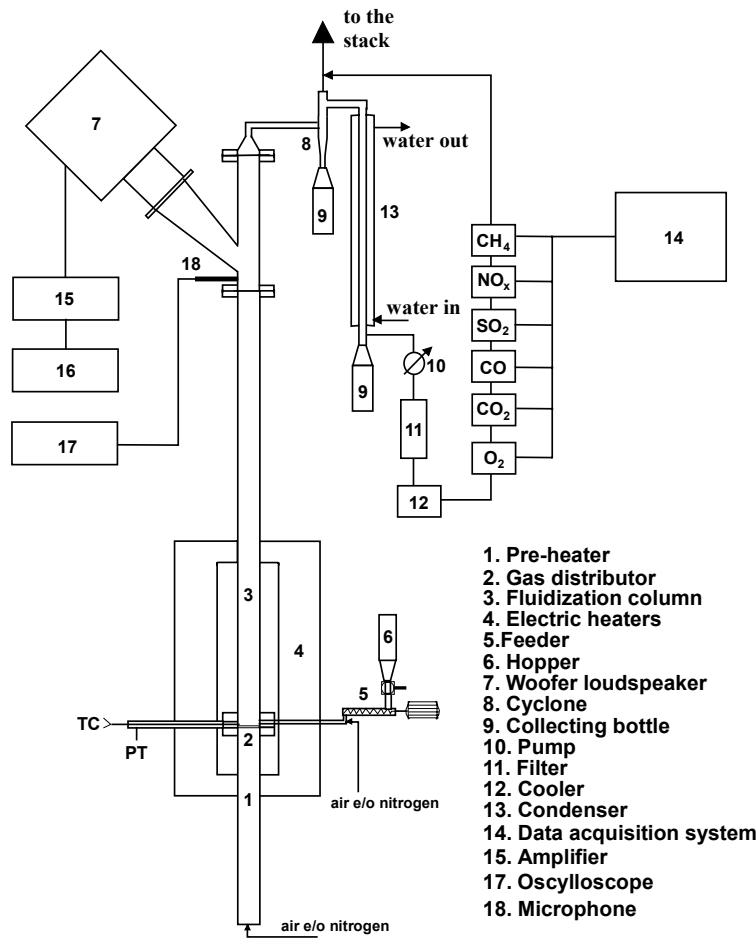


Fig. 1 Sound assisted fluidized bed combustor.

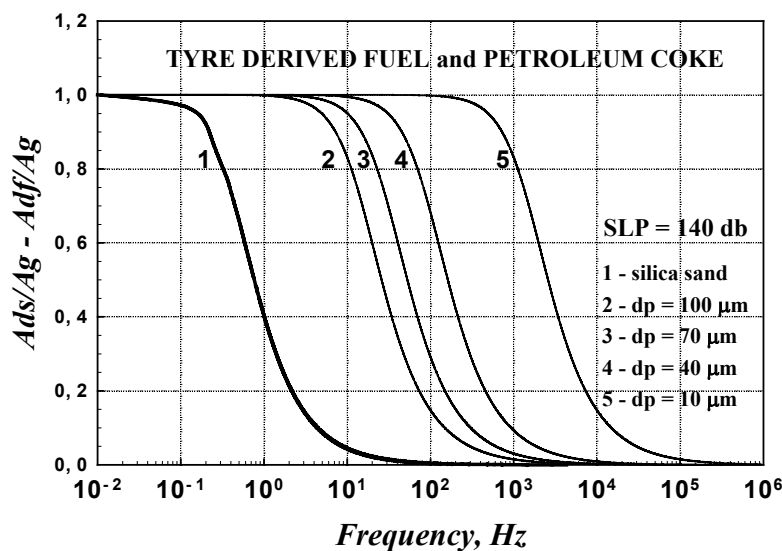


Fig.2 Amplitude of fine particle and coarse particle displacement to amplitude of gas displacement.

application of sound. During experiments, fines escaping the reactor with the flue gasses were collected and analysed to determine their carbon content. Acoustic field intensity and frequency were varied among 130 and 150 dB and among 30 and 200 Hz, respectively. Combustion behaviours of the three fuels were compared in terms of carbon elutriation rate, E_c , bed carbon loading, W_c , and carbon combustion time, τ .

THEORY

During fluidized bed combustion of high volatile fuels, the bed carbon loading is present in two phases: a coarse phase, made of particles having a not elutriable size, and a fine phase, made of particles of elutriable size (Arena U. et al, 1996). Fine particles can interact with bed inert material as well as with combustor internals and walls. The result is that some of fine particles may be subjected to cycles of collisions and attrition phenomena whereas others may move freely in the bed. Application of an acoustic field to a fluidized bed reactor has been proved to increase the residence time of fine particles in the bed (Russo P. et al, 1995). A simplified model has been developed to account for the role of the application of sound to promote adhesion of fine particles on coarse particles (Urciuolo M., 2001). The model assumes that carbon fine particles, of size d_f , and coarse bed inert particles, of size d_s , are suspended in the gas and subjected to the oscillatory perturbation due to sound application. Figure 2 reports the relative displacement of coarse and fine particles, A_{ds} , A_{df} , toward gas particles, A_g . Analysis of the

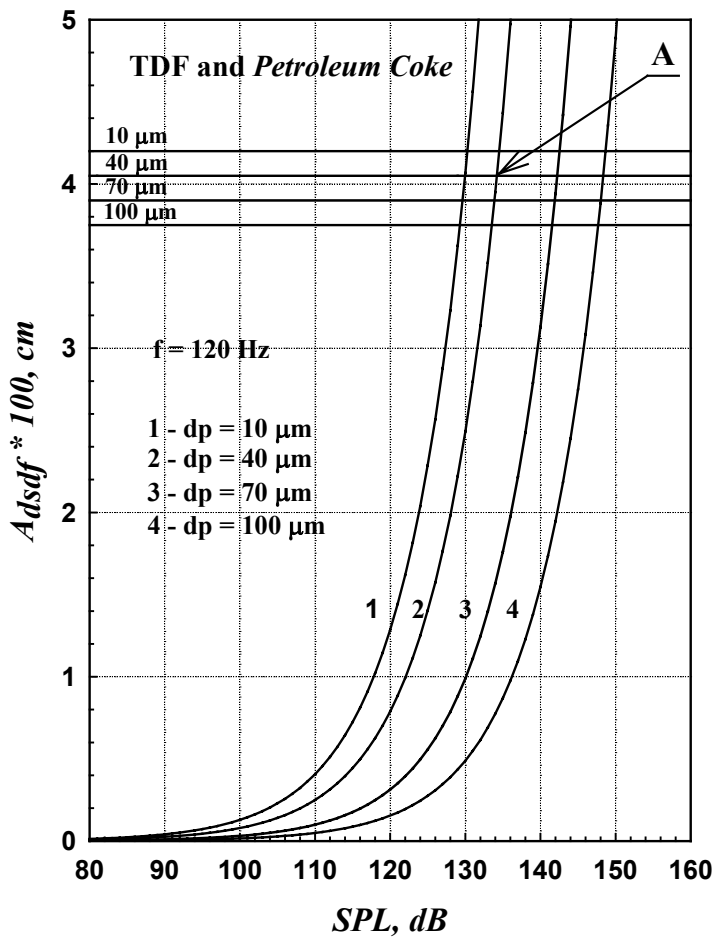


Fig.3 Amplitude of the relative displacement $A_{df,ds}$ vs the intensity of the acoustic field for a frequency of 120 Hz.

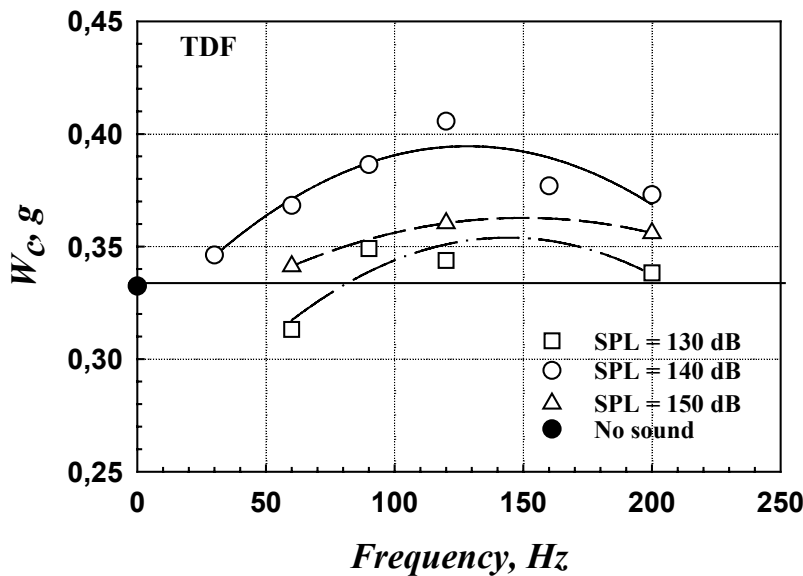


Fig. 4 Effect of the sound frequency on the amount of fixed carbon present to regime in the bed.

figure shows that for relatively low frequency ($f < 10^1 \text{ Hz}$) as well as for relatively high frequency ($f > 10^5 \text{ Hz}$) there is no relative motion between coarse and fine particles. For frequency larger than 10 Hz, coarse particles are fixed in the space and fine particles oscillate depending on their size. For example with reference of 40 μm fine particles, relative motions and in turn coarse/fine particles collisions, are possible in the range of frequency between 10 and 1000 Hz. Figure 3 reports the fine particle displacement for a fixed frequency of 120 Hz and different intensities of the acoustic field. Horizontal lines give the displacement necessary to cause coarse/fine particles collisions. For particle size of 40 μm an intensity of 134 dB is required for the occurrence of collisions (A point in the figure).

EXPERIMENTAL RESULTS AND DISCUSSION

Figures 4 and 5 report the carbon loading in the bed, W_c , and the combustion time, τ , vs the sound frequency f , respectively. Horizontal lines indicate the value of W_c and τ for $f = 0 \text{ Hz}$ and $\text{SPL} = 0 \text{ dB}$. Three different acoustic field intensities are tested under sound assisted combustion runs: 130, 140 and 150 dB. Analysis of the data shows that the application of sound increase bed carbon loading and combustion time. Moreover W_c and τ have a non monotone trend, with acoustic parameters, and the optimum is achieved with a frequency of 120 Hz and an intensity of 140 dB of the acoustic field.

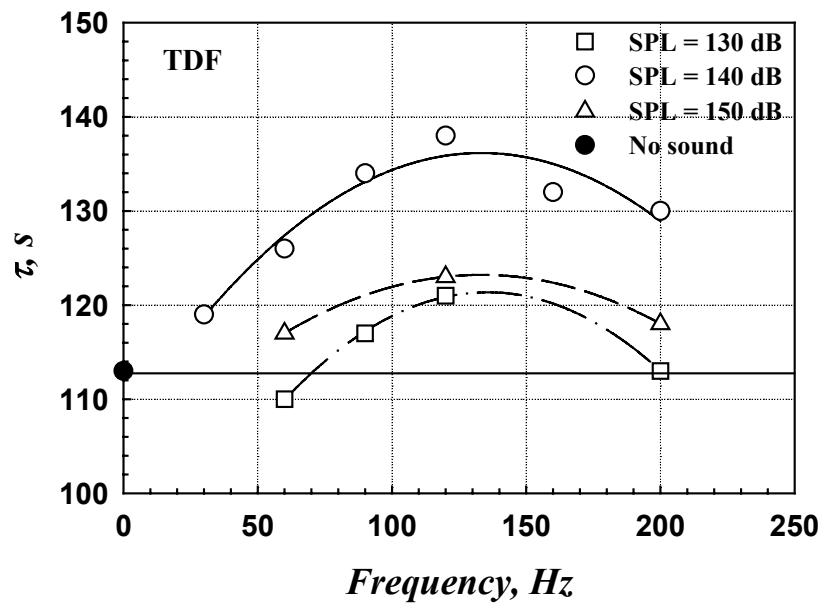


Fig. 5 Effect of sound frequency on the mean residence time of the carbon in the bed.

In summary, the following considerations can be drawn:

- Application of acoustic fields, of opportune intensity and frequency, increases bed carbon loading and combustion time; reduces carbon fines elutriation and increases combustion efficiency.
- For TDF and Petroleum Coke an optima intensity of 140 dB and frequency of 120 Hz of the acoustic fields were found. In these conditions, W_c increases of factors 1.2 for TDF and 1.1 for Petroleum Coke, and τ increase from 113 to 138 s and from 49 to 53 s, respectively. Sound has not effect on Sulcis Lignite combustion behaviours.
- A simplified model of sound assisted fluidization has been developed. Its validity has been tested by comparing the optima intensity and frequency from experiments with the limit intensity and frequency indicated by the model.
- The model is useful for design of the acoustic field to be used in sound assisted fluidized bed combustors.

REFERENCES

- Anthony E. J.: *Fluidized Bed Combustion of Alternative Solid Fuels: Status, Success and Problems of the Technology*, Prog. Energy Combust. Sci., p. 21 (1995).
- Abdulally I. F., Reed K.: *Fluidized Bed Combustion*, ASME, p. 753 (1995).
- Arena U., Chirone R., Salatino P., Symposium Int. on Combustion, The Combustion Institute, **26**:3243 (1996).
- Russo P., Chirone R., Massimilla L., Russo S.: *Powder Techn.*, **82**: 219 (1995).
- Salatino P., Scala F., Chirone R. and Pollesel P.: *Optimization by Air Staging of the Fluidized bed Combustion of Tyre Derived Fuel*, Proc. Conf. Tech. Combust. For Clean Environ., Lisbon, Portugal, **4**:23 (1997).
- Urciuolo M.: *Combustione in Letto Fluidico Vibrato Acusticamente di Combustibili di Varia Natura*, Tesi di Laurea in Ingegneria Chimica, Facoltà di Ingegneria, Napoli (2001).

LOSS OF GASIFICATION REACTIVITY TOWARDS O₂ AND CO₂ UPON HEAT TREATMENT OF CARBONS

Osvalda Senneca and Piero Salatino

Dipartimento di Ingegneria Chimica,
Universita' degli Studi di Napoli *Federico II*
Istituto di Ricerche sulla Combustione - C.N.R.
P.le Tecchio, 80125 Napoli, ITALY

INTRODUCTION

Considerable research effort has been recently devoted to set up kinetic models which account for the occurrence of thermal annealing along with heterogeneous oxidation during gasification of carbon [1-6]. A crucial point is the definition of what is meant as *non-annealed char*. As outlined in Fig. 1, a continuous spectrum of transformations involves the raw fuel and its char. The distinction between pyrolysis and thermal annealing, more operational than conceptual, could be based on the relative time scale (shorter for pyrolysis than for annealing), on the associated volatile matter release (extensive for pyrolysis, negligible for annealing), or on the very chemical nature of transformations (depolymerization and change of carbon hybridization, prevailing during pyrolysis, versus stacking and rearrangement of graphene layers, prevailing during thermal annealing). However a clear cut distinction appears impossible. In the present paper by *non-annealed char* it is meant the solid product of pyrolysis at the point (ξ^* in Fig. 1) at which heterogeneous gasification becomes effective, and by *thermal annealing* the bundle of solid state

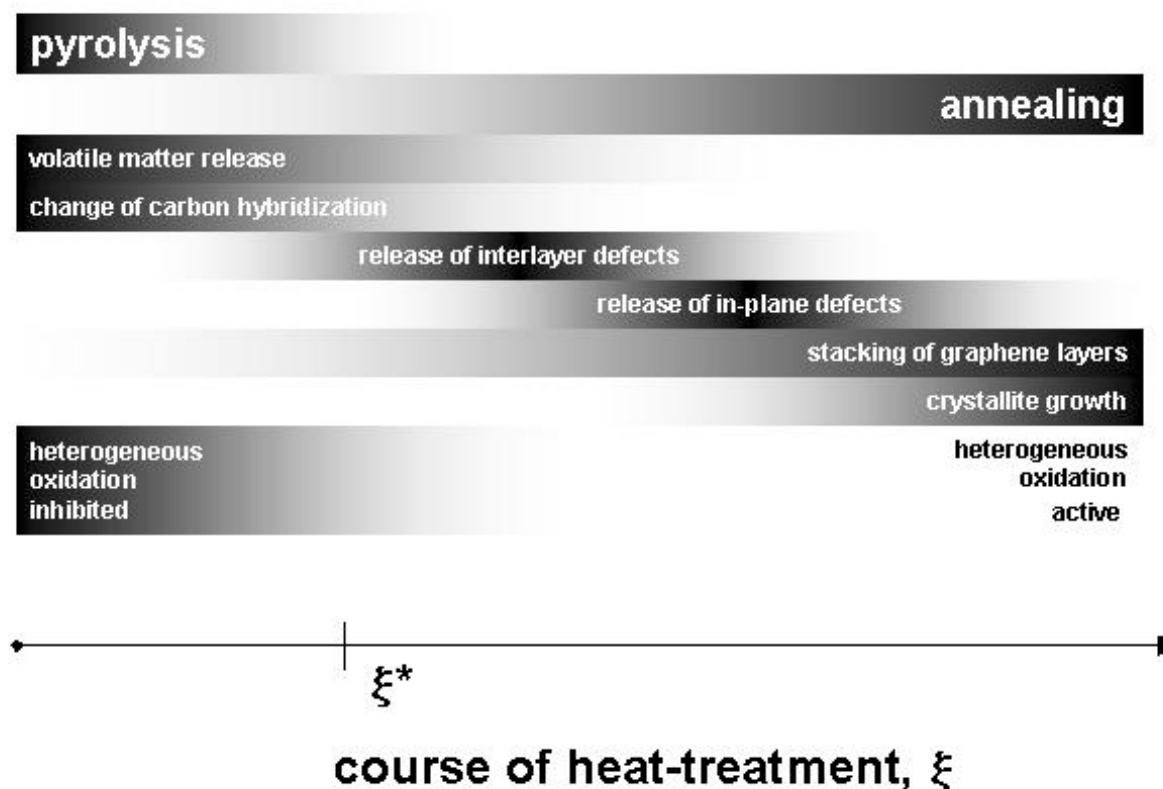


Figure 1

Table 2. Properties of materials

	Pet coke	Ruhr coal	South African coal
<i>Net calorific value</i> <i>kJ kg⁻¹</i>	35100	30400	26300
<i>Proximate analysis(%, dry basis)</i>			
Volatile matter	10.62	31.4	23.1
Fixed carbon	88.91	64.0	61.2
Ash	0.47	4.6	15.7
<i>Ultimate analysis(%, dry basis)</i>			
Carbon	89.05	77.3	68.0
Hydrogen	3.77	4.8	3.8
Sulfur	5.14	1.2	0.6
Nitrogen	1.46	2.1	1.2
Oxygen	0.11	10	10.7
Ash	0.47	4.6	15.7
<i>Free swelling index</i>	-	1	1
<i>Random vitrinite reflectance (%)</i>	-	0.8	0.72
<i>Chemical composition of ashes(%, weight)</i>			
<i>SiO₂</i>	9.81	41.0	44.1
<i>Al₂O₃</i>	5.6	31.8	34.0
<i>CaO</i>	3.08	1.6	8.1
<i>MgO</i>	2.01	1.3	2.2
<i>K₂O</i>	0.1	2.3	0.62
<i>Na₂O</i>	8.37	0.5	0.15
<i>FeO</i>	1.44	17.5	1.53
<i>MnO</i>	0.06	0.04	0.01
<i>TiO₂</i>	0.05	0.9	1.41
<i>P₂O₅</i>	-	0.5	2.35
<i>SO₃</i>	10.3	1.62	2.08
<i>Others</i>	59.18*		3.45

*CuO=0.06, Cr₂O₃=0.16, ZnO=0.20, NiO=7.7, V₂O₅=49.12, MoO₃=0.53, As₂O₃=0.07, CoO=0.04, BaO=0.02

EXPERIMENTAL

Two bituminous coals from the Southern and Northern hemisphere, namely South African (SA) and Ruhr coal (Ru), and a Petroleum Coke (PC), whose properties are reported in Table 1, have been used for the experiments. Carbon samples were ground and sieved in the size range of 75-125 μm prior to any processing.

Samples were heat treated in nitrogen with heating rate H_r to the final temperature T . Isothermal heat treatment in nitrogen for a time t immediately followed. Heat treatment conditions include $T=500^\circ\text{C}-2000^\circ\text{C}$, $H_r=900^\circ-10^{60}\text{C}/\text{min}$; $t=0.2\text{sec}-300\text{min}$. The reactivity of heat-treated samples was measured by thermogravimetric analysis with air at 500°C and with carbon dioxide at 900° .

Equipment used for the experiments include a Rheometrics PL-TG1000M (heating rate up to $1000^\circ\text{C}/\text{min}$ and maximum operating temperature of 950°C .), a Rheometrics PL-TG1500 thermobalance (fixed heating rate of $10000^\circ\text{C}/\text{min}$ with a maximum operating temperature of

transformations occurring thereafter.

Thermal annealing has been shown to involve not only the organic structure, but to induce major changes also within the mineral matter [5,7,8]. It is feasible that the two kinds of microstructural transformations have different effects on gasification reactivity depending on the oxidizer [9]. Moreover the extent of either microstructural transformation depends on the very nature of carbon. In the present work different carbons are subjected to heat treatment and the effects of annealing are checked against both carbon dioxide and oxygen reactivity. The dependence of the loss of reactivity from temperature and duration of heat treatment is described according to the kinetic model proposed by Salatino et al.[1] assuming that the course of annealing can be quantified by an internal coordinate whose rate of change follows an n-th order power law dependence with respect to the fraction of non annealed carbon.

1500°C), a heated-strip reactor (HSR) (maximum heating rate of 10⁶°C/min and maximum temperature of 2200°C).

RESULTS

Experimental results have been fitted to the annealing kinetic expression proposed by Salatino et al. [1]:

$$\frac{R - R_\infty}{R_0 - R_\infty} = [1 + (n - 1)A_d \exp(-E_d/RT)t]^{-1/(n-1)} \tag{1}$$

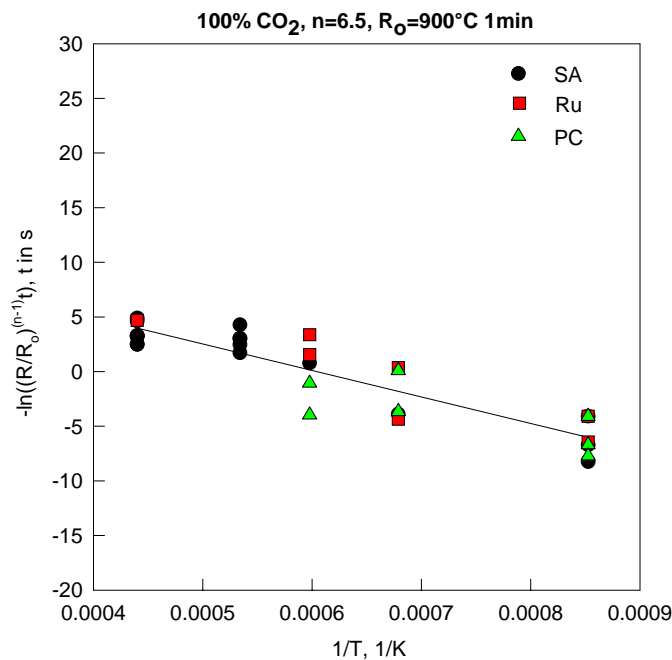


Figure 2

where R₀ and R_∞ are the reactivities of the non-annealed and of the fully annealed materials, respectively. They have been assumed equal to the reactivity of samples heat treated at 900°C for 1min and zero respectively. Results are presented as Arrhenius plots in figures 2 and 3. It can be noted that the fit of experimental points is satisfactory in the case of CO₂ annealing data, yielding the following values of the kinetic parameters:

$$E_d=48 \text{ kcal/mol}; n=6.5; A_d=5 \cdot 10^6 \text{ s}^{-1}$$

The fit was, instead, unsatisfactory in the case of oxygen annealing data. Indeed different trends are observed for mild and severe heat treatment conditions when the extent of annealing is assessed from oxyreactivities. If data points in Fig. 3

are separately fitted to the kinetic model expressed by eq. (1) for mild (T<1200°C) and severe (T>1200°C) heat treatment temperatures, the following sets of kinetic parameters are obtained:

- “mild” heat treatment (T<1200°C): E_d=34 kcal/mol; n=6.5; A_d=2·10³ s⁻¹
- “severe” heat treatment (T>1200°C): E_d=63 kcal/mol; n=6.5; A_d=1·10⁸ s⁻¹ for PC
- E_d=114 kcal/mol; n=6.5; A_d=1·10⁵ s⁻¹ for SA
- E_d=142 kcal/mol; n=6.5; A_d=4·10²¹ s⁻¹ for Ru.

Notably activation energy of thermodeactivation towards oxygen is larger under severe heat treatment conditions than under moderate ones for the coals, whereas it is relatively insensitive to heat treatment temperature for the petroleum coke.

DISCUSSION

Two pathways might be relevant to the different thermodeactivation patterns observed at low versus high heat treatment temperature towards O₂ and CO₂:

- a) transformations involving mineral matter might be extensive beyond a temperature threshold which depends on the chemical nature of ash material and, in turn, on the nature of carbon [8]. Accordingly, differences between thermodeactivation towards O₂ and CO₂ might be explained

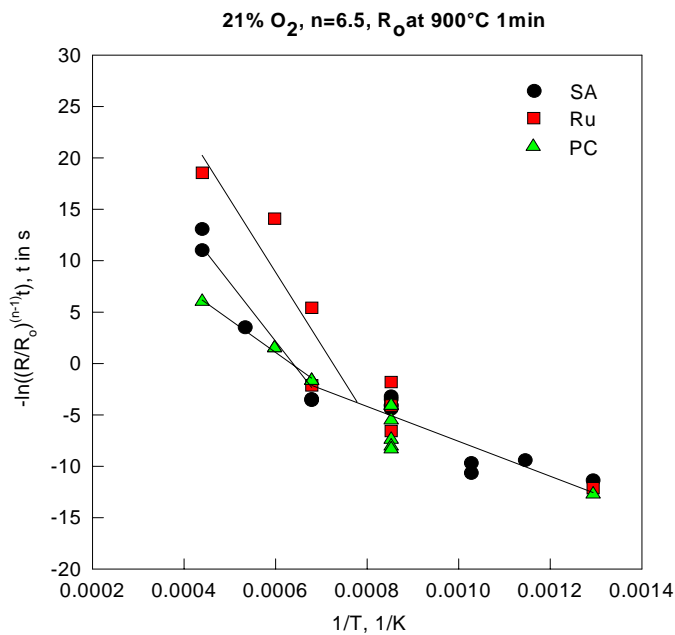


Figure 3

carbon microdomains to the oxidant [9].

in the light of a different role of catalytic versus non-catalytic carbon gasification by the two oxidants.

- b) the very nature of turbostratic carbon structural modifications is dependent on heat treatment temperature. As discussed in Bar-Ziv et al. [7], change of carbon hybridization and loss of aliphatic functionalities should prevail at moderate temperature; graphene layer stacking and rearrangement might be the dominant thermodeactivation mechanism at higher temperature. It can be speculated that oxyreactivity would be affected to a larger extent than carboxireactivity by stacking of graphene layers due to reduced accessibility of

CONCLUSIONS

As far as the loss of oxyreactivity is concerned, different thermodeactivation patterns (reflected by a change of annealing kinetic parameters) are observed at heat treatment temperatures below and above about 1200°C, depending on the carbon. On the contrary, a single set of annealing kinetic parameters fairly well represents the loss of carbon reactivity towards carbon dioxide throughout the temperature range investigated and for all the carbons. It is speculated that changes of the turbostratic carbon structure and modifications of the ash constituents, affecting the heterogeneous reaction of carbon along different pathways for the two oxidants, may both be relevant to the observed behaviour

References

1. Salatino, P., Senneca, O., and Masi, S., *Energy & Fuels* 13: 154 (1999) 1154;
2. Hurt, R. H., Sun, J.-K., and Lunden, M., *Combust. Flame* 113:181 (1998);
3. Russell N.V., Gibbins J.R., Man C.K., and Williamson, J., *Energy & Fuels* 14:883 (2000);
4. Zolin A., Jensen A, and Dam-Johansen, K., *Proc. Comb. Inst.*, 28: 2181 (2000);
5. Feng B., Bhatia S.K., and Barry, J.C., *Carbon*, in press (2002);
6. Suuberg, E.M., *Fundamental Issues in Control of Carbon Gasification Reactivity*, eds. J. Lahaye and P. Ehrburger, Kluwer Academic Publishers, Series E: Applied Sciences **192**, pp. 269-305 (1990).
7. Bar-Ziv, E., Zaida, A., Salatino, P., and Senneca, O., *Proc. Comb. Inst.*, 28:2369 (2000);
8. Senneca, O., Salatino, P., and Masi, S., *Fuel* 77:1483 (1998);
9. Salatino, P., Senneca, O., Masi, S., *Carbon*, 36: 443 (1998).

Puff Production During Incineration Of Sewage Sludge Spiked With Chlorinated Hydrocarbons

Giuseppe Mininni* and Giuseppe Mascolo**

CNR – Istituto di Ricerca sulle Acque;

*Via Reno, 1 – 00198 Roma; **Via Francesco De Blasio, 5 – 70123 Bari

ABSTRACT

Laboratory experiments were carried out to simulate puff production during incineration of sewage sludge. The system for thermal diagnostic studies (STDS) was used. It consists in a pyroprobe and a quartz reactor as first and second thermal treatment, respectively, and in GC/MS system directly connected. Puffs were simulated by injecting a surrogate organic mixture (SOM), constituting of 20 % of toluene, 25 % of chlorobenzene and 55 % of tetrachloroethene, before or after the thermal chamber. Results evidenced that (i) many chlorine containing compounds are formed, being their abundance dependent on the SOM injection point, (ii) among the chlorine containing PICs there are aliphatic as well as aromatic compounds, (iii) the destruction of SOM components is practically independent on the SOM injection point and (iv) toluene is a typical PIC from sludge combustion and its abundance at 700 °C is higher than at 600 °C. Finally, the laboratory investigation confirmed that perturbations are responsible of the appearance in the emissions of a spectrum of organic contaminants whose presence is strictly correlated with the destruction.

INTRODUCTION

Currently over 6.5 millions tons of dry solid sludge are produced in the EU per year. Furthermore the full implementation of the European urban wastewater treatment directive (91/271/EEC) will lead to a substantial increase of the whole sludge production. Among the outlets for sludge disposal (agriculture, landfill and incineration), incineration is expected to increase particularly in those countries where distances to agricultural land make transportation prohibitively expensive and where landfill sites are difficult to realize (Clement and Kagel, 1990).

Although incineration should theoretically result in the conversion of the hazardous organic compounds present in the sludge to innocuous end-products, often such conversion is not fully achieved due to upset conditions observed in full scale incineration (Dellinger et al., 1988). Therefore, the control of toxic organics emitted from incinerators during combustion of wastes is one of the major issues that further limit the widespread application of incineration (Huang and Buckens, 1985; Fångmark et al. 1993; Ghorishi and Altwicker, 1995).

Upset conditions occurring during the incineration generally are responsible to produce intense emissions, which can continue until the perturbation persists. These conditions are due to instantaneous alteration of the composition of the feed stream or modification of the combustion chamber parameters (temperature, oxygen availability) and are responsible of products of incomplete combustion (PICs) formation. In this study preliminary results of experiments carried out on laboratory scale are presented, where dried sewage sludge was subjected to thermal degradation. Puffs production was simulated with instantaneous injection of a SOM, constituting of 20 % of toluene, 25 % of chlorobenzene and 55 % of tetrachloroethene, before or after the thermal chamber.

EXPERIMENTAL

Tests on thermal degradation were carried out with a specific developed System for Thermal Diagnostic Studies (STDS). A detailed description of the system can be found elsewhere (Rubey and Grant, 1988; Mascolo et al., 1997). The system is contained in four integrated sub-assemblies: a control console, a thermal reaction compartment, a cryogenic trapping gas-chromatograph (GC) and a mass selective detector (MSD). In the console sub-assembly, the controls of gas flow rates, gas composition, pressures and residence time are located. The thermal reaction compartment is a modified GC equipped with a pyroprobe (SGE, Melbourne, Australia) as injector which is connected via a 3 mm id silicosteel tube (Restek, Bellefonte, PA, USA) to an interchangeable quartz reactor contained into a Lindbergh high temperature furnace. The exit of the quartz reactor is connected by another silicosteel tube, to a capillary GC column located in a 5890 series II GC that is interfaced, through a transfer line heated to 320 °C, with a 5971 MSD (both from Agilent Technologies, Palo Alto, CA, USA) equipped with an electron impact ion source. During the thermal experiments the GC analytical column (RTX-20, 60 m, 0.32 mm id from Restek) was kept at -60 °C in order to cryofocus the evolved organic compounds into a small band. After completion of the thermal experiment, the compounds trapped at the top of the GC column were separated by raising the oven temperature up to 320 °C at a rate of 15 °C/minute. Electron impact mass spectra, at an electron energy of 70 eV, were recorded by scanning the quadrupole from mass 35 to 550 Dalton at 1.4 scan/s. The background-subtracted mass spectra were matched against those of the NIST mass spectra library and interpreted on the basis of the observed fragmentation.

Dewatered digested sludge used in the experimental tests was sampled from “Bari – West” municipal wastewater treatment plant. It was dried at 105 °C for 7 hours, then grounded, sieved (100 µm) and its organic fraction composition was measured by a EA1108 elemental analyser (Fisons Instruments, Italy): its organic fraction consisted of 57 % C, 7 % H, 30 % O, 5 % N and 1 % S. The SOM mixture consisted of toluene (20%), chlorobenzene (25%), both from Carlo Erba (Milan, Italy), and tetrachloroethene (55%) from Supelco (Bellefonte, PA, USA). In the experimental tests puffs were simulated by injecting 0.1 µL of SOM in the pyroprobe or between it and the reactor. In Fig. 1 is sketched the experimental set-up used.

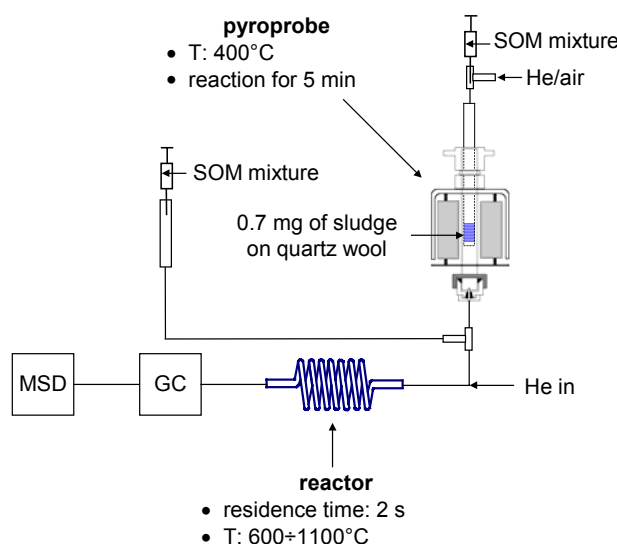


Fig. 1. STDS instrumental set-up for puff production during lab-scale sludge incineration.

In a typical STDS experiment, 0.7 mg of sludge sample was placed into the quartz capillary tube (1.5 mm i.d., 15 mm length from Vitro Dynamics Inc., Rochaway, NJ, USA) and held in

place by quartz wool at both ends. The quartz tube was inserted into the quartz probe which was, in turn, inserted into the pyroprobe, held at 400°C, for first thermal degradation step. 0.1 µL of SOM was instantaneously fed either into the pyroprobe or immediately before the reactor using a typical GC injector and conveyed by a helium flow of 6.1 mL/min.

The reaction in the pyroprobe was carried out under controlled oxygen rich atmosphere (160 % more of the stoichiometric oxygen theoretically required for the sludge combustion) by feeding a variable helium/air mixture (total flow=2.66 ml/min) through the quartz probe. The gaseous mixture from the pyroprobe was swept to the quartz reactor where it was subjected to higher temperatures (600-1100 °C) for a fixed residence time (2 s) which was obtained by properly setting the helium flow rate at the reactor inlet. The thermal reaction products were then transferred into the cryogenic GC chamber, where they were focused on a capillary GC column, separated by a temperature ramp, and identified by MSD.

RESULTS AND DISCUSSION

The results showed that puffs generated both in the pyroprobe and between it and the reactor give rise to the formation of several halogen-containing compounds, reported in Tab. 1, deriving from the incomplete combustion of the SOM mixture and from reaction between radicals generated from SOM decomposition and organic compounds present into the sludge. All these compounds are formed together many other non chlorine containing aliphatic and aromatic organics, not reported in Tab.1, deriving from the thermal decomposition of the organic fraction of the sludge. Results also evidenced that the two different puffs give rise to the formation of the same chlorine-containing compounds. However, their intensity was different being greater when puff is produced after the pyroprobe.

Tab. 1 Principal hazardous organic compounds arising from puff experiments of sludge incineration

Compound	Temperature (°C)					
	600	700	800	900	1000	1100
cianogen chloride		x	x			
CS ₂				x	x	x
etyne dichloro	x	x				
ethene dichloro		x				
benzene	x	x	x	x	x	x
thiofene		x	x	x	x	
ethene trichloro	x	x				
toluene	x	x	x			
tetrachloro ethene	x	x	x			
propene trichloro	x	x				
benzene chloro	x	x	x			
benzene etyl	x	x	x	x	x	
styrene	x	x	x	x	x	
phenol	x	x				
propanone chloro	x	x				

Compound	Temperature (°C)					
	600	700	800	900	1000	1100
benzene dichloro		x				
benzene chloro ethenyl		x				
naphthalene	x	x	x	x	x	x
chloro styrene	x	x				
Chlorophenol	x	x				
naphthalene metyl	x	x	x			
biphenil	x	x	x			
chloronaphthalene		x				
acenaphtylene		x	x			
dichloro naphthalene		x				
dibenzofurane		x				
phenanthrene		x				
naphthalene phenyl		x				
PAHs (high molecular weight)			x	x	x	x

From Fig. 2 it may also be seen that at temperature above 800 °C destruction of the SOM mixture is almost completed and that it is practically independent on the injection point. As far as toluene is concerned, abundance at 700 °C was greater than at 600 °C, thus confirming that this compound is formed as product of sludge incomplete combustion (Mascolo et al., 1997).

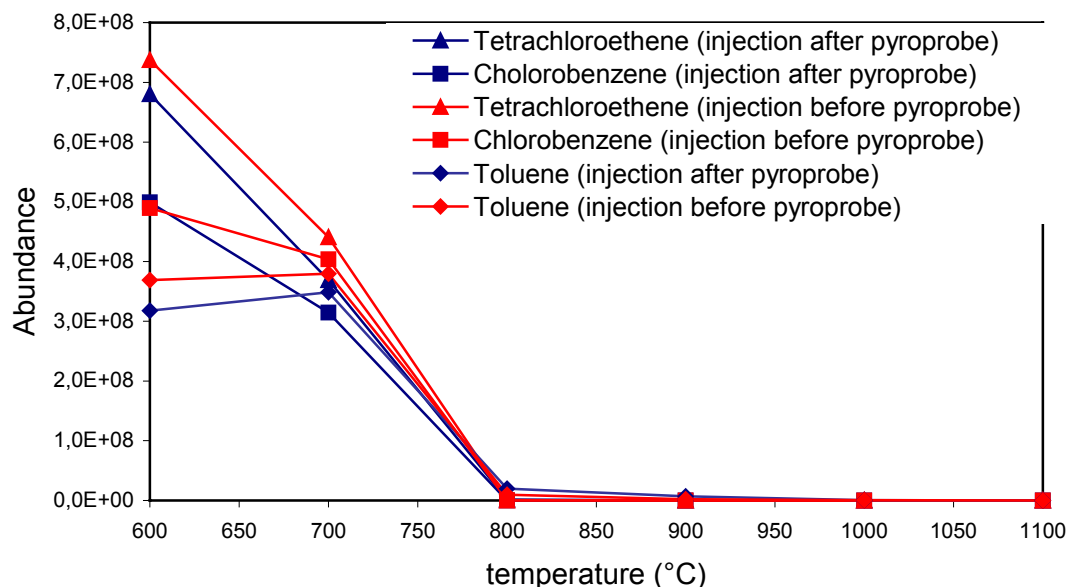


Fig. 2. Thermal degradation pattern of compounds included in the SOM.

CONCLUSIONS

Laboratory experiments carried out to simulate puff production during incineration of sewage sludge evidenced that:

- many halogen containing PICs are formed, being their abundance dependent on the SOM injection point;
- among the halogen containing PICs there are aliphatic as well as aromatic compounds;
- destruction of SOM components is practically independent on the SOM injection point;
- toluene is a typical PIC from sludge combustion and its abundance at 700 °C is higher than at 600 °C.

LITERATURE CITED

- Clement, R. E., Kagel, R. O. Ed., Emissions from combustion processes: origin, measurement, control, Lewis Publishers, Chelsea, MI, USA, 1990.
- Dellinger, B., Taylor, P. H., Lee, C. C., In Second Annual National Symposium on Incineration of Industrial Wastes, San Diego, CA, USA, 9-11 March, 1988.
- Fängmark, I., van Bavel, B., Marklund, S., Strömberg, B., Berge, N., Rappe, C. (1993). Influence of combustion parameters on the formation of polychlorinated dibenzo-p-dioxins, dibenzofurans, benzenes, biphenyls and polyaromatic hydrocarbons in a pilot incinerator. *Environ. Sci., Technol.*, **27**, 1602-1610.
- Ghorishi, S. B. and Altwicker, E. R. (1995). Formation of polychlorinated dioxins, furans benzenes and phenols in the post-combustion region of a heterogeneous combustor: effect of bed material and post-combustion temperature. *Environ. Sci. Technol.*, **29**, 1156-1162.
- Huang, H., Buckens, A. (1985). On the mechanism of dioxin formation in combustion processes. *Chemosphere*, **31**(9), 4099-4117.
- Mascolo G., Spinosa L., Lotito V., Mininni G., Bagnuolo G. Lab-scale evaluations on formation of products of incomplete combustion in hazardous waste incineration: influence of process variables. *Water Science Technology*, 1997, 36(11), 219-226.
- Rubey, W. A., Grant, R. A. (1988). Design aspects of a modular instrumentation system for thermal diagnostic studies. *Rev. Sci. Instrum.*, **59**(2), 265-269.

XXV Event of The Italian Section of the Combustion Institute
Rome 3-6 June 2002

Metal Enrichment in Solid Residues Produced in Sludge Incineration by a Fluidized-Bed Furnace

Marani D., Braguglia C.M. and Mininni G.

**CNR – Water Research Institute – via Reno, 1 – 00198 Rome (Italy)*

INTRODUCTION

The growing quantity of sewage sludge produced in urban wastewater treatment suggests to explore new disposal routes, because the conventional options (such as agricultural utilisation and landfill) are being progressively restricted due to the presence of organic and inorganic pollutants. To this purpose, sludge incineration is gaining increasing interest because of three main advantages: volume reduction up to 80-90%, destruction of organic micropollutants and pathogens, and energy recovery.

Sludge incineration may have an adverse environmental impact due to uncontrolled stack emissions of toxic metals. The metals, which may be present in significant concentration in sewage sludge, include: zinc, lead, copper, chromium, manganese, tin, nickel, and cadmium (Mininni and Santori, 1987). Several studies show that some metals become enriched in the fly ash with respect to their concentrations in the bottom ash and that the enrichment is enhanced in the finer fraction of the fly ash (Gerstle and Albrink, 1982; Lorber, 1986; Balogh, 1996).

Metal partitioning among the incineration residues may be affected by several operating parameters, including combustion temperature, excess air, feed composition (chlorine, sulphur, and water content). With the aim of a better understanding of the potential factors affecting metal speciation and partitioning in sludge incineration a series of pilot tests were carried out in a circulating fluidized-bed combustor. In this paper the behaviour of eight metals (Cd, Cr, Cu, Mn, Ni, Pb, Sn, and Zn) is discussed in the framework of a thermodynamic model of the combustion process.

EXPERIMENTAL

Sewage sludge incineration tests were carried out in a pilot plant located in Bari (Southern Italy), at the site of a large municipal wastewater-treatment plant. Plant capacity is about 250 kg/h of sewage sludge at 20% solids concentration. Equipment main characteristics and process scheme of the pilot-plant are reported elsewhere (Mininni et al., 2000). The pilot-plant tests were performed using dewatered sewage sludge produced in the nearby sewage treatment plant (total solids content about 15%; volatile solids about 65% of the total solids). Sludge was fed either as is or spiked with tetrachloroethylene or with a Surrogate Organic Mixture (SOM) that comprises 25% chlorobenzene, 55% tetrachloroethylene and 20% toluene. Methane was used as auxiliary fuel.

Table 1 summarises the operating conditions of the pilot tests considered here. The total chlorine content in the feed varied from a minimum of 0.03% (tests with sludge alone) to a maximum of 4.8% (tests with addition of SOM). All tests were performed with a large excess of air. Combustion temperatures spanned 821°C to 865°C.

Sampling and analytical procedures to measure the metal content of sludge and ash samples are described extensively elsewhere (Marani et al., 1998; Mininni et al., 2000).

Table 1. Operating conditions of the pilot plant tests

Test #	Feed				Excess Air (%)	T(°C)	Gas residence time (s)
	Sludge (kg/h)	Spike (Type)	Spike (kg/h)	Cl (%)			
1r	250	-	-	0.03	76	841	1.41
3r	250	-	-	0.03	66	851	1.52
4r	245	TCE	5	1.7	74	865	1.33
7r	230	TCE	12.5	4.4	104	821	1.16
13r	227	SOM	21.9	4.8	87	847	1.37
14r	227	SOM	21.9	4.8	115	836	0.93

TCE = Tetrachloroethylene SOM = Surrogate Organic Mixture

In the present study some filter-ash samples were split into several size fractions (sieves of 5, 10, 20, 30, 40 μm) before acid digestion and metal analysis. Major elements of the organic fraction of the feed sludge were analysed using a Carlo Erba elemental analyser (EA1108). Crystallographic analyses of cyclone ash were carried out by X-ray diffractometry using a Scintag model X1 with a Bragg-Bentano geometry, 30 kV $\text{CuK}\alpha$ radiation, in the range $2^\circ \leq 2\theta \leq 70^\circ$, with a scanning step of 0.05° and a count time of 3 seconds per step.

THERMODYNAMIC MODEL

The simple thermodynamic model considered in this work assumes homogeneity and equilibrium conditions in the combustion chamber. The model includes 14 elements (C, H, N, S, O, Cl, Cd, Cr, Cu, Mn, Ni, Pb, Sn, Zn), which represent the input streams of fuel, air, water, the organic fraction of the sludge, and the heavy metals of interest. The calculations were performed using HSC computer code and thermochemical database (Roine, 1997). Figure 1 shows the predicted metal volatilisation at atmospheric pressure and at 850°C as a function of chlorine percentage in the feed. At low chlorine concentration, only Cd and Pb are expected to volatilise in significant proportion. High concentrations of chlorine are expected to induce complete volatilisation of cadmium, copper, lead, and zinc. Nickel and manganese reach about 30% volatilisation at the highest chlorine concentration. On the other hand, chromium and tin volatilisation is never significant across the entire range of experimental conditions (maximum volatilisation percentage is 2 and 10^{-5} for Cr and Sn, respectively).

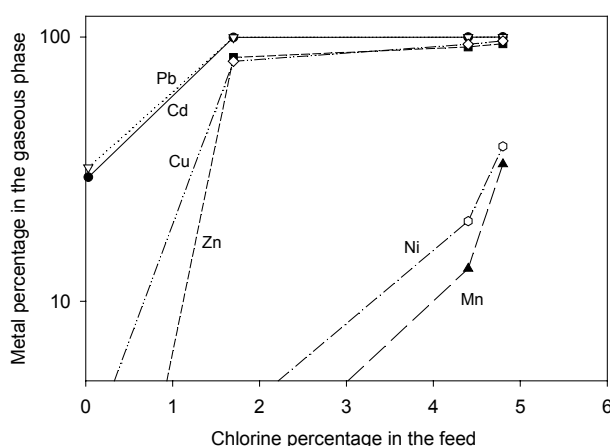


Figure 1. Model prediction of metal volatilisation in the combustion chamber

RESULTS AND DISCUSSION

Metal-concentration (ppm) ranges in the feed sludge were in the following decreasing order: Zn (2796-4213), Cr (240-650), Cu (262-599), Pb (104-137), Mn (75-98), Ni (36-53), Sn (36-

50), and Cd (14-23). The concentration of Ti, used in this work as a reference metal, was in the range 1086-1626 ppm.

Visual and microscopic observations of ash samples showed large amounts of carry-over sand in the cyclone ash. Metal dilution in the ash samples caused by the presence of carry-over sand was calculated using the ratio of titanium concentrations between ash samples and the relevant concentrations in the feed sludge on an inert basis. Titanium was selected as a tracer for sludge incineration residues because: 1) the Ti content of the sand used in the fluidized bed was negligible; 2) Ti is well known as a non-volatile element (Paoletti et al., 2000) and is expected to partition in equal concentrations among the several incineration solid residues. The Ti method for calculating the content of sand in cyclone ash samples showed a satisfactory agreement (within 10%) with the results of direct measurements using X-ray diffraction.

To quantify metal enrichment, an enrichment factor was defined as the ratio between the corrected metal concentration in filter ash and the corresponding concentration in the cyclone ash. Figure 2 shows that enrichment factors span from a minimum of 0.8 for Mn to a maximum of 6.3 for Pb. Due to sampling and analytical uncertainties, in our investigation only enrichment factors above 1.9 are deemed indicative of metal volatilisation in the combustion chamber. Figure 2 shows that Cd and Pb undergo significant enrichment in the filter ash. The enrichment increases with increasing chlorine content of the feed (the tests are plotted in order of increasing chlorine). In contrast, Cu, Cr, Mn, Ni, Sn, and Zn behave as refractory (non-volatile) elements under the experimental conditions used in this investigation. Cd and Pb enrichment in the finer fractions of the solid residues was confirmed by splitting some filter ash samples into fractions of different particle size. Figure 3 compares Cd, Pb, and Cr enrichment factors in different size fractions of filter ash. The enrichment factor of the inert chromium remains below the significance level. On the contrary, Cd and Pb enrichment factors increase with decreasing size, in accordance with the widely accepted hypothesis that metal enrichment is due to metal vaporisation in the combustion chamber and subsequent condensation on the fly-ash particles.

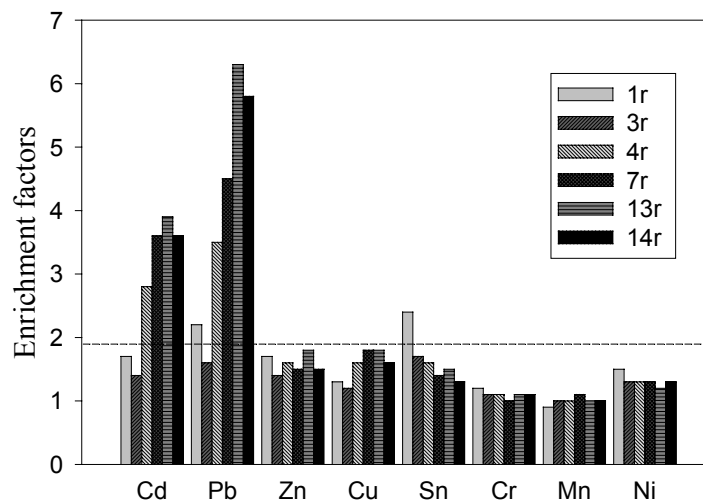


Figure 2. Metal enrichment factors (dashed line shows limit for significant enrichment)

The significant enrichment of Cd and Pb at high chlorine dosage (Fig. 2) is in agreement with the predicted metal volatilisation in the combustion chamber (Fig. 1). The experimental behaviour of Cr and Sn showing enrichment factors below the significance level is also in agreement with the thermodynamic model predicting negligible volatilisation.

By contrast, a clear discrepancy appears between model predictions and experimental behaviour of Cu, Zn, Ni, and Mn, which should form gaseous metal chloride species at high chlorine concentrations, with predicted metal volatilisation as high as 97, 94, 39, and 33%, respectively.

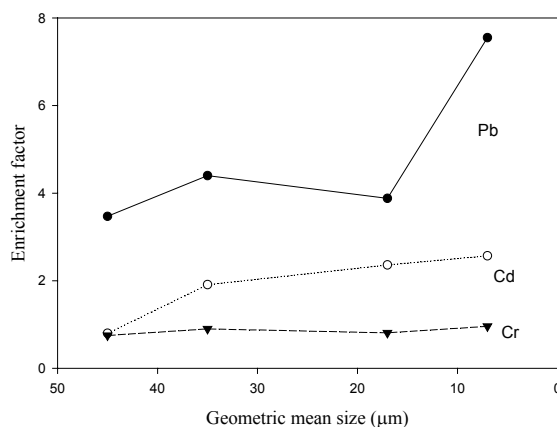


Figure 3. Effect of filter ash size on Cd, Cr, and Pb enrichment

These discrepancies are likely to arise from kinetic limitations due to the very short residence times in the pilot-plant tests (Table 1). Another potential explanation could be an oversimplification of the model chemical system, which neglects potential formation of stable silicates and aluminates, and competing reactions of major elements with chlorine.

CONCLUSIONS

Cd and Pb enrichment increased with increasing chlorine concentration in the incinerator feed and with decreasing particle size. In contrast, Cr, Cu, Mn, Ni, Sn, and Zn did not show significant enrichment, even at high chlorine dosage. The comparison between experimental behaviour and the predictions of a thermodynamic model shows satisfactory agreement for Cd and Pb, as well as for Cr and Sn. In contrast, discrepancies are found in comparing model predictions and experimental results of Cu, Zn, Mn, and Ni. Potential explanations of these discrepancies include kinetic limitations to vaporisation of metallic species and oversimplification of the model chemical system.

REFERENCES

- Balogh, R.: *Water Air and Soil Pollution*, **91**: 249-254 (1996).
- Gerstle, R.W. and Albrinck, D.N.: *Journal of the Air Pollution Control Association*, **32**: 1119-1123 (1982).
- Lorber, K.E.: *Waste Management & Research*, **4**: 3-13 (1986).
- Marani, D., Braguglia, C.M., Bemporad, E. and Mininni, G.: *Annali di Chimica. Journal of Analytical and Environmental Chemistry*, **88**: 887- 899 (1998).
- Mininni, G., Braguglia, C.M. and Marani, D.: *Water Science and Technology*, **41**(8): 61-76 (2000).
- Mininni, G. and Santori, M.: *Agriculture, Ecosystems and Environment*, **18**: 291-311 (1987).
- Paoletti, F., Seifert, H. and Vehlow, J.: *Proceedings of the Combustion Institute*, **23**: 35 (2000).
- Roine, A.: *Outokumpu HSC Chemistry for Windows. Chemical Reaction and Equilibrium Software with Extensive Thermochemical Database*. Outokumpu Research Oy, Pori, Finland, (1997).

The Influence of the Hydration Time on Spent Sorbents Reactivation for Fluidized-Bed Desulphurization Processes

¹Fabio Montagnaro, ¹Piero Salatino,
²Sabato Russo, ²Fabrizio Scala, ²Clelia Zucchini

¹Dipartimento di Ingegneria Chimica, Università degli Studi di Napoli Federico II

²Istituto di Ricerche sulla Combustione, Consiglio Nazionale delle Ricerche
Piazzale Vincenzo Tecchio, 80 - 80125 Napoli (ITALY)

INTRODUCTION

The fluidized-bed combustion technology is very effective in burning solid fuels ensuring also a low environmental impact. Among the main advantages of this technique, there is the possibility of removing SO₂ generated during coal combustion through *in situ* injection of calcium-based sorbents (e.g. limestone). Under typical FBC operating conditions (850°C and 1atm) sorbent particles are subject to rapid calcination in which CaCO₃ decomposes into porous CaO which in turn is able to capture SO₂ to give CaSO₄ (sulphation reaction). The onset of significant diffusional resistances as a low-porosity sulphated shell builds up around a largely unsulphated porous core (this mechanism is generally referred to as “core-shell” sulphation pattern [1]) makes the conversion of CaO into CaSO₄ far from its quantitative completion.

To enhance calcium utilization, different techniques have been proposed in the literature with the aim of reactivating spent sorbents. Among these techniques, a promising one is hydration of the spent sorbent by water or steam [1-4]. This process implies the conversion of the unreacted CaO into Ca(OH)₂. It has been hypothesized that, because of its larger molar volume, Ca(OH)₂ swells inside the particles leading to the formation of cracks and flaws. These would provide enhanced access to gaseous reactants upon further exposure of the reactivated sorbent to sulphur-containing atmospheres. Recently, Scala *et al.* [5] observed that hydration by water is able to promote a pronounced redistribution of sulphur inside the spent sorbent particle structure, which in turn enables further access to unconverted CaO. The authors proposed that a possible pathway of sulphur redistribution could be a solubilization/precipitation mechanism associated with the transport of sulphate ions in the aqueous phase inside the porous structure of the particle.

In this work spent limestone-based sorbents, generated in fluidized-bed desulphurization tests under simulated combustion conditions, were reactivated by means of a hydration process at 25°C (for times ranging from 1 to 24 h) and further reinjected in the fluidized-bed reactor. The final calcium conversion degrees of resulphated sorbent particles were related to the redistribution of sulphur inside the spent sorbent particle structure and to a “molecular cramming” phenomenon, both dependent on the hydration reaction time.

EXPERIMENTAL

Sulphation experiments were carried out at 850°C in a laboratory scale stainless steel atmospheric fluidized-bed reactor, 40mm ID and 1m height, electrically heated. A high-calcium (96.8% CaCO₃) Italian limestone (*Massicci*) was used as sulphur sorbent. The bed material, batchwise injected in the reactor and consisting of mixtures of sorbent (20g in the size range 0.425-0.6 mm) and silica sand (150g in the size range 0.85-1 mm), was fluidized at 0.8m/s for 180min by simulated combustion flue gases consisting of a mixture SO₂+O₂+N₂ with a SO₂ inlet concentration of 1800ppmv. Flue gases at the outlet of the reactor were rapidly cooled down and continuously sampled for SO₂ concentration measurement by a non dispersive infra red analyzer on line (precision and reproducibility ±50ppmv). SO₂ concentration data in flue gases were recorded (with a time step of 1s) in order to calculate the calcium conversion degree during the tests as a function of time.

Sulphated samples were reactivated by hydration in excess water at 25°C for curing times of 1, 2, 3, 6, 10 and 24 h. Batches of sulphated samples (10g) were blended with bidistilled water in sealed polyethylene bags and put in a thermostatic bath having an accuracy of ±0.001°C and operating with

water as thermal-carrier. At the end of curing times, hydrated samples were picked up from the bags, ground under acetone, dried with ether and stored in a desiccator. Furthermore they were characterized by means of X-Ray Diffraction (XRD) analysis, for the determination of the crystalline phases present after the hydration treatment. Batches of reactivated sorbents were resulphated in the fluidized-bed reactor under the same operating conditions as those of the first sulphation test. The sorbent mass in each batch (25.01g) was chosen in order to feed in the reactor the same number of moles of calcium available for the sulphation reaction as in the first sulphation test.

Polished cross sections of sulphated and hydrated sorbent particles, embedded in epoxy resin, were observed under a Scanning Electron Microscope (SEM) equipped with an Energy Dispersive X-ray (EDX) detector for the elemental mapping of sulphur and calcium. The characterization of the main sulphur distribution patterns was carried out with the aid of a novel Computer Controlled SEM (CCSEM) quantitative technique based on an automated statistical analysis of the elemental sulphur mappings of cross sections of sorbent particles [6]. The CCSEM technique was based on an algorithm able to generate probability density functions of pointwise sulphur contents which can be directly related to the sorbent particle sulphation pattern. In this context, bimodal distribution functions are indicative of a core-shell sulphation pattern, while an unimodal distribution function reveals an uniform sulphur distribution throughout the particles cross sections.

RESULTS AND DISCUSSION

Figure 1a) reports the calcium conversion degree as a function of time during the first sulphation test for *Massicci* limestone. It shows that the final value of the calcium conversion degree (X_F) is approximately 0.28. Inspection of Figure 2a), in which SEM micrographs (upper row) and EDX sulphur maps (lower row) of the polished cross sections of a sulphated multiparticle sample are reported, reveals that the core-shell sulphation pattern is dominant for the sulphated limestone. CCSEM analysis results are reported in Figure 3: the sulphated sample shows a bimodal distribution function in which two characteristic peaks can be detected, namely a peak in the low-sulphur-content zone (denoted as the “core zone”) and another in the high-sulphur-content zone (denoted as the “shell zone”). For this sample, values of core-zone area=35% and mean relative sulphur content=33% are calculated (for a thorough analysis on the sulphur distribution patterns occurring during sorbents sulphation refer to Montagnaro *et al.* [6]).

Figure 4 shows XRD analysis results for the sulphated sample hydrated for 1h, the samples

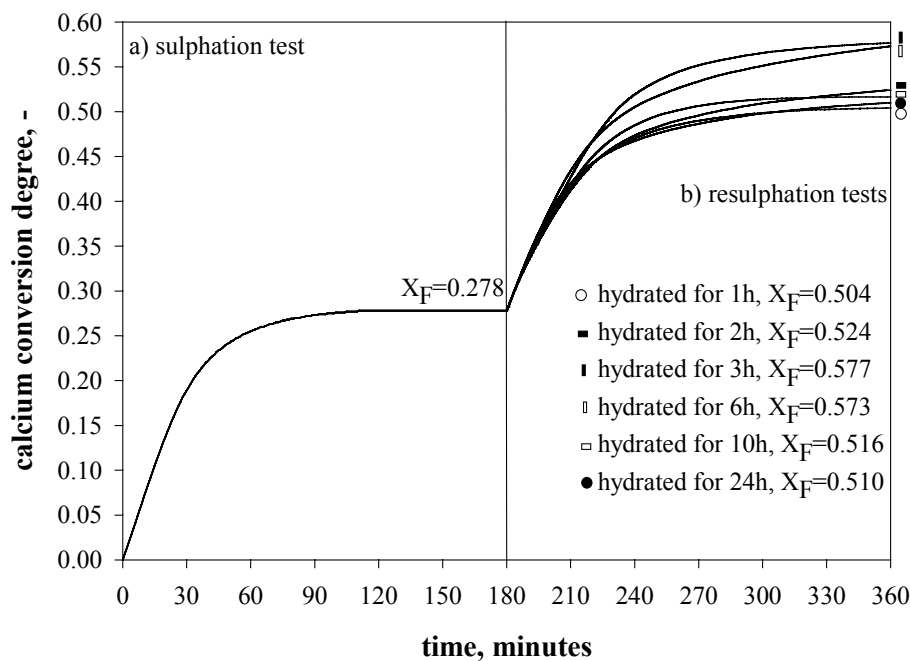


Fig. 1: Calcium conversion degrees as a function of time during sulphation and resulphation tests.

hydrated for different times showing similar results. Only portlandite was detected as hydration product, while anhydrite and quartz were revealed among the unconverted reactants. At all hydration times, the absence of lime shows that it is completely hydrated towards $\text{Ca}(\text{OH})_2$, whereas the presence of anhydrite is due to its scarce tendency to form gypsum-like phases ($\text{CaSO}_4 \cdot n\text{H}_2\text{O}$) in these conditions. The presence of quartz is instead

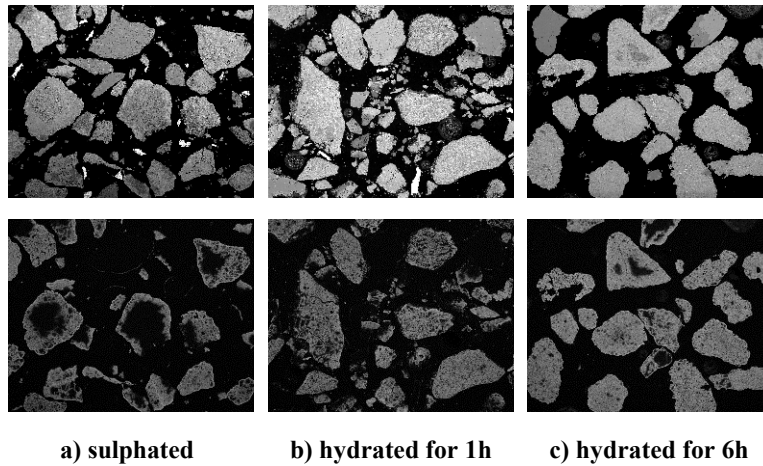


Fig. 2: SEM micrographs (upper row) and EDX sulphur maps (lower row) of cross sections of multiparticle sulphated and hydrated samples.

related to some unavoidable sand impurities in the sample. Therefore XRD data put in evidence that the chemical process of hydration is complete after 1h with the total conversion of CaO into Ca(OH)_2 . Figures 2b) and 2c) report the SEM-EDX analyses on the samples hydrated for 1 and 6 h, showing a pronounced redistribution of sulphur inside the spent sorbent particle structure. The influence of the hydration time on sulphur redistribution can be observed in Figure 3, in which CCSEM analysis results for the two hydrated samples are reported. These data show that the higher the hydration time, between 1 and 6 h, the weaker the bimodal distribution function (core-zone area=25% and mean relative sulphur content=40% for the sample hydrated for 1h; core-zone area=6% and mean relative sulphur content=50% for the sample hydrated for 6h). This is clearly indicative that the sulphur redistribution process is enhanced when the hydration time is higher in the range 1-6 h. Moreover, it is worth noting that no further redistribution was found when applying the CCSEM technique to samples hydrated at times longer than 6h, thus suggesting that the physical process of sulphur redistribution *via* aqueous phase is complete after 6h. On the other hand, hydrated sorbent particles in the samples appeared more “crammed” (*i.e.* more compacted) as the hydration time was increased in the whole range 1-24 h.

Figure 1b) reports the calcium conversion degree as a function of time during resulphation tests of sorbent batches hydrated-reactivated at 1, 2, 3, 6, 10 and 24 h. As a general result, water reactivation of the spent sorbent was highly effective in promoting further sulphur uptake upon resulphation. It can be also observed that the trend of X_F is non-monotonic with the reactivation time, being $X_F=0.504$ for the sorbent hydrated for 1h, reaching a maximum ($X_F \cong 0.57-0.58$) for sorbents hydrated at 3 and 6 h, and then decreasing up to $X_F=0.510$ for the sorbent hydrated at 24h. This trend could be explained taking into account a competition between the sulphur redistribution and the particles cramming phenomena, both influenced by the hydration time.

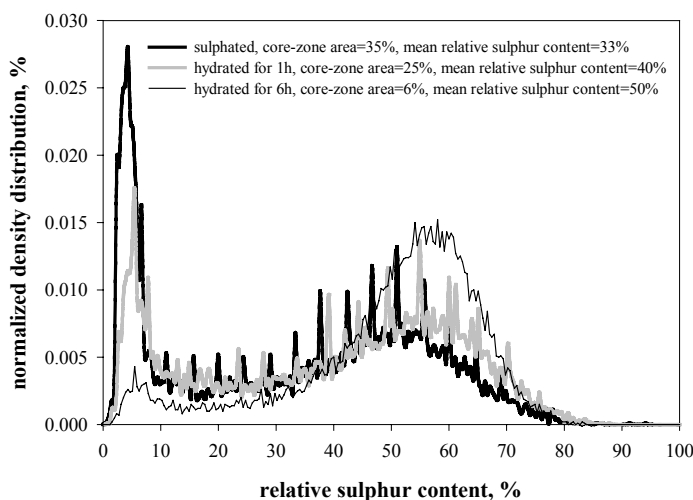


Fig. 3: CCSEM analysis results for multiparticle sulphated and hydrated samples.

In fact, the sulphur redistribution process is greatly enhanced by the hydration time in the range 1-6 h, thus resulting into a positive effect of the reactivation time on the sulphur capture ability of the reactivated samples. On the other hand, cramming phenomena could make hydrated-reactivated sorbent particles less prone to resulphation by partially hindering available calcium to the contact with the flue gases when reinjected in the fluidized-bed reactor. As the effect of sulphur redistribution is complete after 6h while the observed cramming phenomena are enhanced up to 24h, this could

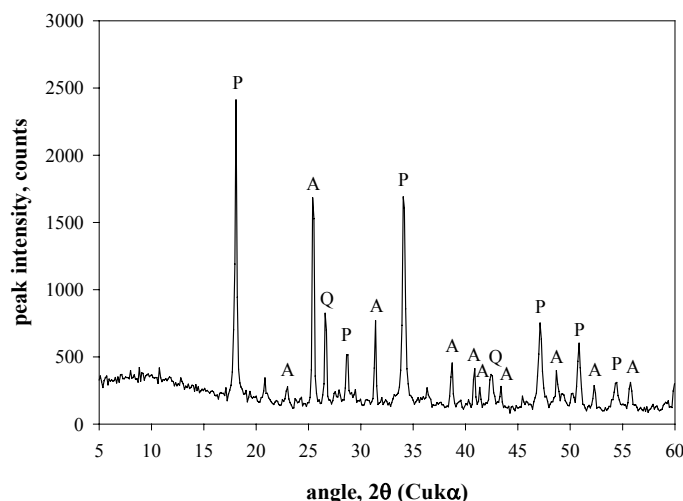


Fig. 4: XRD analysis results for the sulphated sample hydrated for 1h. P=portlandite ($\text{Ca}(\text{OH})_2$); A=anhydrite (CaSO_4); Q=quartz (SiO_2).

result into a negative effect of the reactivation time (in the range 6-24 h) on the sulphur uptake during resulphation.

These results seem to indicate that, under the operating conditions employed in this study, it is possible to locate an optimum range of hydration times as regards the sulphur capture ability of the reactivated sorbent. These data deserve however further investigations to assess the effect of other variables such as the type of sorbent and the hydration temperature.

CONCLUSIONS

A spent limestone-based sorbent, generated by fluidized-bed desulphurization of simulated flue combustion gases, was reactivated by means of a hydration process at room temperature and further reinjected in the fluidized-bed reactor. For the spent sorbent, constituted of CaSO_4 and unconverted CaO , the calcium conversion degree did not exceed ~28%. Sulphated particles were hydrated for times ranging from 1 to 24 hours, and XRD results revealed a complete hydration of CaO at all hydration times. With the aid of a novel CCSEM technique it was pointed out that hydration promoted a pronounced redistribution of sulphur inside the spent sorbent particle structure, thus enabling further access to unconverted calcium oxide. The overall calcium conversion degrees of resulphated sorbent particles ranged from ~50% to ~58%, thus almost doubling the first-stage value. A non-monotonic influence of the hydration time on the resulphation ability was observed and attributed to a competition between sulphur redistribution and a “molecular cramming” phenomenon.

REFERENCES

1. Shearer, J.A., Smith, G.W., Moulton, D.S., Smyk, E.B., Myles, K.M., Swift, W.M., Johnson, I.: *Proceedings of the 6th International Conference on Fluidized Bed Combustion*, p. 1015 (1980).
2. Couturier, M.F., Marquis, D.L., Steward, F.R., Volmerange, Y.: *The Canadian Journal of Chemical Engineering*, **72**:91 (1994).
3. Laursen, K., Duo, W., Grace, J.R., Lim, J.: *Fuel*, **79**:153 (2000).
4. Laursen, K., Duo, W., Grace, J.R., Lim, C.J.: *Fuel*, **80**:1293 (2001).
5. Scala, F., Montagnaro, F., Salatino, P.: *Industrial & Engineering Chemistry Research*, **40**:2495 (2001).
6. Montagnaro, F., Scala, F., Salatino, P.: *Proceedings of the 2nd Mediterranean Combustion Symposium*, **2**:827 (2002).

Selective depolymerization of Polyethylene

D. Pedol, P. Canu

*Dipartimento di Principi e Impianti di Ingegneria Chimica
Università di Padova, Padua - ITALY*

INTRODUCTION

Polymer pyrolysis is a process that can be used to effectively recover chemicals from recycled plastics. Products nature and quantity for each polymer strongly depend upon the process conditions and specifically temperature and residence time. So far literature studies (Milne *et al.* 1996) demonstrated the possibility to vary the amount and length of olefin and alkanes by changes of operating conditions. The possibility to maximize the production of olefins, much more interesting for their intrinsic reactivity, by means of short contact time has been suggested by the Berruti's group, that indicated the existence of an optimal reaction time for HD-PE. Ideally, a significant production of monomer from the corresponding polymer would also be the best solution, since it would mean a perfect closure of the life-cycle of the material. In this contribution the search for this goal has been applied to HD-PE, one of the polymer most widely used, with quite interesting results.

EXPERIMENTAL APPARATUS

Polymer pyrolysis has been carried out in an entrained flow reactor (EFR) where the solids are fed in the form of powders through a heated tubular reactor. Unconverted polymer, solid products, tars and gases are collected after quenching and analyzed. Gas analysis uses a GC with FI and TC detectors. Previous experience with EFR in the study of cellulose pyrolysis has been completely reconsidered because of the specific nature of polymers. During heating, polymers soften and melt before decomposing and then tend to stick to the internal reactor walls, so that the actual residence time of the material in the reactor runs out of control, preventing any systematic investigation of the de-polymerization kinetics. A novel EFR has been designed and characterized where the suspension of powder polymers in N₂ is fed internally to a second, coaxial flux of N₂. The flow rate of the resulting jet must be tuned to the external flow so that it can remain sufficiently coherent up to the end of the reactor, minimizing solids deposition on the internal reactor walls. A detailed experimental study, with CFD validation, has been carried out by using a suitable tracer, resulting in flow maps that allow to design experiments at different flow rate, still preserving the structure of the jet. The feeding system also requires some attention, since a perfectly stable flow rate of solids at a small flow rate is crucial for the kinetics studies and quite difficult to achieve. A properly designed screw feeder fitted the scope.

Design of Experiments

Any EFR is characterized by a longitudinal temperature profile and possibly also a radial one. Neglecting the second, still the presence of a variable temperature along the solids path has several relevant consequences. The most obvious is that a single experiment cannot be associated to a single temperature, but only to a given profile. With the purpose of comparing the effect of temperature on the pyrolysis, results must be reported in terms of a some sort of average temperature, further discussed below. The second is that the density of the flowing gas is varying significantly, resulting in dramatic variations of velocity through the reactor, affecting the total residence time and the heating history of the solids flowing through. The

connection between temperature and velocity can be simply formulated as

$$v_p(z); v_g(z) = v_{IN} T_g(z) / T_{IN} \quad (1)$$

which states that the particles velocity along the axial coordinate z is assumed to equal the gas velocity because of the small size, the latter being directly proportional to the local (ideal) gas temperature. Subscript IN indicates inlet conditions. Gas temperature can be independently measured without solids flow, the pyrolysis of which negligibly affects the gas temperature, and $T_g(z)$ profiles for different oven temperatures can be stored in the form of spline interpolation coefficients for further calculations. An average temperature can be defined in different ways. The most intuitive is a simple spatial average

$$\bar{T}_z = \frac{\int_{z_0}^{z_1} T_g(z) dz}{z_1 - z_0} \quad (2)$$

where z_1 and z_0 are the coordinates between which the temperature is high enough to be significant. Threshold has been set to 300°C as a minimum temperature for some pyrolysis to take place. Actually, the minimum temperature where degradation begins depends on the heating rate, as well known in the field of fast pyrolysis. While 300°C can be the onset of some weight loss in TGA experiments with PE, in our case no transformation can be observed at such a low temperature. However, the temperature threshold for the average temperature calculation is a matter of convention. It serves the scope of distinguishing between geometrical length of the oven and actual temperature profile, so that only the effective part of the length is considered. It must be recalled that the convention on the minimum threshold for T (here 300°C) influences the calculation of the average, so that the values used for data representation and discussion is valid only within this investigation and data analysis, and it can be compared with literature results only qualitatively. But we definitely question the significance of literature data of solids fast pyrolysis uniquely associated to a given temperature, without any discussion of the temperature history, that cannot be a step function by any mean. A more appropriate averaging for T should be:

$$\bar{T}_\theta = \frac{\int_{\theta_1}^{\theta_2} T_g(t) dt}{\theta_2 - \theta_1} \quad (3)$$

where θ is the residence time. Here the temperature is averaged on the base of the time spent by the particle at that specific T value, which can be calculated through the local value of the particle velocity, $v(z)$, being $dt=dz/v(z)$. Again, the two values of residence time correspond to the points limiting the region where T is higher than a minimum threshold. Values calculated through eq. (3) are those reported with the results in the following.

The average temperature can be determined *a posteriori*, from the longitudinal temperature profiles, which changes according to the gas flow rate and oven temperature set. From several measured temperature profiles, an algorithm was developed in order to design new experimental runs with predetermined average temperature and residence time.

RESULTS AND DISCUSSION

Experimental measurements have been carried out using virgin HD-PE in the form of powder, with an average particle size of 95 μm , a weight average molecular weight $M_w = 80000$, and a density of 0.951. A suspension of polymer particle in N_2 is continuously created and fed to the reactor at a flow rate of 0.05 g/min (average, the actual value is determined at the end of each run) in 0.4 NL/min N_2 . The suspension enter the reactor through a central pipe, surrounded by a second gas stream used to stabilize the inner jet, with a variable flow rate, between 4 and 6 NL/min, in order to change the residence time. Reaction course is characterized through

measurements of polymer conversion and gas analysis.

In the following, results are briefly presented in terms of polymer conversion, monomer yields and selectivity. The conversion is determined as the weight difference between the polymer fed and that collected after the reactor. Such a difference involves several products, predominantly gas but also charring deposits along the reactor, particularly in the quench section. Gas yields are calculated as the amount of specific gas in the outlet stream, while the selectivity is meant to be the same amount divided by the converted polymer.

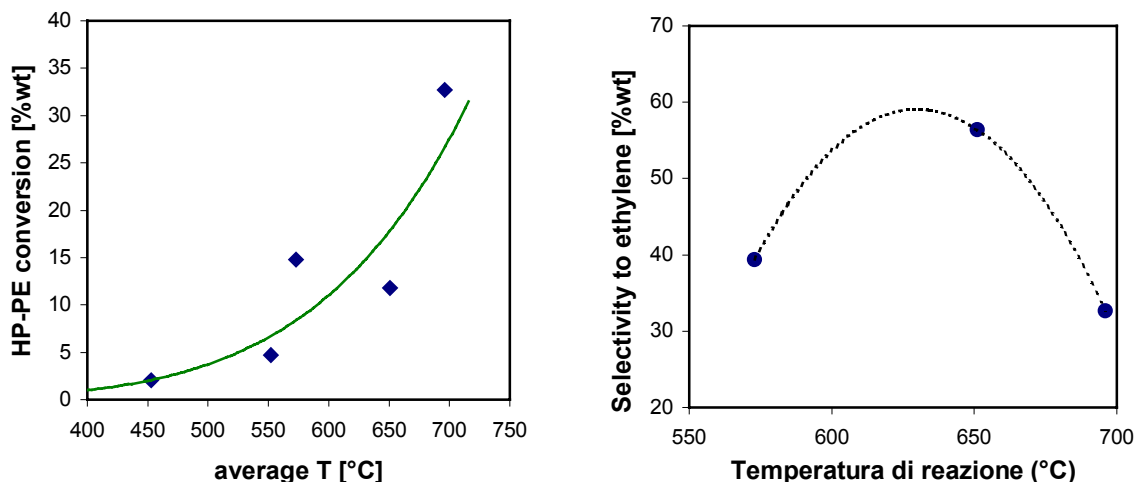


Fig. 1 Effect of temperature on the HD-PE conversion and selectivity to the monomer, at 750 ms residence time.

The role of temperature on the polymer conversion and selectivity to the monomer is depicted in Fig. 1. The residence time has been kept close to a value of 750 ms by varying the oven temperature and secondary N₂ flow rate. Figure clearly shows that the conversion increases with temperature while the amount of ethylene apparently goes through a maximum. The last result must be further confirmed with additional tests, but it is confirmed for propylene also, while the amount of methane increases with temperature. Such a result agree with the hypothesis that olefins are intermediates in the process of degradation of the polymer down to alkanes of progressively lower molecular weight.

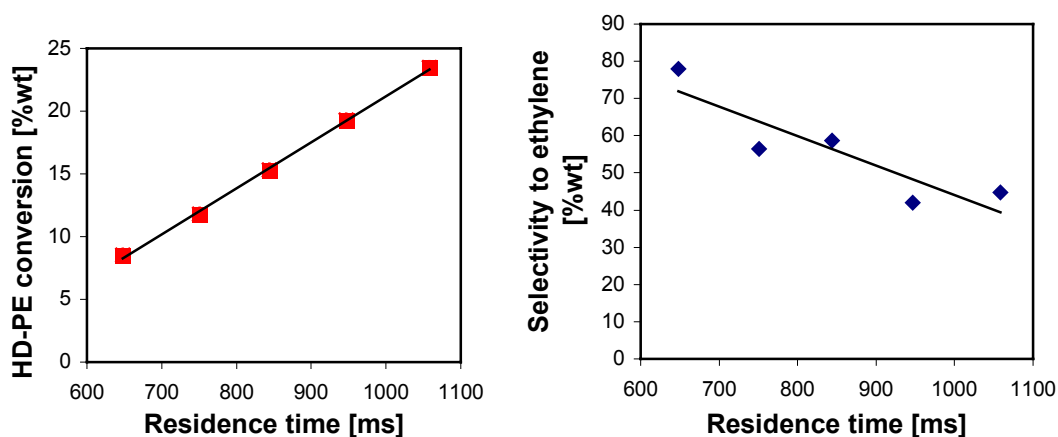


Fig. 2 Effect of residence time on the HD-PE conversion and selectivity to the monomer, at 650 C.

It is particularly important to investigate the role of residence time, in order to provide evidences of such an hypothesis. Some results are reported in Fig. 2. The polymer conversion

clearly decreases with residence time, as expected, while the relative amount of ethylene produced per unit HD-PE converted increases. We believe that this is a clear indication that the olefins, and specifically the monomer, tend to build up in the reactor quite rapidly, but the reaction must be stopped by quenching to keep significant amount of these intermediates before they are further reduced to alkanes. The hypothesis is partially confirmed by the distribution of gaseous products in terms of selectivity reported in Fig. 3.

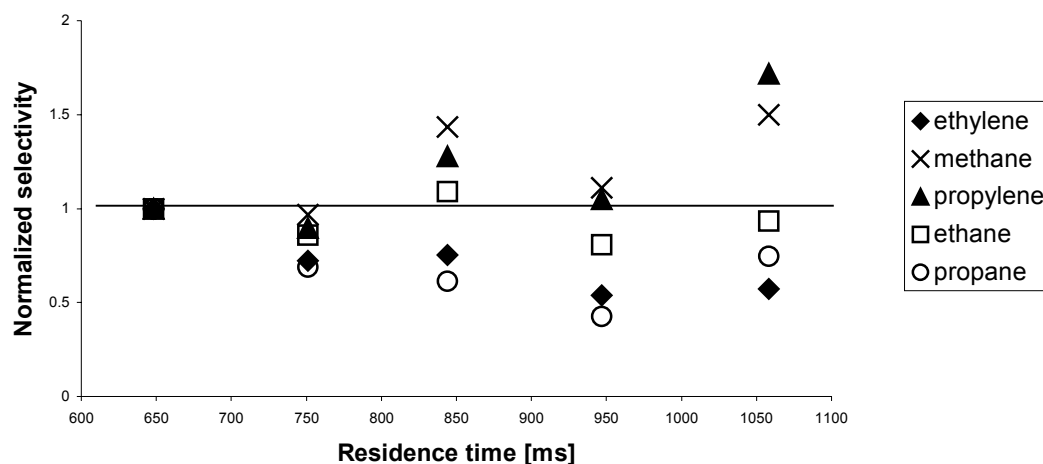


Fig. 3 Effect of residence time on the normalized selectivity to several, at 650 C.

Here the selectivity of all the measured species has been scaled by dividing each value by the one at the lower residence time, for the purpose of comparing the behavior of all of them. It can be seen from Fig. 3 that a longer residence time causes a decrease of selectivity to ethylene, as already shown in Fig. 2, but also propane decreases, while methane and propylene show some increase, and ethane is almost constant. Among these data, only methane is significantly consistent with the interpretation above, based on the ethylene decrease with higher residence time. A larger amount of propylene at longer residence time. We can conclude that the apparatus developed and used in this work is a valuable tool to investigate the mechanism of polymer degradation by pyrolysis, notwithstanding the opposite conclusion of other research groups (Westerhout *et al.* 1996). The EFR also allows to characterize the role of the gas phase reaction by feeding some product or some intermediate together with the solids or simply alone, aiming to obtain sufficient experimental data to validate, discuss and possibly extend kinetic models already suggested (Faravelli *et al.*, 2001).

REFERENCES

- Faravelli T., G. Bozzano, C. Scassa, M. Perego, S. Fabini, E. Ranzi, M. Dente "Gas product distribution from polyethylene pyrolysis" *Journal of Analytical and Applied Pyrolysis* 52 (1999) 87–103
- Milne, B.J., Behie, L.A., Berruti, F. "Recycling of waste plastics by ultrapyrolysis using an internally circulating fluidized bed reactor" *J. Analytical and Applied Pyrolysis*, 51(1) 1999, 157-166
- Westerhout R. W. J. , J. A. M. Kuipers and W. P. M. Van Swaaij "Development, modelling and evaluation of a (laminar) entrained flow reactor for the determination of the pyrolysis kinetics of polymers" *Chem. Engng Sci.*, 51 (10) 1996, 2221-2230

XXV Event of The Italian Section of the Combustion Institute
Rome 3-6 June 2002

Fuels And Combustible Wastes

Giuseppe Mininni* and Riccardo Chirone**

**CNR – Istituto di Ricerca sulle Acque – via Reno, 1 00198 Roma*

***CNR – Istituto di Ricerche sulla Combustione – Piazzale V. Tecchio 80125 Napoli*

ABSTRACT

The paper is an overview of Italian legislation concerning the use of combustibles in industrial plants. In particular gaseous emission limits are compared for fuel combustion and for incineration and co-incineration plants.

INTRODUCTION

The use of fuels in industry is regulated by a number of different laws and governmental decrees, which fix limits for solids and gaseous emissions and restrict their utilization for specific applications. The interest for the utilization of combustible wastes grows as interest in the last years, the reason for that being the disposal and global warming issues and the possible energy recovery from the high quantities of wastes. However, the management of a waste generally requires higher level of precaution due to possible environmental contamination. Accordingly gaseous emission limits are more severe than those valid for fuels. Moreover in waste incineration attention must be given to the presence in the emissions of a wide number of possible contaminants (heavy metals, organic micropollutants, specific compounds in the wastes) that are not considered when a traditional fuel is utilized.

The paper highlights some specific problems of Italian laws and underlines the consequent necessity for a better characterization of combustibles materials.

FUEL COMBUSTION

The use of fuels and their characteristics is regulated by three Italian decrees: DPCM 2 October 1995, DPCM 7 September 2001 and DPCM 12 March 2002 (Table 1). According to data reported in the table fuel oil must have sulphur content lower than 1 %, fixed carbon lower than 15 % and ash content lower than 0.15%. Higher values are allowed for particular uses and applications. This is the case of gasification of heavy hydrocarbons derived from oil refining where higher sulphur content is allowed, but more severe limits in dust, NO₂, SO₂ and CO are imposed. Examples of this are the Saras refinery in Sardinia and Api refinery in Marche. A specific law, just approved from the Italian Parliament, regulates the use of pet-coke in combustion plants. Maximum sulphur content of this fuel used in plants with single burner power higher than 50 MW is fixed at 3%. No limits of sulphur and other pollutants are imposed for the use of pet-coke if used where it is produced. In Italy, pet-coke is produced in Sicily at the Gela refinery. Sulphur content of the fuel is limited to 6% if used in plants where sulphur is fixed in the final product for at least 60% (cement plant and lime production plants).

WASTE COMBUSTION AND INCINERATION

According to the European Directive 91/156 on wastes: “waste shall mean any substance or object in the categories set out in Annex I which the holder discards or intend or is required to

discard". Annex I, among others, includes: production or consumption residues, off-specification products, residues of industrial process (e.g. slags, still bottoms, etc.), residues from raw materials extraction and processing (e.g. mining residues, oil field slops, etc.). This means that the production system determines the qualification of a substance as product or as a waste. A substance is a product whenever is produced with specific characteristics that make possible its use in the same productive cycle. On the contrary, if the process produces a product where contaminants are present and not specifically regulated, such a substance is a waste. In other words when any substance is an undesirable by-product of the production activity this is certainly a waste. Only when the producer is able to demonstrate that the process is conducted precisely to produce a target substance, responding to definite standards, that does not need any further treatment to be used or commercialised, then this substance is really a product.

Application of the above concepts to combustible wastes implies many consequences from the administrative and practical point of view. Directive 2000/76 regulates the use of combustible wastes in incineration or co-incineration processes. In fact, incineration plants are "*any stationary or mobile technical unit and equipment dedicated to thermal treatment of wastes with or without recovery of the combustion heat generated*", while co-incineration plants are "*any stationary or mobile plant whose main purpose is the generation of energy or production of material products which uses wastes as a regular or additional fuel*".

In this perspective there are many examples of activities that should be classified as co-incineration. This is the case of the use of: i.) petroleum refinery residues in power plants; ii.) exhaust oil, dried sludge, RDF in cement and lime factories; iii.) off-specification products in combustion equipments. However there are wastes excluded from the application of Directive 2000/76: vegetable waste from agriculture and forestry; vegetable waste from the food processing industry, if the heat generated is recovered; fibrous vegetable waste from virgin pulp production and from production of paper from pulp, if it is co-incinerated at the place of production and the heat generated is recovered; wood waste with the exception of that containing halogenated organic compound or heavy metals as a result of treatment with wood-preservatives or coating, and which includes in particular such wood waste originating from construction and demolition waste; cork waste; radioactive waste; animal carcasses as regulated by Directive 90/667/EEC without prejudice to its future amendments; waste resulting from the exploration for, and the exploitation of, oil and gas resources from off-shore installations and incinerated on board the installation.

As regards co-incineration plant, it shall be designed, built and operated in such a way that the gas resulting is raised to a temperature of 850 °C for two seconds. Moreover the temperature has to be raised to 1.100 °C when hazardous wastes with a content of more than 1 % of halogenated organic substances, expressed as chlorine, are co-incinerated. An automatic system should prevent feeding of waste until the temperature at start up has been reached to 850 or 1.100 °C, whenever the above temperatures are not maintained and whenever the continuous measurements show that any emission limit value is exceeded due to disturbances or failures of the purification devices.

With reference to incineration plants, they shall be operated to achieve slag and bottom ashes TOC content less than 3 % or their loss on ignition must be less than 5 % of the dry weight of the material. Continuous monitoring of NO_x, CO, total particulate, TOC, HCl, HF and SO₂ is generally required, as well as continuous measurements of temperature near the inner wall (or another representative point of the combustion chamber), oxygen concentration, pressure, temperature and water vapour content of the exhaust gas. Two measurements per year are generally requested of heavy metals, dioxins and furans (4 measurements for the first year of operation).

Limit values for the gaseous emissions of the Directive 2000/76 and the Italian Guidelines of the gaseous emissions relevant to combustion plants and refineries are compared in Table 2. Analysis of the data shows that limits are significantly different and in some cases there are orders of magnitude differences. This is the case of SO₂, gaseous and vapour organic substances and dioxins and furans.

CONCLUSIONS

Classification of a substance as a fuel or a combustible waste is crucial as regards the different emission limits to be applied. From a practical point, incineration and co-incineration plants is required to be operated under specified conditions of temperature, oxygen concentration and residence time. Continuous monitoring of the emissions is also a prerequisite to be respected in the case of incineration.

Italian legislation of combustion plants is not as strict as for incinerators. This is the result of considering that pollutants causing environmental concern are not present in the fuel. In this perspective precise characterization of the combustible material, as far as chemical and physical/chemical properties are concerned, is certainly needed to be sure that utilisation of such substance as a fuel will not cause any environmental pollution and is not an alternatively way to bypass normative regarding wastes incineration.

Such conditions are generally considered in the Italian legislation. However there are concerns regarding the combustion of pet-coke at the place of production, because in such cases there are no fixed limits on the presence of sulphur, nickel, vanadium, PCB and PCT. Moreover, gaseous emissions are regulated as for industry activities, with limits clearly much less stringent than the corresponding ones for incineration and co-incineration plants. The same concerns do not apply to the case of gasification of heavy hydrocarbons derived from oil refining which is indicated as the best available technique for energy recovery from refinery residues in a document of the European Commission (2001).

References: European Commission Directorate General JRC Institute for Prospective Technological Studies (2001): "Integrated Pollution Prevention and Control (IPPC) Reference Document on Best Available Techniques for Mineral Oil and Gas Refineries" 516 pp.

Table 1 Characteristics of fuel oils and heavy hydrocarbons

Parameter	Combustion plants		On site use where fuel is produced		Plants where S is fixed in the final product for at least 60 %
	<50MW	>50MW		Heavy hydrocarbons for gasification	
Calorific value, kJ/kg				>35000 kJ/kg	
Viscosity at 50 °C, mm ² /s	≤91	>91	>91		>91
Sulphur, %	≤1	≤3	≤3	≤10	≤4
Fixed carbon, %	≤15	≤18	≤18		≤18
Ash content, %	≤0.15	≤0.20	≤0.20	≤1	≤0.20
Water, %		≤1.5	≤1.5		≤1.5
Sediments, % in volume		≤0.5	≤0.5		≤0.5
Ni+V, ppm	≤180	≤180-230	≤180-230		≤180-230
PCB/PCT	Absent	Absent	Absent		Absent

Table 2. Comparison of limit at the gaseous emissions according to the Directive 2000/76 and the Italian Guidelines (12/7/1990) relevant to combustion plants and refineries

Parameter	Directive 2000/76 on waste incineration				Italian Guidelines 12/7/1990 on industrial plants
	Daily average values	Half-hourly average values		Ten minutes average value	mg/m ³
		Absolute value	97° percentile over the year		
	mg/m ³	mg/m ³	mg/m ³	mg/m ³	mg/m ³
Total dust	10	30	10		50 -comb. plants of solid fuels, 5-50 MW 50 -comb. plants, ≥ 50 MW 80 -cumulative emission from refineries 100 -comb. plants of liquid fuels, 5-50 MW 100-150 -comb. plants of solid and liquid fuels, ≤5 MW
Gaseous and vaporous organic substance, total organic carbon	10	20	10		50 -comb. plants of solid fuels 300 -comb. plants, ≥ 50 MW 300 -cumulative emission from refineries
Hydrogen chloride (HCl)	10	60	10		30 -cumulative emission from refineries 100 -comb. plants, ≥ 50 MW
Hydrogen fluoride (HF)	1	4	2		
Sulphur dioxide (SO₂)	50	200	20		400 -comb. plants, ≥ 500 MW 600 -combustion FB of solid fuels, <50 MW 1.700 -comb. plants of liquid fuels, <50 MW and of any fuel, 50 - 500 MW 1.700 -cumulative emission from refineries 2.000 -other comb. plants of solid fuels, <50 MW
NO and NO₂, expressed as NO₂ (incineration plants - nominal capacity exceeding 6 t/hr or new incineration plants)	200*	400*	200*		200 -comb. plants, ≥500 MW 500 -comb. plants of liquid fuels, <50 MW 500 -cumulative emission from refineries 650 -comb. plants of solid fuels, <50 MW and of any fuel, 50 - 500 MW
NO and NO₂, expressed as NO₂ (incineration plants, nominal capacity ≤6 t/hr)	400*				
Carbon monoxide (CO)	50 (97° percentile)	100		150 (95° percentile)	250 -comb. plants, ≥50 MW 250 -cumulative emission from refineries
Heavy metals	Sampling period of 0,5-8 h				
Cadmium and compounds, as Cd	Total 0,1**				As, Cr, Co, Ni: 1 mg/m ³ -comb. plants, ≥ 50 MW and cumulative emission from refineries Cd, Hg, Tl: 0,2 mg/m ³ -comb. plants, ≥ 50 MW Cd, Hg, Tl: 0,3 mg/m ³ -cumulative emission from refineries Se, Te: 2 mg/m ³ -comb. plants, ≥ 50 MW Se, Te: 3 mg/m ³ -cumulative emission from refineries Sb, Cr, Mn, Pb, Cu, Sn, V: 10 mg/m ³ -comb. plants, ≥50 MW and cumulative emission from refineries
Thallium and compounds, as Tl					
Mercury and compounds, as Hg	0,1**				
Antimony and compounds, as Sb	Total 1**				
Arsenic and compounds, as As					
Lead and compounds, as Pb					
Chromium and compounds, as Cr					
Cobalt and compounds, as Co					
Copper and compounds, as Cu					
Manganese and compounds, as Mn					
Nickel and compounds, as Ni					
Vanadium and compounds, as V					
Organic micropollutants	Sampling period of 6-8 h, (ng TE/m ³)				
Dioxins and furans	0,1				10.000 total ng/m ³ -comb. plants, ≥50 MW and cumulative emission from refineries

* The limits of NO_x do not apply to plants only incinerating hazardous waste until 1 January 2007

** Including gaseous and vapour forms of the relevant heavy metal emissions as well as their compounds

Characterization of biomass residue after devolatilization in different operative conditions

E. Biagini, L. Tognotti

Dipartimento di Ingegneria Chimica – Università di Pisa - ITALY

INTRODUCTION

Biomass devolatilization process is strongly influenced by operative conditions used. Materials containing high amounts of volatile matter should be characterized from different points of view in order to describe their behaviour in a sufficiently wide range of operative conditions. This allows the feasibility of a practical use of such materials to be evaluated. Furthermore, parameters depending on the actual thermal history of the same material can be obtained for a modellistic approach.

Simple thermogravimetric runs rarely can shed light on the complex phenomena involved during the devolatilization. At low heating rate (HR), a gradual release of different volatile compounds occurs as the temperature increases. Humidity is released at lower temperatures, structural modifications (porosity, fragmentation...) in the solid matrix proceed with continuous but small variations, melting of solid generally occurs when devolatilization process is completed. Vice versa, at high HR, the temperature increases rapidly in the solid particle, so that all phenomena above act simultaneously, interfering each others and giving results not predictable at low HR: for instance, the simultaneous release of volatiles and the melting of solid can swell the particle generating large internal cavities. From a chemical point of view, the kinetics of devolatilization products are influenced by the HR [1,2], because competitive kinetic paths can be supposed (as in the decomposition of cellulose [3 and references herein]). These authors (and also [4,5]) studied the effect of HR on the devolatilization of cellulose or biomass materials, underlying the importance of interactions of different devolatilization stages succeeding as the temperature increases. As a matter of fact, these investigations are conducted using the same apparatus with a range of HR actually narrow.

In this study an experimental method is suggested to study the devolatilization process using different equipment taking advantage of the main characteristics of each one. Biomass materials are expected to give different reactivity varying HR in a very wide range, that is from 1°C/s (TG runs) to 2×10^4 °C/s (wire mesh reactor). The analysis of solid residue in various conditions can also give important results: SEM analysis can reveal structural variations (porosity increase, fragmentation, swelling) that strongly influence the reactivity of char produced.

EXPERIMENTAL

Equipment

Three different equipment on a laboratory scale have been used to characterize the behaviour of different materials during devolatilization: a thermogravimetric balance (Mettler TA 3000), a wire mesh reactor (in the following called with its commercial name, Pyroprobe) and a drop tube reactor (DTR). Different conditions can be programmed according to the specific characteristics of each apparatus. Very different values of reactor temperature, HR and residence time can be achieved, influencing the thermal history of the sample and, hence, the devolatilization process. The main characteristics of each equipment are listed synthetically in table 1. In particular, TG balance is indicated to study the devolatilization process at very low HR: constant HR runs can be performed in which the temperature of the sample follows that programmed with negligible delay. A second employment of the same apparatus allows higher HR to be achieved. In this case (TG isothermal runs), the sample is kept distant from the furnace during the heating up in a nitrogen flow. Once the final temperature is reached the crucible containing the sample is instantaneously immersed in the furnace. The effective HR using this procedure is estimated to be approximately 100°C/s, considering the small quantities of the sample. The Pyroprobe reactor is a commercial wire mesh reactor which was characterized [6] as for thermal profile and mass transfer. The temperature and the HR are extremely higher than the TG balance, thus, more severe conditions can be programmed. A detailed description of DTR can be found elsewhere [7]. A stream of particles is

continuously fed to the oven maintained at constant temperature. Size fraction successfully employed were in the range 100-300 μm . The solid is transported pneumatically with the primary air: the solid flowrate is approximately 0.2 g/min. Both the devolatilization and a partial oxidation are expected to occur: because of the short residence time, the oxidation extent can be limited. The DTR allows experimental runs in conditions similar to those encountered in industrial plants to be performed on a laboratory scale.

	TG (constant HR)	TG (isothermal)	Pyroprobe	Drop Tube Reactor
T max ($^{\circ}\text{C}$)	900	600	1400	1200
HR max ($^{\circ}\text{C}/\text{s}$) nominal value	0.5	-	2×10^4	-
HR max ($^{\circ}\text{C}/\text{s}$) evaluated on sample	0.5	50-100	2×10^3	500-1000
residence time (s)	(...)	(...)	0-200	0.5-1.5
sample mass (mg)	5-10	5-10	3-5	stream of particles
gas environment	N_2	N_2	N_2	O_2/N_2

Table 1. Characteristics of experimental equipment used.

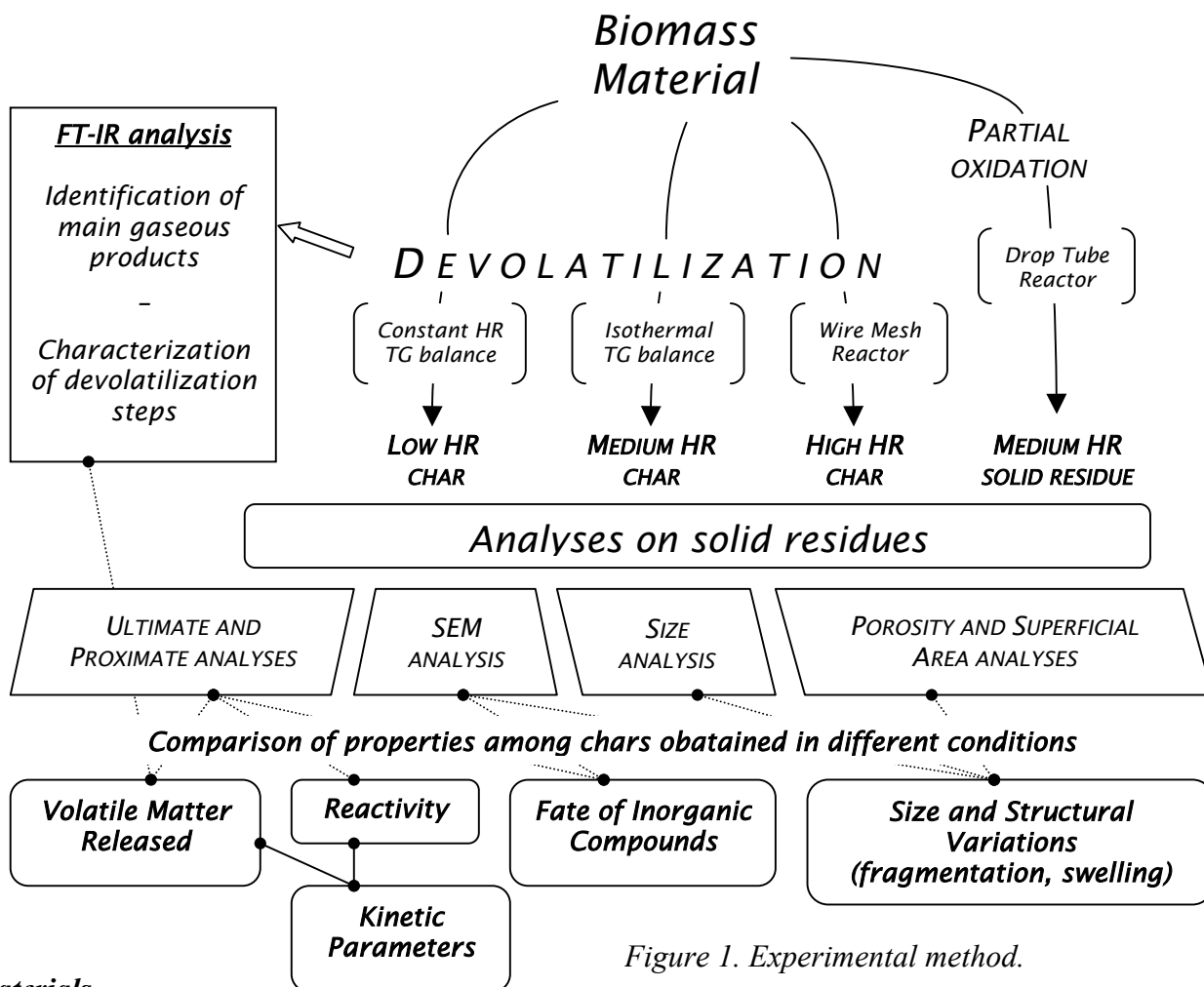


Figure 1. Experimental method.

Materials

Three different biomass materials have been studied, namely, hazelnut shells, olive husks and paper sludge. Furthermore, a reference coal has been tested for comparison. Proximate and ultimate analyses are listed in table 2. At present, an experimental program is in progress for all materials. As schematically shown in figure 1, devolatilization process is performed in different conditions, obtaining low, medium and high HR char from the same material. All analyses indicated in figure 1 allow to evaluate characteristics of solid residues as volatile matter content, reactivity, size and structural variations, which can determine the properties of char. In particular, FT-IR analysis carried out in series during the devolatilization run can provide important information to identify the main gaseous products and, hence, to characterize the devolatilization steps. SEM analysis can be used to observe the average aspect of samples, comparing all cases. Furthermore, it can furnish a punctual size analysis (so that

fragmentation or swelling phenomena can be distinguished). Finally, a semi-quantitative elemental analysis conducted using SEM can be compared to the global ultimate analysis (or ash analysis) in order to investigate the fate of inorganic compounds, especially alkali.

In the following, some significant results are reported among those obtained in this preliminary study.

		coal Kema04	olive residue	hazelnut shells	paper sludge
Ultimate analysis (dry)	C	71.43	51.24	51.0	24.27
	H	4.47	6.69	5.40	3.42
	N	1.12	0.83	1.30	0.51
	S	0.81	0.05	-	0.014
Proximate analysis (as recd.)	Cl	0.265	0.071	-	0.053
	Mois.	5.68	14.03	7.0	54.8
	VM	28.73	67.37	73.0	22.58
	FC	52.6	17.55	18.8	1.36
	Ash	13	1.05	1.2	21.26
HHV (kJ/kg) (dry)		29842	22290	-	8798
LHV (kJ/kg) (dry)		28708	20068	-	5136

Table 2. Analyses of materials.

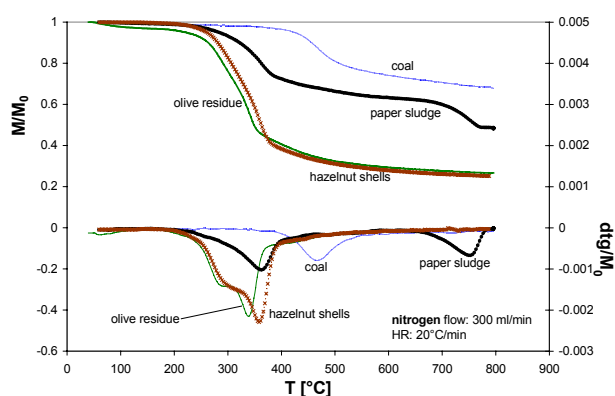


Figure 2. TG constant HR results.

RESULTS

As a first approach, a TG constant HR has been carried out for all materials in order to compare the behaviour of each one and identify the major steps in the process. Weight loss and dtg curves are reported in figure 2 for HR 20°C/min. Olive residue and hazelnut shells show a similar behaviour: the composite peak can be attributed to the devolatilization of main components (cellulose, hemicellulose and lignin). The first peak of paper sludge (approximately at 370°C, as the other lignin-cellulosic materials) can be attributed to the devolatilization of cellulose contained. FT-IR profiles demonstrated that the weight loss at higher temperature (approximately 750°C) is caused by the decomposition of inorganic matter (calcium carbonate), the unique volatile product being CO₂. While biomass materials devolatilize at temperatures between 230 and 420°C, the reference coal needs higher temperature, the temperature for the maximum weight loss rate being 470°C.

Subsequently, different HR have been programmed on the same equipment: in general, the higher the HR, the higher the amount of volatiles released. Furthermore, a certain delay in the devolatilization phenomena can be noticed. In figure 3 the weight loss and dtg curves are reported for paper sludge. As for the organic devolatilization peak, the temperature for the maximum is 363, 353 and 337°C at HR 20, 10 and 5°C/min, respectively. Similar qualitative conclusions can be drawn considering the other materials, for which TG results are not reported.

Isothermal runs have been also carried out on all materials. Weight loss curves are obtained in a

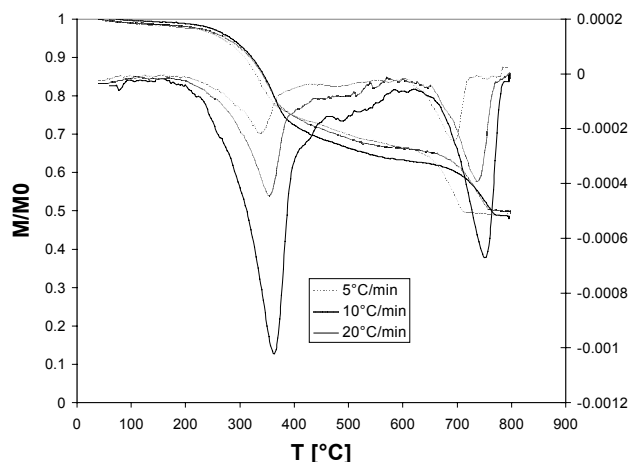


Fig. 3. TG runs at different HR for paper sludge.

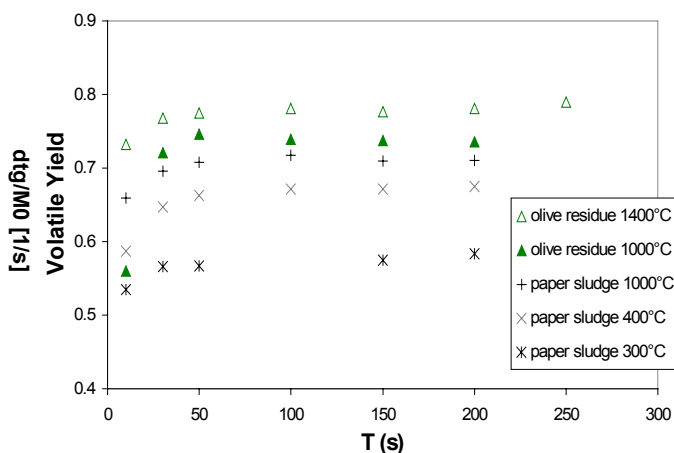


Fig. 4. Isothermal runs in Pyroprobe.

temperature range characteristic for each material where the main devolatilization phenomenon occurs. Different single runs have to be performed in order to obtain the isothermal profile in Pyroprobe. All characteristics (temperature, HR, sample mass...) are maintained unchanged, while the residence time

is varied up to the maximum value (approximately 200 s). At the maximum temperature (1400°C) and HR (2×10^4 °C/s) the highest quantity of volatile matter is supposed to be released. Some isothermal curves for paper sludge and olive residue are reported in figure 4. A comparison between TG and Pyroprobe results, as for the global volatile matter released, is made in table 3. In general, the more severe the operative conditions, the higher the amount of VM released.

Finally, a preliminary SEM analysis has been carried out on two materials (coal Kema04 and paper sludge). The characteristic aspect of a coal particle as received (average size of 100 μm) is reported in

Volatile content	TG runs			PYROPROBE runs	
	5°C/min	10°C/min	20°C/min	1000°C	1400°C
Coal			32.4	27.1	35.4
Olive residue		70.8	71.2	72.7	77.8
Paper sludge	49.8		51	57.3	62.8

Table 3. Comparison of VM released from TG and pyroprobe.

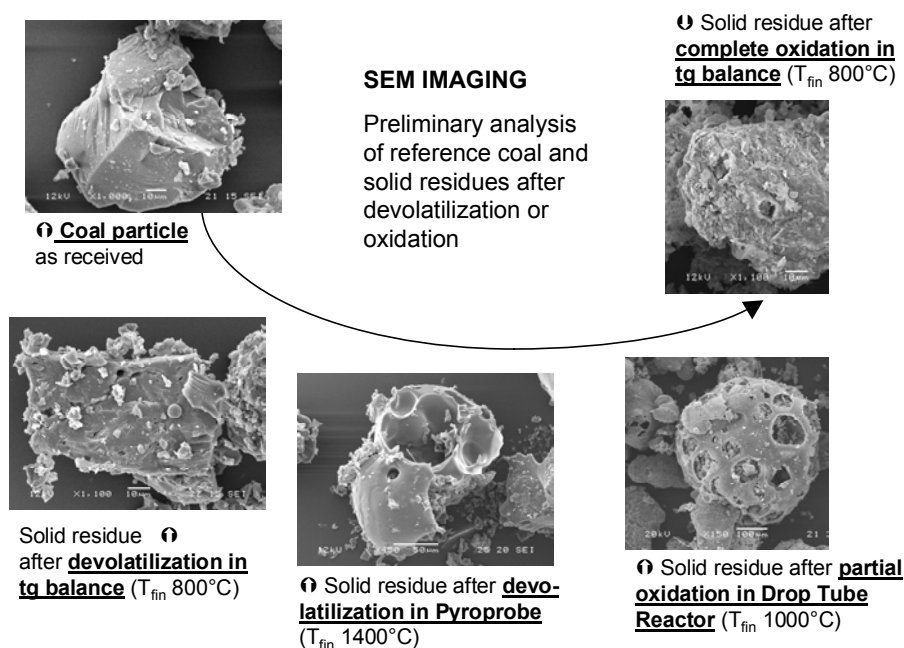


Figure 5. SEM imaging of coal particle and different solid residues.

oxidized in TG, i.e. at low HR: again, superficial indentations and porosity can be observed, with no significant swelling or size variation.

REFERENCES

1. Milosavljevic Ivan, Oja Vahur, Suuberg E.M.: *Ind.Eng.Chem.Res.* **35**:653-662 (1996)
2. Antal M.J.Jr. and Varhegyi G.: *Ind.Eng.Chem.Res.* **34**:703-717 (1995)
3. Piskorz J., Radlein D., Scott D.S.: *J.Anal.Appl.Pyrolysis* **9**:121-137 (1986)
4. Caballero J.A., Font R., Marcilla A., Conesa J.A.: *Ind.Eng.Chem.Res.* **34**:806-812 (1995)
5. Fisher T., Hajaligol M., Waymack B., Kellogg D.: *J.Anal.Appl.Pyrolysis* **62**:331-349 (2002)
6. Bonfanti L., Riccardi J., Semino D., Tognotti.: pp.111-114, *Combustion Meeting 98, XXI Event of the Italian Section of the Combustion Institute*, Salerno, Italy, September (2001)
7. Cioni M., Malloggi S., Biagini E., Tognotti L.: *Paper I-24 Open Meeting on Combustion, XXIV Event of the Italian Section of the Combustion Institute – Combustion and the Environment*, S.Margherita Ligure, Italy, September (2001)

Sub-models for the devolatilization of biomass fuels

E. Biagini, C.Grassi, L.Tognotti

Dipartimento di Ingegneria Chimica – Università di Pisa - ITALY

INTRODUCTION

Biomass devolatilization has been extensively studied during the past decades. Numerous investigations have been also performed on modeling the biomass devolatilization and its major components, which were summarized in several reviews and collected papers [1,5,7,9]. Several kinetic models have been proposed to describe biomass devolatilization [3,8,10]. Their simplicity allows a low computational cost, making them suitable for an efficient implementation in comprehensive codes (CFD). However, these models generally depend on both the biomass composition and the specific operative conditions employed, so that they are strictly applicable to the case considered. Vice versa, some complex models can cover a wide range of operative conditions and material composition (models based on the devolatilization of components, cellulose, hemicellulose, lignin [11]). They need a very high number of parameters and have a high computational cost: as a matter of fact, their implementation in comprehensive codes is impractical.

The crucial point in the devolatilization of biomass materials is the strong dependence of the process (kinetic and main products) on both the composition, which can vary widely, and the operative conditions (temperature, heating rate and residence time). A possible solution is to individuate the sub-model which optimizes the experimental data, starting from a preliminary simple analysis and then choosing among different specific and more complex models covering, globally, a wide range of composition and operative conditions. Simplicity should be guarantee in any case. Neural network model is a different approach, assuring simplicity and the independence from the mathematical description of each single phenomenon. However, a large number of experimental data has to be collected (also from literature) in order to train the model.

EXPERIMENTAL NEEDS

The behaviour of biomass materials during devolatilization is very specific. Compared with coal, the content of volatile matter is higher, the reactivity is higher (biomass materials generally have a range of devolatilization between 200 and 430°C, whereas coal starts roughly after 400°C); the char formed after devolatilization has also completely different characteristics respect to coal, being more reactivity. The composition of biomass varies from one material to another; the chemical composition, cellulose, hemicellulose, lignin and extractives, together with the effect of inorganic materials determines the devolatilization characteristics of biomass. Some examples have been obtained using a thermogravimetric balance for different biomass: olive residue, pine sawdust, hazelnut shells, paper sludge, sewage sludge and a reference coal [13]. The main chemical components of biomasses, significantly different in their chemical structures, determine the specific behaviour during devolatilization; TG and dtg curves are reported in figure 1. Measuring the chemical composition of a

		olive residue	pine sawdust	hazelnut shells	paper sludge	sewage sludge	reference coal
<i>Ultimate analysis (dry)</i>	C	51.24	53	51.0	24.27	52	71.43
	H	6.69	6	5.40	3.42	8	4.47
	N	0.83	0.2	1.30	0.51	6	1.12
	S	0.05	0.08	-	0.014	1.2	0.81
	Cl	0.071	0.02	-	0.053	0.5	0.265
<i>Proximate analysis (as received)</i>	Moist.	14.03	(dry)	7.0	54.8	(dry)	5.68
	VM	67.37	80.6	73.0	22.58	47.8	28.73
	FC	17.55	17.7	18.8	1.36	6.6	52.6
	Ash	1.05	1.7	1.2	21.26	45.6	13

Table 1. Ultimate and proximate analysis for materials studied.

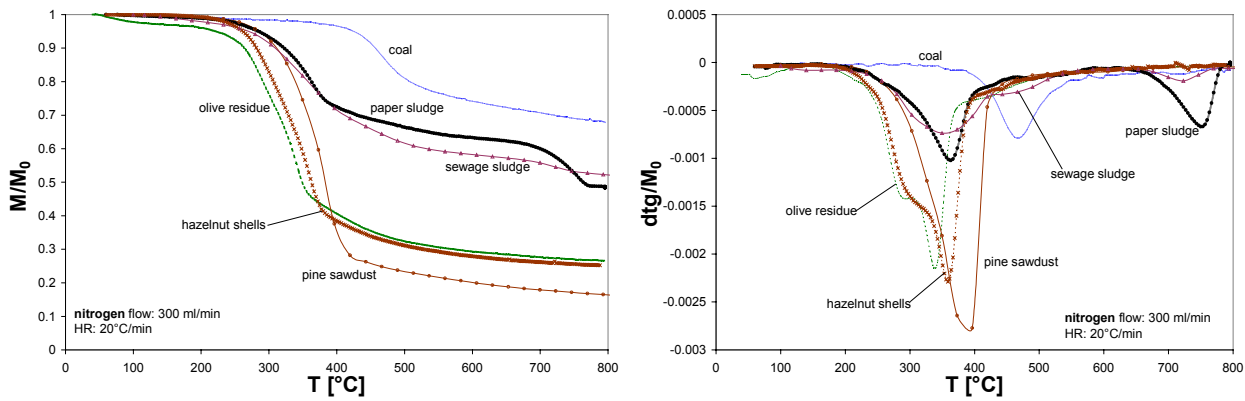


Figure 1. Weight loss and dtg curves for materials studied.

a biomass is a complex and onerous process but necessary from a kinetic point of view. In practice, it is more convenient and easier to perform elemental analysis and proximate analysis of a feedstock, table 1. In order to simulate the behaviour of biomasses, a specific model should be developed starting from the chemical characterisation of the material. In the following a diversified modellistic method is described for biomass materials. Several kinetic sub-models and more complex model, which need the chemical composition as inputs, are used to fit the experimental data. Furthermore, a neural model, which calculates the chemical composition starting from Ultimate and Proximate analyses, was realised overcoming the above cited problems about the direct chemical analysis [14].

MODEL SECTION

From a methodological point of view, every materials should be characterized employing a simple common model, for the purpose of comparison. In general, Single First Order Reaction (SFOR) model is hardly accurate to describe the devolatilization of a material. However, the simplicity and the very low computational cost make it the first step in the fitting of experimental data. This allows to compare materials as for both the activation energy and the pre-exponential factor and, also, to have a starting value for the fitting parameters using more specific and complex models, in a following analysis. These preliminary values are reported in table 2 for all materials, representing the major devolatilization step.

Kinetic parameters	olive residue	pine sawdust	hazelnut shells	paper sludge	sewage sludge	reference coal
E (kJ/kg)	85.6	121.8	71.0	53.2	88.7	139.9
A (s ⁻¹)	1.9x10 ⁵	3.9x10 ⁸	5.7x10 ³	69	2.2x10 ⁵	3.5x10 ⁷

Table 2. Parameters obtained using SFOR model

Subsequently, depending on the specific behaviour of a material, a more complex model should be chosen to fit the experimental data.

Table 3 summarizes synthetically the main characteristics of sub-models tested to simulate the devolatilization of biomass materials. Detailed description of each model can be found in literature [2]. In particular, DAEP model (Distribution Activation Energy Parallel Reaction) is the weighted sum of *n* SFOR models and, hence,

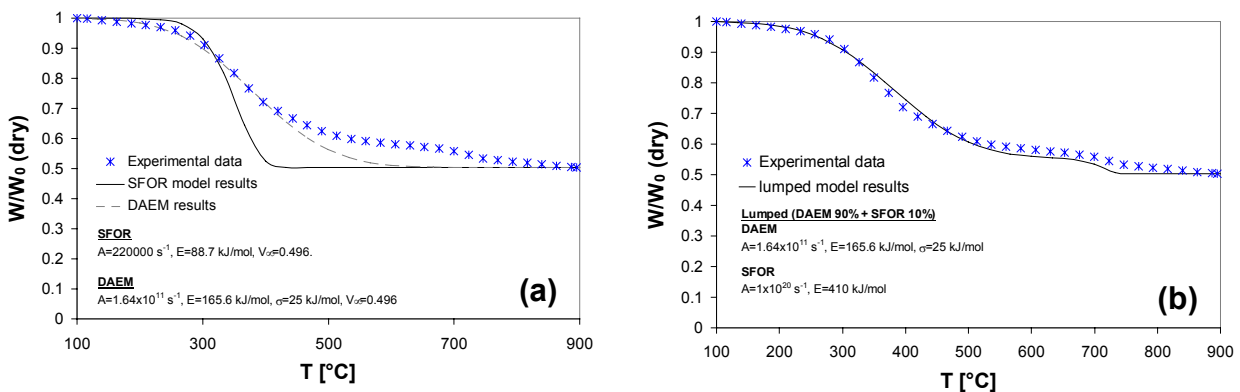


Figure 3. Comparison between experimental and model results on the devolatilization of sewage sludge. (a) SFOR and DAEM results; (b) lumped model results.

allows the devolatilization of composite materials (for which dtg peaks can be easily distinguished) to be modelled. DAEM [1] generally is adopted for heterogeneous materials, assuming the devolatilization process as a series of first order reactions (supposing continuous activation energy distributed on an average value E_0). Lumped model is the weighted sum of a DAEM and a SFOR model, used for heterogeneous materials showing distinguished peaks during the devolatilization.

	Model	Parameters	Properties needed		Applicability	Characteristics
Devolatilization sub-models	SFOR: Single First Order Reaction	2 parameters (A, E)	V^∞ thermal history	Mass (kinetic)	All materials	Simple scheme Low comp. cost
	DAEP: (n SFOR models)	n*2 (A,E)	Chemical composition $n*(V^\infty)$	Mass (kinetic)	Blends, composite materials and multi-stage devolatilization	Simple scheme Low comp. cost
	DAEM: Distribution Activation Energy Model	3 parameters (A, E_0 , σ)	V^∞ thermal history	Mass (kinetic)	All materials especially coals	Simple scheme Medium comp. cost
	Lumped: (SFOR+DAEM)	2+3 parameters	Chemical composition V_1^∞ and V_2^∞ thermal history	Mass (kinetic)	Blends, composite materials and multi-stage devolatilization	Simple scheme Medium comp. cost
	Neural Network model	Minimization of error function on output values	Physical and chemical properties of sample Chemical composition	No balance	Biomass materials	Black box scheme Very low comp. cost
	CHL model	No fitting parameters	Chemical composition operating conditions	Mass and Energy	Biomass Material	Complex model High comp. cost

Table 3. Main characteristics of sub-models tested for the devolatilization of biomasses.

Some examples of application of these models are shown in the following. In figure 2, preliminary kinetic parameters obtained with SFOR model are used to fit experimental data of hazelnut shells pyrolysis. As can be observed, the agreement is good at least up to 400°C. After this temperature, SFOR model is not able to follow the long tail in the weight loss. In some cases, SFOR model is clearly unsuitable to fit complex devolatilization behaviours as that reported in figure 3, for sewage sludge. As a matter of fact, even DAEM can fit the experimental data only partially, up to 450°C. A lumped model (DEAM+SFOR) should be considered to match also the weight loss at high temperature, applying SFOR model to simulate the decomposition of carbonate at 720°C. Finally, DAEP model is used to fit data of pine sawdust. The agreement is quite good, especially considering the composite shape of devolatilization peak (see figure 1). It is worth noting that parameters used in this case are not extracted from experimental data obtained in the present work but they are adopted from literature [9]

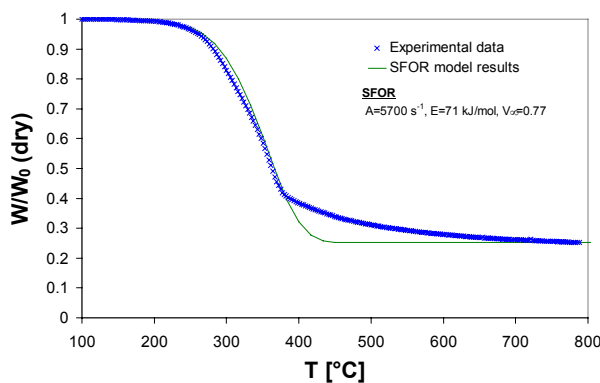


Figure 2. Comparison between experimental and SFOR model results on the devolatilization of a lignin-cellulosic material (hazelnut shell).

introducing the chemical composition of pine wood (cellulose 41%, hemicellulose 32% and lignin 27%). A complete different approach is based on the application of artificial neural network model. From a detailed database [12] collecting data on the devolatilization of 115 different biomasses since 1980, a neural model was trained and tested considering very different operative conditions. The aim of this approach is to obtain an overall description of biomass devolatilization. Details on the development of this model can be found elsewhere [6]. It is applicable to lignin-cellulosic materials and for conditions similar to those used during the training step, these ranges being very wide, maximum temperature 1400°C, heating rate from low (order of magnitude 1°C/s, TG balances) to very high (10⁵ °C/s, wire mesh reactor and laser heaters). No direct fitting parameters are actually needed, once weights for the minimization of the error function were set up during the training. This model is flexible as for the material composition and operative conditions; furthermore, it has a very low computational cost and can be easily

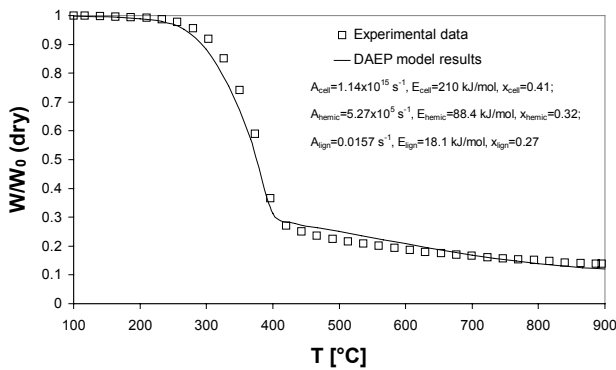


Figure 4. Comparison between experimental and DAEP model (3xSFOR) results on the devolatilization of a lignin-cellulosic material (pine sawdust).

describe the devolatilization of biomass materials. So, several tools with different characteristics have been developed in order to simulate the biomass pyrolysis. These different approaches can be implemented in complex CFD codes in order to model industrial and laboratory scale results.

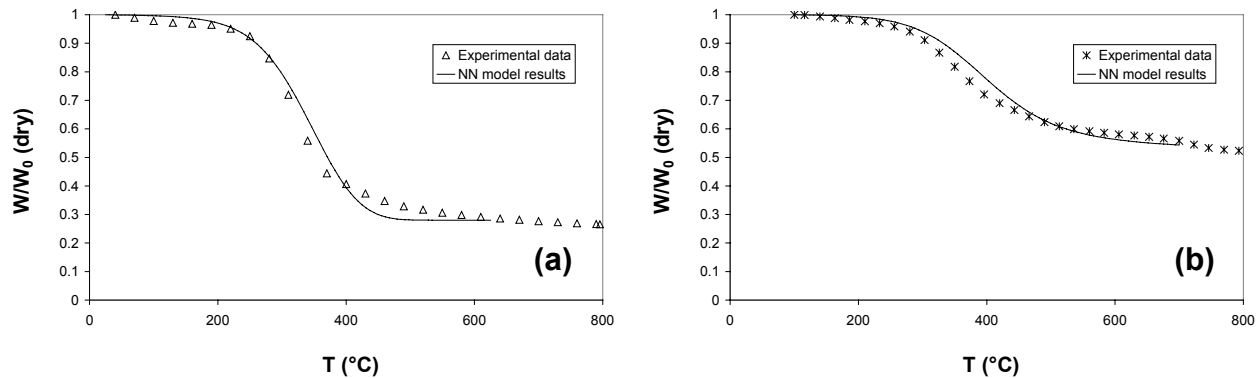


Figure 5. NN model results on the devolatilization of (a) olive residue and (b) sewage sludge.

REFERENCES

1. Anthony D.B., Howard J.B.: *AICHE J.* **22**:625-656 (1976)
2. Biagini E., Lippi F., Petarca L., Tognotti L.: *Fuel* **81**:1041-1050 (2002)
3. Chen Y., Charpenay S., Jensen A., Wójtowicz M. A.: *Twenty-seventh Symp. Combust.- The Combustion Institute* pp.1327-1334 (1998)
4. Fletcher, T. H., Kerstein, A. R., Pugmire, R. J., Grant, D. M.: *Energy & Fuels* **4**: 54-60 (1990)
5. Gaur S., Reed T.B.: *Thermal Data for Natural and Synthetic Fuels*. Marcel Dekker, Inc., New York (1998)
6. Grassi C., Tognotti L. *Paper IV-5 Open Meeting on Combustion, XXIII Event of the Italian Section of the Combustion Institute – Combustion and the Environment*, Ischia, Italy, May (2000)
7. Koufopoulos C.A., Maschio G., Lucchesi A.: *Can J Chem Eng* **67**:75-84 (1989)
8. Liang X.H., Kozinski J.A.: *Fuel* **79**:1477-1486 (2000)
9. Órfão J.J.M., Antunes F.J.A., Figueiredo J.L.: *Fuel* **78**:349-358 (1999)
10. Semino D., Tognotti L.: *Computers Chem Engng* **22**:S699-S702 (1998)
11. Sheng C. and Azevedo J.L.T., *Eleventh International Conference on Coal Science*, October, 2001
12. Tognotti L., Grassi C.: *BIOMASSDEVO – database on the biomass pyrolysis*, Chem. Eng. Dep. – University of Pisa – Italy (1999)
13. Biagini E., Tognotti L.: submitted to *Open Meeting on Combustion, XXV Event of the Italian Section of the Combustion Institute – Combustion and the Environment*, Rome, Italy, June (2002)
14. Grassi C., Tognotti L.: *Poster Session XXVIII International Symposium on Combustion*, Edimburgh, UK, August (2000)

Deposit Prediction from coal-biomass co-combustion

¹ A. Bianchi, M. Cioni, N. Pintus

ENEL-Produzione SpA – Ricerca Via A. Pisano 120 56100 Pisa

SCOPE

Biomass will be more and more important for energy production. By now they can be used in order to reduce the utilization of fossil fuel in coal fired power plants but in this case the deposition of ash on the banks can limit the plant availability (1).

Tests were carried out burning biomass with coal on a 5 MWth experimental furnace sampling ash and deposits. The results are compared with those obtained on a the same facility with other fuels and on full scale boiler fed with coal. Different mixtures of coal with wood and straw were used.

The results of the tests were compared to those obtained with mixtures petcoke-coal on the same facility and with coal on a full scale power plant

The general scope of the work is to find a relationship between the ash deposition tendency and the fuel ash composition. An empirical approach to the deposition modelling was proposed which takes into account the ash composition and the flue gas temperature.

COMBUSTION FACILITIES AND EXPERIMENTAL SET-UP

The tests were carried out on two plants, the S. Gilla 5 MWth simulator and a 640 MWe.

The plant characteristics of the S. Gilla Simulator are the following: This facility is made up by 15 main modules (11 are cooled and 4 are adiabatic), a transition adiabatic module (TAM) and a convective section (CS). The furnace has about 60 ports suitable for gas sampling.

Each module is formed by an external casing (carbon steel) which is internally covered by refractory material. The cooled modules have two cooling loops inside the refractory material.

Actually the furnace configuration simulates a boiler with front/rear burners, reburning injectors and OFA ports, but it could be possible to simulate any kind of boiler by changing the modulus type.

The boiler where the co-combustion tests were performed is a conventional pulverised coal boiler equipped with frontal burners. The mix of fuels was prepared before the tests in an unique proportion, 10% because it was not

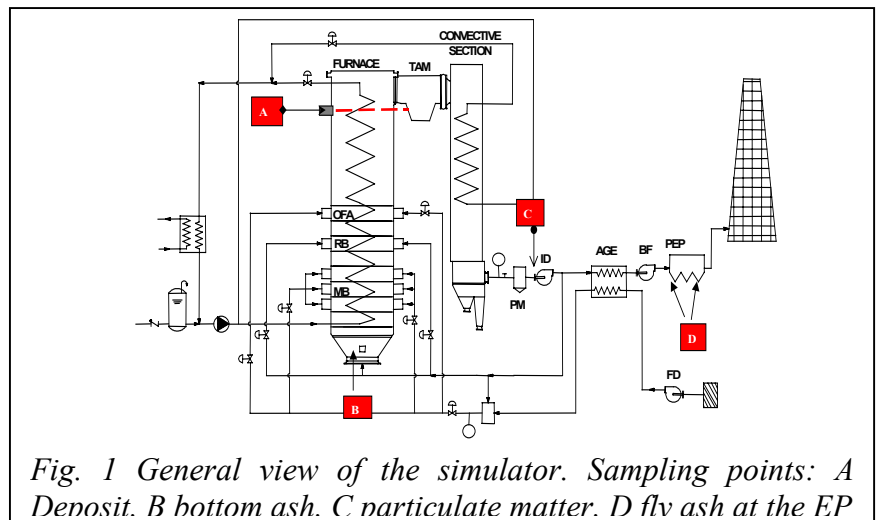


Fig. 1 General view of the simulator. Sampling points: A Deposit. B bottom ash. C narticulate matter. D flv ash at the EP

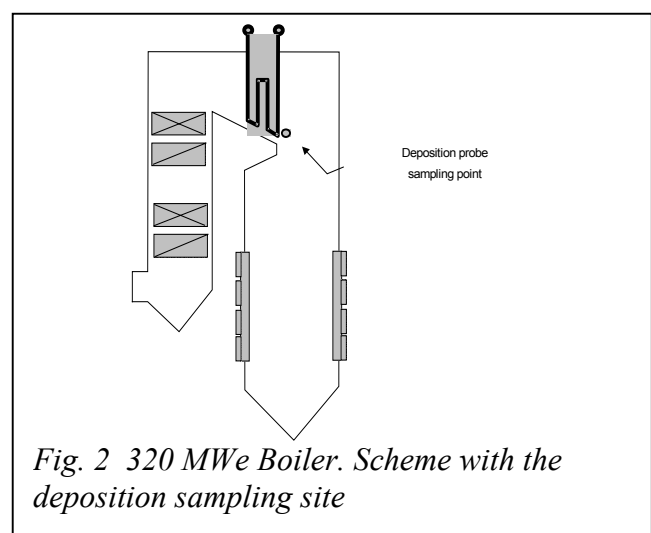


Fig. 2 320 MWe Boiler. Scheme with the deposition sampling site

available an independent feeding line in this plant The boiler is equipped with an SCR, an Electrostatic Precipitator (7 fields) and a wet scrubber in order to meet the regulations for what concerns the emission limits.

The deposit samplings were made for all the tests in a single port with a deposition probe made of a stainless steel tube air cooled 2.5 m long.

During the tests the actual fuel fed, the bottom ash and the fly ash were sampled.

In order to collect deposit samples inside the boiler, a variable length air cooled probe has been developed. It is a 25 mm tube, made of austenitic steel with four thermocouples, 50 cm one far from the other, inserted under the surface (skin) of the metal. The measured temperatures are acquired and recorded.

The Figures 3 shows the probe before the insertion in the flue gas.

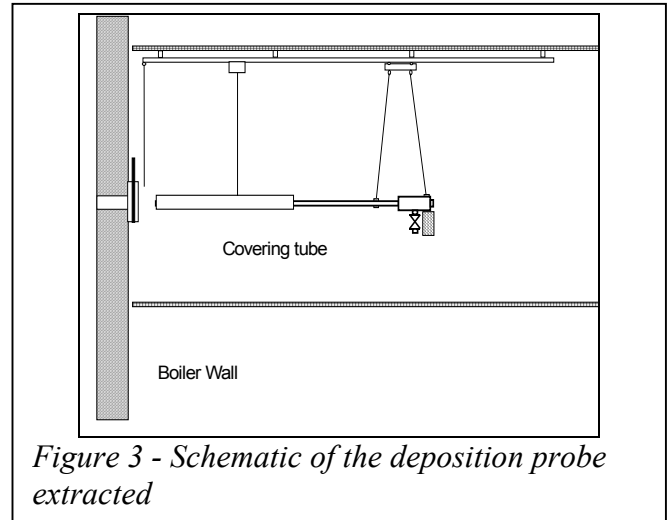


Figure 3 - Schematic of the deposition probe extracted

EXPERIMENTAL RESULTS

The results discussed are relative to the following tests:

- deposition measurements in a full size coal fed plant (640 MWe)
- deposition measurements in the S. Gilla Simulator fed with coal and coal/petcoke mixtures
- deposition measurement in the S. Gilla Simulator fed with coal, coal/wood and coal straw mixtures

On the full scale boiler three coals (South African, American, Chinese) were tested. For each fuel a data matrix containing the Total Deposition Rate and the composition of the soluble part in order to measure Cl, NO3, SO4, Na, K, Mg, Ca as a function of the fuel and the sampling conditions and was obtained (tab. 3).

The Total Deposition Rate measured with a sampling probe in a single point is not the real deposition rate on each single exchanger tube but can be assumed to represent in a correct way the differences between each single fuel-plant set-up. The results of this experimental campaign can be assumed as representative of the behaviour of different coals on a full scale boiler and from the deposit composition some statement can be done on the deposition mechanisms.

Applying the PCA technique to the table 1 data-set it is possible to point-out the differences between the coals. Fig 4 shows the graph of loadings on the first two components relative to the data matrix.

The comments on the graph are the following:

Coal	time	Dist	Sol	F %	Cl	SO4	Na	K %	Mg	Ca	TDR
SA	20	143	3,7	0,08	0,23	67,9	0,73	0,98	0,16	29,7	31,0
SA	20	180	3,9	0,08	0,09	62,0	0,49	0,31	0,26	36,4	21,0
SA	5	35	1,8	0,16	0,64	27,2	0,77	0,25	0,39	69,9	71,5
SA	5	87	2,2	0,13	0,62	29,6	0,99	1,06	0,15	66,6	66,7
SA	5	21	4,5	0,22	0,27	31,8	0,53	0,28	0,00	66,6	48,0
SA	5	120	2,1	0,09	0,35	47,5	0,60	0,66	0,32	50,5	86,8
SA	5	72	2,5	0,11	0,21	36,9	0,42	0,79	0,17	61,4	75,0
SA	5	25	3,2	0,06	0,19	48,2	0,26	0,12	0,10	51,0	84,6
SA	5	5	2,6	0,07	0,12	43,7	0,22	0,00	0,13	55,4	81,3
SA	5	53	2,5	0,07	0,39	32,4	0,50	0,18	0,25	66,1	65,2
SA	5	100	2,4	0,39	1,44	33,9	1,01	0,71	0,25	61,9	69,3
SA	5	150	2,9	0,10	0,25	33,3	0,49	0,71	0,17	64,9	51,5
SA	5	55	2,8	0,24	0,68	31,6	0,80	0,93	0,29	65,3	53,1
SA	5	100	2,6	0,09	0,19	33,3	0,35	0,30	0,14	65,5	60,1
SA	5	140	2,7	0,20	0,60	37,7	0,68	0,58	0,24	59,9	48,8
SA	15	17	3,2	0,09	0,38	58,3	0,48	0,30	0,43	39,8	27,9
SA	15	60	2,6	0,09	0,27	61,1	0,29	0,36	0,39	37,2	30,5
SA	15	110	2,4	0,31	1,26	50,7	1,19	1,19	0,37	44,9	26,6
CIN	10	20	2,0	0,15	0,45	48,4	0,56	1,88	0,29	45,3	28,6
CIN	10	60	2,3	0,15	0,32	37,0	0,38	1,94	0,20	57,9	32,3
CIN	10	120	2,3	0,19	0,30	41,4	0,48	0,76	0,09	51,1	34,4
CIN	10	170	2,2	0,15	0,21	47,6	0,33	0,00	0,05	50,0	45,5
CIN	10	40	2,5	0,22	0,30	42,9	0,25	0,63	0,08	48,3	35,8
CIN	10	70	2,2	0,24	0,32	38,3	0,26	0,66	0,03	53,2	51,1
CIN	10	126	2,1	0,18	0,23	40,7	0,41	0,41	0,03	49,8	61,7
CIN	10	160	1,7	0,16	0,18	47,1	0,23	0,18	0,04	50,5	75,3
AM	10	30	1,1	-0,04	1,08	48,2	2,06	3,04	3,19	39,2	36,4
AM	10	60	1,1	-0,04	0,43	50,7	0,94	2,33	2,58	38,7	41,2
AM	10	90	1,0	0,30	2,19	50,8	0,78	2,15	2,85	36,4	40,0
AM	10	120	1,6	0,46	1,53	52,1	0,67	1,71	1,95	37,6	39,7
AM	10	30	2,0	1,68	0,73	47,4	0,38	1,25	2,22	38,5	24,3
AM	10	60	1,3	0,35	2,13	47,8	0,94	2,18	2,40	35,4	39,6
AM	10	90	1,4	0,88	3,53	47,1	0,62	2,10	3,18	35,7	31,5
AM	10	120	1,6	1,13	4,80	47,8	3,55	2,54	3,51	33,7	32,2

Tab. 1 Deposit composition with different coals on a 640 MWe boiler

The distance from the boiler wall doesn't influence the deposition. TDR and Calcium soluble have high negative, alkaline metals and chloride high positive loadings on factor 1.

Alkaline metals and chloride are correlated and hence probably associated in the deposit and negatively correlated with TDR. Calcium and sulphate are inversely correlated each other even if they constitute the most part of the deposit soluble part.

One of the most important deposition mechanism is then in some way dependent on the calcium condensed on the particles. The behaviour of the different fuels is well documented by the graph of the scores: Fig. 5. Analysing the graph with the loadings graph of the fig. 13 it is possible to identify different zones relative to the coals which produce deposits with different composition: the American (am) coal produces deposits more rich in sodium chloride, the south African coal shows a deposition rate higher containing more calcium. The Chinese coal produces a deposit having an intermediate composition and deposition rate.

Coal and coal/petcoke mixtures were tested at the S. Gilla Simulator. The total deposition rate measured with the two fuels was not significantly different.. The increase of petcoke produces an increase of soluble vanadium and nickel on the deposit, but from these tests it doesn't seem that petcoke could induce an increase of deposition rate.

The plot of loadings points-out that TDR is well correlated with soluble calcium and pH, the same effect found burning coal alone at the full scale 640 MWe boiler.

Another interesting effect is the high value of the PET% loading on the second principal component as if the influence of this secondary fuel was secondary or null on the deposition rate which is relevant on the first principal component.

The amount of soluble deposit is relatively small and tends to increase when TDR decrease. The amount of sticky compounds on the deposit particles is not necessarily high.

The coal biomass co-combustion tests made were 5 in accordance to the following test matrix

Test 1 2	Test 3 4	Test 5 6	Test 7 8	Test 9 10
100% Coal	80% Coal 20% wood	60% coal 40% wood	80% coal 20% straw	60% coal 40% straw

The plant was run in low NOx configuration at constant load of 4 MWth with the previously prepared fuel mixtures on thermal input basis. Before each test the furnace hoppers (bottom and EP) were evacuated in order to obtain fresh samples.

As in the case of coal and petcoke the graph of loadings on the first two components relative to

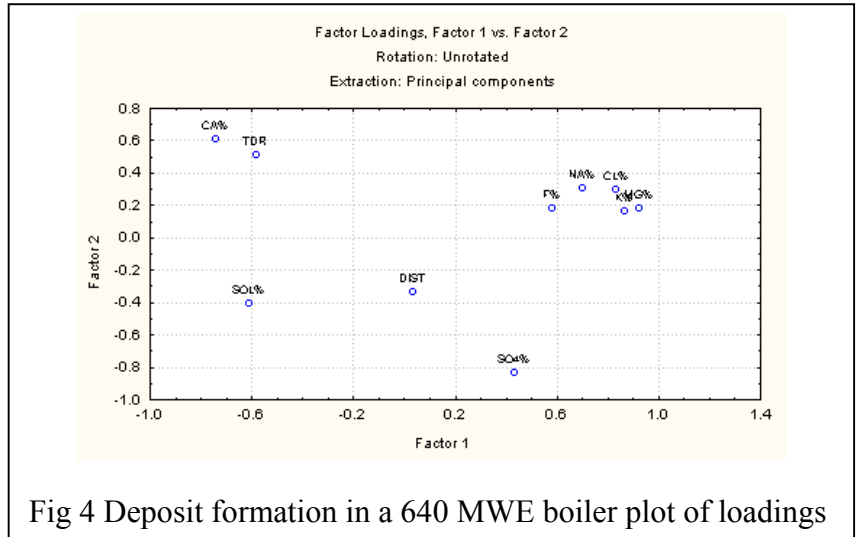


Fig 4 Deposit formation in a 640 MWE boiler plot of loadings

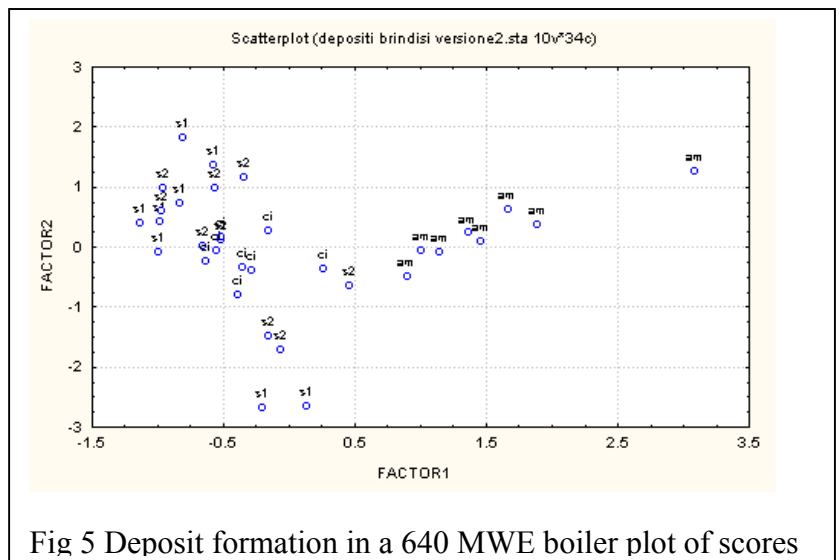


Fig 5 Deposit formation in a 640 MWE boiler plot of scores

the data matrix of the simulator co-combustion tests shows quite well the relationships between the deposit composition variables. The TDR is correlated with K, Na and Cl indicating a mechanism of condensation which involves the alkaline oxides and salts. On the right part of the graph there are the coal %, soluble calcium, magnesium the sulphate which indicate another condensation mechanism which is related to the amount of coal.

The mechanism of deposition is very complex. A physical model that should be able to predict the fouling tendency of a fuel must take into account all the (2) properties of the mineral inclusions in order to be able to describe the behaviour of the ash generated from combustion. These data together with a fluid-dynamic description of the motion field in the exchanger zone can provide such prediction tool. Another

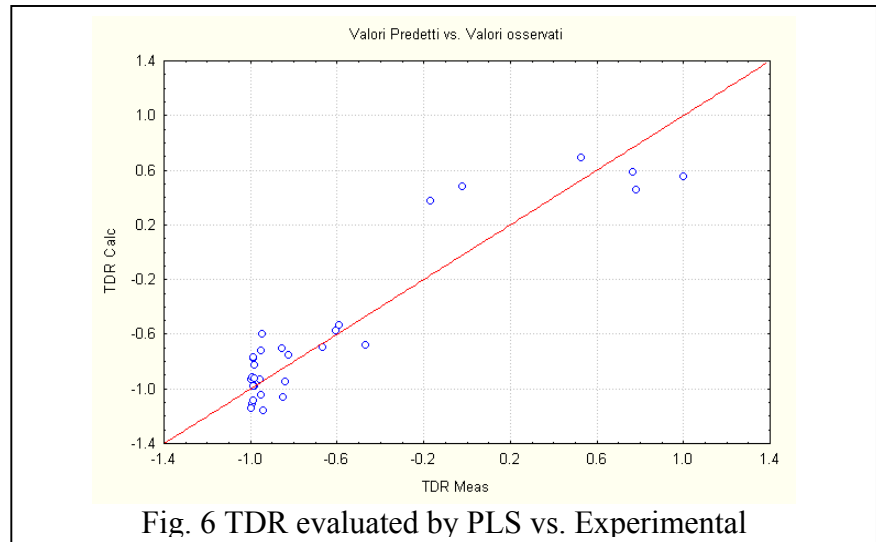


Fig. 6 TDR evaluated by PLS vs. Experimental

approach can be to make an empirical model using the fuel composition and the deposition descriptive parameters as gas temperature probe temperature and total deposition rate measured during the co-combustion tests at the S. Gilla Simulator.

These data were analysed using . It is assumed that deposition depends only on the gas temperature, the tube temperature and on the fuel composition. The regressive technique used in order to predict TDR is PLS (Partial Least Squares) which is able to treat block of variables even if they are correlated each other in order to build a multivariate model.

Fig. 6 shows the results of the application of this technique to the simulator experimental data-set in terms of evaluated Total Deposition Rate (standardised) against the experimental one.

CONCLUSIONS

The formation of deposits during co-combustion of coal and secondary fuels such as petcoke and biomass is a complicated problem which can be approached in a small size furnace.

The results obtained during the tests allowed to understand the role played by some elements present in some refuse in the deposition process.

From the results of the tests it was possible to formulate a new empirical approach to the deposit formation modelling. This approach seems good in predicting the deposition tendency but the model coefficients must be evaluated for every plant where coal and biomass/refuses mixtures are burned.

REFERENCES

1. R.W.Bryers, Fireside Slagging, Fouling, and high temperature corrosion of heat-transfer surface due to impurities in steam-raising fuels *Prog. Energy Comb. Sci.*, **22**:29–120 (1996)
2. F.C.C. Lee, F.C. Lockwood, Modelling ash deposition in pulverised coal fired applications, *Prog. Energy Comb. Sci.*, **25**:117–132 (1999)

ACKNOWLEDGEMENT:

This work was possible with the help of EU. JOULE Contract JOR3-CT98-0198 “DEPOSIT PREDICTION” Prediction of Ash and Deposit Formation for Biomass Co-Combustion.

Combustion behaviour of fast pyrolysed coal, biomasses and their blends

P. Ciambelli, V. Palma, P. Russo, S. Vaccaro, V. Vaiano

Dipartimento di Ingegneria Chimica e Alimentare, Università di Salerno, via Ponte Don Melillo, 84084 Fisciano (SA), Italy.

INTRODUCTION

In the last decade there has been a growing interest toward the study of biomass combustion. Biomass is the third largest primary energy source in the world after coal and oil and it often represents the major source of energy in developing countries [1]. In addition, the use of biomass, to provide partial substitution of fossil fuels, has an additional importance as concerns global warming since biomass combustion has the potential to be CO₂ neutral. This is particularly true for agricultural residue which are periodically planted and harvested [2]. During their growth, these plants remove CO₂ from the atmosphere, for photosynthesis, which is released during combustion.

The efficient use of such materials as fuels in new and existing plants requires the knowledge of their devolatilisation and combustion characteristics in order to properly design the boiler and the burner or to eventually retrofit already running plants. Specifically, when they are employed in plants built for combustion of ordinary fuels such as coal, the study of the interaction occurring during the combustion process is fundamental. The influence of the relatively high volatile release or of the relatively high ash content as well the characteristics of biomass's char combustion may significantly influence the combustion behaviour of the coal biomass blend [3].

The present paper aimed at studying the combustion behaviour of a bituminous coal, two renewable fuels (waste wood and cocoa) and blends of the latter with the former. This was accomplished through the production of chars and the subsequent combustion of such chars.

EXPERIMENTAL

A bituminous coal, and two biomass (waste wood and cocoa) were employed in the experiments. Samples of the single materials and samples of coal-biomass blends at 10 wt% of biomass were prepared and ground below 45 μm . The samples were pyrolysed by a wire mesh reactor (WMR) specifically designed and built for this application. The sample (about 20 mg) was kept at room temperature for 15 min in nitrogen flow (99.999 % purity), then the test was started by heating the sample at $2 \cdot 10^3$ K/s up to 1300 K and stopped after 1 s. Several tests were also performed at an heating rate of 10^4 K/s. In this case the run lasted only 0.1 s to avoid the reaching of temperature above 1300 K.

Temperature-programmed thermogravimetric analysis (TGA) of the samples in air flow was performed with a thermoanalyzer (NETZSCH TA 209). Air flow rate was $20 \text{ cm}^3 \text{ min}^{-1}$ (STP), heating rate was 10 K min^{-1} from 293 to 1250 K.

Isothermal combustion tests of samples were carried out at atmospheric pressure in a quartz flow reactor, connected on-line with CO, CO₂ (NDIR, Uras 10E) and O₂ (paramagnetic, Magnos 6G) Hartmann & Braun analyzers. The feed gas flow rate was $500 \text{ cm}^3 \text{ min}^{-1}$ (STP) and the oxygen molar fraction 0.21. During each test the temperature was kept constant, at 673, 723, 773 and 873 K. The samples were diluted with 180-350 μm quartz particles to a mass ratio of 0.01 to avoid local temperature rises during the test. Carbon

oxidation rate and conversion were calculated from the reactor outlet concentrations of carbon oxides. Further details on the experimental apparatus and procedure are reported elsewhere [4].

Specific surface area (S.S.A.) measurements of the mentioned samples were performed by a sorptometer (Fisons) to establish possible changes in the surface area subsequent to coal and biomass blending and charring. Measurements were carried out by nitrogen adsorption at 77 K after sample's pretreatment in nitrogen flow for 2 hours at 363 K.

RESULTS

Results of sample's pyrolysis in the WMR show that, as expected, cocoa and wood volatile release was very high, i.e. 82 wt% and 90 wt% respectively on d.a.f. basis, while medium volatile content was found with coal K (37 wt%) d.a.f.

Table 1. Surface area measurement of the biomass samples

Sample	raw		char	
	Meas.ed	Calc.ed	Meas.ed	Calc.ed
Cocoa	0.11		13.34	
Wood	0.78		3.08	
Coal K	5.00		0.21	
Blend Coal K-Cocoa	1.98	4.50	1.06	0.26
Blend Coal K-Wood	3.86	4.58	0.57	0.62

Results, reported in table 1, show that the measured SSA's of the blends made with coal K and the two biomasses were much smaller than those calculated by assuming a proportional contribution of the two components in the mixture. In addition, while the S.S.A.'s of both

biomass increase markedly after pyrolysis, coal char S.S.A. is lower than that pertaining to the raw coal. Tests aimed at evaluating the evolution of the char S.S.A. with carbon conversion (X) were performed in the case of cocoa char. Results showed that SSA increases from 13 m²/g at X=0 up to 40 m²/g at X=0.55 with a tendency to remain constant as X further increases.

Results of thermogravimetric tests showed that during the combustion of not charred blends there was not significant influence of each component of the blend on the other during combustion at low temperature (30-1000°C) or, in other words, the blends behaved as though the two components were burned independently. In addition, since the biomass amount in the mixtures was small (10 wt%), the blend's combustion profiles were very similar to that of the coal. The comparison between the combustion profiles of cocoa and wood and their respective chars showed that uncharred samples of both biomasses show two distinct DTG peaks corresponding to the combustion of unhomogeneous material with very different reactivity. Instead, the combustion profiles of the chars of both biomasses show only one peak because of the absence of volatiles. However, while in the case of wood the DTG peak of char occurs in the same temperature range of the second peak of the uncharred sample, cocoa char shows a peak at a temperature intermediate between those of the two peaks of the corresponding uncharred sample. In the case of coal K the combustion profile of the char does not differ significantly from that of the coal. However, the DTG profile of the char is 20 K shifted at higher temperature and does not show the shoulder due to volatiles and observable in the case of the coal. The percent weight loss curves and their derivatives (i.e. DTG), obtained by some of the thermogravimetric analysis of the samples, are reported as a function of the temperature in figures 1 and 2. Specifically, data in fig.s 1 and 2 show the comparisons between the thermogravimetric analyses of charred blends and of the chars of coal k and of the biomass in the blend, for the couple coal-cocoa and coal-wood, respectively. In the case of coal-cocoa couple (fig. 1), as expected, the combustion profile of the blend's char closely follows that of the coal char. Instead, with the coal-wood couple the blend's char appears less reactive than

the coal char, its burnout temperature resulting 30 K higher than that pertaining to the coal char. It is worth noting that, given the char yields of the biomasses under question (wood: 7 wt% and cocoa 11 wt% d.a.f.), the amount of char in the blend deriving from the biomass is very small (1-2 wt%) either in the case of coal-wood couple or in the other case. This means that its influence on the combustion profile of the blend should be negligible, as it is verified in the case of the coal-cocoa blend's char. Therefore, it is more likely that the phenomenon observed in the case of the coal-wood blend's char is due to the biomass's ash interaction with the coal ash/char rather than to the direct influence of the biomass's char. This finding was also confirmed by some results of the combustion tests at constant temperature in the flow microreactor.

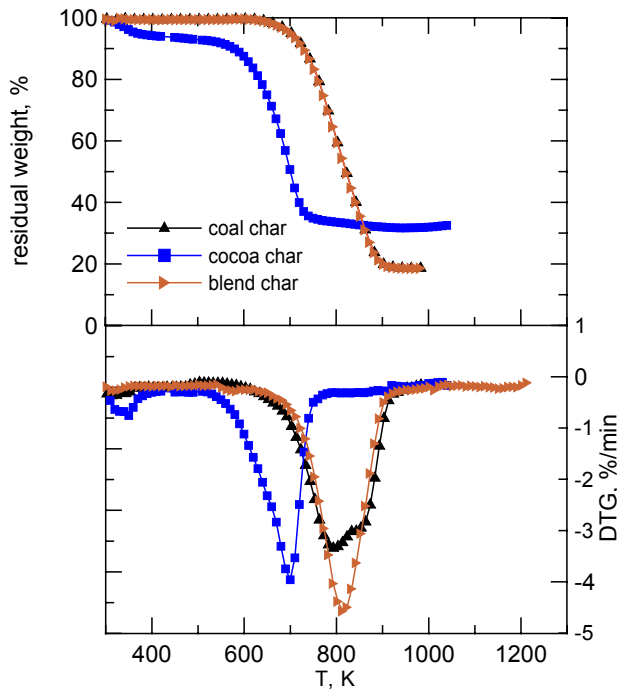


Figure 1 Comparison between TG and DTG profiles of chars of coal K, of cocoa and of their blend

conversion dX/dt ($X=(m_0-m)/m_0$, m and m_0 being the current and the initial mass of carbon in the sample, respectively) as a function of X itself. Constant temperature combustion tests allowed, through the plotting of data in Arrhenius diagrams, the determination of the kinetic parameters of the various char samples, which are summarised in table 2. Here the values of the frequency factor (K_0) and of the apparent activation energy (E_a), calculated at three values of X for each sample, are reported. In the case of cocoa and wood beside results pertaining to chars obtained at an heating rate of 10^3 K/s also findings relative to chars produced at 10^4 K/s are reported. For what concerns the chars obtained at the lower heating rate the analysis of the results shows that i) the most homogeneous char is that derived from wood since both K_0 and E_a remain practically unchanged from $x=0.3$ to $x=0.7$; ii) the combustion behaviours of cocoa char and wood char are very similar because the kinetic parameters of such materials are comparable; iii) the apparent activation energy and the

Ash residue after thermogravimetric analysis in air of the blends made with coal K and the correspondent biomasses are comparable with those estimated from the ash of the single components.

All the char samples, obtained in the WMR, were tested in the flow microreactor under isothermal conditions at 673, 723, 773 and 823 K. Results of such combustion tests, yielded the rate of change of the carbon

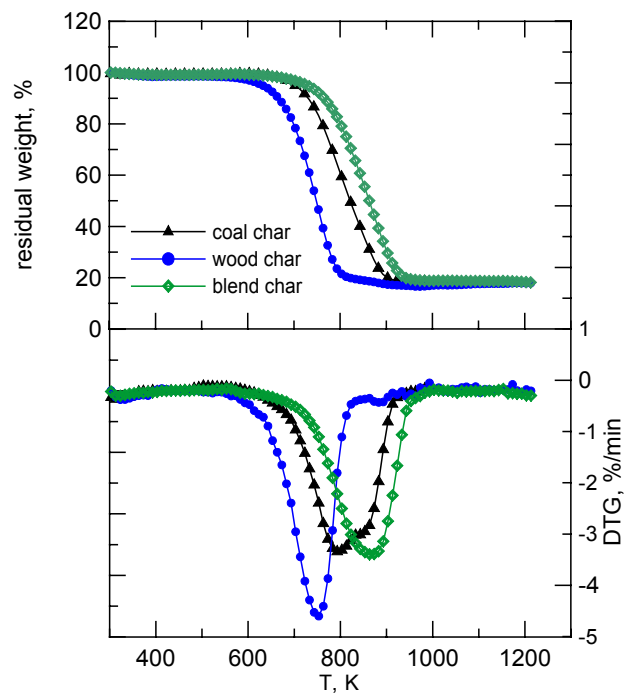


Figure 2 Comparison between TG and DTG profiles of the chars of coal k, of wood and of their blend

frequency factor of coal char increase as X increases; iv) surprisingly, the apparent activation energies of the chars of the blends coal-wood and coal-cocoa are much higher than that of the coal char. This occurs though most (97-99 wt%) of the blend char is actually coal char.

In addition, the comparison of the kinetic parameters in table 2 shows that cocoa and wood chars, obtained at 10^3 K/s and 10^4 K/s, are very similar and that already in the charring process lasted only 0.1 s (10^4 K/s) the chars are completely devolatilised the apparent activation energy being almost constant with the carbon conversion (X) and with the heating rate of charring. In contrast, already coal char obtained at 10^3 K/s shows a significant increase of the apparent activation energy and the frequency factor with the conversion. The situation would become even worse if coal char obtained at 10^4 K/s were considered. This suggests that the coal K char is not completely devolatilised.

Altogether results suggest that a role is likely played by the interaction of the biomass and coal minerals in the blend. Otherwise, it would be quite difficult to justify the lower reactivity of the coal wood blend's char with respect to that measured for the chars of pure samples or the markedly higher apparent activation energies of the blends with respect to those of the single components of the blend.

Table 3. Kinetic parameters of chars produced from various samples. K_0 [min^{-1}], E_a , [kcal/mol].

	X=0.3		X=0.5		X=0.7	
	K_0	E_a	K_0	E_a	K_0	E_a
Coal char	$1.48 \cdot 10^5$	22.26	$8.33 \cdot 10^5$	25.69	$1.52 \cdot 10^7$	31.31
Cocoa char	$0.29 \cdot 10^7$	21.83	$4.76 \cdot 10^7$	26.39	$3.87 \cdot 10^7$	26.76
Cocoa char 10^4 k/s	$9.13 \cdot 10^7$	21.95	$4.27 \cdot 10^7$	23.33	$1.37 \cdot 10^7$	25.55
Wood char	$1.18 \cdot 10^6$	22.28	$4.02 \cdot 10^6$	24.61	$3.36 \cdot 10^6$	25.16
Wood char 10^4 k/s	$0.64 \cdot 10^6$	20.48	$2.09 \cdot 10^6$	22.70	$1.89 \cdot 10^6$	23.42
Coal-cocoa blend char	$2.90 \cdot 10^8$	33.88	$2.01 \cdot 10^8$	33.93	$3.58 \cdot 10^7$	32.11
Coal-wood blend char	$3.64 \cdot 10^8$	34.268	$1.29 \cdot 10^{10}$	40.45	$1.22 \cdot 10^{10}$	41.32

REFERENCES

1. Werther, J., Saenger, M., Hartge E.-U., Ogada, T., Siagi, Z.: *Prog Energy Combust Sci*, **26**:1 (2000).
2. Strehler, A., Stuetzle, W.: *Biomass residue In Hall DO, editor, Biomass*, New York, NY, Wiley, p. 75 (1987).
3. Jenkins, B.M., Baxter, L.L., Miles, Jr.T.R., Miles, T.R.: *Fuel Process Technol Sci*, **54**:17 (1998).
4. Ciambelli, P, D'Amore, M., Palma, V., Russo P., Vaccaro, S. 4th *Int. Conf. on Combustion Technologies for a Clean Environment*, Lisboa, Portugal, 7-11 July (1997).

The Environmental Performance of Alternative Solid Waste Management Options: a Life Cycle Assessment Approach to the Study

U. Arena, M. L. Mastellone and F. Perugini

*Department of Environmental Sciences – II University of Naples
Via Vivaldi – 81100 CASERTA, ITALY*

BACKGROUND

It is now generally accepted that no one single method of waste disposal can deal with all materials in waste in an environmentally sustainable way. An integrated approach to solid waste management can deliver both environmental and economic sustainability. To assess on the whole such sustainability, tools that can predict the environmental and economical burdens of any system are needed.

A Life Cycle Assessment (LCA) methodology is generally considered the best environmental management tool that can be used to this aim, i.e. to understand and compare how a solid waste management system provided *from cradle to grave* [Boustead, 1996; Ademe/Eco-Emballages, 2001; McDougall et al., 2001]. LCA is an internationally standardized method (ISO 14040 to 14043) that makes it possible to evaluate the quantifiable environmental effects of a *system* (it is the industrial system that consumes the energy and raw materials and it is the system that gives rise to emissions, while industry and the consumer are usually concerned with *products*). Furthermore, the technique examines every stage of the life cycle, from raw material acquisition until final end-of-life treatment. Every operation or unit process within a stage is included. For each operation within a stage, the inputs (raw materials, resources and energy) and outputs (emission to air, water and solid waste) are calculated and then aggregated over the life cycle by means of material and energy balances, drawn over the system boundary [Daae and Clift, 1998; Mc Dougall et al., 2001]

This study is part of a joint research project between the Italian Committee for Waste Emergency in Campania and the Department of Environmental Sciences of the Second University of Naples, carried out in co-operation with the Italian National Consortium for Packaging (CONAI) and some companies active in the Campania Region. The LCA-type analysis is focused on various Municipal Solid Waste (MSW) management options that could be applied to the Campania Region. The analysis takes into account that any option influences the environment by consuming resources and releasing emissions and other waste streams, which have to be ultimately disposed, and by replacing energy and conventional products from primary production, which do not have to be produced in case of having available recycling products with suitable properties [Heyde and Kremer, 1999].

GOAL AND SCOPE DEFINITION

The *overall goal* for this project is to develop information and tools to evaluate the environmental performance of alternative MSW management options in the area of Campania Region. The *primary audience* for this effort is the Italian Committee for Waste Emergency in Campania, which is interested to assess energetic and environmental profile of the current management in comparison with some integrated alternatives. However, the considerations and tools developed through the study will also be of value to local governments and solid

waste planners as well as the Italian Consortium for Packaging (CONAI), the industry active in the field of solid waste management, environmental organizations and LCA practitioners.

The function of the system under study is to manage MSW of a given quantity and composition. Therefore, the *functional unit* is defined as the management of 1kg of MSW of a specified composition (that measured as average in Campania). All the activities required to manage the MSW from the time it is sent out for collection to its ultimate disposition (disposal in a landfill, energy recovery from combustion, material recovery from selection and reprocessing) are considered. Therefore, the phases of pre-sorting and collection, transportation, central sorting, biological treatment, thermal treatment and landfilling are individually analysed and quantified in terms of energy and material consumptions as well as of emissions in the environment at local, regional and global level.

The major *unit processes* included in the overall system under study are:

waste management processes (Collection, Transfer Station, Sorting of mixed waste to produce RDF, RDF Combustion with Energy Recovery, Mass Burn Combustion with Energy Recovery, Landfill with energy recovery and Ash landfill) and related processes (Inter-unit process transportation, Electrical energy, Manufacturing of materials from virgin resources).

Note that, like all the other waste options examined in the study, landfilling is a unit process: solid wastes form the inputs, along with some energy to run the process; the process itself involves the decomposition of part of the landfilled waste; the outputs are the final stabilized solid waste, the gaseous and aqueous products of composition, which emerge as landfill gas and leachate and, as in all processes, the amounts and quality of the products as well as the efficiency of the process depend on the inputs and the way that the process is operated and controlled (Fig.1D).

It is assumed that the solid waste enters the *system boundaries* (Fig. 1A-D) when it is delivered to a collection site, whether it is a kerbside collection site or a drop-off site. In agreement with similar studies (Weitz et al., 1999; Beccali et al., 2001; McDougall et al., 2001; Arena et al., 2002), all upstream life cycle activities (raw materials extraction, manufacturing, and use) are assumed to be held constant. Thus, the production of garbage bags and recycling bins has not been included in the study as well as the transport of waste by residents to a collection point. Moreover, the scope of this study does not include bulky items (televisions, refrigerators, etc.), waste from sewage works, construction and demolition waste (building debris and rubble, etc.), green waste from local authorities (pruning waste, etc.) as well as general industrial and commercial waste not collected with the municipal solid waste. Finally, the study does not cover the economic aspects of waste management: no assessment will be made of the economic impact of the various scenarios. LCA can sometimes be combined with an economic environmental impact assessment, but this study does not take such an approach.

MAIN FEATURES OF THE PROPOSED APPROACH

For each of the unit processes, and in order to increase the *data quality*, all the data of interest will derive from on site investigation, i.e. they have been or will be collected (from November 2001 to November 2002) during technical visits to all the plants active in Campania or deduced by official documents and certificate declarations of the same sites. The data quality is furthermore increased by taking into account the specific characterization of the MSW (as well as the process waste) at the various stages, i.e. at the collection, at the sorting facilities, at the energy recovery sites.

The following categories were assumed as principal indicators of environmental impact related to each step in the MSW life cycle:

- consumption of natural resources (gross and net energy consumption; oil consumption;

- water consumption);
- air pollution (increase in the greenhouse effect over 100 years; air acidification; emission to the air of metals and other pollutants);
- water pollution (water eutrophication; discharge of metals and other pollutants into water);
- quantities of solid waste generated (which is strictly related to the volume requirements in landfill).

The comparison between different scenarios of MSW waste management is made by means of the combined use of the collected data, the LCA tool and the international energetic and environmental databank of the Boustead Ltd. To allow comparison of resource consumption and environmental pollution from different management scenarios producing different products, the *basket of products method* [Ebert et al., 1996; Heyde and Kremer, 1999] was applied in this study. This means that, for a fixed input, the basket of products for each of the compared scenarios must be filled with the products of the related recovery method. In other words, when a product cannot be produced from one of the management scenarios (for instance, the landfill does not produce recovered materials), it must be produced from traditional activities (i.e. by using the virgin materials and conventional manufacturing processes) taking into account the related environmental burdens.

RESULTS AND CONCLUSIONS

The whole of collected information will be processed in order to develop the LCA of some options for solid waste management in Campania:

- Option 1. landfill disposal for all the collected wastes;
- Option 2. sorting of all the collected waste to produce RDF and RDF combustion with energy recovery;
- Option 3. mass burn incineration with energy recovery of all the collected waste, with little pre-processing treatment other than the removal of recyclable material and bulky items.

The three options will be quantified and compared in the case of a substantial absence of an home pre-sorting as well as in that of a sorting&collection stage able to reach the minimum target of Italian law (equal to 35% of the generated wastes).

The analytical comparison between the different options, even though on the basis of a not yet completed set of data, already shows the relevant role of the pre-sorting and collection method and the crucial importance of energy recovery step in the different environmental impact categories, on local, regional and global scale.

ACKNOWLEDGEMENTS

The study was carried out with the financial support and the continuous co-operation of the Italian Committee for Waste Emergency in Campania and of CONAI (Italian Consortium for Packaging).

Authors are indebted to Dr. Carlo Di Domenico (Microambiente s.r.l.), which helps in developing original software to create a database for MSW management options completely oriented to Campania Region. The contributions of Domenico Cataldo and Nino Sannolo, which help in the collection of experimental data, are gratefully acknowledged.

REFERENCES

- Ademe and Eco-Emballages, *Municipal Solid Waste : Environmental Impact Levers for Improvement*, Ademe/Eco-Emballages coeditors, Levallois-Perret, France, 2001
- Arena, U., M.L. Mastellone, F. Perugini, "Life Cycle Assessment of a Plastic Packaging

Recycling System”, Final Report of CONAI-DSA Joint Res. Prog. 1999- 2001, submitted to *Int. J. LCA* (2002)

Beccali, G., M. Cellura, M. Mistretta, “Managing Municipal Solid Waste”, *Int. J. LCA*, **6** (4):243-249 (2001)

Brandrup, J. M. Bittner, W. Michaeli, G. Menges, *Recycling and Recovery of Plastics*, Hanser Publ., New York (1996)

Boustead, I., “Theory and Definitions in Ecobalances”, in *Recycling and Recovery of Plastics*, Brandrup et al. (eds), Hanser Publ., New York, pp. 73-93, 1996

Daae, E. and R. Clift, *Environm. Protection Bull.*, **28**:23-25 (1998)

Ebert, F., G. Fleischer, W. Holley, “Life-Cycle Analysis of Recycling and Recovery of Households Plastics Waste Packaging materials”, in *Recycling and Recovery of Plastics*, Brandrup et al. (eds), Hanser Publ., New York, pp. 168-192, 1996

Heyde, M. and M. Kremer, *Recycling and Recovery of Plastics from Packagings in Domestic Waste. LCA-type Analysis of Different Strategies*, Ecomed publishers, Landsberg, Germany (1999)

McDougall, F.R., P. White, M. Franke and P. Hindle, *Integrated Solid Waste Management: a Life cycle Inventory*, 2nd ed., Blackwell Science (2001)

Weitz, K., M. Barlaz, R. Ranjithan, D. Brill, S. Thorneloe, R. Ham, “Life Cycle Management of Municipal Solid Waste”, *Int. J. LCA*, **4** (4):195-201 (1999)

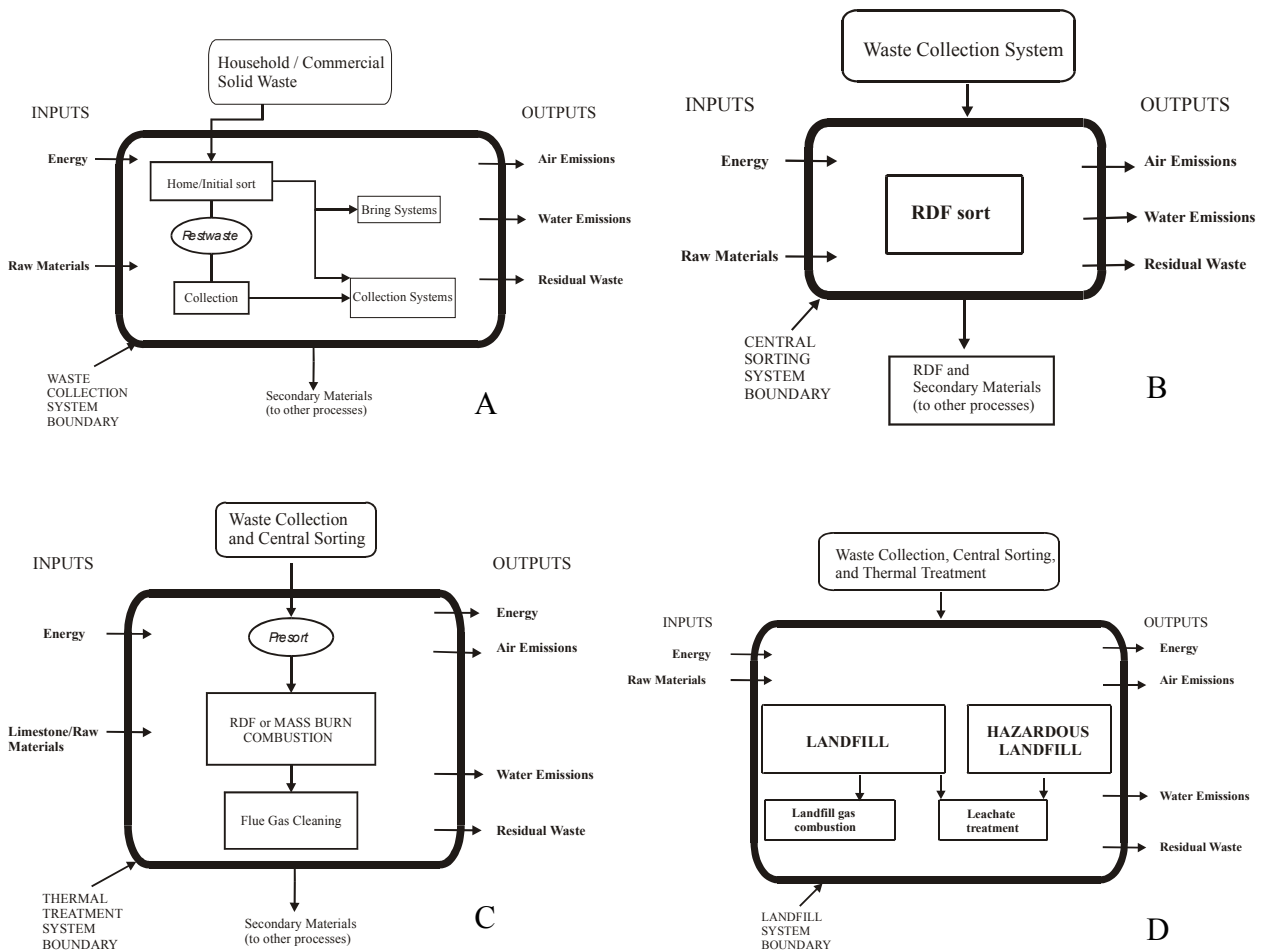


Fig. 1 The system boundaries for the major unit processes included in the overall system.

Chemical Characterisation of Liquids Products from Wood Pyrolysis

C. Branca

*Dipartimento di Ingegneria Chimica - Università di Napoli "Federico II",
Naples - ITALY*

The presence of tarry compounds in the producer gas from biomass gasification is highly undesired because of severe operating problems in internal combustion engines and turbines. In this study the analysis of beech wood derived liquids produced in a laboratory-scale countercurrent fixed-bed gasification plant, is reported. The identification of the main compounds has been achieved by gas chromatography/mass spectrometry (GC/MS) analysis.

INTRODUCTION

The main product of biomass gasification is a gaseous mixture of carbon monoxide, hydrogen, steam, methane and light hydrocarbons with other undesired effluents, such as organic vapours (tars), sodium, potassium and chlorine compounds, ammonia and hydrocyanic acid (1). Particularly problematic is the behaviour of tars, whose content in the gas varies much from one process to another, from about 1 to 180g/Nm³. In order to burn this combustible gas in a second step, this concentration has to be lowered to only 50-500 mg/Nm³ or even brought to zero depending on the applications (1). Fixed-bed, countercurrent (updraft), and concurrent (downdraft) reactors are easier to construct and operate and less expensive than the fluid-bed reactors and present high carbon conversion, long residence times and low ash carry-over. The updraft process is more thermal efficient than the downdraft but the tar content of the gas is very high. However, low-temperature updraft tars are more reactive and thus easier to be removed, than the high-temperature tars produced in much lower amounts by downdraft gasifiers (1,2).

Very few studies on biomass gasification include the analysis of tars, partly because gases are the predominant product of gasification, but also because tars are far more difficult to sample and to analyse. Most of the information presently available on biomass derived tars has been obtained from pyrolysis studies at relatively low temperatures. In this study the main compounds of liquids products obtained under fixed-bed biomass gasification conditions, that is, low pyrolysis temperatures, has been determined by GC/MS analysis. The aim is to provide fundamental information for the formulation of a mechanism of tar formation and destruction during the gasification process, needed for the development of primary measures against tar problem.

EXPERIMENTAL

The liquids analysed in this study has been produced in a laboratory-scale gasification plant which has already been presented elsewhere (1). It consists of a cylindrical steel gasifier in which the biomass (beech wood particle in the tests of interest in this study) is fed at the top by means of a double-slide valve and air is fed at the bottom through a grate with small holes on its surface. Temperature profiles along the gasifier axis are measured by a set of thermocouples placed at different heights. The maximum temperature values (about 1250K for an air flow rate, W_a , of 1.56kg/h) was attained in the gasification/combustion zone, while in the upper section of the gasifier, where biomass devolatilization takes place, the temperature were rather low (580-850K). At the exit of the gasifier, the gas stream enters two condensers,

where steam and tars are condensed and collected at the bottom. The liquids samples have been maintained at low temperature ($<0^{\circ}\text{C}$) until the analysis to minimise degradation.

The liquids analysis has been performed by a Fision GC 8000/MD 800 system, with a quadrupole detector, using a DB-1701 capillary column (60m x 0.25mm i.d., 0.25 μm film thickness). Helium (99.9999%) was used as carrier gas with a constant flow of 1.0ml/min. The oven temperature was programmed from 45°C (4min) to 235°C at a heating rate of $3^{\circ}\text{C}/\text{min}$ and held at 235°C for 13min. The injector (Fision SSL 71) and the GC/MS interface were kept at a constant temperature of 250°C and 235°C respectively. A sample volume of $1\mu\text{l}$ of pyrolysis liquids (4.5% in acetone) were injected. The MS was operated in electron ionisation (EI) mode and the m/z range from 30 to 300 was scanned with a cycle time of 0.3s. Standard mass spectra with 70eV ionisation energy has been recorded.

RESULTS AND DISCUSSION

The total ion chromatogram (TIC) from GC/MS analysis of liquids produced in the laboratory-scale gasifier with an air flow rate (W_a) of 1.56kg/h, is shown in Fig.1. The peaks assignment correspond to the retention time (RT) of some identified compounds listed in Table 1. The identification of the peaks in the chromatograms has been based on computer matching of the mass spectra with the Wiley and NIST libraries, on GC retention times and on comparison with the compounds reported in the literature (5,6).

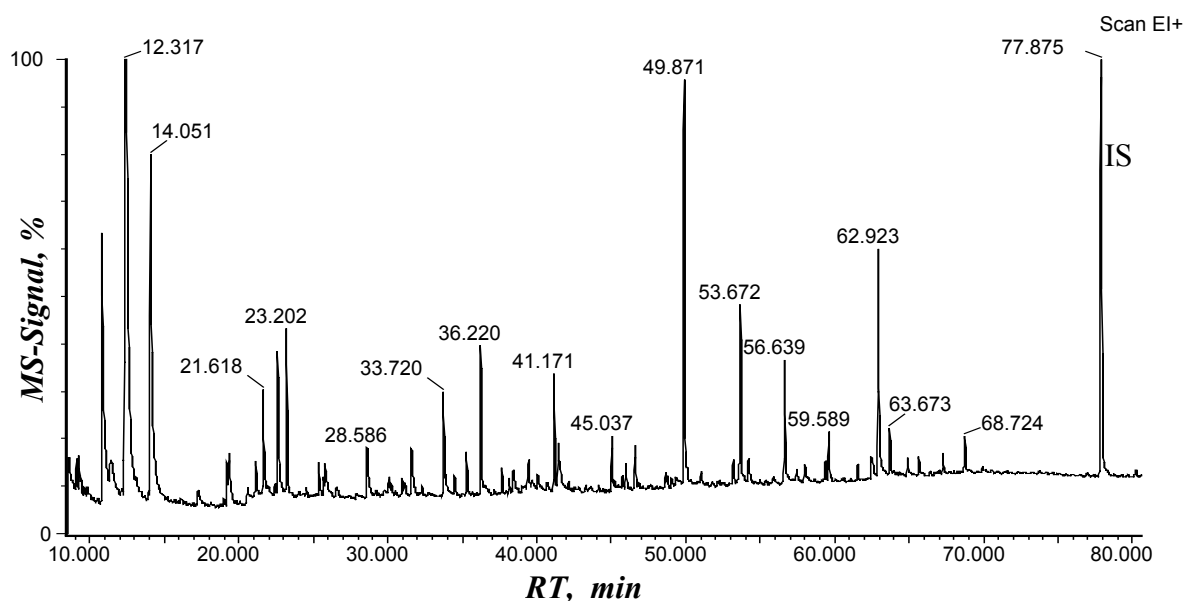


Fig. 1 Total ion chromatogram of tar derived from beech wood gasification ($W_a=1.56\text{kg/h}$) (IS indicates the internal standard peak) .

The chromatogram reflects the chemical complexity of the liquids which is a mixture of hundreds of phenolic and oxygenated etherocyclic compounds. According to previous studies (3), three major classes of tar products can be identified as result of gas-phase secondary reactions. For temperatures below 770K, primary pyrolysis products are constituted by fragments of monomers of the biopolymers of biomass (cellulose, hemicellulose and lignin). They are characterised by the presence of oxygenated compounds such as furane derivatives, carboxylic acids, alcohols, dihydroxyphenols and dimethoxyphenols, that give the primary tar a high reactivity. Beyond 770K, cracking of primary vapours leads to the formation of secondary products including low molecular weight aromatics, such as phenols and olefins.

ID N.	Compound	RT [min]	ID N.	Compound	RT [min]
1	Furan (i)	6.938	39	Phenol (i)	35.257
2	Ethylacetate (i)	9.058	40	Guaiacol (i)	36.220
3	2-Butanone	9.300	41	3-Ethylcyclopenten-2-en-1-one	36.686
4	Propionic acid methylester	9.517	42	o-Cresol (i)	37.622
5	3-Pentanone	9.734	43	2,6-Dimethylphenol (i)	38.369
6	Benzene (i)	10.069	44	p-Cresol (i)	39.337
7	Hydroxyacetaldehyde (i)	10.797	45	m-Cresol (i)	39.412
8	Formic acid (i)	11.468	46	4-Methyl guaiacol (i)	41.171
9	3-Buten-2-one-3-methyl	11.667	47	2,5 + 2,4-Dimethyl phenol	41.549
10	Acetic acid (i)	12.317	48	2,4,6-Trimethyl phenol	42.552
11	2,3-Pentanedione	13.051	49	3-Ethyl phenol	43.590
12	Acetol (i)	14.051	50	3,4-Dimethyl phenol (i)	44.623
13	Propionic acid (i)	17.184	51	4-Ethyl guaiacol	45.037
14	Cyclopentanone	18.918	52	1,4-3,6-dianhydro- α -D-glucopyranose	46.553
15	1-Hydroxy-2-butanone	19.253	53	4-Vinyl guaiacol	47.506
16	Methylacetate	19.251	54	3-Methoxy phenol (i)	48.036
17	Furantetrahydro-2,5-dimethoxy (cis) (i)	20.517	55	Eugenol (i)	48.606
18	2,3-Dimethylpentanal	21.568	56	2-Methoxy-4-propylphenol	48.737
19	Styrene	21.185	57	5-Hydroxymethyl-2-furaldehyde	49.237
20	Furantetrahydro-2,5-dimethoxy (trans) (i)	22.364	58	Catechol	49.603
21	2-Furaldehyde (i)	22.530	59	Syringol (i)	49.871
22	Ethylcaproate (i)	23.202	60	1,2,3-Trimethoxy-5-methylbenzene	50.020
23	Cyclohexanone (i)	24.735	61	Isoeugenol (cis) (i)	50.992
24	α -Angelicalactone (i)	24.787	62	3-Methyl catechol (i)	51.215
25	Furfuryl alcohol (i)	24.960	63	4-Methyl catechol (i)	52.885
26	Acetoxyacetone (i)	25.290	64	Isoeugenol (trans) (i)	53.138
27	2-Methyl-2-cyclopentenone (i)	25.636	65	4-Methyl syringol (i)	53.629
28	2-Acetylfuran (i)	26.483	66	Vanillin (i)	54.172
29	2,5-Hexanedione	29.169	67	Hydroquinone (i)	54.172
30	5-Methyl-2-furaldehyde (i)	30.012	68	4-Ethyl syringol	53.921
31	2-Acetyloxy-1-butanone	30.185	69	Acetoguaiacone	57.388
32	2,3-Dimethylcyclopenten-2-en-1-one	30.469	70	4-Aceton guaiacol (i)	59.322
33	3-Methyl-2-cyclopentenone (i)	30.875	71	4-Propenyl syringol (cis) (i)	61.490
34	(5H)-Furan-2-one (i)	31.546	72	Levogluconan (i)	62.923
35	3-Methyl-5H-furan-2-one	32.252	73	4-Propenyl syringol (trans) (i)	63.673
36	1-Cyclopenten-3-one-2-hydroxy-1-methyl	33.686	74	Syringaldehyde (i)	64.839
37	5-Methyl-5H-furan-2-one	33.836	75	Acetosyringone (i)	67.217
38	Acetophenone	34.719	76	Syringil acetone	68.724

Tab. 1 Results of identification by GC/MS of the compounds in the liquids derived from the beech wood gasification ($W_a=1.56\text{kg/h}$) ((i)=identification by injection of standard sample).

The yields of secondary tar components slight increase with temperatures up to around 1100K followed by more or less steep decrease with further increasing temperatures (3,4). At this

temperature, tertiary tar products appear. The dominant compound types in the tertiary tar class are aromatics which include alkyl aromatics, like naphthalene, anthracene, indene and condensed aromatics (PAH), derived from the polymerisation of low weight hydrocarbons. The liquids analysed in this study is a slight creaked tar dominated by primary pyrolysis products. In fact, due to the low operating temperatures of the updraft gasifier, only the more thermally labile products have been creaked and the tertiary products are totally absent (Table 1). The water content, determined by Karl Fisher volumetric titration method, has been found to be 47% wt of the total liquid mass. Prior to analysis the liquid samples have been filtered to remove any insoluble solids and diluted at 4.5% wt in acetone. Quantitative analysis has been carried out by internal standard (fluoranthene) method. It has been found that two main tar constituents are hydroxyacetaldehyde and levoglucosan, which derived from the decomposition products of cellulose according to two competitive reaction paths (5,6). At temperature of 623K, after a depolymerisation stage taking place between 423-523K, cellulose undergoes transglycosilation to form levoglucosan in high yields. However, the presence of alkali metal (like sodium or potassium) in the biomass inhibits the formation of levoglucosan and leads to different products in particular to hydroxyacetaldehyde (7). Other products present in large amounts are acetic acid and acetol, also carbohydrate-derived products. The less volatile products, corresponding to the peaks in the right part of the chromatogram in Fig.1 (retention time beyond 35min), comprise phenolic and methoxy-phenolic hydrocarbons which are related to the lignin building blocks. Lignin is a complex three-dimensional polymer of hydroxy/methoxy-phenylpropanoids (e.g. coniferyl alcohol) and its pyrolysis give rise to a variety of phenols, in particular para-substituted phenols. The main lignin-derived products in the analysed tar are guaiacol, 4-methylguaiacol, isoeugenol, syringol, eugenol, catechol. The presence of both syringyl and guaiacyl products is typical of the hardwood derived tars, while softwood yield mainly guaiacyl products (8). The secondary products identified are phenol and cresols which yields attain the maximum value at temperature of about 1000K.

CONCLUSIONS

Wood derived liquids obtained in condition of interest for biomass updraft gasification have been characterised by GC/MS analysis. The main components are oxygenated compounds including a variety of low molecular weight carboxylic acids, alcohols, furans (carbohydrate-derived products) and substituted phenols related to the lignin fraction of biomass. The analysis of the dependence of tar composition on pyrolysis conditions and the quantification of the main components are under way.

REFERENCES

1. Di Blasi C., Signorelli G., Portoricco G.: *Ind. Eng. Chem. Res.*, **38**:2571 (1999).
2. Di Blasi C., *Chem. Eng. Sci.*, **55**:2931 (2000).
3. Evans R.J., Milne T.A.: *Energy & Fuels*, **1**:123 (1987).
4. Di Blasi C., Signorelli G., Di Russo C., Rea G.: *Ind. Eng. Chem. Res.*, **38**:2216 (1999).
5. Di Blasi C. and Branca C.: *Ind. Eng. Chem. Res.*, **40**:5547 (2001).
6. Branca C. and Di Blasi C.: *J. Anal. Appl. Pyr.* in press (2002).
7. Di Blasi C., Branca C. and G. D'Errico: *Thermochimica Acta*, **364**:133,(2000).
8. Di Blasi C., Branca C., Santoro A., Perez Bermudez R. A.: *J. Anal. Appl. Pyr.*, **57**:77 (2001).

MODELLING THE COMBUSTION OF MOIST WOOD

A. Galgano

*Dipartimento di Ingegneria Chimica – Università di Napoli “Federico II”,
Naples – ITALY*

An integral model of wood devolatilization has been developed as a first step for a comprehensive combustion model. A sensitivity analysis has been carried out.

INTRODUCTION

Models of wood combustion are useful tools for the design of combustors and the understanding of fire growth. Several researchers studied experimentally and theoretically the transient pyrolysis and burning rates. Previous theoretical work based on numerical solutions can be classified into two categories (Moghtaderi et al.(1997)): detailed partial differential equation models as in Di Blasi (2000a), Di Blasi (2000b), Di Blasi (2002) and Jia et al. (1999), and integral models as in Chen et al. (1993), Moghtaderi et al. (1997) and Spearpoint and Quintiere (2000). Integral model results are generally less accurate than those obtained with detailed PDE models, but they have the advantage to be simpler and less time consuming, so their coupling with CFD models is more convenient.

A research activity is underway for the development of an integral model of wood combustion/gasification of moist wood to be coupled with a CFD code for the numerical simulation of small-scale boilers. The first part of the work, dealing with the devolatilization stage, is discussed here.

PHISICAL DESCRIPTION OF THE PROBLEM

When a wood sample is exposed to a radiative or convective heat flux, it undergoes several processes that can be classified as follows (Moghtaderi et al. (1997)): the preheat phase, the infinite body pyrolysis phase and the finite body pyrolysis phase. As long as the surface temperature is not sufficiently high for the degradation process to start, only heating occurs. Heat is transferred towards the interior of the solid by conduction, and the thickness of the layer, whose temperature is higher than the initial value, increases with time. Surface temperature rises until pyrolysis reaction begins, before the heat penetration depth reaches the centerline: this is the infinite body pyrolysis phase. As the reaction front proceeds, it leaves behind a char layer and volatiles in gas phase. The penetration depth increases until it reaches the centerline of the cylinder: this is the finite body pyrolysis phase.

MATHEMATICAL MODEL

Specific assumptions of the model are as follows: a) the process is one-dimensional in cylindrical coordinates along the radius direction; b) wood properties are constant; c) the material does not melt shrink/expand; d) char reactions are not taken into account; e) the conservation equation of energy for the char layer is stationary; f) a local thermal equilibrium between gas and solid material in the charred material is established; g) heat conduction processes are described by means of an effective thermal conductivity; h) an integral method is used for the solution of the transient energy balance in the virgin wood; i) pyrolysis reaction is kinetically controlled; j) the moisture content is negligible.

The energy equation along the dried wood region (and the related initial conditions) is written as:

$$c_d \rho_d \frac{\partial T_d}{\partial t} = \frac{1}{r} \frac{\partial}{\partial r} \left(r k_d \frac{\partial T_d}{\partial r} \right) \quad (1)$$

$$t = 0 \quad T_d(r, 0) = T_o \quad (1a)$$

The boundary conditions depend on the position of thermal penetration depth. In the preheat phase, the following equations can be written :

$$r = R_\delta \quad \frac{\partial T_d}{\partial r} = 0, \quad T_d(r \leq R_\delta, t) = T_o \quad (1b)$$

$$r = R_o \quad 2\pi L R_o k_d \frac{\partial T_d}{\partial r} = 2\pi L R_o \left[q_{\text{rad}} + h_c (T_{\text{inf}} - T_{\text{ds}}) + \varepsilon \sigma (T_{\text{inf}}^4 - T_{\text{ds}}^4) \right] \quad (1c)$$

In the infinitely thick pyrolysis phase, when the reaction front advances and the thermal penetration depth has not yet reached the centerline of the cylinder, the new boundary conditions are:

$$r = R_\delta \quad \frac{\partial T_d}{\partial r} = 0, \quad T_d(r \leq R_\delta, t) = T_o \quad (1d)$$

$$r = R_p \quad T_d(R_p, t) = T_c(R_p, t) \quad (1e)$$

When the penetration depth reaches the centerline of the cylinder, the boundary conditions reduce to:

$$r = 0 \quad \frac{\partial T_d}{\partial r} = 0 \quad (1f)$$

$$r = R_p \quad T_d(R_p, t) = T_c(R_p, t) \quad (1g)$$

The unsteady propagation of the pyrolysis front can be evaluated according to the following equation:

$$\frac{dR_p}{dt} = -Ae^{-\frac{E}{RT_d(R_p, t)}} \quad (2)$$

Thus the mass loss rate is obtained from:

$$\dot{m}_{\text{vol}} = -2\pi R_p L (\rho_d - \rho_c) \frac{dR_p}{dt} \quad (3)$$

The energy equation in char layer, according to the hypothesis of steady state, with the boundary conditions is:

$$\frac{1}{r} \frac{\partial}{\partial r} \left(r k_c \frac{\partial T_c}{\partial r} \right) - \frac{\partial}{\partial r} (r \rho_g u_g c_g T_c) = 0 \quad (4)$$

$$r = R_p \quad 2\pi L R_p k_c \frac{\partial T_c}{\partial r} = 2\pi L R_p k_d \frac{\partial T_d}{\partial r} - \dot{m}_{\text{vol}} \Delta H_{\text{vol}} \quad (4a)$$

$$r = R_o \quad 2\pi L R_o k_c \frac{\partial T_c}{\partial r} = 2\pi L R_o \left[q_{\text{rad}} + h_c (T_{\text{inf}} - T_{\text{cs}}) + \varepsilon \sigma (T_{\text{inf}}^4 - T_{\text{cs}}^4) \right] \quad (4b)$$

From the mass balance of the gas phase in the char layer and from the boundary condition at the pyrolysis front the following equations are obtained:

$$\frac{\partial}{\partial r} (r \rho_g u_g) = 0 \quad r \rho_g u_g = \frac{\dot{m}_{\text{vol}}}{2\pi L} \quad (5)$$

A quadratic temperature profile along the radius is assumed for the virgin wood. Quadratic temperature profiles have been found to yield satisfactory results for several moving boundary problems and high level heat fluxes (Agarwal et al. (1983), Moghtaderi et al. (1997), Janssens and White (1994)). This assumption give rise to three unknown coefficients (A_1, A_2, A_3):

$$T_d(r, t) = A_1 + A_2 \frac{r - R_\delta}{R_p - R_\delta} + A_3 \left(\frac{r - R_\delta}{R_p - R_\delta} \right)^2 \quad (6)$$

Moreover the thermal penetration depth has to be determined until the finite body pyrolysis phase begins. These variables are obtained by integration of Eqn (1) and by application of the related boundary conditions. A set of two ordinary differential equations is obtained for the evaluation of position and temperature of the pyrolysis front, whereas a non linear algebraic equation is solved for the evaluation of the surface temperature.

RESULTS

A parametric investigation has been carried out by means of the model developed. Thermal and physical properties used in the simulation are obtained from literature(Di Blasi (2000a), Di Blasi and Branca (2001)). Di Blasi et al. (2000) and Di Blasi et al (2001) made experiments of the radiative pyrolysis of beech wood cylinders with 4×10^{-2} m diameter and length, density of 728 kg/m^3 , heat radiation intensities comprised between 27.5 and 80 kW/m^2 . Spearpoint and Quintiere (2001) give absorptivity of dry wood variable in the range 0.60 and 0.72 , depending on the wood species. After thermal exposure begins, this value approaches unity, due to the darkening of the surface as it chars. The assumption that the emissivity is equal to the absorptivity is usually made. Specific heats for dry wood and volatiles are assumed to be respectively 1900 and 2000 J/kg K . thermal conductivity for wood and char are 0.23 and $0.32 \text{ W/m}^2 \text{ K}$, respectively. The heat of pyrolysis has been assumed to be 535 kJ/kg . Pre-exponential factor and activation temperature are $2.2 \times 10^6 \text{ m/s}$ and 17000 K , respectively.

In Fig.1 the effect of heat of pyrolysis on mass flux curve is parametrically shown for an external heat flux of 49 kW/m^2 . After a first period with no mass release (preheating phase), a peak appears owing to pyrolysis. Then the curves fall because of both the insulating effect of the char layer and the reduction of the reaction surface.

In Fig.2 the effects of different external heat flux on the mass loss are shown. As expected, as the heat flux is increased, the conversion process becomes faster and the mass flux peaks higher.

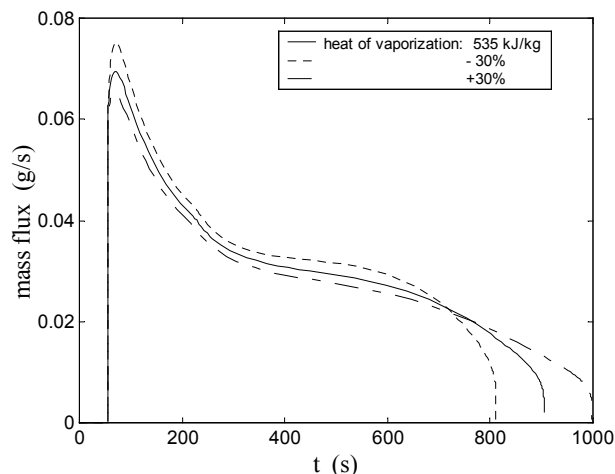


Figure 1. Simulations of the mass loss rate for beech at different values of heat of pyrolysis

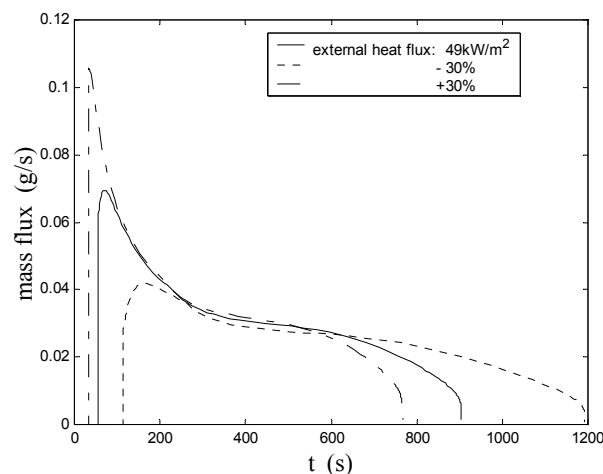


Figure 2. Simulations of the mass loss rate for beech at different values of external heat flux.

CONCLUSIONS

An integral model has been developed and applied to simulate the transient pyrolysis of wood cylinders. Results are qualitatively sound. Validation of the model against experimental data is under way.

REFERENCES

- 1) Agarwal P. K., Genetti W. E., Lee Y. Y., and Prasad S. N., *Fuel*, 63, 1019 (1984).
- 2) Bryden K. M., Ragland K. W. and Rutland C. J., *Biomass and Bioenergy*, 22, 41-53 (2002).
- 3) Chen Y., Delichatsios M. A. and Motevalli V., *Combust. Sci. and Tech.*, 88, 309-328 (1993).
- 4) Moghtaderi B., Novozhilov V., Fletcher D. and Kent J. H., *Fire and Materials*, 21,7-16 (1997).
- 5) Di Blasi C., *Polymer International*, 49, 1-14 (2000a).
- 6) Di Blasi C., *Chemical Engineering Science*, 55, 5999-6013 (2000b).
- 7) Di Blasi C., Hernandez E. G. and Santoro A., *Ind. Eng. Chem. Res.*, 39, 873-882 (2000).
- 8) Di Blasi C., Branca C., Santoro A. and Gonzalez Hernandez E., *Combustion and Flame*, 124, 165-177 (2001).
- 9) Di Blasi C. and Branca C., *Industrial & Engineering Chemistry Research*, 40, 5547-5556 (2001).
- 10) Di Blasi C., Modelling intra- and extra-particle processes of wood fast pyrolysis, *AIChE Journal*, in press 2002.
- 11) Janssens M. and White R. H., *Fire and Materials*, 18, 263 (1994).
- 12) Jia F., Galea E. R. and Patel M. K., *Fire and Materials*, 23, 71-78 (1999).
- 13) Spearpoint M. J. and Quintiere J. G., *Combustion and Flame*, 123, 308-324 (2000).
- 14) Spearpoint M. J. and Quintiere J. G., *Fire Safety Journal*, 36, 391-415 (2001).

Development of a Commercial FB Boiler for Combustion of Renewable Fuels at Small Scale

A. Cante¹, A. De Riccardis², C. Liccardi¹, F. Miccio¹, A. Silvestre¹

1 Istituto Ricerche sulla Combustione – CNR, Napoli (I), miccio@irc.na.cnr.it

2 Tekne srl, SP 328, 73013 Galatina LE (I), tkk.it@tiscalinet.it

INTRODUCTION

The utilization of non conventional fuels (wastes and biomass) poses a serious of disadvantages and problems during boiler operation, like fouling, slagging, ash melting, metal deposition on grids and tubes, agglomeration [1]. Fluidized bed technology seems to be preferable when low process temperature and tolerance toward fuel properties are a prerequisite for the thermal process. In general FB combustion ensures good performances in terms of process reliability, efficiency and emissions [2, 3]. Even if fluidized bed technology is widely applied for thermal processes, there are few commercial applications for combustion at very small scale (i.e. less than 500 kW_t) [3].

In the present work, among the large inventory of non conventional fuels two materials (i.e. olive husks and animal flours) are considered because they are of large interest for application in Italian rural areas.

Olive husks are a typical seasonal by-product of the olive oil industry. Olive husks (virgin or exhaust) are obtained during the production cycle of olive oil from the grinding and pressing of olives or chemical extraction of a residual oil. A further stage of drying is sometimes needed to produce a stable and storable granular material. Olive husks are allowed to be considered as fuel by virtue of a recent Italian normative (DPCM. 60, 12/02/2002).

Animal flours are a by-product of zoo-technical activity. They originate from a proper treatment of carcasses and entrails of slaughtered animals. Animal flours have been used in the past as an additive for animal food. As a consequence of the BSE emergency, such an utilization was forbidden by European and Italian laws. Recently, the utilization of animal flours as fuel to fire furnaces and boilers was allowed, under certain constraints provided by the Italian normative (GU 7/4/2001).

The present research is a cooperation between IRC/CNR and Tekne Srl, a SME operating in the south of Italy. It aims at developing an advanced boiler for the combustion of non conventional fuels. The boiler is based on fluidized bed technology and is conceived as a modular unit for operation also at very low power output (less than 100 kW_t).

EXPERIMENTAL

Experimental facility and technique

A prototype of a bubbling fluidized bed boiler has been designed, developed and built at Tekne Srl of Galatina (LE). The boiler, named TK359, was also recently submitted to the Italian Patent Office (Proposal N. LE-2001-A-000002). The fluidization column has an internal diameter of 300 mm and a total height of 2000 mm. It consists of two distinct sections made by stainless steel. In the bottom the plenum chamber and the air distributor are allocated. The air distributor is a perforated plate having 96 holes with a diameter of 2 mm. A horizontal, water-cooled, bayonet-type 30 mm OD tube is used for heat extraction in order to control the bed temperature. An internal axial cyclone allows de-dusting of the flue gases inside the combustion chamber and storage of separated particles in a collection tank.

The entire vessel is thermally insulated by means of a blanket of ceramic fiber. An optical window is available in the freeboard section of the combustor and allows to observe the surface of the fluidized bed and the presence of flames. Two air streams are normally used: the first one - primary air - fluidizes bed materials, the second one facilitates the transport of the fuel along the overbed feeding line. The fuel is under-bed fed by using an especially designed screw feeder, which is also able to avoid gas percolation from combustion chamber under a moderate pressure drop. Temperature and pressure probes are inserted in various points of the combustion chamber. The flue gases at the cyclone exit are analyzed on-line by means of a LAND (type LANCOM SERIES II) gas analyzer for multiple gaseous species (O_2 , CO, CO_2 , NO_x , C_nH_m).

During each steady-state run, the overall air flow rate was set at a prefixed value and constantly monitored by means of a rotameter; the flue gas concentrations and the set of temperatures were continuously recorded. At the end of the run, powders separated by the cyclone were collected.

Materials

A batch of about 30 kg of quartz sand with a nominal size of 1 mm was normally charged in the fluidization column. The fuels burned during combustion tests were olive husks (both virgin and exhaust) and animal flours. The chemical and physical properties of the fuels are reported in Table I. From the viewpoint of fuel characterization, all fuels exhibit a remarkably high volatiles fraction. A large difference in ash content can be noted between olive husks and animal flours. Virgin olive husks still have a large water content. Nitrogen content of animal flours is relevant. The heating value is that typical of biomass fuels.

Table I - Physical and chemical properties of fuels

Fuel:	Exhaust olive husks	Virgin olive husks	Animal flours
Density, kg/m^3	620	730	800
Low heating value (dry basis), $MJ\ kg^{-1}$	20300	23000	17500
Particle size range, mm	0 - 5	0 - 5	0-2.5
Ash melting temperature, °C			985
Proximate analysis			
Moisture, %	14.0	53.0	2.5
Volatiles (dry basis), %	77.1	79.0	66.0
Ash (dry basis), %	2.6	3.0	29.0
Fixed carbon (dry basis), %	20.3	18.0	5.0
Ultimate analysis (dry basis), %			
Carbon	49.7	52.8	37.0
Nitrogen	1.5	4.0	8.2
Hydrogen	6.1	6.9	5.9
Sulfur	0.0	0.0	0.0
Ash	2.6	3.0	29.0
Oxygen (by diff.)	40.1	33.3	19.9

RESULTS AND DISCUSSION

Tests of steady-state combustion were carried out at typical temperature of FBC, ranging between 800°C and about 860°C. Heat-up was accomplished by means of a pilot LPG burner located above the bed surface and, in parallel, introducing a further LPG stream in the plenum chamber. Since the air-LPG mixture ignites above the bed surface, the flame is

progressively shifted below as temperature increases, leading to a well mixing between flue gases and bed material. As a consequence the heat-up results very fast.

The boiler prototype was firstly fired with olive husks. The combustion was carried out smoothly and reliably, also in the case of virgin olive husks in spite of its huge water content. During combustion of dry olive husks, fuel particles were ignited as soon as they were dropped downward, large flames appeared in the freeboard and extended along the overall section. On the contrary, particles of virgin olive husks ignited only after they reached the bed and were mixed with hot bed solids. In turn, flames at bed surface had the appearance of relatively small and moving flares. The large content of water in virgin olive husks and the tendency to form aggregates of particles have to be considered responsible of longer ignition delay, which prevented the on-set of combustion before particles reached the bed surface.

The concentrations of carbon monoxide, nitrogen oxide and unburned hydrocarbons measured at combustor exit and normalized with reference to 11% oxygen in dry flue gases are reported in Fig. 1. Virgin olive husks exhibit higher concentration of all pollutants with respect to exhausts ones. The jump in CO emission, at a first analysis, might be related to changes that the much higher water content induces in residence time, fuel particle conversion and interaction with fluidized solids. Larger NO_x emissions for virgin olive husks are explained by considering the higher nitrogen content in this material. In Fig. 1 data are also reported concerning the combustion of virgin olive husks during operation with secondary air. The performance of the combustor resulted better in such a case, all concentrations of pollutants and unburned species being depressed. It is well known that the use of secondary air is a counter-measurement adopted to decrease NO_x emissions. Furthermore, the bed material was less intensively fluidized after splitting the air flow into two underbed and overbed streams. As a consequence, comminution phenomena are reduced and the residence time of gases in the bed is increased, resulting in a more efficient fuel conversion.

The low levels of CO concentration achieved during combustion of olive husks is also confirmed by a very low loss in efficiency due to the emissions of carbonaceous particulate at combustor exit. A sample of the ash collected at the cyclone was subjected to chemical analysis, giving C and H contents equal to 0.16 % and 0.01 % by mass, respectively. These low figures denote a very high conversion of combustible matters in the solid residue of the char by virtue of the high fuel reactivity.

Preliminary tests of animal flours combustion are currently in course. A part from a different tuning required to properly feed the combustion chamber, no dramatic consequences by utilization of a different fuel are noted. The fuel is quickly ignited as soon as it enters the combustor. Small and uniformly distributed flames appear above the bed surface. The temperature increase in the freeboard is moderate, denoting an improved combustion mechanism inside the bed, thanks to the very small particle size and the high reactivity. Further, the large thermal inertia of the fluidized bed ensures that the fuel is efficiently converted, even if the fuel feed rate is suddenly varied. This good response to load changing could represent a major advantage of fluidized bed with respect to traditional burners which experienced flame extinction with animal flours when the load varied and needed high furnace temperature in order to stabilize the flame.

Future developments of the research are:

- full characterization at laboratory scale of animal flours;
- complete grid of combustion tests using the boiler prototype;
- minimization of NO_x emissions for both olive husks and animal flours.

REFERENCES

- 1 Werther J., Sanger M., Hartg E.U., Ogada T., Siagi Z., Prog. Energy Combust. Sci. 26:1-27, 2000
- 2 Anthony, E. J.: Prog. Energy Combust. Sci. 21:239-268, 1995
- 3 Howard, J.R., "Fluidized Bed Technology, Adam Hilger Publ., Bristol, 1989
- 4 Trivett G.S., Field R.S. and Mackay G.D., Proc. of 6th Int. Symp. on Coal-Slurry Combustion and Technology, Orlando (FL), 1984

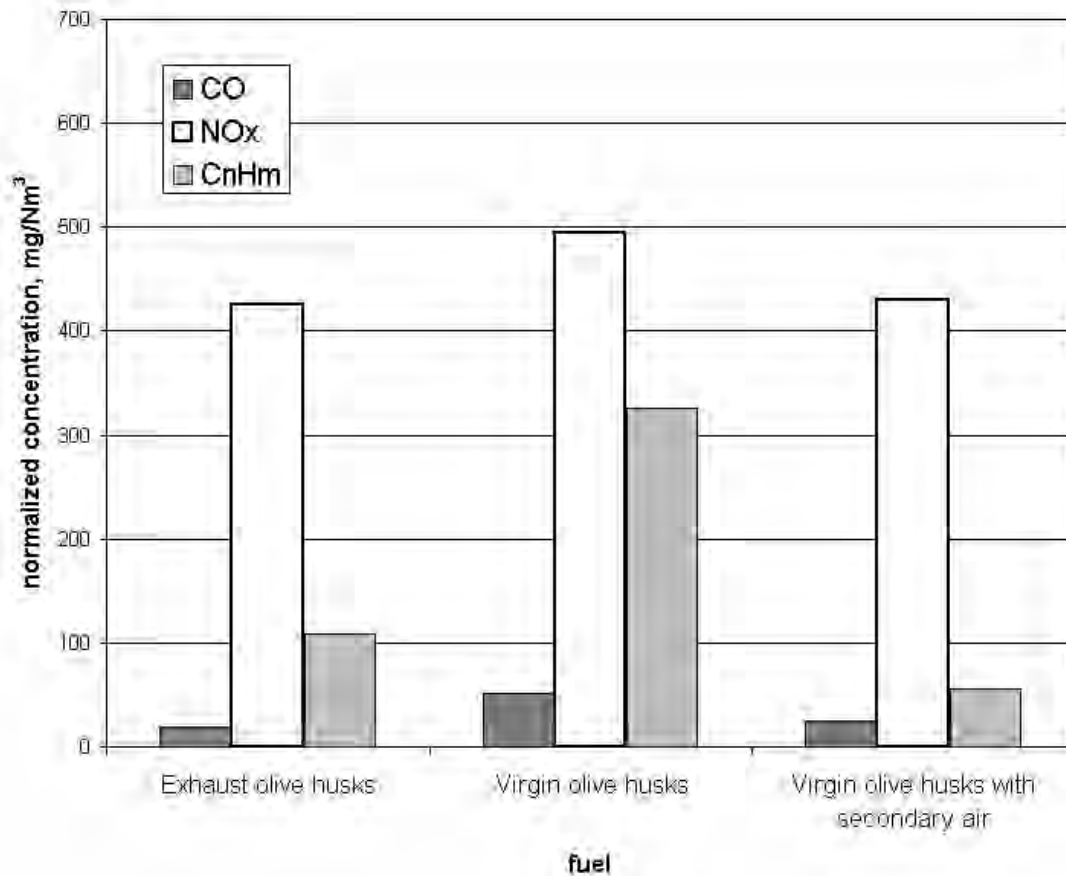


Fig. 1: Concentration of CO, NO_x and C_nH_m during combustion of olive husks under quite similar operating conditions

Char Combustion Kinetics of Biomasses: a Database for Industry

¹N. Rossi, ²M. Falcitelli, ¹P. Ghetti,

1 ENEL S.p.A. Produzione Ricerca, Via A. Pisano, 120 - 56122 Pisa – ITALY

2 Consorzio Pisa Ricerche - P.zza D'Ancona, 1 - 56126 Pisa – ITALY

INTRODUCTION

For both engineering calculations and detailed numerical simulations of coal and biomass fuel combustion processes, rate expressions are required that accurately describe the kinetics of the heterogeneous char oxidation reaction. A series of char oxidation kinetic investigations was recently completed in ENEL Produzione Ricerca laboratories for a suite of biomasses and lignitic coals in the frame of the “BIOFLAM” EU Project. The data set was acquired in a single experimental facility using a standardised experimental procedure (TGA for conversion rates, FRITSCH PARTICLE SIZER ANALYSETTE 22 for Char particle size distribution and CCSEM for morphology) and was analysed in a uniform way to facilitate comparison between chars. The data base consists of global char oxidation kinetic parameters, time-resolved release rates of organic elements and CCSEM scansions of both original biomass particles and derived chars. In the present paper the methodology and the results of the numerical analysis for determining the kinetic parameters are presented.

THEORETICAL MODEL

Char oxidation for small particle sizes (100 μm or less) under typical combustion conditions is controlled both by diffusion through the boundary layer and by reaction kinetics. The reaction products formed at the char surface are assumed to be CO according to the single film model [1]. The char combustion rate for a spherical char particle is therefore determined by the flux of oxygen through the boundary layer. By neglecting the Stephan flow (non-equimolar flow) one obtains

$$N_{O_2} = -C \cdot D_{O_2} \frac{dy_{O_2}}{dr} \quad (1)$$

where C is the total concentration ($C=P/(RT)$) and y_{O_2} , N_{O_2} , D_{O_2} are respectively the mole fraction, the molar flux and the diffusivity of oxygen. By integrating across the boundary layer thickness (δ) one obtains

$$N_{O_2} = \frac{-C_{av} \cdot D_{O_2}}{\delta} (y_{O_2,b} - y_{O_2,s}) \quad (2)$$

where $C_{av} = 2 \cdot P / (R [T_s + T_b])$ is C evaluated at the average particle and bulk gas temperature. By introducing the effective film ($\delta = d/Sh$) and the relation between oxygen flux and carbon flux ($N_{O_2} = -N_C / 2$ since the CO flux equals the carbon flux) one obtains

$$N_C = h_g (y_{O_2,b} - y_{O_2,s}) \quad (3)$$

where $h_g = 2 \cdot C_{av} \cdot D_{O_2} \cdot Sh/d$. The kinetics for char combustion is assumed to be of the first order and it can be described by a global reaction rate for the carbon flux [2]

$$N_C = k_s y_{O_2,s} P \quad (4)$$

where k_s is an Arrhenius expression for the apparent reaction rate. By combining equations (3) and (4) the solution for the carbon flux becomes

$$N_C = y_{O_2,b} \left(\frac{1}{h_g} + \frac{1}{Pk_s} \right)^{-1} \quad (5)$$

The rate constant defined by equation (4) refers to the early stages of combustion when deactivation of char reactivity and ash inhibition of char combustion are still negligible phenomena. In order to determine the kinetic constants for k_s , the conversion rate curves obtained with thermogravimetric analysis were employed. As equation (4) is worth for the early stages of combustion, only the conversion rate measured by the instrument at the first time step Δt was considered.

The conversion measured with TGA is the fractional weight loss of a sample of char due to the oxidation at different temperatures. It is related to the molar flux of carbon by the following equation

$$\frac{wt_loss(t = \Delta t)}{wt_0} = \frac{PM_C}{\rho_p^0} \sum_i p(r_i) N_C(r_i) \frac{S^0(r_i)}{V^0(r_i)} \Delta t \quad (6)$$

where ρ_p^0 is the overall particle density, $p(r_i)$ is the mass fraction of particles of radius r_i and $S_0(r_i)/V_0(r_i)$ is the ratio surface/volume for the particles of radius r_i .

For a spherical char particle, combining equations (5) and (6), the early stage conversion takes the following expression

$$\frac{wt_loss(t = \Delta t)}{wt_0} = 3 \frac{PM_C}{\rho_p^0} y_{O_2,b} \Delta t \sum_i \frac{p(r_i)}{r_i \left(\frac{1}{h_g} + \frac{1}{Pk_s} \right)} \quad (7)$$

For the numerical analysis of the data acquired, equation (7) plotted in function of the temperature was used and the kinetic parameters A and E_a of the Arrhenius

$$k_s = A \exp(-E_a / RT) \quad (8)$$

were determined as best fitting parameters. The parameters applied in the term accounting the diffusion effects h_g were: $Sh = 2$ and $D_{O_2} = 1.523 \cdot 10^{-9} T^{1.67} \text{ m}^2/\text{s}$, as calculated from Lennart-Jones potentials [1].

SUMMARY OF SELECTED EXPERIMENTAL RESULTS AND ANALYSIS

Table 1 summarises the kinetic results for each biomass, comprising in a unique set of combustion parameters. A sensitivity analysis was performed in order to understand the influence of some assumptions of the model on the values found for the kinetic constants. The

Sample Name	Elemen. Carbon Content (dry wt-%)	% ash	Char Density (kg/m ³)	Pre-exp. Factor, A (kg-carb m ⁻² s ⁻¹ atm ⁻¹)	Activation Energy E _a (kJ mol ⁻¹)
Brown Coal # 4052	63.66	4.61	496.12	4.1	130.1
Raw Wood # 4055	49.44	2.21	235.08	5.46 10 ⁻³	102.8
Cacao Pellets # 4056	47.05	7.68	227.23	0.80 10 ⁻³	82.4
Grinded Coal # 4057	71.21	14.84	692.99	100	164.2

Tab. 1 Char Combustion Parameters and Selected Properties for the Suite of Coals Investigated

values of activation energy E_a resulted to have a small dependency on the values of physical parameters such as density ρ_p^0 and shape factor (S^0/V^0) of the particles. Also the order of the reaction (4) was found to have a modest influence on the fitting values of E_a for all the chars. On the contrary the values of the pre-exponential factor A showed a strong dependence on the physical-chemical conditions cited above. Consequently the values of A extrapolated from the measures cannot be used separately from the assumptions of spherical shape for the char particles, first order reaction for char oxidation and the values of char density calculated by the proximate analysis by the following relation

$$\frac{1}{\rho_{char}^0} = \frac{1}{\rho_{org}} \frac{1 - x_{ash}}{x_{FC}} + \frac{1}{\rho_{ash}} \frac{x_{ash}}{x_{FC}} \quad (9)$$

For the apparent density of the organic fraction ρ_{org} and the ash density ρ_{ash} are assumed respectively the means values of 1200 kg/m³ and 2500 kg/m³.

Figure 1 shows the conversion after 1,08 s. versus the temperature for a selection of char investigated: for each char sample both measurements points and the fit curves produced by the numerical analysis are plotted. A pronounced trend is evident in Figure 1: for the two lignites, char reactivity increases with decreasing carbon content of the parent coal, while for the two biomasses that have the same content of carbon, the reactivity increases with decreasing ash content. Moreover, the analysis showed that under the experimental conditions (TGA), characterised by temperature values below those of pulverised coal flames, the oxidation rate of the chars examined is kinetically controlled.

CONCLUSION

The experimental and analytical activity carried out in the frame of the "BIOFLAM" EU Project produced a self-consistent kinetic data base for a suite of biomasses and lignitic coals. This would be an useful tool for both engineering calculations and detailed numerical simulations of coal and biomass fuel combustion processes. The kinetic parameters determined for the analysed samples refer to the early stage oxidation of the char particles, they can be employed within practical combustion codes based on empirical combustion models (CBK like) [3].

REFERENCES

1. Pedersen, L.S., Glarborg, P., Dam-Johansen, K., Hepburn, P.W. and Hesselmann, G.: *Combust. Sci. and Tech*, **132**:251-314 (1998).
2. Hurt, R.H. and Mitchell, R.E.: *24th Symp. (Int) on Combust.*, pp. 1243-1250 (1992).
3. Hurt, R.H., Sun, J-K. and Lunden, M.: *Combust. Flame*, **113**:181-197 (1998).

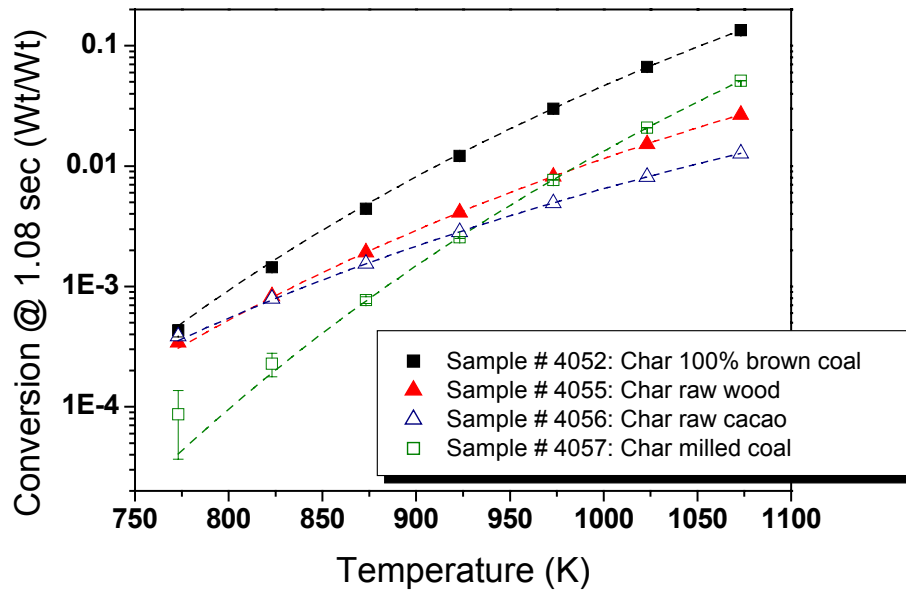


Fig. 1 Early stage conversion of char samples analysed with TGA. The fitting curves represent the equation (7) with the Arrhenius parameters of Table 1

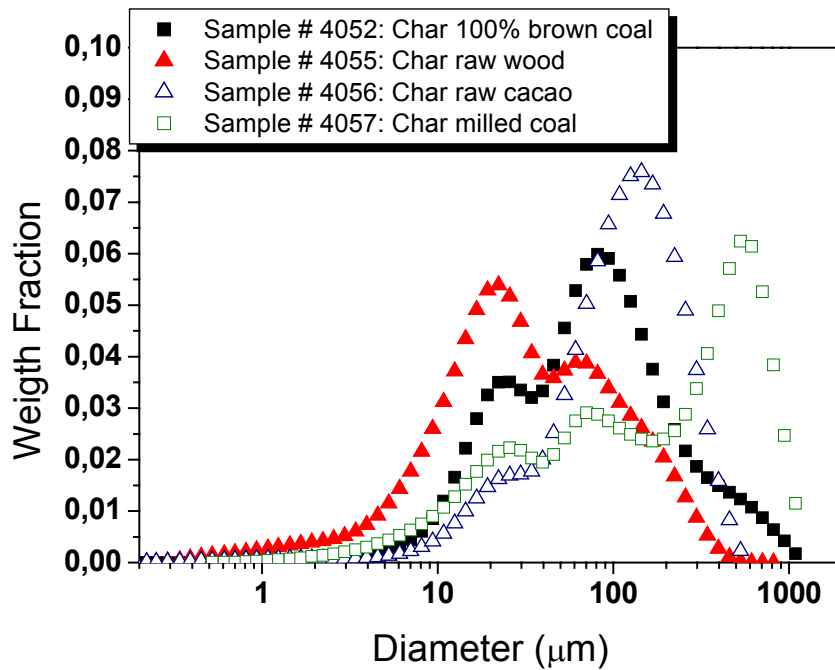


Fig. 2 Particle size distribution for char samples analysed.

Detailed surface chemistry and CFD simulation of CO catalytic combustion

M. Perini, S. Segato, H. Kusar*, P. Canu

DIPIC Università di Padova, Padua - Italy

*KTH, Dept. of Chemical Engineering and Technology, Stockholm – Sweden

INTRODUCTION

Surface reactions occur in a very broad range of industrial applications. Common features are extreme advantages in terms of severity of reaction conditions, increased yield, precise control of selectivity and poor understanding of the intrinsic kinetics. Catalytic combustion is a wide subset of such reactions with two major additional and specific features, i.e. exothermicity and extremely high reaction rate. Both inevitably lead to uneven temperature distribution and sustained auto-acceleration where adiabatic conditions prevail (very often, due to the rate of heat release), ultimately reaching a diffusion limited regime. There is a common need to develop intrinsic kinetics model for surface reactions (Dumesic *et al.* 1993) that could be reliably used in scaling up the processes. However, the validation of detailed mechanisms is often carried out with simplified reactor models, without a satisfactory evaluation of the influence of transport processes. The experimental investigation at short contact time, required to isolate intermediate and transient parts of the mechanism, is difficult to carry out under full control of physical and chemical processes. Modelling must properly account for local heat and mass transfer influences if intrinsic kinetics is sought. Critical use of 2D/3D models (Raja *et al.*, 2000; Deutschmann *et al.*, 1998) can serve the purpose, if satisfactory integration of detailed chemistry is obtained. CO catalytic combustion is a good model reaction to discuss these features. It is very exothermic and fast, almost without by-products. It constitutes a common subset of any carbon-based fuel and its impact is enormous, because of the application in the automotive industry. At the same time, its chemistry is relatively simple, so that a detailed mechanism is still manageable and relatively easy to understand in its operations. Moreover, the role of each step in the mechanism is best seen operating at short contact time. From this point of view, annular reactors are a good option (Beretta *et al.* 1999), that we used to obtain experimental data of CO oxidation on Pt/MgAl₂O₄. In this contribution both aspects of detailed surface mechanism and detailed description of the composition, flow, and temperature fields are addressed.

EXPERIMENTAL APPARATUS

The discussion in the following is based on some experimental data obtained in an annular reactor, developed and characterized at KTH. The reactor consists of an external quartz-tube with a second coaxial mullite tube inside. A thermocouple is placed inside the internal tube to report the catalyst surface temperature. Most of the reactor (0.325 m out of a total length of 0.45 m) is placed inside an oven. The reacting mixture flows in the annular chamber between the two coaxial tubes and reaches the catalyst layer after 0.18 m of heating length. The catalyst used was Pt/MgAl₂O₄ and it was washcoated on the mullite tube for a short length (0.03 m). Tests are carried out in a close sequence, by gradually increasing the oven temperature (3°K/min), allowing to collect a large number of data for several catalyst inlet temperature. Typically, results are obtained as outlet gas composition and catalyst temperature measurements, varying the feed composition and temperature. The feed mixture

Table 1 Gas and surface mechanism for CO/O₂ reaction. $k = A T^b \exp(-E/RT)$. Total site density = $2.7 \cdot 10^{-9}$ moles/cm². Sticking rate expression are in the Motz-Wise form.

		A (mol,cm,s)	b	E (kJ/mol)
G1	CO+O+M=CO ₂ +M	3.20E+13	0	-17.6
G2	CO+O ₂ =CO ₂ +O	1.60E+13	0	171.6
S1	O ₂ +2Pt(S) => 2O(S)	1.80E+21	-0.5	0
S2	O ₂ +2Pt(S) => 2O(S)	0.023 (stick)	0	0
S3	2O(S) => O ₂ +2Pt(S)	3.70E+21	0	213.2
	Coverage parameters for O(S): 0, 0, -60			
S4	O+Pt(S) => O(S)	1.0 (stick)	0	0
S5	CO+Pt(S) => CO(S)	0.84 (stick)	0	0
	Coverage parameters for Pt(S): 0, 1, 0			
S6	CO(S) => CO+Pt(S)	1.00E+13	0	125.5
S7	CO(S)+O(S) => CO ₂ +2Pt(S)	3.70E+21	0	105.0
S8	CO(S)+Pt(S) => C(S)+O(S)	1.00E+18	0	184.0
S9	C(S)+O(S) => CO(S)+Pt(S)	3.70E+21	0	62.8

was always CO in air, at 0.5, 1 and 2%vol. The effect of water in the inlet mixture has also been investigated. Total inlet flow rate has been varied between 0.7 and 2 L/min. Residence time varied between 5.44 ms (2L/min @ 773°K) and 25.35 ms (0.7 L/min @ 473°K).

The experimental data indicate an exponential growth of conversion with increasing inlet temperature, typical of ignition phenomena, and the reach of a maximum rate at high temperature, independently of the mixture fed, marking the onset of a diffusion limited regime. The most important feature shown by the experimental data is the negative effect of CO on the ignition temperature. A larger amount of CO in the feed mixture requires a higher temperature to reach the same degree of conversion.

RESULTS AND DISCUSSION

The experimental data are used in the following to compare and tune the prediction of a detailed surface mechanism. Two issues have been addressed independently, as a first step in the investigation: the actual operating features of the chemical mechanism and the role of transport processes. The mechanism has been investigated through a plug-flow, ideal reactor model. The concentration and temperature distribution are evaluated by means of a CFD code, with simplified chemistry. Eventually, both pieces will merge.

The surface mechanism

Considering that annular reactor can be operated isothermally, our first approach to simulate the data was a simple isothermal plug-flow reactor (PFR) model. The PLUG implementation of such reactor model inside the CHEMKIN 3.6 package has been used since it provides an context to easily test detailed mechanisms. The operating features of the many steps can be discussed and compared. The kinetic mechanism used was extracted from the one of Deutschmann for methane combustion (Deutschmann *et al.*, 2000). Such a mechanism is often quoted as a reference for catalytic combustion of CH₄/air mixture, with some parameter modification not always explained and even misinterpretation (same parameter values, used with different units). The CO subset used here and the corresponding kinetic parameters are reported in Tab. 1. Since the surface mechanism accounts also for oxygen radical adsorption, two reversible reaction in the gas phase that involve radical O has been included, with literature values for the kinetic parameters. It must be recalled that the PFR model does not account for any diffusion process, so its predictions can be compared only to the data where chemical regime prevails. The PFR can also attain a complete conversion, while the

experimental data hardly increase the conversion above the diffusion limited threshold. Results with the literature mechanism severely underestimate the measured values, notwithstanding the total site density used, which is closer to pure Pt than supported one. Moreover, calculations indicate an earlier ignition as the inlet CO increases, contrasting the experimental evidences. In addition, at high CO concentration, calculations show a kink in the conversion vs. T curves close to 25% conversion, apparently dividing two chemical regimes. Eventually, both aspects were explained by the same features of the mechanism, identified through a sensitivity analysis. We varied the pre-exponential factors of each reaction in turn, monitoring the relative effect on the concentration of each species along the reactor. The results (Fig. 1, left) clearly identifies the adsorption/desorption reactions as the key to determine the CO conversion values.

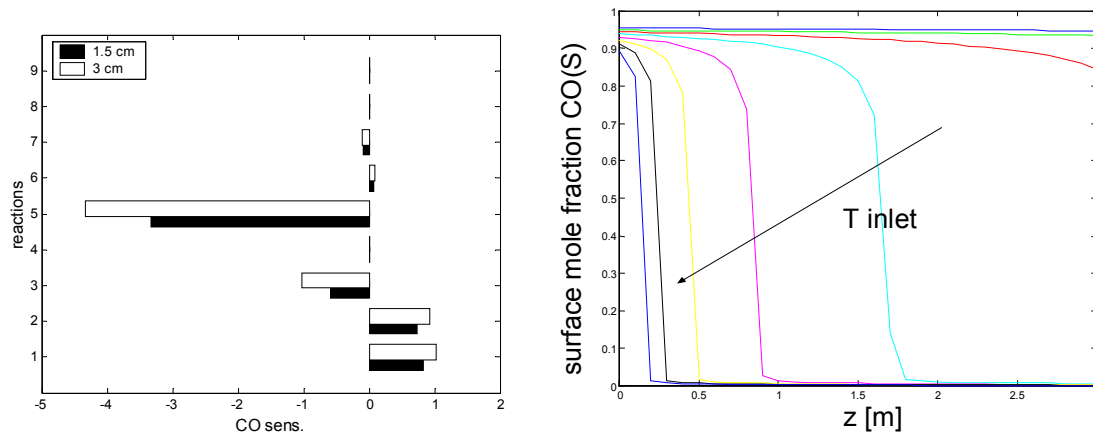


Fig. 1 Relative sensitivity of CO at 500 C, left; CO(S) along the catalyst, right. 2% $[CO]_{in}$.

The competition between CO and O₂ for the surface sites is crucial to determine the ignition behavior. Weakening the O₂ adsorption rate by varying literature parameters leads to a totally different behavior, so that the effect of varying the inlet CO concentration can agree qualitatively with the experiments. Apparently, literature parameters overestimate the adsorption of oxygen with respect to CO, and the overall combustion rate takes advantage of any increase of CO in the gas stream (i.e the literature mechanism predicts a reaction that is starving CO). Although apparently intuitive, it does not reflect the actual behavior of the experimental data. Allowing for a larger surface concentration of CO by altering the adsorption/desorption rates of oxygen, can indeed predict an inhibition by CO. In addition, a weaker O₂ adsorption determines sharp bends in the curves, now predicted for any inlet concentration. A closer inspection to the simulation results at each temperature reveals interesting features of the mechanism. Observing the species concentration profiles along the reactor, one can notice that the surface coverage is dominated by O(S) at small CO concentration, with a surface mole fraction approaching 1. With a larger amount of CO in the gas, the surface occupancy can be reversed, with a dominance of CO(S) up to the point where the CO gas concentration drops below a critical value, as shown in Fig. 1 (right). A sudden switch takes place at a given point in the reactor, from a CO(S) dominated surface to one where O(S) is the most abundant surface intermediate, and again the reaction becomes starving CO(S). The switching point progressively shifts toward the reactor inlet, as the temperature increases. From this point onward, until the end of the reactor, the conversion rate is extremely slow. The circumstances that trigger the sudden change of surface coverage can not be related simply to the temperature, as observed in Fig. 3, but the local concentration plays a role as well. At this switch there is a change in the chemistry of the reaction, resulting in sharp bends on the calculated conversion vs. T curves. By arbitrarily modifying the adsorption/desorption rates of oxygen, we delayed the onset of the regime in which CO is

lacking on the surface, resulting in some better agreement with our experimental data. Once O(S) has gained most of the surface sites, the overall kinetics is completely different, like a totally new reaction. Tuning the parameters in the detailed mechanism to our experimental data, something similar to the kink experimentally observed can be explained, through purely chemical arguments. Note also that the two chemical regime imply that a few parameters are actually significant under different conditions. It can be concluded that CO or O₂ cover the whole surface, the mole fraction of Pt(S) (unoccupied surface sites) and C(S) being always small. The coverage can be totally shifted from CO(S) to O(S), each one using all the surface sites, depending on the amount of CO in the gas phase. The literature parameters fail to predict the process quantitatively, ultimately resulting in wrong qualitative behavior.

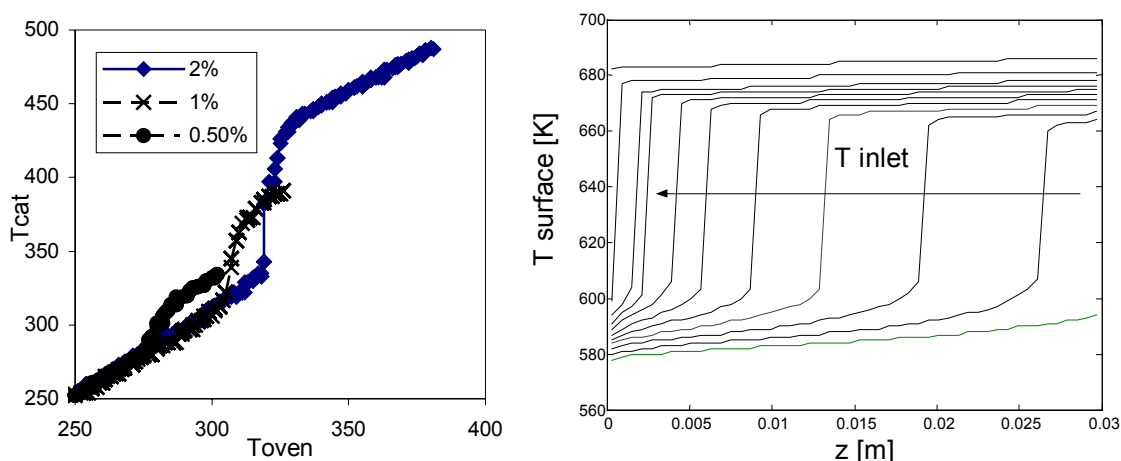


Fig. 2 Temperature at the surface. Measured vs oven temperature, left; predicted, right.

The reactor model

In order to evaluate the appropriate model for the annular reactor used, the temperature on the catalyst surface has been compared with that of the oven. Results are shown in Fig. 2 (left) and clearly indicate that a sharp temperature rise follows the ignition, notwithstanding the small surface-to-volume ratio. Quantitative analysis demonstrated that 0.5 and 1% inlet CO result in a completely adiabatic operation, while 2% requires a higher temperature to ignite, resulting in some heat loss by radiation from the catalyst surface towards the oven itself. A more detailed analysis of temperature and species distribution along the annular chamber has been carried out by means of a commercial CFD code (CFX, AEA Tech.) successfully modified (Canu, 2001) to simulate surface reactions with simplified chemistry. The 2D model confirms the existence of an ignition front that begins at the reactor outlet and regresses towards the inlet. As shown in Fig. 2 (right) the catalyst surface temperature is extremely uneven along the length, and that causes radial gradients as well. It can be concluded that the reactor requires a complete 2D model within which an appropriate surface mechanism must be included and properly analyzed.

REFERENCES

- Dumesic J.A., D.F. Rudd, *et al.*, *The Microkinetics of Heterogeneous Catalysis*, ACS, 1993.
 Raja, L. L., R. J. Kee, O. Deutschmann, J. Warnatz, L. Schmidt, *Catal. Today*, **59**, 47 (2000).
 Deutschmann, O., F. Behrendt, and J. Warnatz, *Catal. Today*, **46** 155 (1998).
 Deutschmann O., Maier I., Riedel U., Stroemann A., Dibble, R. *Catal. Today*, **59** (2000) 141.
 Canu P., *Catal. Today*, **64** (2001) 239.
 Beretta A., Groppi G., Majocchi L., and Forzatti, P. *App. Catal. A: General*, **187**, (1999) 49.

Mechanisms and Kinetics of Catalytic Combustion of Diesel Soot

Debora Fino*, Paolo Fino, Guido Saracco, Vito Specchia

Dipartimento di Scienza dei Materiali ed Ingegneria Chimica,
Politecnico di Torino, Corso Duca degli Abruzzi 24, 10129 Torino, Italy.

*corresponding author: tel./fax: +39-011-5644666/99; e-mail: dfino@athena.polito.it

INTRODUCTION

Catalytic traps are potential candidates for the reduction of Diesel particulate emissions [1]. The catalyst deposited in such devices should lower the soot ignition temperature (about 600°C for non-catalytic combustion) down to the values characteristic of Diesel exhaust gases (180-350°C) so as to enable self-regeneration of the traps. Earlier studies carried out at Politecnico di Torino concerned the development of soot combustion catalysts based on Cs and V oxides for catalytic foam traps [2,3]. Owing to the dynamic nature of the drive, any modelling and design effort of such reactor should take into account proper kinetics for catalytic soot combustion. The aim of this work is to define an intrinsic kinetic law of catalytic soot oxidation with particular reference to the role of mobile catalyst species on the reaction. This law should be markedly influenced by the catalyst-soot contact conditions.

In Fig. 1 the possible contact conditions for non-mobile (such as noble metals, perovskites or CsVO₃) and mobile (e.g. Cs₂O·V₂O₅) catalysts are sketched. As reported in Fig. 1.a, in case of a non-mobile catalyst, the catalytic effect is limited to few contact points between soot and solid catalyst. Conversely, it is enlightened that three different mobility mechanisms and two kinds of indirect catalysis may exist. Catalysts forming volatile compounds at their operating temperatures (e.g. KI coupled with KVO₃, which releases I₂ [4]) operate through a gas-phase transport (Fig. 1.b), whereas catalysts forming liquids (e.g. Cs₂O·V₂O₅), enable a liquid-phase transport of active species. The first option is not interesting as loss of catalyst is actually unavoidable. Conversely, liquid-phase mobility seems to have potential of practical application, provided the catalyst shows low volatility, high viscosity and good filter-material wettability, so as to remain in the filter despite the drag force exerted by the gases.

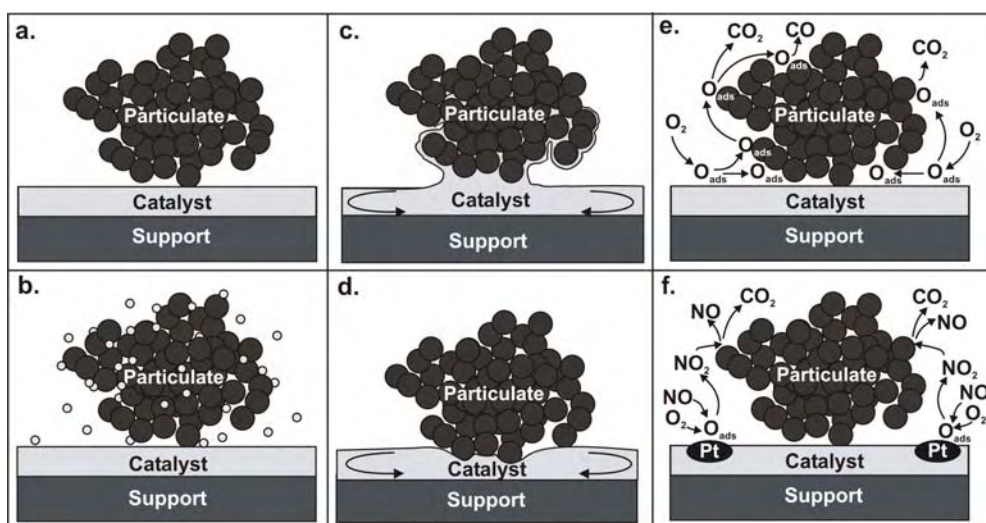


Fig. 1. Catalyst-particulate interactions a. non-mobile catalyst; b. gas-phase mobile catalyst; c. wetting mobile catalyst; d. non-wetting mobile catalyst; e. catalyst promoting oxygen spillover; f. catalyst coupling a NO/NO₂ functionality (indirect catalysis).

In this case it is also possible to distinguish a wetting or non-wetting state: as shown in Fig. 1.c, the catalyst, thanks to favourable surface tension conditions and capillarity forces, can move towards soot agglomerate wetting the entire particulate surface. In a complete non-wetting situation (Fig. 1.d), the formation of eutectic liquids allows the catalyst to rapidly offer new catalytic species to diesel particulate during its combustion. Otherwise, some catalysts can oxidize soot without having intimate physical contact. They catalyse the formation of mobile oxidising species that are more reactive than O_2 . Two main reaction mechanisms are known for indirect-contact catalysts: oxygen spillover and NO_x -aided gas-phase mechanism. Some catalysts can dissociate oxygen and transfer it to the soot particle by spillover [1]. Conversely, Pt can oxidise NO to NO_2 , which is transported via the gas phase over soot particles to oxidize carbon while being reduced to NO [5].

DETERMINATION OF KINETICS AND RELATED PARAMETERS

A kinetic law for diesel particulate catalytic combustion should account for several parameters: e.g. oxygen concentration in the gaseous phase, temperature. The following Arrhenius type reaction rate expression can be proposed. Previous investigations [6] showed that an Arrhenius type expression including power-law dependence on the oxygen partial pressure holds for most diesel combustion catalysts:

$$r = k_{\infty} \exp\left(-\frac{E_a}{RT}\right) p_{O_2}^{\beta} \quad (1)$$

where: p_{O_2} = oxygen concentration; β = reaction order; T = temperature; k_{∞} = pre-exponential constant; E_a = activation energy; R = gas constant.

There are no standard methods of testing the soot oxidation activity of a catalyst and the type of contact applied in each specific study becomes very important. When the soot and catalyst powders are mixed with a spatula the contact mode is *loose* (as to simulate the contact conditions typical of the trap). When mixing is carried out with a mechanical mill, it is possible to define a *tight contact* condition (as to define an intrinsic catalytic activity under optimal contact conditions). It is clear that the performance of a catalyst mixed with soot in tight mode cannot reproduce the tests of real diesel engine and the contact conditions that take place in a trap. On the other hand, it is necessary to perform kinetic and mechanism studies in tight contact so as to establish a good reproducibility of the experiments and determine intrinsic kinetic parameters.

Differential scanning calorimetry (DSC) was performed on mixtures of three catalysts ($CsVO_3$, $Cs_4V_2O_7$, $Cs_2O \cdot V_2O_5$, selected for their prevalent activity) with carbon to measure the heat released as an index of the evolution of catalytic combustion. By varying the temperature rise rate employed from 50 to 720 °C, the activation energies could be evaluated via the Ozawa method [7]. By these means the half conversion temperatures ($T_{50\%}$) were also recorded as an index of catalytic activity. Isothermal reaction (ITR) tests were carried out so as to evaluate K_{∞} and β , using catalyst/carbon mixtures placed in a micro-reactor between two quartz wool layers. The reactor was heated via a PID-regulated electric oven; the temperature was raised up to a constant operating value (in the range 300-450 °C) under helium flow. The reacting gas (characterised by different O_2 concentrations in He: e.g. 5, 2.5 and 1 vol%) was then fed to the micro reactor at the constant rate of 50 ml/min. The carbon dioxide concentration in the gas flowing outlet the micro reactor was analysed by a CO_2 NDIR analyser. The fraction of carbon converted per unit time (r) was calculated for each catalyst and p_{O_2} level at equal carbon-to-catalyst ratios and temperature values.

The reaction order β can instead be derived from ITR data obtained at different p_{O_2} values. The rate of carbon converted per unit time (r) can be calculated for each catalyst and p_{O_2} value

via a simple carbon mass balance, at equal carbon-to-catalyst ratios and temperature values. Hence, β and k_{∞} can be evaluated from the slope and the y-axis intercept of the least-squares fitting line of semi-logarithmic data plots. Conversely, k_{∞} is a function of the catalyst and carbon particle size as well as of the relative amount of such components in the reactants mixture. At least for the cases represented in Fig. 1.a and 1.d k_{∞} is proportional to the number of contact points between carbon and catalyst particles.

Carbon wettability studies were finally carried out inside the oven of an heating microscope by preparing a tablet of graphite above which a small sample of catalyst was placed. The temperature was raised from room temperature up to melting point and beyond with a heating rate of $5\text{ }^{\circ}\text{C}\cdot\text{min}^{-1}$, meanwhile monitoring the contact angle between catalyst and carbon by direct observation.

RESULTS & DISCUSSION

As far as the comparative analysis of the activity of the catalysts towards soot combustion, the TPR curves plotted in Fig. 2 show that all catalysts significantly shift the combustion temperature range towards temperature values lower than those typical of non-catalytic combustion. The activity order in *tight-contact* conditions is $\text{Cs}_4\text{V}_2\text{O}_7 > \text{Cs}_2\text{O}\cdot\text{V}_2\text{O}_5 > \text{CsVO}_3$. The superior activity of cesium pyrovanadate, melting at $870\text{ }^{\circ}\text{C}$, is likely to be attributed to its capability of promoting oxygen spillover (Fig. 1.e)[1]. High mobility of oxygen species is related to the high oxygen-to-vanadium ratio of this compound compared to its two counter parts. Furthermore, the high electro-positivity of cesium (pyrovanadate has the highest Cs-to-V ratio among the considered catalysts) entails an electron-donating effect which should further weaken the stability of V=O bonds [8]. The good catalytic activity shown by the $\text{Cs}_2\text{O}\cdot\text{V}_2\text{O}_5$ is conversely related to its capability of producing a eutectic liquid among its compounds already at $380\text{ }^{\circ}\text{C}$ [9] as confirmed by a specific DSC run performed with the catalyst alone. As mentioned earlier, a specific test was carried out in a heated optical microscope in order to better enlighten whether such a liquid phase was capable of wetting or not the soot (Fig. 1.c or 1.d).

Fig. 3 shows the occurrence of liquid formation when the related temperature is overpassed ($390\text{ }^{\circ}\text{C}$) and that the derived liquid cannot wet the carbon (see the picture taken at $420\text{ }^{\circ}\text{C}$). Hence, the type of contact conditions between the $\text{Cs}_2\text{O}\cdot\text{V}_2\text{O}_5$ eutectic liquid and carbon are those depicted in Fig. 1.d. Conversely, the melting temperature of the less-active CsVO_3 ($641\text{ }^{\circ}\text{C}$) is too high to let liquid formation affect the evolution of carbon combustion, which should be thus governed by the mechanisms depicted in Figs. 1.a and 1.e.

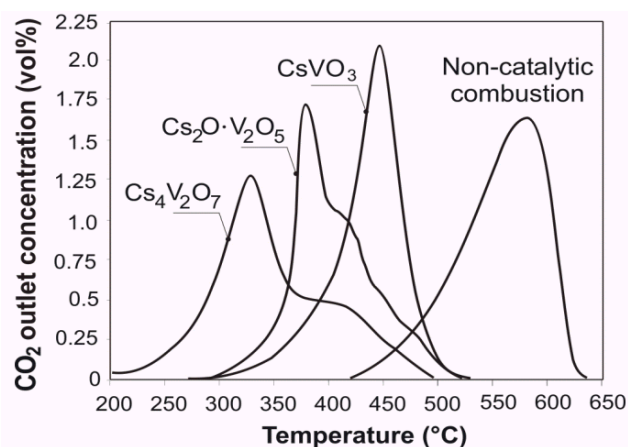


Fig. 2. TPR runs performed with $\text{Cs}_4\text{V}_2\text{O}_7$, $\text{Cs}_2\text{O}\cdot\text{V}_2\text{O}_5$ and CsVO_3 catalysts; non-catalytic carbon combustion is also considered for a comparison.

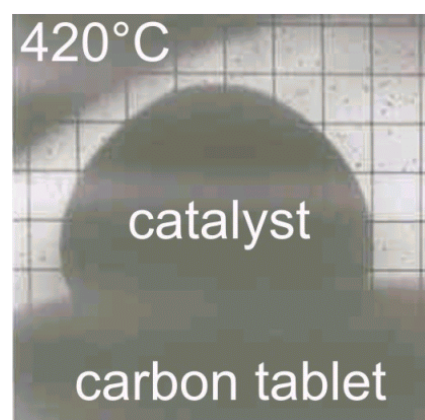


Fig. 3. Picture of a $\text{Cs}_2\text{O}\cdot\text{V}_2\text{O}_5$ catalyst sample obtained in a thermal microscope in calm air at $420\text{ }^{\circ}\text{C}$ (i.e. above the catalyst melting temperature).

Table 1. Prevalent kinetic parameters derived for the different catalysts by use of amorphous carbon as a particulate source.

Catalysts	k_{∞} ($s^{-1}Pa^{-\beta}$)	β	E_a (J/mol) *
CsVO ₃	4.15	1	104
Cs ₄ V ₂ O ₇	10.3	0.68	75
Cs ₂ O·V ₂ O ₅	3811	0.79	123

*non-catalytic diesel soot combustion: 157 kJ/mol

Shifting to the analysis of kinetic data, Table 1 lists the values of the kinetic parameters determined for the combustion of amorphous carbon. The E_a obtained for all the catalysts are much lower than the E_a of non catalytic combustion. The Cs₄V₂O₇ has a very low E_a value, less than half of the non catalytic combustion, which, at least in part justifies its rather low $T_{50\%}$ value. This catalyst should act as an oxygen pump towards carbon, as entailed by its rather low β value, an index of oxygen chemisorption from the atmosphere, according to the Langmuir-Hinshelwood type mechanism. This feature is shared also by another quite active catalyst, Cs₂O·V₂O₅, whose activation energy is surprisingly not as low as it could have been expected. This last catalyst owes its superior activity to a very large k_{∞} factor, a sign of very good contact conditions between its active sites and carbon. Through specific DSC runs carried out in the absence of carbon, this catalyst was in fact found to form low melting point eutectic liquids between its oxide components, which increase the wettability of soot by the catalytic species. Hence, the definition of *mobile* for this catalyst. Since its stability is good (reduced volatilisation and solubility in water; much lower than the Cs₄V₂O₇ one) this mobile catalyst has good potential for application in catalytic traps.

CONCLUSIONS

A mechanism and kinetic analysis has been carried out for three of the most promising catalysts (Cs₂O·V₂O₅, Cs₄V₂O₇, CVO₃) for application in catalytic traps for diesel particulate removal. It has been enlightened that beyond the intrinsic activity of the catalytic species (excellent for the Cs₄V₂O₇ catalyst), their mobility, achieved by the Cs₂O·V₂O₅ via eutectic liquid formation, is a quite important requisite for practical application as a coating for diesel traps. Nevertheless, the application of mobile catalysts for the after-treatment of diesel exhausts requires a careful evaluation of their stability. The severe operating conditions characteristic of the exhaust line of (temperature peaks, high space velocities, etc.) might lead to loss of active compounds by drag or by evaporation. Some encouraging preliminary tests on catalytic foam traps lined Cs₂O·V₂O₅ show only a limited and acceptable catalyst deactivation of this catalyst after prolonged use.

Finally, the derived kinetic expressions are currently being employed in numerical models for the design optimization of this complex type of multifunctional reactor.

REFERENCES

1. van Setten, B.A.A.L., Makkee, M., Moulijn, J.A.: *Catal. Rev. Sci. Eng.*, **43** : 489 (2001).
2. Saracco, G., Badini, C., Russo, N., Specchia, V.: *Appl. Catal. B: Env.*, **21**: 233 (1999).
3. Badini, C., Saracco, G., Russo, N., Specchia, V.: *Catal. Lett.*, **69**: 207 (2000).
4. Badini, C., Saracco, G., Specchia, V.: *Catalysis Letters*, **55**: 201 (1998).
5. Liu, S., Obuchi, A., Uchisawa, O.-J., Nanba, T., Kushiyama, S.: *App. Cat. B. Env.*, **30**: 259 (2001).
6. Ciambelli, P., Corbo, P., Gambino, M., Palma, V., Vaccaro, S.: *Cat. Today*, **27**: 99 (1996).
7. Ozawa T.: *J. Thermal Anal.*, **2**: 301 (1970).
8. Mross, W.D.: *Catal. Rev.-Sci. Eng.*, **25**: 591 (1983).
9. Roth, R.S., Negas, T., Cook, L.P.: *Phase diagrams for ceramists*, Compiled at the National Bureau of Standards, American Chemical Society, Washington (1969).

Catalytic Combustion of Light Alkanes in a Fluidized Bed Reactor under Fuel-Lean Conditions

¹M. Iamarino, ²R. Chirone, ²R. Pirone, ³P. Salatino, ²G. Russo

1 DIFA - Università della Basilicata, Potenza - ITALY

2 Istituto di Ricerche sulla Combustione - C.N.R., Naples – ITALY

3 Dipartimento di Ingegneria Chimica – Università Federico II, Naples - ITALY

INTRODUCTION

Fluidized bed reactors, widely applied in solid fuels combustion systems, represent a promising alternative to honeycomb monoliths for catalytic combustion applications. Despite the low attention by far received, considerable benefits would derive from catalytic combustion processes in fluidized beds mainly due to improved heat transfer properties, enabling, on one side, an efficient heat recovery by means of external or internal cooling devices and preventing, on the other side, undesired temperature profiles and catalyst thermal deactivation due to overheating as recently investigated by Hayhurst et al. (1998).

Recent literature about laboratory-to-large scale fluidized bed catalytic converters encourages further investigation in this field, since, despite the good results obtained with regards to NO_x prevention, major problems like the loss of expensive catalyst due to in-bed abrasion (Marshall e Mleczko, 1994) or fuel segregation phenomena in bubble phase (Mulder et al., 1997) often represented serious process drawbacks.

In the present work, the performance of a premixed fluidized bed catalytic reactor in the combustion of methane and propane is studied. A supported copper based catalyst is used for this purpose. A mathematical model of the converter is also developed, based on the two-phase theory of fluidization. The study aims at characterising on both experimental and theoretical grounds the reactor performance in different experimental conditions.

EXPERIMENTAL

The experimental apparatus consists of a 0.10 m ID fluidized bed reactor surrounded by an electrical oven. Reactor temperature was maintained by means of the oven operated through a PID control system. Continuous monitoring of gas composition was accomplished by on line analyzers (for CO, CO₂, NO_x and CH₄) and a gas-chromatograph (CH₄, C₃H₈).

Fuel was either methane or propane at 0.005 molar fraction. A few experiments were carried out at different fuel molar fractions in order to assess the dependence of the reaction rate on fuel concentration. The bed consisted of 0.7 kg of catalyst (unexpanded bed height H = 0.10 m) or 1.4 kg (H = 0.20 m). Experiments were carried out at two superficial gas velocities, 0.40 and 0.80 m·s⁻¹ (at the reactor temperature). The catalyst consisted of copper dispersed on porous γ -Al₂O₃ spheres (1 mm) recently investigated by Iamarino et al. (2002).

RESULTS AND DISCUSSION

Results of methane and propane combustion tests are reported in Fig. 1 in terms of C/C_{in} as a function of bed temperature. Depending on the mass of catalyst and gas space velocity, fuel conversion is complete at temperatures ranging between 500 and 700°C. Noteworthy, both methane and propane outlet concentrations asymptotically approach 0 as temperature increases, regardless of experimental conditions. This proves that no permanent fuel bypass in

the bubble phase onsets under the experimental conditions tested. This is a consequence of effective interphase mass transfer between bubbles and the emulsion phase, most likely associated with the choice of operating with relatively coarse solids belonging to the B-D group of the Geldart classification of powders.

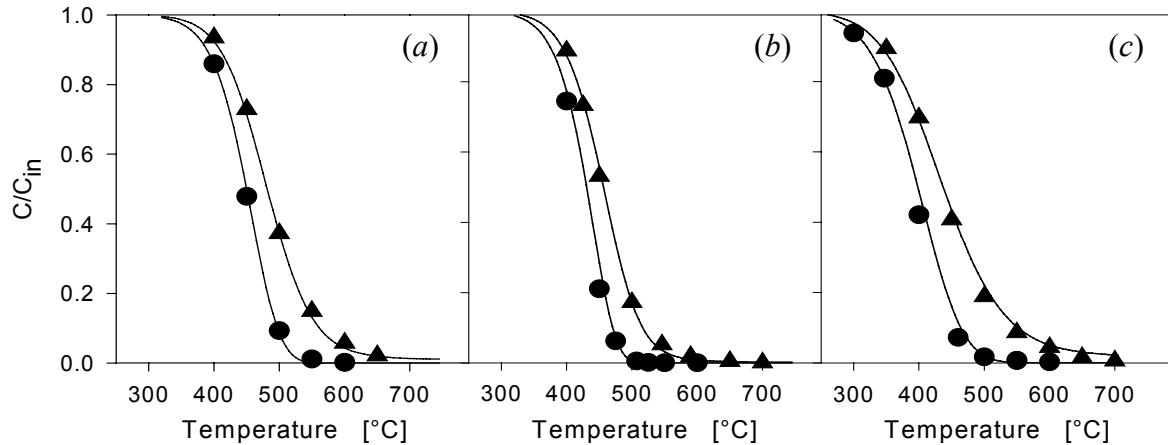


Fig. 1 C/C_{in} measured for CH_4 combustion at $H = 0.10 \text{ m}$ (a) and 0.20 m (b) and for C_3H_8 combustion at $H = 0.10 \text{ m}$ (c). Superficial gas velocities are $0.40 \text{ m}\cdot\text{s}^{-1}$ (●) and $0.80 \text{ m}\cdot\text{s}^{-1}$ (▲). Inlet concentration is 0.5% vol. for all conditions. Solid lines represent model predictions.

THE MODEL

A model of the fluidized bed catalytic converter is reported in Table 1 in dimensionless form and has been developed with the following assumptions:

- the converter is isothermal at temperature T and differential with respect to oxygen;
- the flow pattern is plug flow in both bubble and emulsion phases;
- at the temperatures of interest, the reaction takes place in the emulsion phase only;

Incipient fluidization velocity has been calculated according to Wen and Yu (1966), bubble diameter according to Werther (1976), bubble rise velocity u_b according to Davidson and Harrison (1963), particle-emulsion phase mass transfer coefficient k_g according to Chakraborty and Howard (1981), bubble-emulsion phase mass transfer k_{be} according to Kunii and Levenspiel (1991). The fractional volume δ of the bubble phase has been calculated as the ratio of visible bubble flow u_{b0} and the absolute bubble rise velocity. A value of $4 \cdot 10^{-7} \text{ m}^2 \cdot \text{s}^{-1}$ has been assumed for the intraparticle effective fuel diffusivity of both fuels.

The reaction order m was first assessed by fitting C/C_{in} experimental data corresponding to different inlet fuel concentration at constant temperature (450°C for CH_4 and 350°C for C_3H_8). Data points for methane and propane combustion are well fitted by a reaction order $m=0.7$ for both fuels. Data points relative to all the experimental conditions have been re-plotted in an Arrhenius diagram, assuming $m=0.7$. In the low-temperature range, points are fairly well aligned along straight lines whose slopes and intercepts have been worked out to yield the pre-exponential factor, k_{c0} , and the activation energy, E_a , of the intrinsic kinetic equation, according to eq. 4. These values are: $E_a = 1.25 \cdot 10^5 \text{ J}\cdot\text{mol}^{-1}$ and $k_{c0} = 3 \cdot 10^8 \text{ s}^{-1}$ for methane and $E_a = 7.95 \cdot 10^4 \text{ J}\cdot\text{mol}^{-1}$ and $k_{c0} = 4.5 \cdot 10^5 \text{ s}^{-1}$ for propane.

The kinetic parameters have been used to calculate profiles of C/C_{in} as a function of temperature for the different experimental conditions. The comparison with experimental

results is reported in Fig. 1 and is fairly good throughout the temperature range investigated. This is encouraging as regards the ability of the model to take into account the cooperative role of intrinsic kinetics and of intraparticle, boundary layer and interphase (bubble-to-emulsion phase) diffusional resistances.

Model computations have been further directed to the quantitative assessment of the relative importance of the different processes at work. Figure 2 compares the values of the Damköhler number Da , of the product ηDa between the Damköhler number and the catalyst effectiveness factor, of the mass transfer Stanton number St_m and of the bubble-to-emulsion phase mass transfer index X . It is worth recalling here that Da , St_m and X express the ratio between the gas space-time and the time scales of, respectively, heterogeneous reaction, diffusion across the particle boundary layer and mass transfer between the bubbles and the emulsion phase.

Analysis of Fig. 2 indicates that St_m is orders of magnitude greater than the other numbers throughout the temperature range, hence mass transfer in the boundary layer around the catalyst particle is extremely efficient when compared with other physico-chemical processes occurring in the reactor. This corresponds to $C_s \approx C_e$ in all experimental conditions.

In the low temperature range ($T < 450^\circ\text{C}$ for CH_4 and $T < 400^\circ\text{C}$ for C_3H_8), the conversion rate is controlled by the intrinsic kinetics. Curves for ηDa and Da overlap in this region, hence $\eta=1$ and no internal diffusion limitation onsets in these conditions. On the other hand, X is much greater than Da , i.e. mass transfer between bubbles and emulsion phase is more effective than intrinsic kinetics: this implies $C_b \approx C_e$ in this range.

(1)	$\omega \frac{d\Gamma_b}{d\xi} = -X(\Gamma_b - \Gamma_e)$	balance on fuel in the bubble phase
(2)	$(1 - \omega) \frac{d\Gamma_e}{d\xi} = X(\Gamma_b - \Gamma_e) - St_m(\Gamma_e - \Gamma_s)$	balance on fuel in the emulsion phase
(3)	$St_m(\Gamma_e - \Gamma_s) = \eta Da \Gamma_s^m$	balance on fuel around a single catalyst particle
initial conditions: $\xi = 0 \Rightarrow \Gamma_e = \Gamma_b = 1$		
(4)	$\frac{d\Gamma}{d\xi} = -Da\Gamma^m \Rightarrow \Gamma(\xi = 1) = [1 - (1 - m)Da]^{1/(1-m)}$	low temperatures limiting case
Nomenclature		
$Da = \frac{k_c(1 - \varepsilon_{mf})(1 - \delta)C_{in}^{m-1}H_b}{u_0}$	$X = \frac{6k_{be}\delta H_b}{d_b u_0}$	$St_m = \frac{6k_g(1 - \varepsilon_{mf})(1 - \delta)H_b}{d_c u_0}$
$\phi = \frac{d_c}{6} \sqrt{\frac{k_c C_s^{m-1}}{D_{eff}} \frac{m+1}{2}}$	$\eta = \frac{1}{\phi} \left(\frac{1}{\tanh(3\phi)} - \frac{1}{3\phi} \right)$	
C_b, C_e	fuel molar fractions in bubble, emulsion phase, -;	m reaction order;
C_{in}	fuel molar fraction in the feeding, -;	$u_{0,b0,e0}$ superficial gas velocity in the bed, in bubble and in emulsion, phases, $m \cdot s^{-1}$;
C_s	fuel molar fraction at the catalyst surface, -;	z axial coordinate, m ;
d_c	catalyst particle diameter, m ;	δ bubble phase fractional volume;
d_b	bubble diameter, m ;	ε_{mf} dense phase voidage;
D_{eff}	effective intraparticle diffusivity, $m^2 \cdot s^{-1}$;	$\Gamma_b = C_b / C_{in}$ normalized bubble phase conc.;
H_b	unexpanded bed height, m ;	$\Gamma_e = C_e / C_{in}$ normalized emulsion phase conc.;
k_{be}	mass transfer coefficient between bubble and emulsion phases ref. to bubble surface, $m \cdot s^{-1}$;	$\Gamma_s = C_s / C_{in}$ normalized conc. at the catalyst surface;
k_c	kinetic constant per unit volume of catalyst s^{-1}	$\omega = u_{b0} / u_0$
k_g	mass transfer coefficient between emulsion phase and catalyst ref. to catalyst surface, $m \cdot s^{-1}$;	$\xi = z / H_b$ dimensionless axial coordinate;

Table 1 Model equations

In the intermediate-to-high temperature range, catalyst effectiveness η significantly departs from 1 and ηDa deviates from the intrinsic Da , suggesting that intraparticle diffusional limitations start to play an important role in determining reactor performances. At the upper limit of the temperature range, ηDa approaches, or even overtakes, the interphase mass transfer index X . In this range the conversion rate is controlled by the combined intraparticle diffusion-intrinsic kinetics of heterogeneous reaction at the same time as the bubble-to-emulsion phase mass transfer. The importance of bubble-to-emulsion phase mass transfer is moderate throughout the temperature range investigated. This is consistent with the above reported observation that permanent by-pass of fuel is never observed under any experimental condition tested. Operation at larger gas superficial velocity or smaller catalyst loading might, however, turn out to be critical under this respect.

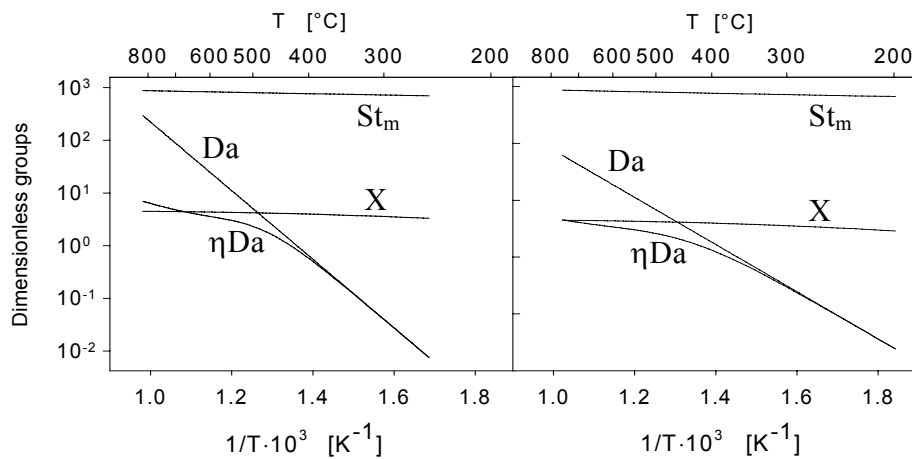


Fig. 2 Evaluation of dimensionless groups from model computations at $H = 0.10$ m and $u_0 = 0.40$ m·s⁻¹ for CH₄ (a) and C₃H₈ (b) combustion.

ACKNOWLEDGMENTS

Regione Campania is acknowledged for financial support to this project (L.R. 31/12/94 N.41 – Art.3 1° comma – Annualità 1998).

REFERENCES

- Chakraborty, R.K., Howard, J.R.: *J Inst Energy* **54**:48 (1981).
- Davidson, J.F., Harrison, D.: *Fluidized Particles*, Cambridge University Press (1963)
- Hayhurst, A.N., John, J.J., Wazacz, R.J.: *Proceedings of the Combustion Institute*, **27**: 3111 (1998).
- Iamarino, M., Chirone, R., Lisi, L., Pirone, R., Salatino, P., Russo, G.: *Catal Today* (in press) (2002).
- Mulder, A., der Kinderen, J., Riphagen, J.: *Twentieth World Gas Conference*, Copenhagen, Denmark, June (1997).
- Kunii, D., Levenspiel, O.: *Fluidization Engineering* (2nd ed), Butterworth-Heinemann, 1991.
- Marshall, K.-J., Mleczko, L.: *Sixth International Conference on Circulating Fluidized Beds*, Würzburg, Germany, August: p. 539 (1999).
- Wen, C.Y., Yu, Y.H.: *AIChE Journal* **12**:610 (1966).
- Werther, J.: in *Fluidization Technology* ed. by Keairns, D.L., vol. 1:215 (1976).

Combustion Synthesis of Perovskite Catalysts

S. Biamino, A. Civera, M. Pavese, P. Fino, G. Saracco, C. Badini*

Dipartimento di Scienza dei Materiali ed Ingegneria Chimica

Politecnico di Torino, Corso Duca degli Abruzzi 24, 10129 Torino, Italy.

* corresponding author: tel./fax: +39-011-5644635/99; e-mail: badini@athena.polito.it

INTRODUCTION

Over the last years the synthesis of innovative ceramic materials for catalytic applications has been the subject of many studies. The main constraints were the reproducibility of the results and the cost and complexity of the processes. Many new synthesis methods were developed based on the use of highly exothermic synthesis reactions. The two most important methods of this type are the combustion synthesis and the self-propagating high-temperature synthesis (SHS) [1]. They differ for the state of aggregation (respectively liquid and solid) of the reagents but both involve reactions which are able to increase the temperature of the synthesis zone over even 2000°C for a short period of time, possibly enabling rapid nucleation and limited growth of the desired products. This would result into a high specific surface area of the obtained materials, which renders them as good candidates for practical applications in the heterogeneous catalysis field.

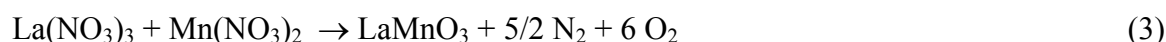
Among the catalytic materials produced by combustion synthesis in our labs, the most important ones are perovskites such as LaMnO₃, LaFeO₃ and LaCrO₃ [2] or other oxides such as LaVO₄ and Al₂O₃ [3,4]. As just mentioned, the high specific area as well as the purity of these oxides, suggests that they can be applied for driving catalytic combustion reactions such as the combustion of diesel-engine soot (catalytic traps) or of natural gas (catalytic burners). This paper describes the characteristics and catalytic performance towards soot and natural gas combustion of some perovskite catalysts produced by the combustion synthesis method.

MATERIALS AND METHODS

The combustion synthesis technique involves different phenomena and reactions that allow the process to be self-sustaining. A homogeneous aqueous solution of metal nitrates (oxidisers) and urea (fuel) is placed into an oven at a constant temperature between 400°C and 800°C; it quickly begins to boil and froth until ignition takes place. The general reaction scheme, to produce e.g. LaMnO₃, is the following (hydration of both lanthanum and manganese nitrates was neglected):



The whole reaction can be regarded as the sum of two different contributions:



Reaction (2), urea combustion ($\Delta H = -520$ kcal/mol), provides the heat necessary to the endothermic transformation of nitrates into the oxide, i.e. reaction (3) ($\Delta H = +127$ kcal/mol). The whole process is over in a few minutes and the result is an inorganic foam that easily crumbles, with a very high specific volume and surface area.

Metal nitrates are the best starting materials because they are very soluble in water and act as an oxygen source during the reaction. In some cases, in order to obtain oxides with a large

specific area, some additives might be required. These must be able at the same time to develop large amounts of gases and to provide the reacting system with more oxygen. Among the different possibilities, NH_4NO_3 is to be preferred because, during its decomposition (reaction 4 below), it can, on the one hand, develop only gaseous products which do not contaminate the oxide and, on the other hand, provide the system with additional heat ($\Delta H = -38$ kcal/mol).



In addition to this it has a low cost and, as the other nitrates, brings more oxygen into the system. It has though to be underlined that ammonium nitrate is a well known explosive and that the handling of this material at an industrial level might employ additional costs linked to process safety.

The prepared oxides were characterised: the crystal structure and the composition were examined by using powder X-ray diffraction (XRD) and EDS, the surface area was measured by a BET measuring apparatus and the morphology was studied by electronic microscopy (SEM and TEM). Furthermore, catalytic activity tests were performed by temperature-programmed- reaction of soot-catalyst mixtures (1:9 mass basis). Air was fed at the constant rate of $50 \text{ ml} \cdot \text{min}^{-1}$ to a fixed-bed micro reactor loaded with about 1 g of the above mixture. All experiments were performed by using, instead of real diesel soot, a dry amorphous carbon which is tougher to burn than real diesel soot, a conservative condition. The reaction temperature was controlled through a PID-regulated oven and varied during a TPR run from 200 to 700°C at a $5^\circ\text{C} \cdot \text{min}^{-1}$ rate meanwhile feeding air at a $50 \text{ Ncm}^3/\text{min}$ rate. The analysis of the outlet reactor gas was performed through NDIR analysers. The conversion peak temperature was registered as an index of catalytic activity. Analogous combustion runs were performed to check the activity of these catalysts towards natural gas combustion by employing a fixed-bed of 0.1 g of catalyst powder and 0.9 g of SiO_2 (0.2-0.7 granulate, used to hinder thermal runaways), sandwiched between two quartz wool layers. The reactor was fed in this case with a gas flow rate of $50 \text{ Ncm}^3/\text{min}$ of the following composition: $\text{CH}_4 = 2\%$, $\text{O}_2 = 18\%$, He = balance.

RESULTS AND DISCUSSION

In the present work the combustion synthesis technique has been successfully applied in the production of perovskite-type oxides of formula LaBO_3 (B = Mn, Fe, Cr). Table 1 shows some interesting features of the prepared perovskites. Firstly, despite the short duration of the combustion synthesis, it is possible to obtain very pure products, as shown by the absence of undesired phases, even after thermal treatment. In addition to this, it is possible to customise both the degree of crystallisation and the BET surface area, by optimising the synthesis conditions (in particular the urea-to-nitrates ratio). It is worth noting that perovskites with quite high values of specific surface area can be obtained.

Table 1. Principal properties of prepared perovskites.

Material	Foreign phases	Crystallisation	Surface area
LaMnO_3	none	poor to good	up to $20 \text{ m}^2/\text{g}$
LaFeO_3	none	poor to good	up to $25 \text{ m}^2/\text{g}$
LaCrO_3	none	poor to good	up to $18 \text{ m}^2/\text{g}$

Catalytic combustion of CH_4 requires high-specific surface area perovskites. It is therefore quite important to obtain a fine crystal size. This is shown in Table 2, where the performance of a high-surface catalyst obtained by combustion synthesis is compared to a lower-specific-

surface-area catalyst obtained by the “citrate” method.

Table 2. Catalytic properties of LaMnO_3 obtained with two different synthesis techniques.

Synthesis Method	surface area [m^2/g]	Temperature of 50% methane conversion [$^{\circ}\text{C}$]
combustion synthesis	18	461
“citrate” method	4	535

On the contrary, for other applications such as catalytic combustion of diesel soot, this parameter is less important. What is there needed is a catalyst having comparable crystal dimensions to diesel soot ones so as to allow good contact conditions between these two counter parts. Fig. 1 shows, in fact, the peak temperature of combustion of diesel soot without catalyst and with different perovskite catalysts. The catalysts belonging to the LaCrO_3 family behave better than the higher-SSA iron or manganese-based oxides.

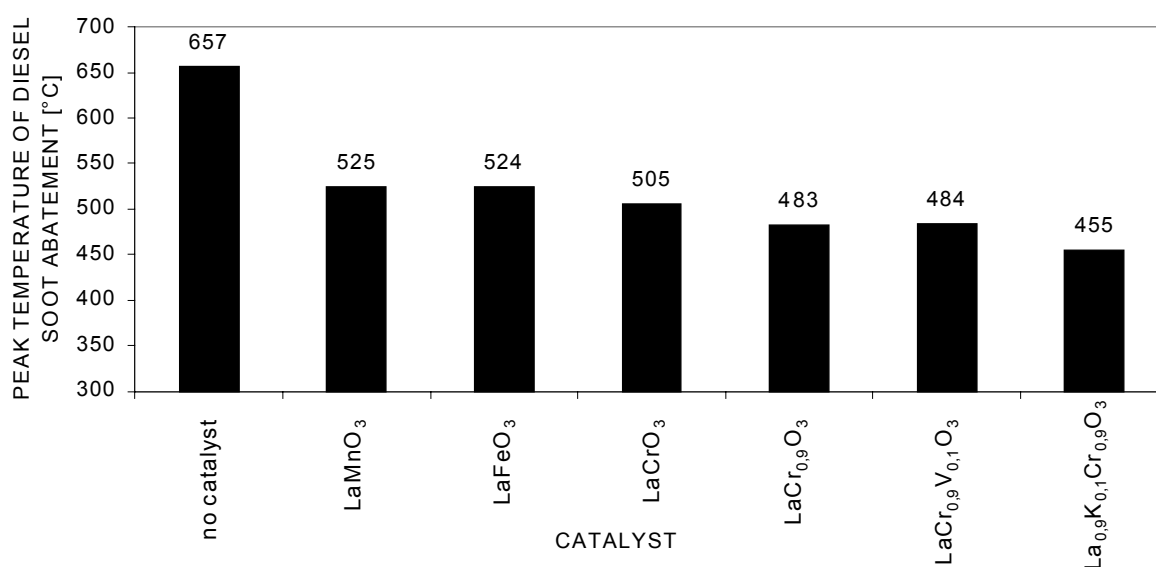


Fig. 1. Catalytic activity of perovskites for catalytic abatement of diesel soot.

In particular, $\text{La}_{0.9}\text{K}_{0.1}\text{Cr}_{0.9}\text{O}_3$ shows the lowest peak temperature (i.e. the highest catalytic activity) at only 455°C . Owing to the nature of chromium, this transition metal can in part undergo a valence shift from Cr^{3+} to Cr^{4+} so as to re-establish electroneutrality, despite the substoichiometric composition of the above mentioned chromite and the partial substitution of trivalent lanthanum by monovalent potassium. The most likely explanation is that the perovskite can act as an oxygen pump towards the soot. Oxygen can indeed be made available to particulate combustion in combination with a temporary shift of Cr valence from $4+$ to $3+$. Oxygen molecules coming from the gaseous atmosphere can re-oxidise the perovskite and set back Cr^{4+} species.

It is surprising to observe that chromites are the most active catalysts family in the field of diesel-soot abatement, while in natural gas combustion both LaMnO_3 and LaFeO_3 work better than LaCrO_3 . Further investigations about the mechanism and the kinetic parameters of reaction among soot and catalyst are essential to explain this behaviour.

The micro-structural characterisation, performed by electron microscopy (TEM and SEM), microanalysis (SEM-EDS) and XRD, allows the authors to confirm that the prepared perovskites maintain the same stoichiometric proportions of the precursors, and, at the same time, to investigate the morphology of the particles. TEM analyses show that, by varying the

combustion synthesis conditions, it is possible to obtain particles of different dimensions. Particularly, Fig. 2 shows two TEM micrographs of LaMnO_3 , synthesised without (Fig. 2a) or with (Fig. 2b) ammonium nitrate in the starting batch. The presence of this additive leads to smaller size of the particles (20 nm, compared to 100 nm for the LaMnO_3 obtained without NH_4NO_3).

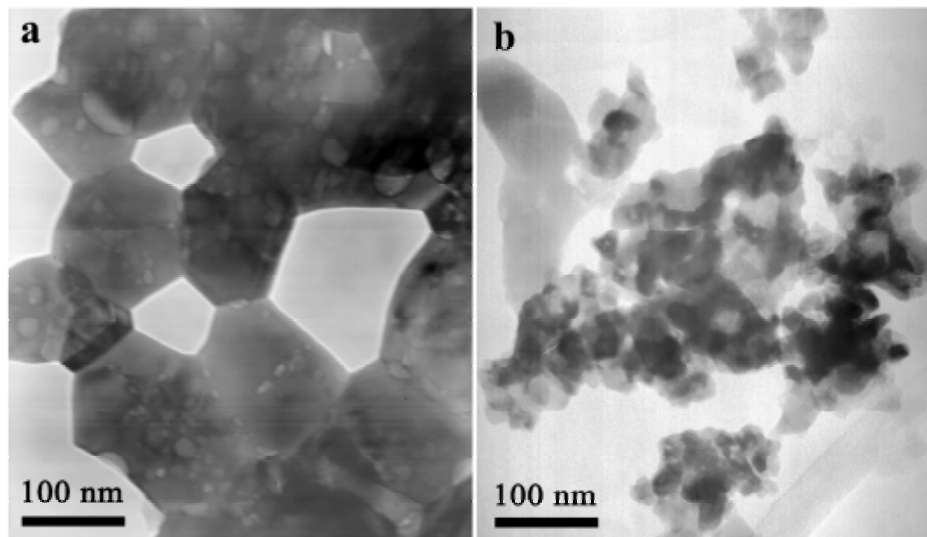


Fig. 2. TEM micrograph of an aggregate of LaMnO_3 particles.

CONCLUSIONS

Combustion synthesis has proved a very interesting technique for the synthesis of many different types of oxides, since it allows quick and economic production of pure materials with high values of specific surface area. In particular, in the field of catalysis these features seem to be very interesting. In the present work, a number of perovskite oxides were produced, both for the abatement of soot emitted from diesel engine and for methane catalytic combustion.

The good level of purity of the products, the wide range of particle dimensions that can be obtained (as small as 10–20 nm), the rapidity of the method and the excellent catalytic activity displayed by some specific catalysts compositions for the two combustion applications addressed, suggest that combustion synthesis can be applied for the in situ deposition of catalysts on monolithic structured supports in the fields of catalytic traps for diesel exhaust treatment [6] (e.g. cordierite or SiC wall-flow honeycombs) or of catalytic burners for domestic-boilers or industrial furnaces [7] (e.g. FaCrAlloy-fibre or mullite-foam burners).

REFERENCES

1. Merzhanov A.G.: *J. of Mat. Proc. Techn.*, **56**: 222 (1996).
2. Manoharan S.S., Patil K.C.: *J. Am. Ceram. Soc.*, **75**(4): 1012 (1992).
3. Kingsley J.J., Patil K.C.: *Mat. Lett.*, **6**(11-12): 472 (1998).
4. Bhaduri S., Zhou E., Bhaduri S.B.: *Nanostructured Mat.*, **7**(5): 487 (1996).
5. Tejuca, L. G., Fierro, J. L.G., *Properties and applications of perovskite-type oxides*, Marcel Dekker Inc.: New York, 1993.
6. Fino, D., Saracco, G., Specchia, V.: *Chem. Eng. Sci.*, in press (2002).
7. Cerri, I., Saracco, G., Specchia, V., Trimis, D.: *Chem. Eng. J.*, **82**: 73 (2001).

Absolute Concentrations of Radical C₂ in Atmospheric Pressure Hydrocarbon Flames

¹M. Marrocco, ¹M. D'Apice, ¹S. Giammartini, ²M. Magaldi, and ²G. P. Romano

1 C. R. Casaccia – ENEA, S. M. di Galeria (RM) - ITALY

2 Dep. of Mechanics and Aeronautics – Univ. of Rome “La Sapienza, Rome - ITALY

ABSTRACT

The C₂ concentration in flames at atmospheric pressure is measured for three fuel-rich combustion environments: acetylene/oxygen, Liquid Petroleum Gas (LPG)/air and methane/air flames. Measurements have been based on spectrographic and two-dimensional Laser-induced Fluorescence (LIF) of the $\Delta v = -1$ d³Π_g-a³Π_u band. The oxy-acetylene flame was utilized to establish a comparison with literature data and absolute values, calibrated through Rayleigh scattering, were found to be distributed within the 10¹⁴ cm⁻³ range.

The induced emission from two Bunsen flames fed with LPG/air or methane/air was also investigated. Accumulated acquisitions were necessary to detect small C₂ quantities in the order of 10¹⁰ cm⁻³ concentrated on the flame front.

INTRODUCTION

The study of transient species produced in combustion processes has attracted a great deal of attention [1]. Among the most studied radicals at atmospheric pressure C₂ has mainly been detected under favorable conditions as those provided by C₂H₂ [2] or C₂H₄ [3] fuels where the strength of the double and triple bond between the carbon atoms is such that the flame chemistry enables C₂ molecules to be released and then detected. To that end Laser-induced Fluorescence (LIF), Degenerate Four Wave Mixing (DFWM), Polarization spectroscopy (PS) and Resonance Coherent Anti-Stokes Raman Spectroscopy (RECARS) have been proven to be the spectroscopic techniques that most easily guarantee enough spatial resolution to cope with the small quantities of C₂ present in the interaction region inside the flames.

LIF spectroscopy is a good candidate to detect the expected low concentration range for C₂ in LPG/air and methane/air flames as it has been applied successfully to evaluate species concentration at the sub-ppm level [1]. It does not have the drawbacks of DFWM where the influence of both the thermal gratings and the normalization procedure might affect the concentration predictions. PS might also be applicable but it suffers from spurious polarization dependence and the absolute measurements are complicated by the rather complex structure of the signal. RECARS is promising but it involves a rather intricate spectral analysis besides the operation of two different laser sources under specific geometrical arrangement.

The current work deals with both spectroscopic and imaging LIF analysis of C₂. The most widely studied C₂H₂/O₂ flame has been used as reference flame to set up the spectroscopic and imaging techniques that have been extended to less studied flames as those generated with fuel-rich premixed LPG/air and CH₄/air mixtures at atmospheric pressure.

EXPERIMENT

The excitation of the C₂ radical has been provided by a tunable dye laser (mod. LDL 20505, LAS GmbH) capable of a nominal linewidth of 0.04 cm⁻¹. It was pumped with a pulse energy of 50 mJ given by the third harmonic of a Nd:Yag laser (mod. CLS400, Quanta System). Two solutions of Coumarin 500 dye were employed in the oscillator and in the amplifying stages of the laser resulting in an output of 6 mJ at 516.5 nm with pulse duration of about 10 ns. The laser beam was treated with mirrors along an optical path to synchronize the arrival of the laser pulse with the optical time gate of the detection system. The pulse energy was anyhow limited to about 4 mJ focused with different lenses depending on the specific experimental run. Collection was carried out at 90 degree.

In the spectroscopic data, a quartz lens with nominal focal length of 254 mm (mod. PLCX-50.8-130.8-UV, CVI) was used to capture the fluorescence from the d³Π_g-a³Π_u band. A second quartz lens of nominal focal length of 75 mm (mod. PLCX-50.8-38.6-UV, CVI) illuminated the entrance slit of a spectrograph. The spectral dispersion of about 5 nm/mm was enough to determine all of the main features of the vibrational bands of the C₂ molecule.

An ICCD detector (mod. EEV47-10, Andor Technology) was employed for all the spectral measurements. This detector has a photoactive area of 1024 × 1024 pixels grouped in a physical square of 13.3 mm per side and it was equipped with the high spatial resolution tube yielding a measured minimum resolution of 21.4 μm. The response uniformity is specified from the manufacturer to be better than 1.74%. The detector was kept at -30 °C corresponding to a dark count rate of about 60 s⁻¹. The gate (controlled with DG535 delay generator, Stanford Research Systems) was set at 100 ns to eliminate the background luminosity and to limit the accuracy of the data to the photon shot-noise even with the lowest LIF counts per pixel. This time gate assured also the synchronization with the arrival of the fluorescence signal promoted after an optical retardation laser line of about 15 m.

In the spectral data the ICCD worked in a full vertical binning mode but the whole active area was used in the image acquisitions. In this latter condition a photographic lens (mod. micro-Nikkor 105mm/2.8 AFD, Nikon) was employed to image the natural emission and the induced fluorescence from the flames.

SPECTRAL DATA

The fuel-rich oxy-acetylene welding torch having a nozzle with an internal diameter of 1 mm was used as reference for the main optical adjustments and for comparison with the results published in literature. To that end a long pass filter having a cut-on wavelength of 550 nm (mod. LPF-550-2.00, CVI) was inserted between the two collecting lenses before the spectrograph. This filter was enough to eliminate unwanted light so that only the main portion of the $\Delta v = -1$ d³Π_g-a³Π_u band contributed to the signal. The focusing lens was a spherical quartz lens of 300 mm (mod. PLCX-50.8-154.5-UV, CVI) resulting in a measured laser beam diameter of about 130 μm so that the height of the laser-flame intersection could be changed with good accuracy. Increasing vertical heights of 3, 15, 30, 70 mm above the burner exit were chosen accordingly to the flame geometry. In such a manner the C₂ amount was probed in significant positions of the flame, that is the reaction zone, the middle and upper section of the luminous mantle and the outer cone. The spectra were accumulated over 10 laser shots, so that 5000 counts per laser pulse were possible on the maximum of the fluorescence response. Unwanted contributes were removed by subtraction of the spectra obtained with off-resonance tuning. As general remark, it must be said that the C₂ production decreases with the height. This behavior is well described in literature [4]. However in the reaction zone the overall spectral response was found less intense than expected. This might due to the interplay of different reasons. First of all a different absolute value of C₂ concentrations. But the

relative local concentrations along the laser path are also affecting the data: in fact the C_2 density is expected to be very localized in the reaction zone, while it should almost homogeneously spread out in the luminous mantle. In addition the laser beam traverses a different length into the actual flame. Furthermore the balance between the spectral laser irradiance and the actual local absorption might play a role without considering the corrections to be made because of wing effects.

The understanding of the previous phenomenology is out of the main interest of the present contribution, but it is clear that spectral data are subjected to limited reliability in the prediction of absolute concentrations even if they still retain a validity for relative measurements. However the concern about the feasibility of the absolute C_2 concentration determination was addressed by running a saturation test. For this purpose the two lowest positions of the laser-flame intersection were chosen ($z = 3$ and 15 mm) and high degree of saturation was observed for both positions.

A Bunsen burner with 9 mm of internal diameter was used to compare the LPG/air and methane/air flames. First attempts to determine a detectable spectral response failed when the interaction volume was kept identical to that of the oxy-acetylene flame. Neither an accumulation of 1000 spectra provided a readable outcome. The lack of a signal was attributed to the strong saturation that limited a lot the overall fluorescence in the viewed solid angle. An enlargement of the focused area was thus the necessary compromise to induce fluorescence from a larger ensemble of C_2 radicals. In addition the background signal was found too much disturbing to distinguish the vibrational band at an acceptable level. Therefore an interferential filter (mod. F40-550-4-2.00, CVI) centered at 550 nm with 40 nm bandwidth was coupled to the previous long pass filter. To avoid other sources of spurious signals each spectrum was compared with one obtained off-resonance. The two different flames were operated at the same Reynolds number ($Re = 1500$) and equal air contribution but with a consequent slight prevalence of the equivalence ratio Φ of the heavier fuel. The laser diameter was enlarged and passed through apertures of 6 mm; nevertheless it was still essential an accumulation of 500 laser shots to provide readable spectra after the corrections for the contribution of spurious signals. The center of the enlarged laser beam entered the flames at three different heights ($z = 3, 15,$ and 35 mm) above the burner and a difference between the two flames can be outlined. As expected in the LPG/air flame the C_2 production is definitely greater than in the methane/air flame but it diminishes with the height. The methane/air flame shows instead a rather constant amount of the radical so that at the highest locations the C_2 quantity almost equals that one produced in the LPG/air mixture. The saturation behavior was finally checked and it appeared in all of the checks.

IMAGES

Absolute concentrations is not so straightforward and probe volume effects have to be avoided with a proper spatial selection [5]. This can be realized through image acquisition. to that end the induced fluorescence from the three flames was imaged on the ICCD equipped with both the long pass and the interferential filter used for the spectrographic purposes. An example of the experimental outcome is reported in Fig. 1 for the three different flames.

The fluorescence of the oxy-acetylene flame (Fig. 1a) was acquired with the best resolution owing to the large amount of the signal. It shows an area of major concentration localized in the upper zone of the hot arch delimiting the conical reacting region. Right above the tip the C_2 production is high, as it results from the bright region, but it decreases within few millimeters. This is in qualitative agreement with the unidimensional LIF reconstruction reported in the work of Aldén et al. [5].

The problem of collecting a small signal from the LPG/air and methane/air flames was

attenuated by viewing an enlarged area of $58 \times 58 \mu\text{m}$ per pixel. This also favored the capture of the main body of the flames into the images. But a 8×8 pixel binning (superpixel) was needed to guarantee enough fluorescence to contrast the noise in the pictures. This means that the resolution was degraded to about $0,46 \times 0,46 \text{ mm}$ of comparable size with the expected flame front dimension. Figs. 1b and 1c summarize some of the results relatively to the Bunsen flames.

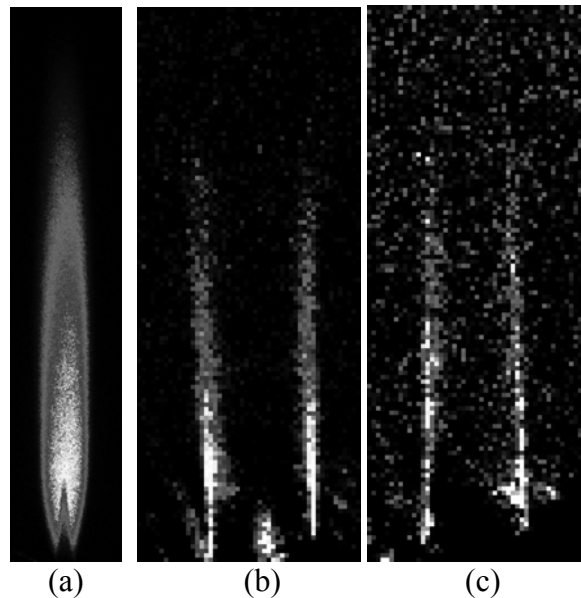


Fig. 1 Images of the C_2 fluorescence: (a) the oxy-acetylene flame with physical resolution of $33 \times 33 \mu\text{m}$ per pixel, (b) the LPG/air flame, and (c) the methane air flame with resolution of $0,46 \times 0,46 \text{ mm}$ per pixel.

Absolute measurements were derived from those images for which saturated conditions were verified, but before data processing a careful calibration was launched by looking at the Rayleigh scattering of the laser in air. This resulted in a maximum C_2 concentration for the oxy-acetylene flame of about $3.4 \times 10^{14} \text{ cm}^{-3}$ with a shot-noise limited signal to noise ratio (SNR) of 10.6 and a detection limit of $2.4 \times 10^{12} \text{ cm}^{-3}$. The measured value seems acceptable when compared with previous evaluations present in literature and ranging between 10^{13} and 10^{15} cm^{-3} . Disagreement with other measurements can be explained in terms of probe volume effects, flame temperature and stoichiometry. The Bunsen flames gave a C_2 distribution localized in the correspondence of the flame front and maximum concentrations of 1.7×10^{10} and $5.2 \times 10^9 \text{ cm}^{-3}$ were found for the LPG/air and methane/air mixtures respectively. This time the detection limit was $3.3 \cdot 10^9 \text{ cm}^{-3}$ with the filter transmission included in the calculation.

REFERENCES

1. Eckbreth A. C.: *Laser diagnostics for combustion temperature and species*. Gordon and Breach Publishers, Amsterdam (1995).
2. Kamiski, C. F., Hughes, I. G., Lloyd, G. M. and Ewart, P.: *Appl. Phys. B* **62**: 39 (1996). And references therein.
3. Allen, M. G., Howe, R. D., and Hanson, R. K.: *Opt. Lett.* **11**: 126 (1986).
4. Aldén, M., Edner, H., and Svanberg, S.: *Appl. Phys. B* **29**: 93 (1982).
5. Salmon, J. T., and Laurendeau, N. M.: *Appl. Opt.* **24**: 1313 (1985).

Optical Emission Spectroscopy on a MILD Combustor

M. Marrocco, V. Visentin, M. D'Apice, S. Giammartini

C. R. Casaccia – ENEA, S. M. di Galeria (RM) - ITALY

INTRODUCTION

Flameless oxidation or the so called MILD (Moderate and Intense Low oxygen Dilution) combustion is an important operational mode of combustion that leads to relevant reduction of pollution in conjunction with considerable energy savings [1]. The basic idea consists in the dilution of local oxygen concentrations by introducing inert gases after a strong preheating of the reactants [2]. This leads to lower temperature gradients as well as limitation of combustion instability.

One of the most striking phenomenological features of MILD combustion is the absence of any visible structure. Spectroscopic studies are then important for the localization of the reaction zones. The current work has the goal of describing relative radical concentrations in a FLOX[®] burner of 40 kW operated with natural gas in working conditions depending on internal temperatures and equivalence ratio. Data show a shift of the reaction zone towards the gas entrance when passing from a rich to a lean mixture. Higher temperatures determine only a more compact spatial extension of the phenomenology.

COMBUSTOR

The burner used in the following tests is a WS – Rekumat C-150, capable of 40 kW. It has been conceived for both operational modes: conventional flame and flameless. The conventional flame is needed for the start-up till temperature is so high that flameless operational mode can be sustained. In this latter mode gas and air are mixed directly in the combustion chamber with gas velocity of about 70 m/s. This high velocity attracts great quantities of combustion products towards the primary zone realizing the internal recirculation necessary to dilute the mixture below 15% of oxygen. The furnace built for this study is called MCD (Mild Combustion Demonstrator). It is made of a ceramic fibre (Caowool) structure. A metallic enclosure contains the internal walls realized in refractory material (pyroblock) and the final shape of the combustion chamber is a parallelepiped with dimensions 1400×700 mm at the base and 700 mm high. When the furnace was operated three optical accesses were available in the horizontal plane at the same height of the gas stream. The reference temperature T_{set} utilized to determine the working conditions was measured by a thermocouple mounted at the top of the chamber. It had a maximum value of 1300 °C.

EXPERIMENT AND RESULTS

The experiments were carried out at different operational conditions. Two temperature settings have been considered ($T_{\text{set}} = 1050, 1150$ °C) and for each T_{set} the equivalence ratio Φ was varied so that it took the value of 0.9, 1.0 and 1.1.

Emission spectroscopy

A spectrograph was employed to search for the relative abundances of radical species in the furnace. Its characteristics are described elsewhere [3]. The spectral analysis was limited to the first two windows closer to the gas inlet because the third did not show any significant

signal. In order to compare directly the detectivities of the radical species in the combustion process the use of special filters was avoided. The search for spectral signatures of OH, CH and C₂ was successfully performed even if the discussion will be limited to the most abundant species, OH. Although relative intensities might be largely different spatial profiles do not differ when considering the other radicals.

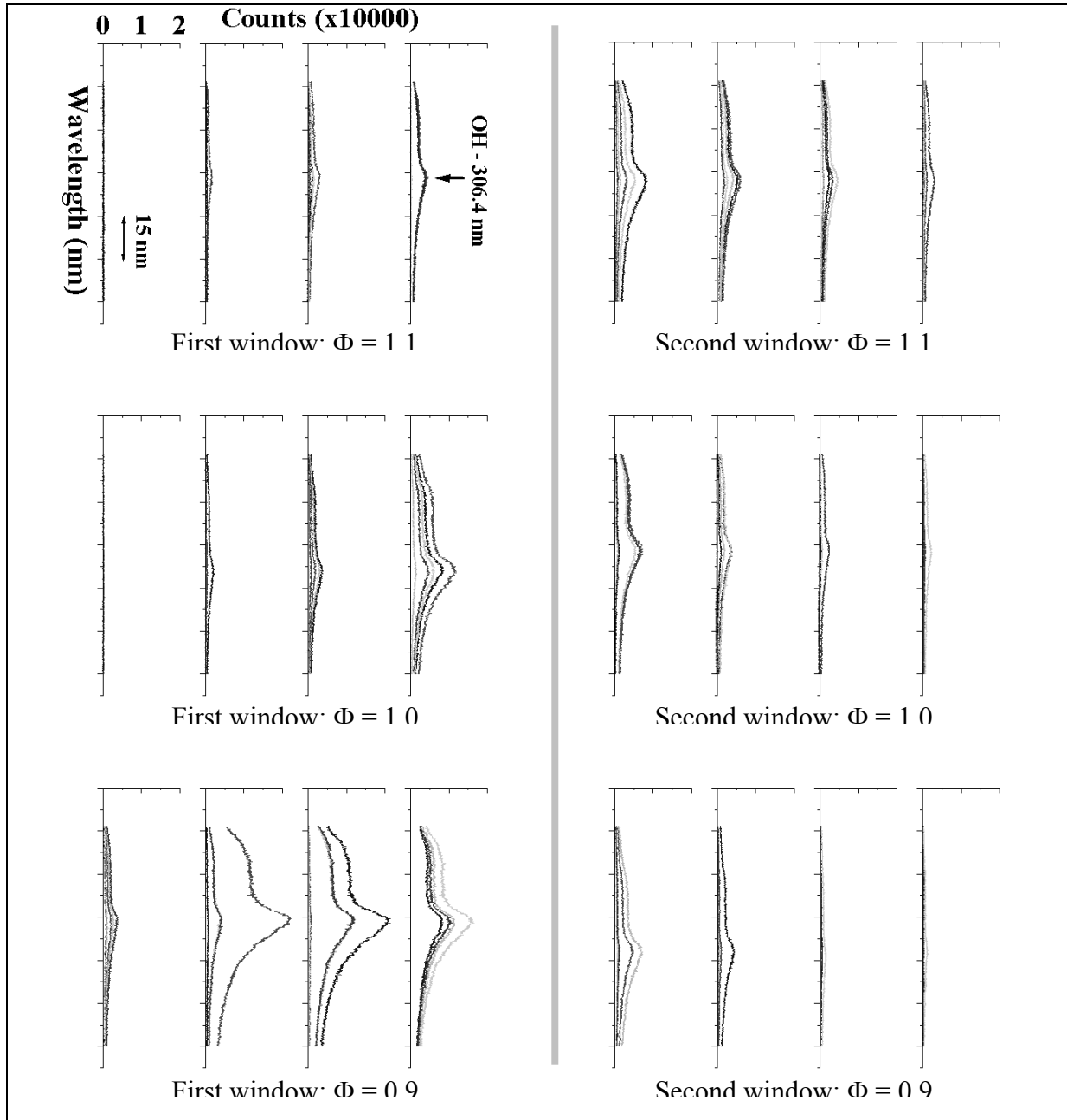


Fig. 1 OH spectra at $T_{set}=1050\text{ }^{\circ}\text{C}$. All the spectra are relative to the same graphic scales reported for the top left plot only.

The reading of the data is rather complex and it deserves a little bit of explanation. The figures are organized like in a table so that they represent the spectra obtained in the side view of the two windows located in the furnace walls. The gas entrance is supposed on the left of Fig. 1. Each window of the furnace has been divided in four sections. Each section corresponds approximately to the cylindrical volume with base given by the collecting lens

area and height determined by the internal width of the furnace. For each section a group of spectra has been reported. They are rotated for space savings so that the wavelength axis lies vertical. Starting from the top of the figures, the rows of spectra correspond to the results obtained for $\Phi=1.1$, 1.0 and 0.9 respectively. The columns are then determined by the spatial positioning of the spectrograph axis with respect to the burner exit. The eight positions have the following distances $z=237, 312, 387, 462, 587, 662, 737, 812$ mm.

The most abundant radical of hydrocarbon combustion is OH. The flameless mode with natural gas does not make any exception to this well known phenomenology. This radical participates in many chemical reactions and it is a good marker of the reaction zone. Its presence is related to high temperatures and therefore it is interesting to check its localization. The most prominent spectral band of OH radicals originates at the transition $A^2\Sigma-X^2\Pi(0,0)$ with wavelength equal to 306.4 nm. This band is degraded to the red. Other bands are also present but their contribution is rather negligible compared to the cited one. For this reason the spectra are centred around 306 nm with relative adjustment depending on the manual rotation of the grating angle.

The data obtained at $T_{\text{set}}=1050$ °C are in Fig. 1 where more than one single spectrum has been reported for each experimental condition. A grey vertical bar divides the data obtained at the two windows. On the left, where the gases come into the furnace, it is possible to recognize a faster ignition of OH production with decreasing values of Φ . In particular, the activity reaches a maximum for $\Phi=0.9$ in all of the four sections of the first window. Fluctuations are of course rather relevant where the OH abundance is the largest, and a more detailed investigation would require a better statistical effort. Nevertheless it remains proven that an advance of the OH radicals towards the gas entrance takes place when passing from a rich to a lean gas mixture. The second window confirms the indication of OH displacement with Φ . The last two sections on the right of the figure for example contain some signal for $\Phi=1.1$ as a consequence of the stretching, while for $\Phi=0.9$ they hardly possess any signal due to the regression of the OH radicals in the proximity of the gas entrance.

The behaviour of OH concentration with the equivalence ratio Φ is reproducible for $T_{\text{set}}=1150$ °C (not shown in the paper). In this case the OH presence is completely confined in the first window at any chosen value of Φ and of course the second window contains a very low level signal only. The OH regression is then more dramatic depending on the higher internal temperatures. As matter of fact the radical production changes moderately along the window optical field for $\Phi=1.1$. Dissimilarly the OH production seems to be attached to the gas entrance for $\Phi=0.9$ and it is already extinguished in the section at the end of the first window. This OH shift must be a consequence of the balance between different ignition times of the relevant reactions caused by the air fluence and the peculiar aerodynamics of the FLOX[®] burner that governs the recirculation.

Images

An ICCD detector (mod. EEV47-10, Andor Technology) was utilized for taking images at the first window where the most interesting features have been put forward by the foregoing considerations. An interferential filter was introduced in front of the ICCD. It had a bandwidth of 10 nm centred at 431.5 nm in correspondence of the main CH spectral emission. Results for $T_{\text{set}}=1150$ °C are given in Fig. 2. Here four images have only been inserted for each condition. The gas entrance is now reversed for graphic reasons and it lies on the right side of the pictures. The images confirm the spectral evidence: at $\Phi=0.9$ they reveal a CH abundance lying in the very proximity of the gas entrance, while at $\Phi=1.1$ the CH luminescence is firmly confined to the central part of the window demonstrating the regression of the production zone towards the gas entrance with decreasing equivalence ratios.

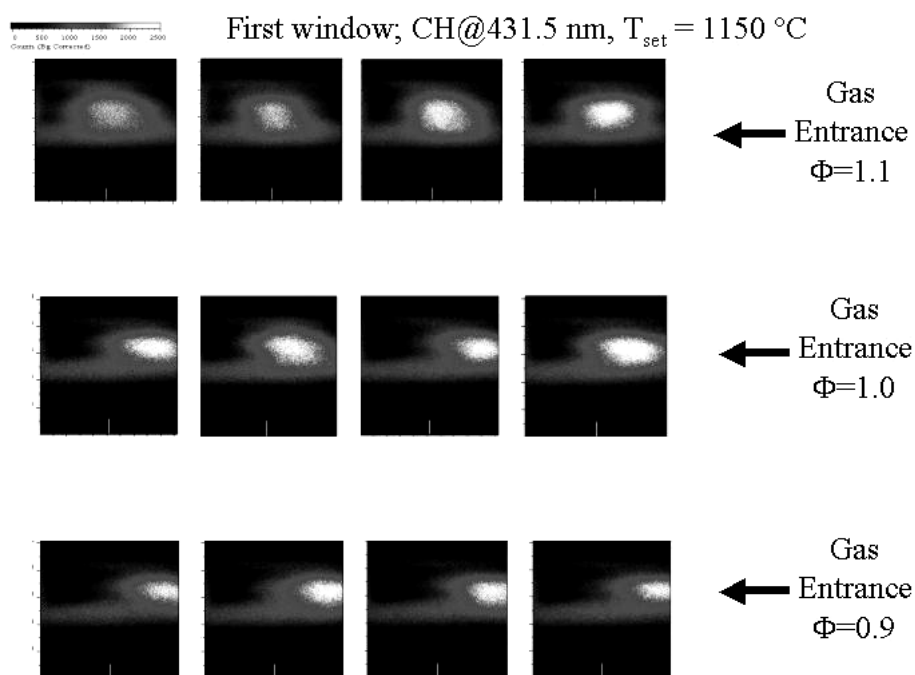


Fig. 2 Pictures of CH taken with an interferential filter at 431.5 nm and bandwidth 10 nm. $T_{set}=1150\text{ }^{\circ}\text{C}$. The four pictures for each Φ correspond to four acquisition time.

The instrumental limits prevented us from observing signals at $T_{set}=950\text{ }^{\circ}\text{C}$. These limitations pertain to the spatial resolution also. In the spectral data resolution is very rough and determined by the physical dimension of the collecting lens having a diameter of 5 cm. This means that the source volume of the signal is confined within the lens area and the furnace width (70 cm). Even though the resolution is rather poor, the spectra contain a dependence on the observing positions located along the furnace length. This can be explained with the help of the images which are surely characterized by a better resolution. They are in fact limited by the pixel dimensions and the collecting optics of the ICCD so that each pixel was capable of capturing light from a squared area of about 0.4 mm per side. The good optical resolution allow the determination of the physical extension of the reaction zone in the direction of the gas injection to about 10 cm for the set temperature corresponding to a stable combustion ($T_{set}=1150\text{ }^{\circ}\text{C}$). Since the furnace has a cylindrical symmetry it is reasonable to conclude that the reaction zone has the same extension in the observing direction too. This conclusion gives then credit to the results obtained with the spectral acquisitions where contributions to the signals originated from an area determined by the collecting lens. In effect its extension is still smaller than the physical extension of the reaction zone and therefore the rough spatial resolution of the spectra does not limit their sensitivity to the spatial changes in the gaseous medium.

REFERENCES

1. Gupta A. K.: *International Symposium on High Temperature Air Combustion and Gasification*, Yokohama, Japan, p. B1-1 (2000).
2. Cavaliere A., de Joannon M., Ragucci R.: *International Symposium on High Temperature Reactants*, Tokio, Japan, p. B4-1 (1999).
3. Marrocco M., Magaldi M., Visentin V., D'Apice M., Cipriani R., and Giammartini S.: *Fourth International Symposium on High Temperature Air Combustion and Gasification*, Rome, Italy (2001).

PIV Post Processing Methods Applied on High Turbulent GT Burners Flames

¹D. Giordano, ²C. Willert, ¹S. Giammartini, ³R. Gallodoro

*1 ENEA –Sezione Tecnologia della combustione, Via Anguillarese n.301
00060 Casaccia (Roma), Italy*

*2 Institut für Antriebstechnik, Deutsches Zentrum für Luft und Raumfahrt (DLR)
D-51170 Köln, Germany*

3 DMA, Univ. di Roma “La Sapienza” Via Eudossiana 18 00184 Roma, Italy

ABSTRACT

The investigation of velocity fields on industrial burner flows is an important and necessary subject of propulsion technology. Actually numerical simulation presents some problem to predict complex combustor in real time flow, due to the general necessity of volume evaluations that involve heavy computational time. Consequently a two dimension diagnostic technique applied on Gas Turbines (GT) burners allows us to point out high turbulent flame properties by means of Mie scattering image analysis and velocity fields post processing techniques. As a matter of fact two industrial burners have been investigated, a conical bluff body burner and a pressurised single sector combustor, by means of the planar technique.

Squishing movements, front flame contours and differential properties have been put in evidence on the annular methane-air burner.

Instantaneous velocity fields and vorticity map, corresponding to swirling movements of kerosene-air mixture flow, have been visualised with 3 bar working condition.

These results are useful for phenomenon understanding, to give boundary condition values for numerical simulations and, finally, to validate numerical results for in-plane flow.

INTRODUCTION

Researches on combustion are continuously finalised to improve combustor efficiency and to reduce fuel consumption and pollutant emissions. These goals involve the analysis of flame properties and flow field description in a wide working range.

Planar PIV technique is already a powerful instrument that reduces operative complexity and costs (respect to three dimensional techniques¹ that generally need of several optical access and higher complexity of the rig) with high resolution of in plane instantaneous velocity field.

The set of flame properties, obtainable with post processing methods, is briefly showed in this work. Local and/or global instantaneous data extracted by a single couple of Mie scattering images (and the corresponding row vector field) can be directly used to initialize numerical simulation calculation and to validate final results.

Firstly, an industrial annular burner (working with methane-air mixture) will be studied and characterised. Axial recirculating movements are imposed by a ring vortex (fixed axially at the outletting duct) that evolves downstream a conical stabiliser (fig.1).

Secondly, a single sector combustor (working at three bar with kerosene-air mixture) will be described with a 2D PIV, even if a swirl movement of the outletting mixture is present.

EXPERIMENTAL FACILITIES

ENEA laboratories equipment

Annular burner (fig.1, left side) works with methane air mixture. It has an external diameter $D_e=25$ mm and an axial stabiliser formed by an inverted frustum of cone $d=15$ mm width (blockage ratio $B_r = 0.37 = d^2/D^2$). PIV measurement are performed by means of a double pulsed Nd:Yag (wave length of 532 nm and power 300 mJ) a CCD camera (484x768 pxs) a Dantec PIV 2000 synchronisation system, a PC and an Al_2O_3 seeder acting on inletting air.

DLR Laboratories equipment

Single sector combustor¹ (fig. 1, right side) was investigated by means of double cavity Nd:Yag laser (energized with 120 mJ per pulse at 532 nm), and visualized with a PCO camera (1280x1024 pxs). The cold air, flowing upstream the air blast nozzle, is seeded by a particle dispenser of SiO_2 .

EXPERIMENTAL RESULTS: IMAGE PROCESSING

High turbulent premixed flame (anchored with squishing and/or swirling movements) can be divided into three regions (fig. 1): 1. non reactive zone, with quite constant temperature, high seeding and lighth density (considered like reference brightness value); 2. reaction zone, where abrupt temperature variation governs gas expansion, involving seeding and light variation; 3. outer front region contemporary affected by combustion and shedding effects.

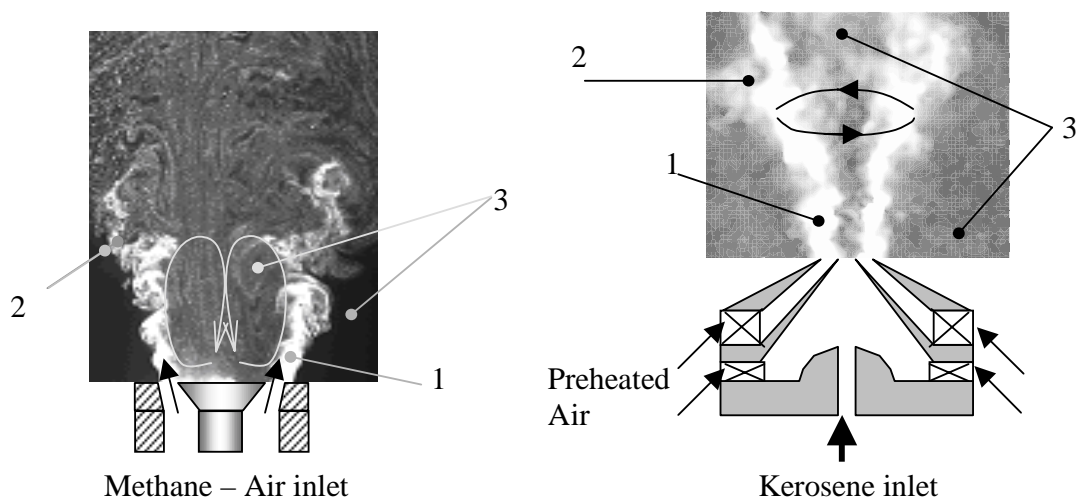


Fig. 1 Three flame regions for: the conical bluff body burner (left side) and the double swirled SSC (right side)

It is possible to extrapolate a qualitative information about front thickness by means of a brightness variation examination method consisting of a comparison between local brightness and reference value obtained by means of light distribution in the outletting jet. This procedure (fig.2) has been validated by theoretical data³ with maximum difference⁴ of 12%.

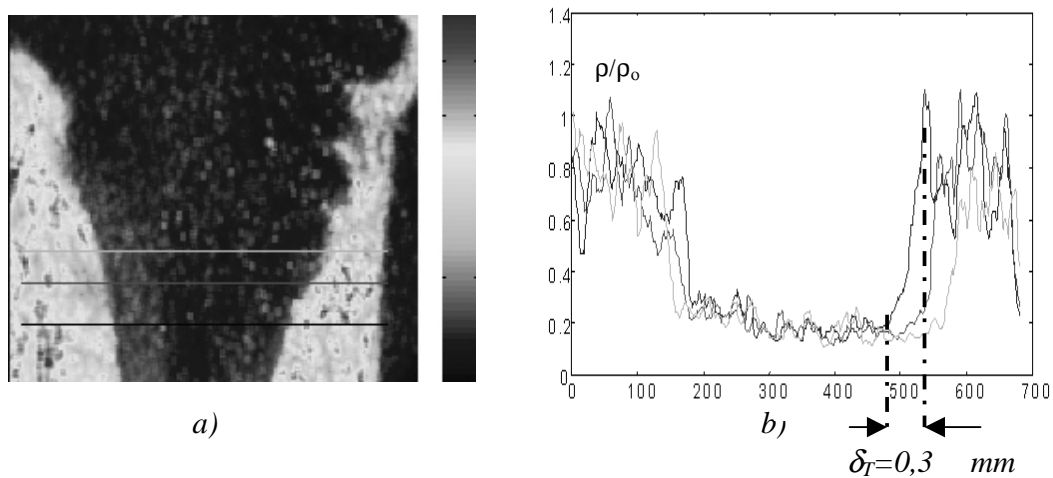


Fig. 2 a) Light density variation representation; b) Diagram relative light density versus radial distance (in pixels, 1 px=32 μ m)

Front flame contour plot (fig.3) is extrapolated by means of the application of a contour tracking system. Front contour is now represented by a row vector, that can be used to evaluate the area, the extension and the curvature of the front. The observation of contour oscillation and curvature distribution allows us to predict combustion regime (wrinkled, corrugated or thickened) The correspondence of maximum front contour curvature with maximum normal divergence zones allows us to validate the above mentioned method and to point out Lewis number effect (causing a reduction or an increasing of local combustion on the base of curvature sign and value²).

Contour plot of the flame overlaid on instantaneous velocity field (fig. 3) allows us to point out combustion effects on velocity distribution and vorticity change.

Front extension obtained by instantaneous data is useful to evaluate turbulent front flame velocity (S_T) on the base of the Guoy's method⁵, with a maximum error of 20%, by means of the ratio:

$$\frac{S_T}{S_L} = \frac{A_L}{A_T}$$

(where S_L is the laminar front velocity, A_T is the turbulent front area and A_L is the laminar front area).

EXPERIMENTAL RESULTS: VELOCITY FIELD ANALISYS

Statistics applied on vector fields gives information about mean velocity fields, on the base of 100 samples.

The comparison between hundreds of local velocities gives us the local mean value (V_{mo}).

Root mean square calculation of local fluctuation evaluated on the base of several instantaneous gives the turbulence distribution.

The difference between instantaneous and mean velocity values allows us to obtain velocity flag u' .

Streamlines calculation is useful to point out flow evolution and vortices behaviour.

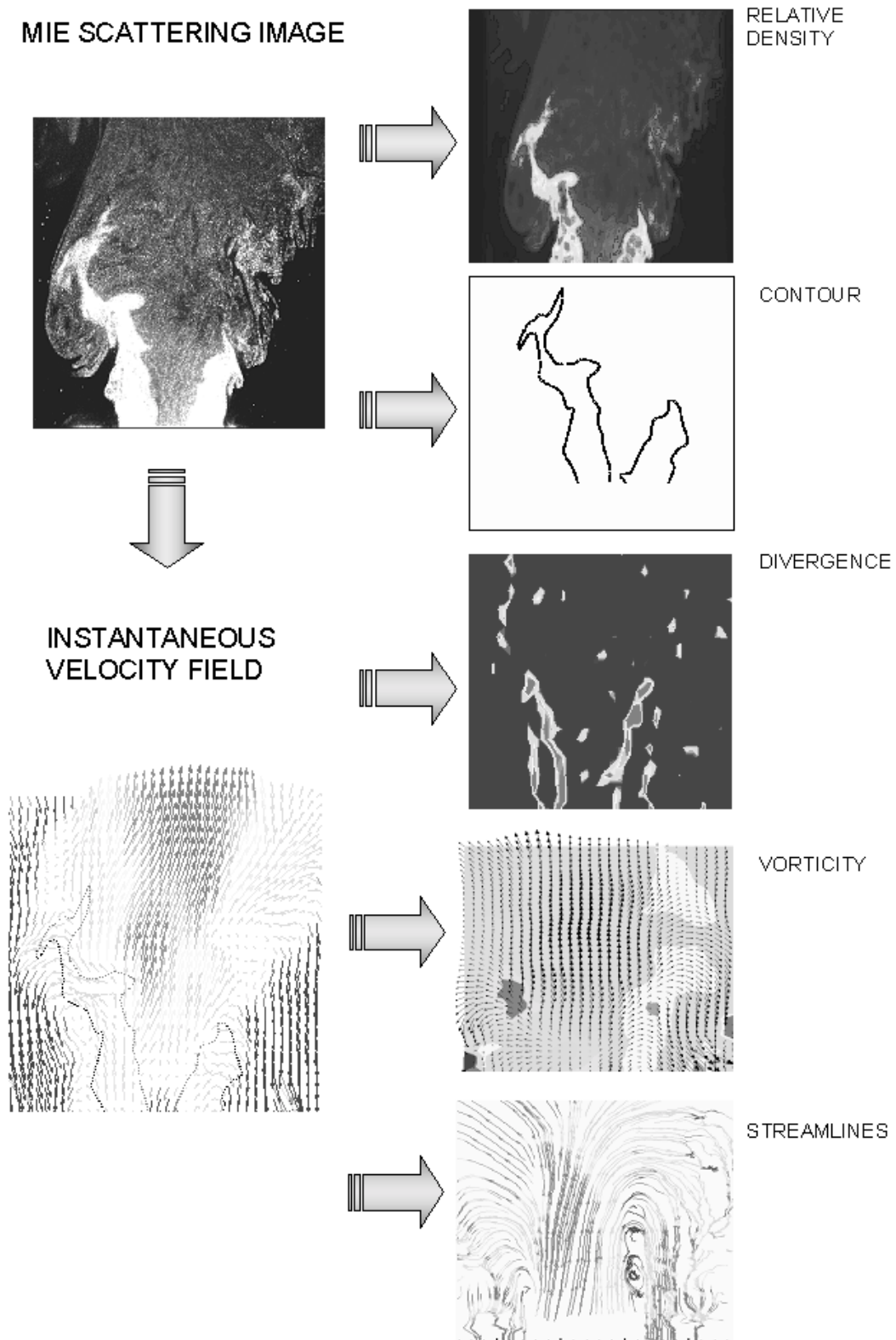


Fig. 3 PIV post processing method results for the conical bluff body burner

Evaluation of normal strain⁶ $\eta=(\partial U/\partial x)+(\partial V/\partial y)$ with constant density gives the regions with out of plane velocity components (where it isn't possible to evaluate the third component⁶); in combustion represents zones crossed by combustive phenomena.

Vorticity evaluation (showed in fig. 3) is obtained by the expression: $\epsilon_{xy}=(\partial U/\partial y)-(\partial V/\partial x)$, that puts in evidence vortices positions.

All these instruments applied on annular methane-air burner allows to evaluate residence time, extrapolated by crossover time⁷, useful to predict NO_x emissions⁷ by means of adiabatic flame temperature evaluation or measurement.

Local experimental data have been used to initialise Large Eddy Simulation (applied on a two dimensional design of the same burner) and validate numerical results with good agreement between calculations and real fields (as reported in another our work presented in this Conference).

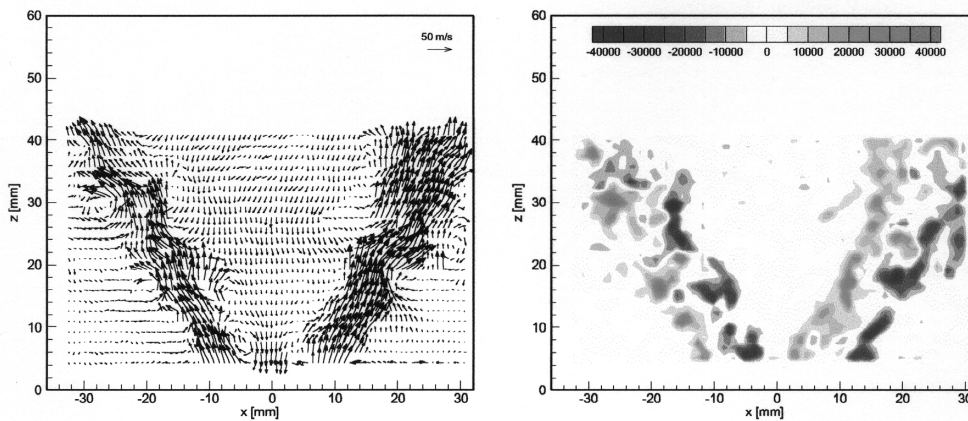


Fig. 4 Example of instantaneous flow inside the pressurized single sector combustor operating at 3 bar: velocity vector map (left), and vorticity map (right). On the right side is shown vorticity field ω_y

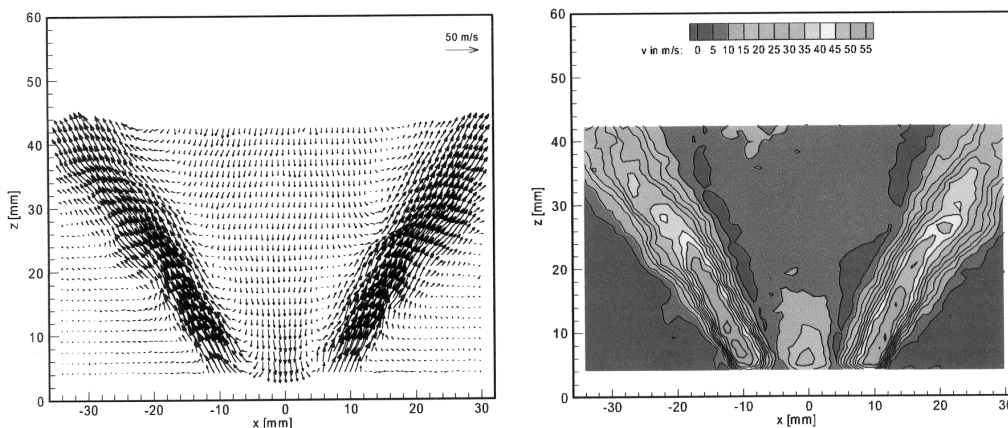


Fig. 5 Average of 13 PIV images of the flow inside the pressurized single sector combustor at 3 bar

The same procedure applied on the single sector high pressure combustor (SSC working at 3 Bar) exhibits a relatively large recirculation area centred above the nozzle exit velocity (fig.4, 5) similar to that found in the former burner, with a down velocity up to 20 m/s. The recirculation also carries unburned radicals of the hot fuel air mixture back toward the nozzle which has a stabilizing effect on flame position and ensures a continuous and complete combustion.

The described recirculation area is easy to identify and it is characterised by the lack of vortical flow between the lobes of the spray cone

CONCLUSIONS

Two different configurations have been examined for combustor geometry by means of PIV post processing methods. Mie scattering images analysis is useful to put in evidence flame front properties like: turbulent flame speed (from area calculation); front thickness (with a maximum error of 20%); front curvature (useful for burning regime detection); front shape. Velocity field processing gives information of instantaneous and mean field, differential properties and vortices behaviours and position. The above mentioned results point out the squishing central movements and the crossing time, useful for pollutant emission preview. The single sector burner has been investigated with a working pressure of 3 bar. Pressure values higher than the former burner ones caused experimental problems (for the not homogeneity of the seeding and for the dusts and powder leaved on glasses inner faces). Instantaneous and mean velocity field seems quite similar. Swirling movements generate an inner recirculating zone rotating in a plane orthogonal to burner axis (on the contrary of the conical case). All of these local and global data are: useful input for numerical code and a validation for calculated fields.

ACKNOWLEDGMENTS

We gratefully acknowledge Prof. Giulio Guy of the University of Rome "Roma Tre" for his insightful comments about image processing and Mr Livio Fabi of IECA Italia S.R.L. who make possible to develop our researches. We acknowledge Mr Augusto Raganelli (IECA Italia) who participated to paper redaction and to Dr Marc Jarius for SSC image data.

REFERENCES

1. Willert, C., Jarius, M.: *4th International Symposium on Particle Image Velocimetry*, Göttingen, Germany, September (2001)
2. Stella A.: *Experimental Investigation of Turbulent Premixed Combustive Flows*, PHD thesis of the University of Rome "La Sapienza", Rome, Italy 2001
3. Peters N.: *Journal of Fluid Mechanics*, **384** (1999)
4. Giordano D., Giammartini S., Manfredi F.: *Proceedings of the Combustion Institute (WIPP)*, **28**:85 (2000)
5. Gaydon A. G., Wolfhard H. G.: *Flames Their Structure, Radiation and Temperature*. Chapman & Hall, London (1960)
6. Willert C.: *Vector field Operatore, Proceedings of DLR Course 2001 "Application of Particle Image Velocimetry – Theory and Practise"*, Gottingen, Germany (2001)
7. Giordano D., Giammartini S., Manfredi F., Guy G.: *Sixth International Conference on Technologies and Combustion for a Clean Environment*, Oporto, Portugal, July (2001)

Multiangular light scattering measurements from soot fractal aggregates in laminar diffusion flames

S. De Iuliis, F. Cignoli, and G. Zizak

CNR- IENI, Istituto per l'Energetica e le Interfasi
Sez. Milano (ex-TeMPE), via Cozzi 53, 20125 Milano, Italy

INTRODUCTION

Sampling of soot in hydrocarbon flames showed that soot consists of fractal aggregates of primary particles. Such aggregates exhibit these basic features: the primary particle diameter, dp , and the fractal dimension, D_f , of the aggregates are nearly constant at a flame location for all aggregates, on the contrary, the number of particles per aggregate changes largely leading to a polydisperse distribution for the resulting aggregate structure [1]. In this work, the angular dependence of the light scattering from soot aggregates in a laminar ethylene diffusion flame has been investigated by using the fractal approach. The main optical parameters such as the gyration radius and the fractal dimension of the aggregates have been inferred. For the interpretation of the data, polydisperse soot distributions have been utilized. These measurements in conjunction with an extinction and an absolute small angle scattering measurement will allow a complete soot characterization. Results compare well with previous measurements in similar flames.

BASIC THEORETICAL BACKGROUND

By carrying out a scattering measurement the resulting average signal can contain only information about some sort of "average" aggregate. Our aim is to find out, among the many, the most reliable of these average aggregates.

The angular dependence of the light scattering from a monodisperse ensemble of aggregates (with the same number, N , of primary particles) is given by:

$$I_{scatt}^m(\theta) = \eta I_0 C_{vv}^p N_a N^2 S(qR_g) \quad (1)$$

where I_0 is the incident light intensity, η is a calibration constant, C_{vv}^p is the vertical scattering cross section of a single primary particle for a vertically polarized light, N_a is the number density of aggregates in the probe volume, and $S(qR_g)$ is the static structure factor depending on the radius of gyration of the aggregates, R_g , and on the scattering wave vector, $q = (4\pi/\lambda) \sin(\theta/2)$. For a polydisperse ensemble of aggregates eq. (1) takes the form of:

$$I_{scatt}^p(\theta) = \eta I_0 C_{vv}^p N_a \int N^2 S(qR_g) p(N) dN = \eta I_0 Q_{vv}(\theta) \quad (2)$$

where $p(N) dN$ represents the normalized population distribution and $Q_{vv}(\theta)$ is the experimental scattering coefficient. Again from sampling measurements, the population distribution has been determined to be represented by a lognormal distribution in the form of:

$$p(N) = (1/(\sqrt{2\pi N \ln\sigma})) \exp(-1/2 (\ln(N/N_{gm})/\ln\sigma)^2) \quad (3)$$

where σ and N_{gm} are the standard deviation and the geometric mean of the distribution, respectively. The determination of the static structure factor $S(qR_g)$ poses severe problems and numerous studies have been conducted on this subject. Two limiting cases have been obtained:

$$S(q R_g) \approx 1 - q^2 R_g^2 / 3 \quad \text{for } q R_g \leq 1 \quad (4a)$$

$$S(q R_g) \sim q^{-D_f} \quad \text{for } q R_g > 1 \quad (4b)$$

Relation (4a) describes the Guinier regime, whereas relation (4b) is characteristic of the power-law regime. The exact form, covering all ranges, is still debated and a number of approximate solutions are found in literature. It could be noticed that the above relationships (4a) and (4b) suggest that measurements at small and large angles could be a satisfactory approach for the determination of R_g and D_f and some attempts have actually been done. Nevertheless, measurements at large angles with visible wavelengths give fractal dimensions substantially lower than the ones observed through sampling. Moreover, at small angles, the measured radius of gyration has a straightforward meaning only for a monodisperse distribution and not for polydisperse ones that are actually found in flames. In fact the use of eq. (4b) in eq.(2) shows that measurements at small angles allow to achieve a mean-squared radius of gyration written as

$$R_{g2m} = (dp/k_f^{1/D_f}) (m_{2+2/d_f}/m_2)^{1/2} \quad (5)$$

where k_f is the prefactor (in the range 5.8 – 9.4) and the $m_i = \sum N^i p(N)$ is the i-th normalized moment of the distribution. It is also well known that by combining measurements of extinction, (K_{abs}), and scattering at small angles (where $S(qR_g)$ is about 1 in the Guinier regime) a volume-mean diameter, D_{30} , of aggregates can be obtained

$$D_{30}^3 f_n = (\lambda / \pi)^3 (4 \pi E(m) Q_{vv}(\theta)) / (F(m) S(q R_g) K_{abs}) \quad (6)$$

In this expression $E(m)$ and $F(m)$ are the usual functions of the refractive index, $m = n - i k$, of soot particles, f_n is the ratio of moments $f_n = m_2 / m_1^2$ and $D_{30}^3 = d_p^3 m_1$ is connected with the primary particles diameter, d_p and the average number of particles per aggregate, m_1 .

It is apparent from eq. (5) and (6) that the measurable quantities (R_{g2m} and D_{30}) depend on different moments of the distribution and therefore can not be combined to derive any meaningful quantity concerning the soot structure. This particular example together with the general fact that measurements allow to achieve an “average” value anyway, points out that the proper assessment of such a quantity is a crucial issue in order to obtain from the experimental data some information about the aggregate structure, that is dp , D_f , and “average” number of particles per aggregate.

From the above it follows that the radius of gyration to be measured must depend on the ratio m_2 / m_1 , as well as D_{30} . Moreover it must be as insensitive as possible to the actual parameters of the aggregate structure and distribution, basically from σ and D_f . The formulation of the radius of gyration that best matches these requirements turns out to be as proposed by Koylu and Faeth [2], measured in the power law regime. This assumes the expression

$$R_{gKF} = (dp / k_f^{1/D_f}) (m_2 / m_1)^{1/D_f} \quad (7)$$

From our numerical calculations R_{gKF} exhibits a stability with respect to σ and D_f higher than any other R_g otherwise defined. Once the value of R_{gKF} and D_f are determined (our procedure is discussed further on), the diameter of primary particles is calculated with the expression:

$$dp^{3-D_f} = (D_{30} f_n) / (k_f R_{gKF}^{D_f}) \quad (8)$$

The total number of primary particles, N_p , is then calculated by the soot volume fraction value obtained through the K_{abs} measurement.

The procedure to determine the value of R_{gKF} is the following. For a given set of values of dp , N_{gm} , σ , and D_f , both R_{gKF} (from Eq. 7) and the angular dependence of the scattering signal (from Eqs. 2, 3) have been calculated by assuming the static structure factor for monodisperse aggregates as given by Lin *et alii*. Then this scattering curve has been fitted using the R_{gKF} and D_f as input parameters. Repeating this procedure several times, allowed to select the fitting curve able to describe the scattering angular distribution in the widest range of input parameters. This fitting curve was used to analyze the experimental data with R_{gKF} and D_f as variables of this fitting procedure, thus determining as output their experimental values.

EXPERIMENTAL SET-UP

The 514 nm vertically polarised green line of a Kr+ Ar+ ion laser was used to induce the soot scattering. The laser beam, after a mechanical chopper, was passed on the major axis of a modified Wolfhard and Parker burner (central slot of 5 mm x 40 mm and two lateral slots of 3 mm x 50 mm) placed on a motorized three axis table and producing an ethylene-air diffusion flame. Scattering signals were detected by means of an assembly including quartz lens, diaphragm, polarizer, vertical slit, interferential filter and photomultiplier, arranged on an annular rotating platform. Care was taken in placing the burner and the laser beam path on the rotation axis of the platform. Signal were processed by a lock-in amplifier, digital voltmeters and PC for data acquisition. The burner adopted was chosen to avoid interference from the external soot layers at angles approaching the forward and backward directions. It was fed with ethylene (0.48 l/min) in the inner slot and air (4.2 l/min) in the external slots. The resulting diffusion flame was analyzed along the vertical axis at different heights above the burner mouth. For each position the radial scattering measurements were collected between 10 and 160 degrees by averaging 500 acquisition at each angle. The resulting trend was obtained from averaging three of such data sets.

RESULTS AND DISCUSSION

Raw data exhibit a marked maximum in the forward direction and, at a lower extent, in the backward direction, thus confirming a non-Rayleigh regime. Correction for sinusoidal variation of the probe volume was introduced together with a correction for self-absorption. Fig. 1 shows the scattered light signal as a function of the scattering wave vector in a log-log scale as measured at three heights above the burner.

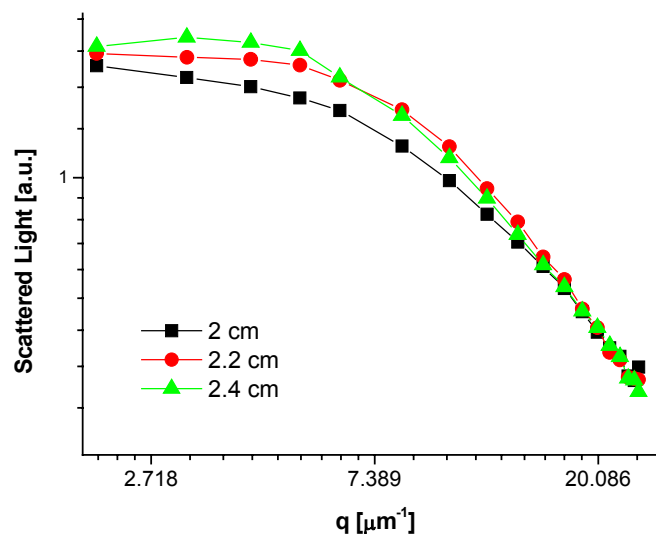


Fig. 1: Scattering signal versus the scattering wave vector at three levels.

The overall shape of the curves reproduces well the typical behavior found in literature with an almost flat beginning in the Guinier regime (small angles), a bending and a linear decrease in the power law regime (large angles). By analyzing these curves it is found that the mean-squared radius of gyration, R_{g2m} , are 126, 122 and 126 nm for the 2.0, 2.2 and 2.4 height respectively. From the slope at high q values of the same curves, the apparent fractal dimension resulted to be 1.06, 1.1 and 1.12 respectively. These values are low in comparison with sampling data confirming the general finding that the slope gives too low fractal dimension [3]. We have applied the previously described fitting procedure with the fitting curve, S_{pol} given by the following expression:

$$S_{pol} = [1 + (5.95168/D_f) (q R_{gKF})^2 + 2.5 (q R_{gKF})^4 - 1.52 (q R_{gKF})^6 + 1.02 (q R_{gKF})^8] J^{-D_f/8}$$

This expression corresponds to the structure factor of the polydisperse distribution characterized by the following choice of parameters: $D_f = 1.6$, $\sigma = 2.1$, $dp = 25$ nm, $N_{gm} = 50$. By fitting the curves of Fig. 1, after normalization, both the D_f and R_{gKF} are determined and the results are reported in the following table.

Height [cm]	D_f	R_{gKF} [nm]
2.0	1.3	103.2
2.2	1.7	87.35
2.4	1.7	89.8

The preliminary results are in general agreement with previous literature data especially with the sampling measurements [3,4]. The results show that the utilized methodology is able to give useful indications about the structure of the soot aggregates. At the moment it is difficult to infer a trend for the aggregation mechanism and further work have to be carried out. From these data the value of the diameter of primary particles and the number concentration of primary particles can be obtained with further measurements of extinction and scattering at small angles, as indicated by eq. (6).

REFERENCES

1. Koylu, U.O, Faeth, G.M.: *Journal of Heat Transfer* , **115**: 409 (1993)
2. Koylu, U.O, Faeth, G.M.: *Journal of Heat Transfer* , **116**: 971 (1994).
3. Bonczyk, P.A., Hall, R.J.: *Langmuir*, **7**: 1274 (1991)
4. Cai, J., Lu, N., Sorensen, C.M., *Langmuir*, **9**: 2861 (1993)

Extra situ-DLS measurements on nanoparticles produced in laminar premixed flames

¹D. Cecere, ²P. Minutolo, ¹A. D'Alessio

¹Università Federico II, Naples-ITALY

²Istituto di Ricerche sulla Combustione –C.N.R., Naples-ITALY

There is an increasing demand for diagnostics to determine the physical and the chemical characteristics of very small particles or molecular clusters in the size range of 1-10 nm produced by various combustion sources. Such compounds are suspected of toxicity, epidemiological results have also showed a causal relationship between particulate matter concentrations in ambient air and increased deaths in several cities around the world (Wichmann et al. 2000).

Because of their size, optical properties, and partial water solubility, combustion generated d=1-10 nm particles may also have significant effects on climate acting as cloud condensation nuclei.

Big difficulties arise in developing diagnostics and in evaluating their performance for particles in this size range which falls into the transition range between the gas and particle phase, and appropriate standards for calibrating these systems are not readily available.

In this paper Dynamic Light Scattering (DLS) technique is used to measure the diameter distribution function of nanoparticles produced in non-sooting, premixed, ethylene/air flames with various C/O ratio.

This technique is based on the study of the intensity fluctuations of the light diffused by nanoparticles suspended in a medium, which are due to Brownian motion. These fluctuations are random and are related to the translational diffusion coefficient D and so to the diameter of the particles. Since the scattering intensity at the detector is dependent upon the position of the particles relative to the detector, the change in particles positions is accompanied by a change in the measured scattering intensity. As a consequence, an ensemble of particles give rise to intensity fluctuation in scattered light. Since the diffusion characteristics of the particles depend on their size and shape, studying the fluctuations of the scattered light by nanoparticles, information about the particle size distribution may be obtained [1].

A typical way to analyze fluctuations of the scattered light signal is by way of its 'autocorrelation function'. The autocorrelation function of the scattered intensity is the convolution of the intensity signal with itself delayed as a function of the delay time. In other words, if the detected intensity is described as a function $I(t)$, then the autocorrelation function of this signal is given by the following expression, where τ is the shift time or delay time since it represents the delay between the original and the shifted signal.

$$G(\tau) = \int_0^{\infty} I(t)I(t + \tau)dt$$

The above function is also called the intensity correlation function, and it is used to describe the correlation between the scattering intensities measured at $t = 0$ and some later time ($t_n = t_0 + \tau$).

In the of any applied forces , the particle position is dictated by the degree of Brownian motion. As such, the measurement of the particle intensity correlation curve is an indirect measure of particle's diffusion coefficient. For light scattered from diffusing molecules the intensity correlation curve exhibits an exponential decay [2], as showed below, indicating that the signal is correlated for short delay times and completely uncorrelated for long delay times.

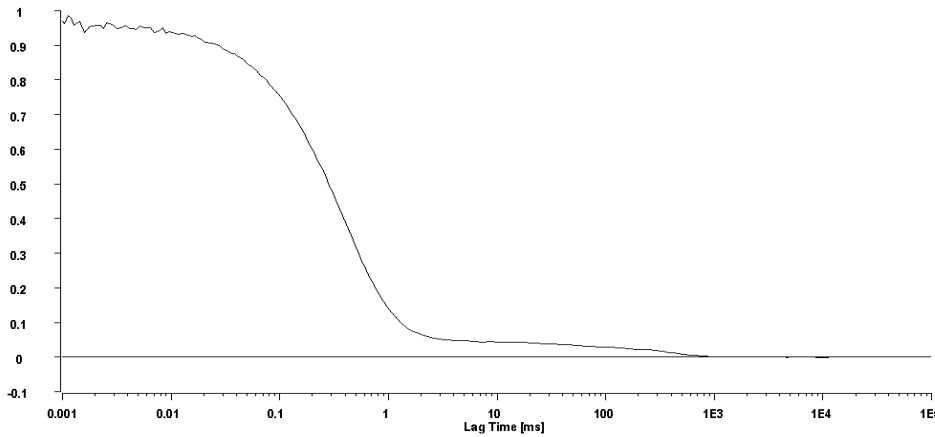


Fig.1: Intensity correlation function

In practice, the continuous intensity correlation function can not be measured. It can however, be approximated with discrete points obtained by a summation over the duration of the experiment. This summation is performed by the correlator, a circuit board composed of various logic chips and operational amplifiers which continuously multiplies and adds measured intensity values.

If the statistics of the measured intensity signal are gaussian (which is true for all diffusion and for most random processes) then the Siegert relation holds true. The Siegert [3] relation states that the normalized intensity autocorrelation function has the form:

$$G (\tau) = A + B \left(g (\tau) \right)^2$$

where A and B are factors dependent on the instrumental configuration and g(τ) is the field correlation function that in the case of non-interacting homogeneous spherical particles with different sizes can be written as a sum of exponential:

$$g (\tau) = \int_0^\infty c(\Gamma) \exp(-\Gamma \tau) d\Gamma$$

being the decay rates $\Gamma = D q^2$ proportional to the particle diffusion coefficient D, ($q = \frac{4\pi n}{\lambda} \sin \frac{\theta}{2}$ is the modulus of the scattering vector fig.2) and c(Γ) represents the normalized intensity weighed distribution of decay rates.

In dynamic light scattering experiments, the radius R of the particle is calculated from the diffusion coefficient D via the Stokes-Einstein equation:

$$D = \frac{k_B T}{6\pi\eta R} C_s$$

where k is the Boltzmann constant, T is the temperature, η is the solvent viscosity, C_s is the Cunningham correction factor C_s [5] that accounts for the increased mobility of the particle in a gas due to non-continuum effects and $f = 6\pi\eta R$ is the frictional coefficient for a compact sphere in a viscous medium.

By definition then, the DLS measured radius is the radius of a hypothetical hard sphere that diffuses with the same speed as the particle under examination.

Typical polydispersity analysis generally involves two steps. In the first one, the modulus of the field autocorrelation function $g(\tau)$ is estimated from the modulus of the experimentally measured autocorrelation function $G(\tau)$.

In the second, $g(\tau)$ is inverted for the distribution of the decay rates. The main objective of the data inversion consists of finding the appropriate distribution of exponential decay functions $c(\Gamma)$, which is consistent with the data and best describes the measured intensity correlation function, this is done by regularization techniques implemented in a program called CONTIN [4].

Experimental set-up.

The PCS experimental set up is shown in fig.1. The laser used is a water-cooled Spectra-Physics Argon laser at an operating wavelength of 488nm.

The detection system for the scattered light consists of a Glan Thompson polarizer and a gradient index lens optical fiber. The signal is sent to the ALV/SO-SIPD detector which uses two photomultipliers and a beamsplitter cube for setting a PSEUDO CROSS correlation detection which is necessary in order to increase the accuracy in the detection of very fast processes.

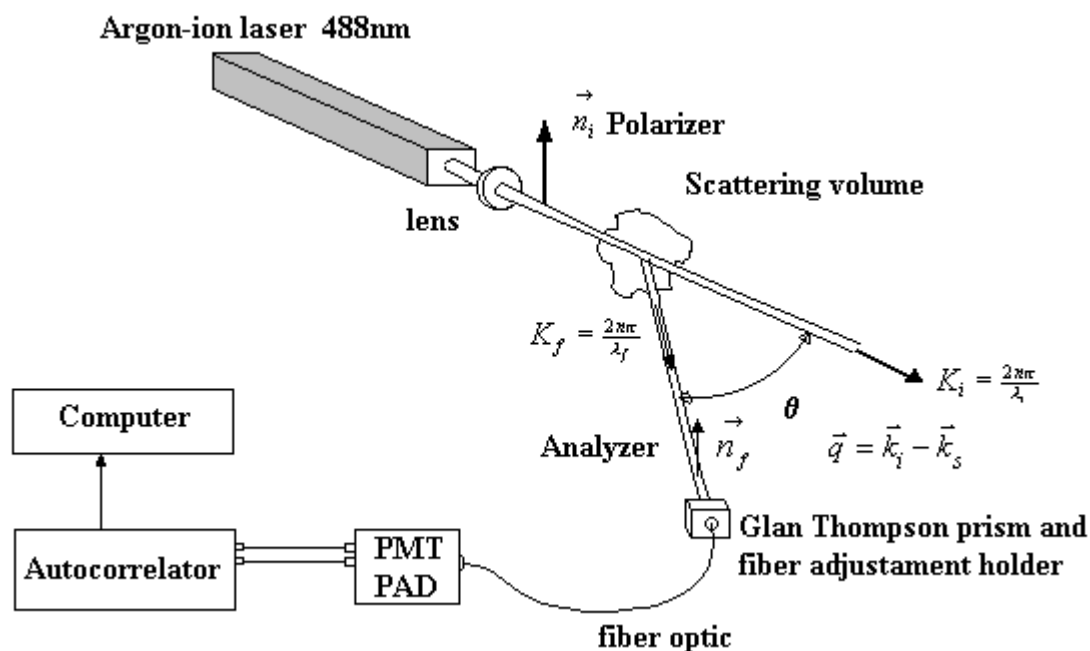


Fig.2: Dynamic Light Scattering apparatus

Both photomultipliers are connected to the same HV-supply and two high speed preamplifiers/discriminators are further used. The correlator is an ALV-6010/200 multiple tau digital correlator with a very fast realtime sampling time of 5 ns. Laminar, premixed, sooting ethylene air flat flames ($C/O=0.69$, $C/O=0.65$) are studied using extra situ sampling techniques.

The flames (cold flow velocity=9.0 cm s⁻¹) are stabilized with a stainless steel plate on a McKenna bronze plate water-cooled, burner. Combustion products are collected by means of an isokinetic water-cooled, stainless steel probe (ID 2mm) placed at different height above the burner, then this material is transported through a sampling line and bubbled in 6ml of water contained in a condenser. The sampling time is of 3h. The particles dispersed in water are finally put in a standard 1 cm path-length quartz cell and analyzed with the DLS set up.

Results and conclusions

The size distribution functions of the particle sampled in two flames, with a different C/O ratio at the height above the burner of 5mm, which are determined by DLS measurements are reported in fig.2.

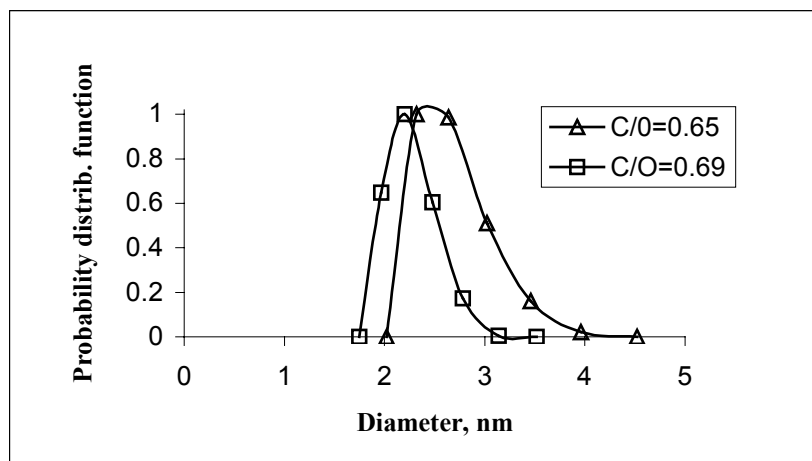


Fig.3: Diameter distribution function for flames with C/O=0.65,0.69 and height above the burner $z=5$ mm.

Under the assumption that the scattering particles behave as hard spheres in dilute solution and within the Rayleigh-Debye theory a weighting of the amplitudes of the decay times distribution is performed to obtain number weighted particle radius distribution functions. The diameters found in Dynamic light scattering experiments are in good agreement with diameters determined by previous studies [6] which used *in situ* light extinction and scattering measurements to determine the size and number concentration of particles. Light scattering/extinction within the experimental uncertainty furnishes the mean diameter $D_{6-3}=2.5$ nm for the two flame conditions, while from the DLS results a slight difference is observed, D_{6-3} is equal to 2.8 nm for the C/O=0.65 flame and 2.4 nm for the C/O=0.69. Further measurements are necessary to confirm a possible trend of the size distribution of the particles with C/O ratio.

References

- [1] Finsky, R., *Particle Sizing by Quasi-Elastic Light Scattering*, Elsevier, 1994
- [2] Berne, B.J., Pecora, R., *Dynamic light scattering* Wiley, New York, 1976
- [3] Wyn Brown, *Dynamic Light Scattering*, Clarendon Press, 1993
- [4] S.W. Provencher, *Comput. Phys. Commun.* 27, 229-242 (1982).
- [5] Gousbet Mean diameters and number densities in premixed flat flames CH₄-O₂ by diffusion broadening spectroscopy, *Applied Optics*, 1986.
- [6] Minutolo, P., Gambi, G., D'Alessio, A., *Proc. 27° Symposium on Combust.*, 1461 (1998).

Characterization of Combustion Produced Nanoparticles by Atomic Force Microscopy

A. Barone, A. D'Alessio, A. D'Anna, M. Malato

*Dipartimento di Ingegneria Chimica, Universita' di Napoli "Federico II"
80125- Napoli Italy*

Introduction

Atmospheric particulate matter of anthropogenic origin is object of great interest because of its influence on health effects [1,2]. Recent toxicological researches demonstrated that small particles harmful effects are enhanced as their size decreases [3].

A significant amount of anthropogenic particles are emitted in form of nanoparticles derived from combustion processes. Results obtained by u.v. light scattering and extinction measurements in soot forming premixed flames showed that nanoparticles with typical dimensions smaller than 3-4 nm are present in the preinception region of soot forming premixed flames and in fuel side of diffusion flames. Furthermore, nanoparticles smaller than 4 nm were found in premixed flames with C/O ratio below the soot threshold, where they emit just a blue light [4]. The problem of this ensemble technique is that it gives only moments of the size distribution of the nanoparticles, and, furthermore, the knowledge of their optical properties (i.e. chemical composition) is required for a correct data interpretation.

Nanoparticles were also studied by High Resolution Transmission Electron Microscopy [5]. The limitation of this technique is that TEM gives only bi-dimensional images of the samples and, in addition, it requires a complex and expensive coating process of the sample with a layer of conducting material.

Atomic Force Microscopy (AFM) offers an interesting new opportunity for the characterisation of nanoparticles. It is based on the mechanical interaction between a tip and the sample surface. The tip, placed at the end of a cantilever, ideally ends with a single atom and is made by hard and non-conducting materials. Scanning the sample surface, this tip generate maps at very high resolution, reproducing sample three-dimensional morphology by taking, using a complex electronics, the trace of attractive or repulsive interactions.

Preliminary application of Atomic Force Microscopy are presented in this paper, with the purpose of describing the morphological properties of carbonaceous nanoparticles sampled from rich premixed laminar flames in different regimes; this results are than compared with data obtained by optical characterization in flames made in some of the observed conditions.

Experimental technique

A McKenna burner was employed to produce different ethylene/air laminar premixed flames with C/O ratios of 0.56, 0.77, 0.92 and 1.0, corresponding to conditions ranging from rich blue flames to fully-sooting flames.

Samples at different heights above the burner were obtained by collecting carbonaceous material on mica substrates by thermophoretic effect. To this aim a special holder mounted over the mobile extension of a one-way acting pneumatic cylinder have been employed, which permits particle sampling with a residence time in flame of about 100 ms. Its small dimensions let the substrate pass through the flame without perturbing significantly the flow downstream. Furthermore, among its feature, there is the possibility to hold substrates different in shapes and thickness (i.e. sampling adapted to different techniques of scanning probe microscopy or electron microscopy).

Tests were performed, preliminarily, by using different materials as substrates, in order to verify the adhesion attitude of the particles. The ideal substrate should show roughness so low to permit to distinguish the observed very small structures by the background noise. Elevated mechanical and chemical resistance to the high flame temperatures and clean surfaces, obtained preferably by cleavage, are other important required features. Thus silica glass, pyrolytic graphite (HOPG) and mica muscovite have been employed for this purpose. The silica glass substrates have been suddenly discarded since the vitreous transition, which causes softening of the material, made unreliable any dimensional and morphological estimations because of a partial entrapment of the particles inside the substrate surface for high exposure times. On the other hand HOPG and muscovite show a very good temperature resistance; but only mica was finally preferred because of its quite perfect cleavage.

A Digital Instruments Nanoscope IIIa™ AFM has been used to observe the nanoparticulate. A *tapping-mode* technique was employed: it consists in putting a cantilever, with a special tip, in oscillation close to the sample, permitting to touch just slightly the deposits. As oscillating frequency is chosen that of the mechanical resonance of the cantilever. Various advantages are present using *tapping-mode*: absence of strong interactions between tip and sample (below 100 pN), observation of samples easily removable from the substrate surface and diminution of undesirable convolution effects.

The *phase detection* tool, present in the electronics of the *tapping-mode* technique, is sensitive to the different viscoelastic properties of the observed materials, and allows to find out further information about morphology and physical properties by measuring the phase shift between the signal that governs the oscillation and the deflexion/oscillation output signal of the cantilever. The Phase Extender electronics permits to acquired in the same time both topography and phase detection. Nanoprobe® Super Sharp Silicon probes, characterized by a very low apical curvature radius (about 2 nm) were employed in order to attenuate the probe-sample convolution effects, a procedure indispensable for the correct detection of very small nanoparticles.

Results and discussion

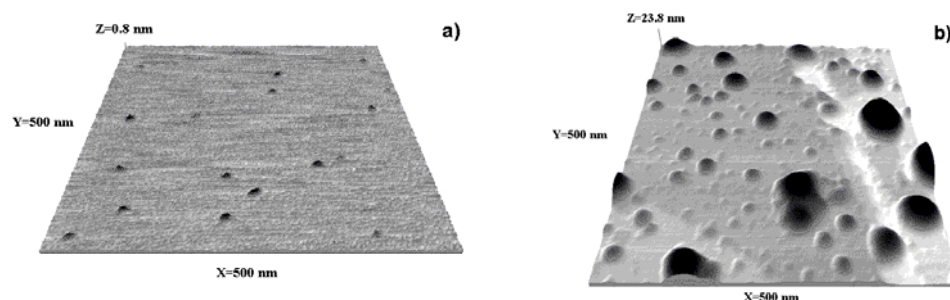


Fig. 1 – AFM images of nanoparticles produced by ethylene/air flames: $C/O=0.56$ at $Hab=5$ mm (a) and $C/O=0.92$ at $Hab=10$ mm (b).

Figure 1 shows an example of AFM scanning on mica substrates exposed to ethylene/air flames for two flames, $C/O=0.56$ at $Hab=5$ mm (a) and $C/O=0.92$ at $Hab=10$ mm (b) respectively.

The electromechanical noise and the electronics (feedback control) put limits to the feasibility of measurements at too strong magnification. It has been verified that the more convenient

condition to study such particles is reached performing measurements on surfaces of 500 x 500 nm. The subtraction via software of a threshold plane to separate the particles from the substrate is a very critical task for the volume calculation. To this aim S.P.I.P.TM ImageMetrology processing software has been used.

An equivalent spherical diameter (ED), calculated for each particle from the volume, and the ratio between the measured height and base diameter (SR), are considered to be parameters useful to this work.

The morphology of the particles shows modifications varying the C/O ratio.

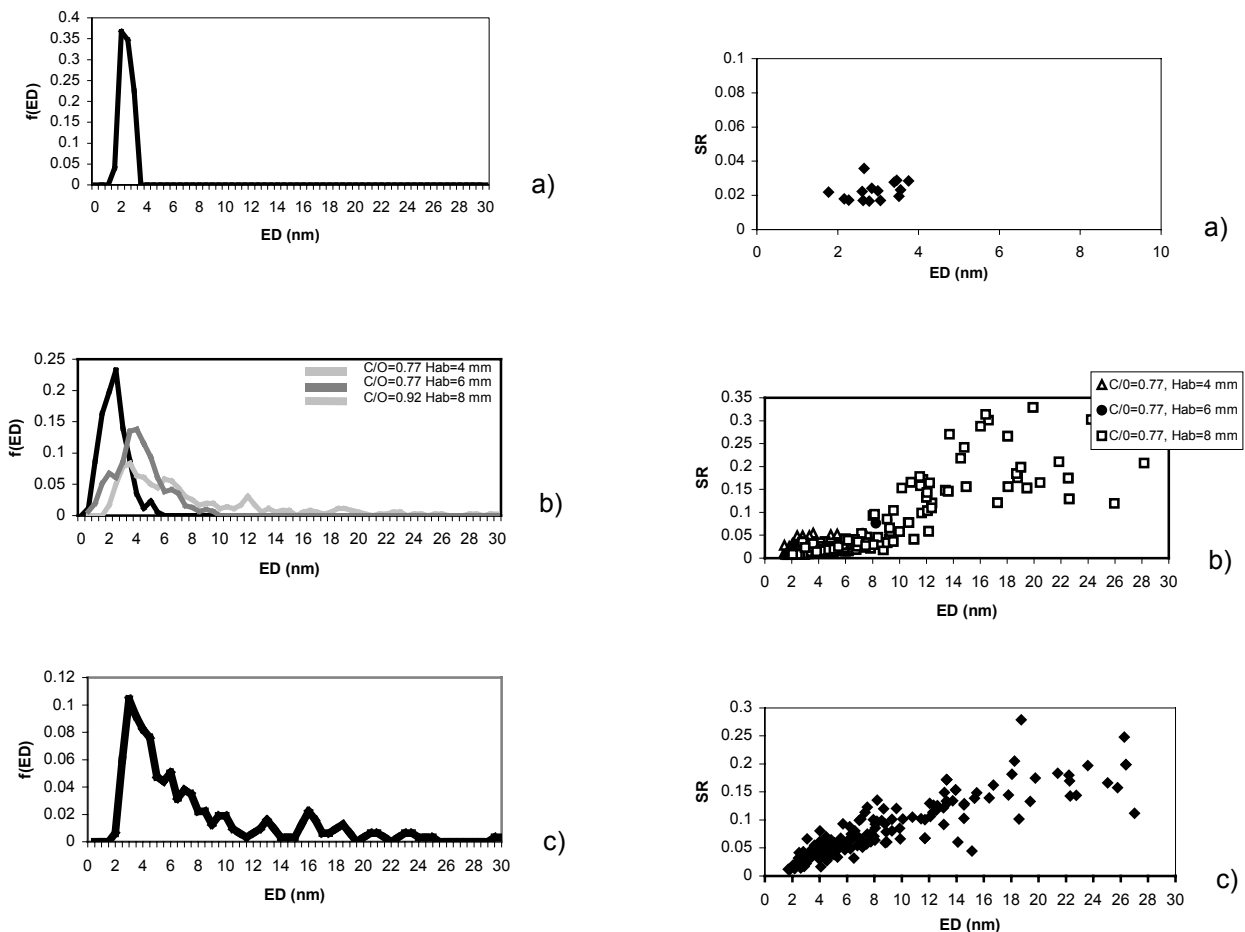


Fig. 2 – Statistics for different flames: $C/O=0.56$ at $Hab=5$ mm (a), $C/O=0.7$ at Hab equal to 4, 6 and 8 mm (b), $C/O=0.92$ at $Hab=10$ mm (c).

Fig. 3 – Sphericity ratios as a function of ED for different flames: $C/O=0.56$ at $Hab=5$ mm (a), $C/O=0.7$ at Hab equal to 4, 6 and 8 mm (b), $C/O=0.92$ at $Hab=10$ mm (c).

Figure 2a reports statistics on a rich blue flame ($C/O=0.56$), with sampling at 5 mm above the burner. A narrow-peaked curve is showed, with a maximum at about 2.4 nm. The particles have a quite circular and very flat shape (Fig. 3a), since the observed particle heights is well below the base diameter.

Fig. 2b shows ED distribution function of a slightly-sooting flame ($C/O=0.77$) for different sampling locations (4 mm, 6 mm and 8 mm). At 4 mm the distribution is peaked at about 2.7 nm and ranges from 1 nm to 6.2 nm (black line). At 6 mm (dark gray line), the particle distribution function broadens extending up to 10 nm with the maximum at 4.5 nm, while at 8 mm a maximum is around 4 nm but the function extends up to 24 nm. The particles detected at 4 and 6 mm have a very flat profile, with a

SR (sphericity ratio) varying from 0.02 to 0.08. At 8 mm, instead, the SR of the particles is similar to those measured at 4 and 6 mm for ED less than 10 nm and jumps to higher values (0.20-0.30 nm) for larger ED particles (see Fig. 3b). Figure 2c, which is relative to a sampling location in the soot inception region of the C/O=0.92 flame, shows a distribution similar to that detected at 8 mm of the C/O=0.77 flame, with a peak centered at about 4 nm and it extends up to 30 nm. Analysis of particle shape reported in Fig. 3c shows a SR behavior close to that measured for C/O=0.77 at Hab=8 mm. This ratio, in facts, increases to values as high as 0.35 for larger particles.

Ethylene/oxygen flames with C/O=1.00 produce maps where only the large particles are present and their SR is between 0.6 and 0.8 (quite spherical). Only equivalent diameters of some single separated particles have been estimated (from 40 to 80 nm).

This preliminary application of Atomic Force Microscopy to the diagnostic of flame generated nanoparticles confirms that the presence of very small nanoparticles. The size and the shape distribution functions are easily obtained and they will be certainly useful in understanding nanoparticles formation mechanism. These results, furthermore, suggest application of the technique to the exhausts of cars and burners in order to furnish further elements to evaluate the nanoparticles impact on the environment.

Remarkable is the quite monodisperse size distribution measured by AFM technique in the lean C/O=0.56 flame and in the slightly-sooting C/O=0.77 flame downstream the reaction zone (4 mm); it is consistent with models of growth of aromatics through a radical-molecule addition mechanism of PAHs, activated by the radicals present in the oxidation zone [6].

The flat shapes exhibited by the young nanoparticles can come out considering this as their own morphology. However the contribution to this shaping to a sort of splash effect on the surface during the thermophoretic capture cannot be excluded.

References

1. Schwartz, J., *Environ. Res.* 64:36 (1994).
2. Hannigan M. P., Cass G. R., Lafleur A. L., Longwell J. P., Thilly W. G., *Environ. Sci. Technol.*, 28:2014 (1994).
3. Lighty, J.S., Veranth, J.M., Sarofim, A.F., *J. Air Waste Manage. Assoc.* 50:1565 (2000).
4. Minutolo, P., Gambi, G., D'Alessio, A., Carlucci, S., *Atmospheric Environment* 33:2725 (1999).
5. Dobbins, R.A., *Combust. Sci. Technol. Book Ser.*, 4:107 (1997).
6. D'Anna, A., Violi, A., D'Alessio, A., and Sarofim, A.F., *Combust. Flame* 127/1-2:1995 (2001).

Matrix-Assisted Laser Desorption/Ionization Time-of-Flight (MALDI-TOF) Mass Spectrometry in the analysis of fuel-rich combustion products: a preliminary study

Barbara Apicella¹, Marcos Millan², Alan A. Herod², Rafael Kandiyoti²

*Istituto di Ricerche sulla Combustione – CNR, P.le Tecchio, 80
80125 Napoli – Italy*

*Department of Chemical Engineering, Imperial College, Prince Consort Road,
London, SW7 2 BY, UK.*

INTRODUCTION

Molecular mass distributions of combustion products (high molecular weight species and soot) obtained burning a fuel under fuel-rich conditions are relevant in determining the mechanism of soot formation. In this work a new approach has been used to evaluate molecular weights of combustion products in a wide range (up to 200,000 u) based on Matrix-Assisted Laser Desorption/Ionization Time-of-Flight (MALDI-TOF) Mass Spectrometry. This technique seemed to be particularly useful in the analysis of very high molecular masses whose structure is completely unknown. In fact it does not need standard molecules with similar chemical structures and it provides a method of transferring large, labile molecules into the gas phase as intact ions, evaluating their molecular weight on the basis of their time of flight.

EXPERIMENTAL

Samples Source and Preparation

The particulate carbonaceous matter was collected in a rich premixed laminar ethylene/oxygen flame, produced on a commercial McKenna burner.

A stainless-steel water-cooled probe was used to sample combustion products along the flame axis. Solid and condensed material collected on the probe walls, on the teflon filter and in an ice-cooled trap placed in the sampling line were extracted by dichloromethane (DCM) to separate the DCM soluble organic material (named “soot extracts”), from the solid carbonaceous material (dry soot), insoluble in DCM.

Polycyclic aromatic hydrocarbons up to 300 u, named GC-PAH, were analysed in the soot extract by gas chromatography-mass spectrometry (GC-MS) on a HP5890 gas chromatograph coupled with an HP5970 mass spectrometer.

More details on experimental procedures are reported in a previous work [1].

The dry soot was washed with dichloromethane (until the disappearance of the fluorescence signal in the exhausted DCM) in order to extract the organic species adsorbed on it.

Soot extracts, dried and weighed, were sonicated in N-methyl-2-pyrrolidinone (NMP) solvent for the following examination by MALDI.

Matrix-Assisted Laser Desorption/Ionization Time-of-Flight (MALDI-TOF) Mass Spectrometry

A Bruker Daltonics Reflex IV MALDI-TOF mass spectrometer instrument was used in linear and reflector mode. The instrument features the 337 nm wavelength of a nitrogen laser with a pulse length of 3 nanoseconds and an acquisition, automation and data processing software package. The spectra were acquired over a range of ion accelerating voltages between 20 and 25 kV. Maximum laser power (90 or 100 %) was used for all spectra since (in this instrument and for these samples) increasing incident laser power levels has been observed to intensify the response of the instrument at high masses. A similar dependence of ion intensity on laser energy has been shown in a previous work for polystyrene polymer using another instrument [2]. For each sample 30 spectra were summed to make up the spectrum.

In order to test the response of the instrument in different molecular mass ranges, a set of polystyrene standards of different nominal peak masses up to 200,000 u were analysed. Polystyrene were examined in presence of a matrix consisting of a mixture of dithranol and silver trifluoroacetate.

Samples were examined both in absence of matrix and in presence of sinapinic acid as matrix.

RESULTS AND DISCUSSION

Matrix-assisted laser desorption/ionisation time-of-flight mass spectrometry (MALDI-TOF MS) was introduced by Karas and Hillenkamp in 1988 [3]. This soft ionisation method was soon established for the determination of high molecular weight biomolecules in a mass range even above 100,000 u. In contrast to other techniques of polymer characterization such as viscometry, light scattering, vapour pressure osmometry, membrane osmometry and size-exclusion chromatography (SEC), absolute molecular weights and molecular weights distributions can be obtained by using MALDI-TOF MS.

Up to now, the MALDI technique was mainly applied to synthetic polymers, as summarised by Nielen in a recent review [4] and only a few work was made on other kind of materials as coal and coal-derived samples [2, 5-8].

The practical limitation of a linear TOF spectrometer is the relatively low mass resolution achievable because of the energy spread of the generated ion packet and other experimental factors such as delayed ion formation and space charge effects. In order to improve the performance, an ion mirror, or reflector may be added to the time-of-flight mass spectrometer (RETOF-MS). The reflector makes use of an electrostatic field to reflect ions through a small angle towards a second detector. Ions with same mass-to-charge ratio but higher kinetic energy, penetrate deeper into the reflector, delaying their time of arrival at the reflector relative to the slower low-energy ions. This effect results in improved resolution in reflector TOF spectra in contrast to linear spectra and an increase in mass accuracy.

As shown in Fig.1 where MALDI of polystyrene standard 11,600 u is reported, the resolution of spectrum is very high and a narrow-distributed PS (polydispersity <1.1) presents peaks with a Poisson distribution centred around the MW (11,600 u). However, PS with MMs higher than 11,600 u are not detectable by reflector mode. By contrast, using the linear detector the resolution is lower but the MM range investigable is bigger than that obtained using reflector detector. In fact even 200,000 u PS is detectable in linear mode with a good signal intensity (not reported here).

As a consequence, simultaneous use of both detectors can assess the MALDI as a very useful technique in the MW investigation of combustion products, also in comparison with the results

obtained using another independent technique, Size Exclusion Chromatography (SEC), and reported in a previous work [9].

By SEC analysis it was found that soot extract was constituted only in part of GC-PAH up to 300 u and that also large molecular mass material was present, including at least three classes of MW estimated to be of order of 1,000,000 u, 100,000-200,000 u and 1000-2,000 u molecular mass. MW attributions were done by using a PS calibration curve (log(MW) vs. elution time) on the basis of the hypothesis that soot extract molecules present the same trend, independent of the different chemical structure. Therefore, the reliability of MW attribution depends on the reliability of this hypothesis.

By contrast, MALDI can be considered an absolute method in the measurement of MW, at least in the analysis of narrowly distributed polymer samples.

MALDI spectra of soot extracts were acquired with and without matrix and in different molecular ranges. Peaks due to GC-PAH up to 300-400 u and to higher molecular mass material up to 2500 u were observable by using both the detectors and without significant differences in presence or in absence of matrix. A better resolution was found in the reflector mode and the RE-TOF spectrum obtained in 500-9000 u range is reported in Fig.2. No signal was observable over 2500 u both using linear and reflector detector and so it is possible to conclude that in soot extracts there are no molecules with MW comprised between 2000-3000 u and 100,000-200,000u (that is the detection limit of MALDI on the basis of PS analyses). This achievement is in a very good agreement with the previous SEC results on soot extracts and it encourages to continue the work in combustion-formed samples analyses, for example extending the application of MALDI technique to dry soot.

Further work is also necessary for testing the reliability of MALDI technique, investigating systematically the effects of all the experimental parameters on spectra resolution and analysing other standard samples, like the sample concentration, the sample-matrix ratio, the extraction voltage, the reflector gain, etc.

REFERENCES

- Ciajolo, A., D'Anna, A., Barbella, R and Tregrossi, A. *Proc. of the Combustion Institute*, 25: 679 (1994).
- Domin, M., Moreea, R., Lazaro, M.J., Herod, A.A., Kandiyoti, R., *Rapid Comm. in Mass Spectr.*, 11: 1845 (1997).
- Karas, M., Hillenkamp, F., *Anal. Chem.*, 60: 2299 (1988).
- Nielen, M.W.F., *Mass Spectrom. Review*, 18: 309 (1999).
- Herod, A.A., Li, C-Z., Xu B., Parker, J.E., Johnson, C.A.F., John, P., Smith, G.P., Humphrey, P., Chapman, J.R., Kandiyoti, R., *Rapid. Comm. in Mass Spectr.*, 8: 815 (1994).
- Herod, A. A., Zang, S-F., Carter, D.M., Domin, M., Cocksedge, M. J., Parker, J.E., Johnson, C.A.F., John, P., Smith, G.P., Johnson, B.R., Bartle, K.D., Kandiyoti, R., *Rapid. Comm. in Mass Spectr.*, 10: 1475 (1996).
- Herod, A. A., Lazaro, M., J., Rahman, M., Domin, M., Cocksedge, M. J., Kandiyoti, R., *Rapid. Comm. in Mass Spectr.*, 11: 1627 (1997).
- Herod, A. A., Lazaro, M., J., Domin, M., Islas, C., A., Kandiyoti, R., *Fuel*, 79: 323 (2000).
- Apicella, B., Ciajolo, A., Suelves, I., Morgan, T., J., Herod, A., A., Kandiyoti, R., accepted for publication on *Comb. Sci. Tech.* (2002).

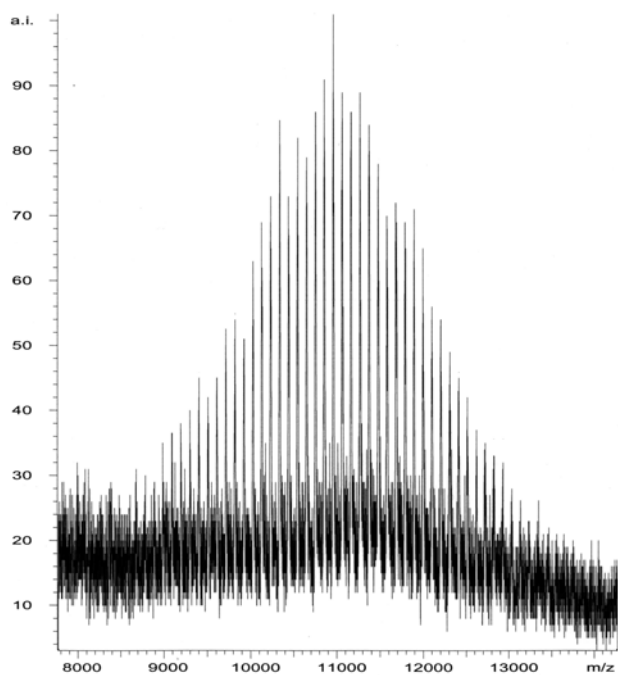


Fig.1 MALDI-TOF spectra of polystyrene standard 11,600 u in dithranol+silver matrix. Reflector mode

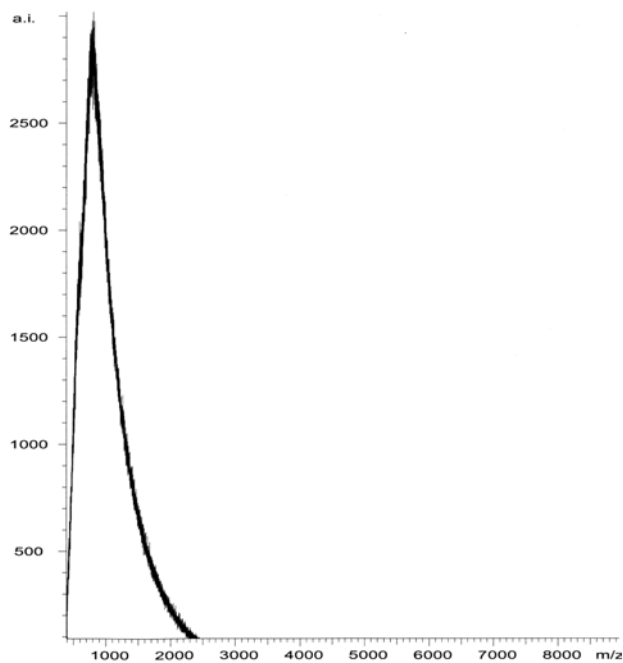


Fig.2 MALDI-TOF spectra high molecular weight species in sinapinic acid matrix. Reflector mode.

Diagnostics of Gas-Mixing in a Bubbling Fluidized Bed

R. Solimene, A. Telesca, A. Marzocchella, R. Ragucci, P. Salatino

Dipartimento di Ingegneria Chimica - Università Federico II, Naples – ITALY
Istituto di Ricerche sulla Combustione – CNR, Naples - ITALY

INTRODUCTION

Gas-mixing phenomena in fuel conversion processes carried out in fluidized bed have been indicated to assume a key role in reactor design and performance optimization. Nevertheless, knowledge of these phenomena is still lacking and calls for more extensive characterization.

Previous studies on gas mixing have been conveniently carried out by dividing the reactor into three sections: the bottom dense bed (further consisting of bubble and emulsion phases), the splash zone and the freeboard. Moreover, it has been proved that the gas-phase reactions take place in bubble phase inside the bed [1] and in the other sections of the reactor. As a consequence, the relative efficiency of gas mixing in these different sections of the reactor largely dictates the location of heat release, as well as temperature and reaction product concentration profiles along the reactor.

Past investigations on gas mixing in fluidized beds were mainly focused on the bottom dense bed adopting several diagnostic techniques (conditional or continuous gas sampling [2,3]; stabilized zirconia-based sensors [4]). Results supported mixing phenomena based on mass transfer between bubble and emulsion phases. On the other hand, limited attention has been paid to mixing phenomena in the splash region and results available in literature are rather contradictory [5, 6].

The present work aims at investigating the gas-mixing phenomena between a single bubble and a fluidized bed reactor. Experimental studies were carried out adopting two diagnostic techniques: one based on time-resolved measurements of the oxygen concentration along the reactor by means of stabilized zirconia-based sensors; one based on the gas flow

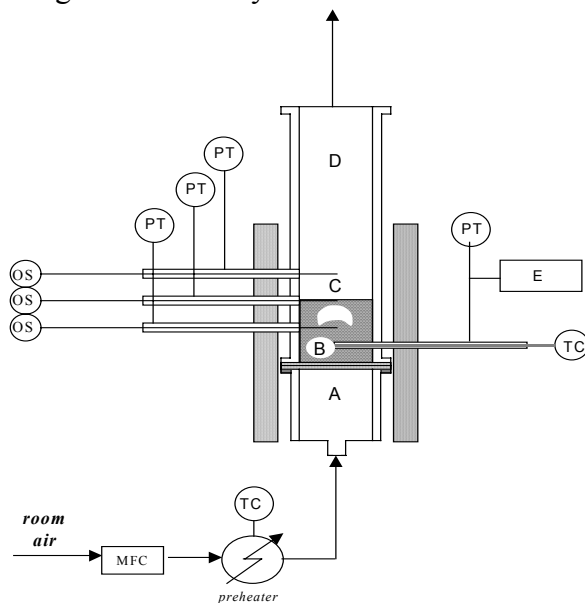


Fig. 1 Plant I. A) windbox; B) fluidized bed; C) splash zone; D) freeboard; E) single-bubble injection device; MFC: mass flow controller; OS: oxygen solid-state sensor; PT: pressure transducer; TC: thermocouple.

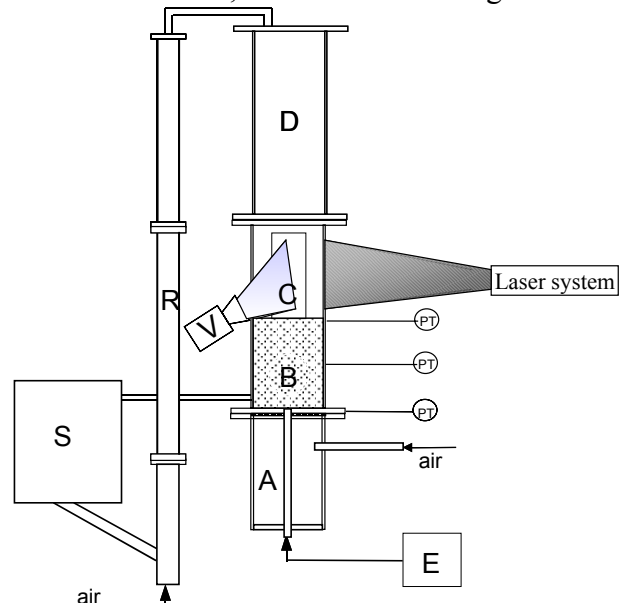


Fig. 2 Plant II. A) windbox; B) fluidized bed; C) splash zone; D) freeboard; E) single bubble injection device; R) riser; S) bed material vessel; V) video camera; PT: pressure transducer.

visualization in the splash zone by means of laser sheet coupled with a synchronized video camera. A theoretical approach to gas-mixing phenomena in the bed region has also been proposed.

EXPERIMENTAL

Table 1 reports the main characteristics of the two experimental facilities and diagnostic techniques adopted. Bed material properties are also reported.

Plant I, sketched in Fig. 1, was described in detail elsewhere [7].

Plant II consisted of a 0.35 m ID Plexiglas tube, 2 m high, operated at atmospheric pressure and room temperature. Three glass windows were fitted in the wall of the column for optical access: two windows are located diametrically facing each other; one is located at 90° with respect to the first two.

Both plants are equipped with a single-bubble injector previously tested in a cold two-dimensional fluidized bed [7]. Single-bubble injection level was at 4 cm above the gas distributor in plant I and at the gas distributor in plant II.

Diagnostics: Plant I is equipped with three oxygen solid-state sensors (special custom-made type SIRO2 C700+) characterized by high spatial and temporal resolution with respect to the investigated phenomena [7]. An acquisition data unit allowed to measure oxygen concentration and pressure signals at a sampling frequency of 1000 Hz for 60 s.

Plant II is equipped with a laser-sheet imaging system consisting of a Nd:YAg laser device, an optical apparatus, a video camera and an acquisition/control data unit. The laser device coupled with the optical apparatus was designed to generate a second harmonic frequency laser-sheet coplanar with the fluidization column axis. The laser sheet was pointed into the fluidization column through the glass windows illuminating an area of about 0.30x0.35 m of the splashing region just above the fluidized bed surface. The video camera was synchronized to the laser-sheet by means of the acquisition/control data unit providing frame-by-frame imaging of the flow patterns at the rate of 30 frames per second.

Materials: Technical air was used as fluidizing gas in both plants. Bed materials characteristics are reported in Table 1. The injected bubble is made of tracing gas: nitrogen in plant I and particles seeded air in plant II. Seeding particles were 1.8 µm silicon carbide small enough to follow gas flow trajectories under tested operating conditions.

Procedure: Beds were kept at incipient fluidization (as indicated by fine monitoring of the pressure drop across the bed) while fluidizing with air at 1123 K (Plant I) or at room temperature (Plant II). A single bubble was generated by suddenly discharging into the

Table 1. Experimental apparatus, materials and diagnostic techniques

	Plant I	Plant II
Fluidization column		
ID x height, m	0.102 x 2.0	0.35 x 2.0
material	Stainless-steel	Plexiglas with glass windows
fluidizing gas distributor	low pressure drop porous plate	low pressure drop perforated plate
Bed material		
	Silica sand	Glass beads
density, kg/m ³	2600	2540
Sauter diameter, µm	328, 950	277
Geldart powder classification	B, D	B
Settled bed height, m	0.14	0.30
Diagnostic technique	Pressure transducers (located at 4, 9, 14 and 19 cm from the gas distributor)	Pressure transducers (located at 2.4 and 5.5 cm from the gas distributor)
	Stabilized zirconia-based sensors (located nearby column axis at 9, 14 and 19 cm from the gas distributor)	Laser-sheet and synchronized video camera system

fluidized bed the tracing gas. The injected bubble diameter, estimated following the procedure reported in [7], was kept at about 4 cm in plant I and at about 10 cm in plant II.

Data logging started before gas tracer bubble injection and lasted for about 1 min.

RESULTS and DISCUSSION

Experiments with solid state sensors: Figure 3 show typical oxygen mole fraction (y_{O_2}) profiles along the reactor versus time measured at the bed surface during single bubble injection in a bed of 300-335 μm silica sand (Fig. 3.I) and 900-1000 μm silica sand (Fig. 3.II). Dashed vertical line marks the beginning of the bubble injection time (t_{inj}) recognized by means of the pressure signal measured in the injector tube. Oxygen concentration profiles highlight the bubble passage (time-period A) and the rich tracer interstitial gas passage (time-period B) for both bed materials [7].

Time-resolved gas-concentration signals measured have been interpreted taking into account: i) mass-transfer between injected bubble and the emulsion phase and ii) gas mixing in the emulsion phase. The first contribution has been described by means of the first-order lumped model proposed by Kunii and Levenspiel [8]. The second contribution has been described assuming plug flow behaviour for the emulsion phase. Model details are reported in Telesca [9]. Figure 4 shows model results in terms of oxygen concentration estimated at the bed surface assuming operating conditions of the experimental tests reported in fig. 3. Elapsed time is calculated since bubble injection. In fig. 4.I sharp decrease of y_{O_2} corresponds to the gas-tracer bubble passage at the bed surface level and the delayed saw-like pattern to the passage of emulsion phase interstitial gas (bubble faster than interstitial fluidization gas). In fig.4.II the earlier saw-like pattern of y_{O_2} profile corresponds to the passage of emulsion phase interstitial gas (interstitial fluidization gas faster than bubble) and the later pulse pattern of y_{O_2} corresponds to the passage of the gas-tracer bubble at bed surface.

Experiments with laser-sheet visualization: Figure 5 shows two typical sequences of frames recorded after bursting of seeded gas bubbles injected at the bottom of the fluidized bed. The dark region indicates gas phase; white regions indicate tracer particles present in the splash region after bubble eruption. The white region observed at the bottom of frames A is bed solids falling down after bubble eruption. Analysis of frames A of both sequences shows that seeded gas (i.e. seeding particles) is released into the splash zone during bubble eruption. Sequence I shows upward motion of the seeded gas and its progressive volumetric spreading. Sequence II shows downward motion of seeded gas and its radial dispersion (seeded gas gradually moves away from the laser-sheet).

Analysis of sequences reported in figure 5 suggests the following tentative conclusions. Gas is

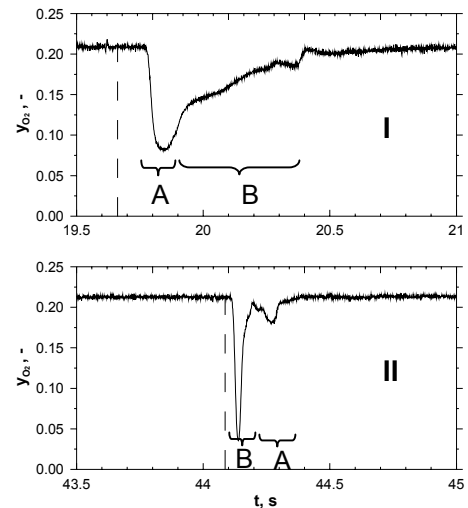


Fig. 3 Oxygen concentration vs. time measured at the bed surface. Bed material: I) 300-355 μm silica sand; II) 900-1000 μm silica sand

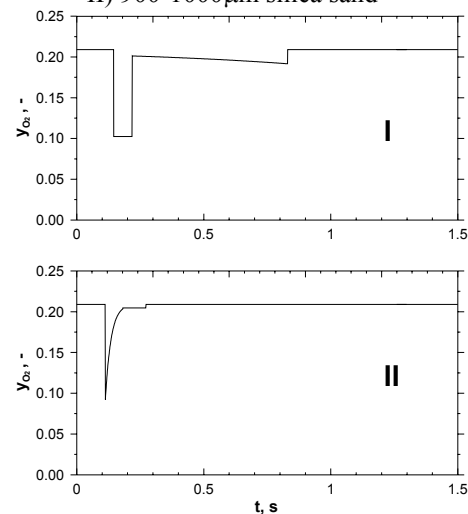


Fig. 4 Oxygen concentration vs. time calculated at the bed surface. Bed material: I) 300-355 μm silica sand; II) 900-1000 μm silica sand

apparently stagnant or even moving downward just above the region of bubble eruption. It moves upward near the wall of the column. This result is probably due to falling back of ejected bed solids that drag gas toward bed surface. This observation is consistent findings of Yorquez-Ramirez and Duursma [5]. Accordingly, gas flow field associated with bubble bursting would not be properly described by turbulence models based on either pulsed jets [10] or upward vortex rings (ghost bubbles) [6].

REFERENCES

1. Dennis, J. S., Hayhurst, A.N., Macklay I.G.: *Nineteenth Symposium on Combustion* p. 1205 (1982).
2. Naruse, I., Ohtake K., Koizumi K., Kuramoto K., Lu, G. Q.: *Twenty-fifth Symposium on Combustion*, The Combustion Institute, p. 545 (1994).
3. Sit, S. P., Grace J. R.: *Chem. Engng Sci.*, **33**:1115 (1978).
4. Stubington, J.F., Chan, S.W.: *J. of Inst. Energy*: 136 (1990).
5. Yorquez-Ramirez, M. I. Duursma, G. R. *Chem. Engng Sci.*, **55**:2055 (2000)
6. Pemberton, S.T., Davidson, J. F.: *Chem. Engng Sci.*, **39**:829 (1984)
7. Solimene, R., PhD annual report (2001)
8. Kunii, D., Levenspiel O., *Fluidization Engineering*, Wiley and Son, NY (1969)
9. Telesca, A., Thesis for the degree in Materials Engineering, Università degli Studi di Napoli Federico II (2002)
10. Horio, M., Taki, A., Hsieh, Y.S., Muchi, I., *Fluidization III*, p. 509 (1980)

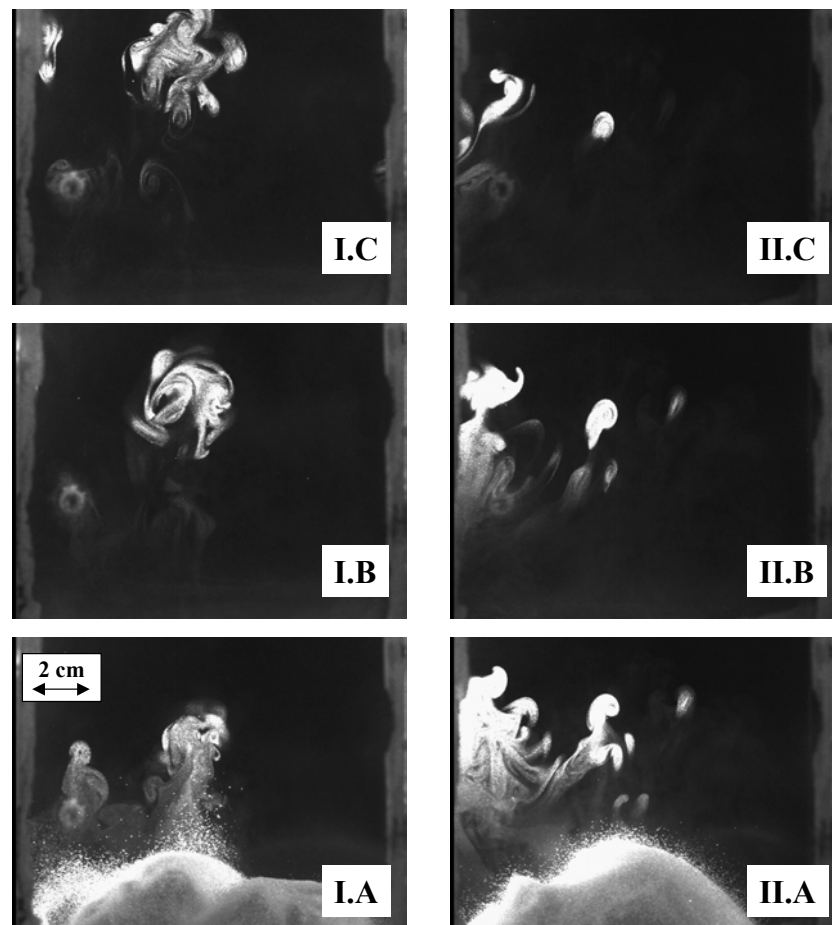


Fig. 5 Video frames of the splash zone recorded after bursting of a seeded gas bubble injected at the bottom of the plant II fluidized bed. Sequence I: A) $t=0$ ms; B) $t=100$ ms; C) $t=233$ ms. Sequence II: A) $t=0$ ms; B) $t=33$ ms; C) $t=100$ ms.

Identification of Average "Hidden" Features of Multiphase Flows Through High Order Statistical Momenta of Quantitative Images

¹R. Ragucci, ²A. Cavaliere, ²A. Sgambati

1 Istituto di Ricerche sulla Combustione - C.N.R., Naples - ITALY

2 Dipartimento di Ingegneria Chimica - Universita Federico II, Naples - ITALY

INTRODUCTION

The aim of this paper is to study how the morphology of a liquid jet in cross-flow conditions can be influenced by characteristic parameters of atomization. The technological reference of this work are the LPP (Lean Premixed Prevaporized) gas turbine systems. In these systems the combustion process occurs in premixed conditions with a very high air excess in order to avoid NO_x forming. The operation of such systems with liquid fuels require a particular care in the preparation of the fuel-air mixture. Fuel injection in an air cross-flow is commonly used to favour a prompt and good mix of air and fuel. This technique presents two main disadvantages: the impact of the liquid jet against the wall; Flashback phenomenon occurring when flame propagation is faster than air velocity allowing for fuel ignition in the inlet duct. To avoid these two disadvantages, the atomization system and the complex coupling between fuel and air steams require particular care in system design. This paper contribute to the general understanding of jet dispersion and its interaction with air flow and attempt to determine a semi-empirical correlation useful to predict liquid jet trajectory in cross-flow conditions.

EXPERIMENTAL SETUP

The experimental system (Fig 1.a) consists of a square section testing chamber with a 25 mm side and long enough to allow for the observation of the whole vaporization process, with quartz windows which makes it optically accessible. The system is completed by a compressor, a tank and a heat exchanger which raises air temperature in the testing chamber to a desired value. The liquid used during the measurements is distilled water, for obvious reasons and because atomization process features doesn't change with liquid type, in accordance with Wu et al.,1997¹.

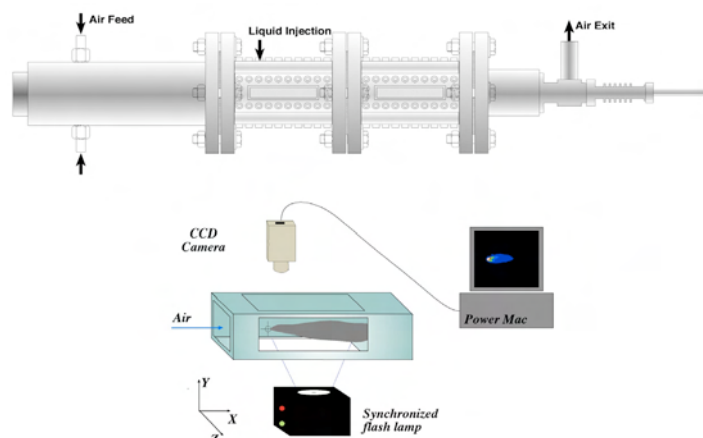


Fig. 1 Schematic of experimental set-up.

IMAGE ACQUISITION

The jet morphology study exploited a shadowgraph technique using a Hamamatsu CCD TV-camera and synchronized xenon flash lamp². Forty 10 bits images (1024 different tonalities of grey) in each experimental condition were acquired. They were sent to a Macintosh computer (Fig 1.b) where they were elaborated by LabVIEW 6 program. A background image, obtained by a exposing the camera in absence of the spray, was subtracted in order to reduce electronic noise. From the obtained images an average image was computed in order to study the bending and penetration of the liquid jet. Using an image binarization routine it was possible to outline the boundaries of single and averaged images in each condition in order to demarcate the spray boundary. The variation both in time and space of image boundaries were used to characterize the jet stability in statistical sense.

RESULTS AND DISCUSSION

It's known that penetration and bending of liquid jet in crossflow conditions are regulated by q -parameter which is the motion quantity stream ratio of liquid and gas $\left[q = \left(\rho_l v_l^2 \right) / \left(\rho_g v_g^2 \right) \right]$.

A very bended jet could be observed when q is low. On the other hand when q is very high the liquid jet penetrates more causing an impact against the wall in extreme conditions. It has been also observed a connection between jet stability and q . In order to study this connection a square mean shifting indicator, s , has been introduced.

$$s = \frac{1}{N} \sqrt{\sum (x_n - x_m)^2}$$

Where x_n is the x coordinate of external boundary of n^{th} image, and x_m is the x coordinate of average image boundary.

The primary goal of this work has been to find a semi-empirical correlation that could assert the liquid jet trajectory if the main atomization parameters are known.

As reference the Wu's study was used but a linear variation of transversal section diameter, in order to consider the transverse section area reduction, was assumed: $D = D_0 \left(1 - z / Z_{jb} \right)$.

In the previous formula D_0 is the nozzle diameter assumed as the initial jet diameter.

The studied model is based on the balance of drag force (responsible of the bending) and inertial force (responsible of the penetration). Once the balance was written there were two parameters to be characterized: the drag coefficient C_D , that has been considered constant even if the cross-sectional diameter was not constant; the jet breakup ordinate, Z_{jb} , that will be later on discussed. To simplify the balance equation's resolution the liquid velocity in the z direction was assumed as constant. Also the ordinate of the liquid jet breakup, Z_{jb} , was considered equal to the curvilinear jet breakup distance L_{jb} .

By integrating twice the forces balance it was obtained a jet trajectory correlation in the form:

$$x = AZ_{jb}^2 \left[\ln \left(\frac{Z_{jb} - z}{Z_{jb}} \right) \left(\frac{Z_{jb} - z}{Z_{jb}} \right) + \frac{z}{Z_{jb}} \right] \quad A = \frac{2C_D}{\pi D_0 q}$$

The correlation is obviously valid for $Z < Z_{jb}$.

The proposed correlation requires the knowledge of Z_{jb} . Although an estimation of this quantity can be based on the aerodynamic theory of jet breakup an experimental procedure has been defined to evaluate Z_{jb} . As mentioned before, for each image an external boundary has been found and from all 40 external boundaries a mean boundary was defined. The error has been plotted as a function of the z coordinate in each experimental condition (Fig. 2).

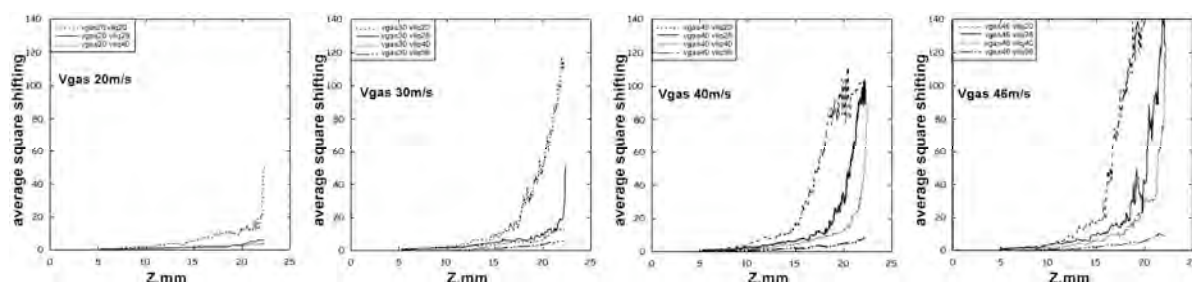


Fig. 2 Square mean shifting indicator versus z for some experimental conditions.

The graph shows, for low values of the ordinate, a slow and regular increase of the square mean shifting error. This phenomenon is caused by a weak atomization. It can be observed that in a particular point, the square mean shifting error plot suddenly increases. This is caused by the breakup of the liquid column. The error increase can be explained by the different behaviour of a liquid column with respect to a cloud of droplets. This justify the assumption of Z_{jb} as the point where the strong increase occurs. This assumption is obviously possible only when the phenomenon of the liquid column breakup occur before the jet impact on the wall of the chamber. Knowing C_D and Z_{jb} it is possible to calculate the jet trajectory using the proposed correlation.

In Fig. 3 the trajectories calculated using the correlation are compared with those obtained using the Wu's and the two Becker's correlations.

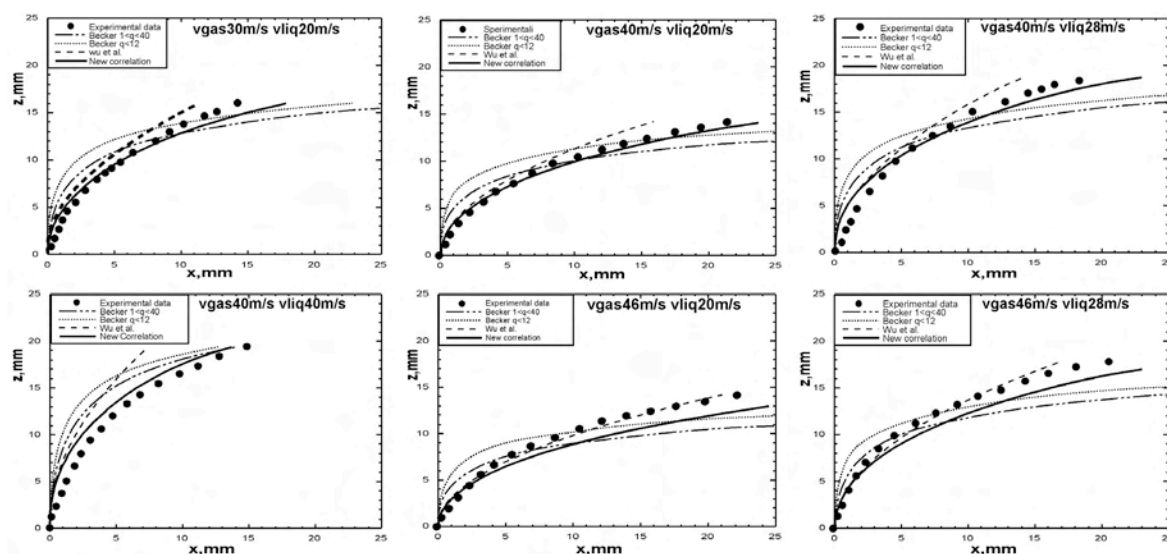


Fig. 3 Comparison between the proposed correlation and the literature's ones.

The correlation proposed in this paper appear to well interpolate the experimental data in the region near to the nozzle as well as Wu's correlation. This is easily explained considering that the two correlations have the same initial slope. Moving away from the nozzle Wu's correlation error increases because it does not consider diameter reduction due to the progress of droplet stripping from the jet. Becker's³ two correlations seems to be less effective than the other ones both close to the nozzle and further downstream.

It is possible to give a numerical evaluation of the effectiveness of the above-mentioned correlations by defining a residual average error as:

$$RAE = \frac{\sum (Z_{ic} - Z_{is})^2}{\sum (Z_{ic} - Z_{is})^2 + \sum (Z_{ic} - \bar{Z}_s)^2}$$

Where Z_{ic} and Z_{is} are the ordinate values of correlation points and experimental points, while \bar{Z}_s is the average value of the experimental point ordinates.

In Fig 4 the RAE for the experimental conditions studied is reported. Full symbols identify the conditions where it's possible to evaluate Z_{jb} while the empty symbols are used for the conditions where the q parameter assumes high value so that Z_{jb} is determined as the mean of breakup distances for the conditions where it is possible to evaluate Z_{jb} . From the plot, Wu's residual mean error is similar to the proposed correlation only for low values of q , while high values of q cause an increase of this error because the cross section area is decreasing in width.

CONCLUSIONS

The real advantage of the proposed correlation consists in the fact that it's applicable for a wider range of q values. In fact, for q values >100 (outside the normal range of q turbine work) there is a kind of low residual error. The functional shape of the proposed correlation, as it has been illustrated, could be a sort of disadvantage. Usually the correlations are written as $z = z(x)$ in order to highlight penetration phenomenon while in this article the correlation is written as $x = x(z)$ in order to highlight the bending phenomenon. It is impossible to analytically invert the proposed correlation because there is a linear and logarithmic shape. On the other hand the proposed correlation can be easily inverted numerically. Future development of this work will be to verify the proposed correlation in high temperature conditions and different nozzle diameters as well as to introduce a correction to take in account the effect of spray cross section deformation.

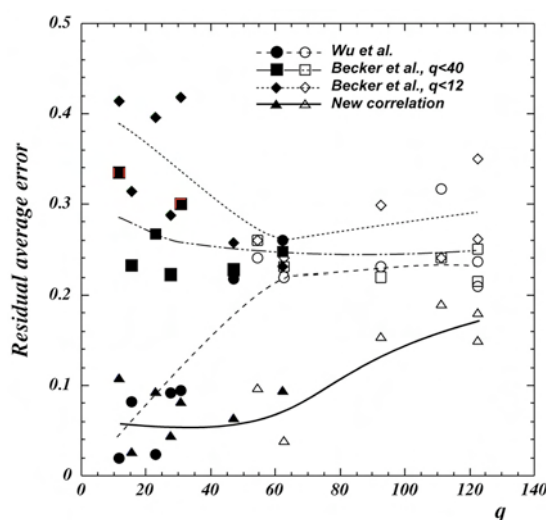


Fig. 4 Residual average error of various correlations versus q parameter.

REFERENCES

- 1) Wu P.-K., Kirkendall K.A. "Breakup Processes of Liquid Jets in Subsonic Crossflows" Journal of Propulsion and Power 1997
- 2) Cavaliere A., Ragucci R., Noviello C.: "Bending and Break-up of a Liquid Jet in a High Pressure Air Flow" The Second Mediterranean Combustion Symposium Sharm El-Sheikh, Egypt, January 6-11, Paper #MCS02-086-III, 2002
- 3) Becker J., Hassa C.: "Breakup and Atomization of a kerosene jet in crossflow of Air at elevated pressure", ILASS-Europe, 1999

Ultraviolet Light Absorption in Flames, Engine Exhausts and Urban Atmosphere

¹A. Borghese, ²G. Basile, ²A. D'Alessio

1 Istituto Motori

CNR P.le Tecchio, 80125 Napoli, Italy.

2 Dipartimento di Ingegneria Chimica

Università "Federico II" P.le Tecchio 80, 80125 Napoli, Italy

INTRODUCTION

Formation and emission of combustion by-products can be thoroughly followed and qualified by means of spectrally resolved optical analysis in the ultraviolet band. Previous data in combustion systems [1][2] and exhausts [3] have been reported in recent years, which led to the assessment of a class of heavy molecular weight organic compounds, also referred to as organic carbon (OC) nanoparticles.

As a further development of those studies, here we report on preliminary optical investigations over open and long paths of urban atmosphere, carried out in terms of ultraviolet-visible extinction spectroscopy. The extension of such technique to much longer optical paths involves the consideration of the unavoidable molecular absorption of atmospheric oxygen, increasing strongly below 240 nm, and of tropospheric ozone, peaking at nearly 260 nm. On one hand, the expected absorption spectrum of both oxygen and ozone sets a reference condition, namely that of an ideally clean atmosphere, whilst, on the other hand, it constitutes a natural optical barrier, preventing feasible investigations over longer optical paths and at lower wavelengths.

EXPERIMENTAL SETUP

Investigations reported on here are based on a conventional scheme of optical extinction spectroscopy, resolved in the spectral band 190-500 nm. Figure 1 shows the experimental apparatus. In the transmitter branch, a Nd:Yag pulsed laser is used as the excitation source of the needed broadband light. The laser beam ($\lambda=1064$ nm) is brought into the focus of a short focal lens in pure nitrogen, where the optical breakdown is induced. The resulting high temperature plasma constitutes the broadband light source, suitable for absorption measurements from visible down to vacuum ultraviolet wavelengths. Its time duration is of tens of nanoseconds and its spatial extension is of the order of 0.01 cubic millimeters [3]. The extremely high intensity emission of the plasma at lower wavelengths is the key-feature that opens up the feasibility of the investigations reported here. The broadband light is collimated by a parabolic mirror and is transmitted through the atmosphere towards two retro-reflectors, placed at two different distances d_1 and d_2 from the source. In the receiver branch, another parabolic mirror collects and focuses the reflected light onto the input slit of a spectrometer, coupled to an intensified and gated CCD camera, which acquires and records the two signals coming from the mirrors. The signals I_1 and I_2 are used to derive the extinction coefficient K_{ext} as function of the wavelength λ , according to the Lambert-Beer law:

$$K_{\text{ext}}(\lambda) = \ln[I_1(\lambda)/I_2(\lambda)]/L$$

where $L=2*(d_2-d_1)$ is the effective path length over which the extinction is averaged.

It is to note that the scheme shown in Fig.1 provides a number of advantages over the conventional spectrophotometry. Firstly, being the extinction coefficient evaluated from the ratio of the two returns I_1 and I_2 , there is no need of the preliminary acquisition of the source spectrum $I_0(\lambda)$, so that instantaneous measurements on a 'single shot' basis can be carried out and, in addition, pulse-to-pulse fluctuations of the light source are canceled out. Also, extension of this scheme to $n>2$ returns allows us to measure extinction spectra of $n-1$ aligned spatial segments.

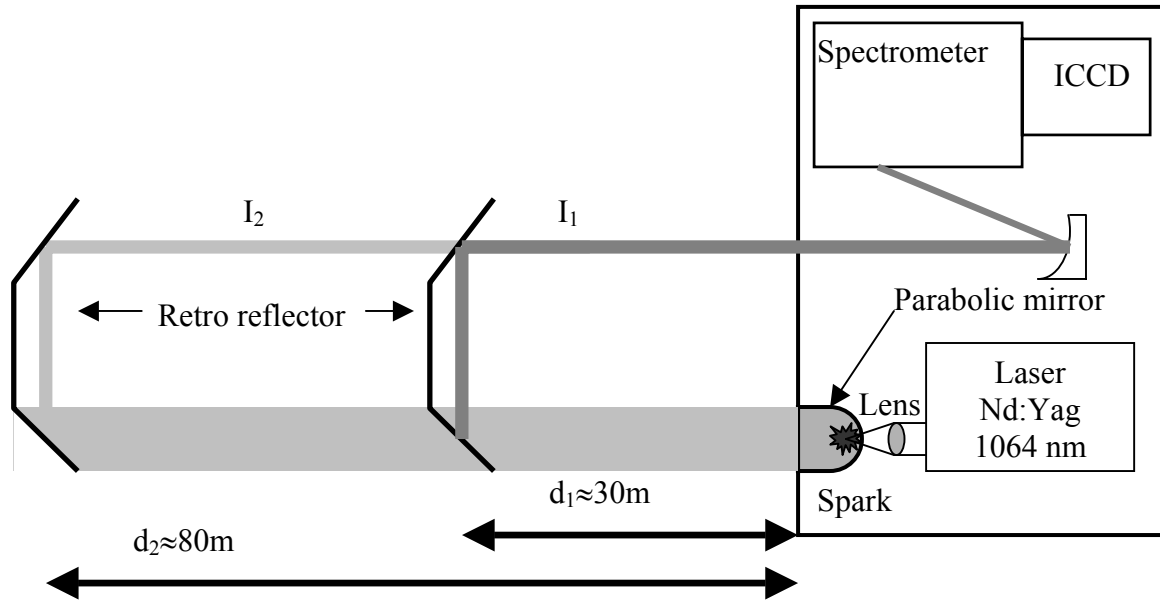


Fig. 1 Experimental set-up.

RESULTS

A typical extinction spectrum of urban atmosphere is reported in Fig.2, where $K_{ext}(\lambda)$, in units of cm^{-1} , is plotted by (•) symbols as a function of wavelength in the spectral range 200-500 nm.

At wavelengths above 300 nm there is no evident absorption, whereas below that value a strong absorption band appears, with increasing intensity at decreasing wavelengths. The observed spectrum can be interpreted as resulting from a number of atmospheric constituents, and given by:

$$K_{ext. atm.} = \sum_i N_i \sigma_i$$

where σ_i is the cross section (in cm^2) of i -th component and N_i is its number concentrations, expressed in units of cm^{-3} [4]. The optical inversion of the extinction spectrum can in principle be carried out once the individual species are identified and their spectral absorption are known. In Fig.2 the absorption spectrum of an ideally clean atmosphere, namely due only to atmospheric oxygen, water vapor and ozone, each at expected concentrations, is also plotted by a dashed line. As a result, an excess absorption is revealed, which peaks at 200 nm and amounts to nearly $10^{-4} cm^{-1}$. Attempts to attribute such excess absorption to known gaseous species failed, due either to unreasonably high concentrations required or to spectral mismatch.

In previous works in combustion system [1] [2] and in engine exhausts [3], we have identified a class of heavy molecular weight organic compounds, also referred to as organic carbon

(OC) nanoparticles, which show spectral features quite distinct from soot or elemental carbon (EC).

These particles have sizes of 2-4 nanometers, exhibit a strong absorption spectrum below 250 nm, increasing at lower wavelengths, and turn out to be nearly transparent above. The reconstruction of the spectral extinction coefficient in terms of the gaseous species cited above and, in addition, of the OC nanoparticles at a mass concentration of $90\mu\text{g}/\text{m}^3$, results in the spectrum shown in Fig.2 by the full line, which fits fairly well the experimental spectrum.

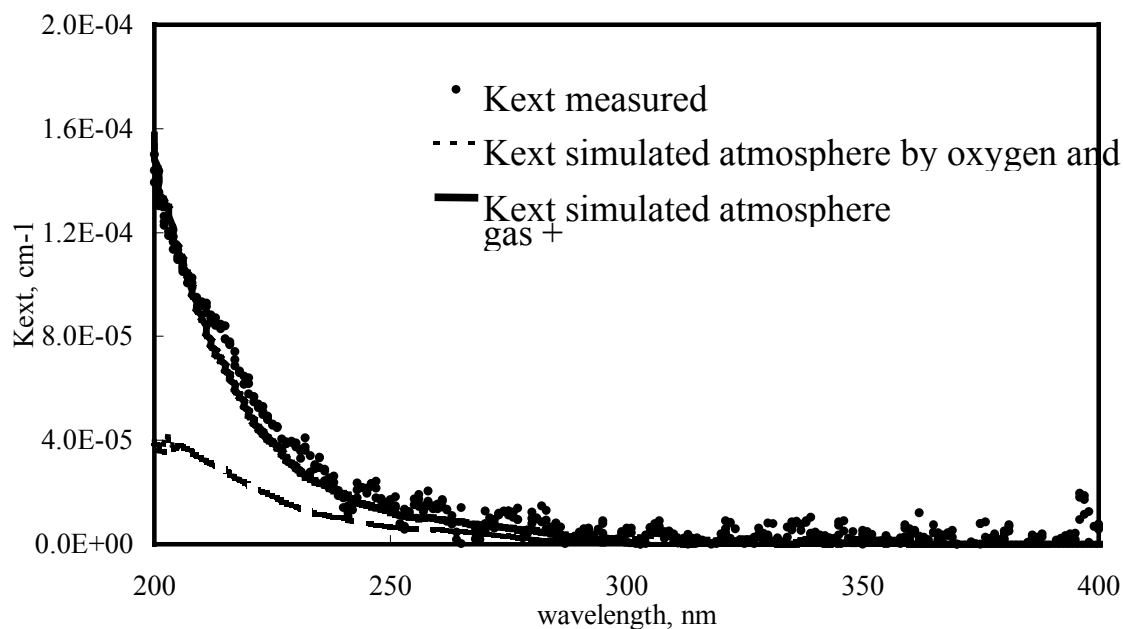


Fig. 2 Comparison between extinction spectra simulated and measured

Further observations have been carried out as function of daytime over thirty hours, from 11.00 of April 23th to 18.00 of April 24th, at the same spatial site. A time-varying spectrally flat background, due to the nucleation/evaporation of suspended water micro-droplets (fog), has been firstly subtracted from the acquired spectra. The resulting data have been inverted in terms of oxygen, water vapor, ozone and OC nanoparticles and the corresponding mass concentrations evaluated. Figure 3 shows the evolutions over the indicated time window of the concentrations of ozone and OC nanoparticles, expressed in $\mu\text{g}/\text{m}^3$. Ozone levels appear to vary according to the known daily dynamics, increasing during the sunny hours, decreasing in the late afternoon and ranging, at the observed time, between few tens up to nearly $160\mu\text{g}/\text{m}^3$. The corresponding levels of OC matter undergo a different evolution, of more difficult interpretation. However, an inverse relationship between ozone and OC nanoparticles seems to establish, which is likely to be related to complex atmospheric, possibly heterogeneous chemistry.

DISCUSSION AND CONCLUSIONS

The preliminary optical investigations on urban atmosphere, reported here, raise a series of interesting issues. Firstly, to our knowledge, it has been demonstrated for the first time the feasibility of open-path atmospheric extinction spectroscopy down to 200 nm, where chemical species of relevant environmental interest can be detected and followed. Oxygen and ozone absorption, widely assumed to constitute an inaccessible natural barrier to optical probes, can instead be accounted for and does not prevent useful insights on atmospheric chemistry, provided that intense enough light sources and suitable optical schemes are exploited.

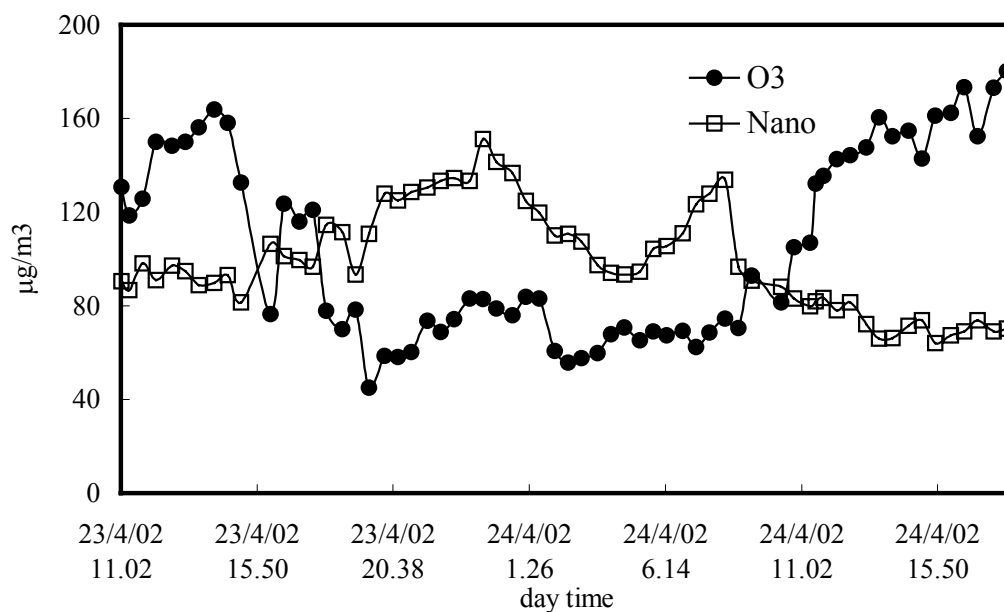


Fig. 3 Concentrations of nanoparticles and O₃ measured during day of 23 and 24 April 2002

Unexpected optical absorption has been revealed below 250 nm, far greater than that due to atmospheric oxygen, which cannot be attributed to known gaseous species at reasonable concentrations. The nature of the chemical species responsible of the observed absorption is still uncertain. The spectral shape strongly suggests that they are heavy-molecular-mass organic compounds of biogenic (e.g. terpenes) and/or anthropogenic (combustion-related) origin.

Calibration of the excess absorption spectra in terms of mass concentrations requires the knowledge of the relevant absorption cross-sections. In this work, we propose to attribute tentatively the observed excess absorption to OC nanoparticles, likely emitted by combustion systems, whose optical properties have been inferred in lab-scale, combustion environments. The assumption relies heavily on the peculiar spectral shapes of the respective absorption bands. The estimated mass concentrations of OC matter suspended in urban atmosphere turn out to fluctuate around 100 µg/m³, a surprisingly high value, far exceeding those typical for PM₁₀. Such concentrations do not vary much as functions of daytime or of traffic conditions, but have been observed to decline temporarily during and after intense rain events.

Finally, it is worth citing related observations, not reported here, which have led to detect similar but much stronger absorption bands in rain samples and even in potable water. Further studies will deal with such new research perspectives.

REFERENCES

1. D'Alessio, A., Barone, A.C., Basile, G., Borghese, A., D'Anna, A., Minutolo, P., Sgro. L.A.: *Chemosphere*, accepted **2002**.
2. Allouis, C.; D'Alessio, A.; Beretta, F.; Borghese, A.: *Proceedings of the Combustion Institute*, **28**:311 (2000).
3. Borghese, A. and Merola, S.S.: *Proceedings of the Combustion Institute*, **27**:2101 (1998).
4. Seinfeld, J. H.; Pandis, S. N. *Atmospheric Chemistry and Physics: From Air Pollution to Climate Change*; John Wiley & Sons, Inc.: NY, 1998.

Dry Flue Gas Desulfurization: Adsorption Mechanism and Sorbent Reactivation

M. Derudi, M. Suardi, D. Gelosa, R. Rota*

Politecnico di Milano

*Dip. di Chimica, Materiali e Ingegneria Chimica "G. Natta" / CIIRCO
via Mancinelli, 7 - 20131 Milano, Italy*

S. Malloggi, E. Sani

ENEL DP / Ricerca

Via Andrea Pisano 120 - 56122 Pisa, Italy

INTRODUCTION

Dry flue gas desulfurization (FGD) processes have become more interesting over the last few years because of its potentiality in low – cost retrofitting of existing plants.

Dry SO₂ removal processes are based on a simple technology, which involves the injection of a dry solid sorbent, typically calcium hydroxide (Ca(OH)₂), into the exhaust duct between furnace and fabric filter. The desulfurization reaction takes place both in the duct as well as on the cake formed on the surface of the particle collection device. However, one of the problems with this technology is its relative small solid utilisation with turns out in high disposal costs.

Several studies were presented in the literature investigating the influence of some operating parameters on the process efficiency for calcium-based sorbents; however they reported contradictory results, in particular concerning the role of temperature and the influence of carbon dioxide on the maximum sorbent conversion.

Consequently, the first aim of this work has been to elucidate, in the well controlled conditions of a laboratory - scale reactor, the effect of some operating conditions on the SO₂ removal by Ca(OH)₂ in the low - intermediate temperature region, that is from 150 up to about 400°C. Once confirmed the low conversion of the solid sorbent achievable with FGD technology, the possibility to increase the Ca(OH)₂ utilisation by reactivating the spent sorbents has been also investigated.

EXPERIMENTAL APPARATUS

The experimental set-up is shown in figure 1. A sand bed reactor working under integral conditions has been used for studying the reaction between gaseous SO₂ and solid Ca(OH)₂. A cylindrical glass-made reactor 840 mm height and 31 mm i.d., located in an electrical tubular oven, was used in all experiments.

Two grams of commercial Ca(OH)₂ (size from 8 to 20 µm, purity larger than 95%) dispersed in 30 g of silica sand (60-200 µm diameter) have been used as a sorbent. Sand dilution allows to maintain isothermal conditions and to avoid the formation of channeling due to particle size enlargement during the gas – solid reactions. The experimental equipment also involves a feeding and humidification system of the gaseous stream as well as an analytical section. Gas flow rates from cylinders (SO₂, CO₂, air and N₂) are regulated through mass flow controllers

* Telephone: +39 0223993154, Fax: +39 0223993180, E-Mail: renato.rota@polimi.it

and mixed to obtain a stream with composition similar to that of the exhausts from a furnace.

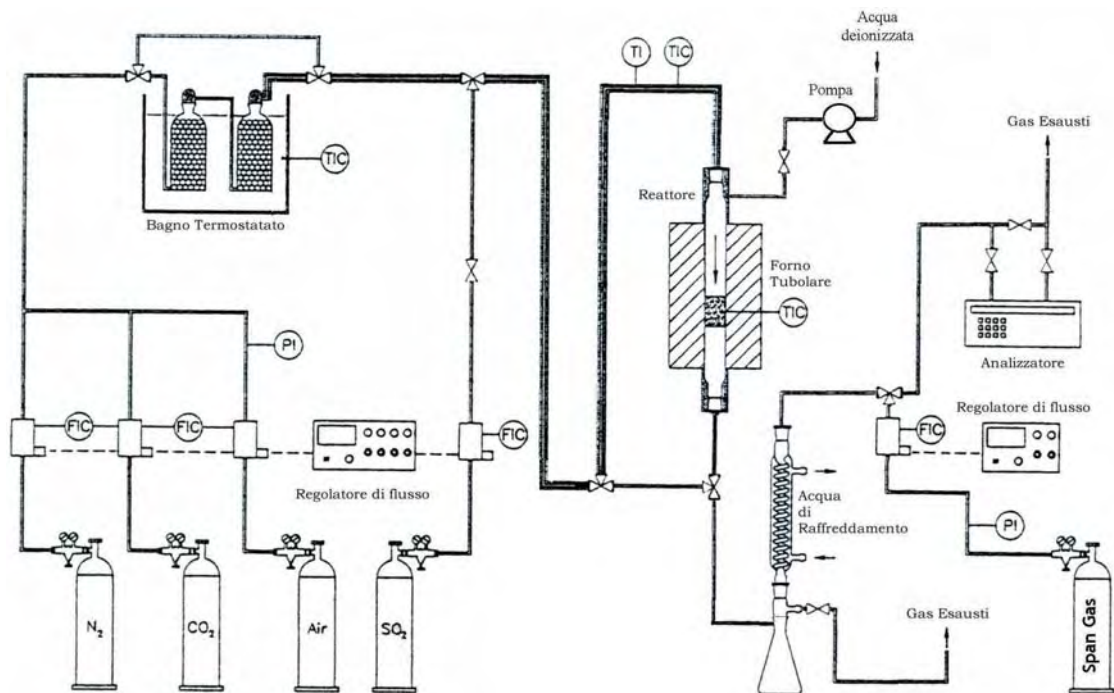


Fig. 1 Schematic diagram of the experimental set-up.

Outlet gas concentrations are measured with a continuous analyzer (HORIBA PG-250) provided by IR detector, allowing the determination of the breakthrough curves (that is, the concentration of SO_2 in the stream leaving the reactor as a function of time). The amount of SO_2 adsorbed by the calcium hydroxide is measured from the difference between the breakthrough curves obtained with and without the sorbent in the packed-bed; an example of a comparison between the two curves is shown in figure 2.

Several preliminary experimental runs were carried out to verify the reliability of the experimental procedure, which has been found to be satisfactory, that is, below 5% in term of sorbent conversion (S/Ca) which is computed as:

$$\frac{S}{\text{Ca}} = \frac{\text{SO}_2 \text{ moles adsorbed}}{\text{initial moles of Ca(OH)}_2}$$

Chemical composition of the reacted sorbent was determined by thermogravimetric analysis (TGA) using helium as carrier gas [1-4]. This allows identifying the amounts of Ca(OH)_2 (that decomposes between 350 and 450°C), CaCO_3 (500-650°C) and CaSO_3 (behind about 1000°C). TGA analysis is an independent method to evaluate the sorbent conversion, which gave results similar to that obtained from the breakthrough curves thus confirming the reliability of the experimental procedure.

RESULTS

Several sets of experiments were performed in order to evaluate the influence of carbon dioxide, water concentration, O_2 concentration and temperature on the sorbent conversion. In all the experimental runs the total gaseous flow rate has been set in the range 2000 - 3000 Nml/min, while the SO_2 concentration in the feed stream was equal to 1000 ppm. Figure 3 summarizes the main results in terms of the sorbent conversion.

It can be noted that the sorbent conversion is not significantly influenced (at least for

temperature values lower than 250°C) by oxydizing conditions (that is, by the O₂ concentration).

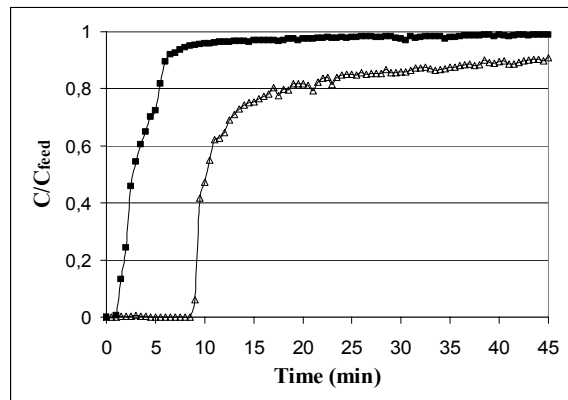


Fig. 2 Example of SO₂ breakthrough curves with (■) and without (Δ) calcium hydroxide.

On the other hand, anhydrous tests have shown a positive effect on the conversion (with respect to the wet gas experiments) at the highest temperature level, which is probably due to a partial decomposition of Ca(OH)₂ to the more reactive CaO. A change in the water content from 4% to 8% has a negligible influence on the solid conversion, as shown in figure 3-b, since the presence of such an amount of water avoids sorbent decomposition.

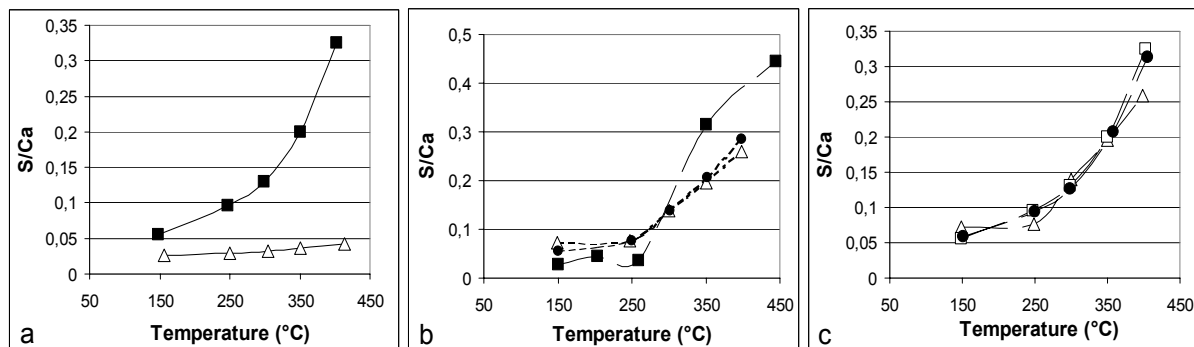


Fig. 3 a) Influence of CO₂: (■) 0%; (Δ) 12%. Feed conditions: 8% H₂O; 2% O₂. b) Influence of water concentration: (■) 0%; (Δ) 4%; (●) 8%. c) Influence of oxygen concentration: (Δ) 0%; (□) 2%; (●) 4%. Feed conditions: 8% H₂O.

As clearly evidenced in figure 3-a the presence of carbon dioxide reduces drastically the sorbent conversion in all the temperature range investigated. Sorbent conversion values as lower as 5%, that is seven times lower than the maximum value obtained without CO₂, have been measured feeding a stream with 12% of CO₂. This means that the low sorbent conversion evidenced in real-size applications, when the presence of carbon dioxide cannot be avoided, has to be ascribed to the competitive carbonation reaction. In the conditions investigated there is a fast reaction between CO₂ and Ca(OH)₂ to form a large amount of CaCO₃ (more than 75% in mole, as measured by TGA analyses). This product reduces the sorbent porosity and reactivity, leading to a very low sulfation of the solid.

SORBENT REACTIVATION

Since the presence of carbon dioxide cannot be avoided in real applications, only a reactivation of spent sorbents can allow to increase the overall solid conversion. The regeneration process investigated in this work consists of a thermal decomposition of calcium carbonate without removing the fixed sulfur. This is possible by heating the spent sorbent for 4 hours up to 550°C. In order to improve CO₂ removal, during the regeneration step the packed-bed has been flushed with a carrier gas, such as nitrogen, wet nitrogen or air. A preliminary set of experiments allowed to verify that the kind of carrier gas does not influence the sorbent reactivation.

The thermal treatment is followed by hydration with wet air for producing calcium hydroxide. The results of several regeneration experiments are summarized in figure 4 where the sorbent conversion values for successive reactivations are reported.

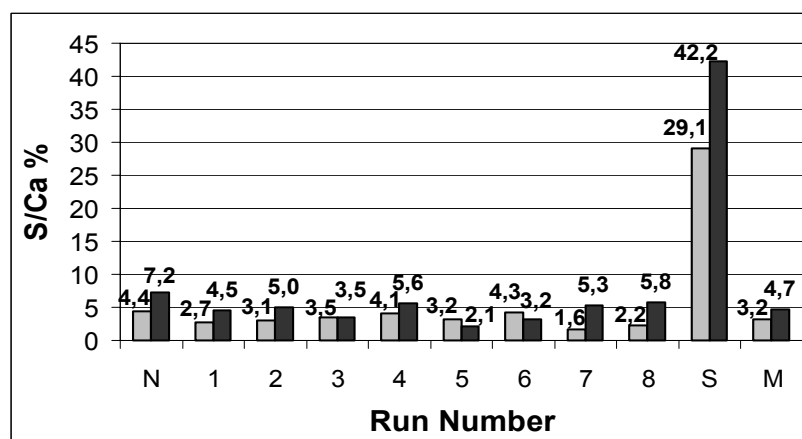


Fig. 4 Influence of sequencing reactivations on the recovering of sorbent activity. $T=300^{\circ}\text{C}$; 1100 ppm SO₂; 12% CO₂; 2% O₂; (■) 6% H₂O; (□) 26% H₂O; N₂ to balance.

In figure 4, N indicates the first test performed, while S and M are respectively the overall conversion reached after 9 runs and the average sorbent conversion on all the tests. We can see that the overall solid utilisation can be increased dramatically since the reactivation can be carried out several times on the same sorbent without any significant loss of activity. Moreover, it can be also seen that a large amount of water in the feed stream (26%) during the FGD process has a significant effect on the sorbent conversion: the average solid conversion increases from 3,2 to 4,7%, while the overall sorbent conversion after 9 tests is equal to 42,2 %.

REFERENCES

1. Fernandez I., Garea A., Irabien A.: *Chem. Eng. Sci.*, **53**: 1869 (1998).
2. Garea A., Viguri J.R., Irabien A.: *Chem. Eng. Sci.*, **52**: 715 (1997).
3. Cortabirte F., Ortiz M.I., Irabien A.: *Thermochim. Acta*, **207**: 255 (1992).
4. Gadalla A. M., Gupta A.: *Ind. Eng. Chem. Res.*, **33**: 1145 (1994).

Kinetic scheme of thermal decomposition of polyvinylchloride

A. Marongiu, F. Robecchi, T. Faravelli, G. Bozzano, M. Dente, E. Ranzi

Dipartimento di Chimica, Materiali e Ingegneria Chimica-Politecnico di Milano – ITALY

INTRODUCTION

In the last years, plastic waste has been mainly disposed of by landfill or incinerated, but these processes are not completely accepted by the actual international policy that is steered to more effective recovery of raw materials and energy. Pyrolysis and gasification processes are promising routes to upgrade the waste. Moreover, pyrolysis of plastic mixtures, based on the decomposition of polymers at different temperatures, allows to treat polymers with the simultaneous decomposition and separation. In typical municipal waste, one of the main plastic component is polyvinylchloride (PVC). Thermal degradation of PVC is a complex process than those of other staple plastic wastes, i.e. polyethylene (PE), polypropylene (PP) and polystyrene (PS). As a matter of facts, whilst PE, PP and PS at quite low temperatures thermally react reducing the polymer chain, PVC pyrolysis involves cross-linking reactions with the formation of polyaromatic structures and carbonaceous residuals (char), eventually chlorinated. Moreover a further “dimension” is required in the chemical description: besides carbon and hydrogen, chlorine has to be introduced in the system. The characterization of the chemistry of PVC pyrolysis claims then some simplifications and lumping procedures to handle the huge amount of intermediate and final products.

The degradation of PVC is a complex chain dehydrochlorination forming conjugated polyene. The PVC pyrolysis is a radical process [Bockhorn et al., 1999], at least at quite high temperatures, above 200°C, where the initiation reaction is the cleavage of C-Cl bonds. The propagation is characterized by two main steps. Initially dehydrochlorination gives rise to the formation of a polyene structure. During this phase benzene and partially naphthalene and phenanthrene are also formed through Diels-Alder reactions between polyene molecules and successive dealkylation. When Cl has been quantitatively released from the melt, as HCl, polyene molecules rearrange and decompose to yield sizeable amounts of alkyl aromatic hydrocarbons. The goal of this work is to model the pyrolysis phenomena of PVC investigating both the degradation mechanism and the product distribution. A semi-detailed kinetic scheme was developed, which provides not only sample weight loss results in isothermal and in dynamic analysis but also dispersion of decomposition products.

KINETIC SCHEME

As already mentioned, the presence of chlorine element, the random formation of double bonds and the intermolecular cross linking reactions give rise to a complex system, characterized by a huge number of compounds from low to very high molecular weight. Increasing the molecular weight the number of possible isomer configurations exponentially increase too. The proposed approach is to simplify the description of the pyrolysis process through the reactions of the single reference monomer unit.

A small set of lumped pseudospecies (representative of large families of compounds) are then sufficient to characterize the system. Due to the lack of space, it is not possible to discuss in detail the characteristic of these reference pseudospecies, which are both molecules, 25, and radicals, 13. The mechanism involves about 250 reactions, whose kinetic parameters are directly derived from analogous rate constants of gas phase elementary reactions, eventually corrected to take into account the transposition in the liquid phase [Ranzi et al., 1997].

Cl radical formed from the C-Cl bond cleavage, abstracts H from a PVC molecule forming HCl (which leaves the system) and a polymeric radical, figure 1. The successive β -scission forms a double bond inside the polymer chain and release another Cl, which rapidly propagates. Formed polyene structures can condense and form through Diels-Alder reactions aromatic compounds. The presence of Cl atoms close to the formed ring and the consequent electronic delocalization reduces the activation energy of the dealkylation reactions. Benzene is then mainly formed during the initial process when most of Cl is still on the polymer chain. When dehydrochlorination is completed the cross linking reactions mainly form alkyl-aromatic species. The interactions between aromatic radicals and/or molecules allow further molecular weight increase and H/C ratio decrease. The result of this process is the formation of char structures of high molecular weight and low H content.

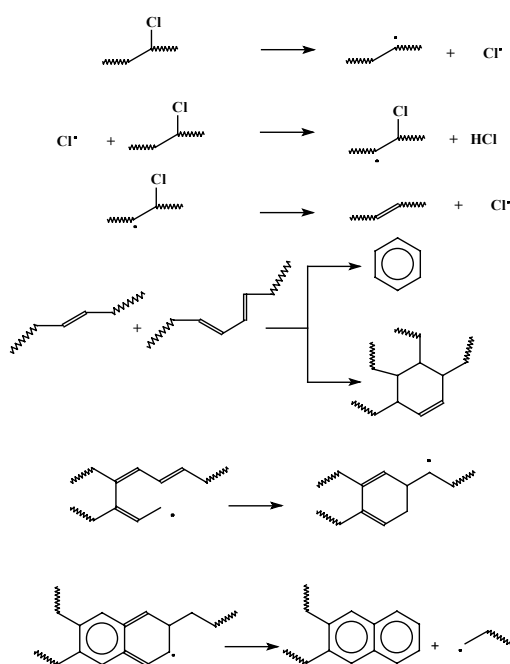


Fig. 1 Main reactions of PVC thermal degradation.

DYNAMIC THERMAL DEGRADATION

The proposed kinetic model has been tested and validated on the basis of different thermogravimetric experiments, both in isothermal or dynamic conditions.

Figures 2 shows a couple of comparisons of dynamic analysis. The experimental data are carried out from two different research groups and refer to different heating rates [Bockhorn et al., 1999; Montaudo et al, 1991]. It is possible to observe the presence of the two mentioned mechanisms.

The initial weight loss begins above about 200°C. During this phase mainly benzene and HCl are formed. At about 350°C the degradation rate decreases. This plateau can be explained by the lower reactivity of the formed alkyl-aromatic radicals resonantly stabilized. Finally further temperature increase (at about 380 – 400 °C) makes faster the radical mechanism and the slope of the degradation curve becomes steeper.

The initial conditions and the computed profiles match very well the experimental measurements in both the examples. The characteristic temperatures at which the degradation curve changes its slope are correctly predicted. The total amount of residue is also correctly reproduced (fig. 2b). On the contrary, in the experiments of Bockhorn et al. (1999), the curve is normalized in comparison with the residual obtained at 500 °C. This normalization does not allow a direct comparison of the char produced.

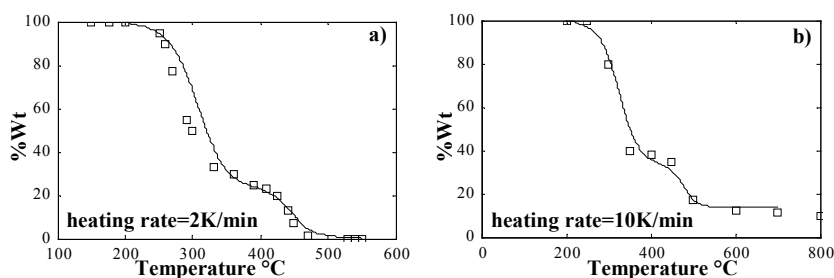


Fig. 2 Dynamic TGA at different heating rate (\square experimental data, — calculated data): a) 2K/min [Bockhorn et al., 1999]; b) 10K/min [Montaudo et al, 1991].

ISOTHERMAL EXPERIMENTAL DATA

An interesting set of experimental thermo-gravimetric analysis carried out in isothermal conditions were reported by Bockhorn et al., 1999. The first set refers to relatively low temperature conditions. These conditions are typically interested by dehydrochlorination phenomena with the simultaneous benzene formation (fig. 3a). The agreement with the theoretical computations is very good. The different degradation curves at different temperatures are well characterized and the reactivity of the system is correctly reproduced. Once again the experimental data are normalized at the residual and char formation cannot be compared. The second set of experiments is characterized by higher temperature levels. These data were performed in order to better investigate the second step of PVC degradation. As a matter of facts, according to what already observed in the dynamic analysis, at 400 – 450 °C the degradation involves mainly the tar formation and its growth to char. The samples were obtained through a particular procedure. Initially a dynamic transformation at heating rate of 2°K/min until 350°C followed by an isothermal at this temperature for 30 minutes allows the complete dehydrochlorination of PVC and the benzene release. The resulting polymer melt is mainly composed by polyene molecules. Successively the sample is instantaneously moved to the final isothermal temperature. In these conditions intermolecular reactions between polyene molecules form alkyl-aromatic molecules, which condensate, losing their alkylation, up to the final char residue. Even though the modeling of this experiments is more difficult to be reproduced and larger uncertainties are introduced, the final comparisons is quite good. The main characteristics of the curves are correctly predicted and the small overprediction of the reactivity observed at lower temperatures is always below 8%.

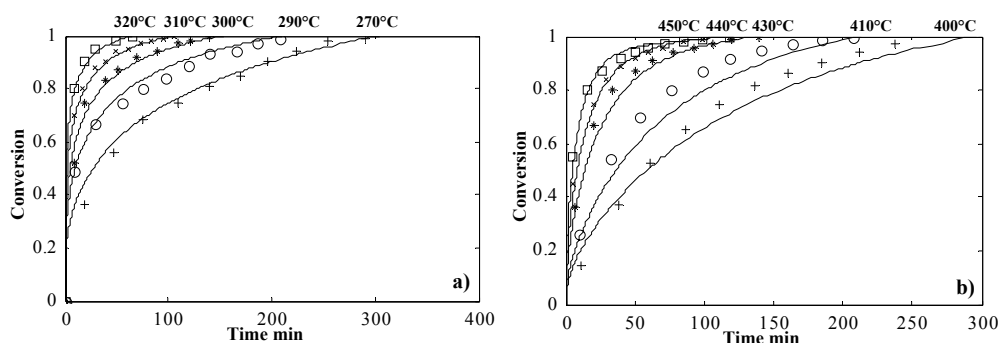


Fig. 3 Isothermal TGA at different temperatures [Bockhorn et al., 1999]: a) first step of degradation; b) degradation of a dehydrochlorinated PVC sample. (Line: predictions; marks: experimental data).

PRODUCTS DISTRIBUTION

As already mentioned, the possibility of this semi-detailed kinetic model lies not only in the possibility of spanning on very wide ranges of operative conditions and type of experiments (dynamic or isothermal), but it has also the intrinsic peculiarity of predicting the product distribution. The importance of such a feature is obvious when the plastic reuse is investigated, but it becomes fundamental in the case of PVC, where possible dangerous chlorinated pollutant can be emitted from the system. Unfortunately, in our knowledge only a few experimental data on product distribution from PVC thermal degradation are available in the literature. McNeill et al. (1995) reported mass fraction distributions from a dynamic pyrolysis with a heating rate of 10 K/min up to 500°C. Table 1 shows the comparison between experimental results and predicted values.

Light gases, C₂ and C₄, were all included in gas. Tar fraction represents the polyaromatic volatile compounds at experimental operative conditions. Chlorinated gases tar and char are

characterized in the scheme. Their amount is also reported in table 1, unfortunately the same detail were not experimentally detected.

(%Wt)	HCl	C ₆ H ₆	Gas	TAR	CHAR	Chlorinated GAS	Chlorinated TAR	Chlorinated CHAR
Predicted	58,1	8	1,0	19	13,6	0,29	2.174e-5	2,2e-3
Experimental McNeill et al. 1995	52,6	6.88	6,6	24,3	9,5	0.12		

Tab. 1 Product massive fraction after a dynamic pyrolysis up to 500°C.

The theoretical HCl released is more than those experimentally observed. The computed value obviously corresponds to the Cl totally present in PVC. The lower experimental amount can be explained either in the measure uncertainties or in the composition of the sample. This discrepancy partially explain the deviation in the gas formation too. The general agreement is satisfactory, considering the many simplifications and further comparisons will increase the

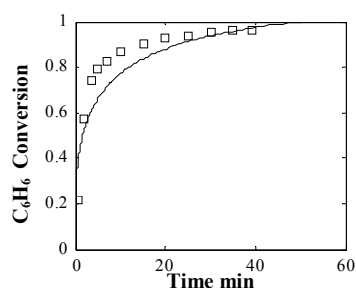


Fig. 4 Benzene evolution during the first degradation step at 290°C [Hornung U., 1997]. (Line: predictions; marks: experimental data)

reliability of the model. Hornung (1997) obtained experimental data of benzene evolution in isothermal TGA. Figure 4 shows the comparison with the calculated results. In this case the agreement is quite good and the same level of accuracy was also observed for different temperatures.

CONCLUSION

A semi-detailed kinetic scheme of the thermal decomposition of PVC has been developed. The mechanistic approach allows to reproduce the degradation in different experimental devices and wide operative conditions. Moreover the

prediction of the product distribution make the model a useful tool not only for the upgrading of plastic wastes but also to investigate the pollutant impact of pyrolysis as process of plastic reuse.

ACKNOWLEDGEMENT

This work was supported by EU under the “HALOCLEAN CONVERSION” project.

REFERENCES

- Bockhorn H., Hornung A., Hornung U.: *J. Anal. App. Pyrolysis*, **50**: 77 (1999).
 Hornung U.: *Bestimmung der Vergasungskinetik von Kunststoffen mit Hilfe eines isotherm betriebenen Kreislaufreaktors*, Fortschritt-berichte VDI, Reihe 3 Nr. 485 (1997).
 Geoffrey M. A.: *Polymer Degradation and Stability*, **64**: 353 (1999).
 McNeill I. C., Memetea L., Cole W. J.: *Polymer Degradation and Stability*, **49**: 181 (1995).
 Montaudo G., Puglisi C.: *Polymer Degradation and Stability*, **33**, 229 (1991)
 Ranzi E., Dente M., Faravelli T., Bozzano G., Fabini S., Nava R., Cozzani V., Tognotti L.: *J. Anal. App. Pyrolysis*, **40-41**: 305 (1997).

Wall-flow catalytic traps for diesel particulate abatement from mobile sources

Emanuele Cauda, Debora Fino, Nunzio Russo, Guido Saracco*, Vito Specchia

*Dipartimento di Scienza dei Materiali ed Ingegneria Chimica,
Politecnico di Torino, Corso Duca degli Abruzzi 24, 10129 Torino, Italy.*

** corresponding author: tel./fax: +39-011-5644654/99; e-mail: saracco@polito.it*

INTRODUCTION

Recent European prescriptions (EEC directive 1999/30/CE) concerning the quality of air in urban areas are more often forcing local authorities to prohibit car circulation in selected days (see the situation of Turin at web site [1]). Particulate matter smaller than 10 μm (the so called PM10), largely produced by diesel engines, is the pollutant more often responsible for this occurrence. These engines dominate the heavy-duty market but they are steadily increasing their penetration in the passenger-vehicle one, owing to their superior efficiency and higher-than-once comfort. However, this trend can face a halt owing to the carcinogenic effect of diesel particulate. The best technical solution to overcome this serious problem lies in the development of particulate traps placed in the exhaust line and capable of filtering diesel particulate down to acceptable concentrations (less than 0.025 g/km are expected for pending 2005 EU regulations). Over time, traps become clogged with particles. The exhaust back-pressure is thus increased which turns into higher fuel consumption. These soot particles can be eliminated by combustion (filter regeneration). However, soot cannot be burned off effectively at temperatures that are likely to occur during normal driving conditions. A way to improve the filter system and to meet the regeneration demands is to use the filter lined with catalyst [2] which facilitates diesel particulate combustion.

Catalytic traps based on wall-flow ceramic monoliths (shallow-bed filtration), combined with an oxidation catalyst deposited onto it, are being developed and tested at our labs. These traps can be periodically regenerated by a peculiar use of last generation Common-Rail Diesel engines: some fuel is post injected and gets burned out by a specific catalytic converter so as to heat up the downstream trap until catalytic combustion of soot is ignited. This paper describes the encouraging results obtained in this context,

EXPERIMENTAL PROCEDURE

Catalyst preparation and characterisation

After a large screening of soot-combustion catalysts, the best catalyst developed was the perovskite $\text{LaCr}_{0.9}\text{O}_3$, obtained by a highly-exothermic and self-sustaining reaction (*combustion synthesis* [3]). A concentrated aqueous solution of various precursors was located in a oven at 600°C for few minutes in a crucible, so as to ignite the very fast reaction:



The catalyst was then ground in a ball mill at room temperature and characterized.

X-ray diffraction (PW 1710 Philips diffractometer) was used to check the achievement of the perovskite structure. Conversely, the activity of the prepared catalyst was analysed by temperature programmed reaction (TPR), according to the standard operating procedures described in detail by Fino et al. [4]: air was fed at the constant rate of 50 $\text{ml} \cdot \text{min}^{-1}$ to a fixed-bed micro reactor constituted of a mixture of carbon and powdered catalyst (1:9 mass basis).

All experiments were performed by using, instead of real diesel soot, an amorphous carbon. This allows to regard as conservative the results obtained because amorphous carbon is more difficult to burn than real diesel soot. The reaction temperature was controlled through a PID-regulated oven and varied from 200 to 700°C at a 5 °C·min⁻¹ rate meanwhile feeding air at a 50 Ncm³/min rate. The analysis of the outlet gas was performed via NDIR analysers.

Catalytic traps preparation

The LaCr_{0.9}O₃ catalyst was deposited by *in situ* combustion synthesis directly over the wall-flow filters. The ceramic support was dipped in the aqueous solution of its precursors and then placed into an oven at 600°C. The aqueous phase was rapidly brought to boil, the precursors mixture ignited and the synthesis reaction took place *in situ*. The support selected was a silicon carbide (SiC) filter produced by IBIDEN (cell structure =14/200, diameter 30 mm, length = 6-12''; pore diameter of channel walls = 9 µm, porosity of channel walls = 42%) which was found to be chemically compatible with the selected catalyst. The load, the adhesion and the thickness of the catalyst deposited onto the monolith were assessed by gravimetric analysis, SEM observation and ultrasonic bath test, respectively. The amount of perovskite deposited was 10 wt% for the catalytic trap tested in the following.

Diesel engine bench tests

The developed traps were tested in the pilot plant sketched in Fig.1 on real Diesel exhaust gases (Kubota 1000 cc IDI engine, capable of up to 23.5 hp at 3000 rpm), where the temperature and gas composition before and after the trap can be controlled and monitored, as well as filtration efficiency and the evolution of the pressure drop through the trap (a sing of soot accumulation therein). A detailed description of the plant was provided by Fino et al. [4].

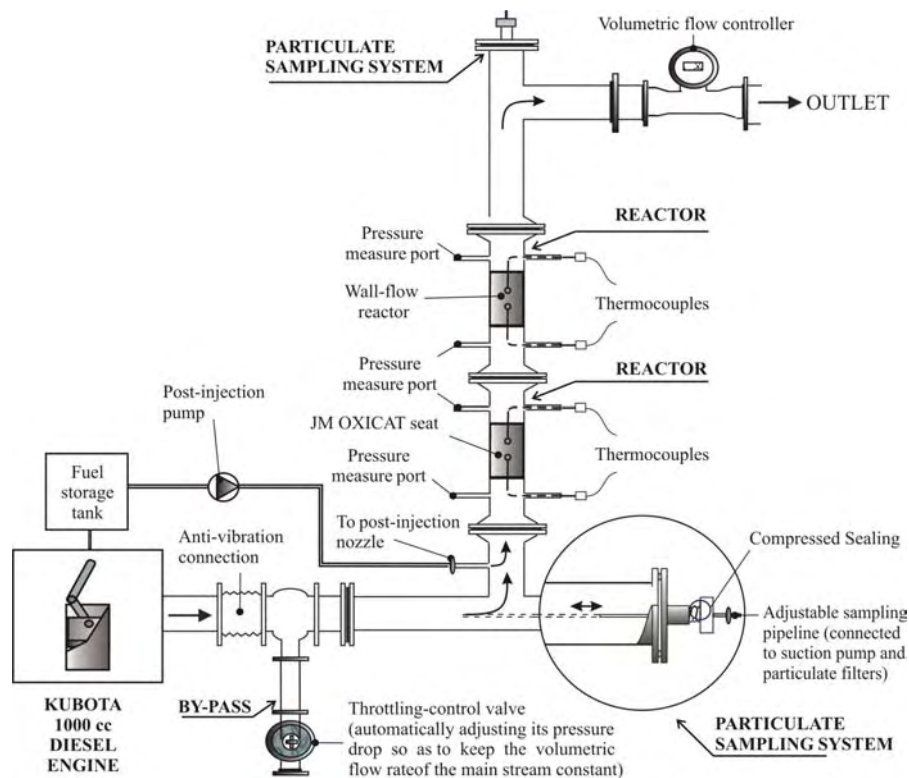


Fig. 1. Schematic view of the engine-bench pilot plant.

The wall-flow was located along the main line of the main exhaust stream. The exhaust gas

superficial velocity across the trap could be controlled at a fixed value by measuring the exhaust flow rate through a volumetric flow controller connected to a throttling valve placed on by-pass exhaust stream. The pressure drop across the trap could be measured by means of differential pressure transducers (VIKA) whereas the trap inlet and outlet temperature was measured by K-type thermocouples at axial position. The soot concentration in the exhaust gases was measured by isokinetic sampling of a small flues-gas flow rate through a pump and by collecting the suspended particulate using a 2-filters system (PALLFLEX 47 TX 40 HI 20-W). Finally, gas phase composition could be monitored through continuous analyser by Elsag-Bailey (NDIR for NO, CO, CO₂, SO₂; FID for overall HC; paramagnetic for O₂). In line with the pending 2005 EU regulations, all the measurements were carried out by using a low-sulfur (<50 ppmw) diesel oil produced by Haltermann.

The standard bench test procedure can be described as follows. The traps is loaded by letting comparatively cold exhaust gases flow inside of it until a 120-150 mbar pressure drop is reached (corresponding to a particulate hold-up of about 10 g·L⁻¹). Then, regeneration is induced by post injecting some fuel with a metering pump and by burning these HC with an oxidizing honeycomb catalyst (OXICAT by Johnson Matthey) placed just upstream the trap. The time needed for complete trap regeneration (e.g. combustion of soot hold-up) is an index of catalyst performance. The higher the catalyst activity the lower the time required.

RESULTS AND DISCUSSION

An index of their activity can be found in the peak temperature (T_p) of their TPR plot: the lower the T_p value, the higher the catalyst activity. The choice of LaCr_{0.9}O₃ was driven by the fact that it entails a CO₂ production peak temperature (T_p) of just 480°C. Owing to the nature of Cr, this transition metal can in part undergo a valence shift from Cr³⁺ to Cr⁴⁺ so as to re-establish electroneutrality, despite its substoichiometric amount. The presence of Cr⁴⁺ was indeed demonstrated to promote an increase of catalytic activity towards carbon combustion [5]. The most likely explanation is that the perovskite can act as an oxygen pump towards soot. Oxygen can be indeed be made available to PM combustion in combination with a temporary shift of Cr valence from 4+ back to 3+. Oxygen molecules coming from the gaseous atmosphere can re-oxidise the perovskite and set the Cr⁴⁺ species back.

As mentioned earlier, LaCr_{0.9}O₃ was thus selected for the catalytic activation of wall-flow monoliths. To these merits, Fig. 2 shows SEM pictures of catalyst lined via *in situ* deposition on the upstream channel-walls of silicon carbide wall-flows traps: the catalyst is strongly bonded to the support and the microstructure obtained appears extremely foamy.

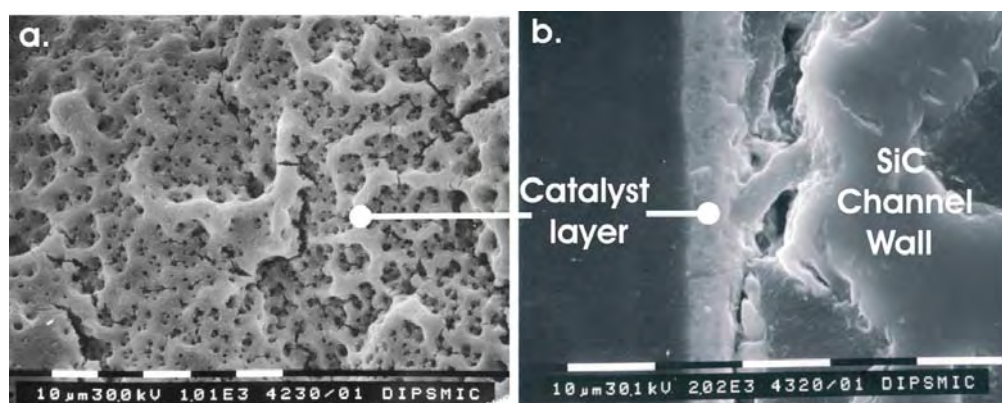


Fig. 2. SEM pictures of layers of LaCr_{0.9}O₃ catalyst deposited on the inlet channel walls of the silicon carbide traps: a. front section; b. cross section.

During combustion synthesis, the decomposition of reacting precursors generates a large

amount of gaseous products in a very short period of time, which leads to a spongy catalyst morphology. This feature represents a great advantage, as it favours the contact between the catalyst and the soot and keeps the pressure drop increase due to the catalyst itself acceptable.

Shifting to the analysis of performance of the developed trap systems, Fig. 3 compares the results of the runs obtained with a catalytic and non-catalytic SiC wall-flow monolith: the results are encouraging. After a trap leading period of about 600 min, in both cases, the regeneration starts as soon as an inlet trap temperature of about 600°C is reached by fuel-post-injection and catalytic combustion. However, the regeneration of the $\text{LaCr}_{0.9}\text{O}_3$ -catalysed trap is much faster than that of the non-catalytic ceramic filter. By these means, it becomes possible to save a significant amount of fuel at any filter regeneration, therefore reducing working costs. It has to be kept into account however that the part of fuel saving cost is compensated by a slight decrease of filter permeability owing to the presence of the catalyst.

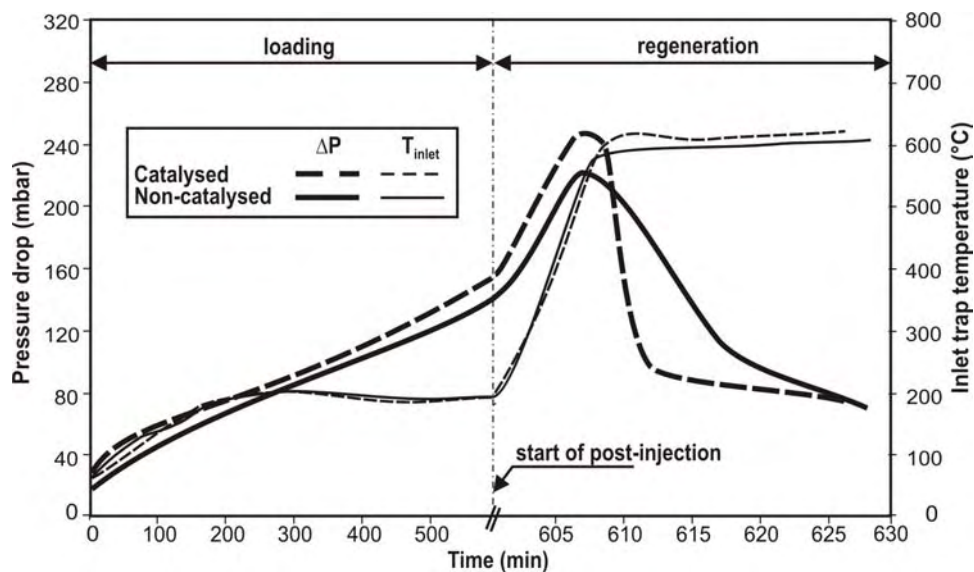


Fig. 3. Trap loading and regeneration cycles for a catalytic ($\text{LaCr}_{0.9}\text{O}_3$) and a non-catalytic wall-flow trap (SiC wall-flow monolith by Ividen).

CONCLUSIONS

The development of the common-rail engines has deeply changed the perspectives in the diesel –exhaust treatment field, by enabling a momentary rise of the exhaust gas temperature for trap regeneration purposes, even if this implies a certain fuel penalty. In this context, wall flow ceramic filters catalyzed with a perovskite compound obtained with the *in situ* combustion synthesis method seem to be very promising, as they entail a reduction of the time required for trap regeneration and of the related fuel penalty. Both experimental and modelling studies are currently in progress to develop new and more active catalysts, to further improve the deposition technique for the sake of reducing the related pressure drop increase, and to design a trap structure optimized for this promising regeneration route.

REFERENCES

1. www.comune.torino.it/ambientecgi/inquinamento.html
2. van Setten, B.A.A.L., Makkee, M., Moulijn, J.A.: *Catal. Rev.- Sci. Eng.*, **43**: 489 (2001).
3. Merzahanov, A. G.: *J. of Mat. Proc. Techn.*, **56**: 222 (1996).
4. Fino, D., Saracco, G. and Specchia, V.: *Chem. Eng. Sci.*, in press (2002).
5. Saracco, G., Scibilia, G., Iannibello, A., Baldi, G.: *Appl. Catal. B: Env.* **8**: 229 (1996).

Emissions from Light Oil Fluidized Combustion: Preliminary Application of an Optical Technique

¹C. Allouis, ¹F. Beretta, ¹F. Miccio, ²M. Miccio, ³G. Olivieri

1 Istituto di Ricerche sulla Combustione - C.N.R., Naples - ITALY

2 Dipartimento di Ingegneria Chimica ed Alimentare, Università di Salerno – ITALY

3. Dipartimento di Ingegneria Chimica - Università Federico II di Napoli, ITALY

In the past, the combustion of conventional gaseous and liquid fuels in Fluidized Bed did not represent an attractive solution for power generation. The interest in reducing the emission of particulate in the atmosphere lead to consider again this technique since it is very efficient; moreover, this process is well known to produce less NO_x, PAH and soot than the conventional ones. In fact, steady combustion of liquids is feasible even in a lower temperature range than that commonly used for solid fuels in Fluid Bed Combustion (FBC).

In spite of the advantages of this kind of combustion, several issues or problems remain to be solved like fuel atomisation and injection, in-bed air/fuel mixing, combustion instability, freeboard temperature peaks, etc.

An experimental and theoretical research on FB combustion of light oils is currently in course with the aim of understanding critical mechanisms of the process and provide a full interpretation of the observed phenomenology (Miccio et al., 2001). This paper presents preliminary results on the formation of conventional pollutants (NO_x, CO, etc.) and on the particulate emitted from a lab-scale fluidised bed fuelled with diesel oil. A particular interest was devoted to the detection of ultrafine particle emission ($d < 10$ nm) by means of light absorption in the UV.

Measurements of emissions were carried out on the exhausts of steady-state tests carried out with a lab-scale, bubbling bed combustor. The unit was 78 mm ID and 3.6 m tall. The fluidization and reaction zones were electrically heated and insulated from outside. Light oil was fed underbed with a horizontal, water-cooled, two-fluid injector, which delivered the fuel through a 1 mm nozzle with a stream of atomization air. The light oil was dosed by a peristaltic pump and its feed rate was determined by continuous weighing.

Conventional composition analysis of exhausts was carried out by sampling gases before the combustor exit and sending them to a battery of O₂, CO₂, CO and NO analyzers after the due conditioning. The concentration of unburned hydrocarbons was expressed as CH₄ equivalent and on-line measured by an *ad-hoc* adaptation of a gas-chromatograph equipped with a flame ionization detector.

TABLE I

Design and operating variables of the experiments

Reactor internal diameter, mm	78
Sand size, mm	0.2-0.4
Fuel nozzle size, mm	1.0
Injector elevation, mm	30
Bed mass, kg	1.8
Excess fluidization velocity ($U-U_{mf}$), $m s^{-1}$	0.3
Dispersion velocity (u_0), $m s^{-1}$	50÷150
Bed temperature, °C	550÷800
Excess air ratio (e)	1.3

Silica sand with an average size of 0.3 mm was used as bed material. The test runs were carried out by varying bed temperature from 550 to 800°C and by keeping constant fluidization conditions (see Table 1). The excess air factor was fixed at the constant value $e = 1.3$. Correspondingly, the diesel oil flow rate was around 200 cm³/h.

Figure 1 reports CO, C_nH_m and NO concentrations at increasing bed temperature as measured by conventional analysis at the reactor exit. CO concentration shows a non-monotonic dependence on the temperature, with a maximum at around 650°C and a fast decay above 700°C. This trend is to be related to an anomalous combustion behavior that was detected during experiments. Actually, in a broad temperature range (from 550 to 700°C) micro-explosions were noted in a random succession; they were associated to acoustic effects, which were clearly detectable by the hear, and to oscillations of the overbed pressure, which were monitored by the instrumentation.

As far as the other unburned species, analysis of Fig. 1 clearly demonstrates that the concentration of hydrocarbons (expressed as methane equivalent) is lower than CO concentration in the entire temperature range covered during the experiments (550-750°C). It is so even at the lowest investigated temperature, i.e. 550°C, where escape of pyrolysis products from the bed could be expected.

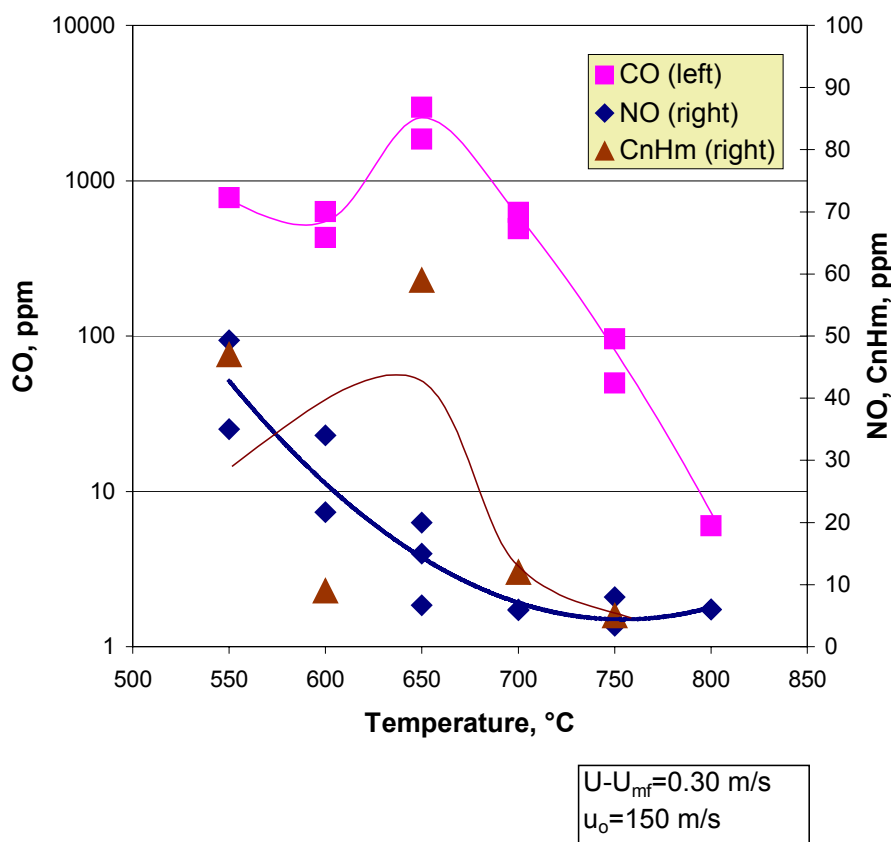


Figure 1- CO, C_nH_m and NO concentrations at reactor exit as a function of bed temperature

The analysis of data concerning NO provides a further confirmation of the anomalous behavior of light oil combustion at low temperatures. Actually, NO concentrations are low as absolute values, but they decrease monotonically with temperature. Higher values of NO concentration were measured in the low temperature range 550-650°C, whereas very small values were determined above 650°C (see Fig. 1), that is when micro-explosions tend to disappear. It is worth noting that the NO generation can be attributed to the thermal mechanism only, the fuel being nitrogen free. Therefore, NO might have been formed at a high concentration in a gas pocket reaching very high temperature following a deflagration; then sampling at the combustor exit smoothes and averages NO concentration.

The investigations via an optical technique were conceived in order to provide

confirmation and additional information to the conventional composition measurements. In particular, they were devoted at checking the presence of ultrafine particles in combustion exhausts.

Absorption measurements were carried out on the exhaust gases of test runs in the temperature range 650-800°C. The optical analysis of the exhaust gas is based on conventional schemes of broad band ultraviolet extinction spectroscopy. A remarkable feature in the extinction experiments is the use of a new kind of light source¹ which exploits the laser-induced breakdown of air, obtained by tightly focusing a pulsed Nd:YAG Q-switched laser beam (8 ns pulse, 200 mJ energy and 8 mm diameter). The resulting plasma kernel is extremely hot, reaching electron temperature up to 10⁵ K, has a lifetime of nearly 20 ns and is spatially confined in a volume of the order of 10⁻² mm³. The detected spectral emission of the light source spreads out from the visible band down to the deep ultraviolet ($\lambda < 190$ nm), a spectral limit imposed by the strong absorption of atmospheric oxygen and by the detector sensitivity. The spectral, spatial and temporal features of the light source proved to enhance the sensitivity of classical optical techniques in recent experiments²⁻⁴. The absorption measurements were based on the analysis of the Lambert – Beer's law:

$$K_{\text{ext}}(\lambda) = (1/L) \cdot \ln[I_0(\lambda)/I(\lambda)] \quad (1)$$

where K_{ext} is the extinction coefficient; λ is the wavelength; L is the optical path and I_0 and I are the incident and attenuated light respectively.

Figure 2 shows the details of the optical set up. The UV-visible radiation, emitted by the Nd-YAG laser plasma, travels through the pipe duct, where the air-diluted exhausts are flown. The transmitted light enters the input slit of a spectrometer, where it is spectrally dispersed, and is recorded by an intensified and gated low-noise CCD detector. The absorption spectra were averaged over 100 shots.

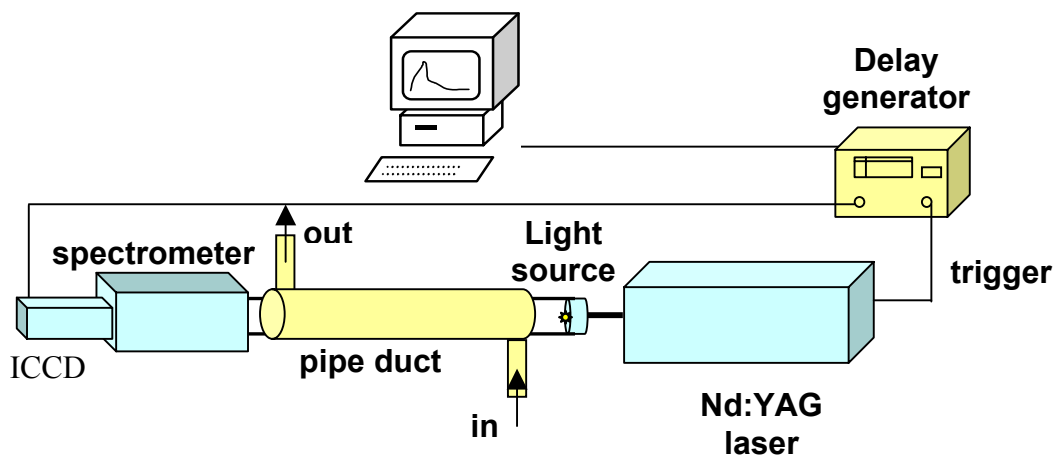


Fig. 2 Experimental Set-up

Figure 3 represents the spectra obtained for the different bed temperatures and background corrected. The data obtained for a bed temperature of 650°C have not been considered because of the poor quality of the signal measured at the exhausts.

In this figure it is possible to note the presence of a significant number of peaks. The most interesting behavior of the absorption spectra is the lack of the strong absorption band between 200 and 240 nm, which is the absorption interval of ultrafine particles ($d < 10$ nm). The analysis in the visible range (400-500 nm) leads to consider the presence of a small

quantity of soot particle since the decreasing slope of the extinction coefficient is close to λ^{-1} law. Further, the NO peak wavelengths were found according to Okabe⁵. However, the optically measured NO values appear 2-3 times larger than those measured by the gas analyzer. A first-approximation analysis of the remaining peaks let us to infer the presence of polycyclic aromatic hydrocarbon and unburned hydrocarbons in the exhausts.

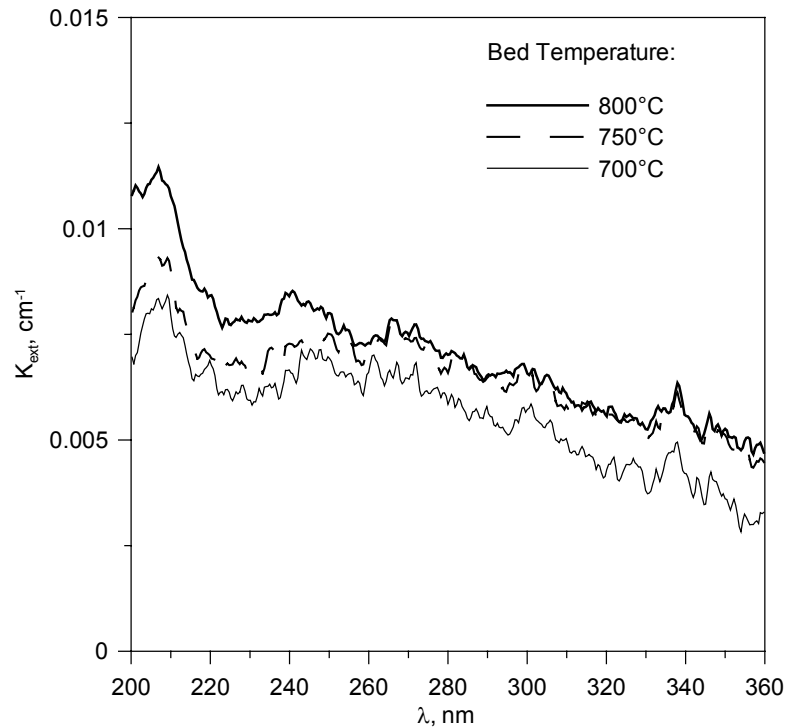


Figure 3 - Absorption spectra obtained at the exhausts of the fluidized bed for different bed temperature

Further tests and a deeper analysis will be performed in order to be able to better identify the numerous peaks that compose the spectra.

ACKNOWLEDGEMENTS

This work has been carried out under the MURST-PRIN (1999-2001 and 2001-2003) financial support.

REFERENCES

1. Borghese, A., Merola, S.S., *Applied Optics* **37**:3977-3983 (1998a)
2. Borghese, A., Merola, S.S., *Proceedings of the Combustion Institute*, **27**:2101-2109 (1998b)
3. Kurz, M., Merola, S.S., D'Anna, A., D'Alessio, A., Borghese, A., *Part. Syst. Charact.* **16**:77-84 (1999)
4. Merola, S.S., Kurz M., Borghese, A., D'Anna, A., D'Alessio, A., **34**:221-241 (1998)
5. Okabe, I., *Photochemistry of small molecules*. Wiley-Interscience Publications, John Wiley and Sons, New York (1978)
6. Miccio F., Miccio M. and Olivieri G., *Proc. of the 16th International Conference on Fluidized Bed Combustion (FBC01)*, Reno, Nevada (USA), paper FBC01-0178 published on CD-ROM by ASME, ISBN 0-7918-3533-5, May 13-16 (2001)

CARBONISATION RATES OF CARBONACEOUS PARTICLES IN PREMIXED LAMINAR FLAMES OF ETHYLENE-AIR

A. Rolando¹, G. Basile¹, P. Minutolo², A. D'Anna¹, A. D'Alessio¹

¹ *Dipartimento di Ingegneria Chimica*

Università "Federico II" P.le Tecchio 80, 80125 Napoli, Italy

² *Istituto di Ricerche sulla Combustione*

CNR P.le Tecchio 80, 80125 Napoli, Italy

INTRODUCTION

In a previous work [1] we had used time resolved temperature measurements performed with a thermocouple inserted in hydrocarbon rich premixed flames to evaluate the emissivity of carbonaceous particles and their carbonization in the process of soot formation. It has been found that the emissivity of carbonaceous nanoparticles remained approximately constant at the value of 0.5 for a certain residence time in flame, thereafter it increased rapidly to values of the order of 0.95. This "induction" time was considered as the half-time of a second order reaction by which the particles with 0.5 emissivity (nanoparticles) were becoming soot, and calculated the kinetic constant of this carbonisation mechanism.

In this work, we apply the same technique to evaluate the activation energy of the carbonization process performing measurements in ethylene/air flames varying the flow of the reacting mixture. In this way, we obtain a wide range of flame temperatures from 1500K to 1800K which allow us to build the Arrhenius diagram and estimate the pre-exponential factor and the activation energy of the process.

SET-UP OF THE EXPERIMENTAL SYSTEM

The experimental set-up for the thermocouple measurements is constituted of a burner to stabilize laminar premixed flames and a fine-wire thermocouple for transient temperature measurements.

The burner is a capillary stainless steel burner for flat premixed flames where C₂H₄/air mixture is fed, with the velocity of the cold gas mixture ranging from 5 to 10 cm/s. The thermocouple is a Pt/13%Rh-Pt thermocouple, whose response time is about 0.2s, with a filaments diameter of 100µm and the diameter of the junction of 330µm. The voltage signal is acquired with a fast analog/digital converter with a resolution of 1 ms and stored in a PC for further analysis. Light absorption spectra in the UV are measured for the determination of the particle volume fraction. The experimental set-up and procedure are reported in [1].

TEMPERATURE MEASUREMENTS

Thermocouple junction is inserted in the flame and held in a fixed position during the measurement. In each measurement, the time response of the thermocouple signal is recorded for about 200s. Different measurements are performed, varying the velocity of the inlet fuel/air mixture, at different heights above the burner.

In about 0.9s, thermocouple junction temperature increases from ambient temperature to a maximum value. This time interval (0.9s) is dependent on the response time of the thermocouple and on the time to insert the junction in the centreline of the flame. After the maximum measured temperature is reached, the temperature of the junction rapidly

decreases if particulate covers the junction. Thus, the junction emissivity increases from 0.2 (platinum) to a final value which is typical of the deposited particles, and is reached when the particulate uniformly covers the junction. This process take about 10 seconds, after that the emissivity remains constant and the further particulate deposition only changes the diameter of the junction. The increase in diameter reduces the temperature of the junction. From the rate of this temperature drop in the time interval 10s-200s, also the density of the deposit layer can be calculated.

The energy-balance on the junction can be written as follows [2]:

$$m_{pl}c_{pl} \frac{dT_j}{dt} = \left[\frac{Nu \cdot k_g}{D} (T_g - T_j) - \varepsilon_j \sigma T_j^4 \right] (4\pi D^2) \quad (1)$$

where m_{pl} , c_{pl} , T_j , D and ε_j are the mass, the temperature, the diameter, the heat specific and the emissivity of the junction, Nu is the Nusselt number, σ is the Stephan-Boltzmann constant, and k_g and T_g are the thermal conductivity and the temperature of the gases (the conduction through the filaments of the thermocouple has been neglected).

The particulate mass flux depositing on the junction because of thermophoretic forces and the consequent diameter variation of the junction is given by the expression [2]:

$$\dot{m}_t = f_v \rho_p \left[0.55 \frac{\mu_g Nu (T_g - T_j)}{\rho_g D T_g} \right] = \frac{\rho_d}{2} \frac{dD}{dt} \quad (2)$$

where f_v , ρ_p , ρ_d are the volume fraction, the density in flame and the deposit density of the particles, μ_g , ρ_g are the viscosity and the density of the gases.

Gas temperature is easily determined when the temperature of the thermocouple reach its maximum value; in fact, in that moment we can assume the thermocouple isn't yet covered and by equation (1), using the emissivity of the platinum and the diameter of the clean junction, we can evaluate T_g .

Emissivity of the particles is determined by equation (1) by the measurements performed in the first ten seconds of the time history of the temperature of the junction. In fact, in this period particulate matter from the gas phase is covering uniformly the thermocouple junction and it is possible to neglect the diameter variation. Consequently, only the emissivity is unknown.

Using the data of the temperature profile in the time range 10s-200s, the density of the material deposited on the thermocouple can be calculated by the system of the two equation (1) and (2). In this period the emissivity is constant, the volume fraction is measured by UV light absorption and so only ρ_d/ρ_p is unknown.

RESULTS

In fig.1 the emissivity values of the particulate deposited on the thermocouple, measured in different flames varying the rate of the inlet mixture, are reported as a function of the flame residence time.

It appears that in all the flames, the emissivity of the particulate deposited on the thermocouple junction sharply increases fom 0.2, the value of platinum, to values between 0.45 and 0.55 just downstream the reaction zone. Later on, the emissivity remains almost constant for a time interval. After this "induction" period, a second rise of the emissivity takes place. The emissivity tends to a final value around 0.95, typical of soot particles [2].

It is quite reasonable to attribute the intermediate emissivity values to carbonaceous nanoparticles. As it was already assessed in the previous work [1] that combined thermocouple measurements with optical UV light absorption and light scattering measurements in order to characterize the flame particulate, in fact it is known that nanoparticles are produced very early in the reaction zone, where the concentration of atoms and radicals is high, and that their size is much smaller than soot particles, so that their presence is associated to relatively low scattering coefficients.

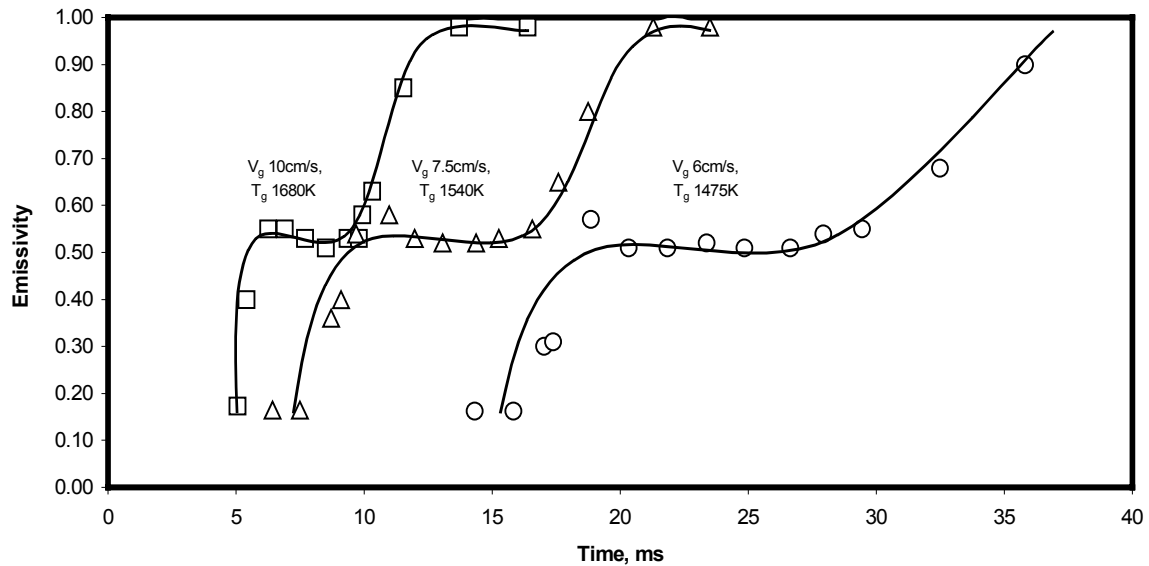


Fig. 1 Emissivity of the particles present in flat premixed flames of ethylene/air with C/O=0.77 and different rates of the inlet fuel/air mixture v_g

The peculiar behavior of the emissivity in premixed flames shown in Fig.1 suggests that the time interval between the first rise in the reaction zone and the second one represents a typical carbonization time during which soot precursor nanoparticles graphitize to form soot [1]. Therefore these data can be used in order to establish the kinetics of this process in premixed flames.

For each flame observed, table I shows the flame temperature T_g , the “induction” time (τ), the volume fraction f_v of nanoparticles measured with UV-absorption technique, and the diameter d of these particles measured with light scattering/absorption.

Table I

V_g (cm/s)	T_g (K)	τ (s)	f_v (cm ³ /cm ³)	d (cm)
5	1440	0.01739	1.50E-07	3E-7
6	1475	0.01058	2.30E-07	3E-7
7.5	1540	0.00690	2.50E-07	3E-7
10	1680	0.00355	3.20E-07	3E-7

The previous work [1] showed that the process is a second order reaction, therefore the lifetime is given by the expression:

$$\tau = \frac{\pi d^3}{6 f_v \cdot K_c} \tag{3}$$

With this formula we calculate the kinetic constant k_c . The Arrhenius plot, i.e. the logarithm of the kinetic constant versus the inverse of temperature $1/T_g$, is reported in fig.2.

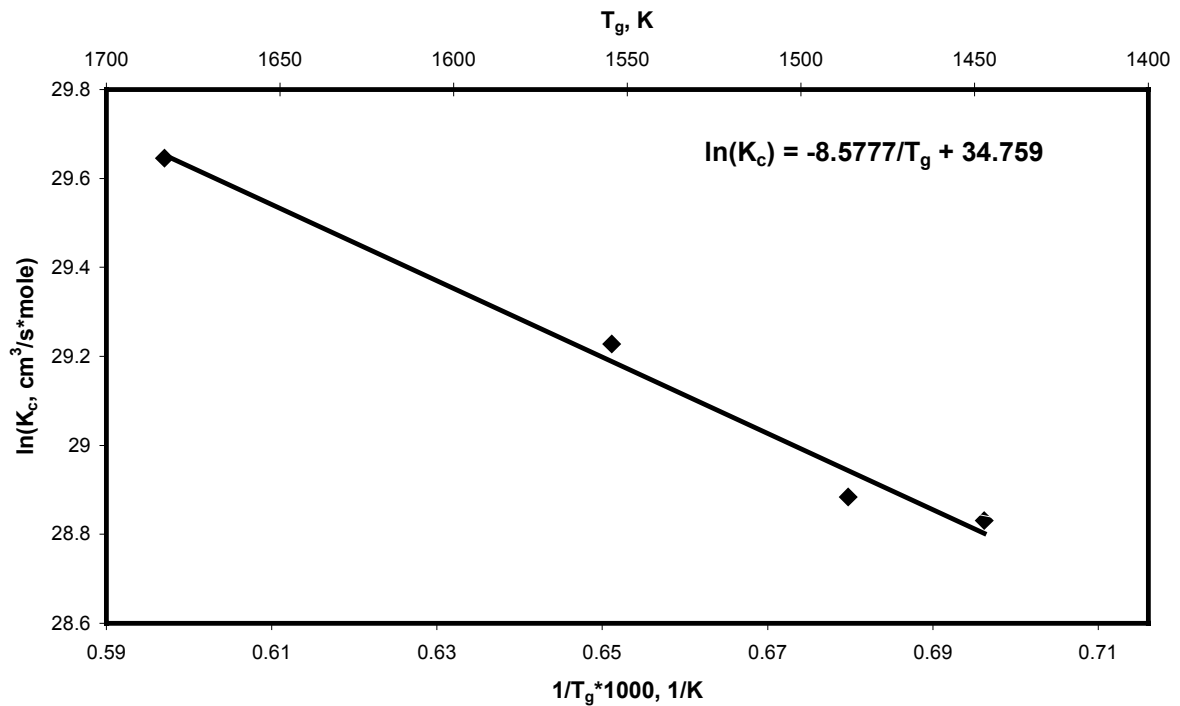


Fig. 2 Arrhenius plot of the carbonization constant

An activation energy of about 17 Kcal/mol and a pre-exponential factor of the order of $1E15$ cm³/s mol can be obtained from the best square fit of the data.

As we have assessed in the previous work [1], it is interesting to note that also the coagulation rate is described by a second order law, the Smoluchowski equation $dN/dt = k_{coag} \cdot N^2$. An average value of the coagulation coefficient, k_{coag} , can be obtained starting from the measurement of the UV absorption and light scattering coefficients [3]. For a flame with C/O=0,77 and velocity of the inlet cold gases equal to 10 cm/s, the two kinetic constants show value almost similar. Moreover, the activation energy calculated by thermocouple measurements is of the same order of the depth of potential well of the overall interaction between two spherical particles of diameter of 3nm [4].

REFERENCES

1. Basile, G., Rolando, A., D'Alessio, A., D'Anna, A., Minutolo, P.: *29th Symposium on Combustion*, Coagulation and carbonization processes in slightly sooting premixed flames (2002)
2. McEnally, C.S., Koylu, U.O., Pfefferle, L.D., Rosner, D.E.: *Combust. Flame*, **109**:701-720 (1997)
3. D'Alessio, A., D'Anna, A., Minutolo, P., Sgro, L. A., Violi, A., *Proc. Comb. Inst.*, **28**:2574 (2000)
4. Mancini Tortora, M., D'Anna, A., D'Alessio, A.: *XXV Event of the Italian Section of the Combustion Institute*, Size-dependent Coagulation of Small Carbonaceous Particles at High Temperature (2002)

Aspetti ambientali della combustione stazionaria

F. Beretta¹, A. Borghese², G. Cascio³, A. D'Alessio⁴, A. Pini³

¹*Istituto di Ricerche sulla Combustione - C.N.R., Napoli*

²*Istituto Motori - C.N.R., Napoli*

³*Agenzia Nazionale per la Protezione dell'Ambiente*

⁴*Dipartimento di Ingegneria Chimica, Università di Napoli "Federico II"*

Effetti globali e locali

Questa comunicazione ha lo scopo di delineare le tendenze evolutive delle nuove tecnologie nei settori della generazione dell'energia e dei trasporti terrestri, in relazione alle istanze di tutela ambientale. Entrambi i settori si basano essenzialmente sui processi di combustione e, quindi, è logico considerare il loro impatto ambientale, sia su scala locale che globale, in termini unitari e comparativi.

L'enfasi corrente su aspetti climatici globali può generare la falsa impressione, alimentata dagli indubbi progressi degli ultimi decenni, che ormai il problema dell'inquinamento atmosferico sia in fase di soluzione e non meriti ulteriori approfondimenti sia scientifici che tecnologici.

Viceversa, i livelli di ozono nella troposfera persistono su valori non soddisfacenti ed il problema degli effetti sulla salute del particolato prodotto in combustione sta appena adesso rivelando le sue dimensioni reali [1,2].

Una diminuzione di interesse sul problema dei sottoprodotti dannosi della combustione si ripercuote sulla ricerca tecnologica per una combustione pulita di tutti i combustibili, siano essi gassosi, liquidi o solidi, che ha per obiettivo l'abbattimento delle barriere ambientali nei prossimi dieci anni.

La chiave per saldare la questione climatica con la tutela della salute e della qualità dell'aria si trova nell'esame più approfondito degli effetti climatici e fisici dei processi radiativi dell'atmosfera. Si è visto come gli stessi composti gassosi ed aerosol, che hanno effetti dannosi sulla salute umana, presentano incrementi radiativi specifici superiori alla CO₂ stessa. Quindi una drastica riduzione delle concentrazioni di ossidi di azoto e zolfo, di composti organici volatili, del particolato carbonioso in tutte le sue forme, nonché dei solfati e dei nitrati, contribuisce in maniera significativa a mitigare l'effetto serra nei prossimi anni. Ciò consente di avere un margine di tempo per provare sul campo le varie tecnologie per la riduzione e cattura dell'anidride carbonica, invece di costringere il mondo industrializzato ad investimenti inutili e/o riduzioni ingiustificate del tenore di vita e della mobilità.

Tecnologie di combustione per energia e trasporti

L'industria dell'energia e quella dei trasporti seguono logiche di prodotto e di mercato largamente diversificate e, naturalmente, perseguono, e presentano all'opinione pubblica, politiche ambientali dai rispettivi punti di vista settoriali. In aggiunta, non può essere sottostimata la questione associata alle fonti dei combustibili e, in particolare, dei loro costi, quale ulteriore variabile indipendente nella definizione del quadro in esame. Pertanto, chi ha la responsabilità della qualità dell'ambiente ha la continua necessità di valutare, sia in termini assoluti che comparativi, gli impatti sulla salute umana, sulla vivibilità e sugli equilibri

climatici locali e globali, senza trascurare i vincoli, le implicazioni e le opportunità di tipo economico su diversi piani.

Il primo punto che appare evidente è che l'aspetto ambientale diventa sempre più determinante per lo sviluppo delle tecnologie dei combustibili, dell'energia e dei trasporti e questa è ormai una evoluzione di tipo irreversibile [3].

L'evoluzione delle tecnologie di combustione, indipendentemente dagli utilizzi, è basata sul progresso nei campi della fluidodinamica, della chimica, delle scienze dei materiali e sull'uso sistematico del controllo elettronico dei processi.

Nel settore dei combustibili, ampi margini di evoluzione si intravedono per quelli solidi, o costituiti da miscele liquide di tagli petroliferi pesanti, per i quali si studiano tecnologie di combustione diverse da quelle convenzionali e sistemi di gassificazione seguiti da combustione in turbine a gas.

Le tecnologie di gassificazione, seguite da sistemi di depurazione dei fumi, sono in competizione con quella del carbone o di residui petroliferi. Il progresso nel campo della pulizia dei gas caldi è centrale per lo sviluppo di questo approccio all'uso energetico del carbone.

Un notevole progresso nel settore energetico è da segnalare nel campo delle turbine a gas, con l'introduzione dei cicli combinati, che consentono un sensibile incremento di rendimento rispetto ai generatori di vapore convenzionali. Anche i cicli a vapore supercritico mostrano progressi essenzialmente legati all'impiego dei materiali a più alta temperatura.

Una linea di sviluppo è la combustione a letto fluido in cui un efficiente scambio di materia ed energia ed un più lungo tempo di residenza nei reattori consentono di condurre le reazioni di ossidazione a temperatura più bassa che nei normali sistemi basati sulla combustione a fiamma. Risultati analoghi possono essere ottenuti senza radicali alterazioni reattoristiche conducendo l'ossidazione previo un forte preriscaldamento dei reagenti e/o un notevole eccesso d'aria comburente. Questa tecnologia, definita combustione dolce o diluita ("mild combustion"), è attualmente in fase di sviluppo sia per la combustione del gas naturale che per tagli petroliferi complessi.

Nel campo della trazione automobilistica, i progressi provengono dalla migliore conoscenza e controllo del reattore "motore a combustione interna. Un controllo più accurato della fase di formazione della miscela, della immissione dei combustibili e della conseguente combustione turbolenta, ha già consentito notevoli riduzioni delle emissioni inquinanti. Ciò è evidente nel caso del particolato carbonioso emesso dai motori diesel con iniezione diretta ad altissima pressione. Inoltre, la imminente introduzione commerciale di architetture di tipo ibrido, che combinano un motore elettrico con uno a combustione interna costituisce un salto evolutivo di grande portata, sia per i maggiori rendimenti energetici, che per la riduzione dell'impatto ambientale. Infatti, è molto più facile minimizzare le emissioni in motori che lavorano in condizioni quasi stazionarie che in ogni regime di carico ed in transitorio, come avviene con i motori attuali.

Una peculiarità del settore dei trasporti, rispetto a quello della produzione elettrica, è costituita dal fatto che il coefficiente complessivo di utilizzo dell'energia, riferito al carico utile, si attesta tuttora su valori estremamente bassi, legati con proporzionalità inversa ai livelli totali dei consumi e delle emissioni. Per tale motivo, il settore dei trasporti è potenzialmente esposto a innovazioni di tipo concettuale di portata ben maggiore degli attuali avanzamenti graduali.

CO₂, effetto serra e gas naturale

Dal punto di vista ambientale, la prospettiva in cui opera il sistema energetico e quello dei trasporti, è essa stessa soggetta ad evoluzione. Negli ultimi anni all'attenzione per gli aspetti locali o regionali dell'inquinamento atmosferico si è sovrapposta quella per gli aspetti globali delle emissioni di origine antropica, che hanno effetti potenziali sugli equilibri climatici. La questione climatica è considerata generalmente di tale rilevanza ed urgenza da richiedere una drastica trasformazione delle tecnologie energetiche e dei trasporti in tempi medio-brevi.

Si va, inoltre, affermando un punto di vista semplificato e cioè che l'effetto climatico dipenda unicamente dall'incremento dell'anidride carbonica nell'atmosfera. La CO₂ è un prodotto stechiometrico della combustione, la cui percentuale diminuisce all'aumentare del rapporto H/C del combustibile. Ciò sposta il problema dalle tecnologie dei processi di combustione alla selezione dei combustibili. Quindi il gas naturale riveste un ruolo privilegiato rispetto al carbone ed ai prodotti petroliferi e, in prospettiva, viene preso in considerazione anche l'impiego dell'idrogeno, sia come vettore energetico che come carburante. Infine, si suggerisce di ritornare ad una politica di risparmio energetico, come durante le crisi petrolifere degli anni '70. Questo indirizzo di pensiero sottende un atteggiamento culturale che ricorre anche in ad altri settori e che in alcuni casi sostiene visioni pessimistiche non sempre fondate [4].

Questa impostazione presenta diversi inconvenienti. In primo luogo, privilegiando il gas naturale si riduce pericolosamente l'offerta energetica rendendo il paese dipendente strategicamente da pochi fornitori. Inoltre, la rete attuale di distribuzione, già oggi vicina al limite della sua capacità operativa, costituisce una strozzatura e il punto debole di tale soluzione. Il ciclo dell'idrogeno, poi, è largamente ipotetico e certamente non maturo tecnologicamente nei tempi ristretti richiesti dall'emergenza ambientale.

Conclusioni

L'analisi delle linee di tendenza delle tecnologie della combustione, in generale, e dei combustibili, della produzione di energia e dei trasporti, in particolare, mostra che esse sono fortemente intrecciate alle questioni ambientali. A sua volta, la questione ambientale si presenta sia come un problema di inquinamento e qualità dell'aria su scala locale, sia come effetto climatico su scala globale.

Le scelte in campo energetico devono rispettare simultaneamente entrambe le esigenze ambientali. Quindi, lo sforzo tecnologico per una combustione pulita va orientato verso tutte le tipologie di combustibili e va associato sia agli sforzi per incrementare i rendimenti energetici, sia a quelli per sviluppare nuovi metodi per la riduzione delle emissioni inquinanti e delle sostanze responsabili dell'effetto serra, siano esse gassose o particellari.

La chiave di collegamento di queste due direzioni tecnologiche è nello sviluppo su scala molto maggiore e coordinata della ricerca scientifica nei campi tradizionalmente separati della combustione e della chimica dell'atmosfera.

Bibliografia

1. Jacobson M.Z.: "Strong radiative heating due to the mixing state of black carbon in atmospheric aerosols", *Nature*, Vol. 409, 8 Feb 2001, p.695-697
2. Hansen J. et al.: "Global warming in the twenty-first century: An alternative scenario", *Proc. Nat. Acad. Sci.*, Vol. 97, p. 9875-9880, (2000)

3. D'Alessio A., Beretta F., Borghese A.: "Studio sullo stato dell'arte e sul potenziale di sviluppo tecnologico nazionale in materia di contenimento delle emissioni inquinanti da processi di combustione", Rapporto finale del contratto tra DIC, Università "Federico II" di Napoli ed Agenzia Nazionale Protezione Ambiente, 2001
4. Lomborg B.: "The skeptical environmentalist: Measuring the real state of the world", Cambridge University Press, ISBN 0 521 01068 3 (2001)

Self-propagating Reactions for Environmental Protection: State of the Art

Daniela Carta, Roberto Orrù* and Giacomo Cao*

*Dipartimento di Ingegneria Chimica e Materiali,
Centro Studi sulle Reazioni Autopropaganti (CESRA),
Unità di Ricerca del Consorzio Interuniversitario Nazionale "La Chimica per l'Ambiente"
and Centro Interdipartimentale di Ingegneria e Scienze Ambientali (CINSA),
Università di Cagliari, 09123 Cagliari, Italy.
Phone: +39-070-675-5058 Fax: +39-070-675-5067
E-mail: cao@visnu.dicm.unica.it*

Integrated environmental protection can be implemented in the process industry as well as energy conversion plants by process redesign, reutilization of residues and safer disposal of wastes with the aim of reducing and avoiding pollutants. Process innovation (i.e. production of the same or similar products using less raw material and energy and decreasing the pollutant output), materials cycles (i.e. recycling of residues and produced wastes so that resources are reduced) and safe waste disposal, represent the characteristic elements of a sustainable development model. In this work we address the use of self-propagating reactions for residues recycling and environmentally benign waste disposal.

It is well known that self-propagating reactions of either solid-solid and gas-solid type has been exploited in the establishment of the technique referred to in the literature with the acronym of SHS (Self-Propagating High-Temperature Synthesis) which represents an attractive alternative to conventional methods of materials synthesis. This technique is characterized by the fact that once the starting mixture is ignited by means of external thermal sources for relatively short times, highly exothermic reactions may propagate through the mixture in the form of a self-sustained combustion wave leading to final products progressively without requiring additional energy, as depicted in Figure 1 (1,2). SHS is also characterized by process simplicity, short reaction time, easy-to-build equipments, low-energy requirements and the possibility of obtaining complex or metastable phases.

Recently, the exploitation of self-propagating reactions for environmental protection has received renewed attention. In particular, interesting results have been obtained in the following areas: fixation and consolidation of high level radioactive wastes (3), treating and recycling of a highly toxic solid waste from electrolytic zinc plants (4,5), degradation of chlorinated aromatics (6,7) and recycling of silicon sludge and aluminum dross produced by semiconductor industries and aluminum foundries, respectively (8).

In particular, self-propagating reactions of thermite type, i.e. a metallic or non-metallic oxide is exothermically reduced by a metal to form more stable products, have been proposed in the literature to address the fixation of high level radioactive wastes. The process consists of reducing the volume of radioactive liquid wastes and fixing products into a highly insoluble polysilicate structure by means of appropriate thermite reactions. The thermite process was preceded by a pre-treatment (evaporation, drying and denitration steps) of the radioactive waste which was originally in the form of an aqueous solution. Through this treatment all the salts present in the waste solution were converted to oxides. Silicon, iron oxide and silica are used to prepare the thermite mixture and to provide the desired reaction rate and final product composition. Leaching tests of radionuclides clearly demonstrate that the technique based on

the occurrence of self-propagating reactions display a higher chemical stability when compared to standard technologies used for radioactive nuclear waste disposal, i.e. their encapsulation in phosphate and borosilicate glass.

Another environmental application of SHS method is the fixation of toxic species typical of hydrometallurgical wastes. Highly toxic solid wastes from electrolytic zinc plants, known as jarosite or goethite depending upon the treatment used for iron removal, are currently obtained as by-products (about 750,000 and 90,000 tons/year in Europe and Sardinia – Italy, respectively). The large production, the high cost of disposal and the increasing difficulty to find suitable disposal locations, clearly provide a demonstration of their environmental impact. Recently, a process of treating and recycling of goethite wastes based upon self-propagating thermite reactions has been proposed. In particular, taking advantage of the relatively high content of iron oxides in the waste, thermite reactions were exploited due to their high exothermic character. It was found that by blending this waste with suitable amount of reducing agents (aluminum, silicon, magnesium and calcium) as well as ferric oxide and igniting the resulting mixture, a combustion wave rapidly travels through the mixture without requiring additional energy, thus converting reactants into two solid products called P_1 and P_2 and a gas mainly containing SO_2 . Product P_2 is distributed in powder form in the reaction chamber walls as a consequence of a probable expulsion occurring during the course of the reaction. On the other hand, product P_1 remains in the same position where the original sample was placed inside the reactor. The occurrence of self-propagating reactions depends upon the combination of reducing agents and the waste content in the starting mixture.

On the basis of the leaching tests performed, the corresponding product P_1 , constituted by an amorphous glassy structure of iron aluminosilicates, was found to fulfill the very restrictive environmental regulations for heavy metals.

Another crucial problem in the area of hazardous waste management is the destruction of organo-chlorine pesticides, polychloric biphenyls, dibenzofurans, dioxins and other synthetically produced derivatives of chlorobenzene. Aromatic rings with halogen substitution are highly resistant to oxidative degradation and the possible emission of even worse by-products appears one of the main disadvantages of conventional incinerator technologies.

Recently, the attention has been directed to the exploitation of self-propagating reactions to degrade chlorinated aromatics. Hexachlorobenzene (C_6Cl_6) and the racemate of 2-(2,4-dichlorophenoxy)-propanoic acid ($C_9H_8Cl_2O_3$), a commercial herbicide known as Dichloroprop- hereafter 2,4DP, were used as chlorinated test species, while calcium hydride was proposed as reducing agent. Relatively low CaH_2 /organohalide benchmark ratios are demanded for the complete reduction of the chloro-organics. At least three moles of calcium hydride are required in the case of hexachlorobenzene and four or five in the case of 2,4-DP.

Consistent concentrations of reaction products has been founded, the total organo-chlorine conversion resulting in each trial greater than 99.999%.

As shown in Figure 2, the transformation of reactants into non-toxic end-products was also confirmed by the X-ray analysis. In the case of hexachlorobenzene (cf. Figure 2a), the burnt powders were found to consist of graphite, $CaCl_2$ and $CaHCl$, the hydride-chloride mixed salt becoming the predominant phase at the larger CaH_2 content. In the case of 2,4-DP (cf. Figure 2b), CaO was also found.

Hydrogen and methane (with CO and CO_2 in the case of 2,4-DP) were the main gaseous products. Traces of benzene, mono-, di- and tri-chlorobenzene, dichloroethylene, dichloromethane, xylene and trimethylbenzene were also detected.

These preliminary results suggest that self-activating processes can be an alternative to conventional thermal treatments of hazardous chlorinated aromatics. The advantages are obvious in that very high temperatures are locally reached with low pressures and under extent-controlled conditions.

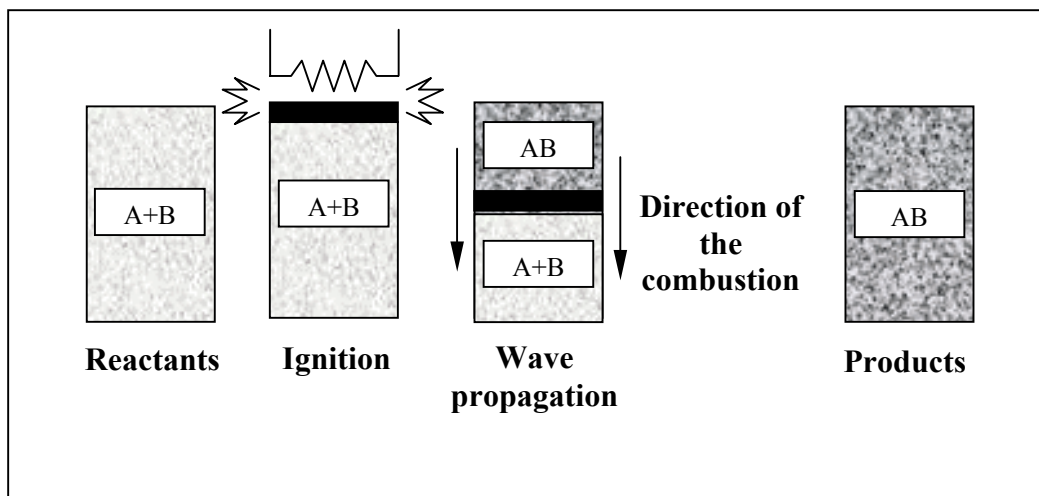


Figure 1

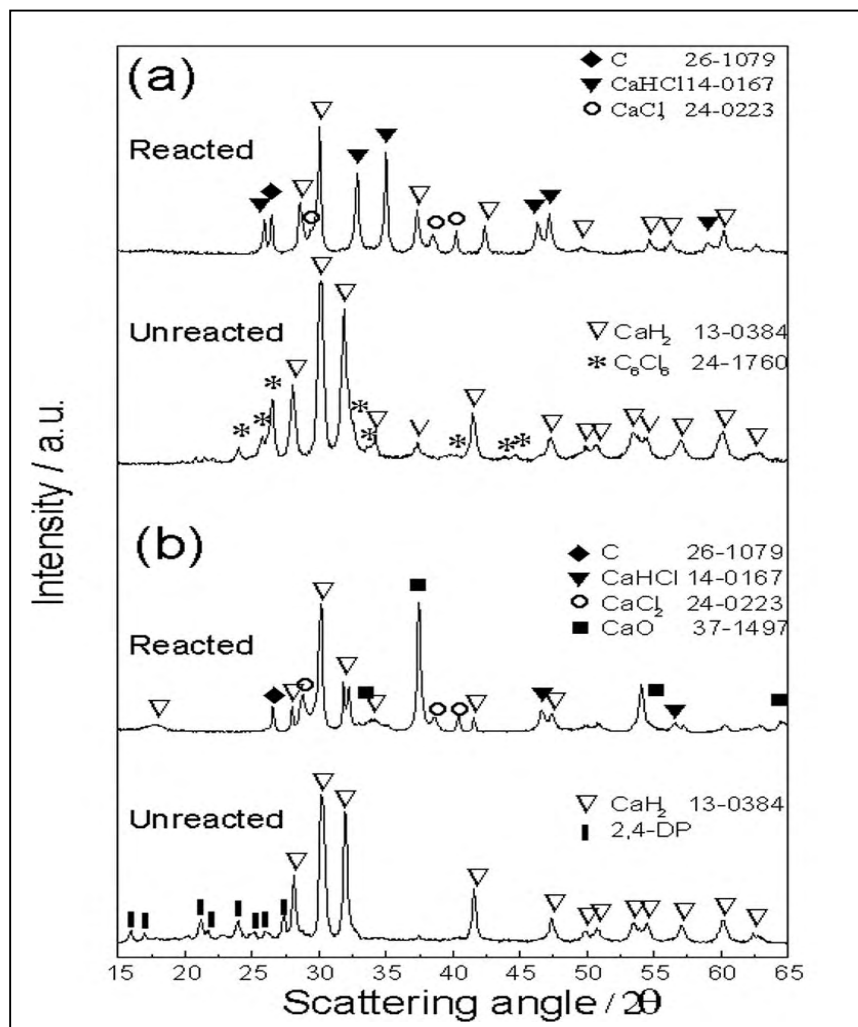


Figure 2

Solid and gaseous reaction products can be easily checked before their discharge. The simplicity and a very low energy requirement are two other merits of the process.

In addition to the application of self-propagating reactions described above and following previous studies related to silicon wastes in zinc smelting, a new recycling process based on the SHS nitriding combustion of silicon sludge from semiconductor industries and aluminum dross from aluminum foundries both to obtain silicon based ceramics has been proposed.

The process treatment of silicon sludge is based on the combination of silicon with nitrogen to form Si_3N_4 . However, since the typical composition of the silicon sludge is Si (26 wt%), Al_2O_3 (14 wt%), ZrSiO_4 (31 wt%), Fe_2O_3 (27 wt%) and CaO (2 wt%), the silicon content is too low to make the nitridation of the sludge possible by SHS. To overcome this problem, reclaimed Si and Al powders produced by silicon and aluminum industries, respectively, were added to the waste.

The product consisted of three different Sialon compositions (i.e. $\text{Si}_6\text{Al}_{10}\text{O}_{21}\text{N}_4$, $\text{Si}_{1.8}\text{Al}_{0.2}\text{O}_{1.2}\text{N}_{1.8}$ and $\text{Si}_3\text{Al}_3\text{O}_3\text{N}_5$), iron silicides (FeSi_2) and monoclinic zirconia (ZrO_2).

It is interesting to note that the product strength is lower than conventional Sialon (about 360 MPa) but may be compared with silicon nitride obtained by reactive sintering (about 250 MPa).

The other SHS recycling process proposed in the literature which makes use of aluminum dross is based on the nitridation of aluminium.

Aluminum dross, whose composition was 75 wt% AlN, 12.5 wt% Al_2O_3 and 12.5 wt% Al, was first pulverized and mixed with reclaimed silicon to make the self-propagation combustion possible.

The resulting mixture was then combusted under nitrogen atmosphere and the resulting product consisted of $\text{Si}_{6-x}\text{Al}_x\text{O}_x\text{N}_{8-x}$ and other Si-Al-O-N phases.

Thus, by taking into account the large world-wide production of silicon wastes from semiconductor industries and aluminum dross, the proposed recycling process based on the exploitation of self-propagating reactions appears to be a promising alternative to the non productive disposal of these wastes.

REFERENCES:

1. Merzhanov, A.G., and I.P. Borovinskaya, *Dokl. Akad. Nauk SSSR*, **204**: 366 (1972).
2. Munir, Z.A., and U. Anselmi-Tamburini, *Materials Science Report*, **3**: 277 (1989).
3. Borovinskaya, I.P., T.V. Barinova, V.I. Ratnikov, V.V. Zakorzhevsky, and T.I. Ignatjeva, *Int. J. SHS*, **1**: 129 (1998).
4. Orrù, R., M. Sannia, A. Cincotti, and G. Cao, *Chem. Eng. Sci.*, **54**: 3053 (1999).
5. M Sannia, R. Orrù, A. Concas and G. Cao, "Self-propagating reactions for environmental protection: Remarks on treatment and recycling of zinc hydrometallurgical wastes", *Industrial Engineering Chemistry Research*, **40**: 801 (2001).
6. Cao, G., S. Doppiu, M. Monagheddu, R. Orru', M. Sannia, and G. Cocco, " *Industrial Engineering Chemistry Research*, **38**: 3218 (1999).
7. G. Cocco, S. Doppiu, M. Monagheddu, G. Cao, R. Orrù, and M. Sannia, " Self-propagating high temperature reduction of toxic chlorinated aromatics", *Int. J. SHS*, **8**, No.4, 521 (1999).
8. Miyamoto, Y., S. Kanehira, and, O. Yamaguchi, "Development of Recycling Process for Industrial Wastes by SHS, " *Int. J. SHS*, **9**: 357 (2000).

Modelling in-Duct Mercury Removal by Activated Carbon Injection in Coal-Fired Power Plants Flue Gas

Fabrizio Scala

*Istituto di Ricerche sulla Combustione - C.N.R.
P.le Tecchio, 80 - 80125 Napoli - ITALY*

INTRODUCTION

In the last decade public concern has risen over the potential risk of toxic elements emitted from anthropogenic sources. Among these, mercury has drawn special attention, because of its high volatility and the increasing level of bioaccumulation in the environment and in the food-chain, with potential risks for human health. Recent studies recognized that about 70-85% of the total anthropogenic mercury emissions are caused by combustion sources, mainly coal-fired utilities and waste incinerators (1,2). Even if mercury emissions from coal-fired plants are very low on a local scale, the large amounts of coal burned worldwide make this source of mercury pollution significant on a global scale.

At typical combustion temperatures mercury is readily vaporized and exits the combustion chamber with the flue gas mainly as elemental mercury (Hg^0). Contrary to other trace metals, mercury does not undergo condensation and passes through traditional air pollution control systems with very low capture efficiency (3). Elemental mercury emitted in the atmosphere is slowly oxidized and then solubilized in rainwater and transported to soil, rivers and lakes where it is transformed into more toxic organic species (e.g. methyl mercury) and assimilated by animals and plants (4). The long life-time in the atmosphere (about one year) makes possible the transportation of mercury even at long distances from the source of emission.

Following extensive experimental research carried out in the last decade, powdered activated carbon injection in flue gas upstream of a particulate matter control device (PMCD) has been indicated as one promising technology for mercury capture in coal-combustors flue gas (1). The powdered activated injection technology offers a number of advantages like: relatively high mercury capture efficiency; production of a non hazardous and non corrosive solid byproduct (possibly regenerable); limited fire or explosion hazards; simple and low cost process design, operation and maintenance; possibility of retrofitting existing plants.

Few models for mercury adsorption by activated carbon injection have been proposed to date (5,6). The scope of the present work was to develop a detailed predictive tool for this process taking into account all relevant mechanisms. The starting point was a recently presented model for the in-duct mercury capture in incinerators (7). In this work the model was employed for the simulation of mercury capture in the duct between the activated carbon feeding point and the PMCD in conditions typical of coal-fired power plants.

THEORY

The system is schematized as a straight duct of constant diameter starting from the activated carbon feeding point and ending at the PMCD. The flue gas is assumed to travel in plug flow along the duct and particles have the same velocity as the flue gas. The model is based on the following assumptions:

1. The relevant mercury species in the gas phase is elemental mercury (Hg^0).
2. The process is not dependent on flue gas composition apart from mercury concentration.

3. Activated carbon particles are spherical, monosized and uniformly dispersed in the gas.
4. The system is at the steady state and both the gas and solid flow rates are constant.
5. The temperature is constant and uniform through the system and pressure losses are neglected, so that gas velocity is constant along the duct.
6. Mercury adsorption on the duct walls is negligible.
7. Mercury adsorption heat effects are neglected due to the trace level concentrations.

The process of mercury vapor adsorption onto activated carbon can be described as a series of three steps: mass transfer from the bulk gas to the external surface of the activated carbon particles. Mass transfer from the external surface to the interior of the particles through the pore structure. Surface adsorption on the internal surface area of the particles. The first step is treated by means of an external mass transfer coefficient. A reasonable assumption is that the particles Sherwood number is equal to the limiting value of 2 relative to stagnant boundary layer. As regards the second step, gaseous diffusion inside the pore network is treated by means of an effective pore diffusion coefficient given by a combination of molecular and Knudsen diffusivities.

Considerable uncertainty exists on the mechanism of elemental mercury adsorption onto activated carbon particles. Both chemisorption and physical adsorption have been suggested as the relevant mechanism. Whatever the mechanism, according to the Langmuir theory the net rate of mercury adsorption on the activated carbon particle surface can be written as the difference between the adsorption rate and the desorption rate:

$$\frac{d\omega}{dt} = k_1(\omega_{max} - \omega)c - k_2\omega \quad (1)$$

where ω is the local mercury uptake on the sorbent and c is the local gas mercury concentration. The mercury mass balance in the gas phase inside the particle pores (in radial coordinates) reads:

$$\varepsilon_p \frac{\partial c}{\partial t} - D_{eff} \left(\frac{\partial^2 c}{\partial r^2} + \frac{2}{r} \frac{\partial c}{\partial r} \right) + \rho_p [k_1(\omega_{max} - \omega)c - k_2\omega] = 0 \quad (2)$$

where ε_p and ρ_p are the sorbent particles porosity and density and D_{eff} is the effective diffusivity. The mercury mass balance in the bulk gas phase in the duct reads:

$$\frac{dc_B}{dt} = - \frac{3\Theta_{AC} D_{eff}}{\rho_p R_p} \frac{\partial c}{\partial r} \Big|_{(R_p, t)} \quad (3)$$

where c_B is the gas bulk mercury concentration, Θ_{AC} the activated carbon loading per unit volume in the bulk gas and R_p the sorbent particle radius. The system of three coupled differential equations (eqs.1-3) has the following initial and boundary conditions:

$$\omega(r, 0) = 0; \quad c(r, 0) = 0; \quad c_B(0) = c_B^{IN} \quad (4)$$

$$\frac{\partial c}{\partial r} \Big|_{(0, t)} = 0; \quad \frac{\partial c}{\partial r} \Big|_{(R_p, t)} = \frac{K_G}{D_{eff}} [c_B(t) - c(R_p, t)] \quad (5)$$

where the mass transfer coefficient is given by $K_G = D_m Sh / 2R_p$. The average mercury uptake in the activated carbon particles in a duct section is simply given by:

$$\bar{\omega}(t) = \frac{(c_B^{IN} - c_B)}{\Theta_{AC}} \quad (6)$$

SORBENT	T, °C	$k_1, m^3/gs$	$k_2, 1/s$	$\omega_{max}, -$	$\rho_p, kg/m^3$	$\epsilon_p, -$	$d_{pore}, \text{Å}$
HGR	120	0.41	7.06E-4	8.4E-2	990	0.5	30
	150	0.7	1.66E-3	2.2E-2			
	200	0.96	4.78E-3	1.1E-2			

Table 1 Adsorptive and physical properties of the sorbent considered.

Solution procedure

After adimensionalization, the boundary-value partial differential equation (eq.5) was reduced to a set of n initial-value ordinary differential equations in time using an orthogonal collocation technique (8). The resulting system of $2n + 1$ ordinary differential equations was integrated using a 5th order Runge-Kutta method with adaptive stepsize control. The number of collocation points (n) and the Runge-Kutta stepsize were adjusted in order to give a total accuracy of 10^{-4} in the value of the output variables. Accordingly $n = 5$ was used.

RESULTS

The model has been applied to one sulfur impregnated activated carbon of practical interest whose adsorptive and physical properties were taken from (9) and are reported in Tab.1. Figures 1 and 2 report the gas bulk mercury concentration decrease and the average mercury uptake on the sorbent as a function of residence time in the duct for different particle sizes (Fig.1) and different system temperatures (Fig.2). Mercury concentration has been normalized with the inlet concentration, while the sorbent mercury uptake with ω_{max} . Both figures show that, as expected, the longer the particle residence time in the duct the larger the mercury capture. Figure 1 clearly points out that small sorbent particles achieve larger mercury capture at all residence times. Below a certain particle size, however, in this case about $10\mu m$, there is not much effect in lowering the particle size. This behavior can be explained by assuming that for large particle sizes intraparticle diffusion resistance is mostly controlling the mercury uptake rate, while for small particle sizes the rate is under kinetic control regime. The effect of the system temperature is significant: curves in Fig.2 show that a temperature decrease from $200^\circ C$ to $120^\circ C$ leads to a mercury capture increase from about 50% to about 80% after 10s of residence time. This result suggests that the adsorption of mercury onto HGR carbon is

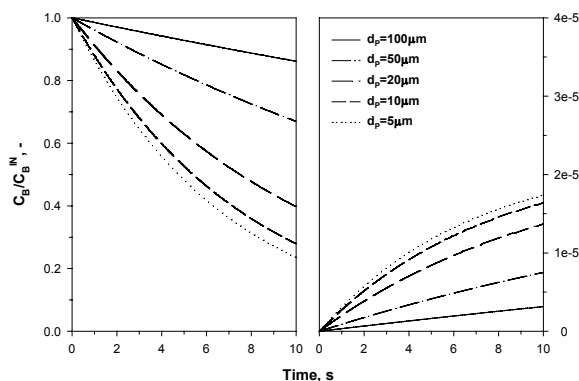


Figure 1 Gas Hg concentration (left) and Hg uptake (right) as a function of residence time in the duct for different particle sizes. $T=150^\circ C$; $c_B^{IN} = 5 \mu g/m^3$; $\Theta_{AC} = 10 g/m^3$.

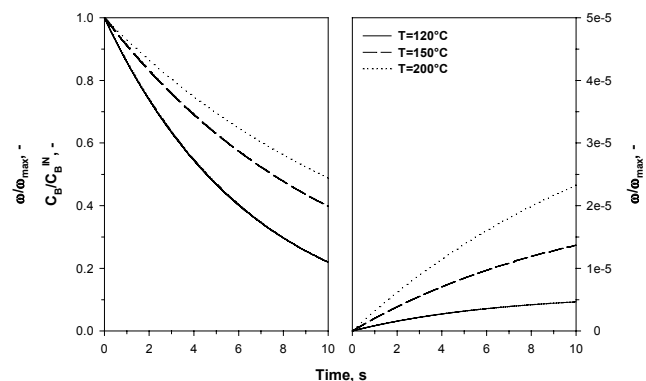


Figure 2 Gas Hg concentration (left) and Hg uptake (right) as a function of residence time in the duct for different temperatures. $d_p=20 \mu m$; $c_B^{IN} = 5 \mu g/m^3$; $\Theta_{AC} = 10 g/m^3$.

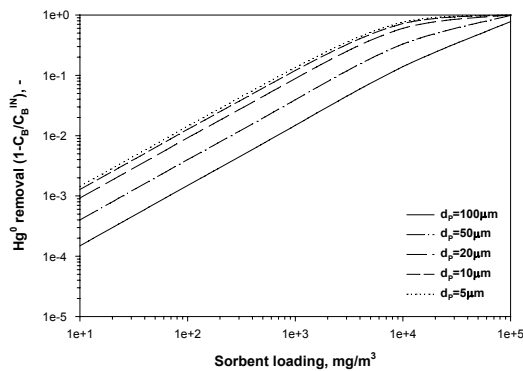


Figure 3 Gas mercury removal as a function of sorbent loading in the duct at different particle sizes. $T=150^{\circ}\text{C}$; $c_B^{IN}=5\mu\text{g}/\text{m}^3$; $t_D=10\text{s}$.

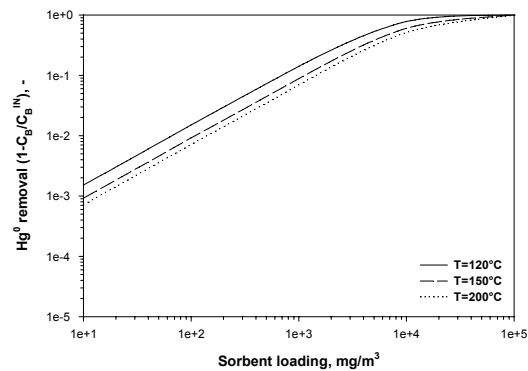


Figure 4 Gas mercury removal as a function of sorbent loading in the duct at different temperatures. $d_P=20\mu\text{m}$; $c_B^{IN}=5\mu\text{g}/\text{m}^3$; $t_D=10\text{s}$.

likely to be of a physical nature. It is interesting to observe that the sorbent mercury uptake figures are some orders of magnitude lower than ω_{max} , indicating a low sorbent utilization.

Figures 3 and 4 report the gas bulk mercury removal as a function of the sorbent loading in the duct at 10s of residence time at different particle sizes (Fig.3) and temperatures (Fig.4). The curves show that in order to obtain mercury removal efficiencies of the order of 90-95%, large loadings of the order of $10\text{-}100\text{g}/\text{m}^3$ have to be used with the sorbent at hand. The best operating conditions are achieved with small particles ($d_P < 10\mu\text{m}$) and low temperatures (120°C).

The influence of the mercury gas inlet concentration was investigated in the range $1\text{-}10\mu\text{g}/\text{m}^3$. No appreciable influence on the mercury removal results was observed at any operating condition. The reason for this behavior is that at the short residence times considered the desorption term ($k_2\omega$) is always negligible so that eq.2 results practically linear in the mercury concentration.

On the whole results of simulations indicate that large sorbent loadings in the duct are needed to obtain high mercury removal efficiencies, due to the short residence time. As a consequence very low utilization of the sorbent is achieved in any case. In order to minimize the sorbent feed rate it is particularly advisable to lower the operating temperature as much as possible. Improvements in the mercury capture performance can be obtained also by increasing the in-duct particles residence time and by decreasing the sorbent particles size.

REFERENCES

1. EPA: *Mercury Study Report to Congress*. Report EPA-452/R-97-003 (1997).
2. Pacyna, J. M.; Munch, J.: *Water, Air & Soil Pollution*, **5**:51 (1991).
3. Sandelin, K.; Backman, R.: *Environmental Science & Technology*, **33**:4508 (1999).
4. Lindqvist, O.: *Waste Management & Research*, **4**:35 (1986).
5. Flora, J. R. V.; Vidic, R. D.; Liu, W.; Thurnau, R. C.: *Journal of the Air & Waste Management Association*, **48**:1051 (1998).
6. Meserole, F. B.; Chang, R.; Carey, T. D.; Machac, J.; Richardson, C. F.: *Journal of the Air & Waste Management Association*, **49**:694 (1999).
7. Scala, F.: *Environmental Science & Technology*, **35**:4367 (2001).
8. Villadsen, J.; Michelsen, M.L.: *Solution of Differential Equation Models by Polynomial Approximation*. Prentice-Hall: Englewood Cliffs, New Jersey (1978).
9. Karatza, D.; Lancia, A.; Musmarra, D.: *personal communication* (2002).

Pilot-Scale Tests of Mercury Removal in Coal Flue Gas through Sorbent Injection

¹N. Pintus, ¹A. Bianchi, ²V. Borghini

1 ENEL Produzione S.p.A. - Ricerca – Pisa - ITALY

2 Final-year undergraduate University - Pisa - ITALY

ABSTRACT

ENEL carried out an experimental campaign to investigate the effectiveness of some commercial sorbents on the mercury removal from the coal flue gas. The tests were performed at the 500 kW_t Livorno pilot plant, equipped with a bag filter. Two commercial sorbents, injected at the inlet of the bag filter, were tested.

An innovative laboratory system, adapted for continuous measurements, was used to monitor alternatively the two forms of speciated mercury (Hg^0 and Hg^{2+}), both at the inlet and the outlet of the bag filter.

The results of the tests with sorbent injection, compared with the baseline values, are presented.

EXPERIMENTAL

Pilot plant description

The tests of mercury removal through sorbent injection have been carried out at the 500 kW_t furnace located in Livorno experimental area. The Figure 1 shows the general scheme of the plant, the sorbent injection point and the sampling points.

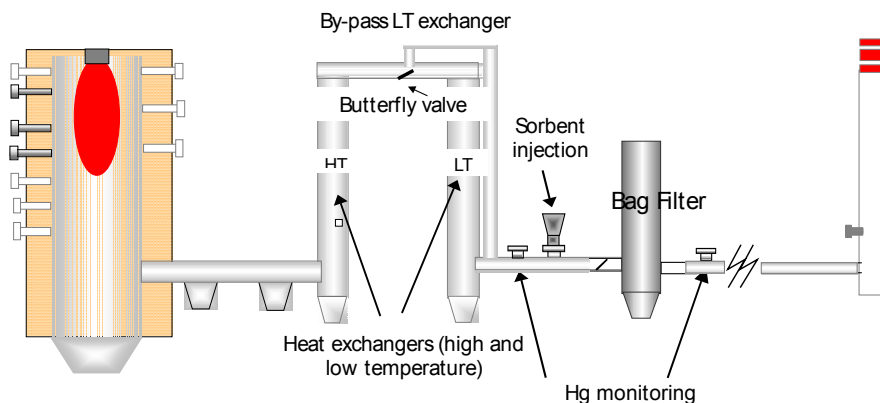


Fig. 1– General scheme of the 500 kW_t facility

Two heat exchangers are used to cool the flue gas; the second one (the low temperature heat exchanger) can be partially excluded in order to regulate the flue gas temperature at the inlet of the bag filter.

Continuous mercury species monitoring in exhaust gas

The Ontario Hydro Method modified has been used to measure the speciated mercury. The modification, described in more detail in [1], allows to reduce both sampling and analysis

length. A laboratory apparatus (FIMS 400 produced by Perkin Elmer for the analysis of mercury in liquids) has been adapted to monitor continuously the two species of mercury, by shifting between two absorbing solutions which are alternatively sent to the Flow Injection Mercury System (FIMS) by a 3-way valve. A steel probe, equipped with a sintered filter, samples the flue gas which passes through a PTFE tube where an absorption solution (KCl for Hg^{++} capture) is mixed with the gas itself. After a gas-liquid separator, the vapour phase passes through the KMnO_4 solution for Hg^0 absorption.

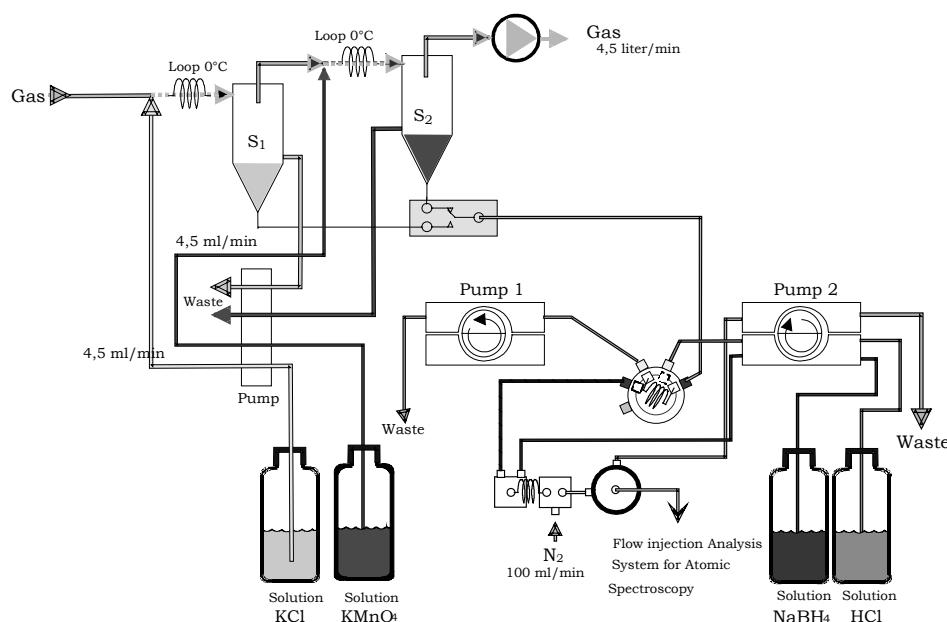


Fig. 2- Flow diagram of the continuous FIMS system

Sorbents

Two commercial sorbents have been tested: GL120® produced by NORIT and Sorbalit® produced by Märker Umwelttechnik GmbH.

The first one is a steam activated carbon with an extra fine particle size; it is especially suitable for the removal of mercury, dioxins and other low concentration trace metals from the flue gases.

The Sorbalit® is a tailor-made mixture of activated carbon (5-6%) and $\text{Ca}(\text{OH})_2$.

The main sorbent characteristics are reported in Table 1.

Table 1- Characteristics of the two sorbents

Parameter		GL120®	Sorbalit®
Total superficial area	m^2/g	54.4	95.5
micropores area	m^2/g	16.6	40.1
mesopores Area	m^2/g	37.7	55.3
macropores Area	m^2/g	0.1	0.1
total pores volume	cc/g	0.14	0.19
micropores volume	cc/g	0.01	0.02
mean diameter	μm	6.4	7.3

Sorbent dosing system

A calibrated cochlea was used to injected the sorbent. Since the minimum operating range of

the cochlea was higher than the minimum dosing rate for GL120 sorbent, we added some calcium carbonate (CaCO_3) as inert carrier to increase the flow rate.

Test conditions

A South African coal was used for the tests. Daily samples of pf were collected in order to evaluate the variability of the mercury in the coal. The mean Hg content in the coal, determined by a dedicated instrument (AMA254), was 0.095 ± 0.023 mg/kg.

The test conditions are reported in Table 2. The load of the furnace was 230 kW_t . The oxygen was about 6%. Two flue gas temperatures have been tested.

Before each trial, baseline measurements were generally performed at the inlet and at the outlet of the bag filter.

Table 2 – Test conditions

Test conditions	PF flow	Flue gas flow	T gas Inlet BF	T gas Outlet BF	Hg in the coal	Dosing rate a.c.	Dosing rate a.c.	a.c./Hg ratio	O ₂
	kg/h	Nm ³ /h	°C	°C	mg/kg	g/h	mg/Nm ³	g/μg	%
Sorbalit HT	36.6	305	209	143	0.078	1000	196.90	21017	5.3
GL120 HT	36.1	326	205	141	0.083	50	153.20	16687	5.85
GL120 LT	35.8	326	187	122	0.091	50	153.56	15433	6.5
Sorbalit LT	36.2	327	182	121	0.102	1000	183.40	16250	6.3

RESULTS

Baseline test. Bag filter Hg removal

Baseline test without sorbent injection has been carried out to measure the removal capacity of the bag filter: Figure 3 shows the speciated mercury (vapor phase) measured at the inlet and the outlet of the bag filter.

From the baseline test it results that the bag filter by itself is able to remove about 60-80% of the total mercury (vapor phase); its effectiveness improves when the content of UBC in the ash increases. The removed fraction of elemental mercury is 70-80%; the abatement of the ionic form is about 60-70%.

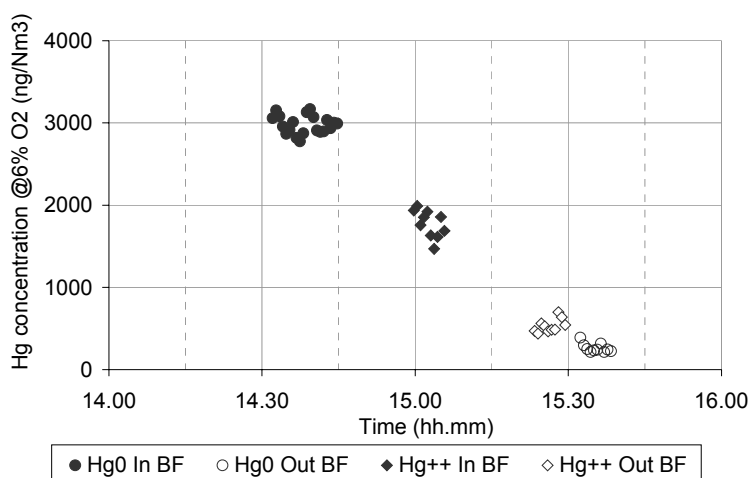


Fig. 3– Hg speciation at the inlet and the outlet of the bag filter

Hg removal by sorbent injection

The two commercial sorbents (GL120 and Sorbalit) have been tested at two flue gas temperatures; the result is, as expected, that the removal capacity increases when temperature get lower. The Figure 4 shows the results of the GL120 injection test at low flue gas temperature; the pressure drop across the bag is reported too. The arrow line bounds the interval of sorbent injection. The dashed line indicates the sootblowing of the bag filter (the pressure drop gets down to 10 mm_{H2O}). The sorbent becomes effective in reducing the ionic form two hours after the beginning of the injection (the temperature in the graphs is the mean working temperature of the bag filter).

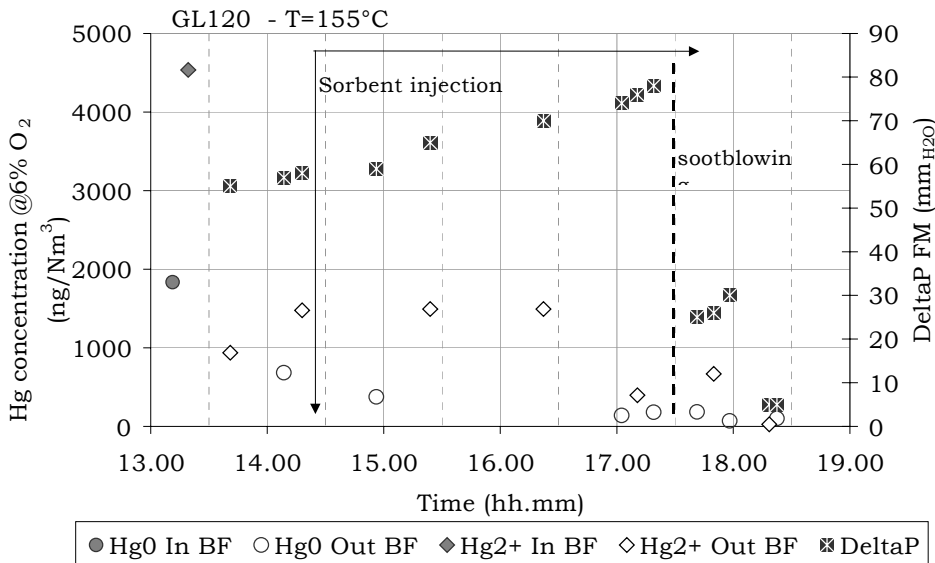


Fig. 4– Test of Hg removal with GL120 injection (LT)

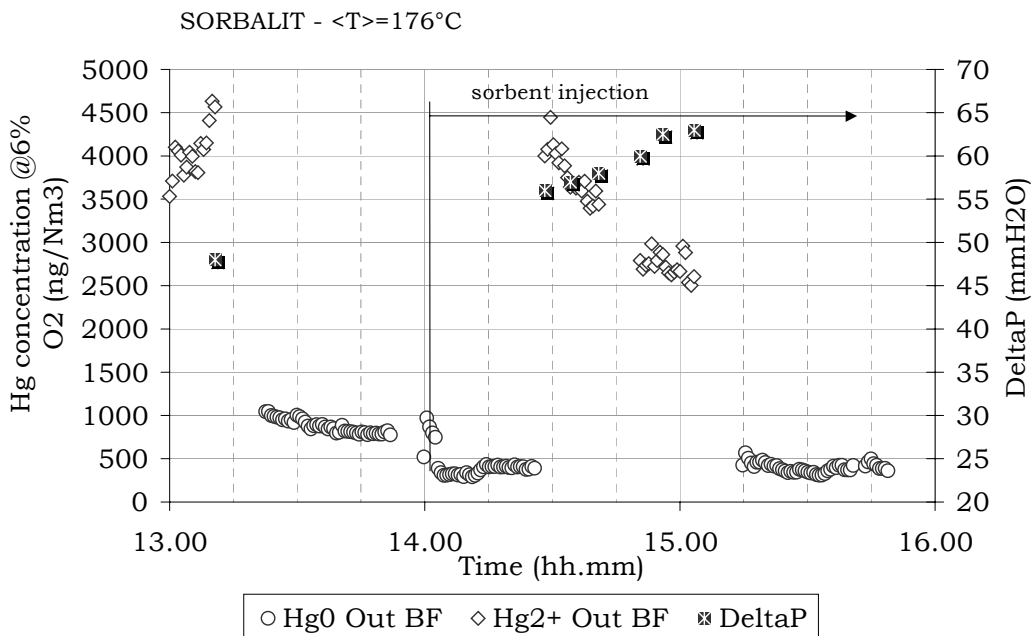


Fig. 5 – Sorbalit injection tests (HT)

The Figure 5 shows the results of Sorbalit injection test for high flue gas temperature ($T=176^{\circ}\text{C}$): the elemental form is promptly removed after the sorbent injection. The effectiveness of the sorbent versus the ionic form is higher when the panel becomes more tick. The same result has been obtained at low temperature ($T=152^{\circ}\text{C}$).

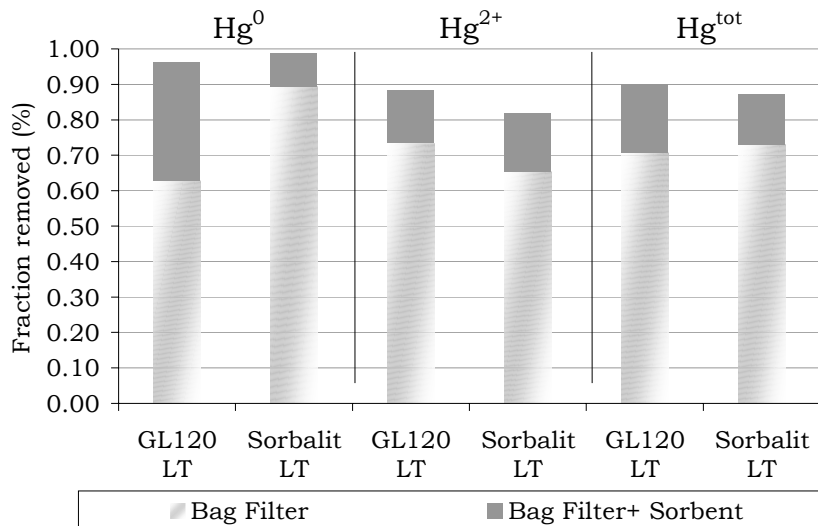


Fig. 6 – Mercury removal (vapour phase) with and without sorbent injection

CONCLUSIONS

The Figure 6 summarises the general results of the tests. The bag filter alone, depending from the UBC content in the ash, is able to reduce about 70%-80% of total mercury. Preliminary results indicate that GL120[®] seems more effective in removing the elemental form and Sorbalit[®] appears more effective towards the ionic form; both sorbents have approximately the same effectiveness in removing total mercury (vapour phase). For both the effectiveness is higher when the flue gas temperature is lower.

REFERENCES

1. Bianchi A., Borghini V., Cioni M. - Continuous Mercury Species Monitoring In Exhaust Gas- Combustion and the Environment - XXIV Event of The Italian Section of the Combustion Institute -S. Margherita Ligure (GE), 16-19 September, 2001

SIZE-DEPENDENT COAGULATION OF SMALL CARBONACEOUS PARTICLES AT HIGH TEMPERATURE

M. Mancini Tortora, A. D'Anna, A. D'Alessio

Dipartimento di Ingegneria Chimica – Università di Napoli “Federico II”, Naples-Italy

INTRODUCTION

Experimental data obtained in rich premixed flame have shown that carbonaceous particles, with typical sizes of few nanometers, are formed just downstream the reaction zone and they coagulate in the past flame region with a rate which is orders of magnitude smaller than that presented by the larger mature soot particles [1,2].

Recently, a kinetic model of PAH formation and growth has been developed. The model reproduce the total amount of particulate matter formed in flames and the concentration and sizes of nanoparticles at their inception[3,4]. The subsequent increase of the sizes of the nanoparticles and the sudden rise of their dimension at the soot threshold still wait for a theoretical explanation.

In this paper we analyse the collisions of clusters of molecules, whose van der Waals interaction is described by Lennard – Jones potentials in order to explain the very low coagulation rate of nanoparticles and the sharp appearance of soot at critical C/O ratio.

COLLISION AND COAGULATION OF SPHERICAL PARTICLES

Collision and subsequent coagulation of particles is a result of their Brownian motion and of the mutual forces of interaction between them. The interactions of macroscopic bodies are due to different kind of force. We consider only van der Waals force between electrical neutre molecules. The origin of van der Waals forces is the quantum mechanical zero-point fluctuations of the electrons in a molecule. A single fluctuation in one particle induces a dipolar interaction in the second one and these compounded interactions yield an attractive force which changes in form with particle separation and size.

The interaction between molecules is modelled by the Lennard – Jones 6-12 potential with both attractive and repulsive terms as a function of r , the separation distance between molecules. In the expression of this potential there are two parameters that characterize the molecular interaction: the minimum of potential ϕ_m and the distance at the minimum r_m . When we consider the interactions of macroscopic particles, all the pair potentials between the molecules in each body are summed. The overall interaction potential between two particles containing q molecule per unit volume is given by $U = \int_{V_1} d_{v1} \int_{V_2} d_{v2} q^2 \phi(r)$ where V_1 and V_2 are the volumes of the particles and $\phi(r)$ is the Lennard-Jones 6-12 potential.

We compare two types of interaction. First, two equal-sized spherical particles; second, two spheres of different radii. The total volume of the two particles is the same in the two case. Figure 1 shows the overall interaction versus dimensionless distance between molecules in both case. An analytic form of the overall potential exists. It's important to highlight that bodies of different size interact in a different way respect to those equal-sized although the total volume of interacting particle is the same.

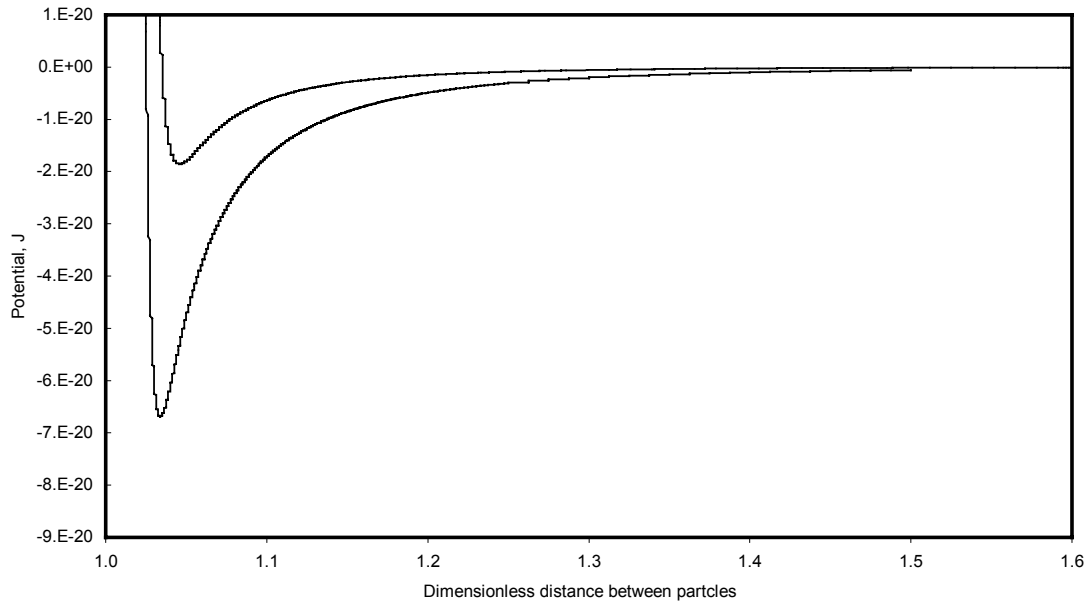


Fig.1 Interaction potential between equal-sized particles(lower curve) and particles of different sizes. ($\phi_m = 6.4173E-21J$, $r_m = 5.29E-10m$ [5]).

The probability of coagulation occurs upon collision is related to the fraction of particles having kinetic energy lower than the depth of potential well ϕ_0 . This fraction can be evaluated from Maxwell-Boltzmann kinetic energy distribution. Thus the sticking probability α , i.e., the number of active collision, is given by:

$$\alpha = 1 - (1 + \theta) \cdot \exp(-\theta)$$

where θ is the dimensionless depth of potential well ($\theta = \phi_0/kT$). For small particles, the depth of the potential well ϕ_0 is low respect to the gas kinetic energy (kT) at flame temperatures. It means that colliding particles have enough energy to escape from the potential well and hence to remain uncoagulated. Conversely, for larger particles the potential well is deeper. The amount of particles with kinetic energy lower than the potential depth increases resulting in an increased coagulation rate.

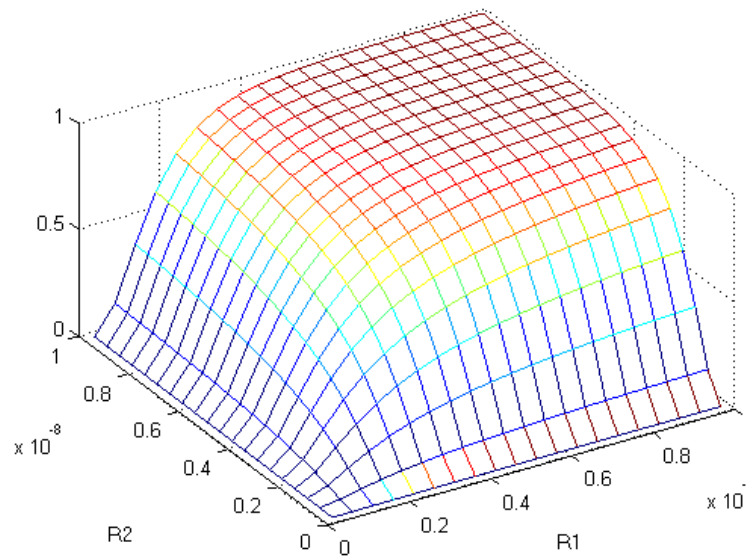


Fig. 2 Sticking probability versus radii of spherical particles

Figure 2 shows a tridimensional plot of α versus the radii of two spherical particles. As particle size increases also the sticking probability increases and even approaches to unity. It is interesting to note that when a small particle is involved in the coagulation process (sizes of the order of 2,3 nm), the sticking probability is very low and never exceeds value high as 0.5 whichever is the size of the colliding particles (see thick line in the tridimensional plot); on the contrary larger particles (sizes larger than 5 nm) have a sticking probability of the order of 0.8-1.

The evaluation of the size distribution function of the nanoparticles due to coagulation has been described by computing the population balance equation using the MAEROS code. Figure 3 compares the computed D_{63} moment of the size distribution along the axis of a 0.77 premixed flame of ethylene/air with those obtained by light scattering and extinction measurements [2]. The coagulation process starts at about 7ms, which corresponds to a height of 4mm in the flame, and it is subsequent to the nucleation of nanoparticles. The process of nanoparticle nucleation is not able to reproduce the sharp increase of the particle size detected between 8 and 10ms but it is necessary to consider a size-dependent coagulation process to follow the growth of nanoparticles to soot particles.

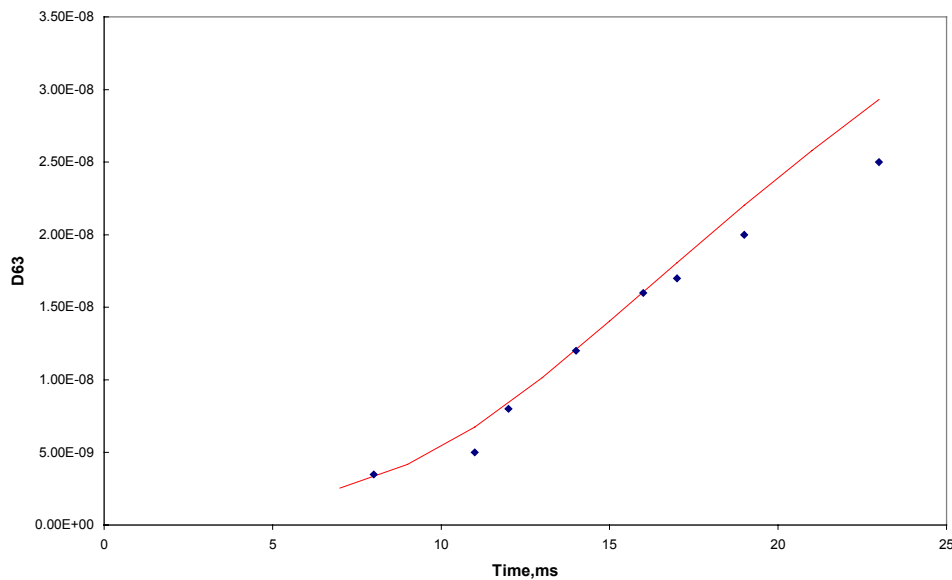


Fig.3 D_{63} evolution in the 0.77 ethylene/air flame. Comparison between model results and experimental data.

Model results agree well with the measured particle sizes in the first region of the flame, when particle size is under 20nm. It should be reminded that the proposed model of particle interaction is valid for very small particles and it fails when particle size increases since other factors influence the interaction between particles.

We conclude that the sticking probability of a small size particle can be correlated with the interaction potential between particles due to van der Waals forces. This model has been able to explain the evolution of the size of nanoparticle along the flame axis and the increase of the size of the particles across soot inception.

REFERENCES

1. D'Alessio, A., D'Anna, A., D'Orsi, A., Minutolo, P., Barbella, R., Ciajolo, A., *Proc. Combust. Inst.* 24: 973-980 (1992).
2. D'Alessio, A., D'Anna, A., Gambi, G., Minutolo, P., *J. Aerosol Sci.* 29(4): 397 (1998).
3. D'Anna, A., Violi, A., *Proc. Combust. Inst.* 27:425-433 (1998).
4. D'Anna, A., Violi, A., D'Alessio, A., Sarofim, A.F. *Combust. Flame* 127:1995-2003 (2001).
5. Wang, H. and Frenklach, M., *Combust. Flame* 96:163-170 (1994)

Optical and Spectroscopic Characterization of a Coflow Ethylene/Air Flame

¹C. Allouis, ¹F. Beretta, ²A. D'Alessio, ²A. D'Anna, ¹P. Minutolo

¹ *Istituto di Ricerche sulla Combustione - CNR, Naples - ITALY*

² *Dipartimento di Ingegneria Chimica - Università di Napoli "Federico II", Naples - ITALY*

INTRODUCTION

The need to control the emission of combustion by-products of environmental concern requires a better physical and chemical understanding of the mechanisms leading to pollutant formation.

A significant research effort on polycyclic aromatic hydrocarbons (PAH) and soot has been undertaken during recent years but many important details remain poorly understood. Particularly, the process whereby the molecular species are transformed to nanoparticles and their coagulation and carbonization to soot particles is still a subject of debate.

The existence of soot precursor nanoparticles has mainly been inferred by spectroscopic and optical characterization in laminar premixed flames and a detailed reaction mechanism has been developed to simulate their formation and growth [1]. Modeling results indicate that the formation and growth of nanoparticles is triggered by the presence in the combustion system of both PAHs and small radicals [2]. This environment is typical of oxidative pyrolytic regimes such as those encountered in the post-oxidation zone of rich premixed flames whereas it is restricted to specific locations of non-premixed combustion systems where the pyrolysis of the fuel is almost decoupled from the oxidation chemistry. Consequently, it is not clear if the formation of carbonaceous nanoparticles similar to those measured in premixed flames is allowed also in diffusion flames.

Thus, the purpose of this communication is to use advanced optical and spectroscopic diagnostics, already tested in premixed flames, for the identification of PAHs, nanoparticles and soot in a coflow ethylene/air flame at atmospheric pressure.

EXPERIMENTAL SYSTEM

Optical and spectroscopic measurements were carried out along the axis of a coflow burner fueled with ethylene/nitrogen mixtures. The burner is a 12 mm diameter uncooled vertical tube for the fuel mixture and a concentric tube (108 mm diam.) for air. The air-annulus was reduced at the burner lip by a ring (i.d. 55 mm) to stabilise the flame. This increased the air velocity by a factor of 4.8 and it only affect the flame height by a few millimetres. The burner is similar to that already used by Mc Enally *et al.* [3] and it has been largely used for the study of PAHs and soot.

The burner can move along the vertical axis and it is quipped with different optical techniques. A Nd:Yag pulsed laser source is employed for spectroscopic measurements. For the determination of the UV absorption spectra, the laser beam ($\lambda=1064$ nm) with an energy of about 200 mJ is condensed into air with a short focal lens, which induces an optical breakdown. The high temperature plasma produces a high intensity light source with time duration of tens of nanoseconds, suitable for absorption measurements in the UV spectral range from 190nm down to the visible [4]. UV-visible extinction measurements were performed using a photomultiplier and two filters centered at 266 ± 10 nm and 532 ± 10 nm. The light scattering measurements are performed using the fourth harmonic of the laser ($\lambda=266$ nm), the laser beam and the detected scattering signals are both vertically polarised.

The detection system consists of a spectrometer coupled to an intensified and gated CCD camera, which acquires and records the signal on a single shot basis.

Laser Induced Fluorescence (LIF) measurements are performed employing the fourth harmonic of the laser at $\lambda_0 = 266$ nm but with a low energy. The LIF signal is collected at 90° and acquired by the a spectrometer-ICCD system. A delay generator provides gating pulses, with suitable delay and exposure times, to the ICCD. All the signals were corrected for flame background and filter attenuation.

RESULTS AND DISCUSSION

UV-visible absorption spectra have been measured in the cylindrical co-ordinate system centered on the flame. The local absorption values are obtained by inverting the measured spectra. Because of the cylindrical symmetry of our flame, this inversion is performed by the Abel transformation.

The absorption spectra detected in the region between 20 and 35mm along the flame axis show a strong absorption coefficient in the UV at 200nm which sharply decreases for longer wavelengths and it is below the detection limit at 350nm. These spectra have been obtained by subtracting the contribution of gaseous compounds, such as CO_2 , H_2O and O_2 , which are known to strongly absorb light in the UV region at flame temperatures.

The spectra detected for heights above the burner larger than 35mm show a similar rise near 200nm, but they are more extended towards the visible. Absorption was below the detection limit up to 20mm from the fuel port.

Figure 1 shows the absorption coefficients detected at 266 and 532nm along the flame axis. Absorption in the visible is attributed only to soot particles. Indeed, the absorption spectrum typical for soot particles extends from UV to visible and exhibits a broad maximum at 230nm. The strong absorption at 200nm is representative of the presence of aromatic compounds. In a first approximation, the absorption coefficient at 532nm can be attributed to soot particles

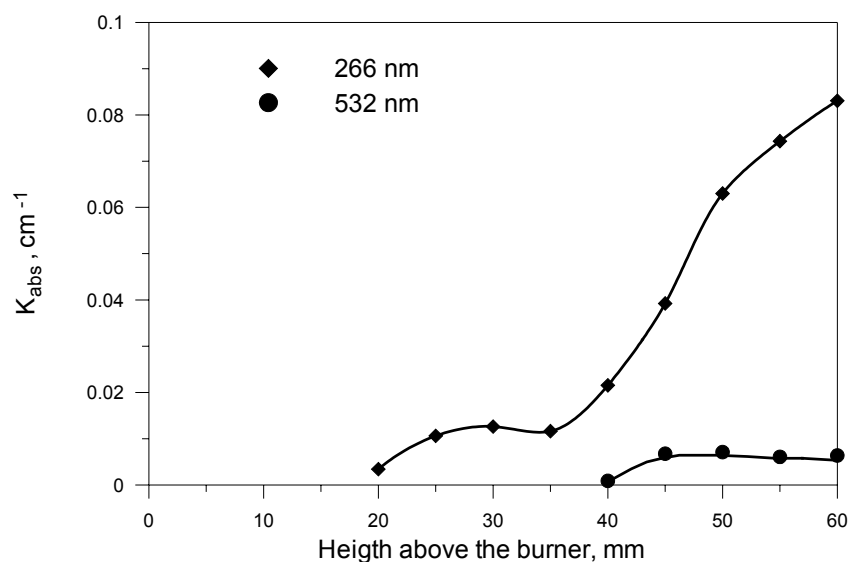


Fig 1 Extinction coefficient at 266 nm and 532 nm measured along the flame axis.

whereas those measured at 266nm are due to the two components: aromatic compounds and soot particles. From the analysis of the absorption profiles it appears that aromatic compounds are formed from fuel pyrolysis and increases up to about 30 mm, thereafter soot is formed.

Laser induced fluorescence spectra have been recorded in order to characterise the aromatic fraction. The fluorescence spectra have been obtained by using the fourth harmonic of the Nd-

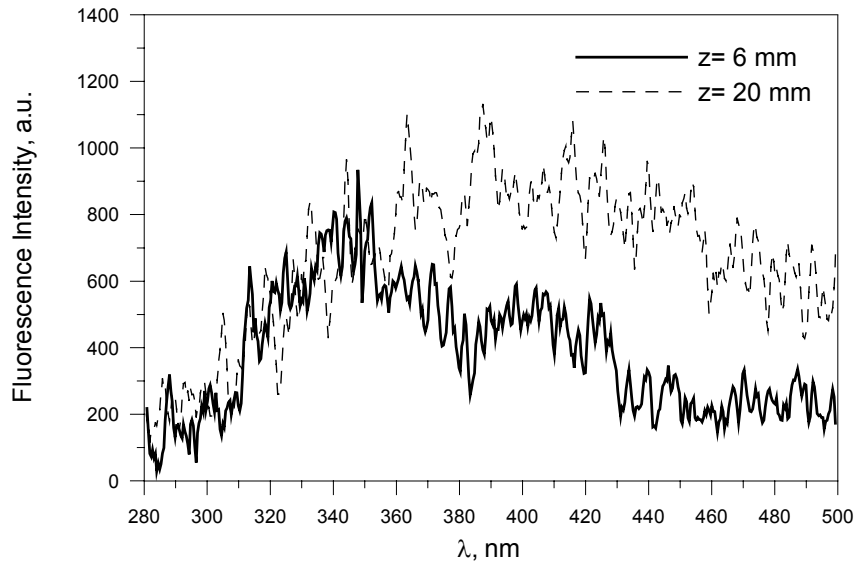


Fig 2 Fluorescence spectra excited at 266 nm measured on the flame axis at different heights above the burner.

YAG laser at 266nm. Figure 2 presents fluorescence spectra measured along the axis of the flame at 6 and 20mm from the fuel outlet. The spectrum detected at 6mm shows a broad maximum centered at about 340nm and a second, less intense, at 410nm whereas in the spectrum detected at 20mm the visible peak is predominant. The UV fluorescence can be mainly attributed to two-, three-ring PAH whereas the fluorescence shifted toward the visible is attributed to four-ring PAHs [5].

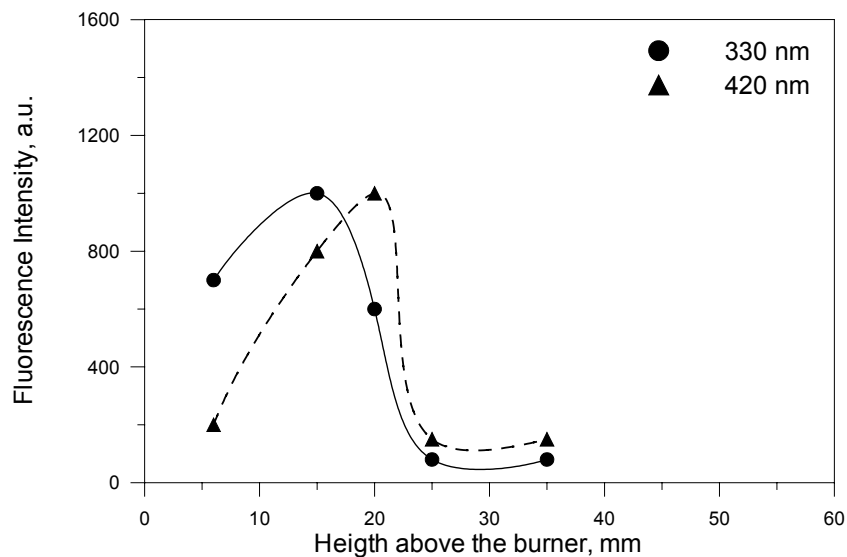


Fig 3 Evolution of two fluorescence wavelengths (330 nm and 420 nm) along the flame axis.

Figure 3 reports the UV-induced fluorescence, on an arbitrary scale, detected at 330 and 420nm as a function of the height above the burner on the flame axis. Two-, three-ring PAHs are rapidly formed from the pyrolysis of the fuel and reach their maximum concentration at about 15mm from the fuel port. The formation of larger PAHs is delayed and peaks at 20mm, thereafter PAHs are destroyed since the fluorescence signal vanishes and it is below

the detection limit. PAHs destruction, however, cannot be attributed to their oxidation since in the analysed flame the main oxidation region is located at about 60 mm on the flame axes. On the other hand UV absorption attributable to aromatic compounds is still present and even increases before the appearance of soot particles. Consequently, it should be hypothesised that the absorption signal is due to aromatic compounds having a very low fluorescence yield.

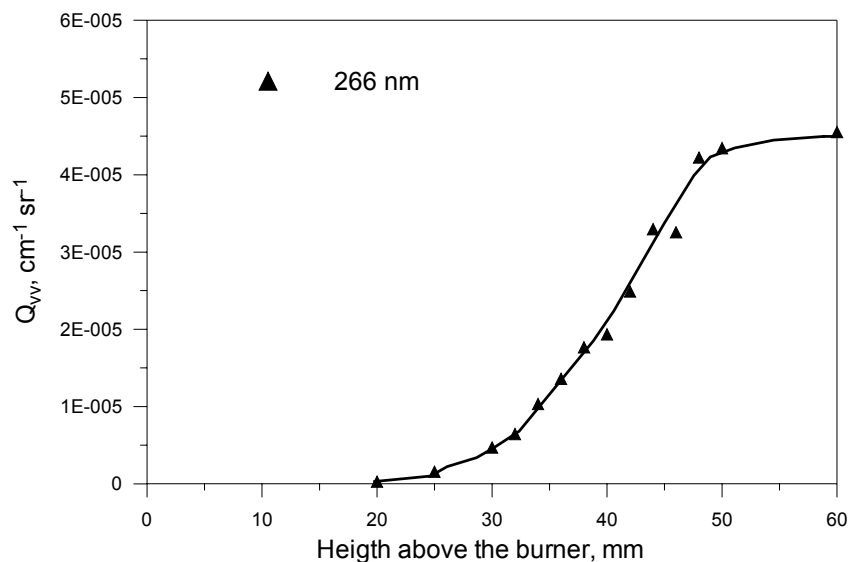


Fig 4 Excess scattering coefficient at 266 nm measured along the flame axis.

In order to characterise these compounds we have also performed scattering measurements. Figure 4 reports the scattering coefficient along the flame axis in excess to gaseous compounds. From the scattering profile it appears that aromatic compounds formed from PAH destruction in the region between 20 and 35mm are species of high molecular mass. After 35mm both the scattering coefficient and the visible absorption strongly increase, thus showing the formation of soot particles.

REFERENCES

- 1) D'Alessio, A., D'Anna, A., Gambi, G., Minutolo, P.: *J. Aerosol Sci.* **29**, 4, 397 (1998).
- 2) D'Anna, A., Violi, A., D'Alessio, A., Sarofim, A.F.: *Combust. Flame* **127**:1995-2003 (2001).
- 3) McEnally, C.S. Pfefferle, L.D.: *Combust. Flame* **121**:575 (2000).
- 4) Borghese, A., Merola, S.S.: *Applied Optics* **37**:3977-3983 (1998).
- 5) Ciajolo, A., D'Anna, A., Barbella, R.: *Combust. Sci. Tech.*, **100**, 271 (1994)

Molecular weight evaluation of combustion related materials

B. Apicella, R. Barbella, A. Ciajolo, Tregrossi, A.
Istituto di Ricerche sulla Combustione - C.N.R., Naples - ITALY

INTRODUCTION AND EXPERIMENTAL APPROACH

The fuel-rich combustion products have been subjected to extensive chromatographic and mass spectral analysis able to isolate individual molecular components. These analyses are particularly adept in the characterization of light and medium weight hydrocarbons that are volatile hydrocarbons (C1-C6) and condensed ring aromatic hydrocarbons from indene (C₉H₈) to coronene (C₂₄H₁₂), respectively.

The heavier hydrocarbon species, including tar and soot, are less amenable to gas chromatographic analysis due to the large molecular weight (MW) coupled with their aromaticity and polarity. In general, chromatographic separation of individual molecular components experiences difficulty because carbonaceous species are typically composed of similar, massive molecules for which the resolving power of chromatography is too low and because the largest part of carbonaceous species is so heavy to be inaccessible to most of the gas chromatographic analyses. Optical spectroscopy as uv-visible absorption and emission can be alternatively used as a direct probe of the aromaticity exploiting the correspondence between optical spectroscopy and excitation of Π electrons typically of aromatic systems. Moreover, the energy of Π transitions are related to the physical size of the aromatic ring systems, i.e. the number of condensed aromatic rings. The lighter aromatics exhibit electronic transitions across the ultraviolet range and the absorption extends toward the visible, sometimes even into the near infrared (NIR) by increasing the size of the aromatic system. Hence, optical spectroscopy is, in line of principle, able to give information on the size of the aromatic ring systems present in the heaviest carbonaceous species.

The changes of the uv-visible spectral shapes of high molecular weight species sampled in the soot formation region of a premixed fuel-rich ethylene flame have been shown in a recent work (1) and related to the growth of the aromaticity. However, first soot particles and high molecular weight species, possible soot precursors, are thought to be composed of a sort of "clusters" of aromatic ring systems bridged by aliphatic chains since infrared analysis has shown that most of the hydrogen population resides on saturated carbon atoms (methyl and methylene groups) (2).

It derives that a complete characterization of a such complex structure requires both the determination of the molecular weight and the size of the aromatic ring systems. This is important also because the knowledge of the structure of soot precursors and of the first soot particles should allow to understand the critical phases of soot inception and growth.

In analogy with the polymer analysis, it has been previously shown that the distribution of the molecular weight of these clusters can be measured by size exclusion chromatography (SEC) (3).

In this work, SEC of tar and soot species, collected in a premixed fuel-rich ethylene flame, has been used to obtain an indication of the molecular mass of tar and soot species whereas the on-line uv-visible absorption analysis of the different SEC molecular mass classes has been utilized to get information on the size of the aromatic ring system units present in these structures.

The analysis is focused on samples collected in the first soot inception region ($Z=4.5$ mm of a

C/O=1 ethylene flame) where tar species were found to reach their maximum flame concentration and the formation of the first soot particles could be just observed (4). Soot particles have been physically separated from the tar species by extraction in dichloromethane and filtration on 0.5 μm Teflon filters. Soot particles deposited on the filter have been sonicated in a powerful organic solvent as N-methyl pyrrolidinone (NMP) obtaining stable “suspensions” of soot that can be subjected to SEC analysis.

The SEC analysis of both tar and soot fractions has been carried out on PL-gel styrene-divinylbenzene column where the column particle sizes are of 5 μm and the pore dimensions are of 50 nm. This column is able to separate polystyrene standards in the 100-100,000 mass atomic units. The on-line detection of SEC eluted species was done with a diode array uv-visible by measuring the absorbance signal at selected wavelengths. Moreover, the diode array system was able to measure the absorption spectrum of the chromatographic peaks in the whole uv-visible range. These spectra will be used in the work to give information on the aromaticity degree.

RESULTS

The separation by size exclusion chromatography is based on the differing penetration degree of the sample molecules into the pores of the stationary phase. Big molecules are early excluded from the pores, i.e. eluted at early elution times, whereas small molecules can enter the pores and elute later on.

Figure 1 reports the SEC chromatograms of the tar and soot species obtained by detecting the absorbance signal at 265 nm (left part of Fig.1) and 450 nm (on the right part of Fig.1) wavelengths. The first significant information given by these chromatograms is that neither

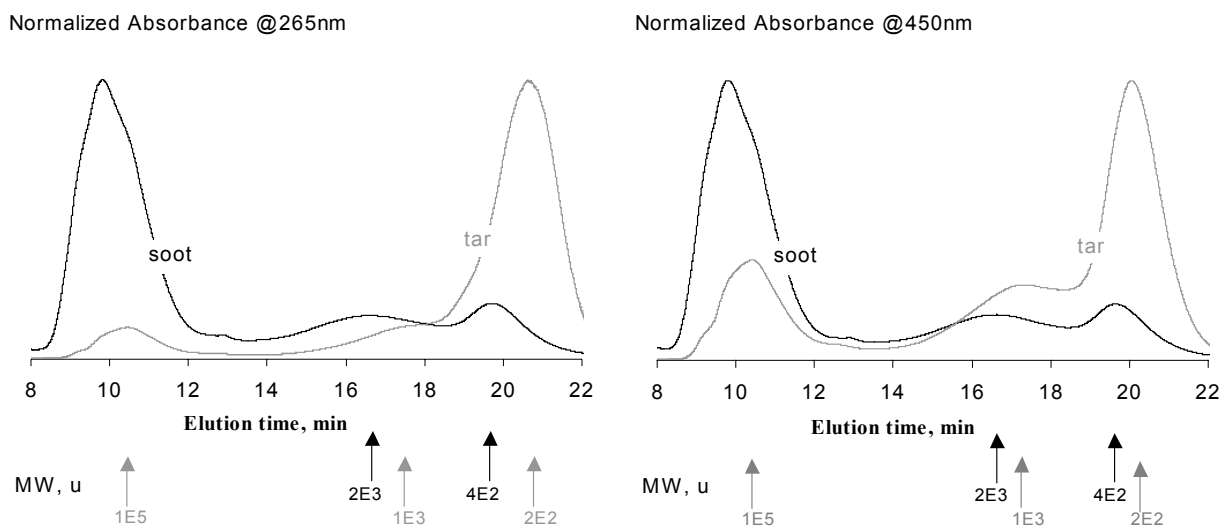


Fig. 1 SEC chromatograms of the tar and soot species measured by uv-visible absorption detector at 265nm (left) and 450nm (right).

tar and soot species present an uniform distribution of molecular weights in the mass range investigated, but peaks in selected molecular weight ranges are well distinct. These findings contradict the general thinking of a soot formation mechanism based on a progressive molecular growth starting from condensed aromatic ring structures of 2-7 ring polycyclic aromatic hydrocarbons up to the first soot particles.

In the chromatogram of tar species a predominant peak at about 20 min elution time demonstrates they mainly consist of relatively low molecular weight species in the 200-400 u MW range and indeed 2-7 ring PAH have been detected in this fraction by means of

gaschromatography-mass spectrometry. A shoulder on the predominant peak indicates the presence of higher molecular weight species (about 1000 u). This shoulder becomes more evident by detection at 450 nm wavelength (on the right chromatogram). A small peak around 100,000 u MW can be also observed (on the left chromatogram) and also this peak is enhanced by detection in the visible at 450 nm wavelength (on the right chromatogram). The higher absorbance in the visible, indicates that, beside to a large MW, the 1000 u and 100,000 u fractions present also a higher aromaticity degree with respect to the PAH fraction.

As expected soot particles exhibit the predominant peak at early elution times, i.e. in the high molecular mass elution range of the column, unfortunately the elution time of this fraction is above the limit of high masses (>100,000 u) where it is impossible to obtain separation since the large size of sample molecules causes the soot molecules to be directly "excluded" from the column.

It is worth to note the presence of lower molecular weight species in the soot fraction that is testified by the appearance of two broad peaks in the low molecular weight elution range (on the right side of the SEC chromatograms). The detection of these species is not enhanced at higher absorption wavelengths (absorption wavelength=450nm) (on the right chromatogram of Fig.1) indicating that the uv-visible spectra of the low and high molecular weight fractions of soot are quite similar. This, in turn, implies that the size of the aromatic ring systems contained in this lower molecular weight soot fraction should be not so different of that contained in the higher molecular weight fraction of soot in the first soot inception region.

This can be better seen in Fig. 2 where the absorption of tar and soot, detected at the apex of the chromatographic peaks, are reported on a log scale as a function of the wavenumber i.e. of the photon energy. The similarities and differences in the absorption spectra are much more striking in this kind of representation.

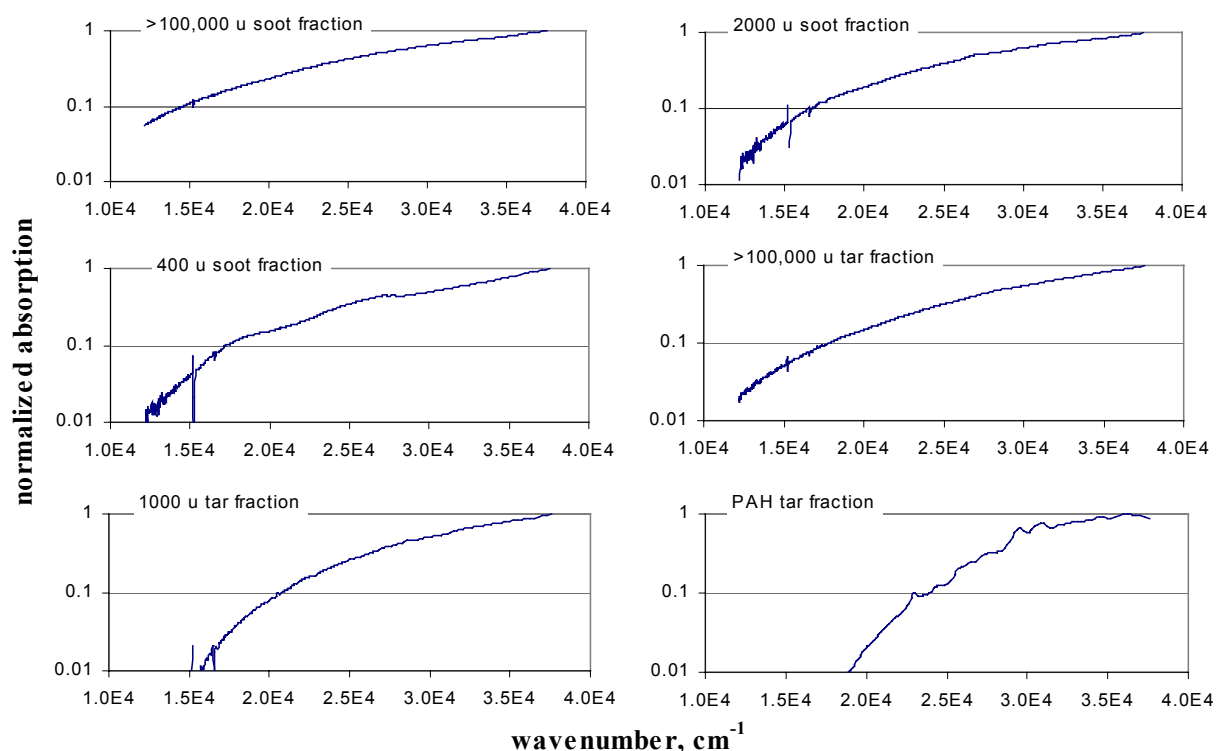


Fig. 2 Normalized absorption of tar and soot fractions measured at the SEC chromatographic peaks apex.

The 200 u peak of tar species exhibits the typical absorption spectrum of two-seven ring PAH that is limited to the high energy region of the spectrum and with the vibrational fine structure of PAH superimposed on a broad absorption. The lack of fine structure in the absorption

spectrum measured on the adjacent shoulder (1000 u) is noteworthy and ascribable to the contributions of many chromophores with overlapping spectra. The heaviest tar fraction (100,000 u) also presents a structureless shape, but much more extended toward low energy absorption range and this indicates the presence of chromophores with large aromatic ring sizes.

The broad shape of the absorption spectrum of 100,000 u tar fraction resembles to the shape of the three sized soot fractions (>100,000 u, 2000 u and 400 u) and more interestingly the spectra of the heaviest tar fractions and of soot fractions exhibit, in the same energy range, quite similar slopes without crossing each other.

This implies that the same repeating aromatic ring unit can be recognized in different molecular weight soot fractions as well as in the heaviest tar fraction.

On the contrary step changes of aromaticity can be observed passing from the species with average molecular weight 200 u (two-seven ring PAH) up to 800-1000 u aromatic species (presumably 15 aromatic rings) and lastly 100,000 u species presenting the same uv-visible spectrum and hence the same aromatic condensation degree of soot particles.

This spectroscopic analysis is relative just to the first soot particles formed in the soot inception region of the flame and this analysis will be in future work extended to mature soot sampled downstream of the flame. Moreover, further work is necessary to assign the number of aromatic rings to the higher molecular weight species in order to have a more quantitative evaluation of aromatic growth process and soot formation.

REFERENCES

1. Apicella, B., Barbella, R., Ciajolo, A., Tregrossi, A.: *24th Event of the Italian Section of The Combustion Institute*, S. Margherita ligure, Italy, September, p. V-43 (2001).
2. Ciajolo, A., Apicella, B., Barbella, R. and Tregrossi, A.: *Comb. Sci. Tech.* **153**: 19 (2000).
3. Apicella, B., Ciajolo, A., Suelves, I., Morgan, T., J., Herod, A., Kandiyoti, R., "Structural characterisation of products from fuel rich combustion: an approach based on size exclusion chromatography" accepted for publication on *Comb. Sci. Tech.* (2002).
4. Ciajolo, A., D'Anna, A., Barbella, R., Tregrossi A., Violi, A. *Proceedings of Combustion Institute*, **26**: 2327 (1996).

Co and Ag Exchanged Zeolites in Lean CH₄-SCR of NO_x

P. Ciambelli, D. Sannino, M. C. Gaudino, I. Buonomo

Dipartimento di Ingegneria Chimica e Alimentare – Università di Salerno, 84084 Fisciano (SA) - ITALY

INTRODUCTION

The use of natural gas (NG) as fuel for automotive applications is based on ecological and economics considerations, like reduced photochemical reactivity and global toxicity, low CO₂ emissions, together with the absence of efficiency loss in lean NG engines. However, because of the misfiring limits, NO_x emissions cannot be satisfactorily controlled by only leaning the air/fuel mixture and catalytic after-treatments are necessary to abate main pollutants as CH₄ and NO_x. Commercial three way catalysts performances are strongly limited by the presence of oxygen in exhaust streams, while metal ion-exchanged zeolites [1] are active catalysts for lean NO_x removal with hydrocarbons in the absence of water. Co-FER was reported as the most active for NO_x reduction with methane [2]. In the presence of water reversible deactivation of Co-FER is observed. Ag-FER catalysts showed usually lower activity than Co-exchanged, with higher tolerance to the presence of water, due to the low propensity of silver to be hydrolysed [1]. Other zeolites have recently been proposed as catalysts for lean DeNO_x with hydrocarbons. Kang [3] has found good activity of Co-SAPO34 for NO_x removal with various hydrocarbons; Bellussi et. al. have reported that Co,Pd-BEA are active in the presence of water for the abatement of NO_x with ethene [4,5].

In this work lean CH₄-DeNO_x activity of Co and Ag exchanged zeolites as ferrierite (FER), beta (BEA), aluminophosphate (APO34) and silicoaluminophosphate (SAPO34) has been investigated.

EXPERIMENTAL

Co-FER and Co-BEA powder catalysts were prepared using Na,K-ferrierite (Engelhard, Si/Al =8.4) and ammonium beta, NH₄⁺-BEA (Zeolyst, Si/Al =12.5) zeolites. Ammonium ferrierite (NH₄⁺-FER) was obtained by exhaustive exchange with aqueous solutions of ammonium nitrate at room temperature. Both ammonium zeolites were ion exchanged at 80°C for different times with 1.6 10⁻² M Co(CH₃COO)₂ aqueous solutions to obtain Co-exchanged samples with various Co loading. Ag-FER and Ag-BEA samples were prepared in the same way of Co catalysts using 0.01 vol. % AgNO₃ solution and performing the exchange at room temperature. Bimetallic Ag,Co-FER and Ag,Co-BEA samples were prepared by further exchange of Ag-ferrierite samples with Co(CH₃COO)₂ aqueous solutions and Co-ferrierite or Co-beta samples with AgNO₃ solution. Since Ag⁺ materials may be sensitive to light, all the procedures involving Ag were carried out in the dark. The samples were dried at 120°C overnight and calcined at 550 °C for two hours.

Ag and Co in aluminophosphate and silicoaluminophosphate with chabasite structure (APO34 and SAPO34) samples were synthesized using a sol-gel method [6], Co acetate and/or Ag nitrate were added directly in the synthesis gel. All the metal-exchanged APO34/SAPO34 samples were dried at 120 °C and heated up to 550 °C, flowing He, and then kept at this temperature for 60 hrs in 10 vol. % O₂, balance He, to remove the template.

The catalytic activity of NO reduction with CH₄ was evaluated with a quartz flow microreactor, electrically heated and equipped with a temperature programmer-controller. The reactor was loaded with powder catalyst (180 to 350 μm particle size). Two on-line IR analysers for the analysis of NO, NO_x and CH₄, concentrations, (HB URAS 10E with NO₂-

NO converter CGO-K) and CO, CO₂ concentrations (HB URAS 10E), and one on-line gas chromatograph (Dani 86.10 HT) for the analysis of O₂, N₂ and N₂O, were used. An analog-digital board (NI, AT MIO16E) was employed for computer acquisition of concentration data from the analysers. Typical experiments were carried out in the temperature range 300-650 °C, feeding 1000 ppm of NO, 100 ppm of NO₂, 1000 ppm of CH₄, 2.5% O₂, balance He (all gases from SOL s.p.a., 99.999% purity grade), with a space velocity of 30,000 h⁻¹. Catalytic tests in wet condition were performed adding water to the feeding gas by a bubble saturator. Metal loading was evaluated by ICP Atomic Emission Spectroscopy after powder samples solubilisation. Micropore volume was obtained from Dubinin elaboration of N₂ adsorption and desorption isotherm at 77 K.

RESULTS AND DISCUSSION

In Tab. 1 the list of the samples is reported with their metal content and micropore volume.

Tab. 1. List of the samples and their main characteristics

Samples	Parent Sample	Exchange time, hrs	Co, wt %	Ag, wt %	Micropore volume, mm ³ /g
FER	-	-	-	-	130
Co(1.3)FER	NH ₄ ⁺ -FER	6	1.32	-	116
Co(2.0)FER	NH ₄ ⁺ -FER	18	2.00	-	-
Co(2.6)FER	NH ₄ ⁺ -FER	24	2.58	-	107
Ag(2.2)FER	NH ₄ ⁺ -FER	40	-	2.20	114
Ag(6.8)FER	NH ₄ ⁺ -FER	301	-	6.80	99
Co(1.7)Ag(2.5)FER	Ag(6.8)FER	67	1.70	2.50	98
Ag(4.0)Co(1.3)FER	Co(1.3)FER	24	1.37	4.03	110
Ag(3.7)Co(2.6)FER	Co(2.6)FER	24	2.56	3.73	104
BEA	-	-	-	-	109
Co(2.9)BEA	NH ₄ ⁺ -BEA	46	2.90	-	113
Co(4.8)BEA	NH ₄ ⁺ -BEA	82	4.80	-	-
Ag(0.3)BEA	BEA	40	-	0.30	129
Ag(2.3)Co(1.6)BEA	Co(2.9)BEA	40	1.60	2.30	120
Ag(2.7)Co(3.2)BEA	Co(4.8)BEA	40	3.20	2.70	106
Co(4.4)APO	-	-	4.4	-	-
Co(3.1)SAPO	-	-	3.1	-	128
Ag(0.3)SAPO	-	-	-	0.30	188

Metal loading for mono or bimetallic catalysts is function of the exchange time and exchange cation. For Ag samples, low metal content was obtained with BEA zeolite with respect to that observed at similar time with FER, the exchange degree being 12% for Ag(2.2)FER and 2.6% for Ag(0.3)BEA.

Different affinity of Ag or Co for different zeolite structures was observed for bimetallic samples: for zeolite BEA the introduction of Ag, starting from Co samples, removes some Co²⁺. With similar procedure of double exchange, Co was not removed from FER matrix [7]. Co-FER samples proved to be very active in NO_x reduction with methane. NO_x conversion depended on the temperature and the cobalt content: the most active sample Co(5.4)FER showed a maximum of 50 % NO_x conversion at 500 °C. CH₄ conversion also increased with Co content. Temperature onset lies around 400 °C, and total conversion is reached at 600 °C for samples with higher amounts of metal. The main products were N₂, CO₂ and water. CO

yield is negligible over the whole temperature range for catalysts with higher Co contents [8]. The activity of all Ag-FER samples was low (NO_x conversion in the 5-10 % range) and poorly dependent of the Ag content. However, Ag-FER catalysts were active in the oxidation of NO to NO₂ in the range 300-500°C (maximum yield of 15 % at 350°C). Higher yield, close to the equilibrium values (27% at 450°C) was achieved with Ag(2.2)FER [7].

In the range 350-650 °C Co-BEA samples showed lower activity of NO reduction than Co-FER catalysts. The main products were again N₂, CO₂ and H₂O, but NO_x reached a maximum conversion value of only 20 % at about 580 °C on Co(2.9)BEA. The onset temperature for CH₄ conversion was about 430 °C and 100 % conversion was achieved at 650 °C. The addition of silver to the Co-BEA samples resulted in decreasing the maximum in NO_x conversion (Fig. 1).

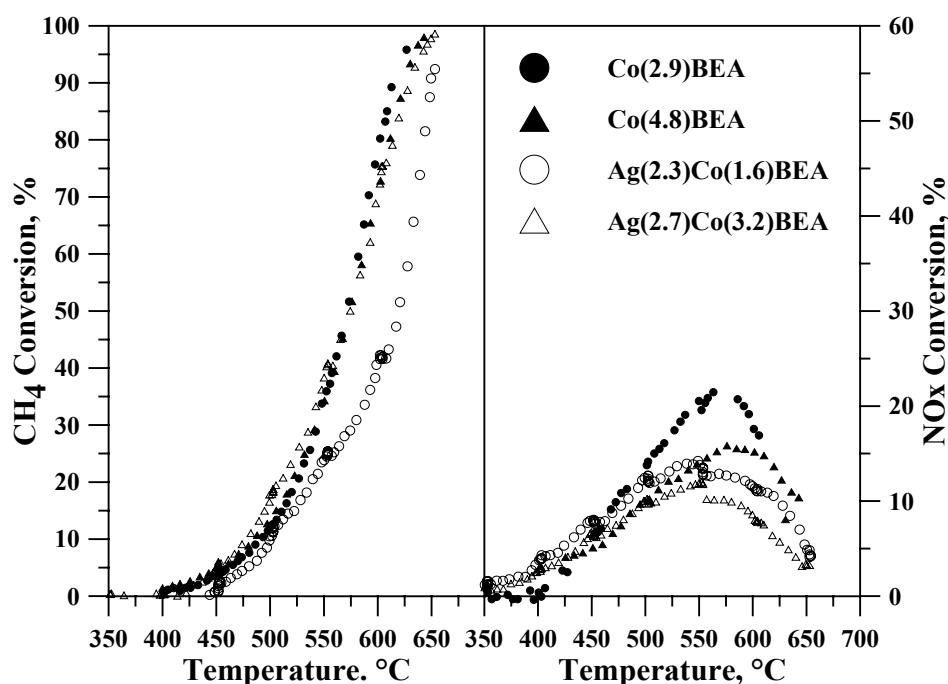


Fig. 1 Comparison of NO_x and CH₄ conversions on Co(2.9)BEA, Co(4.8)BEA, Ag(2.3)Co(1.6)BEA, Ag(2.7)Co(3.2)BEA.

Co-APO34/SAPO34 did not show significant DeNO_x activity with methane in the range 350-600 °C, NO_x conversion reaching at maximum 5%. Methane conversion was comparable with the conversion curve of the reaction carried out in homogeneous condition [9]. No activity was found also for the samples containing Ag.

The effect of the zeolitic matrix is evidenced by the comparison of samples with quite comparable Co content as reported in Fig. 2. Ferrierite resulted the most active zeolite with the following scale of activity: Co-ferrierite > Co-beta >> Co-APO34, Co-SAPO34. Ferrierite structure, characterized by channels at 8- and 10-ring, leads to more favorable Co²⁺ positioning and coordination with respect to three-dimensional structure of BEA at 12-ring but also to chabazite framework for metal-APO34, SAPO34 with 8-ring channels. Presence of octahedral Co²⁺ seems to favor DeNO_x reduction activity.

Bimetallic Ag,Co exchanged ferrierite catalysts were active in the range 300-650 °C. NO_x reduction started after 370 °C, showing a maximum of 20% at 550 °C on the sample Co(1.7)Ag(2.5)FER, with total selectivity to CO₂. Comparison of DeNO_x activity of Co-ferrierite and Ag-ferrierite at similar metal loading (Fig. 3) showed that the presence of Ag enhanced the catalytic activity at low temperature. The presence of both metals in the zeolite

resulted in increased conversion of both NO_x (20% at 550°C) and CH₄ (100% at 650 °C).

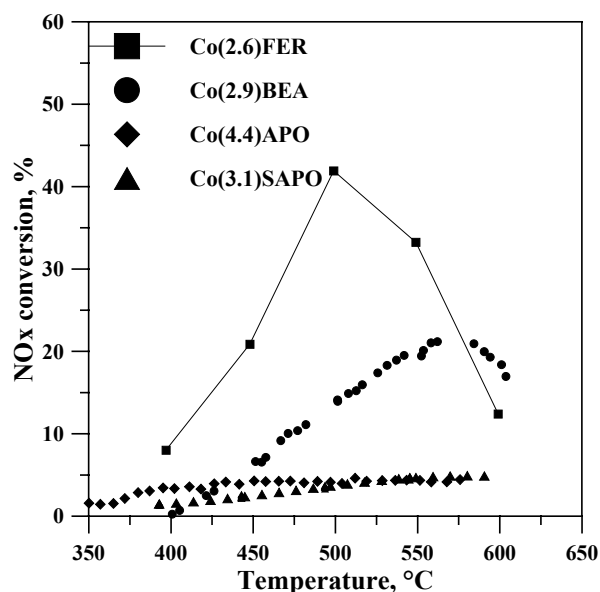


Fig. 2 NO_x conversion for Co(2.6)FER, Co(2.9)BEA, Co(4.4)APO, Co(3.1)SAPO

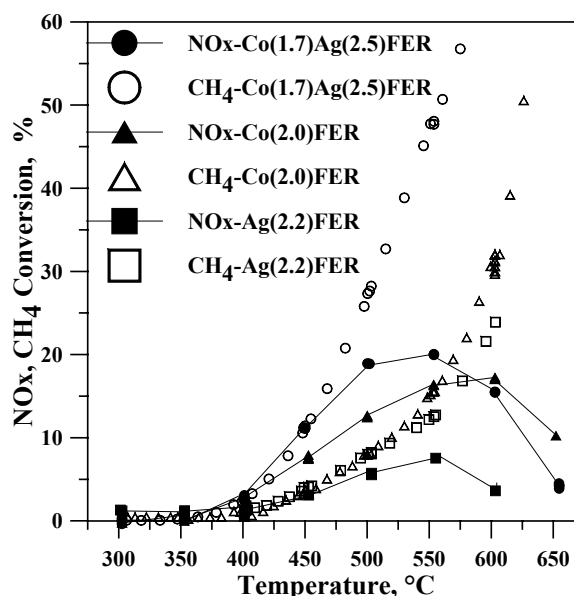


Fig. 3 NO_x and CH₄ conversions for Co(1.7)Ag(2.5)FER, Co(2.0)FER, Ag(2.2)FER

CONCLUSIONS

CH₄-DeNO_x activity of Co and Ag in FER, BEA, APO and SAPO zeolites has been investigated in lean conditions. In monometallic exchanged zeolites Co resulted always more active than Ag. Ferrierite matrix gave better cation siting with the following scale of activity: Co-ferrierite > Co-beta >>> Co-APO34, Co-SAPO34. Bimetallic catalysts showed lower activity for BEA, APO34, and SAPO34 zeolites while the addition of Ag to Co-FER gives higher performances than the relevant monometallic systems in terms of both NO_x reduction and CO₂ selectivity.

REFERENCES

1. Traa Y., Burger B., Weitkamp J.: *Micropor. Mesopor. Mat.*, **30**: 3 (1999).
2. Ciambelli P., Corbo P., Gaudino M.C., Migliardini F., Sannino D.: *Top. Catal.*, **16/17**: 413 (2001).
3. Kang M.: *J. Mol. Catal. A*, **161**: 115 (2000).
4. Tabata T., Kokitsu M., Ohtsuka H., Okada O., Sabatino L.M.F., Bellussi G.: *Catal. Today*, **27**: 91 (1996).
5. Bellussi G., Sabatino L.M.F., Tabata T., Kokitsu M., Okada O., Ohtsuka H.: *Eur. Pat. Appl.*, 739 651, 30 October (1996).
6. Marchese L., Frache A., Gianotti E., Martra G., Causà M., Coluccia S.: *Micropor Mesopor. Mater.*, **30**: 145 (1999).
7. Ciambelli P., Sannino D., Gaudino M. C., Flytzani-Stephanopoulos M.: *in press on Proc. "2nd FEZA Conference"* Taormina-Giardini Naxos-Italy, 1-5 September (2002).
8. Ciambelli P., Sannino D., Gaudino M.C.: *Stud. Surf. Sci. Catal.*, **135**: 329 (2001).